
Electronic Thesis and Dissertation Repository

2-25-2020 11:00 AM

Rare-metal Alkaline Granite from The Arabian Shield, Saudi Arabia

Abdullah A. Aseri, *The University of Western Ontario*

Supervisor: Linnen, Robert L., *The University of Western Ontario*

A thesis submitted in partial fulfillment of the requirements for the Doctor of Philosophy degree in Geology

© Abdullah A. Aseri 2020

Follow this and additional works at: <https://ir.lib.uwo.ca/etd>



Part of the [Geochemistry Commons](#), [Geology Commons](#), and the [Other Earth Sciences Commons](#)

Recommended Citation

Aseri, Abdullah A., "Rare-metal Alkaline Granite from The Arabian Shield, Saudi Arabia" (2020). *Electronic Thesis and Dissertation Repository*. 6822.

<https://ir.lib.uwo.ca/etd/6822>

This Dissertation/Thesis is brought to you for free and open access by Scholarship@Western. It has been accepted for inclusion in Electronic Thesis and Dissertation Repository by an authorized administrator of Scholarship@Western. For more information, please contact wlsadmin@uwo.ca.

Abstract

Mineral deposits of high field strength elements (HFSE) and rare earth elements (REE) are commonly within granites that have experienced strong post-magmatic alterations. There has been a long debate on whether the mineralization is due to magmatic and/or hydrothermal processes. The Arabian Shield hosts several economical rare-metal alkaline granites that are poorly understood. This work aims to evaluate the nature of the mineralization in three rare-metal granites from the Arabian Shield, showing distinct mineralization styles ranging between disseminated mineralization at Al-Ghurayyah, pegmatite and hematized granite at Jabal Sayid, and quartz veins at Dyaheen.

The granites from all three areas are highly evolved and have undergone extreme feldspar fractional crystallization, which led to increases in the contents of incompatible elements in the residual melt. The elevated concentrations of HREE in Al-Ghurayyah and in the mineralized units in Jabal Sayid and Dyaheen suggest crystallization from a fluid-rich melt or interactions with a fluid phase. The textural relationships between ore minerals and rock-forming minerals, in particular zircon and pyrochlore, indicate that the early crystallization occurred in a late-magmatic stage at Al-Ghurayyah, whereas at Jabal Sayid, it occurred in a transitional stage between magmatic and hydrothermal. At Dyaheen, the mineralization is associated with quartz veins and aegirine dykes indicates that it is hydrothermal origin. However, the deformed nature of the quartz veins and the presence of perthite suggests that they formed at high temperature. The hydrothermal stage in Jabal Sayid shows strong hematization and high concentrations of HFSE and REE. In Al-Ghurayyah, the hydrothermal stage is marked by the silicification and the crystallization of columbite as the Nb phase. The total HFSE and REE concentrations do not change with or without silicification.

New age dating from Al-Ghurayyah and Dyaheen confirms the post-orogenic settings of these deposits, and the comparisons of the published Sm-Nd isotopes for the three areas indicate that they have the same source. The melt was developed through magmatic processes and evolved to extreme levels that led to the concentrations of rare-metals. Most of the variations between Al-Ghurayyah, Jabal Sayid, and Dyaheen occur during a late magmatic to a hydrothermal stage.

Keywords

Rare-metal, Alkaline granite, HFSE, REE, Arabian Shield, Al-Ghurayyah, Jabal Sayid, Dyaheen. Columbite, Pyrochlore, Zircon, Gadolinite, Monazite, Xenotime.

Summary for Lay Audience

Rare-metals such as Y and rare earth elements (REE) and Nb, Ta (HFSE) are very important constituents of current advanced technologies and understanding of the processes of the formation of rare-metal deposits are crucial to finding new resources. One of the important sources of these elements is highly evolved rare-metal alkaline granites, that are overprinted by alteration events. The latter makes it difficult to know whether the mineralization was originally formed during the solidification of the melt or by a hydrothermal fluid that developed after solidification. This work examines rare-metal mineralization in alkaline granite in Saudi Arabia and evaluates the roles of magmatic and hydrothermal process in the formation of such deposits. Three rare-metals alkaline deposits from the Arabian Shield were chosen. These deposits have distinct mineralization styles ranging from disseminated at Al-Ghurayyah, pegmatite in Jabal Sayid, and quartz veins in Dyaheen.

The evolution of the chemical composition of the granites at the three deposits involved extreme crystallization of feldspars. This led to increases in the concentrations of HFSE and REE. The study of the texture of ore minerals indicates that at Al-Ghurayyah, the early ore minerals crystallized at the late-magmatic stage, whereas at Jabal Sayid, early mineralization occurred in a transitional stage between magmatic and hydrothermal. At Dyaheen, the mineralization at the rim of the complex deposited from a high-temperature hydrothermal fluid. In Jabal Sayid, strong hematization and elevated concentrations of HFSE and REE occurred in the hydrothermal stage. In Al-Ghurayyah, the hydrothermal stage is marked by the crystallization of late quartz and that is associated with the crystallization of columbite. The total HFSE and REE concentrations do not change with or without silicification.

New age dating from Al-Ghurayyah and Dyaheen confirms the post-orogenic settings of these deposits, and the comparisons of the published Sm-Nd isotopes indicate that they three granites have originated from melting the lower crust of the Arabian Shield. The melt was developed through magmatic processes and evolved to extreme levels that led to the concentrations of rare-metals. Most of the variations between the three deposits occur during a late magmatic to a hydrothermal stage.

Co-Authorship Statement

The field work and samples collection were done by the author and Dr. Robert Linnen (supervisor). During the first two days (of 10 days) of the field work, Dr. Hesham M. Harbi provided us with valuable advice and guidance on the mineralization at Jabal Sayid and Dyaheen.

The zircon age analyses were performed by Dr. Donald W. Davis at the Department of Earth Sciences, University of Toronto, Canada. Dr. Davis performed data acquisition, data reduction and age estimations using a software writing by Davis (1982). These data are used in Chapter 2 and Chapter 5.

Zircon trace elements analyses were obtained by LA-ICP-MS at Great Lakes Institute for Environmental Research (GLIER). J.C. Barrette helped with data acquisition. Dr. Iain Samson and Melissa Price helped with advice and training on how to use data reduction software (Igor and Iolite).

Acknowledgments

I would like to express my gratitude and appreciation to my supervisor Dr. Robert Linnen for the support and guidance I have received during my PhD program. I was honored to know Dr. Linnen and worked under his supervision during my Master and PhD programs for nearly 10 years. His engorgement and constant support during some of the difficult times during my project helped me greatly. I would also like to extend my gratitude to my PhD committee members Dr. David Good from the University of Western Ontario and Dr. Iain Samson from the University of Windsor for their guidance throughout this program.

I would like to thank and dedicate this thesis to my father and mother, Ali Aseri and Rayah Aseri, and my wife and daughter, Rawan and Yara, for their emotional support and prayer during the time I have spent pursuing my graduate degrees. I express my deepest apologies to my parents, brothers and sisters for the unhappiness or discomfort that I might cause due to the many holidays, weddings, social gatherings that I have missed. I would also like to thank my wife for her support, sacrifice, and encouragement that made my work possible.

I would like to acknowledge King Abdul Aziz University for funding my scholarship. I would also like to appreciatively acknowledge a NSERC Discovery grant to Dr. Robert Linnen for supporting this research during the time from January 2020 to the March 2020.

I am appreciative of the assistance that was provided by Dr. Hesham M. Harbi from King Abul Aziz University during the fieldwork, Ahmed Rida for the GIS help and organizing and navigating the Saudi desert, Fahad Al-Refie, Fathi Al-Said, and Abdo Al-Khaldi from King Abdul Aziz University for their help making part of my polished thin sections, Dr. Talal Qadhi for giving me samples and materials from his project on Al-Ghurayyah, and Dr. Rami Bukhsh from King Abdul Aziz University for his help and advice during my fieldwork, Ryan Thigah for his help and support at King Abdul Aziz University. I would like to express my thankfulness to BARIQ mining LTD for accommodating us in their camp during our work in Jabal Sayid and Hdb Ad Dyaheen ring complex. Your generosity made our work easier and more efficient. I would also like to thank Dr. Mustafa Al-Zyadi from the sponsorship management at King Abul Aziz University for his help and support that I have received

throughout my program, Mr Mohsen Mohammed from Saudi Arabia Cultural Bureau in Canada for his help in facilitating my requests and needs.

I am appreciative of the assistance provided by Marc Beauchamp from the University of Western Ontario for all his assistance with electron microprobe analyses, Dr. Alysha Scathain from the University of Western Ontario for her support with the electron microprobe and academic advice, Mary J. Walzak from the University of Western Ontario for her help with Laser Raman Spectroscopy, Cassandra Marion Beauchamp from the University of Western Ontario for her guidance and advice with Laser Raman Spectroscopy, Dr. Roberta Flemming and Fengke Cao from the University of Western Ontario for their help with the XRD analyses, Dr. Donald Davis from the University of Toronto for his help with U-Pb age dating, Melissa Price from the University of Windsor for her help with LA-ICP-MS analyses and data processing with ICP-Pro and Iolite software, J.C. Barrette from the University of Windsor for his help with LA-ICP-MS analyses, Stephen Wood from the University of Western Ontario for his help with polished thin sections preparation.

Special thanks to my friends Fadi Al-Daouk, Talal Alabbasi, Ryan Thigah, Hassene Ben Amara, Alaa Al-Turk, Fahad Al-Zahrani, and Hassene Bouraoui who were very supportive during my work and provided me with invaluable advice and encouragement.

Table of Contents

Abstract.....	ii
Keywords	iii
Summary for Lay Audience.....	iv
Co-Authorship Statement.....	v
Acknowledgments.....	vi
Table of Contents	viii
List of Tables	xiii
List of Figures	xv
List of Appendices	xxx
List of Abbreviations	xxxi
Chapter 1.....	1
1 Rare-metal alkaline granite mineralization in the Arabian Shield, Saudi Arabia.....	1
1.1 Introduction.....	1
1.2 Geochemical background.....	1
1.2.1 High field strength elements	1
1.2.2 Rare earth elements (REE).....	2
1.3 HFSE and REE mineral deposits	3
1.4 Rare-metal mineralization models	4
1.5 Rare-metal alkaline granites in the Arabian Shield	7
1.6 Objectives	9
1.7 Thesis structure	11
1.8 References.....	14
Chapter 2.....	28

2	The petrology and lithology of Al-Ghurayyah Nb, Ta, Zr, Y, REE rare-metal granite, the Arabian Shield, Saudi Arabia.....	28
2.1	Introduction.....	28
2.2	Geological setting	29
2.3	Methodology	32
2.4	Petrography	33
2.4.1	Disseminated mineralization style	34
2.4.2	Aggregate mineralization style	39
2.4.3	Mineral paragenetic sequence in the host granite	40
2.5	Geochemistry	41
2.5.1	U-Pb Zircon age dating.....	43
2.5.2	Composition of feldspars and micas	44
2.6	Discussion.....	44
2.6.1	Magmatic and hydrothermal textures	45
2.6.2	Magmatic evolution and hydrothermal alteration.....	47
2.6.3	HFSE and REE mineralization	50
2.7	Conclusions.....	52
2.8	References.....	52
	Chapter 3.....	91
3	Chemistry and morphology of HFSE and REE minerals at Al-Ghurayyah, the Arabian Shield, Saudi Arabia	91
3.1	Introduction.....	91
3.2	Geology and petrography of Al-Ghurayyah deposit.....	92
3.3	Methodology	95
3.4	Results.....	96
3.4.1	Morphologies of ore minerals.....	96
3.4.2	Compositions of ore minerals	99

3.5 Discussion	103
3.5.1 Magmatic and hydrothermal mineralization	103
3.5.2 Mineralization evolution at Al-Ghurayyah	108
3.6 Conclusion	109
3.7 References	110
Chapter 4	145
4 Rare-metal mineralization at Jabal Sayid, the Arabian Shield, Saudi Arabia: Petrography, lithogeochemistry, and mineral chemistry	145
4.1 Introduction	145
4.2 Geological setting	147
4.3 Methodology	149
4.4 Petrography	151
4.4.1 Aegirine granite	151
4.4.2 Oxidized granite and pegmatite sheets (mineralized units)	151
4.4.3 Rare-metal minerals	153
4.5 Lithogeochemistry	156
4.6 Mineral chemistry	157
4.6.1 Aegirine	157
4.6.2 Zircon	158
4.6.3 Pyrochlore	160
4.6.4 REE minerals	160
4.7 Discussion	161
4.7.1 Magmatic evolution	161
4.7.2 Mineralization and Hydrothermal alteration	163
4.8 Conclusion	166
4.9 References	167

Chapter 5.....	202
5 Rare-metal mineralization at Dyaheen ring complex, the Arabian Shield, Saudi Arabia: petrography, lithogeochemistry, and mineral chemistry.....	202
5.1 Introduction.....	202
5.2 Methodology.....	205
5.3 Petrography.....	208
5.3.1 Monzogranite.....	208
5.3.2 Amphibole-biotite granite.....	208
5.3.3 Aegirine granite.....	209
5.3.4 Alteration.....	209
5.3.5 Mineralization.....	210
5.4 Morphology of ore minerals.....	211
5.4.1 Zircon.....	211
5.4.2 Fergusonite and pyrochlore.....	212
5.4.3 Y and REE minerals.....	212
5.5 Lithogeochemistry.....	213
5.6 U-Pb zircon age dating.....	215
5.7 Mineral chemistry.....	215
5.7.1 Amphibole and aegirine.....	215
5.7.2 Zircon.....	216
5.7.3 Fergusonite and pyrochlore.....	218
5.7.4 REE minerals.....	219
5.8 Discussion.....	220
5.8.1 Magmatic evolution.....	221
5.8.2 Mineralization.....	223
5.9 Conclusion.....	226

5.10References.....	227
Chapter 6.....	271
6 Conclusion	271
6.1 Introduction.....	271
6.2 Geology and petrography.....	272
6.2.1 Mineralization styles and alteration	273
6.3 Chemistry	275
6.4 Age and source.....	281
6.5 Emplacement and evolution of rare-metal deposits in the Arabian Shied.....	283
6.5.1 Late-magmatic stage	284
6.5.2 Hydrothermal stage.....	284
6.6 Conclusion	286
6.7 References.....	287
Appendices.....	309
Curriculum Vitae	414

List of Tables

Table 2-1 Summary of the main rock units in Al-Ghurayyah	62
Table 2-2 List of common minerals in Al-Ghurayyah with abbreviations and mineral formulas	63
Table 2-3 Whole-rock chemical analyses of Al-Ghurayyah.....	64
Table 2-4 EMP analyses of albite, microcline, and mica from the host granite	67
Table 3-1 List of Isotopes used for zircon LA-ICP-MS analyses.....	118
Table 3-2 Classification of zircon from Al-Ghurayyah.....	119
Table 3-3 Classification of pyrochlore from Al-Ghurayyah.....	120
Table 3-4 Classification of columbite from Al-Ghurayyah.....	121
Table 3-5 Average EMPA analyses of zircon.....	121
Table 3-6 Average EMPA analyses of pyrochlore	124
Table 3-7 Average EMPA analyses of columbite.....	126
Table 4-1 Summary of the main rock units at Jabal Sayid mineralization	176
Table 4-2 List of common minerals in Jabal Sayid with abbreviation and formula.....	177
Table 4-3 Whole-rock chemical analyses of Jabal Sayid granite	178
Table 4-4 EMP analyses of Aegirine	180
Table 4-5 Average EMP and LA-ICP-MS analyses of zircon.....	181
Table 4-6 Average EMP analyses of pyrochlore	183
Table 4-7 Average EMP analyses of synchysite and bastnasite	184
Table 4-8 Average EMP analyses of xenotime and monazite	185

Table 5-1 Summary of the main rock units at Dyaheen	238
Table 5-2 List of common minerals at Dyaheen with abbreviations and formulas	239
Table 5-3 Whole-rock Analyses of main rock units at Dyaheen	240
Table 5-4 Table Average EMPA of amphibole and aegirine from Dyaheen	242
Table 5-5 Average EMPA of zircons from Dyaheen.....	243
Table 5-6 Average EMP analyses of pyrochlore from Dyaheen	244
Table 5-7 Average EMP analyses of gadolinite and bastnasite from	246
Table 5-8 Feldspar fractionation model for Dyaheen	248
Table 6-1 Main characteristics of the rare-metal deposits in the current study	295
Table 6-2 Average whole-rock analyses of fresh and altered/mineralized granites at the studied rare-metals	297

List of Figures

- Figure 2-1 A geological map of the Arabian Shield showing the different terranes. The red stars are the locations of some important occurrences of rare-metal granite including Al-Ghurayyah show in the black box (modified after Johnson and Kattan 2012)..... 69
- Figure 2-2 Geological map of Al-Ghurayyah (modified after Elliott et al. 2002) and locations of samples of this study..... 70
- Figure 2-3 Sketch of the composite-body showing the different zones of this unit. 71
- Figure 2-4 Field and petrographic relationships of the amphibole-bearing granite A) Contact between amphibole-bearing granite (light grey) and the common porphyritic granite (pink). B) Crossed polarized light (CPL) image showing snowball quartz with albite inclusions. C) Plane polarized light (PPL) image of arfvedsonite crystals and aegirine surrounded by albite and quartz from amphibole-bearing granite. D) PPL image of Type-2 and pyrochlore in quartz and albite matrix. E) PPL image of trillithionite associated with pyrochlore and zircon in quartz and albite matrix. 72
- Figure 2-5 Main textures and mineralogy of the porphyritic granite and the marginal unit. A) CPL image of snowball quartz from the porphyritic granite showing the alignment of albite and trillithionite inclusions along the growth zones and surrounded by lath-shaped albite from the porphyritic granite. B) CPL image of snowball microcline with inclusions of albite and trillithionite and surrounded by lath-shaped albite from the porphyritic granite. C) Plane polarized light (PPL) image of a fan-shaped muscovite, Type-2 zircon, and rutile that are associated with silica alteration from silicified porphyritic granite. D) PPL image of late quartz associated with acicular columbite, fluorite and chlorite from highly altered granite. E) PPL image of fine-grained euhedral zircons (Type-2) in quartz matrix from the marginal unit. F) CPL image of large trillithionite crystal contains inclusions of euhedral zircons and fine-grained quartz from the marginal unit. G) PPL image of pseudomorph in the marginal unit that altered to chlorite (green), hematite + columbite (dark red to black). H) PPL image of pyrochlore crystals in fine-grained zircon and quartz matrix from the marginal unit. 73

Figure 2-6 Different types of zircon hosted by the granite. A) PPL image of prismatic Type-1 zircon from silicified granite porphyritic granite. B) CL image of Type-1 zircon in A showing Type-1 zircon (core) that was replaced by secondary zircon (bright). C) PPL of a fluid inclusion-rich of the Type-2 zircon from the porphyritic granite. D) BSE image of zircon in C showing bright thorite inclusions and spongy texture. E) PPL image of small bipyramid zircons (Type-2) from the marginal unit. F) CL image of two grains of bipyramid Type-2 zircon showing wide-spaced zoning. G) PPL image of zircon of Type-3 core and Type-4 rim from the composite-body showing. H) CL image of the large zircon grain in G. I) PPL of Type-4 zircon and xenotime overgrowth (reddish rim) from the mineralized quartz vein. J) CL image of two zircons showing xenotime overgrowth over black core Type-4 zircon..... 74

Figure 2-7 Disseminated mineralization from the porphyritic granite and the marginal unit. A) PPL of disseminated zircons (Type-2) and coarse-grained pyrochlore from the marginal unit. B) BSE image of an altered pyrochlore from the marginal unit. The dark core represents early crystallized LREE-rich pyrochlore, whereas the lighter rim is enriched in HREE. The image fluorite surrounding the pyrochlore as well as thorite crystallization on the rim and in cracks C) BSE image of columbite, thorite, and REE-F-carbonate (bastnasite?) crystals associated with chlorite, muscovite and late-quartz from the porphyritic granite. D) BSE image of an altered pyrochlore crystal that was replaced by columbite and Pb-rich pyrochlore associated with bastnasite. E) BSE image of a columbite replaced by aeschynite in the highly altered granite. F) BSE image of acicular columbites associated with chlorite and fluorite in the highly silicified granite. 75

Figure 2-8 Aggregate ore minerals from the aggregate mineralization style. A). PPL of Type-3 and 4 zircons and columbite from the zircon-columbite zone. B) PPL image showing Type-3 & 4 zircons, xenotime and columbite in quartz matrix from the zircon-columbite zone at the composite-body. C-) PPL of interstitial calcite with Type-3 and 4 zircons and rutile in quartz matrix from at composite-body. D) PPL from the zircon-mica zone from the composite-body showing columbite and Type-4 zircon surrounded by hematite in biotite and quartz matrix. E) BSE image of rutile, hematite, and Type-4 zircon in biotite and quartz matrix from the quartz veins. F) PPL image showing the contact between vein-1 and vein-2 from the quartz veins. G) PPL image showing Type-4 zircon and xenotime overgrowth from

vein-1 in the quartz veins. H) BSE image of rutile, aeschynite, Type-4 zircon, cassiterite and hematite from the quartz veins.....	77
Figure 2-9 Mineral paragenesis sequence at Al-Ghurayyah deposit. Red dashed lines represent the boundary of the transitional stage. Dashed black lines represent uncertain beginning and/or end of a mineral crystallization, whereas solid lines represent confirmed beginning and/or end of a mineral crystallization.....	79
Figure 2-10 R1-R2 granite classification diagram (after De La Roche 1980).....	80
Figure 2-11 Tectonic settings discrimination diagram of (Pearce et al. 1984). WPG, within plate granite; ORG, oceanic ridge granite; VAG, volcanic arc granite; Syn/COLG syn-collision granite.....	81
Figure 2-12 Major oxides vs. SiO ₂ . Porphyritic granite has a similar composition to the granite samples from Qadhi and Mufti (2008). Amphibole-bearing granite and the marginal unit have high CaO and F contents. In addition to the high SiO ₂ content, silicide granite has low Al ₂ O ₃ and Na ₂ O, and variable K ₂ O concentrations.	82
Figure 2-13 Chondrite-normalized large-ion lithophile element (LILE), HFSE and REE abundances. The values for CI Chondrite are from Thompson (1982).....	83
Figure 2-14 Chondrite-normalized REE pattern. Chondrite values are from Boynton, 1984.	84
Figure 2-15 Nb vs. Ta, Zr vs. Hf, and Y vs. Ho plots showing a strong geochemical correlation. Lines are least-squares fit of the data.	85
Figure 2-16 U-Pb zircon age dating from different zircon types hosted in different rock units. A) BSE images of analyzed zircon grains. B) inclusion-rich Type-1 zircon from a highly silicified granite. C) Type-2 zircon grains from the porphyritic granite. D) Type-3 zircons from the zircon-columbite zone in the composite-body. Type-4 zircon from the zircon-columbite and the mica-zircon units from the composite-body.....	86
Figure 2-17 Raman spectrum of a mica inclusion from the porphyritic granite. The mica spectrum (black) shows a 91 % match with trillithionite from RRUFF database (ID R040101, 514 nm).	87

Figure 2-18 Normative quartz-albite-orthoclase of Al-Ghurayyah granite samples. The granite data from this work and Qadhi and Mufti, (2008) show a trend toward albite and close to the magmatic trend in F-rich granite (Manning 1981). 88

Figure 2-19 A) Molar whole rock Na +K vs. Si from this study. B) Molar whole rock Na + K vs Al from this study. The diagrams show the effect of preferential silicification of albite over microcline. Orange circles represent that composition if 100 % of albite was replaced by secondary quartz. The line in Figure B is slope of 1, which indicates that Na-K-Al are completely controlled by feldspars. 89

Figure 2-20 Total REE vs Zr+Nb of this study samples. Fresh and least altered granites show a positive correlation indicating that zircon and pyrochlore are the main host of REE. 90

Figure 3-1 A geological map of the Arabian Shield showing the different terranes that constitute the Shield. The red stars are the locations of some important occurrences of rare-metal granite including Al-Ghurayyah, which is shown in the box (modified after Johnson and Kattan 2012). 128

Figure 3-2 A geological map of Al-Ghurayyah deposit showing the main rock units and locations of samples (modified after Elliott et al. 2002). 129

Figure 3-3 Petrology of the rock units in the Al-Ghurayyah. A) Crossed polarized light (CPL) image of a snowball quartz surrounded by albite and microcline from the altered porphyritic granite. The snowball contains inclusion of albite and trilithionite. B) CPL image of a snowball microcline with albite and trilithionite inclusions from the altered porphyritic granite. C) CPL image of a snowball from amphibole-bearing granite showing albite inclusions arranged along the quartz growth zone. D) Plane polarized light (PPL) image of sodic amphibole from the amphibole-bearing granite. E) PPL image of disseminated pyrochlore from the amphibole-bearing granite. F) PPL image of a disseminated Type-2 zircon from the marginal unit. G) PPL of a disseminated pyrochlore, Type-2 zircon, and quartz from the marginal unit. The dark color between grains is due to the presence of chlorite between quartz grains. H) CPL image of a large trilithionite from the marginal unit containing zircon and quartz inclusions. I) PPL image of a large columbite crystal with aggregate Type-3 and 4 zircon from the zircon-columbite zone in the composite-body. J) PPL

image of large columbite with aggregate Type-3 and 4 zircon and siderophyllite from the mica-zircon zone in the composite-body 130

Figure 3-4 A) PPL of a disseminated Type-1 zircon in albite and quartz matrix from the fresh amphibole granite. B) CL image of Type-1 zircon in A. The grain shows clear oscillatory zoning that was overprinted by Type-2 and secondary zircon. C) PPL of a highly altered disseminated Type-1 zircon from the silicified porphyritic granite. D) CL image of Type-1 zircon in B that shows clear oscillatory zoning that was overprinted by secondary zircon. E) CPL image of Type-1 zircon and Type-2 overgrowth showing sharp edges with albite in the matrix from the altered porphyritic granite. F) CL image of Type-1 zircon in C that shows Type-1 zircon with Type-2 overgrowth. G) PPL of Type-2 zircon with spongy texture from the altered porphyritic granite. H) CL image of Type-2 zircon in G. I) PPL image of Type-2 zircon forming sharp contact with albite and quartz from the porphyritic granite. J) BSE image of Type-2 zircon in image (H) showing a patchy zoning. K) PPL image of a disseminated Type-2 zircon from the marginal unit. L) CL image of zircon in (I) showing bimodal zoning. M) PPL image of aggregate Type-3 and Type-4 zircon from the zircon-columbite zone in the composite-body. N) BSE image of zircon in M showing spongy Type-3 in the core, Type-4 on the rim, and xenotime overgrowth. O) CL image of zircon in N..... 132

Figure 3-5 PPL image showing a disseminated pyrochlore (PCL-1) and zircon (Type-1) with albite locally altered to kaolinite. B) PPL image of a pyrochlore forming sharp contact with quartz and albite from the fresh sodic amphibole granite. C) PPL of Pyrochlore (PCL-2) from the marginal unit with disseminating Type-2 zircon. 133

Figure 3-6 BSE image of COLB-1 replacement of PCL-1 from highly altered porphyritic granite. B) BSE image of COLB-2 from the altered porphyritic granite. Light veinlets crosscutting COLB-2 are PCL-3. C) COLB-3 replaced by PCL-3 and aeschynite. D) COLB-3 partially replaced by PCL-3 and aeschynite. Abbreviations: Achy, aeschynite, Chl, chlorite; COLB, columbite..... 134

Figure 3-7 BSE image and WDS X-ray maps showing the internal variation in the composition some zoned zircon. A) Type-1 zircon and Type-2 zircon overgrowth showing

zonation of Hf and Y. B) Bimodally zoned Type-2 zircon. C) Type-4 zircon showing patchy Hf zoning. 135

Figure 3-8 Chemical variation in zircon Composition from Al-Ghurayyah deposit. A) Box and whisker diagram of trace element concentration in the different types of zircon obtained by LA-ICP-MS. B) plot of Si against Zr in a.p.f.u. obtained by EMP analyses. C) plot of Zr against Hf in a.p.f.u. obtained by EMP analyses. D) plot of P against total REE in a.p.f.u. obtained by LA-ICP-MS. The dashed line is slope of 1.1. 136

Figure 3-9 Chondrite normalized REE pattern of Type-1 and 2 zircon. B) Chondrite normalized REE pattern of Type-4 zircon. C) REE normalized pattern of the whole-rock. Normalized values are from Boynton (1984). 137

Figure 3-10 Zircon discrimination of Ce/Ce^* versus Sm/La_N in A and Sm/La_N versus La ppm in B (modified after Hoskin, 2005). Chondrite values are from McDonough and Sun (1995). 138

Figure 3-11 Pyrochlore WDS X-ray maps showing compositional variation in PCL-1 and PCL-2. A) PCL-1 from the fresh sodic amphibole. B) PCL-2 from the marginal unit. 139

Figure 3-12 Chemical composition of pyrochlore. A) A box and whisker plot showing the variable composition of pyrochlore types in Al-Ghurayyah. B) A plot showing the main elements substitute Nb and Ta in the B site. The plot shows PCL-1 a different trend than PCL-1 and 2. Nb_2O_5 against Ta_2O_5 . C) A plot showing major substitution in the A site. The three pyrochlore types show variable substitutions that resulted in the formation of different trends. The general substitution mechanism is represented by the plot in the bottom of Figure C. The slopes in the bottom plots least-square best fit 140

Figure 3-13 Chemical composition of columbite. A) A box and whisker plot showing the variable composition of columbite types in Al-Ghurayyah. B) A plot Nb with Ta in atom per formula unit (a.p.f.u) showing a weak correlation to scattering between the two elements. C) Negative Nb vs Ti in a.p.f.u formed by all columbite types suggesting that Ti is a major substituting element in the B site. D) Fe vs Mn in a.p.f.u plot showing variable negative correlations. COLB-2 and 3 show a similar trend, which is different than the trend formed by COLB-1. E) Mn# versus Ta# showing scattering and the formation of two population of

High Ta# and low Mn# formed mostly by COLB-1 and high Mn# formed and low Ta# formed by COLB-2 and 3. F) A plot showing the main substitution mechanism in the A site. G) plot showing the main substitution mechanism in the B site. The slope in Figures F and G are least-square best fit lines. 143

Figure 3-14 Ternary diagram showing columbite types contents of Ti, Nb, and Ta, and compared to PCL-1 and 2. The diagram shows that COLB-1, PCL-1, and PCL-2 have similar content of Ti, Nb, and Ta and these elements were immobile during the alteration of pyrochlore. 144

Figure 4-1 A geological map of the Arabian Shield showing the different terranes that constitute the Shield. The red stars are the locations of some important occurrences of rare-metal granite including Jabal Sayid deposit. The study is shown in the black box (modified after Johnson and Kattan 2012). 186

Figure 4-2 Geological map of Jabal Sayid deposit (modified after Hackett, 1986) and the location of samples. At the top right corner is a general geological map of Jabal Sayid complex (Modified after Turkistany et al., 1982). The study area is denoted by a dashed orange line..... 187

Figure 4-3 The main rock units in the Jabal Sayid mineralization area. A) Looking southeast, an outcrop of the mineralized units and the aegirine granite. B) A photo of the pegmatite sheets showing the contact with the aegirine granite. C) A photo of the contact between the oxidized granite and the aegirine granite. 188

Figure 4-4 Petrography of the aegirine granite. A) Crossed polarized light image (CPL) of subhedral alkali feldspar and quartz phenocrysts with albite inclusions from the aegirine granite. B) CPL image of euhedral alkali feldspar crystals with albite inclusions. C) A plane-polarized light (PPL) image of prismatic aegirine crystals in albite, and quartz in a perthite matrix. Albite occurs as inclusion in the aegirine D) PPL close up image of prismatic aegirine crystal showing abundant fluid inclusions and a relic of arfvedsonite. E) PPL image of a prismatic aegirine partially replaced by Zircon-1, hematite and quartz, and associated with fresh acicular aegirine. The red dashed lines show the original shape of the prismatic aegirine. F) PPL image of altered acicular aegirine associated with zircon (Zircon-1) in a

quartz matrix. G) CPL image showing large microcline crystals and quartz that contain acicular pseudomorph after aegirine from the oxidized granite. H) PPL image of altered acicular aegirine and sericite in quartz matrix from the oxidized granite. I) CPL image of partially altered monazite to xenotime and bastnasite from the oxidized granite. J) PPL image of a large Zircon-3 -hematite-rich pseudomorph in a quartz matrix from the core of the pegmatite sheet. K) PPL of a large pseudomorph in a quartz matrix from the core of the pegmatite. The pseudomorph consists of hematite, Zircon3, quartz and Synchysite (shown in Fig. 4.6 A and B). L) PPL image showing fluorite with hematite and synchysite from the core of the pegmatite. M) PPL of large snowball quartz contains inclusion of fresh acicular aegirine from the border zone. Zircon-1-rich pseudomorph on the top of the image, which is part of the mineralization associated with the transition stage. N) CPL of large snowball quartz from the border zone, contains fresh acicular aegirine and trapped Zircon-1 pseudomorphs, which is part of the mineralization associated with the transition stage. Bastnasite and hematite occur between grain boundaries. Bastnasite and hematite are part of the mineralization that occurs in the hydrothermal stage. P) CPL image of albite, quartz, and microcline from the border zone form a typical magmatic intergranular texture.

Abbreviations: Qtz: quartz, Ab: albite, Kfs: alkali feldspar, Zrn: zircon, Aeg: aegirine, Arfv: arfvedsonite, acic. Aeg: acicular aegirine, Bst: bastnasite, Schy: synchysite..... 189

Figure 4-5 A) BSE image of Zircon-1 associated with hematite from the aegirine granite B) CL image of Zircon-1 in A. C) CPL image of Zircon-2 rich pseudomorph trapped in a quartz crystal with microcline from the pegmatite boundary. D) BSE image of Zircon-2 in a hematite matrix showing a core of Y-rich zircon and resorbed precipitation texture of Y low zircon from the oxidized granite. E) WDS X-ray map of Zircon-2 internal Y content in D. F) BSE image of a large pseudomorph from the pegmatite core showing Zircon-3 forming veinlets with synchysite and hematite..... 191

Figure 4-6 A) PPL image of large pseudomorphs and acicular synchysite with hematite in a quartz matrix from the core of the pegmatite sheet show B) BSE image of the large pseudomorph in A showing Zircon-3 forming veinlets with synchysite and hematite. C) BSE image of bastnasite that is partially replaced by synchysite and xenotime from the oxidized granite. D) Another BSE image of intensely altered bastnasite that is replaced by synchysite and xenotime. E) PPL image of altered aegirine that is replaced by bastnasite and hematite,

and a partially altered monazite associated with Zircon-2 from the oxidized granite. F) CPL image of aggregates of bastnasite, synchysite, and hematite enclosed by quartz that contains altered acicular aegirine. G) and H) are CPL and BSE images of monazite with partial alteration of xenotime and bastnasite from the oxidized granite. 192

Figure 4-7 A) PPL image of pyrochlore crystals from a pegmatite core. B) BSE image of partially altered pyrochlore that is replaced by Y-rich pyrochlore from a pegmatite core. C) BSE image of pyrochlore in hematite matrix that shows intense alteration to Y-rich pyrochlore. 193

Figure 4-8 Whole-rock litho-geochemistry data of this work compared to previous works data. A) Chondrite-normalized REE pattern of the aegirine granite (chondrite values are from McDonough and Sun, 1995). B) Yb vs. Ta tectonic discrimination diagram (Pearce et al. 1984) showing the within-plate tectonic settings of Jabal Sayid aegirine granite. C) Ratio of Ga/Al vs. Nb concentration in ppm (Whalen et al. 1987) showing the alkalinity nature of Jabal Sayid aegirine granite. D) Ta vs. Nb concentrations. The solid line is a least-square fit has a slope value of 12. E) Hf vs. Zr concentration in ppm forming a trend with a slope of 34. F) The ratio of Zr/Hf vs. Y/Ho of the aegirine granite, oxidized granite, the pegmatite sheets. The box represents the range of charge-and-radius -controlled field proposed by Bau (1996). 194

Figure 4-9 Chemical composition of Aegirine. A) Box and whisker plot showing the variation in the chemical composition of prismatic aegirine and acicular aegirine. B) and C) Si correlates negatively with Fe and Na in atom per formula unit. Prismatic aegirine and acicular aegirine form two different trends in Figure B. Figures D) show the elevated concentration of Zr + Ti in acicular aegirine that is associated with low Fe. 196

Figure 4-10 A) Box and whisker plot showing variations in the chemical composition of zircon types. B) Zr vs. Si in atom per formula unit (a.p.f.u). C) The ratio of Zr/Hf forms a smooth curve with HfO₂ concentration. The Zr/Hf ratio is generally higher than the ratio in the whole-rock suggesting other minerals control these elements. D) The deficiency in the filling of T site ($T_{def} = 1 - \text{cations total of T site}$) forms a strong correlation with Si a.p.f.u. the line represents least square fit with a slope of -0.9. F) A plot that shows the main substitution

mechanism as $M^{n+} + (OH)_n^- + (4-n) H^+ = Si^{4+} + Zr^{4+}$; where M = REE, Y, Fe, Al, and Ca (Caruba et al., 1985)..... 197

Figure 4-11 A) Chondrite-normalized REE diagram of the three main zircon types in Jabal Sayid (chondrite values are from McDonough and Sun, 1995). B) Zircon discrimination of chondrite-normalized ratio of Sm/La with La ppm. C) a discrimination diagram where the chondrite normalized ratios of Ce/Ce* and Sm/La are plot against each other. The grey fields in Figures A and C represent magmatic and hydrothermal zircon (modified after Hoskin,

2005). $Ce/Ce^* = \frac{\left(\frac{Ce_{in\ rock}}{Ce_{in\ chondrite}}\right)}{\sqrt{\frac{La_{in\ rock}}{La_{in\ chondrite}} \times \frac{Pr_{in\ rock}}{Pr_{in\ chondrite}}}}$, $Sm/La_N = \frac{\left(\frac{Sm_{in\ rock}}{Sm_{in\ chondrite}}\right)}{\left(\frac{La_{in\ rock}}{La_{in\ chondrite}}\right)}$. Chondrite values are

from McDonough and Sun (1995)..... 199

Figure 4-12 A) A diagram shows the main substitution mechanism in A site. B) A diagram shows the main substitution mechanism in B site. C) is the main substitution mechanism in pyrochlores. Vac is the vacancy in A site calculated as 1 – total A site cations. D) Is a chondrite-normalized REE diagram of fresh pyrochlores from Jabal Sayid. Most values are above the EMPA detection limit, except for Eu where one half of the detection limit was plotted. 200

Figure 4-13 Chondrite normalized REE pattern of synchysite in A, bastnasite in B, xenotime in C, and monazite in D. One half of the EMP detection limit were plotted for REE value below the detection limit..... 201

Figure 5-1 A geological map showing the different terrane in the Arabian Shield. The red stars are the location of some important rare-metal alkaline granite in the Arabian Shield. The box is showing the location of the study area. (modified after Johnson and Kattan 2012).. 249

Figure 5-2 Geological map of Dyaheen ring complex showing the major rock units and the sample locations (Modified after Radain, 1979)..... 250

Figure 5-3 Photos of mineralized rocks in Dyaheen ring complex. A) Pegmatite dyke in the amphibole-biotite granite. B) Aegirine dyke crosscut aegirine granite. C) Ductile quartz vein crosscut altered aegirine granite..... 250

Figure 5-4 Major rock-forming minerals and alteration minerals in Dyaheen. A) Cross polarized light (CPL) image showing highly selective alteration of highly zoned plagioclase associated with quartz from the monzogranite. B) Plane polarized light (PPL) image of titanite associated with alkali feldspar and quartz from the monzogranite. C) PPL image sodic amphibole with magnetite inclusion. Amphibole is replaced to biotite in a quartz plagioclase matrix from the amphibole-biotite granite. D) PPL image of rounded quartz crystals surrounded by albite crystals and contains inclusions of aegirine from the aegirine granite. E) PPL image of sodic amphibole replaced by aegirine from the aegirine granite. F) CPL image of irregular microcline crystal with albite inclusions in quartz, albite, and aegirine matrix from the aegirine granite. G) PPL image of altered sodic amphibole that is replaced by hematite and fluorite from the amphibole-biotite granite. H) Backscattered electron image (BSEI) of a calcite veinlet associated with albite, biotite, hematite, and fluorite from the amphibole-biotite granite. I) BSEI of calcite veinlets with biotite crosscutting sodic amphibole crystals from the amphibole-biotite granite. the dashed line shows the border of a pseudomorph that contains zircon, hematite, and fluorite. J) BSEI of hematite and fluorite alteration from the amphibole-biotite granite. H) BSEI of fine-grained zircon, fluorite, and hematite replacing sodic amphibole from the amphibole-biotite granite. L) fresh and altered titanite from the altered amphibole-biotite granite. Altered titanite is replaced by calcite and rutile. N) and M) PPL variable degree of hematization associated with fresh aegirine, microcline-perthite, and quartz from the altered aegirine granite..... 251

Figure 5-5 Rock-forming mineral and rare-metal minerals from the aegirine dykes and the quartz veins. A) PPL image of zircons in albite quartz matrix and variable crystal sizes of aegirine from the aegirine dyke. B) PPL image of zircon and pyrochlore in quartz and albite matrix, and large aegirine and perthite crystals from the aegirine dyke. C) PPL image of highly altered rounded pyrochlore crystals from the aegirine dyke. D) PPL of a cluster of acicular aegirine with dark pyrochlore crystals from the deformed quartz vein (Fig. 5.3 C). E) BSEI of image D showing bright pyrochlore inclusion in aegirine..... 253

Figure 5-6 Zircon crystals morphology in Dyaheen. A) PPL image of a prismatic zircon associated with alkali weathered alkali feldspar from the monzogranite. B) BSEI and cathodoluminescence (CL) image of zircon in image A. C) PPL image of inclusion-rich zircon from pegmatites. D) BSEI of the spongy texture of zircon in D. E) PPL image of light irregular zircon crystals from the aegirine granite. F) BSEI of zircon in E. G) and H) are PPL and BSEI of zircons from the aegirine dyke . I) PPL image of a cluster of zircons from the quartz veins. J) BSI image of a spongy texture in zircon from the quartz veins. K) BSEI zircon and gadolinite with inclusions of aegirine from the quartz veins. A close-up image of the gadolinite is in Fig. 5.8 B..... 254

Figure 5-7 Morphology and internal chemistry of fergusonite and pyrochlore from Dyaheen. A) and B) are BSEI's of fergusonite crystals from pegmatite that are replaced by pyrochlore. Stage 1 represents the earliest mineralization in Dyaheen, which is replaced by stage 2 represented by Pb-rich pyrochlore. C) PPL, CL, and wavelength dispersive x-ray spectroscopy (WDS)) maps showing the variable internal chemistry of fergusonite from a ductile quartz vein. D) BSEI and WDS maps show the variable internal chemistry of pyrochlore from the aegirine dyke..... 255

Figure 5-8 Morphology and chemistry of gadolinite and bastnasite. A) PP image, BSEI and WDS maps of early gadolinite associated with fergusonite in quartz matrix from a ductile, quartz vein. B) PP image, BSEI and WDS maps of late gadolinite from a ductile quartz vein. C) PP image, BSEI, and WDS maps of early gadolinite from a ductile quartz vein. D) BSEI of bastnasite and britholite from a ductile quartz vein..... 257

Figure 5-9 A plot of SiO₂ and major oxides concentrations of the main rock units in Dyaheen. Black symbols are from Moghaz et al. (2011). Abbreviations: Amph. grnt, amphibole-biotite granite; Aeg. grnt., aegirine granite; Mz.grnt, Monzogranite..... 259

Figure 5-10 Trace element composition of Dyaheen. A) to C) plots to show the correlation between chemically coherent pairs. D) monzogranite REE chondrite normalized diagram. E) Chondrite normalized REE diagram for the amphibole-biotite granite, aegirine granite, and the aegirine dykes. Chondrite values are from McDonough and Sun, (1995). F) to I) plot of Eu anomaly ($=Eu_N / [\sqrt{Sm_N * Gd_N}]$) and chondrite normalized ratio of La/Yb, CaO wt. %, and

Nb ppm, and Sr ppm. J) a plot of Ba ppm and Sr ppm showing a positive correlation. Arrows resemble the evolution trend of the magma..... 260

Figure 5-11 U-Pb zircon age dating of two zircons from aegirine-rich quartz vein from Dyaheen. Red circles represent analysis points. A) Clear and Inclusion-free zircon from the quartz vein that crosscut the aegirine dyke. B) Dark color, inclusion-rich zircons from the same associated with the clear-zircon. C) Estimated zircon U-Pb age of the clear zircon type. 261

Figure 5-12 Amphibole and aegirine composition from different rock units in Dyaheen. A) Ca and Na content of amphibole in atom per formula unit. B) Variation in trace elements concentration in aegirine from different rock units. C) Fe and Ti in a.p.f.u, showing a negative correlation..... 262

Figure 5-13 Zircon composition from different rock units in Dyaheen. A) Box and whisker plot showing the variable composition of zircons from Dyaheen. B) Hf vs. the ratio of Zr/Hf. Symbols with black rings represent zircons that have samples with whole-rock analyses, which are demonstrated by unfilled circles in the small dashed box. Solid lines represent the tie-line between Hf and Zr/Hf in the host rock and zircons. The dashed line represents the assumed tie line of zircons from the aegirine granite. C) the substitution of Zr+Si by REE+P is followed by most of the zircons from the aegirine granite and the quartz veins. D) Zircons from the aegirine granite show more complex substitutions that involve Nb and Ta. The slope reflects a least-square fit of aegirine dykes (red circles) zircon data points E) Zircon/chondrite normalized REE patterns of the different zircon types. Chondrite values are from McDonough and Sun (1995)..... 263

Figure 5-14 Zircon discrimination of Ce/Ce* versus Sm/La_N in A) and Sm/La_N versus La ppm

in B) (modified after Hoskin, 2005). $Ce/Ce^* = (Ce/Ce_{chondrite}) / \sqrt{\left(\frac{La}{La_{chondrite}}\right) \times \left(\frac{Pr}{Pr_{chondrite}}\right)}$

, $(Sm/La)_N = (Sm/Sm_{chondrite}) / (La/La_{chondrite})$. Chondrite values are from McDonough and Sun (1995). Purple regions are for zircons from Al-Ghurayyah, and red regions are for zircons from Jabal Sayid..... 265

Figure 5-15 Fergusonite chemistry. A) substitution of Y+HREE by LREE that increases from core to rim. The slope of -1 reflects the ideal substitution of LREE for HREE. B) Chondrite normalized REE pattern of Fergusonite. Elements with values below the detection limit are omitted, and the dashed lines show the potential trend. Chondrite's values are from McDonough and Sun (1995)..... 266

Figure 5-16 Nomenclature of pyrochlore group minerals in Dyaheen. The diagram shows the main elements (in atom per formula units) that are present in the A site of pyrochlore. 266

Figure 5-17 Pyrochlore chemistry. A) Nb substitution by Si in a.p.f.u. B) substitution of REE+Y by Pb. C) The decrease in A site vacancy as Pb content increases in pyrochlore. D) The Increase of vacancy in A site as Y content increases in pyrochlore. C) The increase in A site vacancy as the total HREE increase in pyrochlore. F) The slope of -1 reflects the ideal substitutions mechanism in pyrochlore..... 267

Figure 5-18 Gadolinite and bastnasite chemistry. A) Box and whisker plot show the variable composition of the gadolinite types. B) Chondrite normalized REE diagram of early and late gadolinite. C) Chondrite normalized REE diagram of bastnasite. Chondrite's values are from McDonough and Sun (1995)..... 268

Figure 5-19 A) normalized quartz-albite-orthoclase diagram of rocks from Dyaheen. The red line represents the change in granite minima as the F concentration increases in the granitic system at 2 kbars (Manning, 1981). B) Sr Vs. Ba that are commonly controlled by plagioclase and K-feldspar. Plagioclase and K-feldspar vectors were plotted, assuming perfect Rayleigh fractionation. The annotated percentages represent the degree of feldspars fractionation. C) Chondrite normalized REE diagram after 20% and 40 feldspars fractionations from the monzogranite. Chondrite's values are from McDonough and Sun (1995)..... 269

Figure 6-1 A geological map showing the different terrane in the Arabian Shield. The red stars are the location of some important rare-metal alkaline granite in the Arabian Shield. The study areas (modified after Johnson and Kattan 2012)..... 300

Figure 6-2 Simplified geological maps from Al-Ghurayyah (A), Jabal Sayid (B), and Dyaheen 302

Figure 6-3 A) Y vs. Nb ppm tectonic settings discrimination diagram (Pearce et al. 1984). B) Variation in aluminum saturation index (ASI) of the three deposits (Shand 1943). 302

Figure 6-4 A) Box and whiskers plot show the variability in Major oxide composition of the studied areas. B) A chondrite normalized spider diagram showing the mean, max, and min normalized concentrations of REE elements in the fresh studied granites. C) chondrite normalized REE diagram showing the mean, max, and min normalized concentrations of REE elements in the studied granites. Normalized values are from McDonough and Sun (1995)..... 304

Figure 6-5 A) plot of the granite concentrations of Hf ppm and Zr ppm in (A) and Ta ppm vs Nb ppm in (B). The line represents the slope values of Zr/Hf and Nb/Ta..... 304

Figure 6-6 A) Chondrite normalized average REE concentration of zircons from the studied areas Zircon discrimination of Ce/Ce* versus Sm/LaN in B) and Sm/LaN versus La ppm in C) (modified after Hoskin, 2005). $Ce/Ce^* = (Ce/Ce_{\text{chondrite}}) / \sqrt{((La/La_{\text{chondrite}}) \times (Pr/Pr_{\text{chondrite}}))}$, $(Sm/La)_N = (Sm/Sm_{\text{chondrite}}) / (La/La_{\text{chondrite}})$. Chondrite's values are from McDonough and Sun (1995). Purple regions are for zircons from Al-Ghurayyah and red regions are for zircons from Jabal Sayid..... 305

Figure 6-7 Total tetrad effect plot against the ratio of K/Rb in (A), Zr/Hf in (B), and Y/Ho in (C). These elements are sensitive to the change in melt composition (Irber, 1999). Solid lines show the range of CHARAC whereas the dashed line show the minimum value of visible total tetrad effect. The symbols are the same as in Figure 6.5..... 307

Figure 6-8 Cartoon to illustrate the emplacement of the alkaline granite during the post-tectonic time period. The main processes that took place during the late magmatic stage and the hydrothermal stage in Al-Ghurayyah (B) and Jabal Sayid and Dyaheen(C). Abbreviation: Arf, arfvedsonite; Kfs, K-feldspar; Ab, albite; Aeg, aegirine; Bst, bastnasite, Hem, hematite; Zrn, zircon; Pcl, pyrochlore; Plith, polyolithionite; Ms, muscovite; Chl, chlorite, Colb, columbite; Qtz, quartz..... 308

List of Appendices

Appendix A: List of Al-Ghurayyah samples, whole-rock analyses, zircon age data	309
Appendix B : EMP chemical analyses for ore and rock-forming minerals from Al-Ghurayyah	315
Appendix C: List of Jabal Sayid samples, whole-rock analyses, and mineral chemistry.....	352
Appendix D: List of Dyaheen samples, whole-rock analyses, mineral analyses, and zircon age data	371

List of Abbreviations

Mineral	Symbol	Formula	Notes
Quartz	Qtz	SiO ₂	
Albite	Ab	NaAlSi ₃ O ₈	
Microcline	Mc	KAlSi ₃ O ₈	
Alkali feldspar	Kfs	(K,Na)AlSi ₃ O ₈	
Arfvedsonite	Arf	Na ₃ Fe ₅ Si ₈ O ₂₂ (OH,F) ₂	
Aegirine	Aeg	NaFeSi ₂ O ₆	
Muscovite	Ms	KAl ₂ (AlSi ₃ O ₁₀)(OH) ₂	
Trilithionite	Plith	K(Li _{1.5} Al _{1.5})(AlSi ₃ O ₁₀)(F,OH) ₂	
Sericite	Ser	KAl ₂ (Si ₃ Al)O ₁₀ (OH,F) ₂	
Chlorite	Chl	(Fe,Mg) ₅₋₆ (Al,Fe,Si) ₄ (O,OH) ₁₈	
Calcite	Cal	CaCO ₃	
Hematite	Hem	Fe ₂ O ₃	
Magnetite	Mag	Fe ₃ O ₄	
Zircon	Zrn	ZrSiO ₄	
			A = Na ⁺ , Ca ²⁺ , Sn ²⁺ , Sr ²⁺ , Pb ²⁺ , Sb ³⁺ , Y ³⁺ , U ⁴⁺ , H ₂ O
Pyrochlore	Pcl	A ₂ Nb ₂ (O,OH) ₆ Z	or □ Z = OH, F, H ₂ O or □ (vacancy)
Columbite	colb	(Mn,Fe)(Nb,Ta) ₂ O ₆	
Rutile	Rt	TiO ₂	
Thorite	Thr	ThSiO ₄	
Y-fluorite	Y-Fl	(Ca _{1-x} Y _x)F _{2+x}	0.05 < x < 0.3
Fluorite	Fl	CaF ₂	
Aeschnyrite	Achy	(Y,Ln,Ca,Th)(Ti,Nb) ₂ (O,OH) ₆	
Cassiterite	Cst	SnO ₂	
Gadolinite	Gdt	(YREE) ₂ FeBe ₂ Si ₂ O ₁₀	
Bastnasite	Bst	(Ce,La,Nd)(CO ₃)F	
Britholite	Brth	(Y,REE,Ca) ₅ (SiO ₄) ₃ (OH)	
Fergusonite	Frg	YREENbO ₄	
Monazite	Mnz	(Ce,La,Nd)PO ₄	
Thorite	Thr	ThSiO ₄	
Titanite	Tnt	CaTiSiO ₂	
Apatite	Ap	Ca ₅ (PO ₄) ₃ (F,Cl,OH)	
Synchysite	Schy	CaY(CO ₃) ₂ F	
Xenotime	Xtm	(Y,Yb)PO ₄	

Chapter 1

1 Rare-metal alkaline granite mineralization in the Arabian Shield, Saudi Arabia

1.1 Introduction

The increased applications of high field strength elements (HFSE) and rare earth elements (REE) in the current technological industry has led to an increase in demand on these elements. According to the U.S. Geological Survey (Mineral Commodity Summaries, 2019), Brazil produces 88 % of the world production of Nb followed by Canada with 10 %; Congo and Rwanda accounted for 66 % of Ta production; Australia and South Africa produce 57% of the world zirconium, and; China accounted for 80 % of the world production of REE. The most common use of Nb is for steel and superalloy industry; Ta mainly is used to manufacture capacitors for electronics; Zr is used for ceramic, foundry sand, and refractories; Hf is used for superalloy manufacturing; and REE is used for catalysts, ceramic and glass, and metallurgical and alloy applications (U.S. Geological Survey , Mineral Commodity Summaries, 2019). The rapid growth in the demand for these elements has resulted in increased exploration for new resources of rare-metals. This in turn has generated research on understanding the behavior of these elements in different environments and the processes that form economical deposits.

1.2 Geochemical background

1.2.1 High field strength elements

High field strength elements are transition metals that have small ionic radii and high valance states that range between +4 to +5. Examples of HFSE include Nb, Ta, Zr, Hf, Th, U, and Sn. As a result of their high charge to ionic radii ratio, they are incompatible with most rock-forming minerals; thus, they preferentially stay in the residual melt until saturation is attained in an accessory phase that contains one or more of these elements as a major constituent, such as columbite, zircon, thorite, and cassiterite. Moreover, these elements are generally immobile during metamorphism or weathering due to their low solubility in most geological fluids; thus, they are considered useful indicators of the

petrogenesis of ancient igneous and metamorphic rocks (White, 2013). Many HFSE form pairs that share similar charges and ionic radii. For example, Nb-Ta and Zr-Hf have a charge of +5 and +4, respectively, and an ionic radius of 0.61 and 0.64 Å for Nb and Ta; respectively, and 0.72 and 0.71 Å for Zr and Hf, respectively (Shannon, 1976). According to Goldschmidt substitution rules (Goldschmidt, 1937), these pairs enter the mineral structures to the same degree. Therefore, these pair ratios commonly have chondritic values (Nb/Ta 17.6, and Zr/Hf = 36.8; McDonough and Sun, 1995) in rocks and minerals. However, these pairs in the continental crust and in oceanic island basalt can have non-chondritic values (Huang et al., 2011), which indicates that they have undergone fractionation. Bau (1996) proposed a fluid metasomatic model to explain non-chondritic ratios in highly evolved magmatic rocks. However, several authors argued that non-chondritic values could be explained by clinopyroxene fractionation (David et al., 2000; Kogarko, 2016) due to the change in activity coefficients of Zr and Hf in the melt (Linnen and Keppler, 2002). Cerny et al. (1985) stated that Nb/Ta ratio changes greatly during pegmatite evolution due to the higher fluorine-based thermal stability of Ta complexes, which makes Nb available for crystallization earlier than Ta. However, Aseri et al. (2015) showed that fluorine does not affect the solubilities of columbite (MnNb_2O_6) and tantalite (MnTa_2O_6) in haplogranitic melts. Thus, the behavior of HFSE in silicate melts and aqueous fluids remains an area of active research.

1.2.2 Rare earth elements (REE)

Rare earth elements are a group of 14 elements known as the lanthanides, which include La, Ce, Pr, Nd, Sm, Eu, Gd, Tb, Dy, Ho, Er, Tm, Yb, and Lu. Yttrium and scandium are commonly considered as REE because they show similar chemical properties as REE (Balaram, 2019). The REE are subdivided into LREE (La, Ce, Pr, Nd, Sm, Eu, and Gd) and HREE (Tb, Dy, Ho, Er, Tm, Yb, and Lu) based on electron configuration (Rollinson, 1993). The REE are considered as a coherent group and can substitute for one another. Their coherence is a result of the electronic configurations where the 4f shell is progressively filled up to 14 electrons, which leads to identical outer shells (Cesbron, 1989; Henderson, 1996). Moreover, the progressive filling of the inner shell leads to a progressive decrease in size from La to Lu (La = 1.160 to Lu = 0.977 Å effective ionic

radii; Shannon 1976), which is known as lanthanide contraction. REE in geological environments are generally in a trivalent oxidation state. However, some elements can exist in other valence states, such as Eu and Ce, where they can be present as Eu^{2+} and Ce^{4+} . The variation in valence states can be a useful indication of the the oxidation state of the system. Another interesting chemical phenomenon is the tetrad effect, which is the segmentation of a chondrite normalized REE pattern into four segments La-Nd, Sm-Gd, Gd-Ho, and Er-Lu (Masuda and Ikeuchi, 1979). The effect is generated from the variations in exchange interactions of unpaired electrons in the 4f shell, spin-orbit coupling, or crystal field stabilization (Irber, 1999; and references therein). The tetrad effect is manifested in two types, M-type and W-type, where M and W are the shapes of the tetrad (Masuda et al., 1987). The W-type is found in natural waters, whereas the M-type is found in solid products (rocks). The formation of M-type tetrad is a consequence of the separation of W-type by an aqueous phase (Masuda et al., 1987). The occurrence of an M-type tetrad effect in highly evolved granite was often attributed to the interaction with hydrothermal fluid (Bau, 1996, 1991; Irber, 1999) or silicate-fluoride liquid immiscibility (Peretyazhko and Savina, 2010).

1.3 HFSE and REE mineral deposits

Mineral deposits of HFSE and REE + Y are commonly referred to as rare-metal deposits (Linnen et al., 2014). Primary rare-metal deposits are usually associated with carbonatite, (e.g., Bayan Obo, China; Nolan Bore, Australia; Mountain Pass, USA/Canada), alkaline/peralkaline granite (e.g., Ilímaussaq, Greenland; Lovozero and Khibiny, Russia; Nechalacho, Canada), and metaluminous and peraluminous granites and pegmatites (e.g., Pitinga, Brazil; Yichyan, China; Tanco, Canada) (Linnen et al., 2014; Möller et al., 1989).

Carbonatites are igneous rocks that contain more than 50 modal % carbonate minerals (Linnen et al., 2014). Carbonatites are formed from a mantle-derived melt, which might undergo liquid immiscibility or crystal fractionation (Bell et al., 1999). They are considered as one of the most important sources of HFSE and REE deposits. Examples of common rare-metal minerals in carbonatites include: zircon (ZrSiO_4), perovskite ($[\text{Ca}$,

Na, REE] [Ti, Nb, Fe³⁺] O), pyrochlore ([Ca, Na]_{2-x}[Nb, Ti]₂O₆[OH]_{1-y}.nH₂O), monazite ([REE]PO₄), and bastnasite ([REE][CO₃]F).

Metaluminous and peraluminous rare-metal granites and pegmatites are considered to be important sources of Ta, Sn, Li and Cs, and to a lesser extent Nb (Linnen et al., 2014). The deposits are associated with I-type or S-type granites, or A-type peraluminous granites and pegmatites. The mineralization is commonly Ta, Nb, Sn, and W oxides, such as columbite group minerals ([Mn, Fe][Nb, Ta]₂O₆), wodginite, (Mn²⁺Sn⁴⁺Ta₂O₈) cassiterite (SnO₂), and wolframite ([Mn²⁺,Fe²⁺]WO₄), that are disseminated or associated with metasomatic events (Linnen et al 2014).

Rare-metal alkaline/peralkaline granites contain high concentrations of Nb, Ta, Zr, Y, and REE, especially the heavy rare earth element (HREE) that includes Tb, Dy, Ho, Er, Tm, Yb, and Lu. Generally, the alkaline granites are characterized by an alkalinity index (A.I.) of > 1, where A.I. = the molar ratio of (Na + K) /Al (Piilonen et al., 2012). Moreover, alkaline granites can be classified according to their silica saturation into silica over-saturated (quartz-bearing rocks) and silica saturated (feldspar-bearing rocks)/undersaturated (feldspathoids-bearing rocks) (Linnen et al., 2014). The silica saturated/undersaturated peralkaline granites are often given the name agpaitic when the A.I. is equal or larger than 1.2, whereas those with an A.I. of < 1.2 are known as miaskitic. The agpaitic and miaskitic granites mineralogy is distinct. The agpaitic granites are characterized by complex zirconosilicate minerals, such as eudialyte (Na₄[Ca,REE]₂[Fe,Mn]ZrSi₈O₂₂[OH,Cl]₂) and rinkite ([Ca,REE]₄Na[Na,Ca]₂Ti[Si₂O₇]₂F₂[O,F]₂). The miaskitic granites have more simple ore minerals, such as zircon, ilmenite (Fe²⁺TiO₃), and pyrochlore (Möller and Williams-Jones, 2017; Piilonen et al., 2012; Sorensen, 1992). Nevertheless, the term miaskitic has been used to describe silica-bearing alkaline granites with mineralogy similar to the traditional silica-undersaturated miaskitic rocks (Siegel et al., 2018).

1.4 Rare-metal mineralization models

The processes that led to the formation of rare-metals deposits have been a subject of extensive debate, particularly on whether they are formed predominantly by magmatic or

hydrothermal processes (Boily and Williams-Jones, 1994; Borodulin et al., 2009; Feng and Samson, 2015; Gysi and Williams-Jones, 2013; Kovalenko, 1995; Kovalenko and Kovalenko, 1984; Möller and Williams-Jones, 2016; Salvi et al., 2000; Salvi and Williams-Jones, 1990; Van Lichtenvelde et al., 2007, 2010; Vasyukova and Williams-Jones, 2014; Vasyukova et al., 2016; Wang et al., 2003; Zhu et al., 2015). The reason for this debate is the complexity and difficulty of recognizing primary magmatic features that have been overprinted and obscured by secondary hydrothermal processes. The debate can be summarized in three main models: magmatic, hydrothermal, and immiscibility. The magmatic model suggests that the mineralization is due to direct crystallization of the rare-metal minerals from a highly evolved granitic melt (Dostal et al., 2015; Kontak, 2006; Linnen and Williams-Jones, 1993; Novak and Cerny, 1998; Van Lichtenvelde et al., 2009, 2007). For example, Linnen and Williams-Jones (1993) reported high SnO₂ concentration from the core of magmatic garnet from Nong Sua aplite-pegmatite, Thailand. Moreover, they interpreted that the Nb-Ta mineralization in the aplite-pegmatite to have crystallized from a melt. Furthermore, features of primary crystallization were recognized in the HFSE deposits, such as primary zoning in Nb-Ta oxide minerals from Tanco lower pegmatite, Canada (Van Lichtenvelde et al., 2007). The magmatic model is also supported by solubility data of HFSE minerals, which shows that high amounts of HFSE can be carried by a highly fluxed melt (high concentrations of Li, F, B, P) and deposits can be formed through direct crystallization due to the decrease of temperature, alkalis and flux contents (Aseri et al., 2015; Bartels et al., 2010; Fiege et al., 2011; Linnen, 1998; Linnen and Keppler, 1997; Van Lichtenvelde et al., 2010; Watson, 1979). Furthermore, authors in favor of the magmatic model argued against the hydrothermal model due to the lack of metasomatic HFSE in the country rock (Linnen and Cuney, 2005). On the other hand, hydrothermal model studies argued that the mineralized granites resulted from the leaching of metals from the lower part of a pluton by the upward movement of post-magmatic fluids and precipitated them in the apical part, and their model is supported by the frequent association of HFSE mineralization with evidence of alteration events (Beus and Zalashkova, 1964; Pollard, 1989; Yang et al., 2014). The immiscibility model suggests the formation of two immiscible melts due to the accumulation of volatiles and fluxing components in highly evolved melts (Breiter

et al., 1997; Mohamed, 2013; Thomas et al., 2006; Veksler et al., 2002). Thomas et al. (2006) showed the presence of two immiscible peraluminous and peralkaline melts at the Ehrenfriedersdorf pegmatites from Germany. The peralkaline melt had low viscosity and extracts HFSE preferentially. Moreover, Veksler et al. (2002) experimental work showed the possible coexistence of immiscible fluids (aluminosilicate melt, hydrous fluid, and hydrosaline melt) at temperatures ranging from 450 to 900 °C and 0.1 to 0.2 GPa.

Rare-metal deposits associated with alkaline and peralkaline granites have received less attention, probably because they previously have had less economic potential (although, some deposits like Strange Lake, Canada, and Al Ghurayyah, Saudi Arabia potentially have concentrations of HFSE and REE that are close to being economic; Küster, 2009; Linnen et al., 2012). Nevertheless, in the alkaline and peralkaline granitic system, the complex textures and mineralogy (owing to the post-crystallization hydrothermal alteration) that are associated with the mineralization make the interpretation of primary and secondary textures and their relationship to the mineralization challenging. Thus, the same debate on the genesis of rare-metal metaluminous/peraluminous granites is applicable to the alkaline/peralkaline rare-metal granites. Several studies have investigated the processes that are required for these types of rocks to reach economic concentrations (Boily and Williams-Jones, 1994; Feng and Samson, 2015; Finch et al., 2019; Gysi and Williams-Jones, 2013; Hackett, 1986; Harris et al., 1986; Hassanen, 1997; Kovalenko, 1995; Migdisov and Williams-Jones, 2014; Moghazi et al., 2015, 2011; Möller and Williams-Jones, 2016; Qadhi and Moufti, 2008; S Salvi et al., 2000; Salvi and Williams-Jones, 1990, 1996a; Schmitt et al., 2002; Siegel et al., 2018; Turkistany and Ramsay, 1982; Vasyukova and Williams-Jones, 2014; Vasyukova et al., 2016; Vasyukova and Williams-Jones, 2019; Wang et al., 2000, 2003). The main hypotheses on the formation of this kind of deposits includes the involvement of magmatic process, hydrothermal processes, and immiscibility processes, similar to metaluminous and peraluminous granitic systems. The magmatic model suggests that the accumulation of HFSE and REE is a result of extreme fractionation. Kovalenko (1995) interpreted the rare-metal granite of Khaldzan-Buregtey, western Mongolia, to be magmatic based on the field relationships and primary melt inclusion analyses that were homogenized into silicate melts enriched in rare-metals. Moreover, that study demonstrated that post-

magmatic hydrothermal alteration is not necessary for the formation of the deposits, and the rare-metals are concentrated at the magmatic stage. Similarly, Schmitt et al. (2002) provided evidence of magmatic pre-enrichment in Zr, Nb, and REE, which led to the formation of rare-metal mineralization at the Amis Complex, Namibia. Their conclusion was based on melt inclusion analyses that were homogenized into volatile and rare-metal-rich silicate melt, but this study also reported local remobilization of REE during the hydrothermal stage. Boily and Williams-Jones (1994) concluded that the extreme rare-metal enrichment in Strange Lake, Canada, is a result of both fractional crystallization and remobilization of REE and HFSE by low-temperature hydrothermal fluid. The low-temperature REE and HFSE hydrothermal remobilization conclusion agrees with the finding of the previous work of Salvi and Williams-Jones (1990), where leaching and remobilization of REE and HFSE by low temperature meteoric or formational water was interpreted based on fluid inclusion analyses. They further proposed that the mobilization of rare-metals during the hydrothermal stage was via F-complexes (Stefano Salvi et al., 2000; Salvi and Williams-Jones, 1990, 1996a); however, recent studies have shown that REE form more stable complexes with chloride ions (with the LREE being more mobile), whereas F is an important transporting agent for Zr (Gysi and Williams-Jones, 2013; Migdisov et al., 2016; Williams-Jones et al., 2012). Furthermore, Feng and Samson (2015) suggest a hydrothermal role in the addition of HFSE to account for the high concentrations of these elements in pseudomorphs from the T-Zone, Thor Lake, Canada. More recently, the immiscibility model was interpreted for Strange Lake, Canada, based on the observation of immiscible fluoride-silicate melt in melt inclusions (Siegel et al., 2018; Vasyukova and Williams-Jones, 2016, 2014). Vasyukova and Williams (2014) proposed that the Ca and REE preferentially partitioned into the fluoride melt, whereas the silicate melt became enriched in HFSE. Similarly, Siegel et al. (2018) concluded that the highly mineralized pegmatite in Strange Lake, Canada, is the result of the accumulation of the fluoride melt in a volatile-rich silicate melt.

1.5 Rare-metal alkaline granites in the Arabian Shield

The Arabian Shield (Fig. 1.1) formed by the accretion of inter-oceanic island arcs as a result of the closing of Mozambique ocean (Agar, 1992; Nehlig et al., 2002; Robinson et

al., 2014; Stern, 1994). The accretion took place from 900 to 550 Ma and led to an amalgamation of nine distinct terranes: the Asir, Tathlith, Ar-Rayn, Ad-Dawadimi, Afif (and Khida sub-terrane), Ha'il, Jeddah, Hijaz, and Midyan terranes (Johnson et al., 2011). The terranes are marked by the presence of ultramafic bodies within orogenic belts (Agar, 1992; Robinson et al., 2014). After the accretion, a period of extensional tectonism took place during the orogenic collapse. A large volume of alkaline magmatism, associated with this orogenic collapse, was emplaced to form one of the world's largest alkali granite fields (Stoeser, 1986). Radiometric age dating (Rb-Sr) of the alkali granites estimated that this event lasted from 686 to 518 Ma, with younger ages trending toward the northeastern part of the shield (Stoeser, 1986). Several alkaline granites in the Arabian Shield are reported to contain high concentrations of HFSE and REE, including Al-Ghurayyah, Jabal Sayid, Jabal Aja, Umm Al-Birak, and Jabal Hamra (Jackson and Douch, 1986; Johnson et al., 2011; Küster, 2009). It should also be noted that Rb-Sr ages can be reset, so additional age dates are needed to confirm the timing of formation of the different granites.

A-type granites were introduced to the granite classification by Chappell and White (1974) (Chappell and White, 2001) to describe granites that were emplaced in a within-plate tectonic environment. A-type granites are characterized by high SiO₂, Na₂O, K₂O, F, Fe/Mg, HFSE, and REE, and low Ca, Ba, and Sr (Whalen et al., 1987). The source of anorogenic A-type alkaline granites is a subject of an ongoing debate and many genetic models have been proposed to describe the genesis of this type of rock. The proposed models include: 1) residual-modal where A-type granites are a result of high-temperature partial melting of a granulite source that had previously generated an I-type magma (Barker et al., 1975; Collins et al., 1982; Landenberger and Collins, 1996); 2) fractionation of alkaline mantle-derived basalt with or without crustal assimilation (Bonin, 2007; Eby, 1992, 1990; Frost and Frost, 2011; Kemp et al., 2006; Turner et al., 1992; Zhang et al., 2012); 3) melting of lower crust under fluxing of mantle-derived volatiles, melting of lower crust by internal radiogenic heat production, or by underplating mantle-derived magma (Brown, 1994; Frost et al., 2002); 4) high temperature melting of I-type tonalitic granites (Creaser et al., 1991).

The post-orogeny magmatism is marked by the emplacement of calc-alkaline and peralkaline intrusions (Moghazi et al., 2012; Stern et al., 2010). The genesis and development of the post-collision calc-alkaline/peralkaline magmatism in the Arabian-Nubian Shield were investigated by several studies (Ali et al., 2014, 2009; Moghazi et al., 2015, 2012; Stern, 2002, 1994; Stern and Johnson, 2010). Stern and Johnson (2010) concluded that Sm-Nd isotope compositions revealed that the lower crust is formed by juvenile materials from the mantle, and the Nd model age of the lower crust is close to the age of the Arabian-Nubian Shield. Moreover, Stern et al. (2010) excluded the involvement of pre-Neoproterozoic crust in the formation of the Arabian-Nubian Shield. The $\epsilon_{\text{Nd}}(t)$ of the Arabian Shield ranges from ~ 4 to ~ 10 (Moghazi et al., 2012). Thus, partial melting of the lower part of the juvenile Arabian Shield crust with/without direct contribution from upper mantle material led to the formation of the post-origin alkaline granites (Ali et al., 2014; Eyal et al., 2010; Moghazi et al., 2015)

Drysdall et al, (1984) classified of rare-metal granites in the Arabian Shield into Jabal Sayid Type and Al-Ghurayyah type based on geochemical, geological characteristics, host rock, and the associated minerals. The Jabal Sayid type characterized by wholerock compositions with low Al and Na and high Fe, K/Na and enrichment in REE. Moreover, this type has the normative mineralogy of a hematitic silexite. The main minerals include quartz, K-feldspar, and hematite with little or no albite. Jabal Sayid and Jabal Hamra are two examples of this type. Al-Ghurayyah type has a major oxide composition similar to the alkaline granites of Whalen et al. (1987). The mineralization is disseminated in porphyritic to microgranite granite. Major rock-forming minerals include microcline, albite, quartz, sodic amphibole, and zircon. The main feature of this type is the strong enrichment of HREE. Examples of this type include Al-Ghurayyah, Jabal Tawlah, and Umm Al-Birak.

1.6 Objectives

Most alkaline granite-hosted ore deposits lack primary minerals because they have been destroyed by alteration. Furthermore, the abundances of HSF and REE are typically highest within the most intensely altered rocks, concentrated at the apical parts of the intrusions (Kovalenko et al., 2007; Miller, 1996; Salvi and Williams-Jones, 1996b, 1991).

Thus, this leads to a debate on the importance of magmatic versus hydrothermal processes.

The genesis of HFSE and REE mineralization at the rare-metal alkaline granites in Saudi Arabia, despite their importance, has received little scientific attention thus it is not clear whether the models applied elsewhere are also valid for these locations. Consequently, this work studies the mineralization in rare-metal alkaline granites in the Arabian Shield in order to evaluate the roles of magmatic and hydrothermal processes that led to the substantial concentrations of HFSE and REE. Three areas were selected based on their styles of mineralization:

- I. Al-Ghurayyah is characterized by a disseminated mineralization style. This deposit has preserved late-magmatic features, such as intergranular textures and the morphology and chemistry of zircons from the host granite indicate a magmatic environment.
- II. Jabal Sayid is characterized by mineralization that is hosted by pegmatite and hematite-altered granite. This deposit has undergone intense hydrothermal alteration, which is associated with the mineralization. The early hydrothermal mineralogy is partially preserved, which can be used to understand the nature of this stage.
- III. Hdb Ad Dyaheen ring complex (which will be referred to as Dyaheen) is located near Jabal Sayid rare-metal mineralization, and it was suggested that they have the same source (Radain, 1979), in part because they have similar host rock compositions and ages. However, the two deposits show different mineralization styles in which the mineralization in Dyaheen is hosted by quartz veins and an aegirine dykes, whereas at Jabal Sayid, the mineralization is contained in pegmatite sheets and oxidized granite. Another important feature that

distinguishes the two deposits is the absence of the intense hematite alteration at Dyaheen, where the mineralization is associated with relatively fresh rock (in particular the aegirine is fresh). This allows to compare two deposits that share the same source and host rocks but have different mineralization styles.

This study provides new whole-rock lithochemical data for the host rock and detailed mineral chemistry analyses and morphological descriptions for the three deposits. Furthermore, this U-Pb zircon age dates are determined for Al-Ghurayyah and the mineralization in Dyaheen. At each deposit, the magmatic and hydrothermal textures in the host granite and the mineralized units were characterized, and subsequently the genesis of each deposit was evaluated based on the chemical compositions of the ore minerals and the whole rock. The morphologies of the ore minerals were investigated using a polarizing microscope, and a secondary electron microscope (SEM) equipped with energy dispersive spectroscopy (EDS) for mineral identification. The internal chemical variations of ore minerals were determined using wavelength and energy dispersive spectroscopy (WDS and EDS) maps and mineral chemistry analyses by electron microprobe (EMPA). The trace element compositions of zircon were obtained using laser ablation inductively coupled plasma mass spectrometry (LA-ICP-MS), which helped evaluate the environment at which it crystallized.

1.7 Thesis structure

The introduction chapter 1 (the current Chapter) is followed by five chapters that are written as stand-alone publications. These have yet to be submitted to journals, however they will be published after the thesis is completed.

- Chapter 1: Introduction

This chapter provides background information on the geochemistry of the HFSE and REE and the current importance and industry applications of these elements.

Furthermore, this chapter provides an overview of rare-metal deposits and the current genetic models that explain the formation of this kind of deposits, with emphasis on

alkaline/peralkaline rare-metal granites. The occurrences of the rare-metal granites in the Arabian Shield are also discussed briefly. The chapter presents the main issues regarding the formation of rare-metal deposits, the purpose of the study and the methods that will be employed. The chapter also demonstrates the thesis structure with a brief description of the chapter contents

- Chapter 2: The petrology and lithology of Al-Ghurayyah Nb, Ta, Zr, Y, REE rare-metal granite.

This chapter focuses on the petrology and the lithogeochemistry of Al-Ghurayyah. The main objectives of this chapter are to characterize the mineralization through detailed petrographic and mineralogical description of the mineralization and hydrothermal alteration in terms of magmatic and hydrothermal assemblages. The chapter also provides the first estimation of the age of the Al-Ghurayyah deposit using zircon U-Pb geochronology.

- Chapter 3: Morphology and Chemistry of HFSE and REE minerals from Al-Ghurayyah

This chapter investigates the morphology and the chemical compositions of zircon, pyrochlore, and columbite. These data are interpreted in terms of their textural relationships with other rock-forming minerals, which is used to evaluate the roles of magmatic and hydrothermal processes in the formation of Al-Ghurayyah deposit.

- Chapter 4: Rare-metal mineralization in Jabal Sayid

This chapter studies the mineralization in Jabal Sayid deposit and the host granite to evaluate the roles of magmatic and hydrothermal processes that led to the substantial concentrations of HFSE and REE. The study provides new whole-rock lithogeochemical data for the host rock at the northern part of the complex, in addition to textural analysis and detailed mineral chemistry analyses and morphological descriptions for the ore minerals in Jabal Sayid. The morphologies of the ore minerals were studied under a polarizing microscope, and a scanning electron microscope (SEM) equipped with energy dispersive spectroscopy (EDS) for mineral identification. The ore mineral internal

chemical variation was studied using wavelength and energy dispersive spectroscopy (WDS and EDS) maps. This is followed by mineral chemistry analyses from electron microprobe (EMPA). The trace element compositions of zircon were obtained using laser ablation inductively coupled plasma mass spectrometry (LA-ICP-MS), which helped evaluate the chemical evaluation of its crystallization environment. These data were integrated to interpret a general view on the evolution of the magmatic and hydrothermal stages that led to the formation of the mineralized units.

- Chapter 5: Rare-metal mineralization of Dyaheen.

The objectives of this study are to assess the magmatic evolution of Dyaheen ring complex and the hydrothermal stage to evaluate their roles in the formation of rare-metal mineralization. Dyaheen and Jabal Sayid occur in the same terrane, have comparable host rock composition, and similar ages; however, the mineralization styles at these deposits is different, which provides an opportunity to evaluate the importance of different processes on mineralization styles. Moreover, most rare-metal alkaline granites are associated with a heavy post-magmatic alteration that destroys or obscures magmatic and early hydrothermal mineral assemblages (Kovalenko et al., 2007; Miller, 1996; Salvi and Williams-Jones, 1996b, 1991). Thus, the nature of this stage is not well documented. At Dyaheen, the late-magmatic to early-hydrothermal stage mineral assemblages are preserved, which provides the opportunity to understand the nature of this stage that is not possible at similar deposits. This chapter also provides a new age estimation of the mineralization using U-Pb zircon geochronology, and detailed morphology and chemistry of aegirine, amphibole, and rare-metal phases. These were determined from the petrography and litho-geochemistry of Dyaheen rock units, and the evolution of HFSE and REE from petrography and mineral chemistry relationships.

- Chapter 6: Conclusion

This chapter integrates the data from the preceding chapters to compare the Al-Ghurayyah, Jabal Sayid, and Dyaheen deposits in terms of their geology, lithology, ore minerals, and mineral chemistry to evaluate the relative importance of magmatic and

hydrothermal processes to rare metal mineralization. Moreover, the chapter discusses the age of the granites obtained in this study with those from previous studies to constrain the origin of mineralization within the context of the evolution of the Arabian Shield.

1.8 References

- Agar, R.A., 1992. The tectono-metallogenic evolution of the arabian shield. *Precambrian Res.* 58, 169–194. [https://doi.org/10.1016/0301-9268\(92\)90118-8](https://doi.org/10.1016/0301-9268(92)90118-8)
- Ali, K.A., Jeon, H., Andresen, A., Li, S.Q., Harbi, H.M., Hegner, E., 2014. U-Pb zircon geochronology and Nd-Hf-O isotopic systematics of the Neoproterozoic Hadb adh Dayheen ring complex, Central Arabian Shield, Saudi Arabia. *Lithos* 206–207, 348–360. <https://doi.org/10.1016/j.lithos.2014.07.030>
- Aseri, A.A., Linnen, R.L., Che, X.D., Thibault, Y., Holtz, F., 2015. Effects of fluorine on the solubilities of Nb, Ta, Zr and Hf minerals in highly fluxed water-saturated haplogranitic melts. *Ore Geol. Rev.* 64, 736–746. <https://doi.org/10.1016/j.oregeorev.2014.02.014>
- Balaram, V., 2019. A review of applications , occurrence , exploration , analysis , recycling , and environmental impact. *Geosci. Front.* 10, 1285–1303. <https://doi.org/10.1016/j.gsf.2018.12.005>
- Barker, F., Wones, D.R., Sharp, W.N., Desborough, G.A., 1975. The Pikes Peak Batholith, Colorado Front Range, and a model for the origin of the gabbro-anorthosite- syenite-potassic granite suite. *Precambrian Res.* 2, 97–160.
- Bartels, A., Holtz, F., Linnen, R.L., 2010. Solubility of manganotantalite and manganocolumbite in pegmatitic melts. *Am. Mineral.* 95, 537–544. <https://doi.org/10.2138/am.2010.3157>
- Bau, M., 1996. Controls on the fractionation of isovalent trace elements in magmatic and aqueous systems: evidence from Y/Ho, Zr/Hf, and lanthanide tetrad effect. *Contrib Miner. Pet.* 123, 323–333. <https://doi.org/10.1007/s004100050317>

- Bau, M., 1991. Rare-earth element mobility during hydrothermal and metamorphic fluid rock interaction and the: Significance of the oxidation-state of europium. *Chem. Geol.* 93, 219–230. [https://doi.org/10.1016/0009-2541\(91\)90115-8](https://doi.org/10.1016/0009-2541(91)90115-8)
- Bell, K., Kjarsgaard, B.A., Simonetti, A., 1999. Carbonatites — into the twenty-first century. *J. Petrol.* 39, 1839–1845.
- Beus, A.A., Zalashkova, N.Y., 1964. Post-magmatic high temperature metasomatic processes in granitic rock. *Int. Geol. Rev.* 6, 668–681.
- Boily, M., Williams-Jones, A.E., 1994. The role of magmatic and hydrothermal processes in the chemical evolution of the Strange Lake plutonic complex, Quebec-Labrador. *Contrib. to Mineral. Petrol.* <https://doi.org/10.1007/BF00310609>
- Bonin, B., 2007. A-type granites and related rocks: Evolution of a concept, problems and prospects. *Lithos* 97, 1–29. <https://doi.org/10.1016/j.lithos.2006.12.007>
- Borodulin, G., Chevychelov, V.Y., Zaraysky, G., 2009. Experimental study of partitioning of tantalum, niobium, manganese, and fluorine between aqueous fluoride fluid and granitic and alkaline melts. *Dokl. Earth Sci.* 427, 868–873. <https://doi.org/10.1134/S1028334X09050341>
- Breiter, K., Da, J.I.R.I.F.R.Y., Seltmann, R., Thomas, R., 1997. Mineralogical evidence for two magmatic stages in the evolution of an extremely fractionated P-rich rare-metal granite : the Pdlesi Stock , Krus Hory , Czech Republic Podlesı. *J. Petrol.* 38, 1723–1739.
- Brown, M., 1994. The generation , segregation , ascent and emplacement of granite magma : the migmatite-to-crustally-derived granite connection in thickened orogens 36, 83–130.
- Cerny, P., Meintzer, R.E., Anderson, A.J., 1985. Extreme fractionation in rare-element granitic pegmatites: selected examples of data and mechanisms. *Can. Mineral.* 23, 381–421.

- Cesbron, F.P., 1989. Mineralogy of the rare-earth elements, in: Moller, P., Cern, P., Saupe, F. (Eds.), *Lanthanides, Tantalum and Niobium*. Springer, Berlin, Heidelberg, pp. 3–26.
- Chappell, B.W., White, A.J.R., 2001. Two contrasting granite types : 25 years later. *Australian J. Earth Sci.* 48, 489–499.
- Collins, W.J., Beams, S.D., White, A.J.R., Chappell, B.W., 1982. Nature and origin of A-type granites with particular reference to southeastern Australia. *Contrib. to Mineral. Petrol.* 80, 189–200. <https://doi.org/10.1007/BF00374895>
- Creaser, R.A., Price, R.C., Wormald, R.J., 1991. A-type granites revisited: Assessment of a residual-source model. *Geology* 19, 163–166.
- David, K., Schiano, P., Alle, C.J., 2000. Assessment of the Zr / Hf fractionation in oceanic basalts and continental materials during petrogenetic processes 178.
- Dostal, J., Kontak, D.J., Gerel, O., Gregory Shellnutt, J., Fayek, M., 2015. Cretaceous ongonites (topaz-bearing albite-rich microleucogranites) from Ongon Khairkhan, Central Mongolia: Products of extreme magmatic fractionation and pervasive metasomatic fluid: rock interaction. *Lithos* 236–237, 173–189. <https://doi.org/10.1016/j.lithos.2015.08.003>
- Drysdall, a. R., Jackson, N.J., Ramsay, C.R., Douch, C.J., Hackett, D., 1984. Rare element mineralization related in Precambrian alkali granites in the Arabian shield. *Econ. Geol.* 79, 1366–1377. <https://doi.org/10.2113/gsecongeo.79.6.1366>
- Eby, G.N., 1992. Chemical subdivision of the A-type granitoids : Petrogenetic and tectonic implications. *Geology* 20, 641–644.
- Eby, G.N., 1990. The A-type granitoids : A review of their occurrence and chemical characteristics and speculations on their petrogenesis. *Lithos* 26, 115–134.
- Eyal, M., Litvinovsky, B., Jahn, B.M., Zandvilevich, A., Katzir, Y., 2010. Origin and evolution of post-collisional magmatism : Coeval Neoroterozoic calc-alkaline and

- alkaline suites of the Sinai Peninsula. *Chem. Geol.* 269, 153–179.
<https://doi.org/10.1016/j.chemgeo.2009.09.010>
- Feng, Y., Samson, I.M., 2015. Replacement processes involving high field strength elements in the T Zone, Thor Lake rare-metal deposit. *Can. Mineral.* 53, 31–60.
<https://doi.org/10.3749/canmin.1400028>
- Fiege, A., Kirchner, C., Holtz, F., Linnen, R.L., Dziony a, W., 2011. Influence of fluorine on the solubility of manganotantalite (MnTa_2O_6) and manganocolumbite (MnNb_2O_6) in granitic melts - An experimental study. *Lithos* 122, 165–174.
<https://doi.org/10.1016/j.lithos.2010.12.012>
- Finch, A.A., McCreath, J.A., Reekie, C.D.J., Hutchison, W., Ismaila, A., Armour-Brown, A., Andersen, T., Simonsen, S.L., 2019. From mantle to Motzfeldt: A genetic model for syenite-hosted Ta,Nb-mineralisation. *Ore Geol. Rev.* 107, 402–416.
<https://doi.org/10.1016/j.oregeorev.2019.02.032>
- Frost, C.D., Frost, B.R., 2011. On Ferroan (A-type) Granitoids : Their compositional variability and modes of origin Fe-index. *Juornal Petrol.* 52, 39–53.
<https://doi.org/10.1093/petrology/egq070>
- Frost, C.D., Frost, B.R., Bell, J.M., Chamberlain, K.R., 2002. The relationship between A-type granites and residual magmas from anorthosite: evidence from the northern Sherman batholith, Laramie Mountains, Wyoming, USA. *Pre* 119, 45–71.
- Goldschmidt, V.M., 1937. The principles of distribution of chemical elements in minerals and rocks. *juornal Chem. Soc.* 655–673. <https://doi.org/10.1039/JR9370000655>
- Gysi, A.P., Williams-Jones, A.E., 2013. Hydrothermal mobilization of pegmatite-hosted REE and Zr at Strange Lake, Canada: A reaction path model. *Geochim. Cosmochim. Acta* 122, 324–352. <https://doi.org/10.1016/j.gca.2013.08.031>
- Hackett, D., 1986. Mineralized aplite-pegmatite at Jabal Sa'id, Hijaz region, Kingdom of Saudi Arabia. *J. African Earth Sci.* 4. [https://doi.org/10.1016/S0899-5362\(86\)80087-](https://doi.org/10.1016/S0899-5362(86)80087-2)

- Harris, N.B.W., Marzouki, F.M.H., Ali, S., 1986. The Jabel Sayid complex, Arabian Shield: geochemical constraints on the origin of peralkaline and related granites. *J. Geol. Soc. London*. 143, 287–295. <https://doi.org/10.1144/gsjgs.143.2.0287>
- Hassanen, M.A., 1997. Post-collision, A-type granites of Homrit Waggat Complex, Egypt: Petrological and geochemical constraints on its origin. *Precambrian Res.* 82, 211–236.
- Henderson, P., 1996. The rare earth elements: introduction and review, in: Jones, A. p., Wall, F., Williams, C.T. (Eds.), *Rare Earth Minerals: Chemistry, Origin and Ore Deposits*. Chapman & Hall, pp. 1–19.
- Huang, H., Niu, Y., Zhao, Z., Hei, H., Zhu, D., 2011. On the enigma of Nb-Ta and Zr-Hf fractionation-A critical review. *J. Earth Sci.* 22, 52–66. <https://doi.org/10.1007/s12583-011-0157-x>
- Irber, W., 1999. The lanthanide tetrad effect and its correlation with K/Rb, Eu/Eu*, Sr/Eu, Y/Ho, and Zr/Hf of evolving peraluminous granite suites. *Geochim. Cosmochim. Acta* 63, 489–508. [https://doi.org/10.1016/S0016-7037\(99\)00027-7](https://doi.org/10.1016/S0016-7037(99)00027-7)
- Jackson, N.J., Douch, C.J., 1986. Jabal Hamra REE-mineralized silexite, Hijaz region, Kingdom of Saudi Arabia. *J. African Earth Sci.* 4, 269–274. [https://doi.org/10.1016/S0899-5362\(86\)80088-4](https://doi.org/10.1016/S0899-5362(86)80088-4)
- Johnson, P.R.R., Andresen, A., Collins, A.S.S., Fowler, A.R.R., Fritz, H., Ghebreab, W., Kusky, T., Stern, R.J.J., 2011. Late Cryogenian-Ediacaran history of the Arabian-Nubian Shield: A review of depositional, plutonic, structural, and tectonic events in the closing stages of the northern east African Orogen. *J. African Earth Sci.* 61, 167–232. <https://doi.org/10.1016/j.jafrearsci.2011.07.003>
- Kemp, A.I.S., Hawkesworth, C.J., Paterson, B.A., Kinny, P.D., 2006. Episodic growth of the Gondwana supercontinent from hafnium and oxygen isotopes in zircon. *Nature* 439, 580–583. <https://doi.org/10.1038/nature04505>
- Kogarko, L.N., 2016. Geochemistry of fractionation of coherent elements (Zr and Hf)

during the profound differentiation of peralkaline magmatic systems: A case study of the Lovozero Complex. *Geochemistry Int.* 54, 1–6.

<https://doi.org/10.1134/S0016702916010079>

Kontak, D.J., 2006. Nature and origin of a LCT-suite pegmatite with late-stage sodium enrichment, Yarmouth County, Nova Scotia. I. Geological Setting and Petrology. *Can. Mineral.* 44, 563–598.

Kovalenko, V.I., 1995. The peralkaline granite-related Khaldzan-Buregtey rare metal (Zr, Nb, REE) deposit, western Mongolia. *Econ. Geol.* 90, 530–547.

<https://doi.org/10.2113/gsecongeo.90.3.530>

Kovalenko, V.I., Kovalenko, N.I., 1984. Problems of the origin, ore-bearing and evolution of rare-metal granitoids. *Phys. Earth Planet. Inter.* 35, 51–62.

[https://doi.org/10.1016/0031-9201\(84\)90033-5](https://doi.org/10.1016/0031-9201(84)90033-5)

Kovalenko, V.I., Yarmolyuk, V. V., Kozlovsky, a. M., Kovach, V.P., Sal'nikova, E.B., Kotov, a. B., Vladykin, N. V., 2007. Two types of magma sources of rare-metal alkali granites. *Geol. Ore Depos.* 49, 442–466.

<https://doi.org/10.1134/S1075701507060025>

Küster, D., 2009. Granitoid-hosted Ta mineralization in the Arabian-Nubian Shield: Ore deposit types, tectono-metallogenic setting and petrogenetic framework. *Ore Geol. Rev.* 35, 68–86. <https://doi.org/10.1016/j.oregeorev.2008.09.008>

Landenberger, B., Collins, W.J., 1996. Derivation of A-type granites from a dehydrated charnockitic lower crust: Evidence from the Chaelundi Complex, Eastern Australia. *J. Petrol.* <https://doi.org/10.1093/petrology/37.1.145>

Linnen, R.L., 1998. The solubility of Nb-Ta-Zr-Hf-W in granitic melts with Li and Li + F: Constraints for mineralization in rare metal granites and pegmatites. *Econ. Geol.* 93, 1013–1025. <https://doi.org/10.2113/gsecongeo.93.7.1013>

Linnen, R.L., Cuney, M., 2005. Granite-related rare-element deposits and experimental constraints on Ta-Nb-W-Sn-Zr-Hf mineralization, in Linnen RL and Samson IM,

eds., rare-element geochemistry and mineral deposits., in: Geological Association of Canada, GAC, Short Course.

Linnen, R.L., Keppler, H., 2002. Melt composition control of Zr/Hf fractionation in magmatic processes. *Geochim. Cosmochim. Acta* 66, 3293–3301.
[https://doi.org/10.1016/S0016-7037\(02\)00924-9](https://doi.org/10.1016/S0016-7037(02)00924-9)

Linnen, R.L., Keppler, H., 1997. Columbite solubility in granitic melts: consequences for the enrichment and fractionation of Nb and Ta in the Earth's crust. *Contrib. to Mineral. Petrol.* 128, 213–227. <https://doi.org/10.1007/s004100050304>

Linnen, R.L., Samson, I.M., Williams-Jones, A.E., Chakhmouradian, A.R., 2014. Geochemistry of the Rare-Earth Element, Nb, Ta, Hf, and Zr Deposits, in: *Treatise on Geochemistry*. Elsevier, pp. 543–568. <https://doi.org/10.1016/B978-0-08-095975-7.01124-4>

Linnen, R.L., Van Lichtervelde, M., Černý, P., 2012. Granitic pegmatites as sources of strategic metals. *Elements* 8, 275–280. <https://doi.org/2113/gselements.8.4.275>

Linnen, R.L., Williams-Jones, A.E., 1993. Mineralogical constraints on magmatic and hydrothermal Sn-W-Ta-Nb mineralization at the Nong Sua aplite-pegmatite, Thailand. *Eur. J. Mineral.* 5, 721–736. <https://doi.org/10.1127/ejm/5/4/0721>

Masuda, A., Ikeuchi, Y., 1979. Lanthanide tetrad effect observed in marine environments. *Geochem. J.* 13, 19–22.

Masuda, A., Kawakami, O., Dohmoto, Y., Takenaka, T., 1987. Lanthanide tetrad effects in nature: Two mutually opposite types W and M. *Geochem. J.* 21, 119–124.

McDonough, W.F., Sun, S. -s., 1995. The composition of the Earth. *Chem. Geol.* 120, 223–253. [https://doi.org/https://doi.org/10.1016/0009-2541\(94\)00140-4](https://doi.org/https://doi.org/10.1016/0009-2541(94)00140-4)

Migdisov, A., Williams-Jones, A.E., Brugger, J., Caporuscio, F.A., 2016. Hydrothermal transport, deposition, and fractionation of the REE: Experimental data and thermodynamic calculations. *Chem. Geol.* 439, 13–42.

<https://doi.org/10.1016/j.chemgeo.2016.06.005>

- Migdisov, A.A., Williams-Jones, A.E., 2014. Hydrothermal transport and deposition of the rare earth elements by fluorine-bearing aqueous liquids. *Miner. Depos.* 49, 987–997. <https://doi.org/10.1007/s00126-014-0554-z>
- Miller, R.R., 1996. Structural and textural evolution of the strange Lake Peralkaline rare-element (NYF) granitic pegmatite, Quebec-Labrador. *Can. Mineral.* 34, 349–371.
- Moghazi, A.-K.M., Iaccheri, L.M., Bakhsh, R.A., Kotov, A.B., Ali, K.A., 2015. Sources of rare-metal-bearing A-type granites from Jabel Sayed complex, Northern Arabian Shield, Saudi Arabia. *J. Asian Earth Sci.* 107, 244–258. <https://doi.org/10.1016/j.jseaes.2015.04.042>
- Moghazi, A.M., Ali, K.A., Wilde, S.A., Zhou, Q., Andersen, T., Andresen, A., El-enen, M.M.A., Stern, R.J., 2012. Lithos Geochemistry , geochronology , and Sr – Nd isotopes of the Late Neoproterozoic Wadi Kid volcano-sedimentary rocks , Southern Sinai , Egypt : Implications for tectonic setting and crustal evolution. *LITHOS* 154, 147–165. <https://doi.org/10.1016/j.lithos.2012.07.003>
- Moghazi, A.M., Harbi, H.M., Ali, K.A., 2011. Geochemistry of the Late Neoproterozoic Hadb adh Dayheen ring complex, Central Arabian Shield: Implications for the origin of rare-metal-bearing post-orogenic A-type granites. *J. Asian Earth Sci.* 42, 1324–1340. <https://doi.org/10.1016/j.jseaes.2011.07.018>
- Mohamed, M.A., 2013. Immiscibility between silicate magma and aqueous fluids in Egyptian rare-metal granites: melt and fluid inclusions study. *Arab. J. Geosci.* 6, 4021–4033. <https://doi.org/10.1007/s12517-012-0664-9>
- Möller, P., Černý, P., Saupe, F., 1989. Rare earth mineral deposits and their industrial importance, in: *Lanthanides, Tantalum and Niobium*. Springer Berlin Heidelberg, Berlin, Heidelberg, pp. 171–188. https://doi.org/10.1007/978-3-642-87262-4_6
- Möller, V., Williams-Jones, A.E., 2017. Magmatic and hydrothermal controls on the mineralogy of the basal zone, nechalacho REE-Nb-Zr deposit, Canada. *Econ. Geol.*

- 112, 1823–1856. <https://doi.org/10.5382/econgeo.2017.4531>
- Möller, V., Williams-Jones, A.E., 2016. Petrogenesis of the Nechalacho Layered Suite, Canada: Magmatic evolution of a REE–Nb-rich nepheline syenite intrusion. *J. Petrol.* 57, 229–276. <https://doi.org/10.1093/petrology/egw003>
- Nehlig, P., Genna, A., Asfirane, F., 2002. A review of the Pan-African evolution of the Arabian shield. *GeoArabia* 7, 103–124.
- Novak, M., Cerny, P., 1998. Niobium-tantalum oxide minerals from complex granitic pegmatites in the Moldanubicum, Czech Republic. *Can. Mineral.* 36, 659–672.
- Peretyazhko, I.S., Savina, E.A., 2010. Tetrad effects in the rare earth element patterns of granitoid rocks as an indicator of fluoride-silicate liquid immiscibility in magmatic systems. *Petrology* 18, 514–543. <https://doi.org/10.1134/S086959111005005X>
- Piilonen, P.C., McDonald, A.M., Poirier, G., Rowe, R., Larsen, A.O., 2012. The mineralogy and crystal chemistry of alkaline pegmatites in the Larvik Plutonic Complex, Oslo rift valley, Norway. Part 1. Magmatic and secondary zircon: implications for petrogenesis from trace-element geochemistry. *Mineral. Mag.* 76, 649–672. <https://doi.org/10.1180/minmag.2012.076.3.15>
- Pollard, P.J.G.C. and G.P.A. with the D. of G.-H.D. of T. and N., 1989. Geologic characteristics and genetic problems associated with the development of granite-hosted deposits of tantalum and niobium, in: Möller, P., Černý, P., Saupé, F. (Eds.), *Lanthanides, Tantalum and Niobium*. Springer Berlin Heidelberg, Berlin, Heidelberg, pp. 240–256.
- Qadhi, T., Moufti, A., 2008. Geochemical characteristic of the rare-metal rich granite in the Ghurayyah-Dubbagh Area, north western Arabian Shield, Saudi Arabia. *Ann. Geol. Surv. Egypt* XXX, 149.
- Robinson, F.A., Foden, J.D., Collins, A.S., Payne, J.L., 2014. Arabian Shield magmatic cycles and their relationship with Gondwana assembly: Insights from zircon U-Pb and Hf isotopes. *Earth Planet. Sci. Lett.* 408, 207–225.

<https://doi.org/10.1016/j.epsl.2014.10.010>

- Salvi, Stefano, Fontan, F., Monchoux, P., Williams-Jones, a. E., Moine, B., 2000. Hydrothermal mobilization of high field strength elements in Alkaline Igneous Systems: Evidence from the Tamazeght complex (Morocco). *Econ. Geol.* 95, 559–575. <https://doi.org/10.2113/gsecongeo.95.3.559>
- Geochim. Cosmochim. Acta* 60, 1917–1932. [https://doi.org/10.1016/0016-7037\(96\)00071-3](https://doi.org/10.1016/0016-7037(96)00071-3)
- Salvi, S., Williams-Jones, A.E., 1996. The role of hydrothermal processes in concentrating high-field strength elements in the Strange Lake peralkaline complex, northeastern Canada. *Geochim. Cosmochim. Acta* 60, 1917–1932. [https://doi.org/10.1016/0016-7037\(96\)00071-3](https://doi.org/10.1016/0016-7037(96)00071-3)
- Salvi, S., Williams-Jones, A.E., 1991. Reply to Comment by T. C. Birkett and R. R. Miller on “The role of hydrothermal processes in the granite-hosted Zr, Y, REE deposit at Strange Lake, Quebec/Labrador: Evidence from fluid inclusions.” *Geochim. Cosmochim. Acta* 55, 3447–3449. [https://doi.org/10.1016/0016-7037\(91\)90504-X](https://doi.org/10.1016/0016-7037(91)90504-X)
- Salvi, S., Williams-Jones, A.E., 1990. The role of hydrothermal processes in the granite-hosted Zr, Y, REE deposit at Strange Lake, Quebec/Labrador: Evidence from fluid inclusions. *Geochim. Cosmochim. Acta* 54, 2403–2418. [https://doi.org/10.1016/0016-7037\(90\)90228-D](https://doi.org/10.1016/0016-7037(90)90228-D)
- Schmitt, A.K., Trumbull, R.B., Dulski, P., Emmermann, R., 2002. Zr-Nb-REE mineralization in peralkaline granites from the Amis Complex , Brandberg (Namibia): Evidence for magmatic pre-enrichment from melt inclusions. *Econ. Geol.* 97, 399–413.
- Shannon, R.D., 1976. Revised effective ionic radii and systematic studies of interatomic distances in halides and chalcogenides. *Acta Crystallogr. Sect. A Cryst. physics, diffraction, Theor. Gen. Crystallogr.* 32, 751–767.

- Siegel, K., Vasyukova, O. V., Williams-Jones, A.E., 2018. Magmatic evolution and controls on rare metal-enrichment of the Strange Lake A-type peralkaline granitic pluton, Québec-Labrador. *Lithos* 308–309, 34–52.
<https://doi.org/10.1016/j.lithos.2018.03.003>
- Sorensen, H., 1992. Agpaitic nepheline syenites : A potential source of rare elements 7, 417–427.
- Stern, R.J., 1994. ARC Assembly and continental collision in the Neoproterozoic East African Orogen: implications for the consolidation of Gondwanaland. *Annu. Rev. Earth Planet. Sci.* 22, 319–351.
<https://doi.org/10.1146/annurev.ea.22.050194.001535>
- Stern, R.J., Ali, K.A., Lie, J.P., Johnson, P.R., Kozdroj, W., Kattan, F.H., 2010. Distribution and significance of pre-Neoproterozoic zircons in juvenile Neoproterozoic Igneous rocks of the Arabian-Nubian Shield. *Am. J. Sci.* 310, 791–811. <https://doi.org/10.2475/09.2010.02>
- Stoeser, D.B., 1986. Distribution and tectonic setting of plutonic rocks of the Arabian Shield. *J. African Earth Sci.* 4, 21–46. [https://doi.org/10.1016/S0899-5362\(86\)80066-5](https://doi.org/10.1016/S0899-5362(86)80066-5)
- Thomas, R., Webster, J.D., Rhede, D., Seifert, W., Rickers, K., Förster, H., Heinrich, W., Davidson, P., 2006. The transition from peraluminous to peralkaline granitic melts : Evidence from melt inclusions and accessory minerals. *Lithos* 91, 137–149.
<https://doi.org/10.1016/j.lithos.2006.03.013>
- Turkistany, A.R., Ramsay, C.R., 1982. Mineralized apogranite associated with alkali granite at Jabal Sa'id, Kingdom of Saudi Arabia. *Deputy Ministry Miner. Resour.* PP-1, 78-88.
- Turner, S.P., Foden, J.D., Morrison, R.S., 1992. Derivation of some A-type magmas by fractionation of basaltic magma : An example from the Padthaway Ridge , South Australia. *Lithos* 28, 151–179.

- U.S. Geological Survey, 2019, Mineral commodity summaries 2019: U.S. Geological Survey, 200 p., <https://doi.org/10.3133/70202434>.
- Van Lichtervelde, M., Holtz, F., Hanchar, J.M., 2010. Solubility of manganotantalite, zircon and hafnon in highly fluxed peralkaline to peraluminous pegmatitic melts. *Contrib. to Mineral. Petrol.* 160, 17–32. <https://doi.org/10.1007/s00410-009-0462-x>
- Van Lichtervelde, M., Melcher, F., Wirth, R., L, M. V, M, F., W, R., Van Lichtervelde, M., Melcher, F., Wirth, R., 2009. Magmatic vs. hydrothermal origins for zircon associated with Tantalum mineralization in the Tanco pegmatite, Manitoba, Canada. *Am. Mineral.* 94, 439–450. <https://doi.org/10.2138/am.2009.2952>
- Van Lichtervelde, M., Salvi, S., Beziat, D., Linnen, R.L., 2007. Textural features and chemical evolution in tantalum oxides: Magmatic versus hydrothermal origins for Ta mineralization in the Tanco Lower pegmatite, Manitoba, Canada. *Econ. Geol.* 102, 257–276. <https://doi.org/10.2113/gsecongeo.102.2.257>
- Vasyukova, O., Williams-Jones, A.E., 2016. The evolution of immiscible silicate and fluoride melts : Implications for REE ore-genesis. *Geochim. Cosmochim. Acta* 172, 205–224. <https://doi.org/10.1016/j.gca.2015.09.018>
- Vasyukova, O., Williams-Jones, A.E., 2014. Fluoride-silicate melt immiscibility and its role in REE ore formation: Evidence from the Strange Lake rare metal deposit, Quebec-Labrador, Canada. *Geochim. Cosmochim. Acta* 139, 110–130. <https://doi.org/10.1016/j.gca.2014.04.031>
- Vasyukova, O. V., Williams-Jones, A.E., 2019. Tracing the evolution of a fertile REE granite by modelling amphibole-melt partitioning, the Strange Lake story. *Chem. Geol.* 514, 79–89. <https://doi.org/10.1016/j.chemgeo.2019.03.030>
- Vasyukova, O. V., Williams-Jones, A.E., Blamey, N.J.F.F., 2016. Fluid evolution in the Strange Lake granitic pluton, Canada: Implications for HFSE mobilisation. *Chem. Geol.* 444, 83–100. <https://doi.org/10.1016/j.chemgeo.2016.10.009>
- Veksler, I. V., Thomas, R., Schmidt, C., 2002. Experimental evidence of three coexisting

- immiscible fluids in synthetic granitic pegmatite. *Am. Mineral.* 87, 775–779.
- Wang, R., Zhao, G., Wang, D., Lu, J., Xu, S., 2000. Differentiation and accumulation of fluids in A-type granites: Evidence from accessory mineral study. *Chinese Sci. Bull.* 45, 1609–1613. <https://doi.org/10.1007/BF02886223>
- Wang, R.C., Chen, X.M., Hu, H., Liu, C.S., Xu, S.J., Fontan, F., de Parseval, P., 2003. Accessory minerals in the Xihuashan Y-enriched granitic complex, southern China: A record of magmatic and hydrothermal stages of evolution. *Can. Mineral.* 41, 727–748.
- Watson, E.B., 1979. Zircon saturation in felsic liquids: Experimental results and applications to trace element geochemistry. *Contrib. to Mineral. Petrol.* 70, 407–419. <https://doi.org/10.1007/BF00371047>
- Whalen, J.B., Currie, K.L., Chappell, B.W., 1987. A-type granites: geochemical characteristics, discrimination and petrogenesis. *Contrib. to Mineral. Petrol.* 95, 407–419. <https://doi.org/10.1007/BF00402202>
- White, W.M., 2013. *Geochemistry*. John Wiley & Sons.
- Williams-Jones, A.E., Migdisov, A.A., Samson, I.M., 2012. Hydrothermal mobilisation of the rare earth elements--a tale of “ceria” and “yttria.” *Elements* 8, 355–360.
- Yang, L., Hinsberg, V.J. Van, 2019. Liquid immiscibility in the CaF₂-granite system and trace element partitioning between the immiscible liquids. *Chem. Geol.* 511, 28–41. <https://doi.org/10.1016/j.chemgeo.2019.02.017>
- Yang, W.-B., Niu, H.-C., Shan, Q., Sun, W.-D., Zhang, H., Li, N.-B., Jiang, Y.-H., Yu, X.-Y., 2014. Geochemistry of magmatic and hydrothermal zircon from the highly evolved Baerzhe alkaline granite: implications for Zr–REE–Nb mineralization. *Miner. Depos.* 49, 451–470. <https://doi.org/10.1007/s00126-013-0504-1>
- Zhang, X., Yuan, L., Xue, F., Zhang, Y., 2012. Contrasting Triassic ferroan granitoids from northwestern Liaoning, North China: Magmatic monitor of Mesozoic

decratonization and a craton – orogen boundary. *Lithos* 144–145, 12–23.

<https://doi.org/10.1016/j.lithos.2012.03.022>

Zhu, Z.Y., Wang, R.C., Che, X.D., Zhu, J.C., Wei, X.L., Huang, X., 2015. Magmatic-hydrothermal rare-element mineralization in the Songshugang granite (northeastern Jiangxi, China): Insights from an electron-microprobe study of Nb-Ta-Zr minerals. *Ore Geol. Rev.* 65, 749–760. <https://doi.org/10.1016/j.oregeorev.2014.07.021>

Chapter 2

2 The petrology and lithology of Al-Ghurayyah Nb, Ta, Zr, Y, REE rare-metal granite, the Arabian Shield, Saudi Arabia.

2.1 Introduction

Rare-metal alkaline granites contain high concentrations of high field strength elements (HFSE) and rare earth elements (REE). The Arabian Shield hosts one of the largest alkaline granite fields in the world, forming about 2 % of its area (Moghazi et al., 2011; Stoesser, 1986). Many of these granites are enriched in Nb, Zr, Y, and REE, such as Al-Ghurayyah and Jabal Sayid (Fig. 2.1) (Harris et al., 1986; Küster, 2009; Moghazi et al., 2011; Turkistany and Ramsay, 1982). The mineralization is usually disseminated throughout the granites (e.g., Al-Ghurayyah, Qadhi and Moufti, 2008) or concentrated in aplites and pegmatites in the apical zones of the granites (e.g., Jabal Sayid Drysdall et al., 1984; Turkistany and Ramsay, 1982).

Several studies have investigated the mineralized rare metal granite in the Arabian Shield (Ali et al., 2014; Drysdall et al., 1984; du Bray, 1986; Elliott, 1983; Elliott et al., 2002; Hackett, 1986; Moghazi et al., 2015, 2011; Qadhi and Moufti, 2008; Radain et al., 1981; Staatz and Brownfield, 1986; Turkistany and Ramsay, 1982). These studies mostly described the host rock and provided whole-rock chemistry of the granites (Jabal Sayid, Al-Ghurayyah, Hdb Ad Dyaheen).

Al-Ghurayyah is one of the most prospective silica-rich alkaline HFSE deposits in the world (Küster, 2009). In 2006, Tertiary Minerals PCL published an evaluation of Al-Ghurayyah and estimated an inferred ore resource of 385 million tons grading 245 g/t Ta₂O₅, 2840 g/t Nb₂O₅, 8915 g/t ZrO₂, and 1270 g/t Y₂O₃ (Cheetham et al., 2007). It was discovered in 1964 during an airborne geophysical survey. Since then, only a few studies have investigated the deposit and provided petrographic and geochemical data (Elliott et al., 2002; Qadhi and Moufti, 2008). The only published discussion of the mineral chemistry of the deposit was a report by the USGS (Staatz and Brownfield, 1986). The

report included geochemical analyses of zircon, thorite, synchysite (reported as doverite ($\text{CaY}(\text{CO}_3)_2\text{F}$) by Staatz and Brownfield, 1986), and senaite (a rare mineral with composition $\text{Pb}(\text{Ti, Fe, Mn})_{21}\text{O}_{38}$). Qadhi and Mufti (2008) studied Al-Ghurayyah granite and provided information on the whole rock chemistry and described the modal mineralogy of the granite. They suggested that Al-Ghurayyah is related to the nearby Al-Dabbagh batholith. Nonetheless, the ore mineral chemistry has yet to be characterized. The only age determination of Al-Ghurayyah is a Rb-Sr whole-rock isochron method (Qadhi and Mufti, 2008). Because of the high mobility of Rb and Sr during post-crystallization events, the Rb-Sr isochron ages may not represent the age of the intrusion or the mineralization (Nebel and Mezger 2008), thus additional age dating is needed.

This study aims to characterize Al-Ghurayyah rare-metal granite through detailed petrographical and mineralogical descriptions. The age of the granite and the mineralization will be constrained by U-Pb age dates from zircon so that the granite can be interpreted in terms of its metallogenic setting. Moreover, the study will investigate the relative importance roles of magmatic and hydrothermal processes in the formation of Al-Ghurayyah rare-metal deposit.

2.2 Geological setting

The closing of the Mozambique Ocean led to the formation of the Arabian Shield through the accretion of inter-oceanic island arcs (Agar, 1992; Nehlig et al., 2002; Robinson et al., 2014; Stern, 1994). The accretion took place from 900 to 550 Ma and led to an amalgamation of nine distinct terranes: the Asir, the Tathlith, the Ar-Rayn, the Ad-Dawadimi, the Afif (and the Khida sub-terrane), the Ha'il, the Jeddah, the Hijaz, and the Midyan terranes (Johnson et al., 2011) (Fig. 2.1). The terranes are marked by the presence of ultramafic bodies within orogenic belts (Agar, 1992; Robinson et al., 2014). The Arabian Shield accretion was followed by a period of extensional tectonism during an orogenic collapse and the emplacement of a large volume of alkaline magma that formed one of the world's largest alkali granite fields (Stoeser, 1986). The radiometric age dating (Rb-Sr) of the alkali granites estimated the emplacement time to be between 686 and 518 Ma, with younger ages trending toward the northeastern part of the shield (Stoeser, 1986). Several alkaline granites in the Arabian Shield are reported to contain

high concentrations of HFSE and REE, such as Dyaheen, Um-Alberak, and Jabal Hamra (Jackson, 1986; Jackson and Douch, 1986; Johnson et al., 2011; Küster, 2009). However, Al-Ghurayyah alkaline granite is considered to have the greatest economic potential (Cheetham et al., 2007; Küster, 2009).

Al-Ghurayyah is a post-collisional within-plate A-type alkaline granite located in northwest Saudi Arabia (Fig. 2.1) (Johnson et al., 2011; Küster, 2009; Qadhi and Moufti, 2008). The granite is a part of the Midyan terrane and intruded the sedimentary-volcanoclastic succession of Silasia Formation (>710 Ma; Johnson, 2006). The Midyan terrane is 50 to 60 km wide and bordered by the coastal plain of the Red Sea to the west, Phanerozoic sedimentary cover to the east, the shore of the Red Sea and the Gulf of Aqaba to the north and Yanbu suture zone at the south. It consists of layered mafic volcanoclastic and volcanic rocks of Al-Zaam and the Bayda Groups that are locally deformed and have been metamorphosed to amphibolite facies. The layered rocks of the Al-Zaam and the Bayda were intruded by the Muwaylih plutonic suite (725-710 Ma U-Pb zircon) (Johnson, 2006), the Qazaz diorite-monzogranite-syenogranite super suite (635-620 Ma U-Pb zircon), and the Al-Bad granite suite (597.4 ± 4.8 U-Pb zircon; Robinson et al., 2014). The Al-Bad super suite is a collective term for post-orogenic intrusions in the Midyan terrane. It consists of alkaline granite and syenogranite and hosts several occurrences of uranium, rare-earth elements, niobium, and fluorine-rich granites, such as Al-Ghurayyah and Jabal Tawlah (Johnson, 2006).

Al-Ghurayyah is located in the north-central part of the Midyan terrane. It was suggested that Al-Ghurayyah is co-magmatic with the large Dabbagh alkaline granite complex located 2 km west of Al-Ghurayyah (Johnson et al., 2011; Qadhi and Moufti, 2008). Al-Ghurayyah is a small sub-circular stock (900 m in diameter) that consists of several outcrops that are separated by Quaternary sediments (Fig. 2.2). The main rock type at Al-Ghurayyah is a medium-grained to porphyritic pink granite that locally is red and gray granite due to the alteration of iron-rich minerals (sodic amphibole and aegirine). The granite experienced variable degrees of silicification, chlorite alteration, and muscovite alteration, but alteration intensity increases near quartz veins. In the north-east part of Al-Ghurayyah, silicification is more intense. The contact of Al-Ghurayyah granite with

country rocks (the Silasia formation) where exposed is sharp. Near the contact with the country rocks, a marginal unit was recognized, and it is characterized by a fine-grained pinkish color that changes light pink to dark-brown to reddish-brown at the contact with the country rock. The contacts of the marginal unit with the country rock and the porphyritic granite are sharp. The marginal unit was described as a country rock by Elliott et al. (2002); however, its mineralogical composition does not match the description of volcanic metasediment of the country rock. A unique composite-body that consists of four segments was observed to cut the main granite in the southern part of the intrusion (Fig. 2.3). The composite-body has an irregular shape and is in sharp contact with Al-Ghurayyah porphyritic granite. It consists of zones of quartz, zircon-columbite, K-feldspar (microcline) and mica-zircon zones.

Two types of quartz veins can be recognized in Al-Ghurayyah. The first type is white quartz veins with variable fluorite concentrated in the center of the vein (white-quartz vein). The thickness of these veins ranges from 10 to 30 cm. This type is not mineralized and usually is present near fault zones. This type will not be investigated in this study. The second type is greyish white quartz pods and veins that are less common relative to the white quartz veins and are smaller (5-10 cm thick). They are mineralized with zircon and columbite. The mineralogy is variable with some veins containing up to 40% microcline and 5% muscovite in addition to quartz. This type will be referred to as the quartz veins in this study. The main rock units in Al-Ghurayyah are summarized in Table 2.1.

Several faults cut the granite, which resulted in the formation of four large blocks that are now sub-circular bodies approximately 300 meters in diameter, and three small bodies ranging from 50 to less than 100 meters in diameter. The main fault is east-west trending and passes through the middle of the intrusion (Elliott et al., 2002). Additionally, the granite was cut by several mafic and felsic dykes..

2.3 Methodology

Samples from the host granites, marginal unit, and quartz veins were collected for petrographic and geochemical studies (Fig. 2.2). Polished thin sections were prepared in the Department of Earth Sciences at the University of Western Ontario, Canada, and the Faculty of Earth Sciences, at King Abdul Aziz University, Jeddah, Saudi Arabia.

Polished thin sections were studied using a petrographic microscope and a scanning electron microscope equipped with energy dispersive spectroscopy (SEM-EDS) to obtain mineralogical, texture and mineral composition data at the Department of Earth Sciences at the University of Western Ontario, Canada. Major elements compositions of minerals and backscattered electron images (BSEI) were obtained using a JEOL JCM 6000 benchtop SEM equipped with EDS (B-SEM). Data were collected at 15 kV acceleration voltage at high vacuum mode. Quantitative mineral compositions, cathodoluminescence (CL), and EDS analyses were determined on a JEOL JXA-8530F field-emission electron microprobe (EMPA) at Earth and Planetary Materials Analysis Laboratory at the University of Western Ontario, Canada. The analytical conditions of the EMPA were 20 kV probe current, 40-60 nA accelerating voltage and beam diameter ranging from 1 to 15 micrometer. The standards were synthetic zircon for Zr and Si, rutile for Ti, albite for Na and Al, fayalite for Fe for iron in mica, fluorite for F, orthoclase for K, anorthite for Ca. Pure metal standards (serial 2AG-METM25-44, Astimex Standards Limited) were used for iron in oxide accessory minerals, Mn, Th, and U.

Raman spectroscopy was used to identify the types of mica that show low EMPA totals. Raman analyses were carried out using Renishaw InVia Refelex Raman Spectrometer with a 514nm wavelength at Surface Science Western the University of Western Ontario, Canada. The collected data were compared to the RRUFF database using CrystalSleuth software (Laetsch and Downs, 2006).

Ages were determined from U-Pb analyses of zircon. The zircon crystals were selected from the host granite and mineralized rocks of Al-Ghurayyah. Ages were determined at the University of Toronto using a laser-ablation inductively coupled plasma mass spectrometer (LA-ICP-MS) technique. An NWR excimer laser was used with 20 micrometer beam diameter, 7 to 10 repetition rate, and 3.6 to 4.3 J/cm² energy. Five

passes were taken on each analysis spot. The ICP system is an Agilent 7900 ICP-MS. Ar gas flow was 0.85 L/min with 20 milliseconds were used as wash delay. The analyzed isotopes were ^{88}Sr , ^{206}Pb , ^{207}Pb , ^{208}Pb , ^{232}Th , ^{238}U . Strontium was used as an indicator of alteration. Before starting the analyses, and the analyzed spots were pre-ablated to clean them from any dust or unwanted material on the surface. To avoid losing U with drilling in the grains, a rastering technique was followed to obtain a large material amount with less drilling. In sample were the desired areas for analysis are zoned, a line technique was followed. Data reduction was performed using a portogram written by Davis (1982). Zircon standard was from zircon sample DD91-1 from Lac Fourniere pluton, the Pontiac and Abitibi subprovinces, Quebec (Davis, 2002), and sample DD85-17 from mafic tonalite, Marmion batholith, south-central Wabigoon subprovince, Canada (Tomlinson et al., 2003).

Lithochemical analyses of samples from the porphyritic granite, marginal unit, and quartz veins were carried out by Activation Laboratories Ltd (Actlabs), Ancaster, Ontario, Canada. Samples were crushed and pulverized using mild steel. Lithium metaborate/tetraborate fusion glass pellets were digested in a weak nitric acid solution. Major and trace elements were analyzed using fusion ICP and ICP-MS technique. The analyzed oxides and elements and the limits of detection are summarized in Appendix A. Analytical precision was calculated from duplicate analyses and ranges from 0.1 to 5 relative % for major elements, 0.5 to 8 relative % for REE and HFSE, and up to 20 % for other trace elements. Fluorine analysis was performed by the ion-selective electrode technique. In this technique, samples were fused with lithium metaborate/tetraborate in an induction furnace to release the fluoride ions to the matrix and then dissolved in dilute nitric acid. Next, the solution was complexed with an ionic strength adjusted with ammonium citrate buffer before the analysis. The fluoride ion electrode is immersed in this solution to measure the fluoride-ion activity directly. An automated fluoride analyzer from Mandel Scientific is used for the analysis.

2.4 Petrography

Mineralization of HFSE and REE minerals in Al-Ghurayyah occurs in all of the rock units except for the white-quartz veins. Disseminated and aggregate styles were identified

in Al-Ghurayyah. The disseminated mineralization style is present in the amphibole-bearing granite, the porphyritic granite and the marginal unit, whereas the aggregate mineralization style occurs in the composite-body and the quartz veins. Therefore, the petrography of Al-Ghurayyah will be discussed based on these two mineralization styles. Table 2.2 contains the name and mineral formula of common minerals observed in Al-Ghurayyah.

2.4.1 Disseminated mineralization style

The disseminated mineralization style is hosted by amphibole-bearing granite, porphyritic granite, and the marginal unit. The amphibole-bearing granite is rare and only observed in one locality in the southern bodies (Fig. 2.4 A). This granite is light grey, medium-grained and consists of 40 to 45 % plagioclase, 25 % quartz, 20 to 25 % microcline, < 5 % sodic amphibole, and < 1 % mica (trilithionite) based on visual estimation of mineral proportions. Accessory minerals are zircon and pyrochlore. All the plagioclase in Al-Ghurayyah occurs as lath-shaped subhedral crystals of albite (determine by electron microprobe, see below) and forms the bulk of the matrix. Quartz occurs as fine-grained (100 μm) subhedral to rounded crystals in the matrix with albite. Quartz also occurs as large phenocrysts (1 mm) that display a snowball texture with inclusions of albite arranged along the growth boundaries (Fig. 2.4 B). K-feldspar occurs as subhedral to anhedral grains that ranges in size from 300 μm to 1 mm, that display cross-hatched twinning, which is interpreted as microcline. Sodic amphibole occurs as subhedral crystals with strong dark blue to green pleochroism (Fig. 2.4 C). Zircon is present as disseminated, subhedral, dark brown to dark yellow, prismatic crystals, which show a close spatial-temporal association with pyrochlore (Fig. 2.4 D & E). Pyrochlore occurs as euhedral to subhedral yellow crystals ranging in size from 100 to 200 μm . Pyrochlore typically displays a reddish to dark brown alteration rim (Fig. 2.4 D & E).

The dominant rock type in Al-Ghurayyah is the porphyritic granite and followed by the medium-grained granite. The porphyritic and the medium-grained granite have the same mineralogical composition. Visual estimation of the granite mineralogical composition indicates that it consists of approximately 40 % quartz, 35 % albite, 20 % K-feldspar (microcline), and < 1 % mica (trilithionite). Quartz, and less commonly microcline, form

large euhedral to subhedral phenocrysts (up to 10 mm) and display a snowball texture where albite, fine-grained quartz, zircon, pyrochlore, and mica crystals (trilithionite) are trapped along quartz growth zones (Fig. 2.5 A and B). Quartz in the matrix is fine-grained (100 μm) and anhedral. The fine-grain quartz is found as inclusions in the large quartz phenocryst (20 μm) indicating early crystallization of the fine-grain quartz. Albite occurs as lath-shaped crystals (200 μm) making up about 80 % of the matrix minerals and has intergranular contacts with fine-grained quartz, zircon, and pyrochlore. Microcline is generally medium-grained anhedral crystals intergrown with albite in the matrix. Locally, microcline phenocrysts display a snowball texture, which contains inclusions of trilithionite and albite (Fig. 2.5 B). Accessory minerals include zircon, which is the most common HFSE mineral followed by pyrochlore, and secondary columbite, and rutile. Secondary minerals include chlorite, muscovite, columbite, rutile, fluorite, and hematite. Two types of mica were recognized in the host granite. The first type occurs in the matrix and as inclusions in the phenocryst minerals (quartz and microcline) and forms < 1 % of the modal content of the rock. The average composition of this type is close to a trilithionite composition (determined by electron microprobe and confirmed by Raman spectroscopy, Table 2.4, and Fig. 2.17). The second type is more abundant and forms up to 3 % of the modal content of the highly altered rock. It is associated with late quartz (silicification) and occurs as fan-shape crystals that locally are replaced by chlorite. The average composition of this type is close to end-member muscovite (Table 2.4). Previous studies have described sodic amphibole and sodic pyroxene as common mafic minerals in the porphyritic granite and the medium-grained granite (Küster, 2009; Qadhi and Moufti, 2008; Staatz and Brownfield, 1986); however, sodic amphibole and pyroxene are not common minerals in most of the samples collected in this study and their occurrences are limited to the grey granite unit identified at the south body.

In the disseminated mineralization style, at least two alteration events can be recognized. The first event is not widespread and samples affected by this event show hematite staining, which indicates to the alteration of Fe-rich mafic minerals (sodic-amphibole). The second alteration event is silicification and it is common. It occurs in variable intensity and is commonly associated with secondary muscovite. In this type of alteration, a late quartz occurs as irregular large crystals or veinlets that replace albite. In highly

silicified rocks, albite is rare to absent, whereas microcline is the common feldspar phase. Muscovite alteration is associated with silicification, where it is commonly present as fan-shaped crystals and associated with late quartz secondary zircon and acicular columbite, rutile, and fluorite (Fig. 2.5 C and D).

The marginal unit is fine-grained and consists of 70 to 80 % quartz and albite (very difficult to distinguish between them due to the fine grain size), 10 to 15 % zircon, 5 % trillithionite, 1 % anhedral poikilitic microcline, 1 % pseudomorphs (chlorite and hematite), and 1 % pyrochlore and opaque minerals (Fig. 2.5 E-F). The CIPW norm of the marginal unit is 35% quartz, 48 % albite, and 7% orthoclase. Quartz occurs as anhedral to rounded crystals that are < 10 μm across. Zircon occurs as equant-shaped euhedral, bipyramid crystals that are < 30 μm across. It occurs as disseminated crystals throughout the rock and is present as inclusions in trillithionite and microcline (Fig. 2.5 E & F). Microcline occurs in the matrix as 1 mm irregular crystals that encompass other matrix minerals. Trillithionite occurs as 10 to 1000 μm flakes with a poikilitic texture. The inclusions in trillithionite are mostly euhedral zircon and rounded quartz crystals (Fig. 2.5 F). Locally, trillithionite is replaced by quartz and hematite. The abundance of opaque minerals, zircon and chlorite increases noticeably near the contact with the country rock. The marginal unit contains chlorite-hematite pseudomorphs of what might have been sodic-amphibole or pyroxene (henceforth referred to as pseudomorph) (Fig. 2.5 G). The pseudomorph consists of hematite, chlorite, and quartz, \pm zircon, \pm columbite. Hematite in the pseudomorphs occurs as acicular crystals that are oriented parallel to each other, which might have been controlled by the cleavage planes of the precursor mineral. Near the country rocks, pseudomorphs were not observed; however, chloritization is more abundant and is present along grain boundaries of quartz and zircon (Fig. 2.5 H). Pyrochlore is partially altered to aeschynite, Y-fluorite, and REE-fluorocarbonate. Microcline, zircon, and the majority of trillithionite crystals appear fresh and are not affected by chlorite-hematite alteration.

2.4.1.1 Ore mineralogy of the disseminated style

Ore minerals were identified by EDS semi-quantitative analyses or/and EMPA quantitative analyses in addition to their optical properties (Table 2.2). In the

disseminated style, the main HFSE and REE minerals in the host granite are zircon, pyrochlore, columbite, and rutile, \pm aeschynite, \pm fluorocarbonate. In the marginal unit, the main HFSE and REE minerals are zircon, columbite, Y-fluorite, and aeschynite \pm thorite, \pm REE-fluorocarbonate. Zircon is the most common HFSE mineral in all rock types at Al-Ghurayyah. Its size and crystal habit are variable and two dominant textural types can be identified in the same rock: Type-1 and Type-2 zircons (Fig. 2.6 A - D). Type-1 zircon is disseminated in the matrix of the porphyritic granite. It has a brown to reddish color, subhedral to anhedral equant-shaped crystals, and ranges in size from 100 to 500 μm (Fig. 2.6 A & B). Type-1 zircon has inclusion-rich zones usually concentrated at the rim. The inclusion-rich zones contain fluid and mineral inclusions, such as thorite, and hematite. Type-1 zircon displays medium to wide-spaced oscillatory zoning with a dark core and a light rim in the backscattered electron (BSE) and cathodoluminescence (CL) images (Fig. 2.6 B). Commonly, Type-1 zircon is replaced by a bright secondary zircon that occurs as veinlets and overgrowths that can be recognized in the BSE images. Some zones show metamictization and appear as black zones in the CL and BSE images. Type-2 zircon in the porphyritic granite is present as euhedral to anhedral equant crystals with the length to width ratio of approximately 1:1 (Fig 2.6 C & D). Rarely, Type-2 zircon occurs as a small (10 μm) euhedral bipyramid inclusions in the snowball quartz. Type-2 zircon is commonly associated with columbite, muscovite, chlorite, and rutile disseminated in the porphyritic granite. Some crystals of this type have fluid and mineral inclusion-rich cores and inclusion-free rims. Type-2 zircon is the only type observed in the marginal unit (Fig 2.6 E), where it occurs as euhedral bipyramid equant crystals about 10 μm across. Zircon in the marginal unit is similar to Type-2 zircon in the porphyritic granite in terms of composition and morphology (especially the euhedral zircon trapped in snowball quartz), thus it is classified as Type-2 zircon (Table 2.5). Type-2 zircon shows wide-spaced zoning to a lack of zoning in CL images.

In the disseminated mineralization style, pyrochlore and columbite are the main Nb-bearing minerals, whereas aeschynite is less common. In the porphyritic granite, pyrochlore is present as disseminated crystals that form an intergranular texture with albite. Pyrochlore occurs as light yellow anhedral crystals 15 to 50 μm across. The altered

pyrochlore is replaced by Y-pyrochlore, Pb-pyrochlore \pm columbite, and \pm REE-fluorocarbonate minerals. In the marginal unit, pyrochlore occurs as anhedral to irregularly-shaped grains with inclusions of zircon and quartz \pm hematite. Here, altered pyrochlore is replaced by Y-fluorite and thorite (Fig. 2.7 A&B).

Columbite is present in the porphyritic granite as prismatic subhedral crystals about 100 μm across that locally contain patches and veinlets of aeschynite. Columbite is commonly present as clusters with zircon, thorite, and rutile \pm REE-fluorocarbonate minerals, associated with muscovite and chlorite (Fig. 2.7 C). Locally, columbite replaces pyrochlore in highly altered granite, which was then replaced by Pb-pyrochlore (Fig. 2.7 D) or aeschynite (Fig. 2.7 E). Moreover, columbite in highly altered granite occurs as bladed crystals that radiate from margins of late quartz crystals and are associated with Type-2 zircon \pm fluorite (Fig. 2.7 F). In the marginal unit, columbite occurs as clusters with other Y-Nb oxide minerals such as Nb-aeschynite. The clusters of Nb oxides are present as a replacement of pyrochlore near the contact with the country rocks.

In the disseminated mineralization style, REE and Y are hosted by zircon, pyrochlore, Y-fluorite, aeschynite, and REE fluorocarbonate minerals. Zircon and Y-rich pyrochlore host the bulk of HREE in the porphyritic granite (detailed chemical analyses are reported in Chapter 3). The light REE are hosted by a variety of minerals, such as early pyrochlore, REE-fluorocarbonate, and rarely monazite. The REE-fluorocarbonate minerals occur in small abundances in the porphyritic granite associated with muscovite and fluorite alteration or have replaced pyrochlore (Fig. 2.7 C &D). In the marginal unit, the main hosts of the HREE are Y-fluorite, zircon, and pyrochlore.

Tin was previously assumed to be present as a substitution in Nb-rich minerals (Qadhi and Moufti, 2008). In this study, cassiterite was observed as small rounded crystals (5 μm) disseminated in the highly silicified granite (at the contact with quartz vein) and associated with aeschynite and Ti-Y oxide minerals. Cassiterite was also observed in the quartz vein, which will be discussed below. This the first time cassiterite is reported at Al-Ghurayyah as the main Sn phase.

2.4.2 Aggregate mineralization style

The aggregate mineralization style is hosted by quartz veins and the composite-body (Fig. 2.8). Zircon, columbite and rutile, \pm xenotime, \pm thorite are the main HFSE and REE minerals. The composite-body contains the highest concentrations of this style of mineralization. It consists of several zones that are marked by the enrichment of at least one mineral that forms more than 50 modal % of the zone. The zones are quartz, zircon-columbite, K-feldspar, and mica-zircon zones. This body resembles a pegmatite body; however, the only pegmatite feature in this body is the large crystal size in the K-feldspar zone (up to 20 cm) and the bulk composition is not igneous. This suggests that the composite-body is metasomatic in origin. The quartz zone consists of variable grain sizes of quartz that range from approximately 100 μm to larger than 2 cm across. The zircon-columbite zone consists of approximately 40% zircon, 10% columbite, 5% rutile and 1% xenotime, which are embedded in a quartz matrix that forms about 20% of the rock (Fig. 2.8 A & B). Calcite is present in the zircon-columbite zone around the edges of vugs and locally as interstitial calcite (Fig. 2.8 C). The K-feldspar zone consists completely of microcline with cross-hatched twinning. The mica-zircon zone consists of 60% Fe-rich mica, 20 to 25% zircon, 10% hematite, < 5% quartz, < 1% columbite, < 1% thorite and minor amounts of REE-fluorocarbonate (Fig. 2.8D & E). The Fe-rich mica (biotite) has a composition near siderophyllite (Table 2.4). The Fe-rich mica and quartz form the matrix and all other minerals exist as inclusions forming poikilitic texture. Hematite commonly occurs along the biotite cleavage planes (Fig. 2.8 E).

In the composite-body, the zircon-columbite and mica-zircon are the only mineralized zones. In these two units, zircon is present as subhedral to anhedral crystals that range from 100 to 500 μm long. Two types of zircon are observed in this unit: Type-3 and Type-4 zircons. Type-3 zircon occurs as reddish-brown inclusion-rich grains. Type-4 occurs as transparent and colorless inclusion-poor crystals (Fig. 2.8 B). Type-3 zircon contains fluid inclusions, as well as inclusions of hematite and thorite. Type-4 zircon is present as individual crystals or as overgrowths on Type-3 zircon. Both types of zircons lack oscillatory zoning in CL images. Columbite is the main Nb mineral in the composite-body and occurs as subhedral prismatic crystals ranging from 100 to 900 μm

across. Locally, columbite contains inclusions of Type-3 and Type-4 zircons. The rare earth elements in the composite-body are mostly hosted by zircon, less commonly xenotime in the zircon-columbite unit, and by REE-fluorocarbonate in the mica-zircon unit. Xenotime occurs as overgrowths on euhedral Type-4-zircon (Fig. 2.8 B). Locally, xenotime is present as interstitial grains between Type-3 and Type-4 zircons.

The aggregate style of mineralization also occurs in the quartz vein. The quartz veins consist of variable concentrations of microcline, muscovite, and chlorite that locally form about 30 % of the vein volume, with the remainder being quartz. Some quartz veins only consist of quartz, muscovite, chlorite and ore minerals. In one sample of the quartz veins, two types of quartz are present with different grain sizes and associated minerals, which suggests more than one generation of quartz. The first quartz generation (vein-1) occurs as anhedral quartz crystals (200 -500 μm) (Fig. 2.8 F). Quartz vein-1 hosts colorless, euhedral to subhedral and bipyramid zircons that are 50 to 100 μm across. These zircons are distinguished by inclusion-rich cores and inclusion-free rims that are locally rimmed by xenotime. This type of zircon is similar to Type-4 zircon, thus will be giving the same name. The second generation of quartz vein (vein-2) is fine-grained (less than 100 μm) anhedral quartz. Quartz vein-2 hosts zircon and a variety of oxides including columbite, samarskite, aeschynite, rutile, and cassiterite (Fig 2.8 H). In quartz vein-2, zircon is inclusion-rich, subhedral to anhedral (up to 100 μm across), and pinkish to light-red color. This type has a morphology similar to Type-3 zircon and thus given giving the same name. All zircons hosted by the quartz veins lack oscillatory zoning in CL images. Columbite and aeschynite were identified by EDS, and they are present as prismatic subhedral to anhedral elongated crystals (50 to 100 μm across) associated with rutile, hematite, and cassiterite. Cassiterite in the aggregate mineralization style was only observed in the quartz veins where it occurs as small irregular inclusions (<10 μm) in rutile (Fig 2.8 H).

2.4.3 Mineral paragenetic sequence in the host granite

The mineral paragenetic sequence of Al-Ghurayyah host granite is summarized in Figure 2.9. The porphyritic granite contains rare pseudomorphs with only weak Fe oxide staining with fresh albite and microcline. Sodic amphibole is the only Fe-rich mafic

mineral that was observed in Al-Ghurayyah granite; however, it is rare. This suggests the alteration of sodic amphibole was selective where albite and microcline were not affected. Zircon (Type-1 and 2) and early pyrochlore were observed formed an intergranular texture with albite, microcline and quartz (Fig. 2.4 D and F). Albite, microcline, and quartz continued to crystallize in late-magmatic stage. Trilithionite also formed a typical magmatic texture with matrix minerals (Fig. 2.4 B and F) and as inclusions in quartz and microcline phenocrysts (Fig. 2.5 A and B), which indicates an early crystallization in the magmatic stage. Snowball quartz and microcline are the last minerals to form in the magmatic stage and may have continued to crystallize in the transition stage minerals. The metasomatic stage is marked by the alteration of early magmatic zircon (Type-1 and 2) and pyrochlore and the formation of columbite, chlorite and secondary zircon (Fig. 2.7 C to F). Moreover, Type-3 and 4 zircons crystallized during this stage in the composite-body and the quartz veins, in addition to xenotime rutile and cassiterite. The last metasomatic stage is marked by the alteration of columbite to Y-HREE-rich late pyrochlore.

2.5 Geochemistry

Representative whole-rock analyses for the porphyritic granite, the marginal unit, and the quartz veins are given in Table 2.3. The whole-rock analyses of the porphyritic granite and the amphibole-bearing granite were plotted on the R1-R2 diagram for plutonic rock classification (De la Roche et al., 1980) and compared to the fresh Al-Ghurayyah samples from Qadhi and Mufti (2008) (Fig. 2.10). The majority of the samples plot within the alkaline granite field. A few of the samples from Qadhi and Mufti (2008) also plot in the quartz-syenite and syenite fields. However, Al-Ghurayyah may have undergone alteration due to the lack of fresh sodic amphibole (as previous works have suggested), thus results must be treated with caution. The tectonic setting of Al-Ghurayyah was evaluated using Pearce et al. (1984) Nb and Y discrimination diagram (Fig. 2.11). The samples indicate that the granite formed in a within-plate environment, consistent with the previous interpretation of the tectonic settings of Al-Ghurayyah (Qadhi and Moufti, 2008).

The porphyritic granite (lacks sodic amphibole, but contains fresh feldspars) from this study has an average major oxides composition of 72.38 ± 1.36 , wt. % SiO_2 ; $13.19 \pm$

1.51 wt. % Al_2O_3 ; 5.32 ± 1.09 , wt. % Na_2O and 2.76 ± 0.71 wt. % K_2O (Fig. 2.12). Al_2O_3 , or Na_2O are negatively correlated with SiO_2 . The altered granite (silicified granite) has high concentrations of SiO_2 and K_2O , and low concentrations of Al_2O_3 and Na_2O relative to granitic samples with no silicification. Relative to the porphyritic granite, the marginal unit contains elevated concentrations of F, CaO, and Fe_2O_3 . Generally, the amphibole-bearing granite and the porphyritic granite have similar compositions to those of Qadhi and Mufti (2008). Moreover, the amphibole-bearing granite and the porphyritic granite samples of this study have comparable whole-rock compositions.

On a spider plot (Fig. 2.13), Al-Ghurayyah is characterized by low TiO_2 , P_2O_5 , CaO, and Sr, which indicate feldspar, a Ti-bearing mineral and apatite were major phase that fractionated prior to the emplacement of Al-Ghurayyah (Moghazi et al., 2011).

Furthermore, Al-Ghurayyah granite contains concentrations of Rb ranging from 541 to 1270 ppm in the amphibole-bearing and porphyritic granites and up to 2700 ppm in highly silicified rocks. The ratio of K/Rb ranges between 49.30 to 90 in the amphibole-bearing and porphyritic granites, and from 39.90 to 77.15 in highly silicified granite.

These values are lower than the reported values in crustal rocks (from 150 to 350; Anders and Grevesse, 1989) and chondrite (from 150 to 350; Taylor, 1965), which indicates that Al-Ghurayyah underwent crystal/melt fractionation prior to emplacement.

Al-Ghurayyah granite is also characterized by elevated concentrations of Zr, REE, Y, Nb, Th, U, and Zn relative to alkaline granite from the Arabian shield (Moghazi et al, 2011; Moghazi et al, 2014; Radain, 1979) (Fig. 2.13). The porphyritic granite contains an average concentration of 5835 ppm Zr, 1262 ppm Nb, 174 ppm Ta, 963 ppm Y, and 1022 ppm total REE (ΣREE). In the altered rocks, the average concentrations of Zr, Nb, Ta, Y, and ΣREE are very similar: 5175 ppm, 1280 ppm, 109 ppm, 995 ppm, and 912 ppm; respectively. The granites are characterized by Zr/Hf ratios ranging from 13.62 to 29.96 in the amphibole-bearing and porphyritic granites, and from 12.61 to 27.97 in the altered granite. The ratio of Nb/Ta in the granites is close to the normal Nb-Ta ratio in crustal rocks (11 to 12; Green, 1995) ranging from 6.95 to 13.50 in fresh and silicified rocks. On a Chondrite-normalized REE pattern (Boynnton, 1984), Al-Ghurayyah displays a negative Eu anomaly ($\text{Eu}/\text{Eu}^* = 0.06$) and a heavy rare earth elements (HREE) enriched pattern

with an average La/Yb = 0.1 (Fig. 2.14). The marginal unit contains extremely high concentrations of Zr (1.3 wt. %), Hf (527), Y (1.9 wt. %), Nb (0.24 wt. %) and Σ REE (0.88 wt. %). In the REE normalized pattern plot, the marginal unit shows the highest concentrations of REE. The REE pattern is similar to that of the porphyritic granite with lower relative abundances of Er and lower relative abundances of Yb and Lu. The quartz veins have high Hf (5520 ppm), Sn (1200 ppm), and Th (999 ppm) (Table 2.3).

On a chondrite-normalized REE plot (Chondrite values are from Boynton, 1984), Al-Ghurayyah rocks are characterized by a HREE-enriched pattern (La/Yb = 0.27) and negative Eu anomaly (Fig. 2.14). In Figure 2.15, Nb vs. Ta, Zr vs. Hf, and Y vs. Ho show positive correlation with each other. The lack of fractionation relative to one another suggests that their behaviors are controlled by crystallization of a single mineral (e.g. zircon, columbite, and pyrochlore).

2.5.1 U-Pb Zircon age dating

The main challenge of analyzing granitic zircon is the abundance of Th-bearing inclusions. In addition, some samples contain high common lead concentration that exhibit high variability. In some grains, Th peaks were observed in multiple cycles of rastering LA-ICP-MS analysis, indicating the presence of thorite inclusions that were also observed in BSE-EDS analyses. Consequently, the only zircons that could be successfully dated belong to Type-1 zircon from the altered granite, Type-2 zircon from the porphyritic granite, Type-3 and Type-4 zircons from the zircon-columbite zone from the composite-body, and Type-4 zircon from the mica-zircon zone from the composite-body (Fig. 2.16 A). The $^{206}\text{Pb}/^{238}\text{U}$ versus $^{207}\text{Pb}/^{235}\text{U}$ isochrons plots for the analyzed zircons are shown in Figure 2.16 (B to E). Type-1 zircon from the altered granite has a small inclusion-free zone. A line scan and raster techniques were used to analyze the grains. However, the zircon estimated ages were 749.9 ± 5.9 Ma for the line scan and raster techniques. This age is older compared to other age dates from the porphyritic granite and the composite-body, and older than the average alkaline granite in the shield (686 ± 26 Ma; Johnson et al., 2011). The old age of zircon is potentially because it is inherited zircon and its age does not reflect the crystallization age of Al-Ghurayyah. A single Type-2 zircon from the host granite gave an average estimated age of 554 ± 89

Ma. The average estimated age of Type-3 and Type-4 zircons from the composite-body are 647 ± 32 Ma and 631 ± 7 Ma, respectively.

2.5.2 Composition of feldspars and micas

In order to compare the compositions of albite and microcline in the matrix, phenocrysts (microcline), and inclusions in the quartz and microcline phenocrysts in porphyritic granite, the compositions albite and microcline were obtained by EMPA and are summarized in Table 2.4. Albite analyses are from the matrix and from trapped albite in snowball quartz and microcline from the porphyritic granite. Analyses of microcline were from phenocrysts and anhedral microcline in the matrix from the porphyritic granite. The mineral formulas for both minerals were calculated based on 8 oxygens. The concentration of CaO in albite has an average of 0.01 wt. % and is below the detection limit (0.01 Ca %) in microcline. Albite contains an average of 0.1 wt. % K₂O and microcline contains 0.33 wt. % Na₂O (Table 2.5).

Mica EMP analyses are from the early mica (trilithionite) crystals in the matrix and from inclusions in microcline from the porphyritic granite, late mica from the highly silicified granite, and Fe-rich mica from the mica-zircon zone in the composite-body. The results are summarized in Table 2.5. In order to confirm that the early mica is trilithionite, Raman spectra of three crystals from the matrix and from the snowball phenocrysts (quartz and microcline) were acquired. These spectra were compared to the RRUFF database using CrystalSleuth software (Laetsch and Downs, 2006) that has the same laser wavelength (514). The results show a 91 % match to trilithionite (Fig. 3.17 A). Thus, Li content of trilithionite was estimated by the correlation of Li with other elements, such as Si, Mg, F, and Rb (Tischendorf et al., 2004, and references therein). The equation used to estimate Li in micas with < 3 % MgO, < 26% Al₂O₃, and F > 4% is:

$$\text{Li}_2\text{O (wt.\%)} (0.289 * \text{SiO}_2) - 9.658$$

2.6 Discussion

Al-Ghurayyah alkaline granite has high concentrations of Zr, Nb, Y, and REE relative to alkaline granite from the Arabian shield (Moghazi et al, 2011; Moghazi et al, 2014;

Radain, 1979). This enrichment pattern is typical of post-tectonic rare-metal alkaline granites in the Arabian Shield and is consistent with a within-plate tectonic environment. The estimated age of the granite is 554 ± 89 Ma, whereas in the composite-body it ranges from 647 ± 32 Ma (Type-3 zircon) to 631 ± 8 Ma (Type-4 zircon). Thus, the ages of the mineralization and the granite are the same within the error of the method. Moreover, these ages agree with other dates of alkaline granites in the northwestern part of the Arabian Shield (625 ± 5 Ma to 577 ± 4 Ma; Hedge, 1984). Johnson et al., (2011) reported that Al-Ghurayyah age is reasonably constrained by the age of the nearby Dabbagh pluton (577 ± 4 Ma U-Pb zircon) reported by Hedge (1984) and the 666 Ma U-Pb previously estimated age was possibly from an inherited zircon (error not reported). The estimated age of Al-Ghurayyah from this study shows that Al-Ghurayyah is approximately 630 Ma (mostly constrained by the composite-body data), which is slightly older than the Dabbagh pluton. The zircons used in this study are co-genetic with the granite and from the composite-body that crosscut the porphyritic granite, and thus not inherited zircons. This, in turn, implies that Al-Ghurayyah is not co-genetic with the Dabbagh pluton, as previously suggested.

2.6.1 Magmatic and hydrothermal textures

One of the approaches to understanding the nature of the mineralization in rare-metal alkaline granites is to study the magmatic and hydrothermal mineral textures and their relationships to the mineralization. The problem with this approach is that this type of rock may have undergone multiple hydrothermal events that might not be related to the mineralizing event, and magmatic textures are commonly overprinted.

The amphibole-bearing granite and porphyritic granite are characterized by a porphyritic to medium-grained texture. Albite in the matrix displays an intergranular magmatic texture with zircon, pyrochlore, trillithionite, and anhedral microcline. One of the unusual texture that occurs in Al-Ghurayyah granite is the snowball texture, which is commonly within quartz and less commonly microcline phenocrysts (Fig. 2.5 A & B). Snowball textures are common in topaz-bearing granites (e.g., Breiter et al., 2013; Kovalenko, 1995; Muller and Seltnmann, 1999), but have less commonly been reported in peralkaline granites (Costi et al., 2009; Kempe, 1999; Miller, 1996; Moghazi et al., 2011; Spandler

and Morris, 2016). The origin of the snowball texture is controversial, and it has been attributed to either magmatic (Costi et al., 2009; Kovalenko, 1995; Poutiainen and Scherbakova, 1998), or metasomatic (Kempe, 1999) processes. At Al-Ghurayyah, the snowball phenocrysts are late phases that have trapped most of the matrix minerals. Muller and Seltmann (1999) reported a similar snowball texture in a sample from the third intrusion (SG3) of the Schellerhua Granite Complex in Germany. In their samples, some albite crystals are arranged around quartz phenocrysts and others are trapped in the phenocryst. The albite arrangement inside and around the snowball quartz was attributed to the growth rate of the quartz phenocrysts, where high growth rate resulted in the entrapment of matrix minerals. Furthermore, Muller and Seltmann (1999) concluded that this texture is an indicator for a fluid-saturated melt enriched in F and Li. Miller (1996) and Siegel et al. (2017) reported the occurrence of snowball texture at the Strange Lake peralkaline granitic pegmatite, Canada. The formation of snowball texture was ascribed to late-stage growth from an interstitial residual melt. At Al-Ghurayyah, the occurrence of minerals with high F and Li content such as trilithionite in an intergranular texture indicates that the melt was also enriched in these compounds. The albite inclusions in snowballs have end-member composition. Moreover, snowball microcline and albite inclusions in the snowball microcline all have end-member compositions. Based on the binary solid-solution system of K-feldspar-albite (Bowen and Tuttle, 1950), the formation of pure end-members is not realistic under magmatic conditions. However, experimental work showed that calcic plagioclase could evolve isothermally to form albite with an end-member composition from a melt that has experienced undercooling (London, 2014). Therefore, the snowball textures at Al-Ghurayyah most likely formed from a late-stage melt that was enriched in water and other fluxes.

Only one granite sample (GHA5 Fig. 2.2) contains sodic amphibole (arfvedsonite), although Qadhi and Mufti (2008) reported the presence of arfvedsonite in the fresh granite of Al-Ghurayyah. The lack of sodic amphibole inclusions in quartz and microcline snowballs suggests that the replacement of sodic amphibole took place before the formation of the snowball phenocrysts. Comparing the whole-rock composition of the porphyritic granite (with no sodic amphibole) from this study to the amphibole-bearing granite from this study and Qadhi and Mufti (2008) shows very comparable

compositions. These differences in the mineralogical composition and the similarity in the whole-rock composition suggest that the alteration of amphibole was mainly limited to the mineralogical level without significantly changing the bulk rock composition, at least for the major oxide contents. Moreover, the scarce presence of pseudomorphs after sodic amphibole in the porphyritic granite and the typical magmatic texture in the porphyritic granite indicate that the sodic amphibole replacement took place during the magmatic stage. The replacement might be a result of the interaction of sodic-amphibole with the late melt or coexisting aqueous fluid. Notably, this event was limited to the sodic amphibole as the feldspars remained unaltered. In the second alteration (silicification), microcline was stable, but albite was replaced by quartz and fan-shaped muscovite in highly altered rocks.

The marginal unit is one of the most highly mineralized zones relative to other rock units at Al-Ghurayyah. It has a high concentration of F (2.4 wt. %) as well as high concentrations of Fe_2O_3 and MgO, and low K_2O relative to porphyritic granite. Fluorite is always associated with pyrochlore and contains high Y and HREE concentrations. The juxtaposition of the marginal unit with the porphyritic granite at the contact with the country rocks and the fine-grained texture suggest rapid crystallization by quenching. The quenched phase may be related to the late melt that formed the porphyritic granite; however, the interaction with the metasedimentary country rock may have changed the composition by adding Fe, Mg, and Ca. The similar zircon composition from this unit to Type-2 zircon in the granite indicates that the two zircons are likely from the same source (Chapter 3). Moreover, the whole-rock chondrite-normalized REE pattern of the marginal unit is very similar to the normalized-chondrite REE pattern of the granite, which further supports that they were formed from the same source. Thus, it is possible that the marginal unit resulted from the same late melt that formed porphyritic granite.

2.6.2 Magmatic evolution and hydrothermal alteration

The petrographic relationships and geochemical data illustrate that magmatic and post-magmatic processes have both played significant roles in the formation of the Al-

Ghurayyah deposit. The whole-rock spider diagram shows significant negative anomalies of Sr, Eu, Ba, K, Ti, and P (Fig. 2.13), which suggest that the melt evolution involved fractionation of feldspar, Fe-Ti oxide, mica, and apatite. In Figure 2.15, Zr vs. Hf, Nb vs. Ta, and Y vs. Ho ratios are nearly constant, which indicates that their concentrations are controlled by zircon, pyrochlore and columbite. The common presence of F and Li minerals such as fluorite and trilithionite at Al-Ghurayyah indicates that the melt was rich in F and Li as well as H₂O. Moreover, the normalized quartz-albite-orthoclase plot (Fig. 2.19) shows that Al-Ghurayyah granite composition lies near the H₂O saturated granite minima melt at 1 kbar with at 2 wt.% F (fresh sample GHA5 with sodic amphibole). Experimental studies have demonstrated that at equilibrium between vapor phase and siliceous melt, F is preferentially partitioned into the siliceous melt (Borodulin et al., 2009; London et al., 1988; Van Groos and Wyllie, 1969; Webster, 1990). Thus, the increase in F concentration in the melt causes a significant decrease in the solidification temperature. Moreover, experimental studies on the solubility of HFSE and REE demonstrate that the presence of flux components, F in particular, in the melt increase the solubility of HFSE and REE accessory phases in the melt (Aseri et al., 2014; Bartels et al., 2010; Fiege et al., 2011; Keppler, 1996; Linnen, 1998). Therefore, the combined effects of lowering the crystallization temperature and the increased solubility led concentration of incompatible elements in the residual melt. The variation of the quartz-albite-orthoclase composition along a trend toward the albite apex is consistent with the shift of the granite minimum composition with increasing Li-F contents, which indicates magmatic processes dominated. Moreover, the fresh granites show a low Zr/Hf ratio (22.2 on average) and a very low K/Rb ratio (64.3 on average). Linnen and Keppler (2002) demonstrate that the low values of Zr/Hf can be the result of fractional crystallization. However, Irber (1999) and Bau (1996) argued that the low values indicate magmatic-hydrothermal alteration and may suggest the presence of volatiles, such as H₂O, Li, F, and B. Furthermore, the granite shows a whole-rock REE pattern characterized by the enrichment of HREE over LREE with an M REE pattern (Fig. 2.14), which resembles a tetrad effect. The tetrad effect in the lanthanides of whole-rock analyses was calculated following the method of Irber (1999) where the total tetrad effect of tetrad 1 and 3 (TE_{1,3}) is:

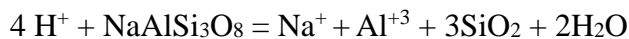
$$TE_{1,3} = \left[\left\{ \left(\frac{Ce}{Ce^t} \right) \times \left(\frac{Pr}{Pr^t} \right) \right\}^{0.5} \times \left\{ \left(\frac{Tb}{Tb^t} \right) \times \left(\frac{Dy}{Dy^t} \right) \right\}^{0.5} \right]^{0.5}$$

Where Ce^t , Pr^t , Tb^t , and Dy^t represent the values of chondrite normalized Ce, Pr, Tb, and Dy values that lie on a hypothetical straight line between La and Nd, and Gd and Ho. Values larger than 1 express the amount of total tetrad effect. Al-Ghurayyah granite shows an average total tetrad effect of 1.4 (Table 2.7). However, there is no correlation between the total tetrad effect and total REE, Zr, Hf, Nb, and Ta contents in the rocks. High lanthanide tetrad effect has been attributed to a melt interaction with an aqueous fluid (Bau, 1991; Irber, 1999; Jahn et al., 2001). Duc-Tin and Keppler (2015) have demonstrated experimentally that the tetrad effect in highly evolved granite may have resulted from monazite or xenotime fractionation. By contrast, Irber (1999) showed that mineral fractionation is unlikely to produce a tetrad effect and suggested that the tetrad effect has resulted from magma-fluid interaction during late-stage crystallization of the granite after the magma-fluid separation. Monecke et al., (2002) argued against the formation of the tetrad effect after the magma-fluid split where no mirroring concave tetrad effect was found in hydrothermal fluorite and greisen, and they suggested that the tetrad effect must have developed before the magma-fluid split or inherited from a fluid phase during or after emplacement of the magma. Given the low K/Rb ratio and the non-charge-and-radius control of trace elements (Zr/Hf), it is most likely that the tetrad effect in Al-Ghurayyah granite was developed due to magma-fluid interaction rather than mineral fractionation.

2.6.2.1 Silica alteration

Figure 2.18 shows that the highly silicified samples plot along the quartz-orthoclase tieline, which is a non-magmatic trend and indicates that the altered granites are silicified and have also experienced Na loss. Figure 2.19 A shows a negative correlation between the molar abundances of Na + K and Si. By contrast, Figure 2.19 B shows a positive correlation between the molar abundances of Na + K and Al with a slope near 1. In highly silicified granite, all albite has been replaced by quartz, microcline, and muscovite. This suggests that albite was preferentially altered over microcline during silicification.

In order to maintain the same positive slope of Na +K vs. Al, equal amounts of Na and Al must have been removed. To test this hypothesis, the rock quartz-albite-orthoclase normative composition was recalculated assuming 100 % silicification of albite and via:



The resulting slope is similar to the original slope, which demonstrates the assumption of preferential silicification of albite over microcline is a viable explanation to explain the range of rock compositions.

2.6.3 HFSE and REE mineralization

High concentrations of flux components (Li and F) in the late-magmatic stage result in increases in the solubility of HFSE and REE accessory phases. It has been demonstrated that zircon solubility is highly dependant on the alkalinity and the flux content of the melt (Aseri et al., 2014; Bartels et al., 2010; Fiege et al., 2011; Keppler, 1996; Linnen, 1998; Linnen and Keppler, 2002, 1997). In alkaline melts, experimental work showed that zircon and hafnon solubility increase with increasing F content of the melt, and showed that hafnon is more soluble than zircon (Aseri et al., 2014). Moreover, zircon is known to incorporate Hf, HREE, and Y (Erdmann et al., 2013; Hoskin and Schaltegger, 2003; Rubin et al., 1989) owing to the similarity in the ionic radii of Hf and Zr (0.83 Å for Hf and 0.84 Å for Zr, Shannon, 1976), and the close HREE ionic radii to zircon (Lu 0.977 Å, Shannon, 1976). The substitution of Zr by Hf in zircon occurs via simple $\text{Hf}^{4+} = \text{Zr}^{4+}$ substitution. The difference in ionic charge between Zr and Y and REE restricts simple substitution. By contrast, Y and REE substitute for Zr in zircon via coupled substitution to compensate for the charge difference. The coupled substitution can occur at two structural sites (common) via $(\text{Y}, \text{REE})^{3+} + \text{P}^{5+} = \text{Zr}^{4+} + \text{Si}^{4+}$, or at one structural site via $(\text{Y}, \text{REE})^{3+} + \text{P}^{5+} = 2 \text{Zr}^{4+}$ (Hoskin and Schaltegger, 2003). Another important host of HFSE and HREE is pyrochlore. At Al-Ghurayyah granite, pyrochlore is the stable Nb-Y-REE phase under late-magmatic to metasomatic conditions, whereas columbite is the stable phase in the highly silicified granite, the composite-body, and the quartz veins. Zircon and pyrochlore are the early crystallized HFSE accessory minerals in the amphibole-bearing and porphyritic granites. Moreover, the fresh rock contents of Zr, Hf,

and HREE are controlled by zircon, whereas pyrochlore controls Nb, Y, LREE, and HREE (yttropyrochlore) (Fig. 2.20). Magmatic zircons (Type-1 and 2, Chapter 3) from porphyritic granite contains Y and heavy rare earth elements (Σ HREE) (Table 3.5, Chapter 3). Based on petrographic observations, zircon and pyrochlore in porphyritic granite crystallized contemporaneously with albite during a late-magmatic to early metasomatic stage. Pyrochlore shows a wide range of REE and Y contents. Early crystallized pyrochlore (PCL-1 and 2, Chapter 3) is enriched in LREE, whereas metasomatic pyrochlore (PCL-3, Chapter 3) is enriched in HREE and Y and associated with fluorite and REE-fluorocarbonate minerals where they replaced early pyrochlore and metasomatic columbite.

The metasomatic stage is demonstrated by the variable degrees of silicification of Al-Ghurayyah granite. During silicification, pyrochlore was no longer a stable phase, and it was replaced by columbite, Y-fluorite, thorite, REE-F-carbonate, xenotime, and monazite. This can be seen in Figure 2.20, where Zr + Nb vs. REE in the silicified granites are highly scattered, which indicates that REE contents in these rocks are no longer controlled by zircon and pyrochlore only. Textural observations showed that columbite crystallized as a secondary phase associated with secondary zircon, late quartz and fluorite (Fig 2.5 D). Moreover, columbite and zircon (Type-3 and 4) are common phases in quartz veins and the composite-body and associated with trace amounts of fluorocarbonate and xenotime. The presence of these elements in the mineralized quartz veins and the composite-body demonstrates that the HFSE and REE were mobile at least locally. Experimental studies and natural systems have demonstrated the important role of F, Cl, and C in the mobilization of HFSE and REE by aqueous fluids (Boily and Williams-Jones, 1994; Gysi et al., 2016; Haas et al., 1995; Salvi and Williams-Jones, 1996; Vasyukova and Williams-Jones, 2014; Webster et al., 1989). It has been argued that the strong association of H^+ and F^- (to form HF) and the solubility of REE-F solids limit the transportation of REE as fluoro-complexes and suggest the REE are more likely to be transported as REE-chloride or sulfate complexes (Migdisov et al., 2016; Migdisov and Williams-Jones, 2014). Gysi and Williams-Jones (2013) proposed a model that involves a HCl-HF fluid that formed a pathway during acidic alteration and led to the mobilization of Zr and REE. In Al-Ghurayyah, the crystallization of zircon, xenotime,

rutile, and columbite \pm aeschynite in the quartz veins could possibly be due to the mobilization of HFSE and REE by an exsolved F-rich fluid from the consolidating granite.

2.7 Conclusions

Al-Ghurayyah is an A-type alkaline granite in northwestern Arabian Shield. It is enriched in Nb, Ta, Zr, Hf, Y, and HREE. Two mineralization styles were identified: disseminated style hosted by the porphyritic granite and the marginal unit, and aggregate style hosted by the quartz veins and the composite-body. In the disseminated style, the main HFSE and REE minerals are zircon, pyrochlore, and columbite, and rutile. The main HFSE and REE minerals in the aggregate mineralization style are zircon, columbite, rutile, and xenotime, \pm cassiterite. The study reported, for the first time, the occurrence of cassiterite in the quartz vein and rarely in the highly altered granite.

The estimated U-Pb zircon age of the granite was 554 ± 89 Ma, and the estimated age from zircons in the composite-body ranges from 647 ± 32 to 631 ± 8 Ma. These ages agree with the age of the alkaline magmatism in the terrane. Moreover, the estimated age of Al-Ghurayyah is older than the nearby Dabbagh pluton, which was previously suggested to be co-magmatic with Al-Ghurayyah.

The granite has a low K/Rb ratio and non-chondritic Zr/Hf ratio in addition to the large total tetrad effect (1.4), which suggests crystallization from a fluid-rich melt.

Furthermore, the petrographic observations and lithochemical data suggest that the crystallization occurred during late-magmatic to metasomatic conditions. During this stage, early pyrochlore and early zircon have crystallized by late-magmatic processes. The transition from late-magmatic to metasomatic conditions can be inferred by the alteration magmatic zircon and pyrochlore to form columbite and metasomatic zircon at the early metasomatic stage, and the alteration of columbite to Y and HREE-rich pyrochlore and fluorite \pm REE-fluorocarbonate at a late-metasomatic stage.

2.8 References

Agar, R.A., 1992. The tectono-metallogenic evolution of the Arabian Shield.

- Precambrian Res. 58, 169–194. [https://doi.org/10.1016/0301-9268\(92\)90118-8](https://doi.org/10.1016/0301-9268(92)90118-8)
- Ali, K.A., Jeon, H., Andresen, A., Li, S.-Q., Harbi, H.M., Hegner, E., 2014. U–Pb zircon geochronology and Nd–Hf–O isotopic systematics of the Neoproterozoic Hadb adh Dayheen ring complex, Central Arabian Shield, Saudi Arabia. *Lithos*. <https://doi.org/10.1016/j.lithos.2014.07.030>
- Anders, E., Grevesse, N., 1989. Abundances of the elements: Meteoric and solar. *Geochim. Cosmochim. Acta* 53, 197–214.
- Aseri, A.A., Linnen, R.L., Che, X.D., Thibault, Y., Holtz, F., 2014. Effects of fluorine on the solubilities of Nb, Ta, Zr and Hf minerals in highly fluxed water-saturated haplogranitic melts. *Ore Geol. Rev.*
- Bartels, a., Holtz, F., Linnen, R.L., 2010. Solubility of manganotantalite and manganocolumbite in pegmatitic melts. *Am. Mineral.* 95, 537–544. <https://doi.org/10.2138/am.2010.3157>
- Bau, M., 1996. Controls on the fractionation of isovalent trace elements in magmatic and aqueous systems : evidence from Y / Ho , Zr / Hf , and lanthanide tetrad effect 323–333.
- Bau, M., 1991. Rare-earth element mobility during hydrothermal and metamorphic fluid rock interaction and the: Significance of the oxidation-state of europium. *Chem. Geol.* 93, 219–230. [https://doi.org/10.1016/0009-2541\(91\)90115-8](https://doi.org/10.1016/0009-2541(91)90115-8)
- Boily, M., Williams-Jones, A. E., 1994. The role of magmatic and hydrothermal processes in the chemical evolution of the Strange Lake plutonic complex, Quebec-Labrador. *Contrib. to Mineral. Petrol.* 118, 33–47. <https://doi.org/10.1007/BF00310609>
- Borodulin, G., Chevychelov, V.Y., Zaraysky, G., 2009. Experimental study of partitioning of tantalum, niobium, manganese, and fluorine between aqueous fluoride fluid and granitic and alkaline melts. *Dokl. Earth Sci.* 427, 868–873. <https://doi.org/10.1134/S1028334X09050341>
- Breiter, K., Svojtka, M., Müller, A., 2013. *Lithos* Behavior of trace elements in quartz

- from plutons of different geochemical signature : A case study from the Bohemian Massif , Czech Republic 176, 54–67. <https://doi.org/10.1016/j.lithos.2013.04.023>
- Cheetham, P., Whitehead, D., Fitch, C., 2007. Tertiary-Annual-Report-2007-website-version-revised.
- Costi, H.T., Dall’Agnol, R., Pichavant, M., Rämö, O.T., 2009. The peralkaline tin-mineralized madeira cryolite albite-rich granite of pitinga, amazonian craton, brazil: Petrography, mineralogy and crystallization processes. *Can. Mineral.* 47, 1301–1327. <https://doi.org/10.3749/canmin.47.6.1301>
- Davis, D.W., 2002. U-Pb geochronology of Archean metasedimentary rocks in the Pontiac and Abitibi subprovinces, Quebec, constraints on timing, provenance and regional tectonics. *Precambrian Res.* 115, 97–117. [https://doi.org/10.1016/S0301-9268\(02\)00007-4](https://doi.org/10.1016/S0301-9268(02)00007-4)
- Davis, D.W., 1982. Optimum linear regression and error estimation applied to U-Pb data. *Can. J. Earth Sci.* 19, 2141–2149. <https://doi.org/10.1139/e82-188>
- De la Roche, H., Leterrier, J., Grandclaude, P., Marchal, M., 1980. A classification of volcanic and plutonic rocks using R 1 R 2 -diagram and major-element analyses — Its relationships with current nomenclature. *Chem. Geol.* 29, 183–210. [https://doi.org/10.1016/0009-2541\(80\)90020-0](https://doi.org/10.1016/0009-2541(80)90020-0)
- Drysdall, a. R., Jackson, N.J., Ramsay, C.R., Douch, C.J., Hackett, D., 1984. Rare element mineralization related in Precambrian alkali granites in the Arabian shield. *Econ. Geol.* 79, 1366–1377. <https://doi.org/10.2113/gsecongeo.79.6.1366>
- du Bray, E.A., 1986. Specialized granitoids in the southeastern Arabian Shield-case history of a regional assessment. *J. African Earth Sci.* 4, 169–176. [https://doi.org/10.1016/S0899-5362\(86\)80077-X](https://doi.org/10.1016/S0899-5362(86)80077-X)
- Duc-Tin, Q., Keppler, H., 2015. Monazite and xenotime solubility in granitic melts and the origin of the lanthanide tetrad effect. *Contrib. to Mineral. Petrol.* 169, 1–26. <https://doi.org/10.1007/s00410-014-1100-9>
- Elliott, J.E., 1983. Peralkaline and peraluminous Granites and Related Mineral Deposits

of the Arabian Shield, Kingdom of Saudi Arabia.

- Elliott, J.E., Al-Yazidi, S., Al-Eissa, A., Al-Shammeri, A., Hashem, A.I., Tarabulsi, Y., 2002. Exploration of the Ghurayyah radioactive granite, Kingdom of Saudi Arabia. Saudi Geol. Surv. open-file, x.
- Erdmann, S., Wodicka, N., Jackson, S.E., Corrigan, D., 2013. Zircon textures and composition: refractory recorders of magmatic volatile evolution? *Contrib. to Mineral. Petrol.* 165, 45–71. <https://doi.org/10.1007/s00410-012-0791-z>
- Fiege, A., Kirchner, C., Holtz, F., Linnen, R.L., Dziony, W., 2011. Lithos Influence of fluorine on the solubility of manganotantalite (MnTa_2O_6) and manganocolumbite (MnNb_2O_6) in granitic melts — An experimental study. *Lithos* 122, 165–174. <https://doi.org/10.1016/j.lithos.2010.12.012>
- Green, T.H., 1995. Significance of Nb/Ta as an indicator of geochemical processes in the crust_mantle system. *Geochemical Geol.* 120, 347.
- Gysi, A.P., Williams-Jones, A.E., 2013. Hydrothermal mobilization of pegmatite-hosted REE and Zr at Strange Lake, Canada: A reaction path model. *Geochim. Cosmochim. Acta* 122, 324–352. <https://doi.org/10.1016/j.gca.2013.08.031>
- Gysi, A.P., Williams-Jones, A.E., Collins, P., 2016. Lithogeochemical vectors for hydrothermal processes in the Strange Lake peralkaline granitic REE-Zr-Nb deposit. *Econ. Geol.* 111, 1241–1276. <https://doi.org/10.2113/econgeo.111.5.1241>
- Haas, J.R., Shock, E.L., Sassani, D.C., 1995. Rare earth elements in hydrothermal systems: estimates of standard partial molal thermodynamic properties of aqueous complexes of the rare earth elements at high pressures and temperatures. *Geochim. Cosmochim. Acta* 59, 4329–4350.
- Hackett, D., 1986. Mineralized aplite-pegmatite at Jabal Sa'id, Hijaz region, Kingdom of Saudi Arabia. *J. African Earth Sci.* 4, 257–267. [https://doi.org/10.1016/S0899-5362\(86\)80087-2](https://doi.org/10.1016/S0899-5362(86)80087-2)
- Harris, N.B.W., Marzouki, F.M.H., Ali, S., 1986. The Jabel Sayid complex, Arabian Shield: geochemical constraints on the origin of peralkaline and related granites. *J.*

- Geol. Soc. London. 143, 287–295. <https://doi.org/10.1144/gsjgs.143.2.0287>
- Hedge, C.E., 1984. Precambrian geochronology of NW KSA,.
- Hoskin, P.W.O., Schaltegger, U., 2003. The composition of zircon and igneous and metamorphic petrogenesis. *Rev. Mineral. Geochemistry* 53, 27–62.
<https://doi.org/10.2113/0530027>
- Irber, W., 1999. The lanthanide tetrad effect and its correlation with K/Rb, Eu/Eu*, Sr/Eu, Y/Ho, and Zr/Hf of evolving peraluminous granite suites. *Geochim. Cosmochim. Acta* 63, 489–508. [https://doi.org/10.1016/S0016-7037\(99\)00027-7](https://doi.org/10.1016/S0016-7037(99)00027-7)
- Jackson, N.J., 1986. Distribution , nature and origin of trondhjemite in the Arabian Shield ; a reconnaissance survey 4, 99–103.
- Jackson, N.J., Douch, C.J., 1986. Jabal Hamra REE-mineralized silexite, Hijaz region, Kingdom of Saudi Arabia. *J. African Earth Sci.* 4, 269–274.
[https://doi.org/10.1016/S0899-5362\(86\)80088-4](https://doi.org/10.1016/S0899-5362(86)80088-4)
- Jahn, B.M., Wu, F., Capdevila, R., Martineau, F., Zhao, Z., Wang, Y., 2001. Highly evolved juvenile granites with tetrad REE patterns: The Woduhe and Baerzhe granites from the Great Xing'an Mountains in NE China. *Lithos* 59, 171–198.
[https://doi.org/10.1016/S0024-4937\(01\)00066-4](https://doi.org/10.1016/S0024-4937(01)00066-4)
- Johnson, P.R., 2006. Explanatory notes to the map of Proterozoic geology of western Saudi Arabia, Saudi Geological Survey Technical Report SGS-TR-2006-4.
- Johnson, P.R.R., Andresen, A., Collins, A.S.S., Fowler, A.R.R., Fritz, H., Ghebreab, W., Kusky, T., Stern, R.J.J., 2011. Late Cryogenian-Ediacaran history of the Arabian-Nubian Shield: A review of depositional, plutonic, structural, and tectonic events in the closing stages of the northern east African Orogen. *J. African Earth Sci.* 61, 167–232. <https://doi.org/10.1016/j.jafrearsci.2011.07.003>
- Kempe, U., 1999. Magmatic and Metasomatic Processes During Formation of the Nb-Zr-REE Deposits Khaldzan Buregte and Tsakhir (Mongolian Altai): Indications from a Combined CL-SEM Study. *Mineral. Mag.* 63, 165–177.
<https://doi.org/10.1180/002646199548402>

- Keppler, H., 1996. Constraints from partitioning experiments on the composition of subduction-zone fluids. *Nature*. <https://doi.org/10.1038/380237a0>
- Kovalenko, V.I., 1995. The peralkaline granite-related Khaldzan-Buregtey rare metal (Zr, Nb, REE) deposit, western Mongolia. *Econ. Geol.* 90, 530–547. <https://doi.org/10.2113/gsecongeo.90.3.530>
- Küster, D., 2009. Granitoid-hosted Ta mineralization in the Arabian-Nubian Shield: Ore deposit types, tectono-metallogenic setting and petrogenetic framework. *Ore Geol. Rev.* 35, 68–86. <https://doi.org/10.1016/j.oregeorev.2008.09.008>
- Laetsch, T., Downs, R., 2006. Software for identification and refinement of cell parameters from powder diffraction data of minerals using the RRUFF Project and American Mineralogist Crystal Structure Databases.
- Linnen, R.L., 1998. The solubility of Nb-Ta-Zr-Hf-W in granitic melts with Li and Li + F: Constraints for mineralization in rare metal granites and pegmatites. *Econ. Geol.* 93, 1013–1025. <https://doi.org/10.2113/gsecongeo.93.7.1013>
- Linnen, R.L., Keppler, H., 2002. Melt composition control of Zr/Hf fractionation in magmatic processes. *Geochim. Cosmochim. Acta* 66, 3293–3301. [https://doi.org/10.1016/S0016-7037\(02\)00924-9](https://doi.org/10.1016/S0016-7037(02)00924-9)
- Linnen, R.L., Keppler, H., 1997. Columbite solubility in granitic melts: consequences for the enrichment and fractionation of Nb and Ta in the Earth's crust. *Contrib. to Mineral. Petrol.* 128, 213–227. <https://doi.org/10.1007/s004100050304>
- London, D., 2014. A petrologic assessment of internal zonation in granitic pegmatites. *Lithos*. <https://doi.org/10.1016/j.lithos.2013.10.025>
- London, D., Hervig, R.L., Morgan, G.B., 1988. Melt-vapor solubilities and elemental partitioning in peraluminous granite-pegmatite systems: experimental results with Macusani glass at 200 MPa. *Contrib. to Mineral. Petrol.* 99, 360–373. <https://doi.org/10.1007/BF00375368>
- Migdisov, A., Williams-Jones, A.E., Brugger, J., Caporuscio, F.A., 2016. Hydrothermal transport, deposition, and fractionation of the REE: Experimental data and

- thermodynamic calculations. *Chem. Geol.* 439, 13–42.
<https://doi.org/10.1016/j.chemgeo.2016.06.005>
- Migdisov, A.A., Williams-Jones, A.E., 2014. Hydrothermal transport and deposition of the rare earth elements by fluorine-bearing aqueous liquids. *Miner. Depos.* 49, 987–997. <https://doi.org/10.1007/s00126-014-0554-z>
- Miller, R.R., 1996. Structural and textural evolution of the strange Lake Peralkaline rare-element (NYF) granitic pegmatite, Quebec-Labrador. *Can. Mineral.* 34, 349–371.
- Moghazi, A.-K.M., Iaccheri, L.M., Bakhsh, R.A., Kotov, A.B., Ali, K.A., 2015. Sources of rare-metal-bearing A-type granites from Jabel Sayed complex, Northern Arabian Shield, Saudi Arabia. *J. Asian Earth Sci.* 107, 244–258.
<https://doi.org/10.1016/j.jseaes.2015.04.042>
- Moghazi, A.M., Harbi, H.M., Ali, K.A., 2011. Geochemistry of the Late Neoproterozoic Hadb adh Dayheen ring complex, Central Arabian Shield: Implications for the origin of rare-metal-bearing post-orogenic A-type granites. *J. Asian Earth Sci.* 42, 1324–1340. <https://doi.org/10.1016/j.jseaes.2011.07.018>
- Monecke, T., Kempe, U., Monecke, J., Sala, M., Wolf, D., 2002. Tetrad effect in rare earth element distribution patterns: A method of quantification with application to rock and mineral samples from granite-related rare metal deposits. *Geochim. Cosmochim. Acta* 66, 1185–1196. [https://doi.org/10.1016/S0016-7037\(01\)00849-3](https://doi.org/10.1016/S0016-7037(01)00849-3)
- Muller, A., Seltmann, R., 1999. The genetic significance of snowball quartz in high fractionated tin granites of the Krusne Hory / Erzgebirge, Mineral Deposits, Processes to Processing. Lodnon.
- Nehlig, P., Genna, A., Asfirane, F., 2002. A review of the Pan-African evolution of the Arabian shield. *GeoArabia* 7, 103–124.
- Pearce, J.A., Harris, N.B.W., Tindle, A.G., 1984. Trace element distribution diagrams for the tectonic interpretation of granitic rocks. *J. Petrol.* 25, 956–983.
<https://doi.org/10.1093/petrology/25.4.956>
- Poutiainen, M., Scherbakova, T.F., 1998. Fluid and melt inclusion evidence for the origin

- of idiomorphic quartz crystals in topaz-bearing granite from the Salmi batholith, Karelia, Russia. *Lithos* 44, 141–151. [https://doi.org/10.1016/S0024-4937\(98\)00052-8](https://doi.org/10.1016/S0024-4937(98)00052-8)
- Putnis, A., 2009. Mineral Replacement Reactions. *Rev. Mineral. Geochemistry* 87–124. <https://doi.org/10.2138/rmg.2009.70.3>
- Qadhi, T., Moufti, A., 2008. Gheochemical characteristic of the rare-metal rich granite in the Ghurayyah-Dubbagh Area, north western Arabian Shield, Saudi Arabia. *Ann. Geol. Surv. Egypt* XXX, 149.
- Radain, A.A.M., Fyfe, W.S., Kerrich, R., 1981. Origin of Peralkaline Granites of Saudi Arabia. *Contrib. Miner. Pet.* 358–366. <https://doi.org/10.1007/BF00398932>
- Robinson, F.A., Foden, J.D., Collins, A.S., Payne, J.L., 2014. Arabian Shield magmatic cycles and their relationship with Gondwana assembly: Insights from zircon U–Pb and Hf isotopes. *Earth Planet. Sci. Lett.* 408, 207–225. <https://doi.org/10.1016/j.epsl.2014.10.010>
- Rubin, J.N., Henry, C.D., Price, J.G., 1989. Hydrothermal zircons and zircon overgrowths, Sierra Blanca Peaks, Texas. *Am. Mineral.*
- Salvi, S., Williams-Jones, A.E., 1996. The role of hydrothermal processes in concentrating high-field strength elements in the Strange Lake peralkaline complex, northeastern Canada. *Geochim. Cosmochim. Acta* 60, 1917–1932. [https://doi.org/10.1016/0016-7037\(96\)00071-3](https://doi.org/10.1016/0016-7037(96)00071-3)
- Shannon, R.D., 1976. Revised effective ionic radii and systematic studies of interatomic distances in halides and chalcogenides. *Acta Crystallogr. Sect. A Cryst. physics, diffraction, Theor. Gen. Crystallogr.* 32, 751–767.
- Siegel, K., Williams-Jones, A.E., van Hinsberg, V.J., 2017. The amphiboles of the REE-rich A-type peralkaline Strange Lake pluton – fingerprints of magma evolution. *Lithos* 288–289, 156–174. <https://doi.org/10.1016/j.lithos.2017.07.012>
- Spandler, C., Morris, C., 2016. Geology and genesis of the Toongi rare metal (Zr, Hf, Nb, Ta, Y and REE) deposit, NSW, Australia, and implications for rare metal

- mineralization in peralkaline igneous rocks. *Contrib. to Mineral. Petrol.* 171, 1–24.
<https://doi.org/10.1007/s00410-016-1316-y>
- Staatz, M.H., Brownfield, I.K., 1986. Trace-and minor-element mineralogy of the microgranite at Ghurayyah, Kingdom of Saudi Arabia.
- Stern, R.J., 1994. Arc assembly and continental collision in the Neoproterozoic East African Orogen: Implication for the Consolidation of Gondwanaland. *Ann. Rev. Earth Planet Sci.* 22, 319–351.
- Stoeser, D.B., 1986. Distribution and tectonic setting of plutonic rocks of the Arabian Shield. *J. African Earth Sci.* 4, 21–46. [https://doi.org/10.1016/S0899-5362\(86\)80066-5](https://doi.org/10.1016/S0899-5362(86)80066-5)
- Taylor, S.R., 1965. The application of trace element data to problems in petrology. *Phys. Chem. Earth* 6, 133–213. [https://doi.org/10.1016/0079-1946\(65\)90014-5](https://doi.org/10.1016/0079-1946(65)90014-5)
- Tischendorf, G., Rieder, M., Förster, Gottesmann, B., Guidotti, C. V., 2004. A new graphical presentation and subdivision of potassium micas. *Mineral. Mag.* 68, 649–667. <https://doi.org/10.1180/0026461046840210>
- Tomlinson, K.Y., Davis, D.W., Stone, D., Hart, T.R., 2003. U-Pb age and Nd isotopic evidence for Archean terrane development and crustal recycling in the south-central Wabigoon subprovince, Canada. *Contrib. to Mineral. Petrol.* 144, 684–702.
<https://doi.org/10.1007/s00410-002-0423-0>
- Turkistany, A.R., Ramsay, C.R., 1982. Mineralized apogranite associated with alkali granite at Jabal Sa'id, Kingdom of Saudi Arabia. *Deputy Ministry Miner. Resour.* 78–88.
- Van Groos, A., Wyllie, P.J., 1969. Melting relationships in the system NaAlSi₃O₈-NaCl-H₂O at one kilobar pressure, with petrological applications. *J. Geol.* 77, 581–605.
- Vasyukova, O., Williams-Jones, A.E., 2014. Fluoride-silicate melt immiscibility and its role in REE ore formation: Evidence from the Strange Lake rare metal deposit, Quebec-Labrador, Canada. *Geochim. Cosmochim. Acta* 139, 110–130.
<https://doi.org/10.1016/j.gca.2014.04.031>

Webster, J.D., 1990. Partitioning of F between H₂O and CO₂ fluids and topaz rhyolite melt - Implications for mineralizing magmatic-hydrothermal fluids in F-rich granitic systems. *Contrib. to Mineral. Petrol.* 104, 424–438.
<https://doi.org/10.1007/BF01575620>

Webster, J.D., Holloway, J.R., Hervig, R.L., 1989. Partitioning of lithophile trace elements between H₂O and H₂O + CO₂ fluids and topaz rhyolite melt. *Econ. Geol.* 84, 116–134. <https://doi.org/10.2113/gsecongeo.84.1.116>

Table 2-1 Summary of the main rock units in Al-Ghurayyah

Rock Type	Description	Mineralization
Porphyritic granite	Pink color. Consists of quartz, albite, and K-feldspar. Accessory minerals are chlorite, muscovite, annite, \pm hematite, and opaque and ore minerals. Phenocrysts are quartz and microcline whereas the matrix consists of albite and accessory minerals. The quartz phenocryst (less common microcline) display snowball textures that contain inclusions of albite, quartz, trillithionite, and \pm euhedral zircon crystals aligned along the quartz growth zones.	Ore minerals are disseminated mostly zircon, pyrochlore, columbite, rutile, and REE-fluorocarbonate.
Marginal unit	Fine-grained quartz, albite with variable grain size and coarse-grained trillithionite and chlorite. Chlorite and hematite concentrations increase toward the contacts with the country rocks.	Highly enriched in very fine-grained bipyramid zircon (10 μ m). Pyrochlore is interstitial to poikilitic. Columbite is more concentrated near the contact with the country rocks. REE-fluorocarbonate is common near altered pyrochlore
Composite-body	Highly mineralized with zones enriched in zircon and columbite. Calcite and fluorite are common. The zones are quartz, zircon-columbite, K-feldspar, and mica-zircon.	Columbite, zircon, thorite, rutile, and xenotime
Quartz veins	Mainly consists of quartz. Locally with microcline and mica	Columbite, rutile, zircon, xenotime \pm fluorocarbonate

Table 2-2 List of common minerals in Al-Ghurayyah with abbreviations and mineral formulas

Mineral	Symbol	Formula	Notes
Y-fluorite	Y-Fl	$(Ca_{1-x}Y_x)F_{2+x}$	$0.05 < x < 0.3$
Muscovite	Ms	$KAl_2(AlSi_3O_{10})(OH)_2$	
Pyrochlore	Pcl	$A_2Nb_2(O,OH)_6Z$	A = Na ⁺ , Ca ²⁺ , Sn ²⁺ , Sr, Pb ²⁺ , Sb ³⁺ , Y, U ⁴⁺ , H ₂ O or □ Z = OH ⁻ , F ⁻ , H ₂ O or □ (vacancy)
Columbite	colb	$(Mn,Fe)(Nb,Ta)_2O_6$	
Zircon	Zrn	$ZrSiO_4$	
Rutile	Rt	TiO_2	
Thorite	Thr	$ThSiO_4$	
Quartz	Qtz	SiO_2	
Albite	Ab	$NaAlSi_3O_8$	
Microcline	Mc	$KAlSi_3O_8$	
Trilithionite	Plith	$K(Li_{1.5}Al_{1.5})(AlSi_3O_{10})(F,OH)_2$	
Fluorite	Fl	CaF_2	
Chlorite	Chl	$(Fe,Mg)_{5-6}(Al,Fe,Si)_4(O,OH)_{18}$	
Calcite	Cal	$CaCO_3$	
Aeschnite	Achy	$(Y,Ln,Ca,Th)(Ti,Nb)_2(O,OH)_6$	
Cassiterite	Cst	SnO_2	
Arfvedsonite	Arf	$Na_3Fe_5Si_8O_{22}(OH,F)_2$	

Table 2-3 Whole-rock chemical analyses of Al-Ghurayyah

	Marginal	Vein	Silicified porphyritic granite					Porphyritic granite				Amphibole-
	Unit											granite ¹
	GHA-1A	GHA26	GHA18A	GHA18B	GHA24	GHA25	GHA4B	GHA7	GHA10	GHA12	GHA17A	GHA5
SiO ₂	66.77	78.18	86.73	85.52	85.97	74.79	81.32	73.4	72.14	70.54	73.43	70.97
Al ₂ O ₃	10.76	1.86	5.1	5.22	5.17	12.26	7.56	11.34	13.95	14.79	12.69	12.87
Fe ₂ O ₃ (T)	3.63	0.72	2.19	1.85	2.57	1.64	2.26	3.77	2.05	1.38	2.05	2.39
MnO	0.023	0.05	0.031	0.026	0.052	0.073	0.032	0.067	0.059	0.029	0.023	0.08
MgO	0.19	0.03	0.07	0.06	0.11	0.03	0.06	0.07	0.07	0.05	0.08	0.05
CaO	2.62	0.21	0.09	0.31	0.13	0.17	0.34	0.53	0.47	0.18	0.17	2.04
Na ₂ O	5.08	0.18	0.2	0.1	0.15	3.11	0.13	4.89	5.23	6.85	4.32	4.94
K ₂ O	1.07	1.3	3.99	4.14	3.65	5.83	5.73	1.83	3.36	2.59	3.26	3.38
TiO ₂	0.091	0.113	0.09	0.178	0.072	0.092	0.156	0.163	0.081	0.097	0.103	0.07
P ₂ O ₅	0.01	0.23	0.14	0.1	0.02	0.01	0.02	0.01	0.01	0.01	0.01	0.01
F	2.2	0.14	0.01	0.01	0.01	0.17	0.06	0.33	0.24	0.03	0.01	1.17
L.O.I	2.61	0.39	0.36	0.65	0.78	0.62	0.83	1.07	0.98	0.74	1.02	1.76
Total	95.1	83.4	99	98.2	98.7	98.8	98.44	97.5	98.6	97.3	97.2	99.72

Contineu Table 2.3												
Be	9.0	87.0	4.0	5.0	6.0	21.0	6.0	7.0	8.0	10.0	11.0	11.0
Zn	990.0	330.0	570.0	640.0	1130.0	1980.0	120.0	2780.0	610.0	1000.0	1110.0	590.0
Ga	53.0	7.0	20.0	20.0	28.0	58.0	32.0	64.0	71.0	77.0	61.0	56.0
Ge	5.0	6.0	3.0	3.0	4.0	6.0	3.0	5.0	4.0	5.0	4.0	5.0
Rb	297.0	562.0	1230.0	1300.0	1180.0	2700.0	1380.0	594.0	968.0	541.0	1030.0	1270.0
Sr	1193.0	5.0	7.0	9.0	8.0	15.0	9.0	10.0	19.0	8.0	11.0	100.0
Y	18800.0	3922.0	1619.0	1168.0	577.0	1052.0	561.0	1303.0	595.0	909.0	1045.0	548.0
Zr	12640.0	100900.0	3875.0	1979.0	3751.0	5882.0	10390.0	8837.0	4332.0	5378.0	4794.0	3453.0
Nb	2390.0	554.0	1550.0	1310.0	1380.0	972.0	1190.0	1660.0	949.0	1280.0	1160.0	992.0
Sn	94.0	1200.0	75.0	524.0	162.0	613.0	1.3	95.0	65.0	76.0	49.0	65.0
Sb	1.1	17.2	0.9	0.7	2.0	3.1	4.5	1.3	0.7	0.8	0.8	0.5
Cs	0.9	3.1	2.1	2.3	3.0	7.0	106.0	1.9	1.8	1.8	3.8	3.1
Ba	106.0	25.0	52.0	37.0	34.0	23.0	34.0	21.0	13.0	27.0	29.0	45.0
La	257.0	3.5	45.8	40.5	43.1	37.3	21.2	85.0	58.7	43.3	40.0	47.0
Ce	739.0	10.7	135.0	117.0	125.0	109.0	51.2	248.0	161.0	92.9	107.0	132.0
Pr	93.4	1.6	14.5	12.4	13.0	11.4	6.3	25.9	18.3	14.6	11.9	14.6
Ce	739.0	10.7	135.0	117.0	125.0	109.0	51.2	248.0	161.0	92.9	107.0	132.0
Pr	93.4	1.6	14.5	12.4	13.0	11.4	6.3	25.9	18.3	14.6	11.9	14.6
Nd	327.0	7.0	40.9	33.7	34.0	30.4	27.8	72.2	49.8	44.5	33.2	41.9
Sm	212.0	10.4	21.2	16.8	13.8	14.4	16.2	34.2	20.3	23.2	17.0	18.3
Eu	4.9	0.4	0.5	0.4	0.3	0.4	1.0	0.7	0.4	0.5	0.4	0.4
Gd	429.0	32.5	36.7	28.0	18.8	25.9	30.0	46.7	26.9	33.9	26.8	24.0
Tb	202.0	26.0	18.4	14.0	9.0	13.9	11.2	20.5	11.3	15.3	13.7	9.3

Contineu Table 2.3												
Er	1830.0	634.0	225.0	196.0	105.0	159.0	124.0	193.0	103.0	187.0	176.0	81.6
Tm	287.0	146.0	39.9	44.5	23.1	32.4	26.7	36.2	19.7	39.2	35.3	15.7
Yb	1670.0	1280.0	255.0	341.0	193.0	247.0	223.0	266.0	147.0	309.0	255.0	115.0
Lu	208.0	231.0	36.5	53.0	28.7	36.5	37.5	39.5	22.2	48.5	35.1	16.7
Hf	527.0	5520.0	149.0	157.0	135.0	422.0	544.0	399.0	193.0	395.0	160.0	194.0
Ta	177.0	41.5	152.0	130.0	138.0	115.0	141.0	239.0	143.0	154.0	160.0	133.0
W	23.0	7.0	8.0	6.0	10.0	7.0	10.0	12.0	9.0	8.0	15.0	5.0

1- Amphibole-bearing granite. 2- LREE (La, Ce, Nd, Sm, and Gd). 3- HREE (Tb, Dy, Ho, Er, Tm, Yb, and Lu). 4- Eu/Eu^* ($Eu_{normalized} / \sqrt{(Sm_{normalized} * Gd_{normalized})}$) normalized chondrite values are for C1 chondrite (Boynton, 1984). $Fe_2O_3(T)$ as total iron; LOI is the weight of volatiles lost on ignition. $TE_{1,3}$ is the total tetrad effect of tetrad 1 and 3 following the method of Irber (1999)

Table 2-4 EMP analyses of albite, microcline, and mica from the host granite

	Albite		Microcline		Trilithionite		Muscovite		Fe-rich mica ¹	
	N = 3	±	N = 3	±	N = 11	±	N = 5	±	N = 4	±
Na ₂ O	11.64	0.01	0.33	0.01	-	-	-	-	0.05	0.0
SiO ₂	68.01	0.11	65.13	0.02	56.5	3	44.88	1	44.63	2.2
Al ₂ O ₃	18.54	0.11	17.98	0.49	15.9	3	30.97	1.6	9.31	0.7
CaO	0.01	0.00	0.00	0.00	-	-	0.05	0.02	0.05	0.0
K ₂ O	0.10	0.02	16.24	0.20	10.8	0.3	10.02	0.9	9.20	0.1
FeO	0.80	0.07	0.44	0.32	4.1	0.8	4.59	1	27.31	1.0
SrO	b.d	b.d	b.d	0.02	-	-	-	-		
Li ₂ O ²	-	-	-	-	6.7	1	-	-		
MgO	-	-	-	-	0.4	0.9	0.06	0.02	1.27	0.2
TiO ₂	-	-	-	-	0.38	0.7	0.06	0.03	3.41	0.5
ZnO	-	-	-	-	0.64	0.3	0.42	0.77	0.06	0.0
F	-	-	-	-	7.5	0.8	1.24	0.25	2.25	0.3
H ₂ O*	-	-	-	-	0.41		8.0	-	0.05	0.0
-O=F ₂	-	-	-	-	3.33		0.55	-	44.63	2.2
Total	99.15	0.19	100.13	0.31	99.59		99.99	-	95.46	

Table 2.4 Continued

Atom per formula unit					
	Albite	Microcline	Trilithionite	Muscovite	Fe-rich mica ¹
Na	1.0	0.03	-	-	0.01
Si	3.0	3	3.74	3.18	3.72
Al	0.97	0.98	1.15	2.58	0.94
Ca	-	-	-	-	0.00
K	0.01	0.96	0.91	0.91	1.00
Fe	0.03	0.02	0.23	0.27	1.95
Li	-	-	1.80	-	-
Mg	-	-	0.04	0.01	0.14
Ti	-	-	0.02	-	0.22
Zn	-	-	0.03	0.02	0.00
Total	5	5	7.91	6.97	8.00

1 Fe-rich mica has composition close to siderophyllite. 2 Li was estimated by the correlation of Li with other elements such as Si, Mg, F, and Rb (Tischendorf et al., 2004, and references therein). The equation used to estimate Li in micas with < 3 % MgO, < 26% Al₂O₃, and F > 4% is: Li₂O (wt%) (0.289 * SiO₂) – 9.658. b.d, below detection. * H₂O is estimated by difference to 100 %.

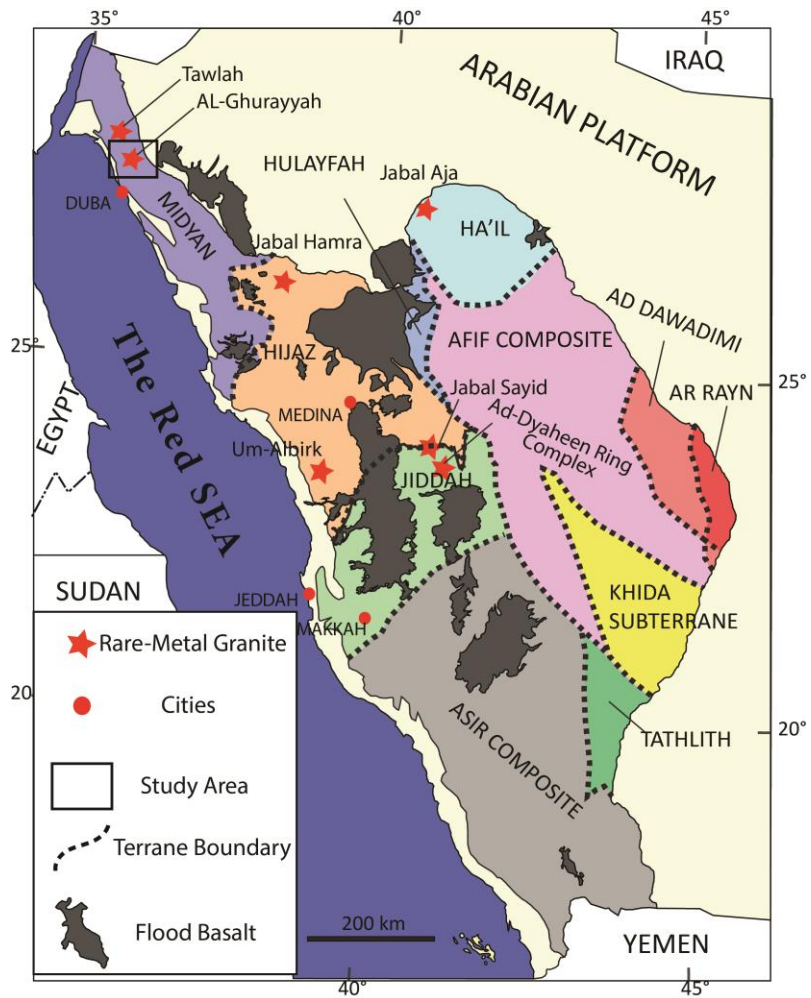


Figure 2-1 A geological map of the Arabian Shield showing the different terranes. The red stars are the locations of some important occurrences of rare-metal granite including Al-Ghurayyah show in the black box (modified after Johnson and Kattan 2012)

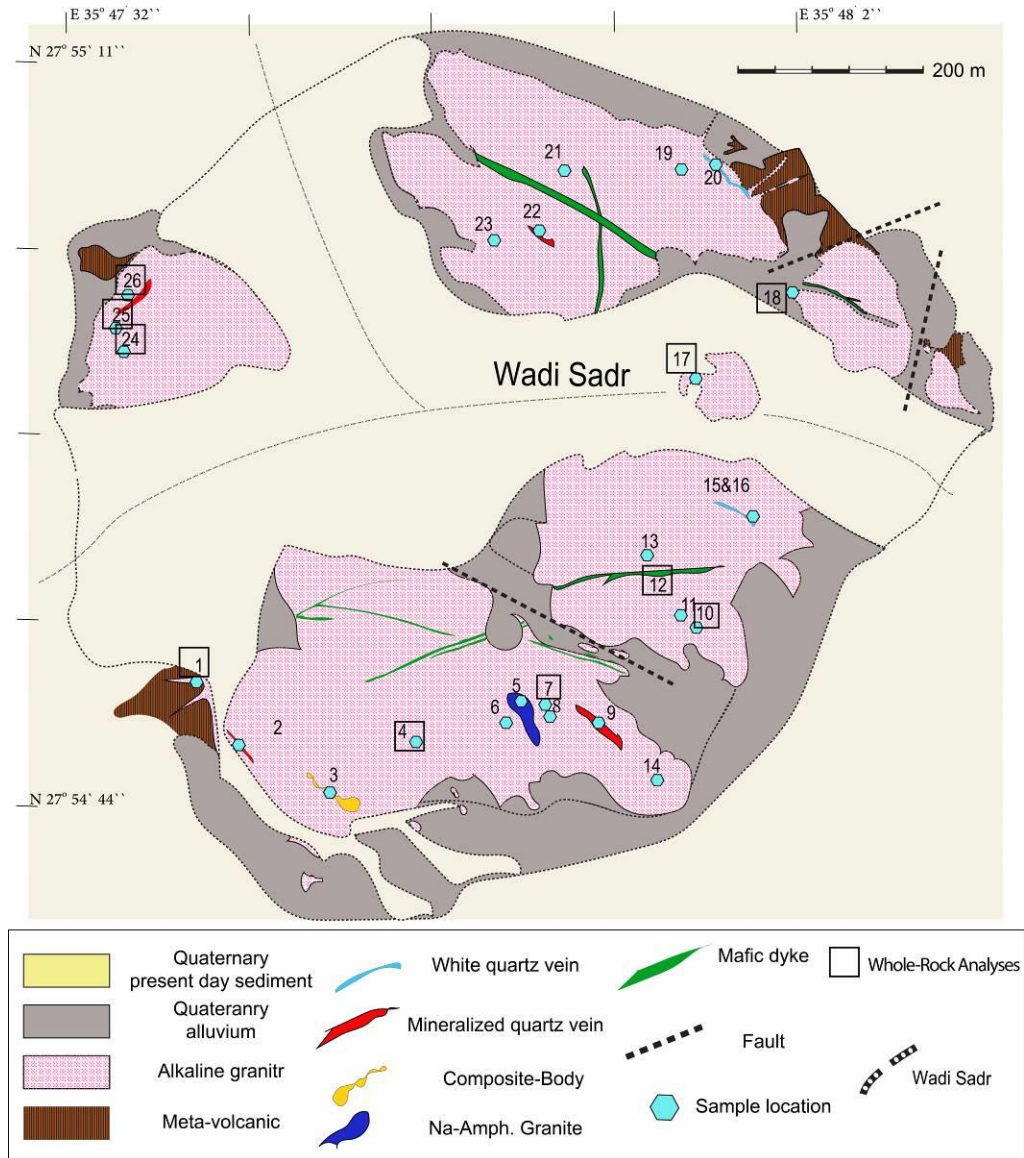


Figure 2-2 Geological map of Al-Ghurayyah (modified after Elliott et al. 2002) and locations of samples of this study

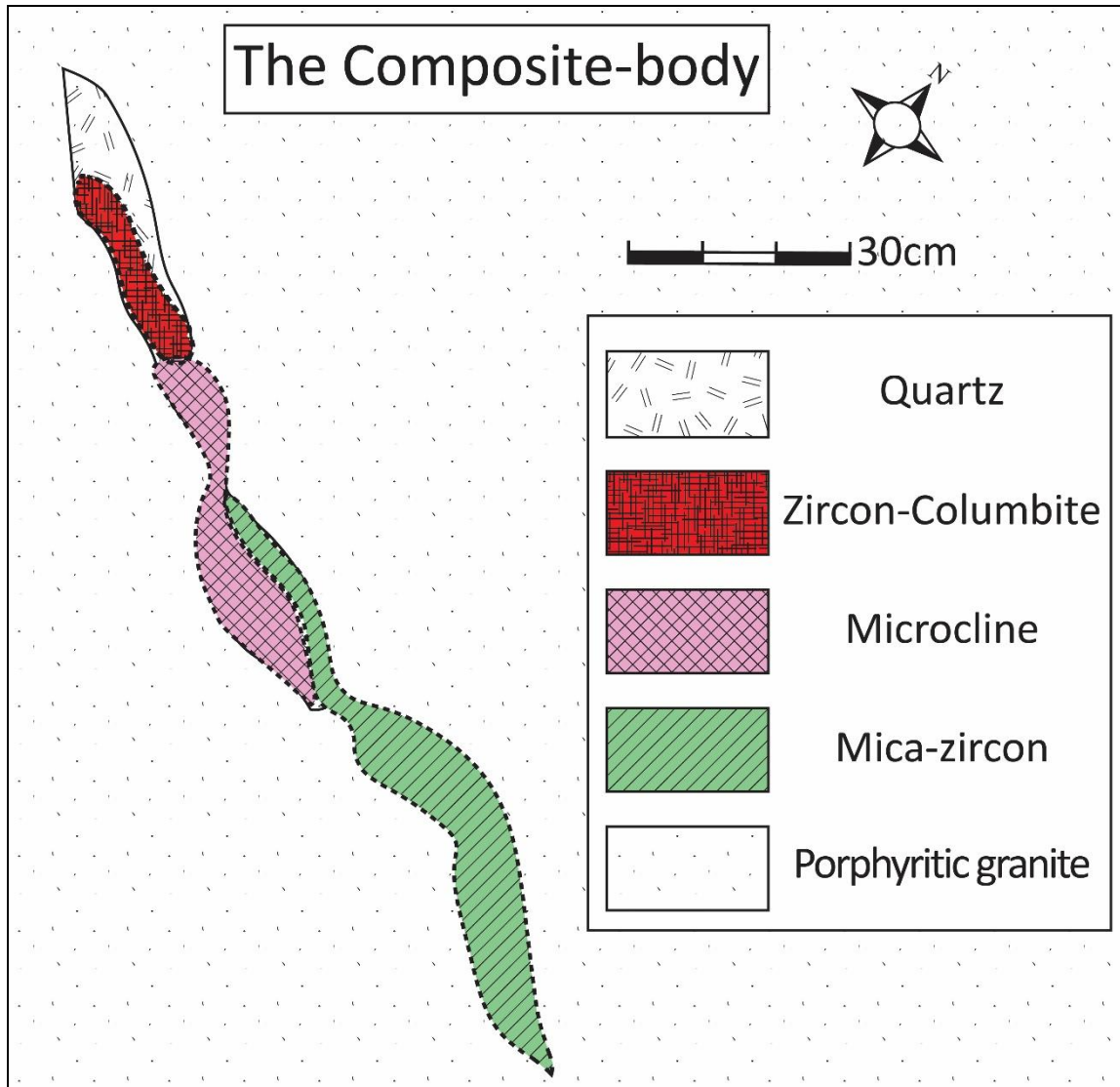


Figure 2-3 Sketch of the composite-body showing the different zones of this unit.

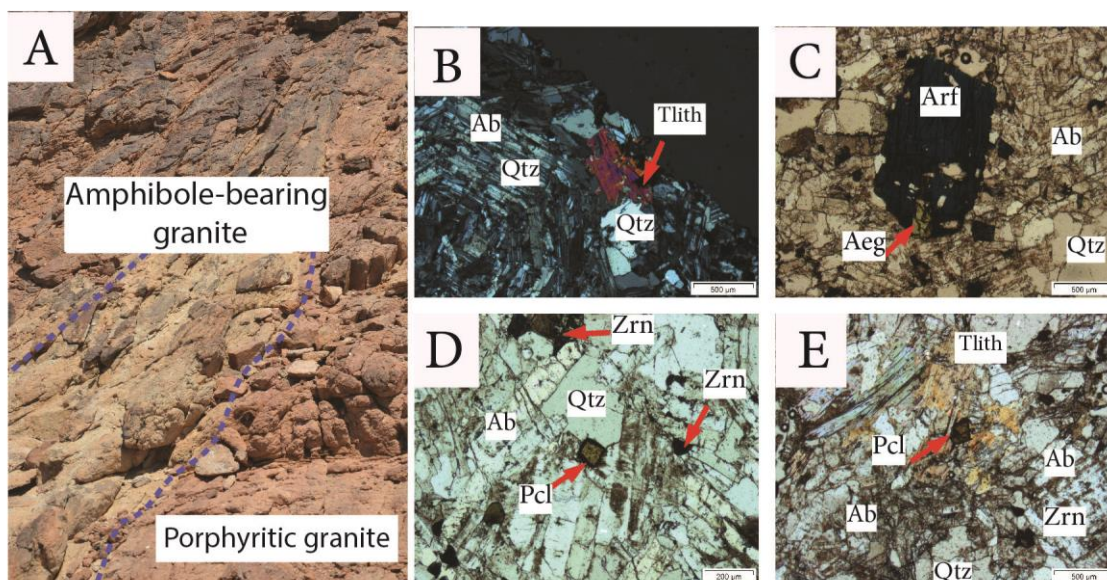


Figure 2-4 Field and petrographic relationships of the amphibole-bearing granite A) Contact between amphibole-bearing granite (light grey) and the common porphyritic granite (pink). B) Crossed polarized light (CPL) image showing snowball quartz with albite inclusions. C) Plane polarized light (PPL) image of arfvedsonite crystals and aegirine surrounded by albite and quartz from amphibole-bearing granite. D) PPL image of Type-2 and pyrochlore in quartz and albite matrix. E) PPL image of trilithionite associated with pyrochlore and zircon in quartz and albite matrix.

Abbreviations: Ab. Albite, Tlith. Trilithionite, Qtz. Quartz, Zrn. Zircon, Aeg. Aegirine, Arf. Arfvedsonite, and Pcl. Pyrochlore

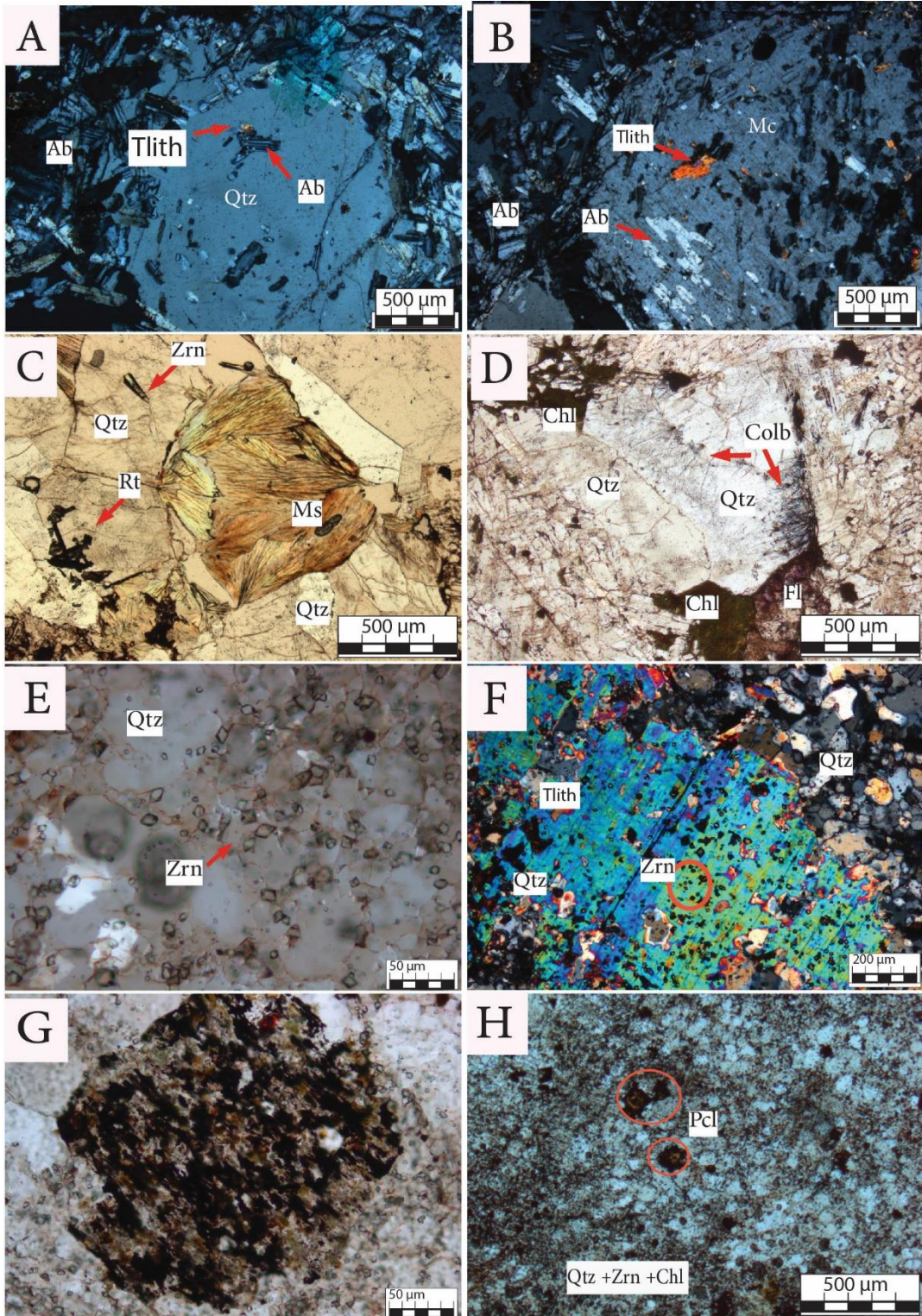


Figure 2-5 Main textures and mineralogy of the porphyritic granite and the marginal unit. A) CPL image of snowball quartz from the porphyritic granite showing the alignment of albite and trillithionite inclusions along the growth zones

and surrounded by lath-shaped albite from the porphyritic granite. B) CPL image of snowball microcline with inclusions of albite and trillithionite and surrounded by lath-shaped albite from the porphyritic granite. C) Plane polarized light (PPL) image of a fan-shaped muscovite, Type-2 zircon, and rutile that are associated with silica alteration from silicified porphyritic granite. D) PPL image of late quartz associated with acicular columbite, fluorite and chlorite from highly altered granite. E) PPL image of fine-grained euhedral zircons (Type-2) in quartz matrix from the marginal unit. F) CPL image of large trillithionite crystal contains inclusions of euhedral zircons and fine-grained quartz from the marginal unit. G) PPL image of pseudomorph in the marginal unit that altered to chlorite (green), hematite + columbite (dark red to black). H) PPL image of pyrochlore crystals in fine-grained zircon and quartz matrix from the marginal unit.

Abbreviations: Ab. albite, Tlith. trillithionite, Qtz. quartz, Mc. microcline, Chl. chlorite, Colb. columbite, Zrn. zircon, Fl. fluorite, Pcl. pyrochlore. Rt, rutile.

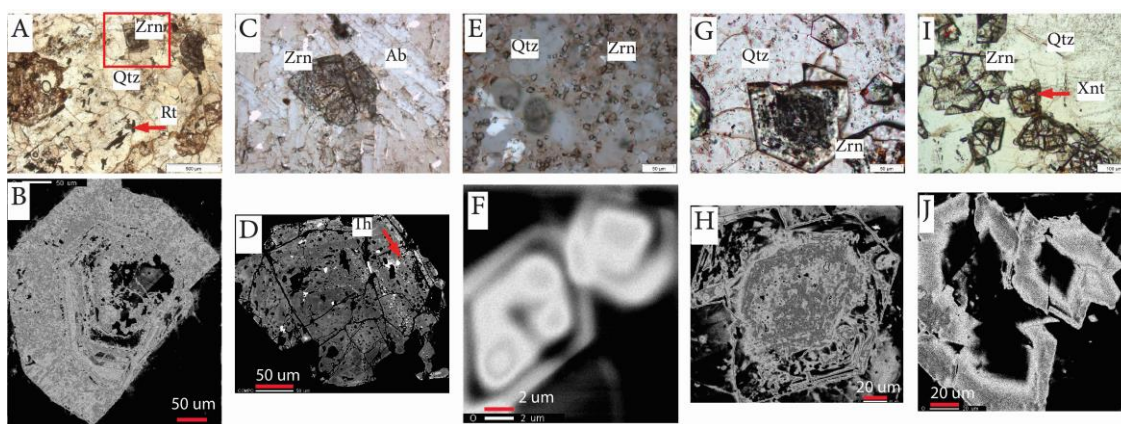


Figure 2-6 Different types of zircon hosted by the granite. A) PPL image of prismatic Type-1 zircon from silicified granite porphyritic granite. B) CL image of Type-1 zircon in A showing Type-1 zircon (core) that was replaced by secondary zircon (bright). C) PPL of a fluid inclusion-rich of the Type-2 zircon from the

porphyritic granite. D) BSE image of zircon in C showing bright thorite inclusions and spongy texture. E) PPL image of small bipyramid zircons (Type-2) from the marginal unit. F) CL image of two grains of bipyramid Type-2 zircon showing wide-spaced zoning. G) PPL image of zircon of Type-3 core and Type-4 rim from the composite-body showing. H) CL image of the large zircon grain in G. I) PPL of Type-4 zircon and xenotime overgrowth (reddish rim) from the mineralized quartz vein. J) CL image of two zircons showing xenotime overgrowth over black core Type-4 zircon.

Abbreviations: Ab. albite, Qtz. quartz, Zrn. zircon, Rt. rutile, Th. thorite.

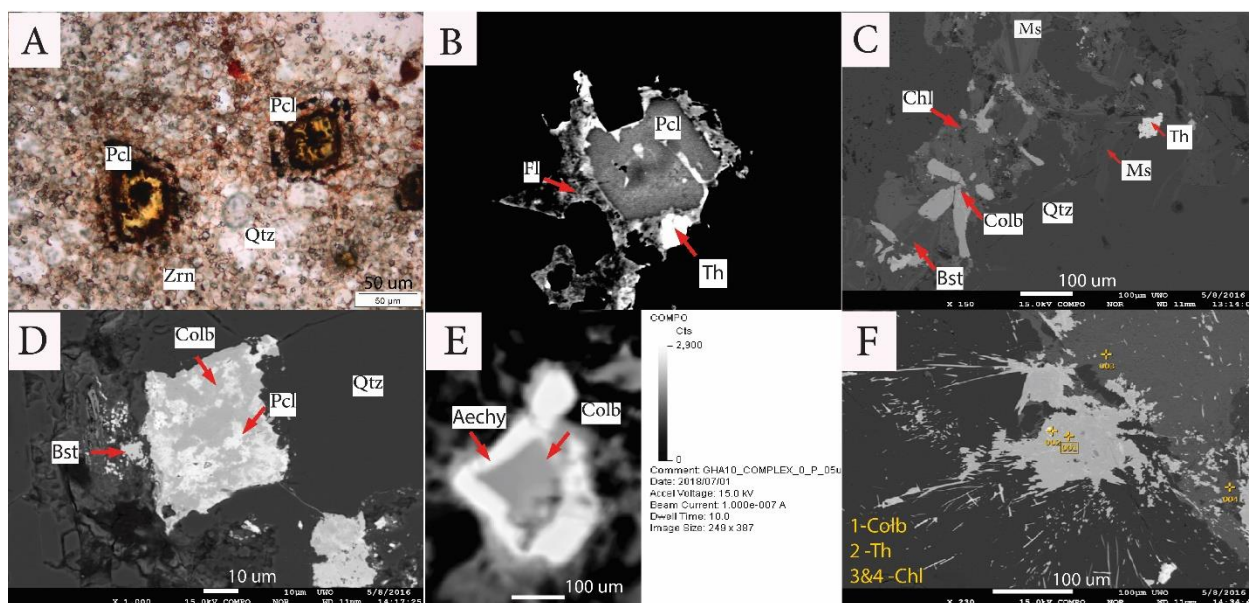


Figure 2-7 Disseminated mineralization from the porphyritic granite and the marginal unit. A) PPL of disseminated zircons (Type-2) and coarse-grained pyrochlore from the marginal unit. B) BSE image of an altered pyrochlore from the marginal unit. The dark core represents early crystallized LREE-rich pyrochlore, whereas the lighter rim is enriched in HREE. The image fluorite surrounding the pyrochlore as well as thorite crystallization on the rim and in cracks C) BSE image of columbite, thorite, and REE-F-carbonate (bastnasite?) crystals associated with chlorite, muscovite and late-quartz from the porphyritic granite. D) BSE image of

an altered pyrochlore crystal that was replaced by columbite and Pb-rich pyrochlore associated with bastnasite. E) BSE image of a columbite replaced by aeschynite in the highly altered granite. F) BSE image of acicular columbites associated with chlorite and fluorite in the highly silicified granite.

Abbreviations: Ab. Albite, Qtz. Quartz, Chl. Chlorite, Colb. Columbite, Zrn. Zircon, Fl. Fluorite, Pcl. Pyrochlore, Bst. Bastnasite, Aechy. Aeschynite, Ms. Muscovite, Th. Thorite.

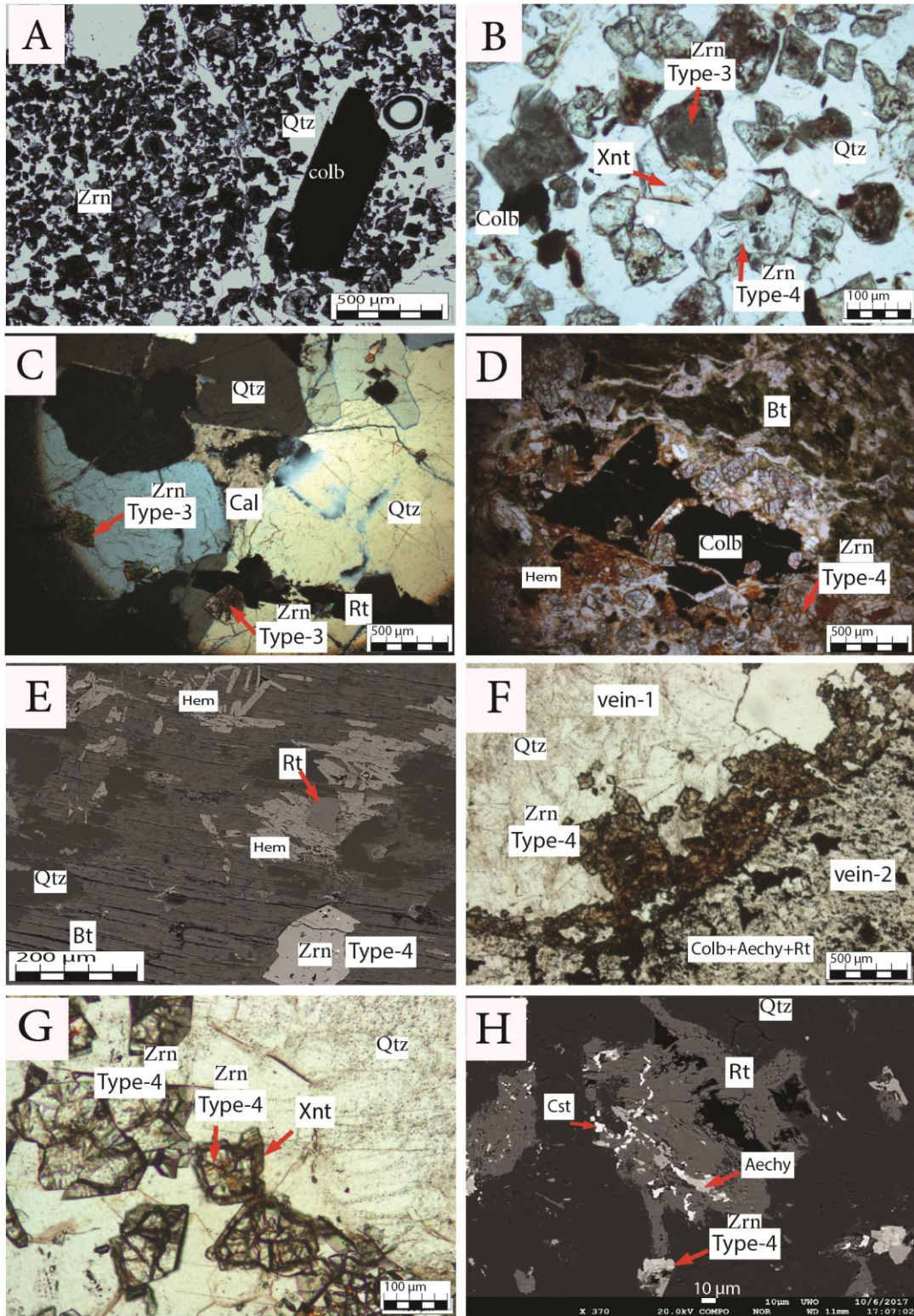
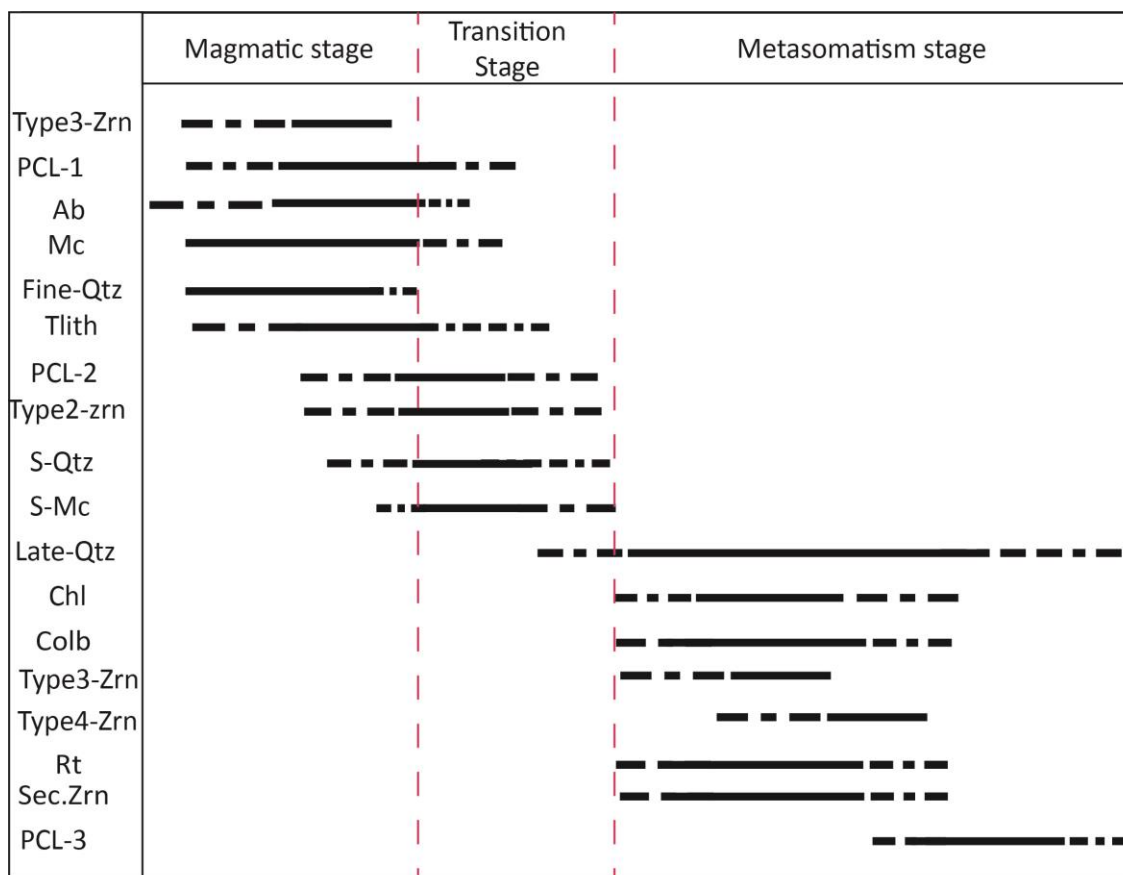


Figure 2-8 Aggregate ore minerals from the aggregate mineralization style. A). PPL of Type-3 and 4 zircons and columbite from the zircon-columbite zone. B) PPL

image showing Type-3 & 4 zircons, xenotime and columbite in quartz matrix from the zircon-columbite zone at the composite-body. C-) PPL of interstitial calcite with Type-3 and 4 zircons and rutile in quartz matrix from at composite-body. D) PPL from the zircon-mica zone from the composite-body showing columbite and Type-4 zircon surrounded by hematite in biotite and quartz matrix. E) BSE image of rutile, hematite, and Type-4 zircon in biotite and quartz matrix from the quartz veins. F) PPL image showing the contact between vein-1 and vein-2 from the quartz veins. G) PPL image showing Type-4 zircon and xenotime overgrowth from vein-1 in the quartz veins. H) BSE image of rutile, aeschynite, Type-4 zircon, cassiterite and hematite from the quartz veins.

Abbreviations: Qtz. quartz, Bt. biotite, Colb. columbite, Zrn. zircon, Fl. fluorite, Cst. cassiterite, Aechy. aeschynite, Ms. muscovite, Th. thorite. Cal. calcite, Hem. hematite, Rt. Rutile, Xnt. xenotime.



Ab: albite; PCL-1 & 2 : magmatic pyrochlore; S-Mc: snowball microcline; Fine-Qtz: fine-grained quartz; S-Qtz: snowball quartz; L-Qtz: late-quartz; Type-1 zircon; Type2-Zrn: Type-2 zircon; tlith: trillithionite; Type3 & 4-Zrn: Type-3 & 4 zircons from the composite-body and the quartz veins; Rt: rutile; Chl: chlorite; Colb: columbite; PCL-3, hydrothermal pyrochlore. Sec.Zrn: secondary zircon from the porphyritic granite.

Figure 2-9 Mineral paragenesis sequence at Al-Ghurayyah deposit. Red dashed lines represent the boundary of the transitional stage. Dashed black lines represent uncertain beginning and/or end of a mineral crystallization, whereas solid lines represent confirmed beginning and/or end of a mineral crystallization.

R1-R2 Plutonic Chemical Variation Diagram

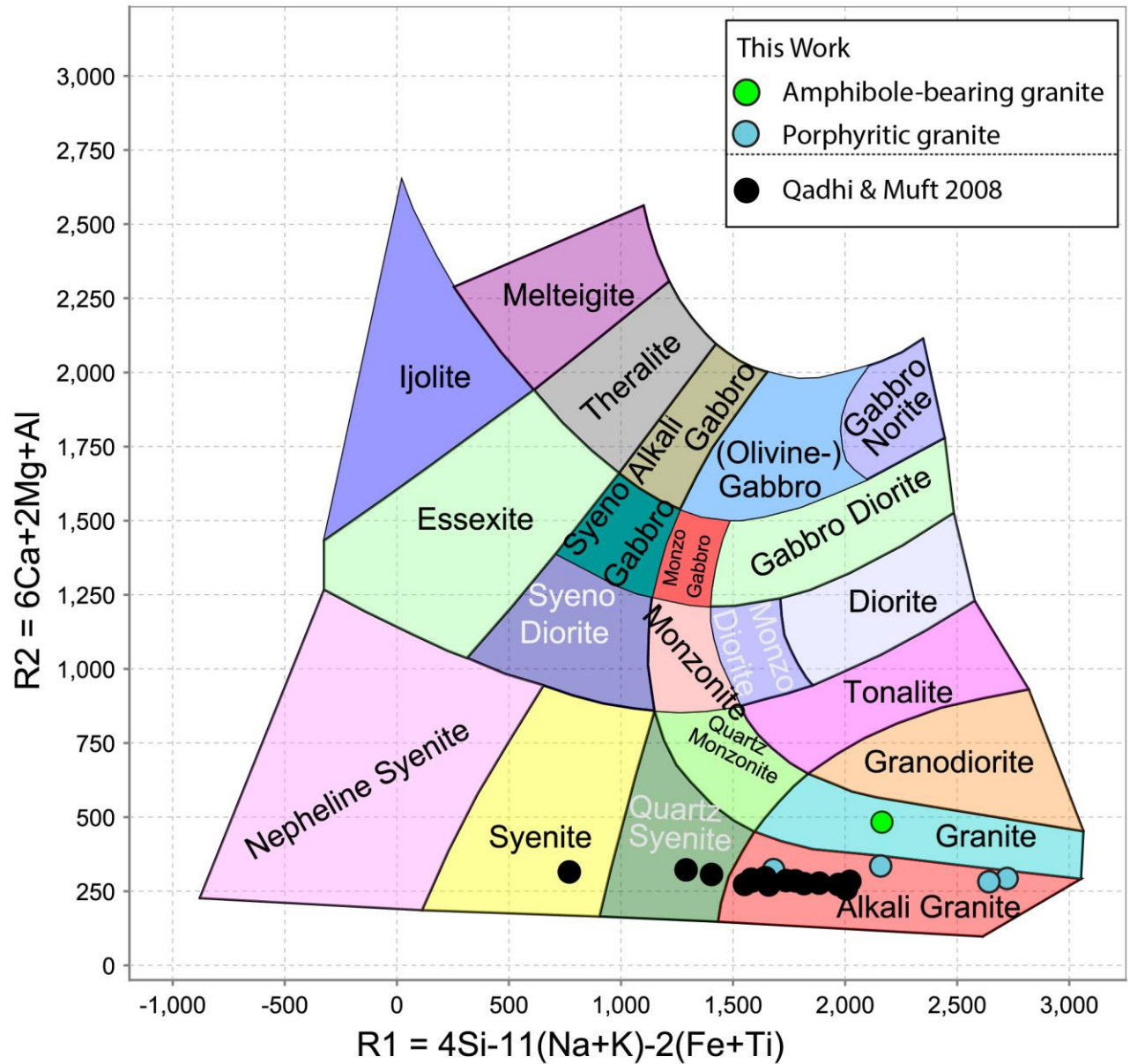


Figure 2-10 R1-R2 granite classification diagram (after De La Roche 1980).

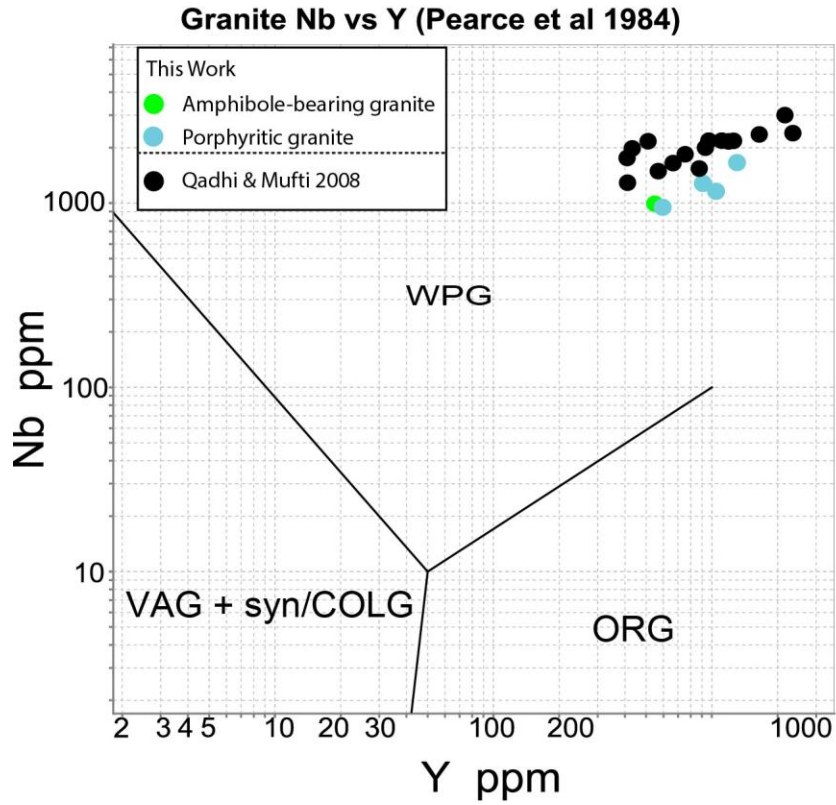


Figure 2-11 Tectonic settings discrimination diagram of (Pearce et al. 1984). WPG, within plate granite; ORG, oceanic ridge granite; VAG, volcanic arc granite; Syn/COLG syn-collision granite.

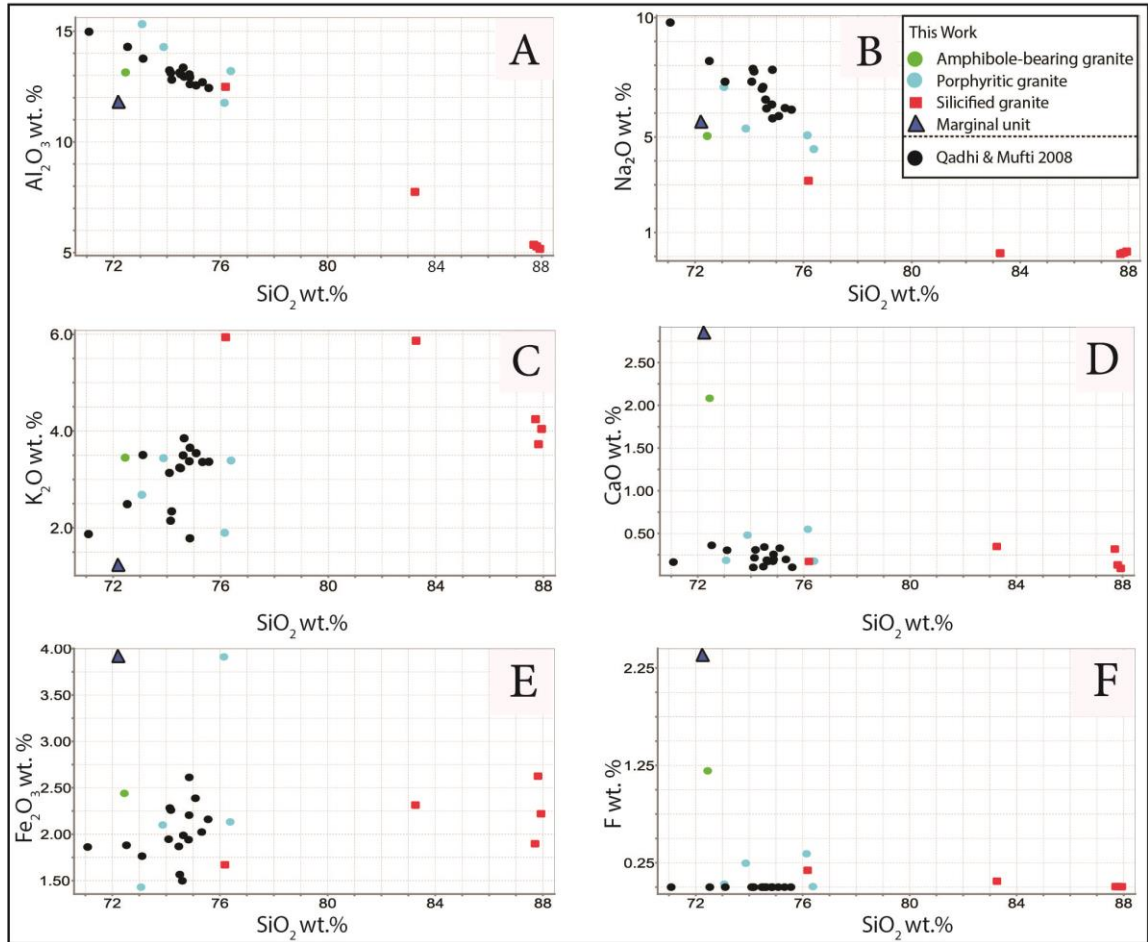


Figure 2-12 Major oxides vs. SiO₂. Porphyritic granite has a similar composition to the granite samples from Qadhi and Mufti (2008). Amphibole-bearing granite and the marginal unit have high CaO and F contents. In addition to the high SiO₂ content, silicide granite has low Al₂O₃ and Na₂O, and variable K₂O concentrations.

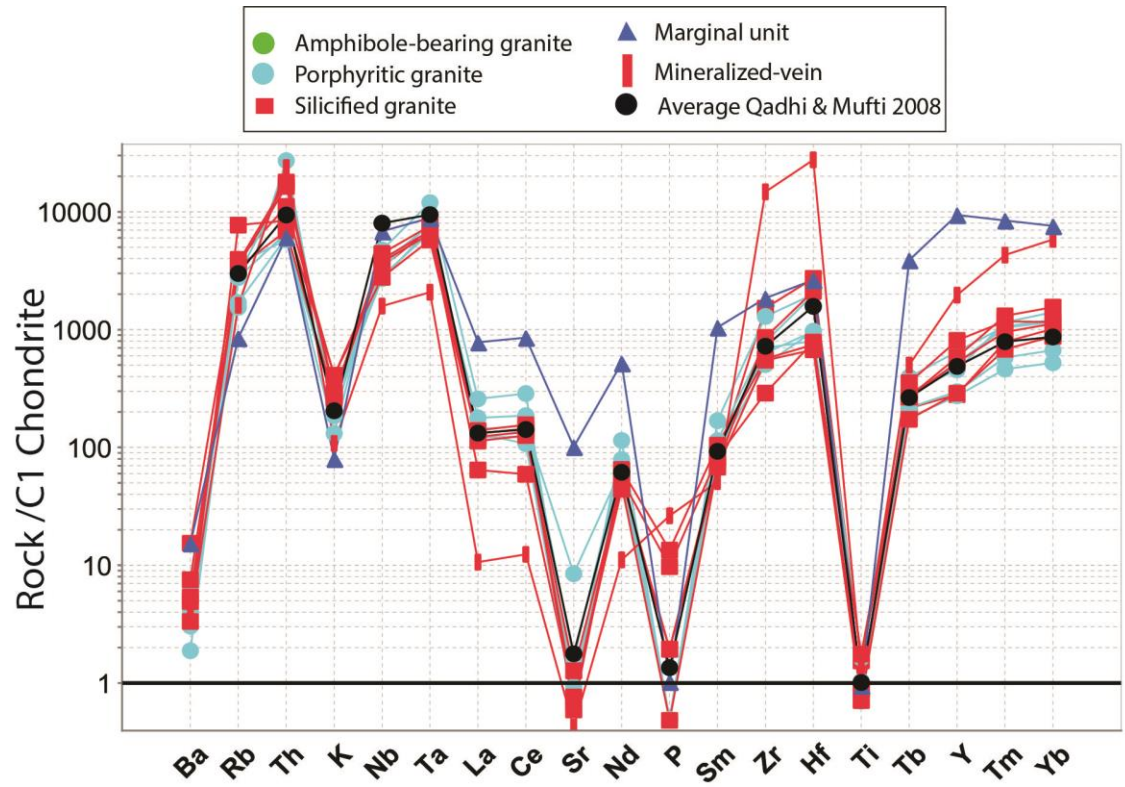


Figure 2-13 Chondrite-normalized large-ion lithophile element (LILE), HFSE and REE abundances. The values for C1 Chondrite are from Thompson (1982).

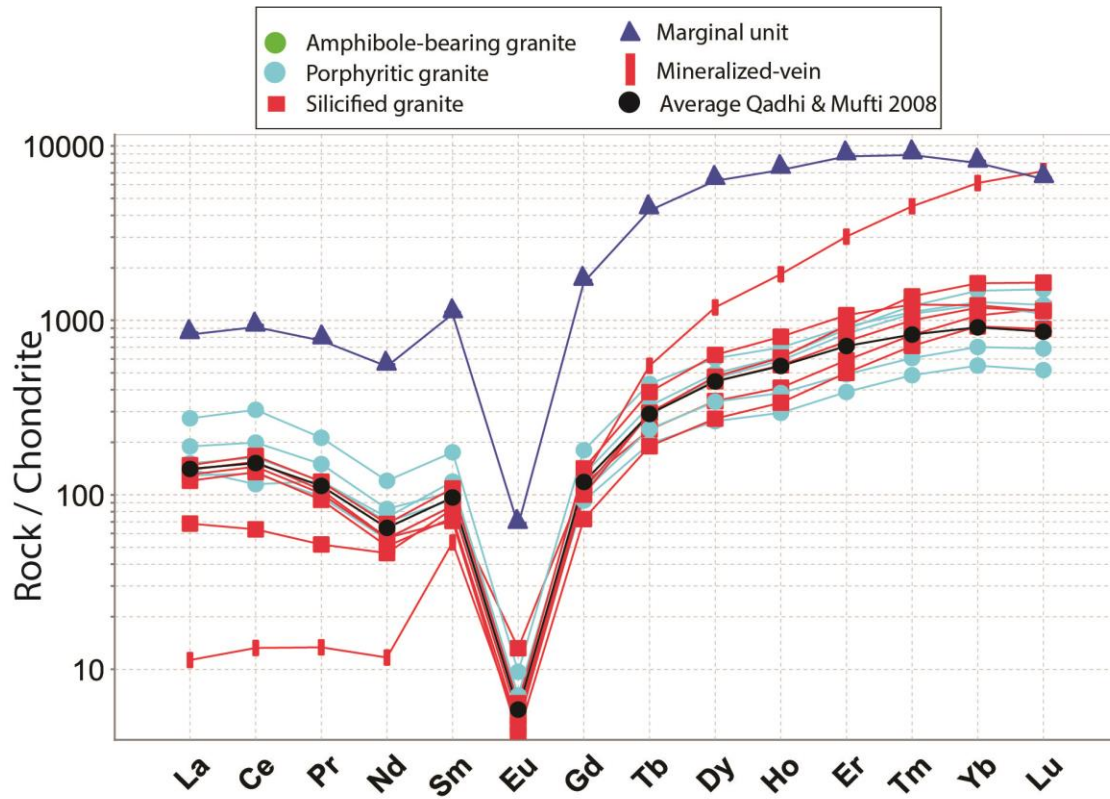


Figure 2-14 Chondrite-normalized REE pattern. Chondrite values are from Boynton, 1984.

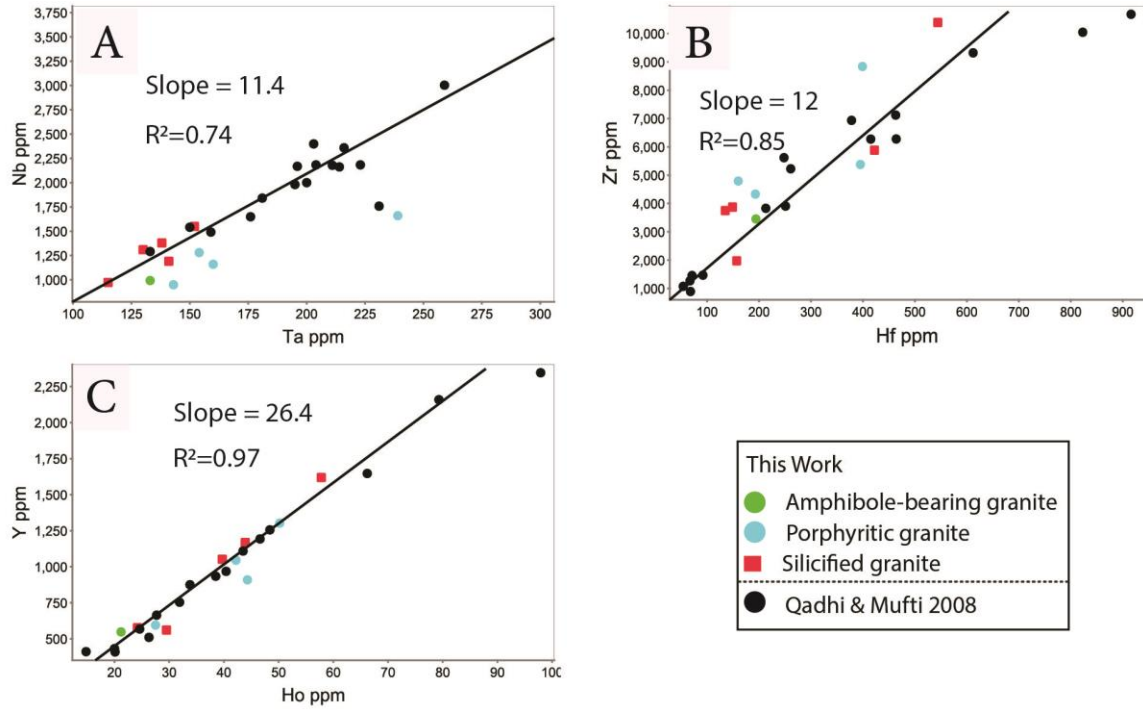


Figure 2-15 Nb vs. Ta, Zr vs. Hf, and Y vs. Ho plots showing a strong geochemical correlation. Lines are least-squares fit of the data.

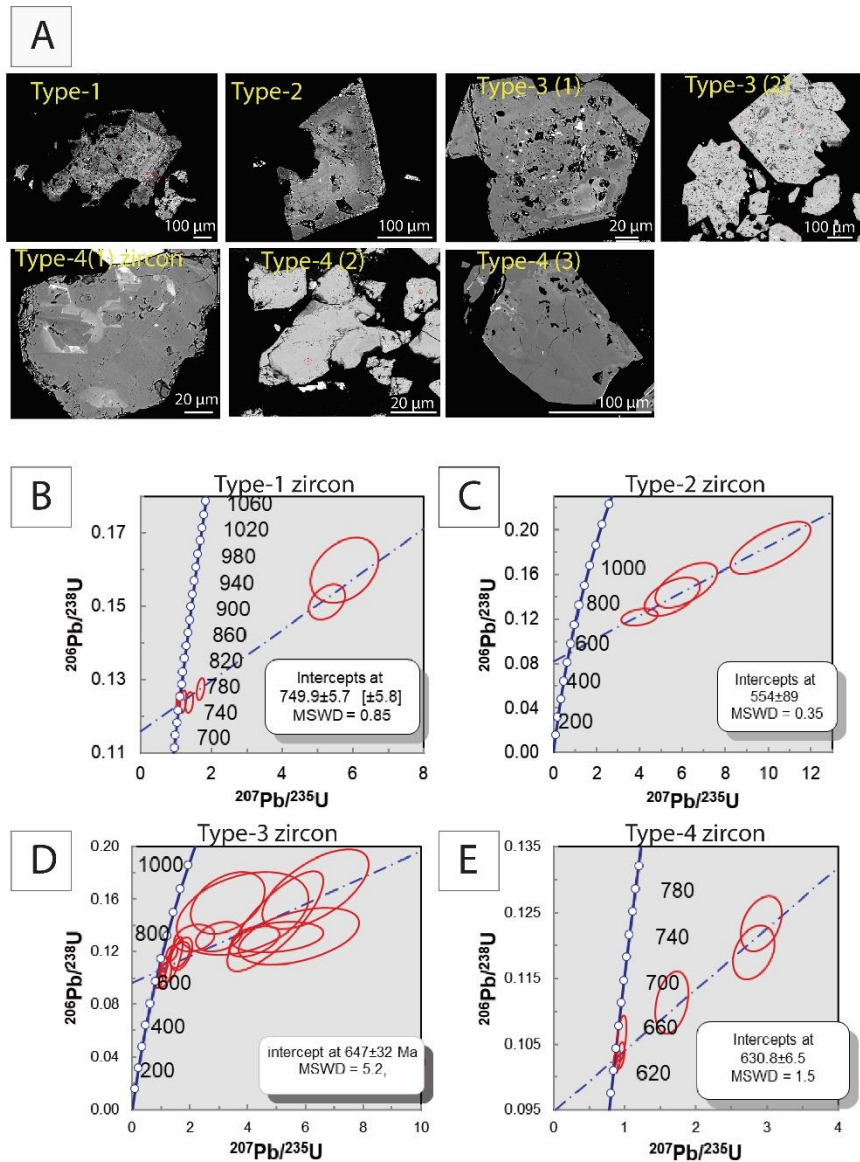


Figure 2-16 U-Pb zircon age dating from different zircon types hosted in different rock units. A) BSE images of analyzed zircon grains. B) inclusion-rich Type-1 zircon from a highly silicified granite. C) Type-2 zircon grains from the porphyritic granite. D) Type-3 zircons from the zircon-columbite zone in the composite-body. Type-4 zircon from the zircon-columbite and the mica-zircon units from the composite-body.

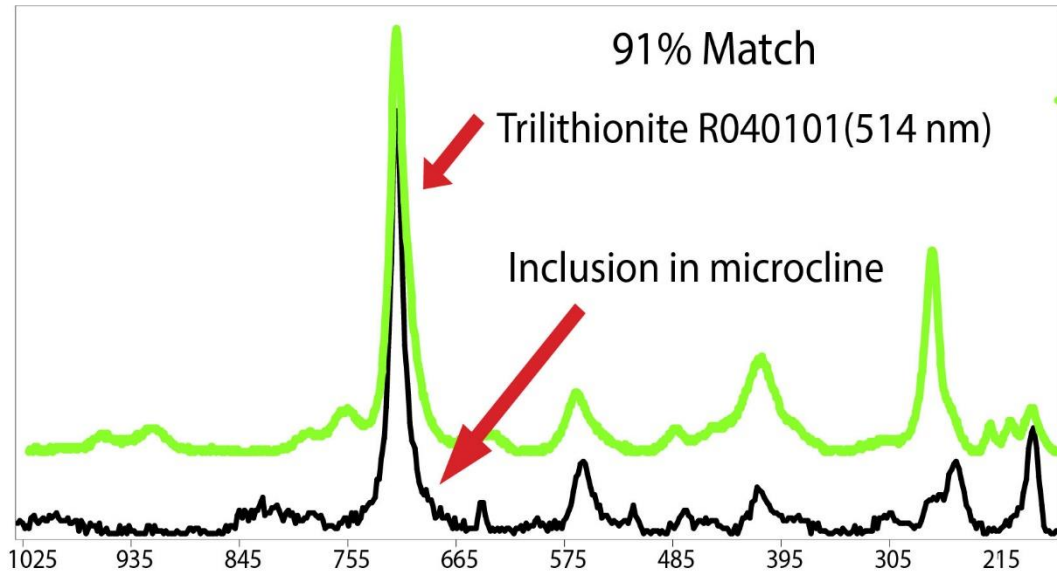


Figure 2-17 Raman spectrum of a mica inclusion from the porphyritic granite. The mica spectrum (black) shows a 91 % match with trilithionite from RRUFF database (ID R040101, 514 nm).

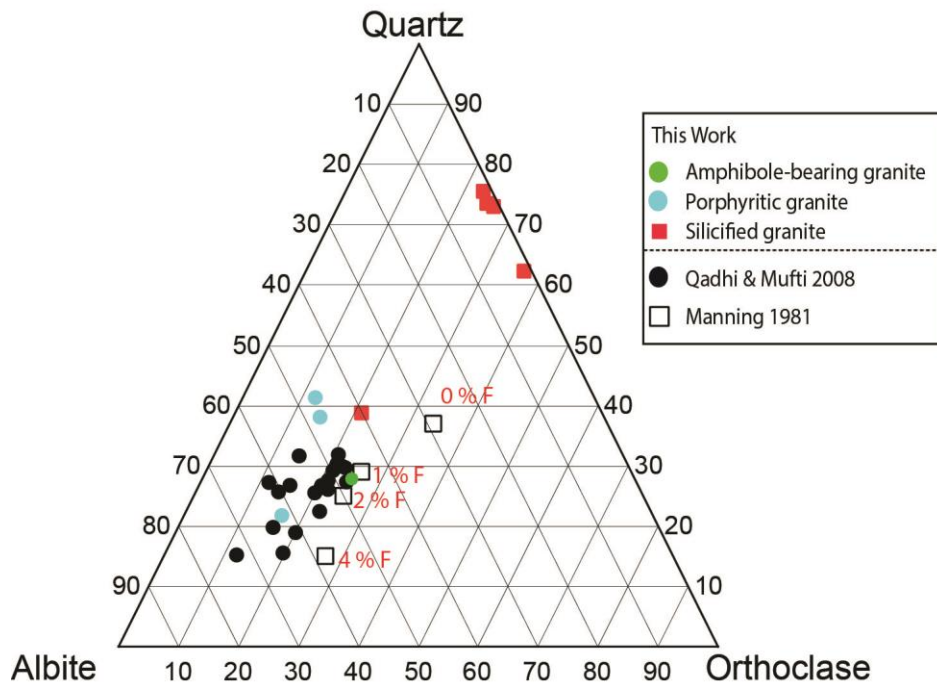


Figure 2-18 Normative quartz-albite-orthoclase of Al-Ghurayyah granite samples. The granite data from this work and Qadhi and Mufti, (2008) show a trend toward albite and close to the magmatic trend in F-rich granite (Manning 1981).

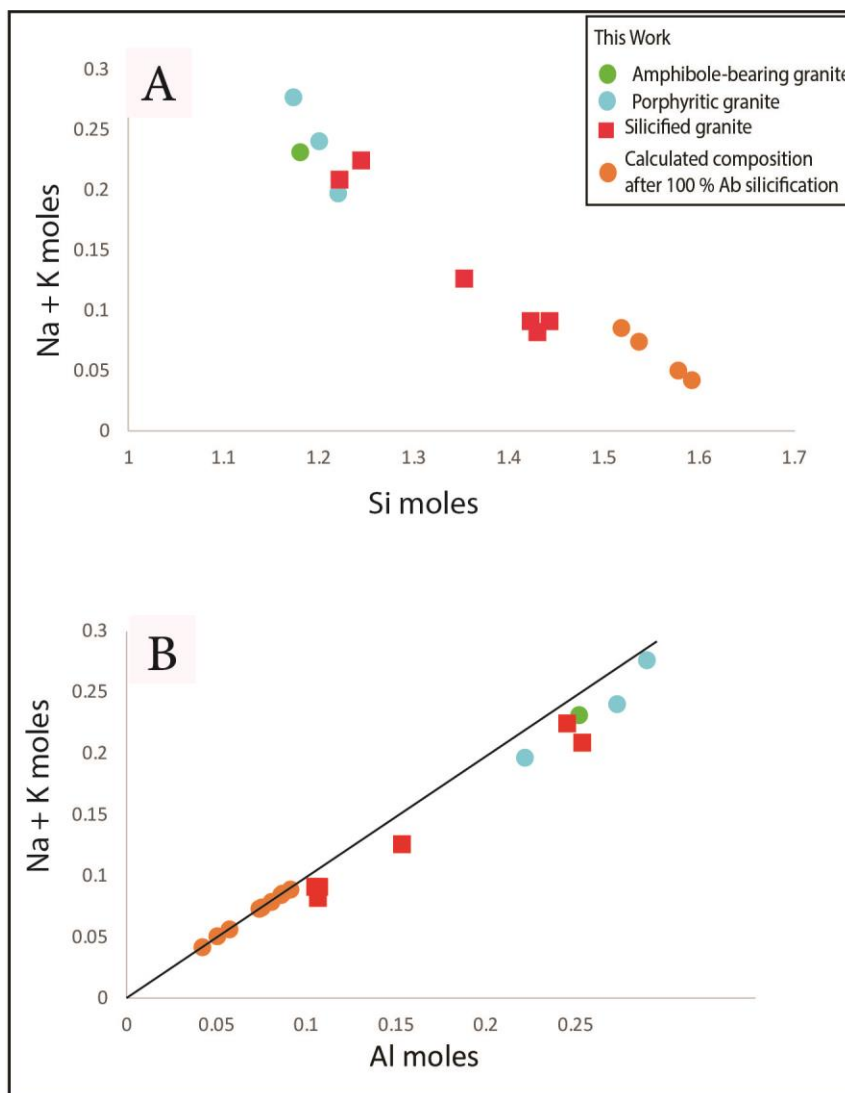


Figure 2-19 A) Molar whole rock Na +K vs. Si from this study. B) Molar whole rock Na + K vs Al from this study. The diagrams show the effect of preferential silicification of albite over microcline. Orange circles represent that composition if 100 % of albite was replaced by secondary quartz. The line in Figure B is slope of 1, which indicates that Na-K-Al are completely controlled by feldspars.

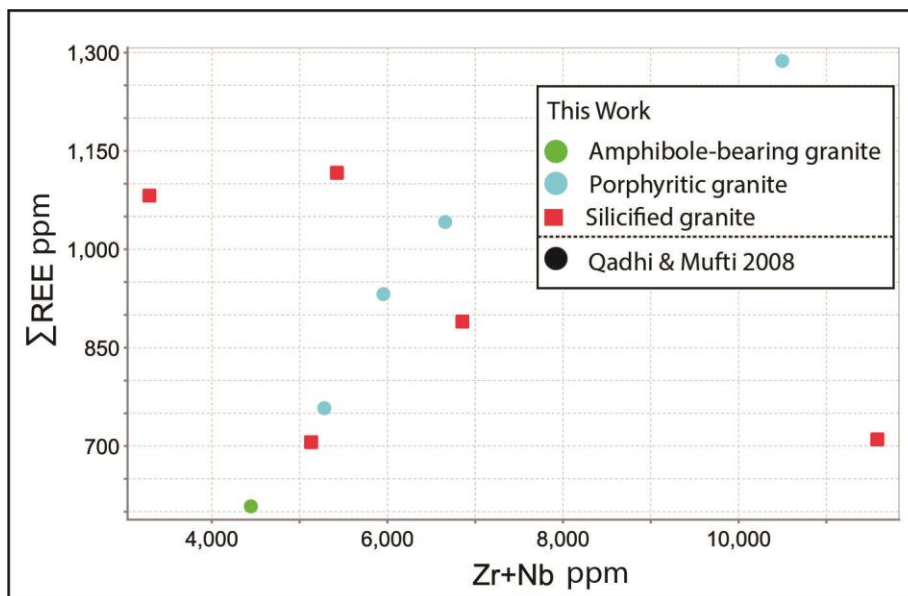


Figure 2-20 Total REE vs Zr+Nb of this study samples. Fresh and least altered granites show a positive correlation indicating that zircon and pyrochlore are the main host of REE.

Chapter 3

3 Chemistry and morphology of HFSE and REE minerals at Al-Ghurayyah, the Arabian Shield, Saudi Arabia

3.1 Introduction

High field strength elements (HFSE) and rare earth elements (REE) are essential components in advanced optical, electronics, and space technologies. This has led to high demand for these elements. Future sources of these metals include rare-metal alkaline granites, which contain high concentrations HFSE and REE. Some examples of these granites are Al-Ghurayyah (Saudi Arabia), Motzfeld (Greenland), Khaldzan-Buregtey (Mongolia), and Strange Lake (Canada) (Linnen et al., 2014). The rare-metal alkaline granites are associated with post-orogenic tectonic settings (Dostal, 2016). In most ore deposits hosted by alkaline granites the primary zircon and pyrochlore have been destroyed by alteration. However, the abundances of HFSE and REE increase with alteration intensity, leading to a debate on the importance of magmatic versus hydrothermal processes.

Al-Ghurayyah is an exceptional case because both zircon and pyrochlore are preserved in the magmatic and hydrothermal stages. This provides an excellent opportunity to examine the magmatic to hydrothermal transition, that is obscured in most deposits.

Al-Ghurayyah rare-metal alkaline granite (Fig. 3.1) is one of the most prospective HFSE deposits in alkaline granite in the world (Küster, 2009) with an inferred resource of 385 million tons grading 245 g/t Ta₂O₅, 2840 g/t Nb₂O₅, 8915 g/t ZrO₂, and 1270 g/t Y₂O₃ (Cheetham et al., 2007). The majority of HFSE and REE are hosted by zircon, pyrochlore, and columbite with lesser amounts of aeschynite, xenotime, cassiterite, and REE-fluorocarbonate minerals. Nevertheless, the mineralization remains poorly studied except for few geological reports (Elliott et al., 2002; Staatz and Brownfield, 1986), and one published paper (Qadhi and Moufti, 2008), or as a part of larger scale studies that investigate the mineralization associated with felsic rocks (Drysdall et al., 1984; Jackson, 1986; Küster, 2009; Ramsay, 1986).

The texture and composition of the host rock are complex. The magmatic stage is overprinted by a metasomatic stage (Chapter 2), and the two stages are difficult to distinguish. However, the magma evolution and the post-magmatic events can be further evaluated from the chemistry and morphology of accessory minerals. For example, zircon is known as a refractory mineral, and it has been used for age dating and petrogenetic modelling (Chen and Zhou, 2017; Hoskin and Schaltegger, 2003; Pettke et al., 2005; Yang et al., 2014). Moreover, zircons that have crystallized in magmatic and hydrothermal environments have characteristic morphologies and chemical signatures (Chen and Zhou, 2017; Corfu et al., 2003; Fu et al., 2009; Hoskin, 2005; Hoskin and Schaltegger, 2003; Pettke et al., 2005; Schaltegger, 2007; Wu et al., 2018; Yang et al., 2014). In Al-Ghurayyah, zircon is the most common accessory mineral and occurs in most of the rock units (Chapter 2). It is associated with other ore minerals, such as pyrochlore and columbite, in addition to other accessory minerals, such as xenotime, aeschynite, and samarskite.

This study will investigate the morphology and chemistry of zircon, pyrochlore, and columbite to evaluate the roles of magmatic and hydrothermal processes and how they contribute to the formation of the mineralization at Al-Ghurayyah deposit. This will be accomplished by studying the textural relationships between ore minerals and rock-forming minerals. Cathodoluminescence (CL), and wavelength and energy dispersive spectroscopy (WDS and EDS) mapping will be used to study the internal chemical variation. This will be followed by mineral chemistry analyses from electron microprobe (EMPA), and laser ablation inductively coupled plasma mass spectrometry (LA-ICP-MS).

3.2 Geology and petrography of Al-Ghurayyah deposit

Al-Ghurayyah is a small sub-circular stock (900 m in diameter) that is exposed by several outcrops separated by Quaternary sediments and located in the north-central part of the Midyan terrane (Fig. 3.1) (Johnson et al., 2011; Qadhi and Moufti, 2008). It forms sharp contacts (where exposed) with metasedimentary-metavolcanic Silasia Formation (>710 Ma; Johnson, 2006) (Fig. 3.2). The main rock unit at Al-Ghurayyah is a medium-grained to porphyritic pink granite that consists of approximately 40 % quartz, 35 % albite, 20 %

K-feldspar (microcline), and < 1 % mica (trilithionite). Quartz, and less commonly K-feldspar, form large euhedral to subhedral phenocrysts (up to 10 mm) and display a snowball texture where albite, fine quartz, zircon, pyrochlore, and mica crystals (trilithionite) occur along quartz growth zones (Fig. 3.3 A and B). Quartz in the matrix is fine-grained (100 μm) and anhedral. Albite occurs as lath-shaped crystals making up approximately 80 % of the matrix minerals and forms an intergranular texture with fine-grained quartz, zircon, and pyrochlore. K-feldspar is microcline, which is identified by the cross-hatched twinning. Microcline is generally medium-grained anhedral crystals intergrown with albite in the matrix, and locally displays a snowball texture (Fig. 3.3 B). Early mica has a trilithionite composition (Chapter 2) and commonly occurs as inclusions in snowball phenocrysts (Fig. 3.3 A and B). Late mica has a muscovite composition and commonly occurs as an alteration mineral associated with silicification (Chapter 2). Amphibole-bearing granite is rare and only observed in one locality in the southernmost outcrop (Fig. 3.2). This granite is light grey, medium-grained and consists of 40-45 % plagioclase, 25 % quartz, 20-25 % microcline, < 5 % sodic amphibole, and < 1 % mica (trilithionite) based on visual estimation of mineral proportions. Quartz occurs as fine-grained subhedral to rounded crystals in the matrix with albite, or as large phenocrysts that display a snowball texture with inclusions of albite (Fig. 3.3 C). Albite occurs as lath-shaped crystals that form the bulk of the matrix. Commonly, albite occurs as inclusions in phenocryst minerals, such as quartz and K-feldspar. K-feldspar occurs as subhedral to anhedral grains marked by cross-hatched twinning, which is interpreted as microcline. Sodic amphibole occurs as subhedral crystals with strong dark blue to green pleochroism (Fig. 3.3 D). Zircon is present as disseminated, subhedral, dark brown to dark yellow prismatic crystals that show a close spatial-temporal association with pyrochlore (Fig. 3.3 E).

At the contact with the country rock, a marginal unit was recognized, which is a fine-grained aplite with a pinkish color that changes to dark-brown to reddish-brown at the contact with the country rock (Fig. 3.2). This unit is approximately 0.6 m wide and is present along the exposed contact with the country rock. It consists of 70 to 80 % quartz and albite (very difficult to distinguish between them due to the fine grain size; < 10 μm), 5 to 10 % zircon, 5 % large flakes (1 mm) poikilitic trilithionite, 1 % anhedral poikilitic

microcline (from 100 μm to 1mm), 1 % pseudomorphs (chlorite and hematite after sodic amphibole), and 1 % pyrochlore (50 μm) and opaque minerals. Quartz occurs as small anhedral to rounded crystals that are < 10 μm across. Zircon is present as euhedral bipyramid equant crystals < 30 μm across. They occur as disseminated crystals throughout the thin section (Fig. 3.3 F) and are present as inclusions in trillithionite and microcline (Fig. 3.3 G). Microcline occurs in the matrix as large irregular crystals (1 mm) that encompass other matrix minerals. Trillithionite occurs as 10 to 1000 μm flakes with a poikilitic texture. The inclusions in trillithionite are mostly euhedral zircon and quartz (Chapter 2 Fig. 2.5 E & F).

A unique composite-body that consists of four segments crosscuts the porphyritic granite in the southern part of the intrusion (Fig. 3.2). The composite-body has an irregular shape and is in sharp contact with Al-Ghurayyah granite (Fig. 2.3, Chapter 2). It consists of zones of zircon-columbite, K-feldspar (microcline) and mica-zircon. The mica-zircon zone is radioactive, with greater than 10000 counts per second (cps) total alpha, beta, and gamma radiation measured using a handheld Technical Association radiation detector. The zircon-columbite zone consists of approximately 40% zircon (100 to 500 μm), 10% columbite (100 to 900 μm), 5% rutile (100 μm), and 1% xenotime (50 μm), all embedded in a quartz matrix that forms approximately 20% of the rock (Fig. 3.3 I). The K-feldspar zone consists of monominerallic microcline with cross-hatched twinning. The mica-zircon zone consists of 60% Fe-Mica (siderophyllite, Chapter 2) (200 μm to 1 mm), 20 to 25% zircon (100 to 500 μm), 10% hematite (100 μm), < 5% quartz, < 1% columbite (100 to 900 μm), < 1% thorite and minor amounts of REE-fluorocarbonate (Fig. 3.3 J).

Two types of quartz veins are present at Al-Ghurayyah. The first type is white quartz veins with variable fluorite that is concentrated in the center of the vein. Veins range in thickness from 10 to 30 cm, are typically not mineralized, and generally occur near fault zones. This type will not be investigated in this study. The second type is greyish white quartz pods and veins that are less common relative to the white quartz veins and smaller (5-10 cm thick). The mineralogy is variable with some veins containing up to 40% microcline and 5% muscovite in addition to quartz.

3.3 Methodology

Samples from the host granites, the marginal unit, and the quartz veins were collected for petrographic study and mineral microanalyses. Polished thin section slides were prepared in the Department of Earth Sciences at the University of Western Ontario, Canada, and the Faculty of Earth Sciences, at King Abdul Aziz University, Jeddah, Saudi Arabia. Polished thin sections were studied using a petrographic microscope and a scanning electron microscope equipped with energy dispersive spectroscopy (SEM-EDS) to obtain mineralogical, texture and mineral composition data at the Department of Earth Sciences at the University of Western Ontario, Canada. Semi-quantitative major and minor element compositions of minerals and backscattered electron images (BSEI) were obtained using JEOL JCM 6000 benchtop SEM equipped with EDS (B-SEM). Data were collected at 15 kV acceleration voltage at high vacuum mode. Quantitative mineral compositions, cathodoluminescence (CL), and EDS analyses were determined on a JEOL JXA-8530F field-emission electron microprobe (EMPA) at Earth and Planetary Materials Analysis Laboratory at the University of Western Ontario, Canada. The analytical conditions of the EPMA were 20 kV probe current, 40-60 nA accelerating voltage, beam diameter ranging from 1 to 15 microns, 10 to 60 seconds counting time on the main peak, and 5 to 30 background counting time. The standards were synthetic zircon for Zr and Si, rutile for Ti, albite for Na and Al, fluorite for F, orthoclase for K, anorthite for Ca. Pure metal standards (serial 2AG-METM25-44, Astimex Standards Limited) were used for iron in oxide accessory minerals, Mn, Nb, Ta, Hf, Pb, Th, and U. The Smithsonian REE phosphate (NMNH 168484-116499) standard was used for REE analysis. In order to resolve the REE peak and background overlaps, corrections were made by performing a slow scan on WDS crystals (LIF, LIFH, and LIFL) to identify the elements with peak and background overlaps. The contributions of overlaps to the main peaks were measured and then subtracted from the main peak (element overlaps and the amounts of overlap are given in Appendix B).

In order to obtain the trace element contents of zircons, laser ablation inductively coupled plasma mass spectrometry (LA-ICP-MS) analyses was performed at the Great Lakes Institute for Environmental Research (GLIER) at the University of Windsor, Ontario,

Canada. The analyzed zircons were from Type-1, Type-2, and Type-4 (see classification below). Type-3 zircon was not analyzed due to the high abundance of mineral and fluid inclusions and the laser beam size, which was larger than the inclusion-free areas. The analyses were obtained using a Photon-Machines 193 ArF excimer laser with 20 micrometers beam diameter, 20 Hz repetition rate, and 1.63 J/cm² energy. The ICP system is an Agilent 7900 ICP-MS. Ar gas flow was 0.82 L/min with 30 milliseconds were used as wash delay. NIST 610 was used as an external standard the Zr concentrations from EMPA analyses were used as the internal standard. In zoned grains, the average concentration of Zr of the ablated area was used as the internal standard. The data processing and data reduction were done using IGORPro and Iolite software (Paton et al., 2011). The isotope list and the average detection limits are summarized in Table 3.1.

3.4 Results

3.4.1 Morphologies of ore minerals

Disseminated and aggregate mineralization styles at Al-Ghurayyah occurs in all rock units except for the white quartz veins (Chapter 2). The disseminated mineralization style is present in the porphyritic granite and the marginal unit, whereas the aggregate mineralization style occurs in the composite-body and the quartz veins. Each style has a distinct mineral assemblage and morphology of the ore minerals. The main HFSE and REE minerals at Al-Ghurayyah are zircon, pyrochlore, and columbite. Other HFSE and REE minerals that are less abundant and/or occur as replacement products of the main ore minerals include aeschynite, samarskite, rutile, xenotime, REE-fluorocarbonate, and Y-fluorite.

3.4.1.1 Zircon

Zircon is the most common HFSE mineral and occurs in all of the rock units at Al-Ghurayyah. Based on morphology and the host rock, zircon was classified into four types (Table 3.2 and Fig. 3.4). Type-1 zircon is disseminated in the matrix of the porphyritic granite where it occurs in an intergranular texture with albite, microcline and quartz (Fig. 3.4 A to F). This zircon is clear to light brown, but altered grains are darker and reddish.

It has subhedral to anhedral shapes, and overall crystals are equant and range in size from 100 to 500 μm . In plane-polarized light, Type-1 zircon locally displays zoning due to the presence of inclusion-rich zones concentrated at the rim. Type-1 zircon displays medium to wide-spaced oscillatory zoning with a dark core and a lighter rim in the backscattered electron (BSE) and cathodoluminescence (CL) images (Fig. 3.4 B, D, and F). Type-2 zircon occurs as disseminated crystals in the porphyritic granite and the marginal unit (Fig. 3.4 F to L). In the porphyritic granite, Type-2 zircon is clear to greyish color subhedral to anhedral crystals that range in size from 50 to 500 μm . Type-2 zircon is rarely present as small (10 μm) euhedral bipyramid inclusions in the snowball quartz in the porphyritic granite, similar to the disseminated zircons in the marginal unit. Zircons in the marginal unit show wide-spaced bimodal zoning to a lack of zoning in CL images (Fig. 3.4 J to L). Due to the similarity in morphology and composition, zircons from the marginal unit are classified as Type-2 zircon.

Another type of zircon was observed as a replacement after Type-1 and 2 zircons as secondary zircon veinlets and overgrowths. This type is easy to distinguish from Type-1 in BSEI and CL images where it occurs as bright veinlets that crosscut Type-1 or as bright rims (Fig. 3.4 B, D, F, and H). However, Type-2 zircon is difficult to distinguish from the secondary zircons because they both give bright BSE and CL images. Nevertheless, the secondary zircon shows a rough surface due to its spongy texture (Fig. 3.4 B and H), which is typical of secondary phases (Putnis, 2009). The secondary zircon is locally associated with chlorite, muscovite, and hematite \pm columbite (COLB-2, see classification below), and rutile.

In the aggregate mineralization style, zircon was classified into Type-3 and Type-4. Type-3 zircon crystals have a dark brown to reddish color, are subhedral to anhedral and range in size from 200 to 500 μm (Fig. 3.4 M to O). This type is mineral and fluid inclusion-rich with the mineral inclusions being predominantly hematite and thorite. Type-3 zircon lacks zoning in BSE and CL images and is associated with columbite (COLB-3, see classification below), hematite, and rutile, \pm fluorite, calcite, and xenotime. Type-4 zircon is present as individual crystals or as overgrowths on Type-3 zircon. It occurs as transparent and colorless subhedral to anhedral crystals that range in size from

50 to 400 μm . This type is also characterized by a low abundance of inclusions, and its zoning is patchy to absent. This type is commonly associated with columbite and rutile, and commonly has xenotime overgrowths.

3.4.1.2 Pyrochlore

Pyrochlore is the main Nb phase in the porphyritic granite and the marginal unit. Pyrochlore was classified into primary and secondary pyrochlore based on the textural relationships with rock-forming minerals and the alteration events (Table 3.3). The primary forms a typical magmatic intergranular texture in porphyritic granite and marginal unit. It was subclassified into PCL-1, which occurs in the porphyritic granite and PCL-2, which occurs in the marginal unit. The secondary pyrochlore (PCL-3) occurs as a replacement after columbite and primary pyrochlore in porphyritic granite and marginal unit.

PCL-1 occurs in the porphyritic granite and is associated with Type-1 zircon. This type occurs as light yellow euhedral to subhedral crystals that range in size from 15 to 50 μm across (Fig. 3.5 A and B). It is present as disseminated crystals that form an intergranular texture with albite in the porphyritic granite (Fig. 3.5 A). The color at the rim of the crystals changes to dark brown and reddish (Fig. 3.5 B), where it is replaced by a variety of minerals including fluorite (and Y-fluorite), columbite, samarskite, and aeschynite \pm REE fluorocarbonate.

The second type PCL-2 occurs in the marginal unit as disseminated crystals and associated with Type-2 zircon (Fig. 3.5 C). Pyrochlore-2 is present as yellow anhedral crystals that are approximately 25 μm across and locally contain inclusions of quartz. Moreover, this type displays bimodal zoning in WDS X-ray maps.

The secondary PCL-3 occurs as a replacement after the primary pyrochlore in the porphyritic granite and the marginal unit, and a replacement mineral after columbite in the porphyritic granite, the composite-body and the mineralized quartz veins (Fig. 3.6). The PCL-3 occurs as small zones (1 to 5 μm) at the rim of primary pyrochlore and

columbite, and as veinlets that crosscut columbite. In addition to the precursor mineral remnants, this type is associated with Y-samaraskite, rutile, and Y-aeschynite.

3.4.1.3 Columbite

Columbite is the main Nb mineral in the composite-body and the mineralized quartz veins. However, it is locally present in the silicified porphyritic granite, which is associated with fluorite, chlorite, muscovite, and late quartz (Fig. 3.6). Based on the associated mineral assemblage and the morphology, columbite can be classified into three types (Table 3.4). The first type of columbite (COLB-1) is present as a replacement of the primary pyrochlore (PCL-1 and PCL-2) and occurs as narrow rims and as veinlets, or as small crystals (20 μm across) in highly altered pyrochlore (Fig. 3.6 A). The second type (COLB-2) occurs as subhedral crystals with variable sizes (10 to 300 μm across) associated with chlorite, Type-2 zircon, muscovite, rutile, and hematite in the porphyritic granite (Fig. 3.6 B). It is partially replaced by PCL-3 and aeschynite that occur as veinlets crosscutting the columbite crystals. The third type of columbite (COLB-3) occurs in the composite-body and the mineralized quartz vein as subhedral prismatic crystals that range in size from 100 to 900 μm across (Fig. 3.6 C and D). This type is associated with Type-3 and Type-4 zircons, rutile, hematite, and xenotime.

3.4.2 Compositions of ore minerals

The results of electron microprobe analyses of zircon, pyrochlore, and columbite and the LA-ICP-MS trace element concentrations of zircon are summarized in Tables 3.5, 3.6, and 3.7.

3.4.2.1 Zircon

Electron microprobe and LA-ICP-MS analyses of zircons show major differences between the four zircon types in major and trace element contents (Table 3.5). LA-ICP-MS analyses were obtained from Type-1, 2, and 4 zircons. Type-3 zircon is inclusion-rich, which makes it difficult to analyze using a laser beam.

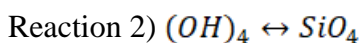
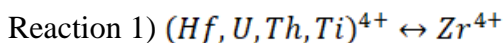
The zircon stoichiometry is calculated by normalizing to the total cations assuming full occupancy by Si, Ti, Al, and P (Speer, 1982). Hafnium can enter zircon structure by a

simple substitution where 1 atom of Hf^{4+} substitutes 1 atom of Zr^{4+} (Hoskin and Schaltegger, 2003), which stoichiometrically can be represented by $(\text{Zr}_{1-x}\text{Hf}_x)\text{SiO}_4$. A coupled substitution is common in zircon, where REE^{3+} and P^{5+} substitute for Zr^{4+} and Si^{4+} , which stoichiometrically can be represented by $(\text{Zr}_{1-x}\text{REE}_x)(\text{Si}_{1-y}\text{P}_y)\text{O}_4$ (Hoskin and Schaltegger, 2003; Speer, 1982).

In Type-1 zircon, the oscillatory zoning is manifested as variations in Hf and REE + Y, where Hf increases from core to rim and REE + Y decrease (Fig. 3.7 A and B). Type-2 zircon has a comparable composition to Type-1 except for an increase in the overall Hf concentration at the crystal rims. Type-3 and Type-4 have high Hf relative to Type-1 and Type-2 zircons and show sector and patchy zoning with respect to Hf (Fig. 3.7 C). The secondary zircon has a composition that range between those of Type-2 zircon and those of Type-3 and 4 zircons (Fig. 3.8 C).

Figure 3.8 A shows the trace elements concentrations in Type-1, 2 and 4 obtained by LA-ICP-MS using box and whisker diagrams. The Figure shows that all zircon types have high concentrations of a variety of non-formula elements. Type-1 and 2 contain high concentrations of P, Li, Th, and REE; whereas Type-4 has high Ti, and Fe, and Type-2 and 4 have high Sc. In Figure 3.8 B, atom per formula unit (a.p.f.u) concentrations of Zr and Si in all zircon types are scattered, and similarly Zr is not correlated with Hf. In Figure 3.8 C, Type-1 zircon data points are clustered at low Hf and high Zr, as are the majority of Type-2 zircon, whereas Type-3, 4 and the secondary zircon have high Hf concentrations. The plot of total REE against P a.p.f.u shows that data points of Type-1, 2, and 4 form a positive correlation with P with a slope close to 1 (Fig. 3.8 D). According to Hoskin and Schaltegger (2003), the incorporation of trace elements in zircon can occur through:

Simple substitution



Coupled substitution

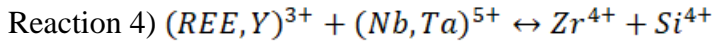
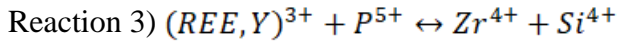


Figure 3.8 D suggests a coupled substitution and indicates that substitution in zircon is likely controlled by reaction (3)

All zircons are enriched in heavy REE similar to the whole-rock REE contents (Fig. 3.9 A to C). Type-1 and Type-2 zircons have a positive Ce anomaly and negative Eu anomaly, whereas Type-3 and Type-4 display flat Ce and negative Eu anomalies, respectively.

The normalized ratio of Sm/La_N ($(Sm/La)_N = (Sm/Sm_{chondrite})/(La/La_{chondrite})$) and

$Ce/Ce^* = (Ce/Ce_{chondrite}) / \sqrt{\left(\frac{La}{La_{chondrite}}\right) \times \left(\frac{Pr}{Pr_{chondrite}}\right)}$ of zircons are plotted in

Figure 3.10 A, using the discrimination diagram proposed by Hoskin (2005). Type-1 and Type-2 zircons range from the magmatic to hydrothermal fields. On the other hand, Type-4 zircon plots closer to the hydrothermal zircon but lies outside both fields. In Figure 3.10 B, La concentration is plotted against Sm/La_N. Most of the data points fall outside the magmatic and hydrothermal fields with many points of Type-1 and Type-2 zircons being closer to the magmatic field.

3.4.2.2 Pyrochlore

Pyrochlore analyses are summarized in Table 3.6. The stoichiometries of pyrochlore were calculated by normalizing cations to the total cations in the B site (total of 2) according to the general formula of pyrochlore group minerals $A_{2-m}B_2X_{6-w}Y_{1-n} \cdot pH_2O$, where A = Na, Ca, Fe²⁺, REE, Pb, Y, U, and Th; B = Nb, Ta, Ti, Al, Fe³⁺, and Sn; X = O and OH; and Y = O, OH, and F, with m = 0 – 1.7, w = 0 – 0.7, and n = 0 – 1 being vacancies in A, X,

and Y, respectively, and $p = 0 - 2$ H₂O molecules in defect pyrochlore (Lumpkin and Ewing, 1996). Vacancy in the A site was calculated by assuming the difference to the total occupancy of the site A (2). The low cation total (<4) in Table 3.6 could be due to the vacancy in the A site (Lumpkin and Ewing, 1996) or the migration of Na during the electron microprobe analyses (Zhao et al., 2015). Another possibility is the presence of elements that are not detectable by EMP, such as Li. However, Li is not known to occur in pyrochlore.

The results show major differences between the pyrochlore types. In a single grain, pyrochlore shows internal chemical variations that are manifested as oscillatory zoning in PCL-1 and patchy to bimodal zoning in PCL-2. These variations are mainly due to variations in Ta, U, Ti, and REE contents (Fig. 3.11).

The comparison of the three pyrochlore types displays significant differences in their concentrations of Nb, Ca, U, LREE, and Y (Fig. 3.12 A). PCL-1 and PCL-2 have comparable Nb and Ta concentrations, whereas PCL-3 has low Nb and Ta contents and high Ti and Si. Moreover, PCL-1 differs from the other types by the relatively high LREE content (Fig. 3.12 A). PCL-2 is characterized by high Ca and Na concentrations, whereas PCL-1 show high Na and low Ca relative to PCL-3. PCL-3 is chemically distinguished by the higher Y and HREE and low LREE, Ca, and Na concentrations (Fig. 3.12 A). Figure 3.11 B shows the main elements that substitute for Nb and Ta in a.p.f.u. In PCL-1 and most of PCL-2, Ti is the main element that substitutes for Nb and Ta. Some PCL-2 analyses show scattering suggesting involvement of other elements. PCL-3 and some analyses from PCL-2 show negative correlation with Nb and Ta. Thus, Si and Ti are the main elements substituting for Nb + Ta, which is indicated by the strong correlation that Nb + Ta forms with Ti + Si (Fig. 3.12 B). The A site, the total of $\text{Na}^+ + \text{Mn}^{2+} + \text{REE}^{3+} + \text{Y}^{3+} + \text{vacancy}$, forms a strong correlation with Ca^{2+} in PCL-2 and 3, and U^{4+} in PCL-1 (Fig. 3.12 C). The main substitution mechanism in the A site is demonstrated by the equation $\text{Na}^+ + \text{Mn}^{2+} + \text{REE}^{3+} + \text{Y}^{3+} + \text{vacancy} = \text{Ca}^{2+} + \text{U}^{4+} + \text{Fe}^{2+} + \text{Pb}^{2+}$. This is shown by the strong correlation and slope of 1 in Figure 3.12 (C). However, this equation is not balanced, and it is likely that a coupled reaction in the hydroxyl site may also be involved e.g., $\text{OH}^- = \text{O}^{2-}$.

3.4.2.3 Columbite

The stoichiometries of columbite were calculated by normalizing to the total cations in the B site according to the general columbite formula $A B_2 O_6$, where $A = Fe, Mn, Mg, Ca, REE, \text{ and } Y$; and $B = Nb, Ta, Ti, W, \text{ and } Sn$ (Table 3.7). The different types of columbite have different Fe, Mn, Ta, Ti contents. COLB-1 has a distinctive composition that can be distinguished from COLB-2 and COLB-3, which have a similar chemical composition (Table 3.7 and Fig. 3.13 A). COLB-1 is characterized by relatively low Nb, Mn, and relatively high Ta, Fe, U, and Ti (Fig. 3.13 A). COLB-2 and COLB-3 have relatively high Nb and Mn, and relatively low Fe, Ta, and Ti (Fig. 3.13 A).

In an atom per formula unit (a.p.f.u) diagram, Nb content exhibits poor correlation with Ta in all columbite types (Fig. 3.13 B). In all columbite types, Ti shows a negative correlation with Nb (Fig. 3.13 C). Fe and Mn contents show negative correlation in all columbite types, suggesting that these elements substituted for each other (Fig. 3.13 D). COLB-1 shows a low Mn# (Mn# = the atomic ratio of $Mn/(Mn+Fe)$) ranging from 0.13 to 0.36, whereas COLB-2 shows a higher Mn# ranging from 0.21 to 0.57 and Mn# in COLB-3 ranges from 0.26 to 0.57. All columbite types show comparable Ta# (Ta# = the atomic ratio of $Ta/(Ta+Nb)$) with average values of 0.05, 0.03, and 0.03 in COLB-1, 2, and 3, respectively (Fig. 3.13 E). Figure 3.13 F and G show the main substitution mechanisms in the A and B sites, respectively. In Figure 3.13 F, Fe mainly substitutes for Mn in COLB-2 and 3, whereas in COLB-1, REE, Y, Pb, and U in addition to Fe substitute for Mn. This is also shown in Figure 3.13 D, where COLB-1 forms a different trend than that in COLB-2 and 3. In Figure 3.13 G, Ti + Sn substitute Nb + Ta in the B site.

3.5 Discussion

3.5.1 Magmatic and hydrothermal mineralization

3.5.1.1 Zircon

Chemical composition and textural observations have been used to discriminate between the different types of zircon (Corfu et al., 2003; Erdmann et al., 2013; Fu et al., 2009;

Hoskin and Schaltegger, 2003; Pupin, 1980; Schaltegger, 2007). For example, oscillatory zoning is attributed to magmatic zircon (Corfu et al., 2003; Pidgeon, 1992; Silver and Deutsch, 1963). However, others argued that hydrothermal zircons might also show oscillatory zoning (Hoskin and Schaltegger, 2003; Schaltegger, 2007). Type-1 zircon from the porphyritic granite shows oscillatory zoning in CL images that was crosscut and partially overprinted by Type-2 zircon and later by the secondary zircon (Figure 3.4 A and F and Fig. 3.7 A and B). The oscillatory zoning in Type-1 is a characteristic feature that distinguishes it from the associated Type-2. Zircons of Type-2, 3, and 4 show patchy to bimodal, or lack of zoning (Fig. 3.4 F to O and Fig. 3.7 B and C). Types-1 and 2 typically form an intergranular texture with albite and K-feldspar (Fig. 3.4 A to I). Locally, Type-1 zircon contains spongy zones at the rim, which indicates that zircon rims have undergone interaction with a fluid phase that formed the secondary zircon (Schaltegger, 2007).

The differences in the chemical composition of the four zircons type further support the morphological classification. The trace element contents in zircons have been used to discriminate hydrothermal and magmatic zircon signatures (Chen and Zhou, 2017; Fu et al., 2009; Hoskin, 2005; Hoskin and Schaltegger, 2003; Pettke et al., 2005; Schaltegger, 2007; Wu et al., 2018; Yang et al., 2014). Hydrothermal zircon is characterized by high abundances of LREE and non-formula elements, such as Li, Fe, Ca, Nb, and Ta (Fu et al., 2009; Hoskin, 2005; Pettke et al., 2005b; Wu et al., 2018). Moreover, magmatic zircon commonly displays positive Ce anomalies unlike hydrothermal zircon (Hoskin and Schaltegger, 2003; Hoskin, 2005).

From Figure 3.8 A and Table 3.5, it can be shown that all zircon types contain high concentrations of various non-formula elements. Moreover, Type-1 and 2 zircons have higher REE contents than Type-4 zircon. This can be seen in Figure 3.9 A, where Type-4 zircon shows relatively low REE contents, and generally, zircon types from this study have relatively low LREE contents. Figure 3.9 A shows that Type-1 and Type-2 zircon have steep REE patterns with positive Ce anomalies and deep negative Eu anomaly, whereas Type-4 shows a flat to slightly negative Ce anomaly and negative Eu anomaly. The strong Ce anomalies in Type-1 and 2 zircons are similar to what is commonly

reported in magmatic zircons (Wu et al., 2018; Yang et al., 2014). The low Ce anomaly is expected from hydrothermal zircons; however, the negative Ce anomaly is unexpected. The main reason for the presence of high or low Ce and Eu anomalies is attributed to the ratios of Ce^{3+} / Ce^{4+} and Eu^{2+} / Eu^{3+} that are controlled by oxygen fugacity, where under oxidized conditions Eu^{3+} and Ce^{4+} are common (Ballard et al., 2002; Hoskin and Schaltegger, 2003; Liang et al., 2006; Yang et al., 2014). Europium can occur as Eu^{2+} and Eu^{3+} , and Eu^{3+} is relatively more compatible in zircon; hence, a negative Eu anomaly should not co-exist with a positive Ce anomaly. Nevertheless, negative Eu anomalies are very common in zircon with a positive Ce anomaly (Erdmann et al., 2013; Feng, 2014; Fu et al., 2009; Hoskin, 2005; Hoskin and Schaltegger, 2003; Pettke et al., 2005; Wu et al., 2018; Yang et al., 2014). Hoskin and Schaltegger (2003) suggested that the Eu anomaly in zircon is inherited from an Eu-depleted melt. The whole-rock REE pattern of Al-Ghurayyah has a pronounced negative Eu anomaly (Fig. 3.9 C), which was interpreted as being the result of plagioclase fractionation (Chapter 2). Thus, it is reasonable to assume that the negative Eu anomaly in zircon from Al-Ghurayyah is due to the granite melt having had a negative Eu anomaly due to plagioclase fractionation and not due to the oxidation states of the crystallization environment of zircon. Furthermore, zircon with negative Ce and Eu anomalies were reported from zircon in zone VI in No. 112 Pegmatite Kelumute, Chinese Altai (Lv et al., 2018). The unusual anomaly of zircon was attributed to the pre- to syn-crystallization of Mn-Fe oxyhydroxides that preferentially depleted Ce. In this study, there are no Ce-rich (or even LREE) minerals associated with Type-3 and 4 zircons. The only common mineral with a significant REE content is pyrochlore, and Ce is the most abundant LREE in this mineral (Table 3.6). Thus, if zircon crystallization was preceded by pyrochlore crystallization, this could explain the low abundance of LREE in Al-Ghurayyah and the reason for the low Ce anomaly present in Type3 and Type-4 zircons.

In the discrimination diagram proposed by Hoskin (2005), Type-1 and Type-2 zircon plot in an array that trends across both magmatic zircon and hydrothermal zircon fields in the Sm/La_N vs Ce/Ce^* diagram (Fig. 3.10 A), whereas Type-4 zircon plots near the hydrothermal field but at lower Ce/Ce^* values (Fig. 3.10 A). In Figure 3.10 B, La concentration is plotted against Sm/La_N . Most of the data points fall outside the magmatic

and hydrothermal fields, but many points of Type-1 and Type-2 zircons are closer to magmatic values.

Fu et al. (2009) have observed that data of hydrothermal zircons from different deposits fall outside of the hydrothermal discrimination field and suggested that these discrimination diagrams are not robust.

Thus, if the textural relationships of Type-1 and 2 zircon with rock-forming minerals are considered with the apparent trending from magmatic to hydrothermal fields, this suggest that Type-1 and 2 zircon crystallized during the transition from a magmatic to a metasomatic environment. The common occurrence of Type-3 and 4 zircon in the composite-body and the mineralized quartz veins in addition to their REE pattern (Type-4) suggests that they have crystallized in a metasomatic environment.

3.5.1.2 Pyrochlore and columbite

Based on textural observations, PCL1 is coeval with Type-1 zircon (Fig. 5A). Moreover, PCL-1 forms an intergranular texture with albite and quartz in the matrix. This pyrochlore displays well-defined oscillatory zoning in WDS X-ray maps (Fig. 3.11 A), which is a common feature in magmatic pyrochlore (Bambi et al., 2012; Sharygin et al., 2009; Walter et al., 2018). The second type of pyrochlore (PCL-2) is commonly associated with Type-2 zircon, and it occurs mostly in the marginal unit. This type lacks zoning or has bimodal zoning (Fig. 3.11 B). Moreover, PCL-1 and PCL-2 occurrences are limited to the porphyritic granite and the marginal unit. The chemical compositions of pyrochlore displays clear differences between the three types. PCL-1 has relatively low Ca and Na and high REE + Y and U, which occupy most of the A site (Fig. 3. 12 C). The difference in composition between PCL-1 and PCL-2 suggests that they were formed from a melt that had a different composition. PCL-1 has relatively low Ca and Na contents relative to PCL-2, although it is coeval with albite. This suggests that during crystallization pyrochlore preferentially incorporated REE, Pb, and Th, whereas Na preferentially partitioned into albite. Moreover, the whole-rock Ca content of the porphyritic granite is low (and from 0.17 to 0.53 wt.% in the porphyritic granite), which may explain the lower Ca concentration in PCL-1. Therefore, it is most likely that PCL-1

crystallized from a medium with a low Ca concentration (late magmatic to early hydrothermal). PCL-1 is coeval with the magmatic zircon Type-1, which indicates that PCL-1 is also magmatic in origin. The second type of pyrochlore (PCL-2) is common in the marginal unit and has higher Ca and Na, and an intermediate LREE concentration relative to PCL-1. This change in the chemistry relative to PCL-1 indicates a change in the melt composition to a higher Ca concentration. This agrees with the whole-rock analyses, where the marginal unit has a higher Ca concentration (2.62 wt.% CaO). The increase in Ca in the marginal unit may be due to the interaction with the metasedimentary country rocks. The association of PCL-2 with Type-2 zircon and the occurrence of both minerals in the marginal unit that is interpreted to represent a quenched melt (Chapter 2) suggests a magmatic origin of PCL-2. The secondary pyrochlore (PCL-3) is a late phase that replaces earlier pyrochlore and columbite and is associated with aeschynite. Textural observations show that PCL-3 occurs as veinlets that crosscut Nb-rich phases (pyrochlore and columbite), or as reaction rims on primary pyrochlore and columbite (Fig. 3.6). PCL-3 contains high Y and HREE, which indicates crystallization from a late-stage hydrothermal fluid with high concentrations of Y and HREE.

Columbite in the porphyritic granite commonly occurs as a replacement mineral after pyrochlore, as in COLB-1, or as individual grains associated with alteration minerals, such as secondary zircon, chlorite, muscovite and fluorite, as in COLB-2. COLB-3 is mostly concentrated in the composite-body and the mineralized quartz vein and associated with Type-3 and 4 zircon (Fig. 3.3 I and J, and Fig. 3.6). The chemical composition of COLB-1 differs from the other columbite types (Fig. 3.13). In terms of Ta # and Mn #, all columbite types in Al-Ghurayyah deposit lack gradual increases in a single grain or for each compositional type. The increase in Ta # is an expected feature for magmatic columbite because Ta concentration increases as the magma evolves by fractional crystallization (Cerny et al., 1985; Linnen and Cuney, 2005; Linnen and Keppler, 1997; Mingqian Wu et al., 2018). Moreover, columbite shows variable Nb/Ta ratios that have an average of 12.40, 20.80, and 22.18 in COLB-1, COLB-2, and COLB-3, respectively. The Nb/Ta ratio in COLB-1 is close to the magmatic ratio in crustal rock (11 to 12; Green, 1995). This ratio is most likely to have been inherited from the replaced

pyrochlore, which has a comparable ratio (13.3 in PCL-1 and 2). In contrast, COLB-2 and COLB-3 have much higher Nb/Ta ratios, that further support their metasomatic origin. In Figure 3.14, PCL-1 and COLB-1, 2 and 3 contents of Ti, Nb, and Ta were plotted on a ternary diagram. PCL-1 and COLB-1 show similar Ti, Nb, and Ta contents, which suggests that these elements were immobile during PCL-1 alteration and the formation of COLB-1. This also supports the metasomatic origin of COLB-1.

3.5.2 Mineralization evolution at Al-Ghurayyah

The textural and chemical observations of the ore minerals revealed the presence of at least 3 mineralization events. The first stage is late-magmatic to early metasomatic, which is indicated by the crystallization of Type-1 zircon and PCL-1 as a magmatic phase and Type-2 as a late magmatic to an early metasomatic phase. This stage was more oxidizing, which resulted in a positive Ce anomaly in zircon (Type-1 and 2). This stage was followed by a metasomatic stage where Type-1 and Type-2 zircon, and PCL-1 in the porphyritic granite were altered as indicated by the spongy zircon rims and the replacement of PCL-1 by COLB-1. The hydrothermal nature of this stage is demonstrated by the coexistence of chlorite, muscovite, and hematite with COLB-2, and secondary zircon. The crystallization order of COLB-1 and COLB-2 is difficult to establish because the two types do not occur together.

At the marginal unit, the first stage is manifested by the crystallization of Type-2 zircon and PCL-2. The second metasomatic stage is manifested in the alteration of PCL-2 to columbite, which is associated with fluorite, Y-fluorite and minor/trace amounts of REE-fluorocarbonate and aeschynite. The composite-body and the mineralized quartz veins represent the metasomatic fluid responsible for the second stage and the crystallization of Types-3 and 4 zircon and COLB-3. The low LREE contents in this stage (the steep positive REE pattern and low LREE and negative Ce anomaly in Type-4 zircon) is likely related to a residual metasomatic fluid that was preceded by the crystallization of a LREE-bearing phase, such as pyrochlore. The comparable composition of COLB-2 and 3 indicate that they are likely genetically related, which is indicated by the Ti-Nb, Ta-Nb, and Mn-Fe trends in Figure 3.13 B to C, and the trend observed in Figure 3.14. The last mineralization stage (Stage 3) is characterized by relatively high HREE and fluorine

alteration, where pyrochlore and columbite are intensely altered and replaced by Y-rich pyrochlore, aeschynite, and Y-rich fluorite \pm samarskite \pm REE-fluorocarbonate. This suggests a late HREE mobilization in an F-rich fluid. Nevertheless, the role of F in the mobilization and mineralization of HFSE is controversial. The critical role of F in addition to Cl and CO₂ in the mobilization of HFSE and REE has been demonstrated in experimental and natural systems (Boily and Williams-Jones, 1994; Gysi et al., 2016; Haas et al., 1995; Salvi and Williams-Jones, 1996; Vasyukova and Williams-Jones, 2014; Webster et al., 1989). However, other experimental studies have argued that at high temperature, H⁺ and F⁻ are highly associated (to form HF) and that REE are more likely to be transported as REE-chloride or sulphate complexes (Migdisov et al., 2016; Migdisov and Williams-Jones, 2014). Moreover, Finch et al., (2019) argued that late-stage fluorine-rich fluid was able to mobilize elements such as U and Pb, but not Nb, Ta, and Hf, based on their observation of pyrochlore alteration where Nb and Ta ratio remains unchanged after the alteration. Furthermore, they also suggested that F content in the fluid is not the only factor that controls the mobility of HFSE, and other parameters may influence the mobility, such as pH and redox state.

At Al-Ghurayyah deposit, the alteration of PCL-1 and the formation of COLB-1 without changing Ta and Nb ratio suggests that Nb and Ta were immobile. However, the presence of columbite (COLB-2) with very different compositions in the same rock, and COLB-3 in the mineralized quartz veins and the composite-body indicate that at some point in the metasomatic stage, Nb and Ta were mobile. Similar behavior was observed in rare-element mineralization in the Songshugang granite, northeastern Jiangxi, China; where columbite group minerals occur in veinlets that crosscut early magmatic mineralization (Zhu et al., 2015).

3.6 Conclusion

The textural, morphological, and chemical study of ore minerals in Al-Ghurayyah indicates that the HFSE and REE mineralization began during a late-magmatic stage by the crystallization of Types 1 & zircon and PCL-1 & 2, and continued to the metasomatic stage where columbite and Types-3 & 4 crystallized and followed by PCL-3 pyrochlore. This makes Al-Ghurayyah exceptionally well-suited to examine the magmatic to

hydrothermal transition. This is because elsewhere primary ore minerals are commonly altered in other miaskitic silica-rich rare-metal alkaline granite deposits and the original mineralogy can only be inferred from the shape of the pseudomorphs and the alteration mineral assemblages (Gysi and Williams-Jones, 2013; Kovalenko, 1995; Miller, 1996; Salvi and Williams-Jones, 1990). At the late-magmatic stage, Type-1 zircon and PLC-1 pyrochlore, and later Type-2 zircon crystallized with major minerals that formed a typical intergranular magmatic texture. Similarly, in the marginal unit PCL-2 and Type-2 zircon crystallized in a fine-grained matrix due to fast crystallization by quenching (Chapter 2). The interaction of this melt with the country rocks may have changed its composition, which explains that high Ca, Fe, and Mg concentrations in the marginal unit. Moreover, this also led to the crystallization of PCL-2 that has different composition than PCL-1 (Ca-rich). This stage was followed by metasomatic stage represented by the alteration of Type-1 and 2 zircon and PCL-1 by the secondary zircon and COLB-1 and the crystallization of COLB-2 that is associated with chlorite and muscovite in the porphyritic granite. The composite-body and the quartz veins contain high concentrations of Type-3 and 4 zircon and COLB-3 that all show metasomatic characteristics. The composite-body and the quartz veins may resemble the metasomatic fluid that altered the granite the porphyritic granite and formed the secondary zircon and columbite (COLB-1 and 2).

3.7 References

- Ballard, J.R., Palin, J.M., Campbell, I.H., 2002. Relative oxidation states of magmas inferred from Ce^{IV}/Ce^{III} in zircon: Application to porphyry copper deposits of northern Chile. *Contrib. to Mineral. Petrol.* 144, 347–364.
<https://doi.org/10.1007/s00410-002-0402-5>
- Bambi, A.C.J.M., Costanzo, A., Gonçalves, A.O., Melgarejo, J.C., 2012. Tracing the chemical evolution of primary pyrochlore from plutonic to volcanic carbonatites: the role of fluorine. *Mineral. Mag.* 76, 377–392.
<https://doi.org/10.1180/minmag.2012.076.2.07>
- Boily, M., Williams-Jones, A. E., 1994. The role of magmatic and hydrothermal

- processes in the chemical evolution of the Strange Lake plutonic complex, Quebec-Labrador. *Contrib. to Mineral. Petrol.* 118, 33–47.
<https://doi.org/10.1007/BF00310609>
- Cerny, P., Meintzer, R.E., Anderson, A.J., 1985. Extreme fractionation in rare-element granitic pegmatites: selected examples of data and mechanisms. *Can. Mineral.* 23, 381–421.
- Cheetham, P., Whitehead, D., Fitch, C., 2007. Tertiary-Annual-Report-2007-website-version-revised.
- Chen, W.E.I.T.E.I.T., Zhou, M.-F., 2017. Hydrothermal alteration of magmatic zircon related to NaCl-rich brines: Diffusion-reaction and dissolution-reprecipitation processes. *Am. J. Sci.* 317, 177–215. <https://doi.org/10.2475/02.2017.02>
- Corfu, F., Hanchar, J.M., Hoskin, P.W.O., Kinny, P., 2003. Atlas of zircon textures. *Rev. Mineral. Geochemistry* 53, 469–500. <https://doi.org/10.2113/0530469>
- Dostal, J., 2016. Rare metal deposits associated with alkaline/peralkaline igneous rocks. *Rev. Econ. Geol* 18, 33–54.
- Drysdall, a. R., Jackson, N.J., Ramsay, C.R., Douch, C.J., Hackett, D., 1984. Rare element mineralization related in Precambrian alkali granites in the Arabian shield. *Econ. Geol.* 79, 1366–1377. <https://doi.org/10.2113/gsecongeo.79.6.1366>
- Elliott, J.E., Al-Yazidi, S., Al-Eissa, A., Al-Shammeri, A., Hashem, A.I., Tarabulsi, Y., 2002. Exploration of the Ghurayyah radioactive granite, Kingdom of Saudi Arabia. *Saudi Geol. Surv.* open-file, x.
- Erdmann, S., Wodicka, N., Jackson, S.E., Corrigan, D., 2013. Zircon textures and composition: refractory recorders of magmatic volatile evolution? *Contrib. to Mineral. Petrol.* 165, 45–71. <https://doi.org/10.1007/s00410-012-0791-z>
- Feng, Y., 2014. Hydrothermal geochemistry and mineralizing processes in the T Zone , Thor Lake Rare-element deposit , Northwest Territories 341.

- Finch, A.A., McCreath, J.A., Reekie, C.D.J., Hutchison, W., Ismaila, A., Armour-Brown, A., Andersen, T., Simonsen, S.L., 2019. From Mantle to Motzfeldt: A genetic model for syenite-hosted Ta,Nb-mineralisation. *Ore Geol. Rev.* 107, 402–416.
<https://doi.org/10.1016/j.oregeorev.2019.02.032>
- Fu, B., Mernagh, T.P., Kita, N.T., Kemp, A.I.S., Valley, J.W., 2009. Distinguishing magmatic zircon from hydrothermal zircon: A case study from the Gidginbung high-sulphidation Au-Ag-(Cu) deposit, SE Australia. *Chem. Geol.* 259, 131–142.
<https://doi.org/10.1016/j.chemgeo.2008.10.035>
- Green, T.H., 1995. Significance of Nb/Ta as an indicator of geochemical processes in the crust_mantle system. *Geochemical Geol.* 120, 347.
- Gysi, A.P., Williams-Jones, A.E., 2013. Hydrothermal mobilization of pegmatite-hosted REE and Zr at Strange Lake, Canada: A reaction path model. *Geochim. Cosmochim. Acta* 122, 324–352. <https://doi.org/10.1016/j.gca.2013.08.031>
- Gysi, A.P., Williams-Jones, A.E., Collins, P., 2016. Lithogeochemical vectors for hydrothermal processes in the Strange Lake peralkaline granitic REE-Zr-Nb deposit. *Econ. Geol.* 111, 1241–1276. <https://doi.org/10.2113/econgeo.111.5.1241>
- Haas, J.R., Shock, E.L., Sassani, D.C., 1995. Rare earth elements in hydrothermal systems: estimates of standard partial molal thermodynamic properties of aqueous complexes of the rare earth elements at high pressures and temperatures. *Geochim. Cosmochim. Acta* 59, 4329–4350.
- Hoskin, P.W.O., 2005. Trace-element composition of hydrothermal zircon and the alteration of Hadean zircon from the Jack Hills, Australia. *Geochim. Cosmochim. Acta* 69, 637–648. <https://doi.org/10.1016/j.gca.2004.07.006>
- Hoskin, P.W.O., Schaltegger, U., 2003. The composition of zircon and igneous and metamorphic petrogenesis. *Rev. Mineral. Geochemistry* 53, 27–62.
<https://doi.org/10.2113/0530027>
- Jackson, N.J., 1986. Mineralization associated with felsic plutonic rocks in the Arabian

- Shield. *J. African Earth Sci.* 4, 213–227. [https://doi.org/10.1016/S0899-5362\(86\)80083-5](https://doi.org/10.1016/S0899-5362(86)80083-5)
- Johnson, P.R., 2006. Explanatory notes to the map of Proterozoic geology of western Saudi Arabia, Saudi Geological Survey Technical Report SGS-TR-2006-4.
- Johnson, P.R.R., Andresen, A., Collins, A.S.S., Fowler, A.R.R., Fritz, H., Ghebreab, W., Kusky, T., Stern, R.J.J., 2011. Late Cryogenian-Ediacaran history of the Arabian-Nubian Shield: A review of depositional, plutonic, structural, and tectonic events in the closing stages of the northern east African Orogen. *J. African Earth Sci.* 61, 167–232. <https://doi.org/10.1016/j.jafrearsci.2011.07.003>
- Kovalenko, V.I., 1995. The peralkaline granite-related Khaldzan-Buregtey rare metal (Zr, Nb, REE) deposit, western Mongolia. *Econ. Geol.* 90, 530–547. <https://doi.org/10.2113/gsecongeo.90.3.530>
- Küster, D., 2009. Granitoid-hosted Ta mineralization in the Arabian-Nubian Shield: Ore deposit types, tectono-metallogenic setting and petrogenetic framework. *Ore Geol. Rev.* 35, 68–86. <https://doi.org/10.1016/j.oregeorev.2008.09.008>
- Liang, H.Y., Campbell, I.H., Allen, C., Sun, W.D., Liu, C.Q., Yu, H.X., Xie, Y.W., Zhang, Y.Q., 2006. Zircon Ce⁴⁺/Ce³⁺ ratios and ages for Yulong ore-bearing porphyries in eastern Tibet. *Miner. Depos.* 41, 152–159. <https://doi.org/10.1007/s00126-005-0047-1>
- Linnen, R.L., Cuney, M., 2005. GLinnen, R.L., Cuney, M., 2005. Granite-related rare-element deposits and experimental constraints on Ta-Nb-W-Sn-Zr-Hf mineralization, in Linnen RL and Samson IM, eds., rare-element geochemistry and mineral deposits., in: Geological Association of Canada, in: Geological Association of Canada, GAC, Short Course.
- Linnen, R.L., Keppler, H., 1997. Columbite solubility in granitic melts: consequences for the enrichment and fractionation of Nb and Ta in the Earth's crust. *Contrib. to Mineral. Petrol.* 128, 213–227. <https://doi.org/10.1007/s004100050304>

- Linnen, R.L., Samson, I.M., Williams-Jones, A.E., Chakhmouradian, A.R., 2014. Geochemistry of the rare-earth element, Nb, Ta, Hf, and Zr deposits, in: *Treatise on Geochemistry*. Elsevier, pp. 543–568. <https://doi.org/10.1016/B978-0-08-095975-7.01124-4>
- Lumpkin, G.R., Ewing, R.C., 1996. Geochemical alteration of pyrochlore group minerals: Betafite subgroup. *Am. Mineral.* 81, 1237–1248.
- Lv, Z.H., Zhang, H., Tang, Y., 2018. Lanthanide tetrads with implications for liquid immiscibility in an evolving magmatic-hydrothermal system: Evidence from rare earth elements in zircon from the No. 112 pegmatite, Kelumute, Chinese Altai. *J. Asian Earth Sci.* 164, 9–22. <https://doi.org/10.1016/j.jseaes.2018.05.031>
- Migdisov, A., Williams-Jones, A.E., Brugger, J., Caporuscio, F.A., 2016. Hydrothermal transport, deposition, and fractionation of the REE: Experimental data and thermodynamic calculations. *Chem. Geol.* 439, 13–42. <https://doi.org/10.1016/j.chemgeo.2016.06.005>
- Migdisov, A.A., Williams-Jones, A.E., 2014. Hydrothermal transport and deposition of the rare earth elements by fluorine-bearing aqueous liquids. *Miner. Depos.* 49, 987–997. <https://doi.org/10.1007/s00126-014-0554-z>
- Miller, R.R., 1996. Structural and textural evolution of the strange Lake Peralkaline rare-element (NYF) granitic pegmatite, Quebec-Labrador. *Can. Mineral.* 34, 349–371.
- Paton, C., Hellstrom, J., Paul, B., Woodhead, J., Hergt, J., 2011. Iolite: Freeware for the visualisation and processing of mass spectrometric data. *J. Anal. At. Spectrom.* 26, 2508–2518.
- Pettke, T., Audéat, A., Schaltegger, U., Heinrich, C. a., 2005. Magmatic-to-hydrothermal crystallization in the W-Sn mineralized Mole Granite (NSW, Australia). Part II: Evolving zircon and thorite trace element chemistry. *Chem. Geol.* 220, 191–213. <https://doi.org/10.1016/j.chemgeo.2005.02.017>
- Pidgeon, R.T., 1992. Recrystallisation of oscillatory zoned zircon: some

- geochronological and petrological implications. *Contrib. to Mineral. Petrol.* 110, 463–472. <https://doi.org/10.1007/BF00344081>
- Pupin, J.P., 1980. Zircon and granite petrology. *Contrib. to Mineral. Petrol.* 73, 207–220. <https://doi.org/10.1007/BF00381441>
- Qadhi, T., Moufti, A., 2008. Geochemical characteristic of the rare-metal rich granite in the Ghurayyah-Dubbagh Area, north western Arabian Shield, Saudi Arabia. *Ann. Geol. Surv. Egypt* XXX, 149.
- Ramsay, C.R., 1986. Specialized felsic plutonic rocks of the Arabian Shield and their precursors. *J. African Earth Sci.* 4, 153–168. [https://doi.org/10.1016/S0899-5362\(86\)80076-8](https://doi.org/10.1016/S0899-5362(86)80076-8)
- Salvi, S., Williams-Jones, A.E., 1996. The role of hydrothermal processes in concentrating high-field strength elements in the Strange Lake peralkaline complex, northeastern Canada. *Geochim. Cosmochim. Acta* 60, 1917–1932. [https://doi.org/10.1016/0016-7037\(96\)00071-3](https://doi.org/10.1016/0016-7037(96)00071-3)
- Salvi, S., Williams-Jones, A.E., 1990. The role of hydrothermal processes in the granite-hosted Zr, Y, REE deposit at Strange Lake, Quebec/Labrador: Evidence from fluid inclusions. *Geochim. Cosmochim. Acta* 54, 2403–2418. [https://doi.org/10.1016/0016-7037\(90\)90228-D](https://doi.org/10.1016/0016-7037(90)90228-D)
- Schaltegger, U., 2007. Hydrothermal zircon. *Elements* 3, 51–79. <https://doi.org/10.2113/gselements.3.1.51>
- Sharygin, V. V., Sobolev, N. V., Channer, D.M.D.R., 2009. Oscillatory-zoned crystals of pyrochlore-group minerals from the Guaniamo kimberlites, Venezuela. *Lithos* 112, 976–985. <https://doi.org/10.1016/j.lithos.2009.03.049>
- Silver, L.T., Deutsch, S., 1963. Uranium-Lead Isotopic Variations in Zircons: A Case Study. *J. Geol.* 71, 721–758. <https://doi.org/10.1086/626951>
- Speer, A., 1982. Zircon, in: Ribbe, P.H. (Ed.), *Orthosilicate*. Mineralogical Society of

America, Blacksburg, pp. 67–112.

Staatz, M.H., Brownfield, I.K., 1986. Trace-and minor-element mineralogy of the microgranite at Ghurayyah, Kingdom of Saudi Arabia.

Vasyukova, O., Williams-Jones, A.E., 2014. Fluoride-silicate melt immiscibility and its role in REE ore formation: Evidence from the Strange Lake rare metal deposit, Quebec-Labrador, Canada. *Geochim. Cosmochim. Acta* 139, 110–130.
<https://doi.org/10.1016/j.gca.2014.04.031>

Walter, B.F., Parsapoor, A., Braunger, S., Marks, M.A.W., Wenzel, T., Martin, M., Markl, G., 2018. Pyrochlore as a monitor for magmatic and hydrothermal processes in carbonatites from the Kaiserstuhl volcanic complex (SW Germany). *Chem. Geol.* 498, 1–16. <https://doi.org/10.1016/j.chemgeo.2018.08.008>

Webster, J.D., Holloway, J.R., Hervig, R.L., 1989. Partitioning of lithophile trace elements between H₂O and H₂O + CO₂ fluids and topaz rhyolite melt. *Econ. Geol.* 84, 116–134. <https://doi.org/10.2113/gsecongeo.84.1.116>

Wu, Mingqian, Samson, I.M., Zhang, D., 2018. Textural features and chemical evolution in Ta-Nb oxides: Implications for deuteric rare-metal mineralization in the yichun granite-marginal pegmatite, Southeastern China. *Econ. Geol.* 113, 937–960.
<https://doi.org/10.5382/econgeo.2018.4577>

Wu, Ming-qian, Tian, B., Zhang, D., Xu, G., Xu, W., Qiu, K., 2018. Zircon of the No. 782 deposit from the Great Xing'an Range in NE China: Implications for Nb-REE-Zr mineralization during magmatic-hydrothermal evolution. *Ore Geol. Rev.* 102, 284–299. <https://doi.org/10.1016/j.oregeorev.2018.09.006>

Yang, W.-B., Niu, H.-C., Shan, Q., Sun, W.-D., Zhang, H., Li, N.-B., Jiang, Y.-H., Yu, X.-Y., 2014. Geochemistry of magmatic and hydrothermal zircon from the highly evolved Baerzhe alkaline granite: implications for Zr–REE–Nb mineralization. *Miner. Depos.* 49, 451–470. <https://doi.org/10.1007/s00126-013-0504-1>

Zhao, D., Zhang, Y., Essene, E.J., 2015. Electron probe microanalysis and microscopy:

Principles and applications in characterization of mineral inclusions in chromite from diamond deposit. *Ore Geol. Rev.* 65, 733–748.

<https://doi.org/10.1016/j.oregeorev.2014.09.020>

Zhu, Z.Y., Wang, R.C., Che, X.D., Zhu, J.C., Wei, X.L., Huang, X., 2015. Magmatic-hydrothermal rare-element mineralization in the Songshugang granite (northeastern Jiangxi, China): Insights from an electron-microprobe study of Nb-Ta-Zr minerals. *Ore Geol. Rev.* 65, 749–760. <https://doi.org/10.1016/j.oregeorev.2014.07.021>

Table 3-1 List of Isotopes used for zircon LA-ICP-MS analyses

Isotope	L.O.D (ppm)	Isotope	L.O.D (ppm)
Li⁷	0.4	Eu¹⁵³	0.05
Al²⁷	0.7	Gd¹⁵⁷	0.2
Si²⁹	2120	Tb¹⁵⁹	0.04
P³¹	60.2	Dy¹⁶³	0.2
Sc⁴⁵	1.0	Ho¹⁶⁵	0.03
Ti⁴⁸	1.4	Er¹⁶⁷	0.2
Fe⁵⁷	70	Tm¹⁶⁹	0.04
Y⁸⁹	0.05	Yb¹⁷¹	0.2
Nb⁹³	0.05	Lu¹⁷⁵	0.03
Sn¹²⁰	1.3	Hf¹⁷⁷	0.3
La¹³⁹	0.05	Ta¹⁸¹	0.04
Ce¹⁴⁰	0.04	Pb²⁰⁸	0.1
Pr¹⁴¹	0.03	Th²³²	0.2
Nd¹⁴⁶	0.2	U²³⁸	0.04
Sm¹⁴⁷	0.2		

L.O.D Limit of detection

Table 3-2 Classification of zircon from Al-Ghurayyah

Type	Description	Host rock
Type1	Light brown and transparent subhedral grains (250 to 500 μm). Well zoned and has fluid inclusion rich rim. Crosscut by secondary zircon and overgrown by Type 2. The core is metamict and appears dark in Cl. Associated with albite, microcline, and pyrochlore	Porphyritic granite
Type2	Variable in size (20 to 300 μm) and occurs as light pink to murky subhedral crystals and locally contain fluid inclusions. Patchy zoning to un-zoned and crosscut by secondary zircon. It is bipyramid in the marginal unit and smaller in size.	Porphyritic granite and marginal unit
Type3	Variable in size (50 to 300 μm) and occurs as brown to dark brown subhedral to anhedral crystals. It contains a high amount of fluid and mineral inclusion. Associated with columbite, hematite and columbite. Type-4 occurs as an overgrowth	Composite body and mineralized quartz veins
Type4	Variable in size (50 to 300 μm) and occurs as light color and transparent. contains low amount of fluid and mineral inclusions. Associated with columbite, hematite, columbite, rutile, and xenotime	Composite body and mineralized quartz veins
Secondary zircon	Small veinlets crosscut Type-1 and 2 in the porphyritic granite and the amphibole granite.	

Table 3-3 Classification of pyrochlore from Al-Ghurayyah

Types	Description	Host rock
PCL-1	Light yellow subhedral to anhedral crystals (15 to 50 μm across). Fresh crystals are well zoned and crosscut by type 3 pyrochlore. Associated with Type-1 zircon in the porphyritic granite and forms intergranular texture with albite, microcline and quartz. Replaced by columbite, PCL-3, samarskite, and REE-F-carbonate	Porphyritic granite
PCL-2	Light yellow anhedral crystals. (60 to 100 μm across). Poorly zoned. Associated with hematite, quartz, Type-2 zircon, and replaced by Y-fluorite PCL-3, columbite, samarskite, and REE-F-carbonate.	Marginal unit
PCL-3	Occurs as veinlets and replacement mineral on columbite and Type-1 and Type-2 pyrochlore.	Porphyritic granite, marginal unit, and mineralized quartz vein

Table 3-4 Classification of columbite from Al-Ghurayyah

Types	Description	Host rock
COLB-1	Small veinlets and fine-grained crystals replacing pyrochlore.	Porphyritic granite, mineralized quartz vein, and marginal unit
COLB-2	Occurs as small subhedral crystals (less than 50 um). Associated with chlorite, Type-2 zircon, hematite, quartz, and rutile	Porphyritic granite
COLB-3	Large subhedral prismatic crystals (100 um to 500 um). Usually associated with Type-3 and 4 zircon, fluorite, quartz, and rutile	Composite-body, mineralized quartz vein, and in fluorite rich altered granite

Table 3-5 Average EMPA analyses of zircon

	Type-1		Type-2		Type-3		Type-4		Secondary	
EMPA	N = 29	±	N = 19	±	N = 12	±	N = 9	±	N = 7	±
HfO₂	1.73	0.5	2.72	1.2	4.01	0.9	3.46	0.4	2.47	1.0
SiO₂	31.58	0.4	32.15	0.7	31.85	0.4	32.15	0.4	31.84	0.5
ThO₂	0.18	0.1	0.13	0.1	0.69	1.5	0.04	0.1	0.40	0.7
ZrO₂	62.25	1.0	61.95	1.8	62.22	1.1	61.44	2.1	62.02	1.3
P₂O₅	0.42	0.1	0.21	0.1	0.15	0.1	0.07	0.1	0.31	0.2
Y₂O₃	1.06	0.5	0.41	0.3	0.09	0.1	0.39	0.5	0.66	0.3
Dy₂O₃	0.12	0.01	0.05	0.1	0.01	0.0	0.04	0.04	0.06	0.0
Ho₂O₃	0.02	0.02	0.01	0.0	0.00	0.0	0.01	0.01	0.00	0.0
Lu₂O₃	0.08	0.04	0.08	0.0	0.03	0.0	0.07	0.1	0.08	0.1
UO₂	0.03	0.03	0.02	0.0	0.02	0.0	0.00	0.01	0.02	0.0
Er₂O₃	0.35	0.12	0.19	0.1	0.07	0.0	0.12	0.1	0.22	0.1
Tm₂O₃	0.07	0.03	0.04	0.0	0.01	0.0	0.03	0.03	0.06	0.0
Yb₂O₃	0.68	0.2	0.52	0.2	0.32	0.1	0.48	0.4	0.61	0.3
Total	98.8	1.3	99.0	2.4	100.0	2.1	99.4	2.2	99.0	1.9
Zr/Hf	35.98		22.80		15.52		17.76		25.11	

Continue Table 3.5					
	Atom per formula unit (a.p.f.u) ¹				
	Type-1	Type-2	Type-3	Type-4	Secondary
Si	0.99	0.99	1.00	1.00	0.99
Al	0.00	0.00	N.A.	0.00	N.A.
Ti	0.00	0.00	N.A.	0.00	N.A.
P	0.01	0.01	0.00	0.00	0.01
T	1.00	1.00	1	1.00	1.00
Hf	0.02	0.02	0.04	0.03	0.02
Zr	0.95	0.93	0.95	0.93	0.94
REE	0.01	0.00	N.A.	0.00	N.A.
Th	0.00	0.00	N.A.	0.00	N.A.
U	0.00	0.00	N.A.	0.00	N.A.
Pb	0.00	0.00	N.A.	0.00	N.A.
Y	0.02	0.01	0.00	0.01	0.01
M	0.99	0.97	0.99	0.97	0.97
N.A. trace element analyses are not available					

Continue Table 3.5						
LA-ICP-MS (ppm)	Type-1		Type-2		Type-4	
	Average (N = 3)	±	Average (N = 7)	±	Average (N = 8)	±
Li	39	61	37	41	4	4
Al	530	857	373	277	417	397
P	163333	4041	167938	8858	162314	15348
Sc	1230	430	1206	518	176	96
Ti	550	6	572	26	575	27
Fe	43	30	42	14	1205	1112
Y	n.a		n.a	-	1950	1785
Nb	10980	893	835	322	1897	1692
Ta	495	230	374	198	624	596
Sn	70	109	36	28	3447	3311
La	1	2	0	0	0	0
Ce	7	2	10	11	1	2
Pr	0	0	0	0	0	0
Nd	1	1	1	0	1	2
Sm	3	1	3	2	0	0
Eu	0	0	0	0	0	0

Gd	36	3	28	26	5	7
Tb	44	5	34	29	6	7
Dy	901	119	707	543	141	193
Ho	398	57	313	212	74	113
Er	2277	272	1876	994	546	813
Tm	523	51	471	186	184	246
Yb	4527	516	4454	1387	2202	2401
Lu	622	109	615	156	384	349
Pb	11787	1745	14168	8943	28700	5365
Th	55	20	48	14	70	34
U	136	125	76	52	37	19

N= number of samples. Standard deviation represents 1 σ . No trace elements analyses for Type-3 zircon due to high inclusions and the large laser beam size. 1- zircon formula was calculated by normalizing to the total cations in T (1). Trace element concentrations used in zircon formula calculation are the average trace element concentrations obtained by LA-ICP-MS. Trace element analyses for zircon Type-3 and secondary zircon are not available due to the high inclusions in zircon Type-3 and the small size of the secondary zircon.

Table 3-6 Average EMPA analyses of pyrochlore

	PCL-1		PCL-2		PCL-3	
	N=8	±	N=24	±	N=6	±
F	2.19	1.7	0.59	1.4	0.55	0.5
SiO₂	n.a		0.18	0.4	2.35	0.7
Na₂O	2.19	2.8	4.88	1.5	0.20	0.1
La₂O₃	2.30	0.5	1.53	0.4	0.08	0.1
Ce₂O₃	6.93	1.6	4.00	0.9	0.26	0.2
Gd₂O₃	0.43	0.1	0.17	0.0	0.43	0.1
TiO₂	4.86	0.7	4.18	0.7	3.20	1.8
CaO	1.18	0.4	6.95	1.3	2.00	0.9
ThO₂	1.04	1.8	1.23	1.2	1.71	1.2
Nb₂O₅	55.40	1.8	55.09	2.8	42.33	2.0
Y₂O₃	1.79	1.2	1.96	1.8	19.01	8.1
Nd₂O₃	1.64	0.2	0.86	0.2	0.13	0.1
Pr₂O₃	0.66	0.2	0.33	0.1	0.03	0.0
Eu₂O₃	0.00	0.0	0.02	0.0	-0.01	0.0
Dy₂O₃	0.57	0.3	0.51	0.2	3.21	0.9
Ho₂O₃	0.08	0.1	0.09	0.1	0.87	0.3
Lu₂O₃	0.04	0.0	0.02	0.0	0.32	0.2
UO₂	5.05	2.5	3.97	1.7	2.32	1.8
Ta₂O₅	4.17	0.6	4.16	0.4	2.23	1.5
MnO	0.13	0.0	0.06	0.1	0.63	0.5
Sm₂O₃	0.56	0.1	0.34	0.1	0.28	0.1
Tb₂O₃	0.08	0.0	0.05	0.0	0.26	0.0
FeO	0.09	0.1	0.76	0.9	3.65	2.5
Er₂O₃	0.24	0.2	0.34	0.3	3.61	1.6
Tm₂O₃	0.09	0.0	0.13	0.1	0.65	0.3
Yb₂O₃	0.22	0.2	0.34	0.3	3.74	1.6
PbO	2.56	0.8	3.45	1.4	2.00	3.3
SnO₂	0.24	0.1	0.16	0.0	0.13	0.1
Total	94.72	5.4	96.35	5.1	96.17	10.2
Nb/Ta	13.3		13.3		19.0	

Continue Table 3.6

Atom per formal unit ¹			
	PCL-1	PCL-1	PCL-1
Si	-	0.01	0.19
Nb	1.67	1.69	0.20
Ti	0.24	0.21	1.56
Ta	0.08	0.08	0.05
Sn	0.01	0.00	0.00
B site	2.00	2.00	2.00
Ca	0.08	0.51	0.03
Na	0.28	0.64	0.17
REE	0.33	0.21	0.36
Th	0.02	0.02	0.03
Y	0.06	0.07	0.82
U	0.08	0.06	0.04
Mn	0.01	0.00	0.04
Fe	0.00	0.04	0.25
Pb	0.05	0.06	0.04
A site	0.91	1.62	1.80
Total	2.91	3.62	3.8

n.a not analyzed; N, number of analyses; ± is 1 sigma standard deviation

1- mineral formula was calculated by normalizing to the total cations in the B site.

Table 3-7 Average EMPA analyses of columbite

	COLB-1		COLB-2		COLB-3	
	N = 13	±	N = 11	±	N = 19	±
SiO₂	1.72	1.4	0.11	0.2	0.04	0.1
La₂O₃	0.05	0.0	0.05	0.0	0.03	0.0
Ce₂O₃	0.05	0.0	0.05	0.0	0.03	0.0
Gd₂O₃	0.10	0.1	0.06	0.1	0.04	0.0
TiO₂	4.92	1.2	3.08	2.2	1.90	1.2
CaO	0.19	0.2	0.12	0.2	0.03	0.0
ThO₂	0.11	0.1	0.15	0.4	0.02	0.0
Nb₂O₅	64.06	2.6	70.31	4.9	72.73	4.0
Y₂O₃	1.16	1.3	1.11	1.5	0.31	0.2
Nd₂O₃	0.03	0.0	0.02	0.0	0.01	0.0
Pr₂O₃	0.01	0.0	0.01	0.0	0.01	0.0
Eu₂O₃	0.03	0.0	0.06	0.0	0.06	0.0
Dy₂O₃	0.44	0.2	0.47	0.3	0.26	0.2
Ho₂O₃	0.07	0.0	0.09	0.1	0.05	0.0
UO₂	1.83	1.5	0.20	0.3	0.17	0.3
Ta₂O₅	5.17	1.3	3.38	1.3	3.39	2.0
MnO	4.72	1.8	8.55	2.1	9.32	1.8
Sm₂O₃	0.19	0.0	0.14	0.0	0.13	0.0
Tb₂O₃	0.03	0.0	0.04	0.0	0.02	0.0
FeO	13.51	1.7	11.25	1.3	11.20	1.7
Er₂O₃	0.28	0.2	0.27	0.2	0.14	0.1
Tm₂O₃	0.12	0.0	0.11	0.0	0.09	0.0
Yb₂O₃	0.35	0.2	0.49	0.3	0.29	0.1
PbO	0.71	0.4	0.37	0.2	0.29	0.0
SnO₂	0.58	0.2	0.56	0.4	0.22	0.2
Total	100.4	4.7	101.1	6.3	100.8	5.3
Nb/Ta	12.4		20.8		21.4	

Continue Table 3.7

	a.p.f.u.		
	COLB-1	COLB-2	COLB-3
Si	0.02	0.00	0.00
Ti	0.21	0.13	0.08
Nb	1.67	1.80	1.86
Ta	0.08	0.05	0.05
Sn	0.01	0.01	0.00
A site	2.00	2.00	2.00
Mn	0.23	0.41	0.45
Fe	0.65	0.53	0.53
U	0.02	0.00	0.00
Th	0.00	0.00	0.00
Pb	0.01	0.00	0.00
Ca	0.01	0.01	0.00
Y	0.00	0.00	0.00
REE	0.03	0.02	0.01
B site	0.96	0.98	0.99
Total	2.96	2.97	2.99

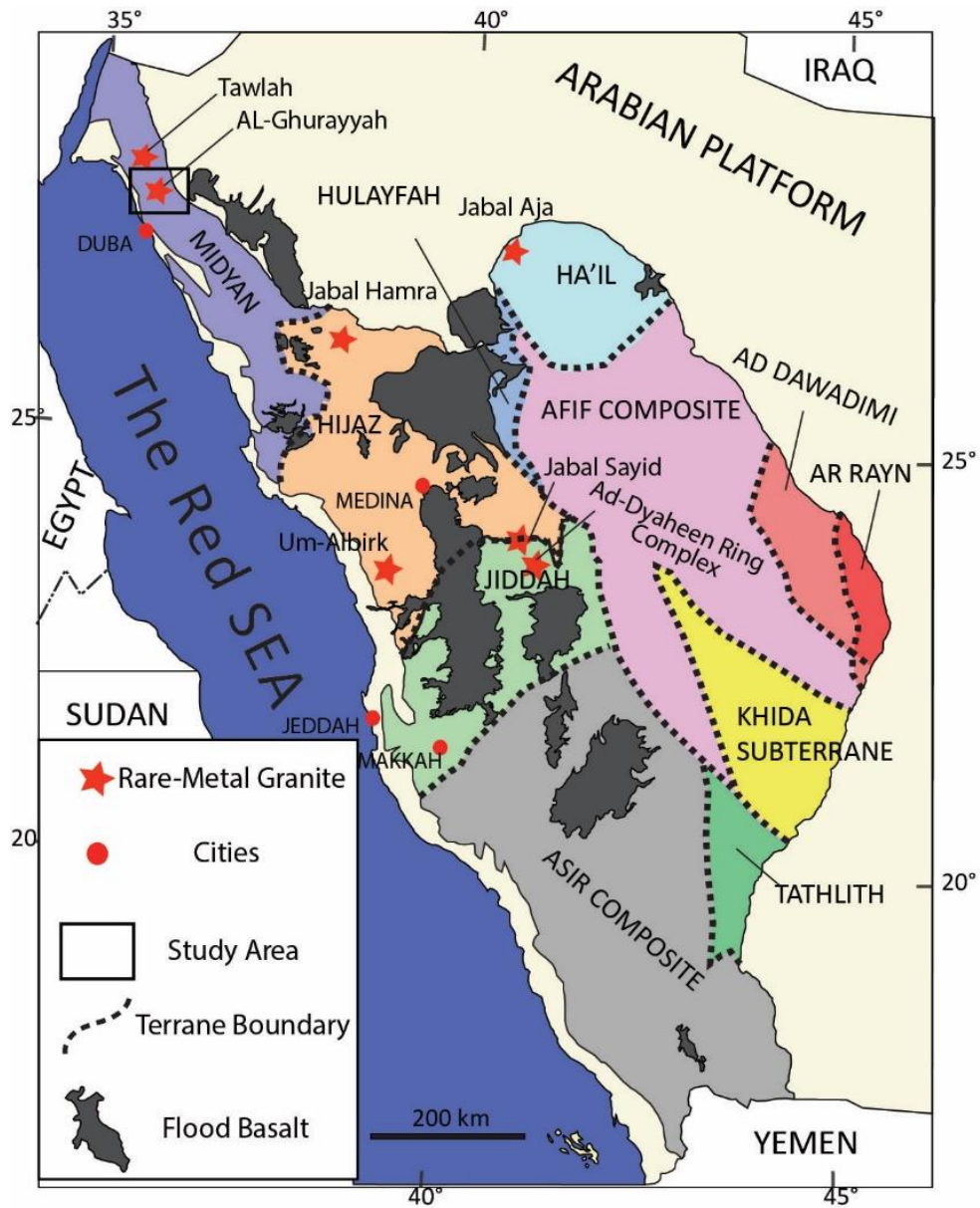


Figure 3-1 A geological map of the Arabian Shield showing the different terranes that constitute the Shield. The red stars are the locations of some important occurrences of rare-metal granite including Al-Ghurayyah, which is shown in the box (modified after Johnson and Kattan 2012).

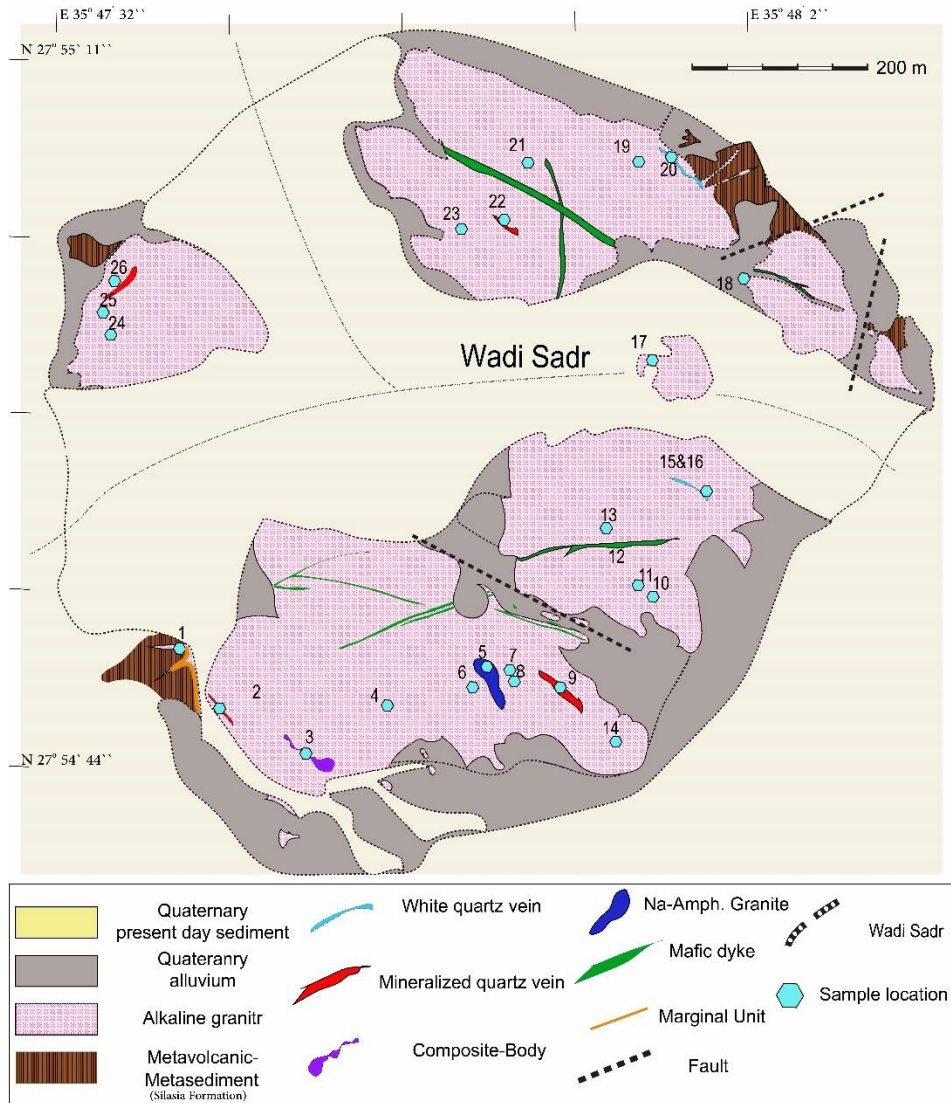


Figure 3-2 A geological map of Al-Ghurayyah deposit showing the main rock units and locations of samples (modified after Elliott et al. 2002).

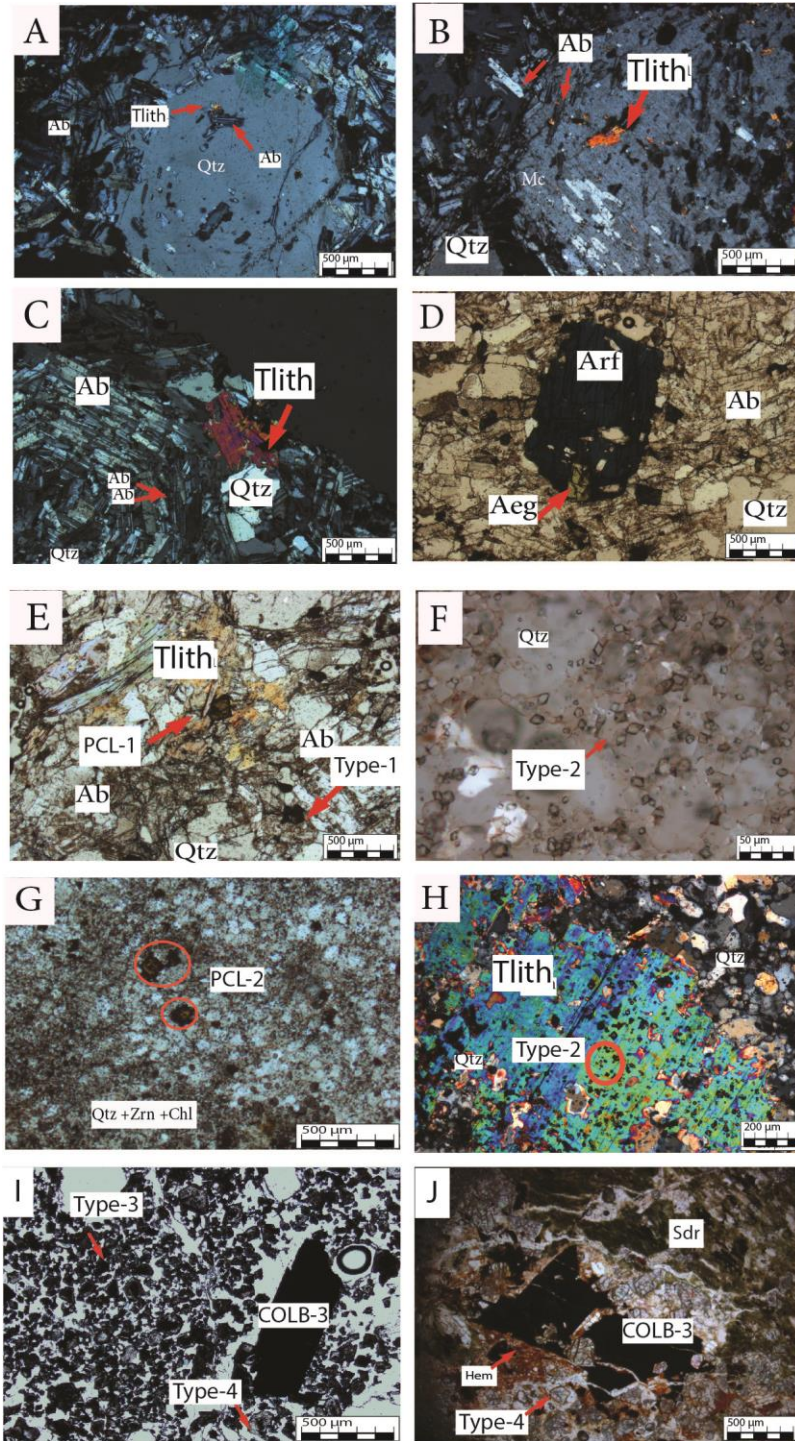


Figure 3-3 Petrology of the rock units in the Al-Ghurayyah. A) Crossed polarized light (CPL) image of a snowball quartz surrounded by albite and microcline from the altered porphyritic granite. The snowball contains inclusion of albite and trilithionite. B) CPL image of a snowball microcline with albite and trilithionite

inclusions from the altered porphyritic granite. C) CPL image of a snowball from amphibole-bearing granite showing albite inclusions arranged along the quartz growth zone. D) Plane polarized light (PPL) image of sodic amphibole from the amphibole-bearing granite. E) PPL image of disseminated pyrochlore from the amphibole-bearing granite. F) PPL image of a disseminated Type-2 zircon from the marginal unit. G) PPL of a disseminated pyrochlore, Type-2 zircon, and quartz from the marginal unit. The dark color between grains is due to the presence of chlorite between quartz grains. H) CPL image of a large trillithionite from the marginal unit containing zircon and quartz inclusions. I) PPL image of a large columbite crystal with aggregate Type-3 and 4 zircon from the zircon-columbite zone in the composite-body. J) PPL image of large columbite with aggregate Type-3 and 4 zircon and siderophyllite from the mica-zircon zone in the composite-body

Abbreviations: Qtz, quartz; Ab, albite, Amp, amphibole; Zrn, zircon; Tlith, trillithionite, PCL, pyrochlore; Colb, columbite.

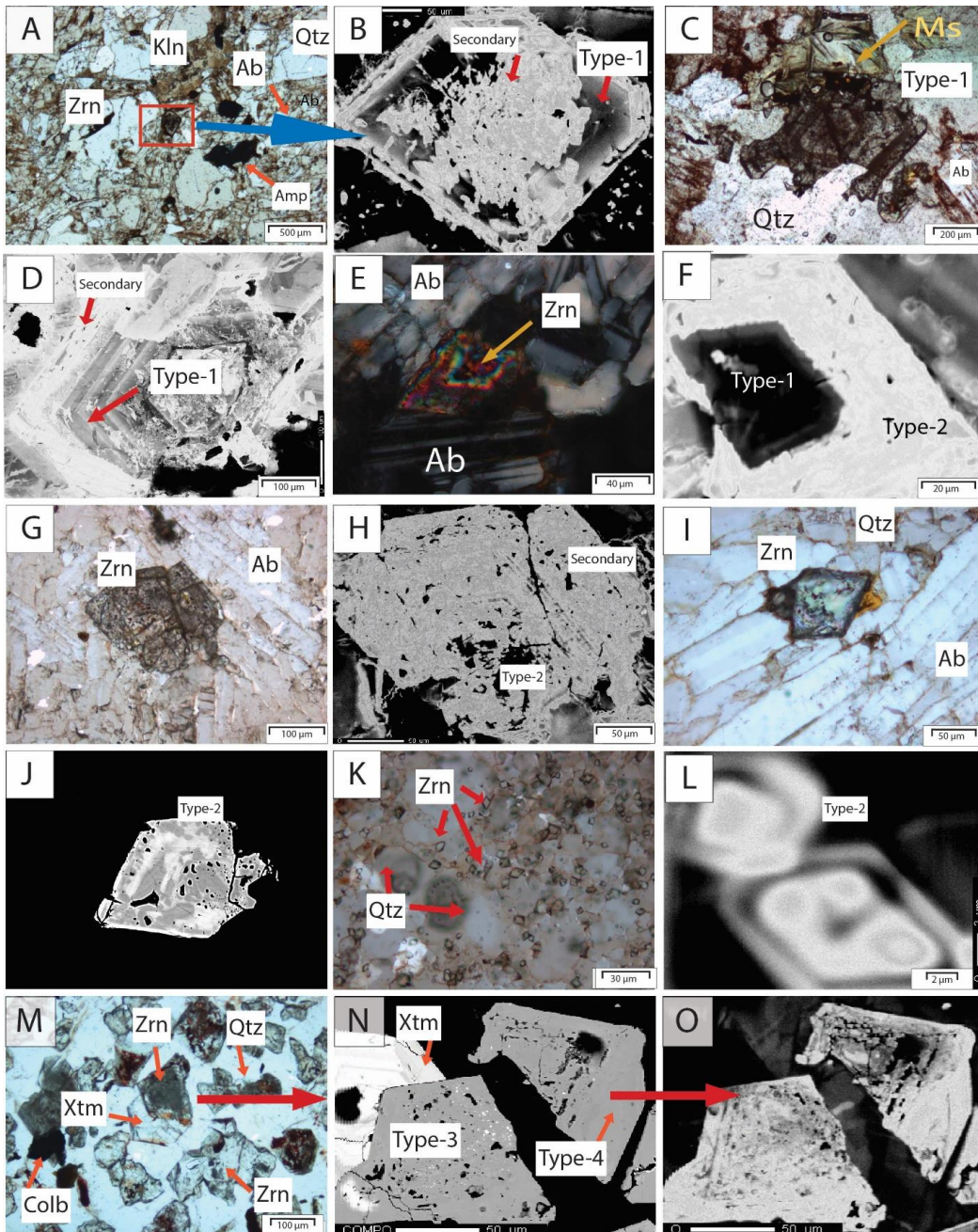


Figure 3-4 A) PPL of a disseminated Type-1 zircon in albite and quartz matrix from the fresh amphibole granite. B) CL image of Type-1 zircon in A. The grain shows clear oscillatory zoning that was overprinted by Type-2 and secondary zircon. C) PPL of a highly altered disseminated Type-1 zircon from the silicified porphyritic granite. D) CL image of Type-1 zircon in B that shows clear oscillatory zoning that was overprinted by secondary zircon. E) CPL image of Type-1 zircon and Type-2 overgrowth showing sharp edges with albite in the matrix from the

altered porphyritic granite. F) CL image of Type-1 zircon in C that shows Type-1 zircon with Type-2 overgrowth. G) PPL of Type-2 zircon with spongy texture from the altered porphyritic granite. H) CL image of Type-2 zircon in G. I) PPL image of Type-2 zircon forming sharp contact with albite and quartz from the porphyritic granite. J) BSE image of Type-2 zircon in image (H) showing a patchy zoning. K) PPL image of a disseminated Type-2 zircon from the marginal unit. L) CL image of zircon in (I) showing bimodal zoning. M) PPL image of aggregate Type-3 and Type-4 zircon from the zircon-columbite zone in the composite-body. N) BSE image of zircon in M showing spongy Type-3 in the core, Type-4 on the rim, and xenotime overgrowth. O) CL image of zircon in N.

Abbreviations: Qtz, quartz; Ab, albite, Amp, amphibole; Zrn, zircon; Kln, kaolinite; Ms, muscovite; Xtem, xenotime; Colb, columbite; Secondary, secondary zircon.

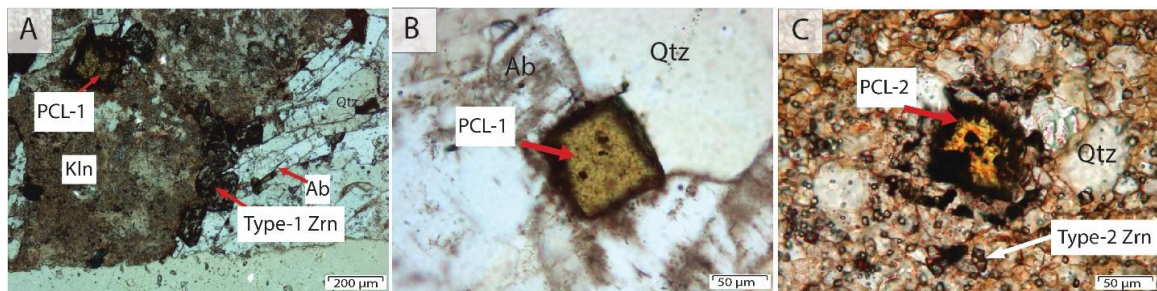


Figure 3-5 PPL image showing a disseminated pyrochlore (PCL-1) and zircon (Type-1) with albite locally altered to kaolinite. B) PPL image of a pyrochlore forming sharp contact with quartz and albite from the fresh sodic amphibole granite. C) PPL of Pyrochlore (PCL-2) from the marginal unit with disseminating Type-2 zircon.

Abbreviations: Qtz: quartz, Ab: albite, Kln: kaolinite; PCL, pyrochlore.

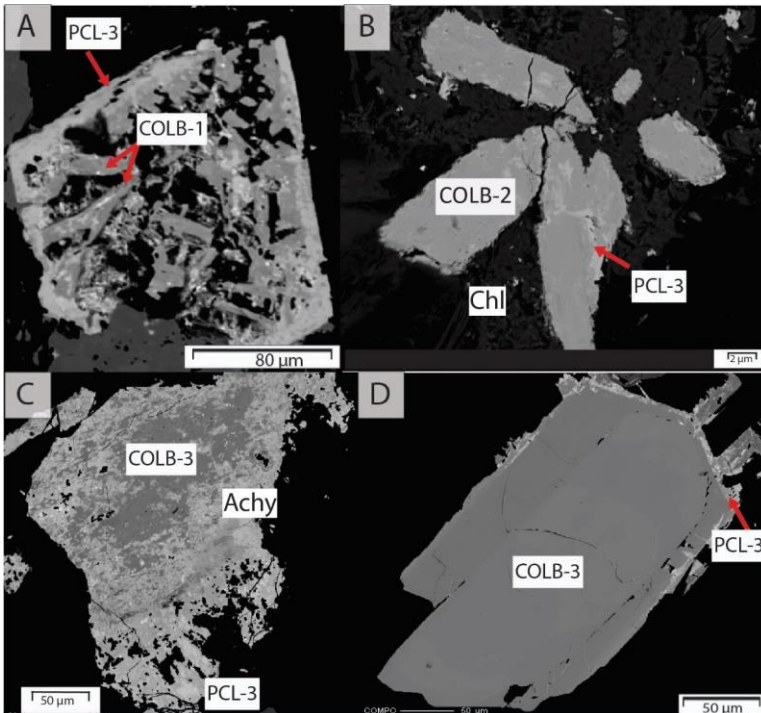


Figure 3-6 BSE image of COLB-1 replacement of PCL-1 from highly altered porphyritic granite. B) BSE image of COLB-2 from the altered porphyritic granite. Light veinlets crosscutting COLB-2 are PCL-3. C) COLB-3 replaced by PCL-3 and aeschynite. D) COLB-3 partially replaced by PCL-3 and aeschynite. Abbreviations: Achy, aeschynite, Chl, chlorite; COLB, columbite

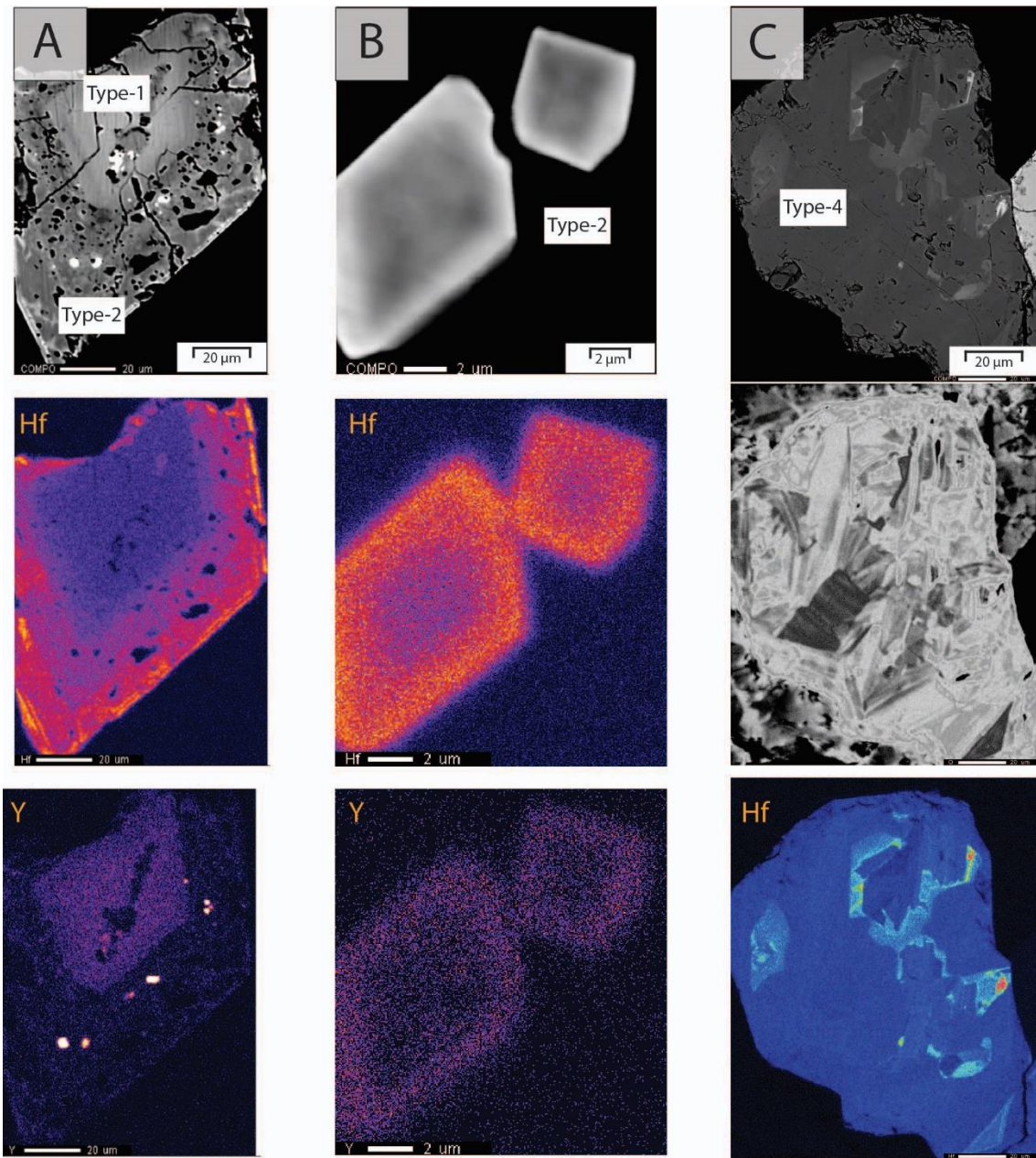


Figure 3-7 BSE image and WDS X-ray maps showing the internal variation in the composition some zoned zircon. A) Type-1 zircon and Type-2 zircon overgrowth showing zonation of Hf and Y. B) Bimodally zoned Type-2 zircon. C) Type-4 zircon showing patchy Hf zoning.

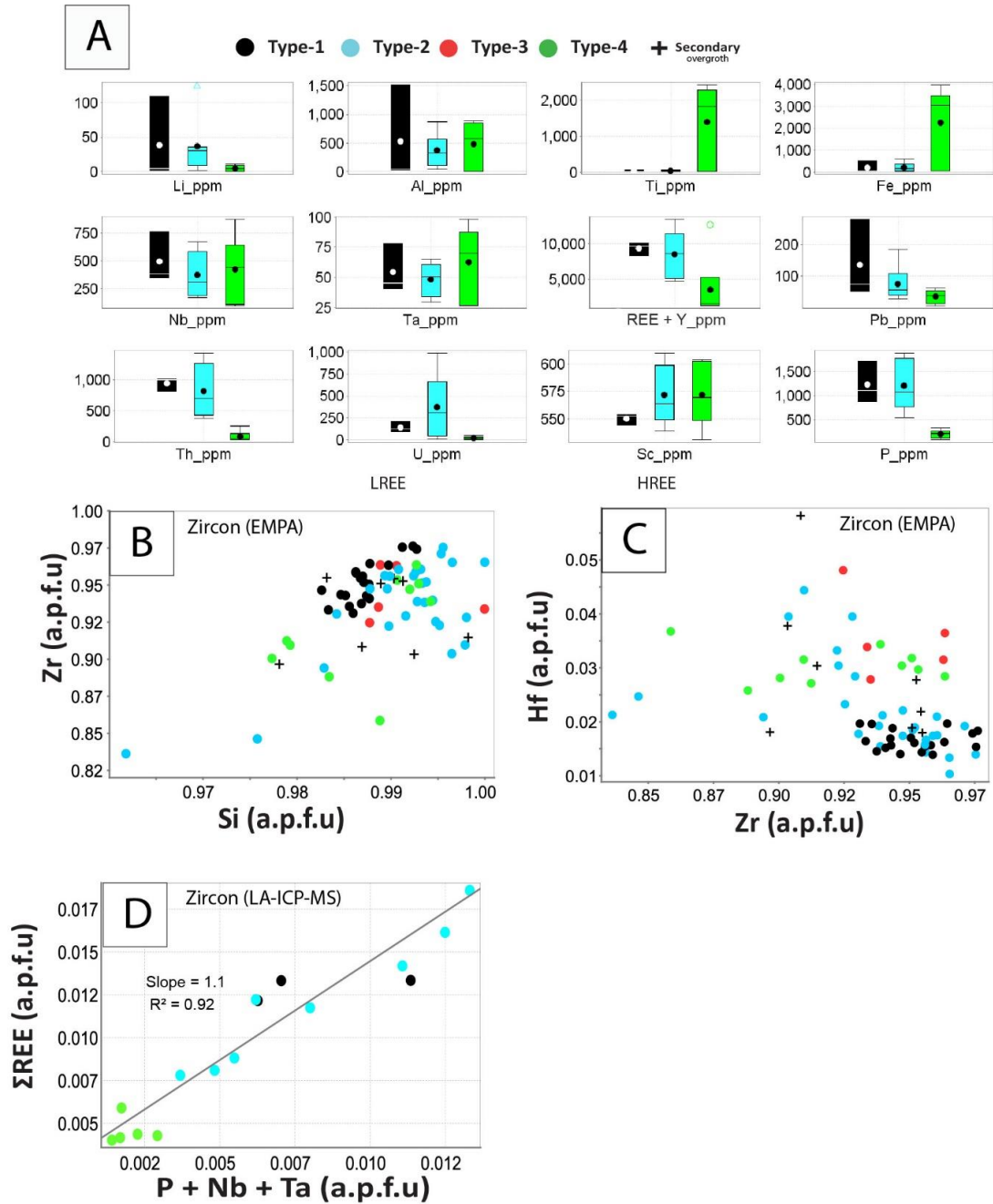


Figure 3-8 Chemical variation in zircon Composition from Al-Ghurayyah deposit.

A) Box and whisker diagram of trace element concentration in the different types of zircon obtained by LA-ICP-MS. **B)** plot of Si against Zr in a.p.f.u. obtained by EMP analyses. **C)** plot of Zr against Hf in a.p.f.u. obtained by EMP analyses. **D)** plot of P against total REE in a.p.f.u. obtained by LA-ICP-MS. The dashed line is slope of 1.1.

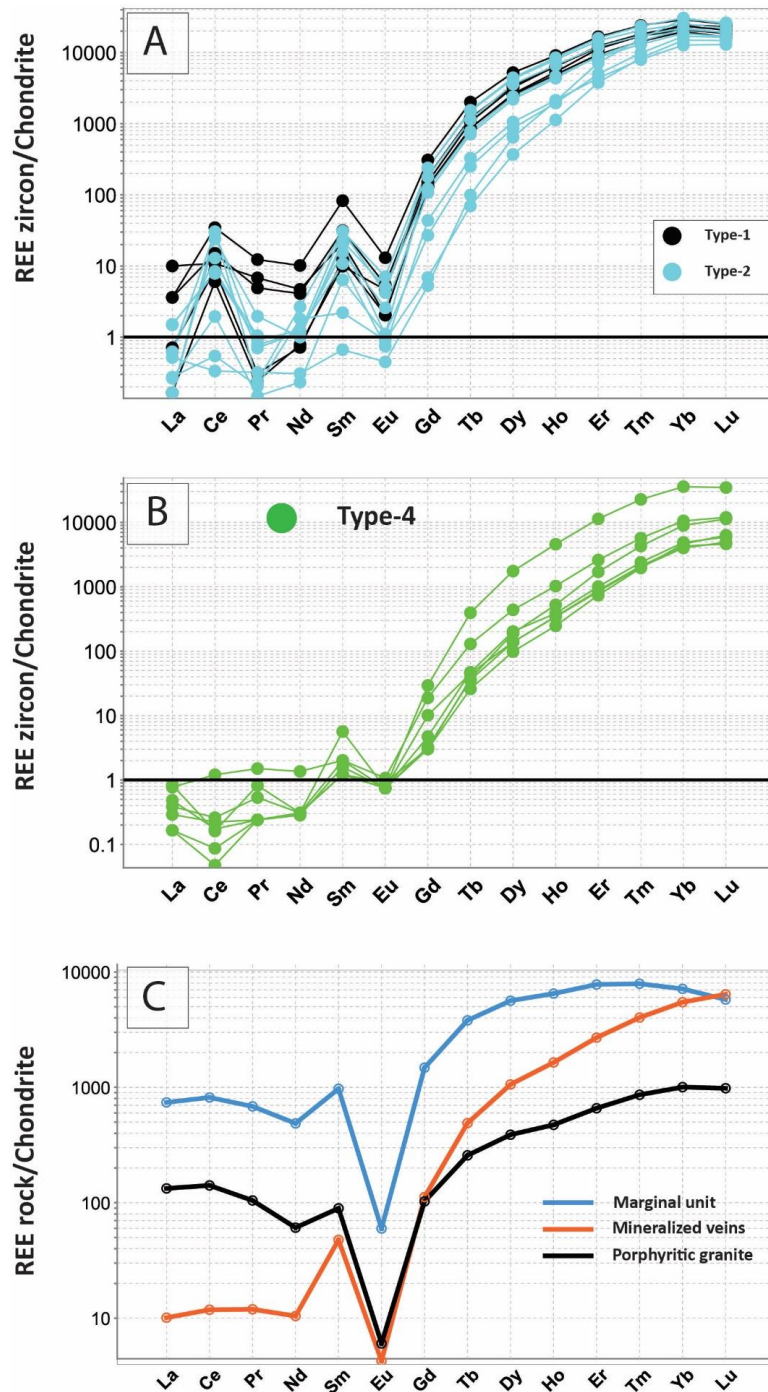


Figure 3-9 Chondrite normalized REE pattern of Type-1 and 2 zircon. B) Chondrite normalized REE pattern of Type-4 zircon. C) REE normalized pattern of the whole-rock. Normalized values are from Boynton (1984).

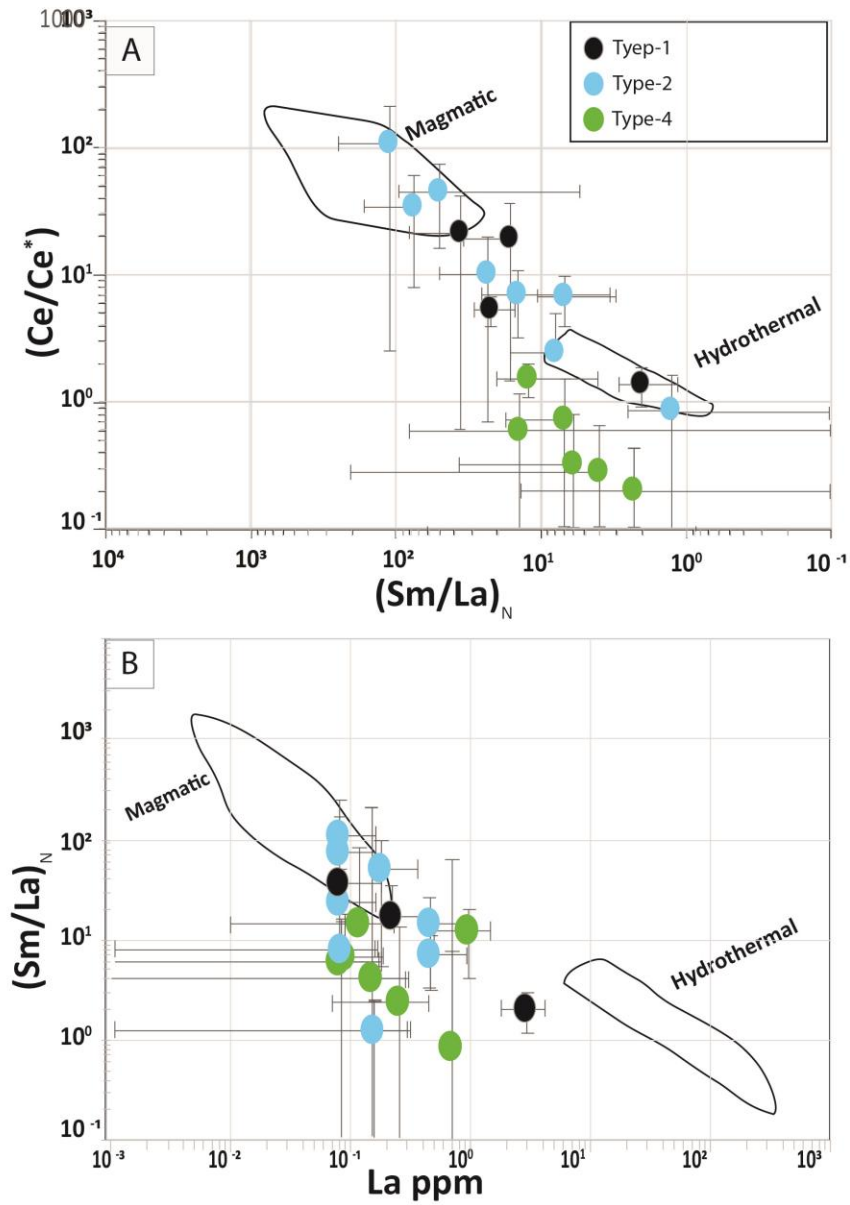


Figure 3-10 Zircon discrimination of Ce/Ce^* versus Sm/La_N in A and Sm/La_N versus La ppm in B (modified after Hoskin, 2005). Chondrite values are from McDonough and Sun (1995).

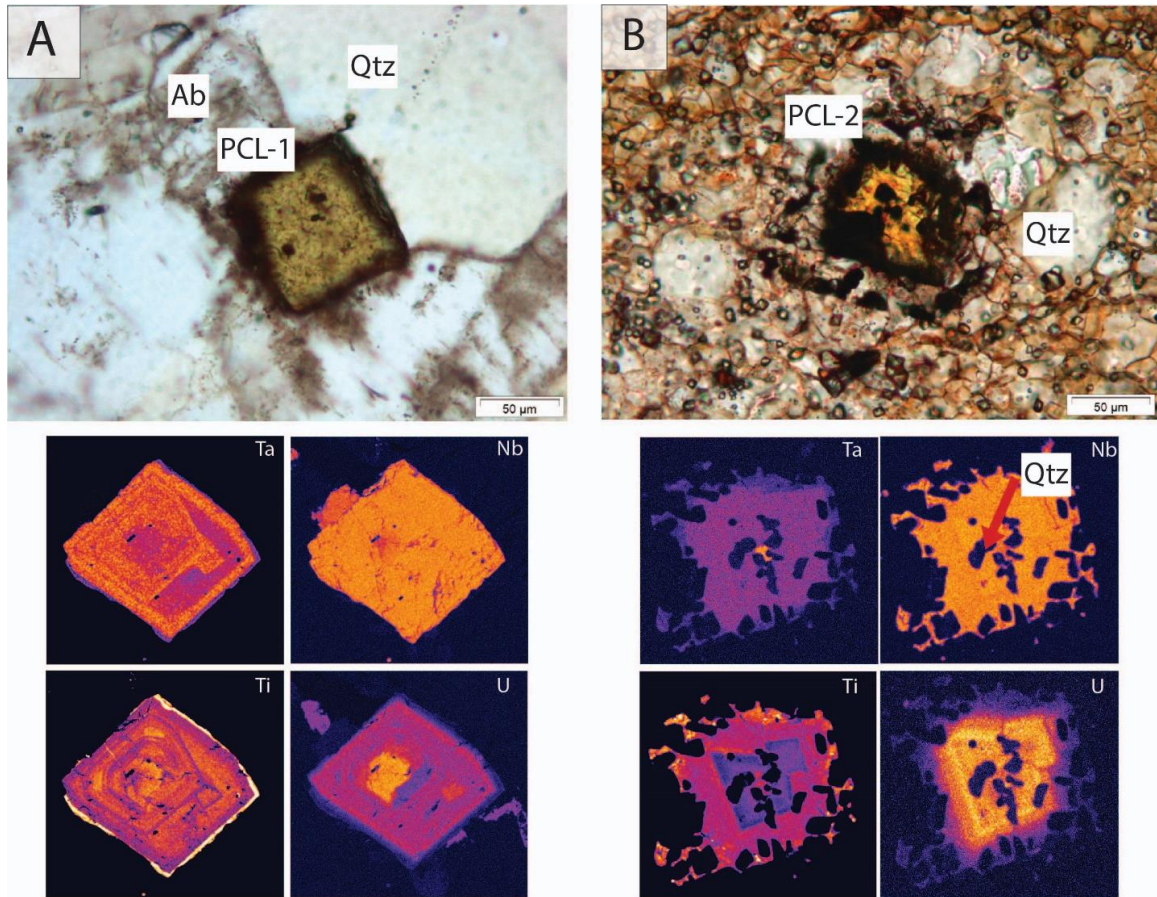


Figure 3-11 Pyrochlore WDS X-ray maps showing compositional variation in PCL-1 and PCL-2. A) PCL-1 from the fresh sodic amphibole. B) PCL-2 from the marginal unit.

Abbreviations: Qtz: quartz, Ab: albite

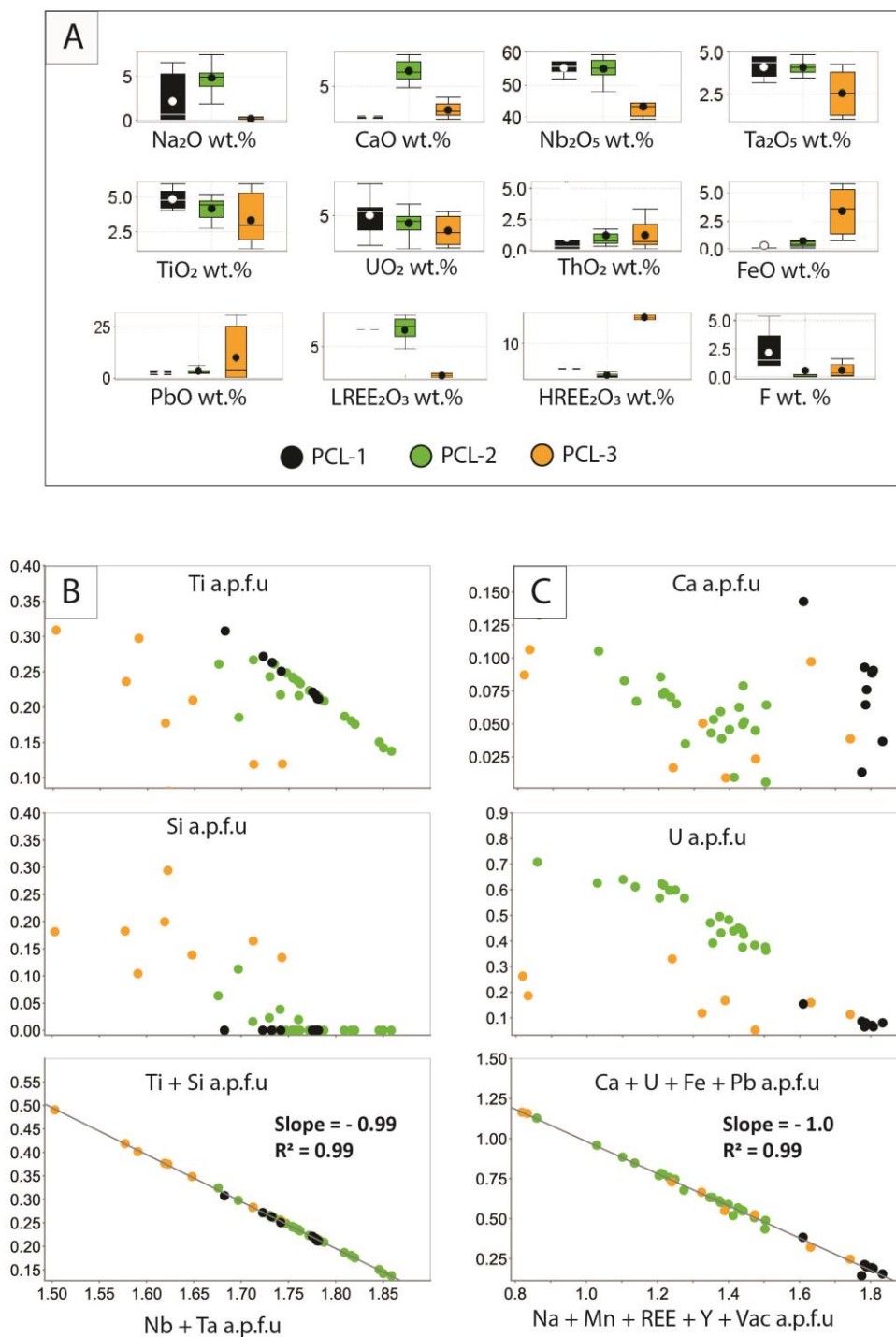


Figure 3-12 Chemical composition of pyrochlore. A) A box and whisker plot showing the variable composition of pyrochlore types in Al-Ghurayyah. B) A plot showing the main elements substitute Nb and Ta in the B site. The plot shows PCL-1 a different trend than PCL-1 and 2. Nb_2O_5 against Ta_2O_5 . C) A

plot showing major substitution in the A site. The three pyrochlore types show variable substitutions that resulted in the formation of different trends. The general substitution mechanism is represented by the plot in the bottom of Figure C. The slopes in the bottom plots least-square best fit

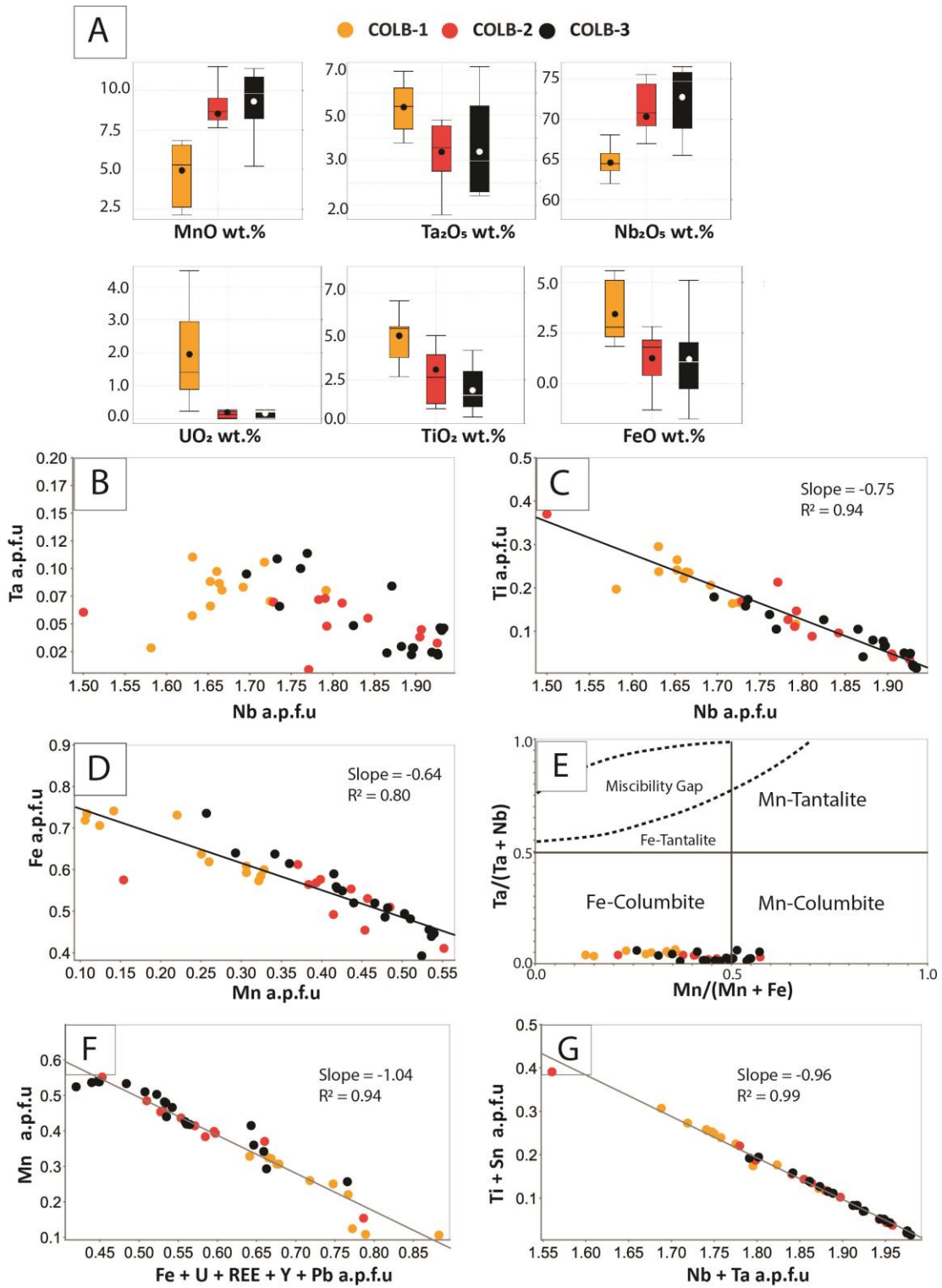


Figure 3-13 Chemical composition of columbite. A) A box and whisker plot showing the variable composition of columbite types in Al-Ghurayyah. B) A plot Nb with Ta in atom per formula unit (a.p.f.u) showing a weak correlation to scattering between the two elements. C) Negative Nb vs Ti in a.p.f.u formed by all columbite types suggesting that Ti is a major substituting element in the B site. D) Fe vs Mn in a.p.f.u plot showing variable negative correlations. COLB-2 and 3 show a similar trend, which is different than the trend formed by COLB-1. E) Mn# versus Ta# showing scattering and the formation of two population of High Ta# and low Mn# formed mostly by COLB-1 and high Mn# formed and low Ta# formed by COLB-2 and 3. F) A plot showing the main substitution mechanism in the A site. G) plot showing the main substitution mechanism in the B site. The slope in Figures F and G are least-square best fit lines.

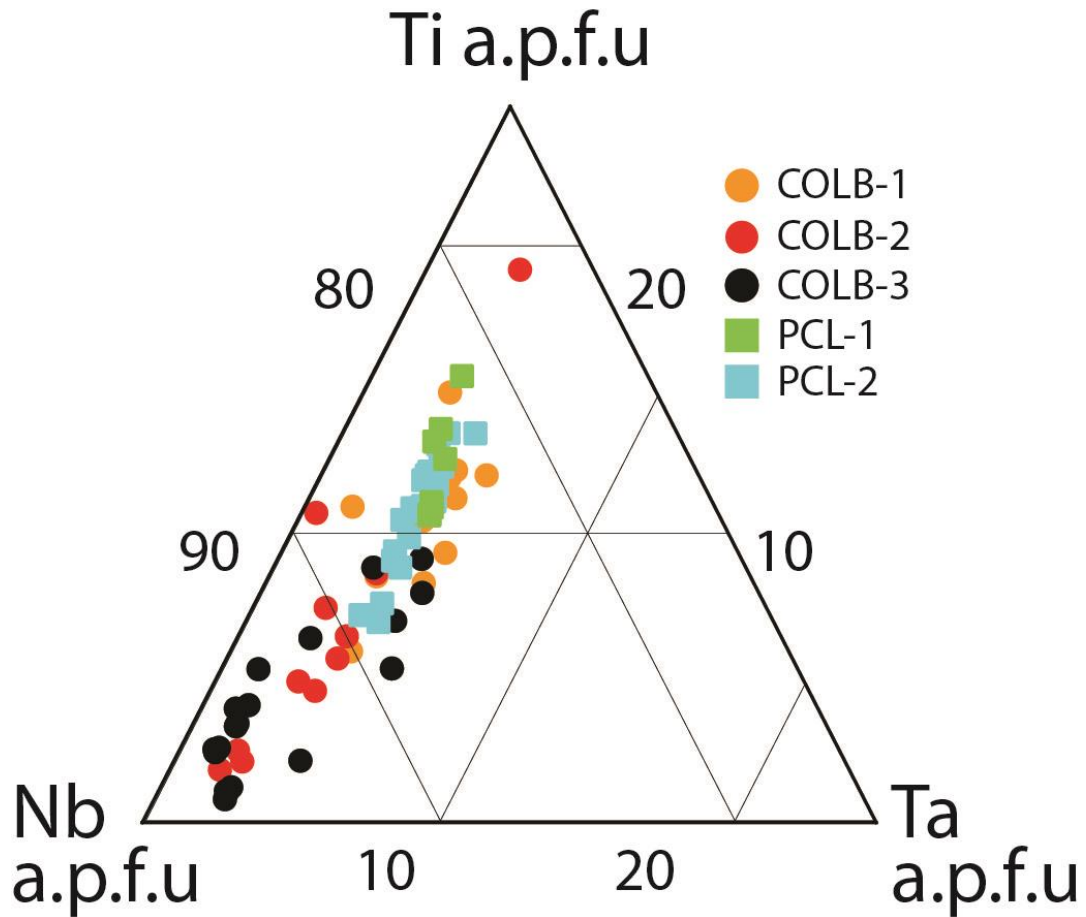


Figure 3-14 Ternary diagram showing columbite types contents of Ti, Nb, and Ta, and compared to PCL-1 and 2. The diagram shows that COLB-1, PCL-1, and PCL-2 have similar content of Ti, Nb, and Ta and these elements were immobile during the alteration of pyrochlore.

Chapter 4

4 Rare-metal mineralization at Jabal Sayid, the Arabian Shield, Saudi Arabia: Petrography, lithogeochemistry, and mineral chemistry

4.1 Introduction

Rare-metal alkaline granites contain high concentrations of high field strength elements (HFSE) and rare earth elements (REE = La, Ce, Pr, Nd, Sm, Eu, Gd, Tb, Dy, Ho, Er, Yb, and Lu), which make them an important source of critical metals. Other sources of critical metals include carbonatites (Bayan Obo, China), and metaluminous and peraluminous granite and pegmatite (Pitinga, Brazil; Yichyan, China; Tanco, Canada; Linnen et al., 2014). Based on the degree of silica saturation, alkaline granites can be classified into silica-under saturated and silica-saturated. Silica-undersaturated granites are characterized by high concentrations of Na-bearing minerals such as nepheline, sodalite, sodic amphibole, and aegirine, and contain complex zirconosilicate minerals. This type is commonly given the name agpaitic rock where the molar $\text{Na}+\text{K}/\text{Al}$ ratio is equal or higher than 1.2 (Sorensen, 1992). The best well-known examples for this type include Ilímaussaq, Greenland; Lovozero and Khibiny, Russia; and Nechalacho, Canada. The silica-saturated granites are sometimes referred to as miaskitic where they have an A.I. of < 1.2 (Sorensen, 1992). They are characterized by the presence of alkali feldspars, quartz, sodic amphibole, zircon, and pyrochlore and have simpler ore mineral composition, such as zircon, ilmenite, and pyrochlore (Möller and Williams-Jones, 2017; Piilonen et al., 2012; Sorensen, 1992). The best-known examples include Khaldzan-Buregtey, Mongolia; Strange Lake, Canada; and Al-Ghurayyah, Saudi Arabia.

Jabal Sayid deposit is one of the most important rare-metal deposits in the Arabian Shield due to its economic potential. The Jabal Sayid deposit is a part of Jabal Sayid complex, which is an A-type intrusion that was formed in a post-collisional environment (Radain et al., 1981). The deposit was discovered in 1956, and it has been a subject to several geological and lithogeochemical studies (Hackett, 1986; Harris et al., 1986; Moghazi et al., 2015; Radain et al., 1981; Staatz and Brownfield, 1985; Turkistany and

Ramsay, 1982). The deposit was estimated to have a reserve of 58 million tonnes containing 450 ppm La, 1040 ppm Ce, 3325 ppm Y, 1077 Nb, and over 19000 ppm Zr (Hackett, 1986). The age of the granite was estimated to be 593 ± 2.4 Ma by U-Pb age dating of zircon (Moghazi et al., 2015). Furthermore, Moghazi et al. (2015) concluded that the Jabal Sayid alkaline granite has an initial ϵNd of +4.9 to +5.3. These values are within the Arabian Shield range, which was interpreted to resemble juvenile crust that ranges from $\approx +4$ to $\approx +10$ (Moghazi et al., 2012; Stern et al., 2010).

The processes that resulted in enrichments of HFSE and REE in A-type alkaline granites have been the focus of many studies (e.g., Boily and Williams-Jones, 1994; Feng and Samson, 2015; Gysi and Williams-Jones, 2013; Kovalenko, 1995; Möller and Williams-Jones, 2016; Salvi et al., 2000; Salvi and Williams-Jones, 1990; Vasyukova and Williams-Jones, 2014; Vasyukova et al., 2016; Wang et al., 2003). The main hypotheses for the formation of this kind of deposits include: 1) magmatic model due to extreme fractionation (Boily and Williams-Jones, 1994; Kovalenko, 1995); 2) magmatic and hydrothermal model where magmatic process enriched the residual melt in HFSE and REE and later a hydrothermal stage increased their concentrations to economical levels (Gysi and Williams-Jones, 2013; Salvi et al., 2000; Salvi and Williams-Jones, 1996); 3) fluoride-silicate melt immiscibility, where the fluoride melt fractionated REE and enriched the silicate melt in HFSE (Siegel et al., 2018; Vasyukova and Williams-Jones, 2014; Vasyukova et al., 2016).

The silica-saturated type of alkaline granites particularly is not understood because the bulk of the studies were focused on silica-undersaturated alkaline granites. In order to better constrain the magmatic and hydrothermal processes in these systems, three examples of silica-saturated alkaline granites from the Arabian shield are chosen, each with unique mineralization styles. These deposits are Al-Ghurayyah (disseminated), Jabal Sayid (pegmatites), and Dyaheen (veins). This chapter discusses the mineralization at Jabal Sayid, whereas mineralization in Al-Ghurayyah is discussed in Chapters 2 and 3, and Dyaheen is discussed in Chapter 5.

Previous work on the Jabal Sayid complex and associated deposits have provided valuable lithogeochemical and petrological information. However, the only known work that provided the compositions of the ore minerals was by Staatz and Brownfield (1985) and the concentrations of La, Ce, Y, Nb, Ta, Th, U, Zr, and Sn were reported. Hackett (1986) provided an estimate of the ore reserve based on the Staatz and Brownfield (1985) geological report. Since then, there has been no new work focusing on the mineralized area of the complex. This study characterizes the mineralization in Jabal Sayid deposit and the host granite for the purpose of evaluating the roles of magmatic and hydrothermal processes that led to the substantial concentrations of HFSE and REE. Jabal Sayid offers the opportunity to assess the late-magmatic and early-hydrothermal stage because these two stages are exceptionally well preserved. New whole-rock lithogeochemical data for the host rock at the northern part of the complex are combined with detailed mineral chemical analyses and morphological descriptions for the ore minerals in Jabal Sayid to constrain the magmatic and the hydrothermal stages that led to the formation of the mineralized units. This was done through studying magmatic and hydrothermal textures in the host granite and the mineralized units, which were then further constrained by the chemical compositions of the ore minerals and the whole rock. The morphologies of the ore minerals were studied using a polarizing microscope and a secondary electron microscope (SEM) equipped with energy dispersive spectroscopy (EDS) for mineral identification. The internal chemical variation of the ore minerals was determined using wavelength and energy dispersive spectroscopy (WDS and EDS) maps, followed by point analyses by electron microprobe (EMPA). Finally, the trace element compositions of zircon were obtained using laser ablation inductively coupled plasma mass spectrometry (LA-ICP-MS), which helped characterize the chemical evolution of its crystallization environment.

4.2 Geological setting

The accretion of the Arabian Shield took place between 900 to 550 Ma ago (Agar, 1992; Nehlig et al., 2002; Robinson et al., 2014; Stern, 1994) when several inter-oceanic island arcs were amalgamated to form the Arabian Shield (Fig. 4.1). The collision of the island arcs resulted in the formation of eleven distinct terranes: the Asir, Tathlith, Khida, Ar-

Rayn, Ad-Dawadimi, Afif, Ha'il, Hulayfah, Jeddah, Hijaz and Midyan terranes (Johnson et al., 2011). The terranes are marked by the presence of ultramafic bodies within the orogenic belts (Agar, 1992; Robinson et al., 2014). The accretion of the Arabian Shield was followed by a period of extensional tectonism during orogenic collapse, and the transition between collisional and extensional environments is demonstrated by the association of dyke swarms and the presence of volcanic rocks in molasse-basins that are associated with calc-alkane and alkaline granite emplacement, which are dated about 686 to 518 Ma (Stoeser, 1986). The post-collision period is associated with the emplacement of a large volume of alkaline magmatism that formed one of the world largest alkali granite fields (Stoeser, 1986). Several of the post-collision alkaline granites are considered to be specialized granites that are characterized by high concentrations of Nb, Ta, Zr, Y, REE, Th and U (Drysdall et al., 1984; Küster, 2009).

The Jabal Sayid rare-metal granite (also written as Jabal Sai'd and Jabal Sayed) is located within the Jeddah terrane, near the Bi'r-Umq suture, between the Hijaz and Jeddah terranes (Fig. 4.1). The Jeddah terrane covers an area of 56000 km² and is bordered by the Hijaz terrane from the north, the Afif composite terrane from the east, the Asir composite terrane from the south and, the Red Sea coastal plain from the west. Jabal Sayid rare-metal granite is part of the larger Jabal Sayid complex, which consists of syenogranite and alkaline granite (Moghazi et al., 2015) that intruded the Hufayryah tonalite (780-760 Ma, Johnson, 2006) and the Dumah granodiorite (Harris et al., 1986; Radain, 1979). The core of the complex is syenogranite (573 ± 22 Ma Rb-Sr; Hackett, 1986), and the western margin of the complex is intruded by a porphyritic peralkaline granite. The complex is cut by a north-west trending fault. The rock units located north the fault are known as Jabal Sayid granite, and the units located south the fault are known as the Hdab as Sharar granite (Moghazi et al., 2015).

Jabal Sayid rare-metal granite is located on the northern margin of Jabal Sayid complex (Fig. 4.2). The main rock units in Jabal Sayid are summarized in Table 4.1. The mineralized part of the complex was previously termed apogranite (Harris et al., 1986) and consists of an oxidized granite and pegmatite sheets that enclose the host aegirine granite in irregular contacts. The oxidized granite is situated between the host granite and

the pegmatite. The pegmatite is a sheet-like body with 2 km strike length that dips 45 to 75 degrees to the north (Fig. 4.3). The contact between the pegmatite sheets and the oxidized granite is sharp; however, the oxidized granite near the pegmatite sheets experienced variable degrees of hematization ranging from mildly to highly hematized. The pegmatite sheets locally display well-developed quartz, feldspar, and altered pyroxene, that are coarse-grained (up to 1 mm in length) compared to the fine-grained (100 to 250 μm) and highly hematized margin. A handheld radiation detector (model TBM-3S) was used to locate mineralization. The areas with strong mineralization are commonly hematized and gave up to 10,000 counts per second (cps) total alpha, beta, and gamma radiation. The mineralogy of the oxidized granite is obscured by the intense hematitic alteration. The host aegirine granite is medium-grained and shows a variable degree of alteration near the contact with the pegmatite. South of the mineralized units (pegmatite sheets and oxidized granite), the granite is weathered and shows porphyritic texture where alkali feldspar and altered arfvedsonite occur as phenocrysts. Moreover, the granite and the pegmatite sheets were cut by late white quartz veins. The quartz veins are mostly barren, except for trace amounts of galena.

4.3 Methodology

Samples from the host granite, the pegmatite sheets, and the oxidized granites were collected for petrographic and litho-geochemical analyses. Polished thin section slides were prepared in the Department of Earth Sciences at the University of Western Ontario, Canada, and the Faculty of Earth Sciences, at King Abdul Aziz University, Jeddah, Saudi Arabia. The polished thin section slides were studied using a petrographic microscope and a scanning electron microscope equipped with energy dispersive spectroscopy (SEM-EDS) to obtain mineralogical, textural, and mineral composition data. The analyses were completed at the Department of Earth Sciences at the University of Western Ontario, Canada. Major elements mineral composition and backscattered electron images (BSEI) were obtained using a JEOL JCM 6000 benchtop SEM equipped with EDS (B-SEM). Data were collected at 15 kV acceleration voltage at a high vacuum mode. Quantitative mineral compositions, cathodoluminescence (CL), and EDS analyses were determined on a JEOL JXA-8530F field-emission electron microprobe (EMPA) at Earth and Planetary

Materials Analysis Laboratory at the University of Western Ontario, Canada. The analytical conditions of the EPMA were 20 kV probe current, 40-60 nA accelerating voltage, and a beam diameter ranging from 1 to 15 micrometer. The standards were synthetic zircon for Zr and Si, rutile for Ti, albite for Na and Al, fayalite for Fe for iron in aegirine, fluorite for F, orthoclase for K, anorthite for Ca. Pure metal standards (serial 2AG-METM25-44, Astimex Standards Limited) were for Fe in oxide accessory minerals, Mn, Nb, Ta, Hf, Pb, Th, and U.

Smithsonian REE phosphate (NMNH 168484-116499) standard was used for REE analysis. In order to resolve the REE peak and background overlaps, corrections were made by performing a slow scan on WDS crystals (LIF, LIFH, and LIFL) to identify the elements with peak and background overlaps. The amount of overlap that contributes to the main peak was measured and then subtracted from the main peak (Appendix C).

In order to obtain the trace element content of zircon, grains were analyzed by laser ablation inductively coupled plasma mass spectrometry (LA-ICP-MS) at the Great Lakes Institute for Environmental Research (GLIER) at the University of Windsor, Ontario, Canada. Zircon-1, Zircon-2, and Zircon-3 (classification discussed below) were analyzed on a Photon-Machines 193 nm ArF excimer laser with 20 micrometer beam diameter, 20 Hz repetition rate, and 1.63 J/cm² energy. The ICP system is an Agilent 7900 ICP-MS. Ar gas flow was 0.82 L/min, with 30 milliseconds used as wash delay. NIST 610 was used as an external standard, and the concentration of Zr obtained using EMPA was used as an internal standard. In zoned grains, the average concentration of Zr of the ablated area was used as the internal standard. The data processing and data reduction were done using IGORPro and Iolite software (Paton et al., 2011). The isotope list and the average detection limits are summarized in Appendix C.

The whole-rock composition was determined by Activation Laboratories Ltd (Actlabs), Ancaster, Ontario, Canada. Samples were crushed and pulverized using mild steel. The powder was fused using lithium metaborate/tetraborate and then digested in a weak nitric acid solution. Major and trace elements were analyzed using inductively coupled plasma-mass spectrometry (ICP/ICP-MS). The analyzed oxides and elements and the limits of

detection are summarized in Appendix C. Analytical precision was calculated from duplicate analyses, and ranges from 0.1 to 5 relative % for major elements, 0.5 to 8 relative % for REE and HFSE, and up to 20 % for other trace elements. Fluorine was analyzed by ion-selective electrode technique. In this technique, samples were fused with lithium metaborate/tetraborate in an induction furnace to release the fluoride ions to the matrix and then dissolved in dilute nitric acid. Next, the solution was complexed with ionic strength adjusted with ammonium citrate buffer before the analysis.

4.4 Petrography

4.4.1 Aegirine granite

The aegirine granite is the dominant rock in the mineralized area of Jabal Sayid. It is porphyritic and consists of 40 to 45 % quartz, 30 % alkali feldspar, 15 to 20 % albite, and 5 to 10 % amphibole/aegirine by visual estimation. Quartz occurs as large subhedral grains (1mm) that locally contain inclusions of tabular albite (Fig. 4.4 A and B). The alkali feldspar occurs as large euhedral to anhedral grains (0.6 to 1mm) of microcline and microcline-perthite that locally contain albite inclusions (Fig. 4.4 B). Albite occurs as lath-shaped grains in the groundmass mantling perthite and microcline crystals and as inclusions in quartz and K-feldspar (Fig. 4.4 A to B). Aegirine occurs as large subhedral to anhedral prismatic-shaped crystals that are up to 1 mm long. It displays intermediate pleochroism from light yellowish green to green (Fig. 4.4 C and D). Near the contact with the mineralized area, the aegirine granite shows alteration of aegirine to hematite, zircon, and quartz that are arranged in prismatic shape (pseudomorph after prismatic aegirine). This altered aegirine granite contains another type of aegirine that is present as acicular crystals (acicular aegirine) that are partially altered to quartz, zircon, and hematite (Fig. 4.4 E and F). Secondary minerals are usually associated with the alteration of prismatic aegirine and acicular aegirine alteration and include iron oxide (hematite), fluorite, zircon, and minor amounts of bastnasite.

4.4.2 Oxidized granite and pegmatite sheets (mineralized units)

The HFSE and REE mineralization in Jabal Sayid is concentrated in the oxidized granite and the pegmatite sheets. The oxidized granite contains clusters of hematite, zircon,

bastnasite, and quartz \pm xenotime, synchysite, and monazite that are arranged to form acicular shape pseudomorphs (after aegirine). The high abundance of pseudomorphs gives the oxidized granite its dark red color. The oxidized granite consists of 45-50 % quartz, 25-30 % pseudomorphs and ore minerals, 10-15 % microcline, < 5 % albite, < 0.5 % sericite and < 0.5 disseminated pyrochlore (volume % by visual estimation). Quartz forms the bulk of the groundmass and encompasses all other minerals. The quartz has an irregular shape, but it is in sharp contact with microcline (Fig. 4.4 G). The pseudomorphs range in size from 20 μm to about 1 mm (Fig. 4.4 H). Locally, hematite occurs in the matrix outside the pseudomorphs as fan-shaped crystals in that commonly contain inclusions of altered pyrochlore and thorite. Microcline occurs as euhedral to subhedral crystals that range from 400 μm to 1 mm that display crosshatch twinning. Ore minerals typically occur as replacement minerals in the pseudomorphs; however, isolated crystals of monazite, bastnasite, and pyrochlore are also present (Fig. 4.4 I). Albite occurs as anhedral prismatic-shaped crystals in the groundmass with microcline that ranges in size from 100 to 300 μm . Sericite occurs as light brown to dark yellow, small, and irregular-shaped fibrous crystals that are associated with hematite (Fig. 4.4 G and H). Other secondary minerals include Fe-chlorite (chamosite), and a Zn- aluminosilicate (identified by EDS). The chemical analyses of Zn- aluminosilicate is only by EDS; thus the mineral cannot be characterized, however; Zn is known to substitute in aluminosilicate structure, such as chlorite, and could possibly be baileychlore ($[\text{Zn}, \text{Fe}^{2+}, \text{Al}, \text{Mg}]_6[\text{Si}, \text{Al}]_4\text{O}_{10}[\text{OH}]_8$) (Rule and Radke, 1988).

The pegmatite sheets locally show a well-developed core (10 to 15 cm) and a border zone (1 to 3 cm). The core consists of 70-75 % quartz, 20-25 pseudomorphs (after aegirine), 5-10 % K-feldspar, and > 1 % pyrochlore (by visual estimation). Quartz encompasses all minerals and forms the groundmass (Fig. 4.4 J and K). The alkali feldspar in the pegmatite is microcline as indicated by the cross-hatched twinning. Microcline occurs as euhedral to subhedral crystals and locally contains hematite along cleavage planes. Pseudomorphs (after aegirine) occur as elongated prisms that are up to 1 cm in length (Fig. 4.4 J and K). The pseudomorphs have variable mineral composition; however, they typically consist of 80 to 90 % quartz, 5 to 10 % zircon, 5 to 10 % hematite, and 5 %

synchysite ± monazite. Fluorite occurs with hematite and REE-fluoro-carbonate minerals (Fig. 4.4 L).

The border zone of the pegmatite (1 to 3 cm) is medium-grained and consists of 40 % quartz, 25 % K-feldspar, 20 % pseudomorphs, and opaque minerals, < 10 % albite, and < 5 % acicular aegirine. The mineralogy of this part of the pegmatite is comparable to the oxidized granite mineralogy; however, the acicular aegirine is less altered, and the unit generally is less hematized (Fig. 4.4 M to P). The main difference between the border and the core of the pegmatite is the size of the pseudomorphs, where they are smaller at the border (30 to 100 µm), and the low abundance of albite in the core of the pegmatite (> 1 %) (Fig. 4.4 N and P). Moreover, bastnasite is more abundant relative to the core, whereas in the core synchysite is the most abundant REE phase. Quartz occurs as euhedral to subhedral crystals (500 µm) containing numerous acicular aegirine and pseudomorphs after prismatic aegirine that form a snowball texture (Fig. 4.4 M and N). The K-feldspar is microcline as indicated by the cross-hatched twinning. Aegirine occurs as euhedral to subhedral acicular crystals that range from 50 to 200 µm long. The acicular aegirine that is commonly included in quartz is arranged along the quartz growth zones (Fig. 4.4 M and N). Microcline is present as anhedral crystals in the groundmass and contains acicular pseudomorph inclusions. Microcline crystals have planar crystal boundaries when they are in contact with quartz. Pseudomorphs generally consist of zircon, bastnasite, hematite, and quartz. Hematite and rare-metal minerals, such as synchysite and bastnasite also occur along grain-boundaries and in cracked grains (Fig. 4.4 N and P).

4.4.3 Rare-metal minerals

The rare-metal minerals are mostly concentrated in the mineralized oxidized granite and the pegmatite sheets. In the oxidized granite and the pegmatite sheets, the main rare-metal minerals are zircon, synchysite, bastnasite, pyrochlore, monazite, and xenotime. Zircon is the main rare-metal mineral in the aegirine granite near the oxidized granite and pegmatite sheets. Trace amounts of bastnasite and pyrochlore are also present in this unit, and are typically associated with altered mafic minerals.

4.4.3.1 Zircon

Zircon is one of the most common rare-metal minerals at Jabal Sayid. In the aegirine granite, zircon is a secondary phase and only observed in samples that are proximal to the mineralized units. Zircon is classified based on the host rock into Zircon-1 in the aegirine granite, Zircon-2 in the oxidized granite and Zircon-3 in the pegmatite sheets.

Nevertheless, this is a general classification, and each type could be further subclassified, as more than one generation of zircon can occur in the same rock. This would require a detailed study of zircon and would be a topic for a future work.

Zircon-1 occurs as aggregates of transparent to light-grey, subhedral, equant crystals that range in size from 5 to 50 μm that are commonly associated with altered prismatic aegirine and acicular aegirine (Fig. 4.4 E and F). Moreover, Zircon-1 is present as aggregates with quartz and hematite that replaced prismatic aegirine. Zircon-1 shows no zoning and appears homogenous in BSEI; however, Zircon-1 locally shows wide-spaced oscillatory zoning in CL images (Fig 4.5 A and B). In the oxidized granite, Zircon-2 optically is similar to the secondary zircon in the aegirine granite. Moreover, Zircon-2 occurs as aggregates in the matrix of the oxidized granite, associated with hematite. Backscattered electron images (BSEI) show that this zircon is irregularly zoned with resorbed-reprecipitation textures (Fig. 4.5 D). The irregular zoning is defined by a high Y concentration in the core and low Y concentration at the margin (Fig. 4.5 E). In the pegmatite sheets, Zircon-3 occurs as aggregates of light-yellow to greyish crystals (< 50 μm) that are arranged to form small veinlets inside pseudomorphs of aegirine (Fig. 4.5 F).

4.4.3.2 REE minerals

The most common REE minerals are synchysite, bastnasite, xenotime, and monazite. The concentrations of these minerals vary according to the host rock. Furthermore, pyrochlore and zircon contain significant REE, up to 20 wt. % and 15 wt. %, respectively. However, this section describes the morphology of synchysite, bastnasite, xenotime, and monazite.

Synchysite is the main HREE mineral in the pegmatite sheets, and its abundance increases from the border to the core. It is commonly associated with Zircon-3 and hematite \pm fluorite in the pseudomorphs and in the matrix. It occurs as reddish-brown acicular

crystals that range in size from 20 to 500 μm (Fig. 4.6 A and B). In the oxidized granite, synchysite is less abundant compared to the core zone of the pegmatite. It occurs as a replacement with xenotime after bastnasite (Fig. 4.6 C and D).

Bastnasite is the predominant light REE (LREE = La, Ce, Pr, Nd, Sm, Eu, and Gd) mineral in the oxidized granite and the border zone of the pegmatite sheets. Bastnasite generally occurs as pale yellow to slightly reddish prismatic crystals that range in size from 30 μm to 0.5 mm. It is commonly replaced by xenotime and synchysite (Fig. 4.6 C and D). Moreover, it occurs with hematite and monazite in the matrix or has replaced acicular aegirine (Fig. 4.6 E and F). Bastnasite in the core of the pegmatite is scarce to absent.

Monazite occurs as light-pink, large subhedral crystals that are 0.5 mm long (Fig. 4.6 G and H). It is locally replaced by other REE minerals, such as xenotime and bastnasite \pm synchysite (Fig. 4.6 H). Monazite is the second most common LREE phase in the oxidized granite and the border zone of the pegmatite, where it comprises about 5 to 10 % of the total LREE minerals, and it is less abundant in the pegmatite core.

Xenotime occurs with synchysite that replaced bastnasite (Fig. 4.6 C, D, and H). It is the main host to the HREE in the oxidized granite and the border zone with synchysite. In the pegmatite sheets, xenotime is less abundant.

4.4.3.3 Pyrochlore

Pyrochlore is the main Nb phase in Jabal Sayid. It is present in the oxidized granite and the pegmatite sheets and in minor amounts in the aegirine granite near the oxidized granite. Pyrochlore occurs as disseminated translucent-yellow euhedral bipyramid crystals that are 10 to 50 μm across (Fig. 4.7 A). It displays oscillatory zoning, which is visible in polarized light under and in the BSEI (Fig. 4.7 B). In the oxidized granite, pyrochlore is commonly replaced by a Y-rich variety of pyrochlore and aeschynite (Fig. 4.7 C).

4.5 Lithogeochemistry

Representative whole-rock analyses of the fresh aegirine granite and the mineralized oxidized granite are given in Table 4.3. Because the current work focused on the northern part of the complex that contains the alkaline granite and the mineralization, data from Moghazi et al. (2015) were used for comparison and to cover a larger area of Jabal Sayid alkaline granite.

The major oxide composition of the aegirine granite is characterized by high SiO_2 (74.8 to 76.28 wt. %) and Fe_2O_3 (2.95 to 3.94 wt. %), and has moderate concentration of Na_2O (3.74 to 4.86 wt. %), K_2O (3.71 to 3.97 wt. %), and Al_2O_3 (10.25 to 10.25 wt. %), and low CaO (0.31 to 0.77 wt. %), TiO_2 (0.06 to 0.08 wt. %), MgO (0.20 to 0.24 wt. %), and MnO (0.02 to 0.09 wt. %). The aegirine granite contents of Na_2O and to a lesser extent K_2O decrease with increasing SiO_2 , whereas Al_2O_3 displays no correlation with SiO_2 (Table 4.3). In Figure 4.8 (A), chondrite-normalized REE (Boynnton, 1984) of the aegirine granite shows a negative slope with a negative Eu anomaly and an average chondrite normalized La/Yb (La_N/Yb_N) ratio of 5.9. The aegirine granite has average trace element contents of 768 ppm Zr, 16 ppm Hf, 82 ppm Nb, 7.4 ppm Ta, 78 ppm Pb, 28 ppm Th, 17 ppm U, 136 ppm Y, and 646 total REE (ΣREE). In order to characterize Jabal Sayid tectonic environment, Yb was plotted with Ta (in ppm) using the Pearce et al., (1984) tectonic discrimination diagram (Fig. 4.8 B). All of Jabal Sayid aegirine granite samples plot in the within-plate tectonic field. In Figure 4.8 C, the ratio of Ga/Al was plotted with Nb ppm using the diagram of Whalen et al. (1987). All samples plot in the A-type granite field. Figure 4.8 (D and E) shows plots of geochemically coherent elements Nb with Ta in (D) and Zr with Hf in (E). These elemental pairs are not expected to be fractionated during magmatic processes (Irber, 1999). In Figure 4.8 (D), aegirine granite samples from this work and samples from the alkali feldspar granite from Moghazi et al. (2015) form a trend with slope ≈ 12 , whereas Zr with Hf (Fig. 4.8 E) form a trend with a slope ≈ 34 . Furthermore, the ratio of Zr/Hf is compared to the ratio of Y/Ho in Figure 4.8 (F). Most of the aegirine granite samples were plot in CHARGE-and-RADIUS-Controlled (CHARAC) field, which represent formation under magmatic condition according to Bau (1996).

The oxidized granite generally has a variable major oxide composition, and is characterized by high concentrations of Fe_2O_3 (5.25 to 15.45 wt. %) and CaO (0.36 to 1.3 wt. %). Moreover, the oxidized granite displays relatively low concentrations of Al_2O_3 (3.75 to 7.58 wt. %), Na_2O (0.11 to 2.04 wt. %), and a slight decrease in SiO_2 (69.56 to 74.56 wt. %) and K_2O (2.50 to 3.56 wt. %) relative to the aegirine granite.

The oxidized granite shows a remarkable increase in the contents of trace elements relative to the aegirine granite. The chondrite-normalized REE diagram (Fig. 4.8 A) shows that the oxidized granite and the pegmatite samples have a flat to slightly HREE enriched pattern with a La_N/Yb_N of 4.3 and negative Eu anomaly ($\text{Eu}/\text{Eu}^* = 0.1$). The average trace element concentrations in the oxidized granite are 9524 ppm Zr, 163 ppm, 1397 ppm Nb, 135 ppm Ta, 761 ppm Pb, 633 ppm U, 12353 ppm Y, and 14337 ppm ΣREE . In Figure 4.8 (F), The oxidized granite samples and samples from the pegmatite sheets plot outside the CHARAC field.

4.6 Mineral chemistry

4.6.1 Aegirine

The compositions of acicular and prismatic aegirine were obtained using EMPA, and the average compositions are summarized in Table 4.4. The aegirine mineral formula was calculated based on the general formula $\text{M}_2\text{M}_1\text{T}_2\text{O}_6$ where $\text{M}_2 = \text{Na}, \text{Ca}, \text{Li}, \text{Mn}^{2+}, \text{Fe}^{2+}, \text{Mg}^{2+}$; $\text{M}_1 = \text{Al}, \text{Ti}^{4+}, \text{Fe}^{3+}, \text{Ti}^{3+}, \text{Zr}^{4+}, \text{Zn}^{2+}, \text{Mg}^{2+}, \text{Fe}^{2+}, \text{Mn}^{2+}$; $\text{T} = \text{Si}, \text{Al}, \text{Fe}^{3+}$ (Morimoto, 1988) and the mineral formula was calculated by normalizing cations to 4 and then adjusting the $\text{Fe}^{3+}/\text{Fe}^{2+}$ ratio to achieve a 6 oxygen total. Generally, the analytical totals range from 95.3 to 98.4 wt%. This is probably due to the presence of other elements that are not detected by the electron microprobe, such as Li or elements with an atomic number smaller than 5. The analyses that have low M1 site totals commonly show high Zr concentration, which may suggest that other elements could be present in the aegirine structure, such as Hf and REE. The M2 site filling ranges between 0.89 and 1.0, which also suggests the presence of elements that were not analyzed in this site. However, no additional elements were indicated by WDS scans across the wavelength range of TAP and PATH crystals, that were performed on several aegirine crystals.

Both prismatic and acicular aegirine have low Al_2O_3 concentrations (Fig. 4.9 A) and MgO and MnO concentrations that are near or below the detection limit. In comparison between the two types of aegirine, prismatic aegirine is characterized by high CaO and low ZrO_2 and TiO_2 , whereas acicular aegirine is characterized by high TiO_2 and ZrO_2 , and low CaO and Fe_2O_3 (Fig. 4.9 A).

Silicon shows a negative correlation with Fe and Ca in a cation per formula unit diagram (Fig 4.9 B and C). In Figure 4.9 B, acicular and prismatic aegirine form two separate trends. An a.p.f.u. plot of $\text{Zr} + \text{Ti}$ versus Fe shows that the two aegirine types form two clusters with one having a high $\text{Zr} + \text{Ti}$ and a low Fe represented by acicular aegirine, and the other represented by prismatic aegirine with a low $\text{Zr} + \text{Ti}$ concentrations (Figure 4.9 D).

4.6.2 Zircon

The average major (by EMPA) and trace element (by EMPA and LA-ICP-MS) compositions of Zircon-1 from the aegirine granite, Zircon-2 from the oxidized granite, and Zircon-3 from the pegmatite sheets are given in Table 4.5. The stoichiometry of zircon was calculated based on the empirical zircon formula $\text{M}_1\text{T}_1\text{O}_4$ (Speer, 1982), where $\text{M} = \text{Zr}, \text{Hf}, \text{REE}, \text{Y}, \text{Fe}^{3+}, \text{Th}, \text{U}, \text{and Pb}$; and $\text{T} = \text{Si}, \text{Ti}, \text{Nb}, \text{Ta}, \text{and P}$. This was done by normalizing cations to M site total of 1. This calculation method was followed due to the possible substitution of $(\text{SiO}_4)^{4-}$ by 4OH^- (Fron del, 1953; Nasdala et al., 2009). Hafnium can enter zircon the structure by a simple substitution where 1 atom of Hf substitutes for 1 atom of Zr^{4+} (Hoskin, 2003), which stoichiometrically can be represented by $(\text{Zr}_{1-x} \text{Hf}_x) \text{SiO}_4$. A coupled substitution is common in zircon, where REE^{3+} and P^{5+} substitute for Zr^{4+} and Si^{4+} , which stoichiometrically can be represented by $(\text{Zr}_{1-x} \text{REE}_x)(\text{Si}_{1-y} \text{P}_y)\text{O}_4$ (Hoskin, 2003; Speer, 1982). A common feature in all zircon types is the low analytical totals (Table 4.5 and Fig. 4.10 A). Many authors have encountered this problem from altered, porous, and metamict zircon (Fron del, 1953; Geisler et al., 2003; Mathieu et al., 2001; Nasdala et al., 2009; Smith et al., 1991; Speer, 1982), which was attributed to the presence of high concentrations of $\text{OH}/\text{H}_2\text{O}$ and sub-nanometer voids. The total cations in the T sites in Zircon-1, Zircon-2 and Zircon-3 are 0.94, 0.88, and 0.74, respectively.

All zircon types in Jabal Sayid show distinct chemical compositions in both major and trace elements (Fig. 4.10 and Fig. 4.11). The plot of Si with Zr atom per formula unit (a.p.f.u) shows a clustering of Zircon-1, whereas Zircon-2 and Zircon-3 show a positive correlation (Fig. 4.10 B). The plot of Zr/Hf ratio with Hf wt. % shows a smooth curve where Zircon-1 has the lowest ratio with an average of 61, whereas Zircon-2 and 3 have a higher ratio average of 86 and 82, respectively (Fig. 4.10 C). The deficiency in the T site ($T_{\text{def}} = 1 - \Sigma \text{ cations in T}$) shows a strong correlation with Si a.p.f.u (Fig. 4.10 D). If the deficiency is assumed to be due to the presence of OH or H₂O, then Figure 4.10 (E)

shows the possible major substitution mechanism as $M^{n+} + (OH)_n^- + (4-n) H^+ = Si^{4+} + Zr^{4+}$; where M = REE, Y, Fe, Al, and Ca (Caruba et al., 1985). In a chondrite-normalized REE diagram (Fig. 4.11 A), all zircon types show a positive REE pattern with flat Ce anomaly and negative Eu anomaly. Zircon-3 shows a low LREE concentration and a HREE concentration closer to that of Zircon-1 and 2, which results in an average La_n/Yb_n of 8×10^{-5} . Zircon-1 and Zircon-2 have higher concentrations of LREE relative to Zircon-3; however, Zircon-2 shows a HREE concentration similar to Zircon-3 and is more REE fractionated relative to Zircon-1 with average La/Yb ratios of 6×10^{-3} and 1×10^{-2} for Zircon-2 and Zircon-1, respectively.

Hoskin (2005) proposed diagrams to discriminate magmatic and hydrothermal zircon. The fields from these diagrams together with the results from this study are plotted in Figure 4.11 B and C. In Figure 4.11 B, chondrite-normalized Sm/La ratios (chondrite values from McDonough and Sun, 1995) were plotted against La concentration. Zircon-1 and Zircon-2 plot near the hydrothermal field, whereas Zircon-3 plotted between the magmatic and hydrothermal field due to low La and higher Sm concentrations. In Figure 4.11 C, all zircon from this study plot outside the discrimination boxes due to the low Ce anomaly. Although Figure 4.11 B and C show that Zircon-3 is closer to the magmatic field of Hoskin (2005) than the other types, this origin can be rejected based on textural constraints, where Zircon-3 forms small veinlets associated with hematite and synchysite alteration. The relatively low LREE abundance is due to a very low LREE/HREE ratio in the environment from which Zircon-3 has crystallized from, or a co-crystallization of Zircon-3 with LREE-rich phases, such as monazite and pyrochlore. Monazite does occur

with Zircon-3, however, in low abundance. Pyrochlore is common in the core of the pegmatite sheets and associated with Zircon-3 and the pyrochlore associated with Zircon-3 contains high concentrations LREE (discussed below).

4.6.3 Pyrochlore

The average microprobe analyses of fresh and altered pyrochlore are summarized in Table 4.6. The mineral formulae were calculated by normalizing cation total in the A site to total cations in the B site ($\sum \text{Nb, Ta, Ti, and Si}$) according to the empirical formula of pyrochlore group minerals $\text{A}_{2-m}\text{B}_2\text{X}_{6-w}\text{Y}_{1-n} \cdot p\text{H}_2\text{O}$, where A = Na, Ca, Fe^{2+} , REE, Pb, Y, U, and Th; B = Nb, Ta, Ti, Al, Fe^{3+} , and Sn; X = O and OH; and Y = O, OH, and F, with $m = 0 - 1.7$, $w = 0 - 0.7$, and $n = 0 - 1$ are vacancies in A, X, and Y, respectively, and $p = 0 - 2$ H₂O molecules in defect pyrochlore (Lumpkin and Ewing, 1996). Pyrochlore from the core zone of the pegmatite dyke is fresh, whereas those from the oxidized granite are highly altered to Y-rich pyrochlore (yttropyrochlore) and aeschynite. The fresh pyrochlore is Pb-rich, plumbopyrochlore, which has average concentrations of 44.35 ± 4.4 wt.% Nb₂O₅, 3.72 ± 0.60 wt. % Ta₂O₅, 26.38 ± 7.2 wt. % PbO, 0.6 ± 0.4 Na₂O, 2.40 ± 0.1 wt. % TiO₂, 3.3 ± 0.5 wt. % CaO, and 10.5 ± 2.0 wt. % total REE, where Ce, La, and Nd form 88 % of the total LREE content. The total LREE, Na, and vacancy (Vac.= 1- the total of A-site cations) display a negative correlation with the total of Ca, Pb, Fe, and the total HREE (Fig. 4.12 A). Similarly, Nb +Ta forms a strong negative correlation with Si + Ti (Fig. 4.12 B). This suggests a coupled substitution in the A and B site according to $(\text{Ca, Pb, Fe, HREE}) + (\text{Si+Ti}) = (\text{LREE+Na}) + (\text{Nb+Ti}) + \text{Vac}$ (Fig. 4.12 C). In a chondrite normalized REE pattern of fresh pyrochlore (chondrite values from McDonough and Sun, 1995), the REE pattern has a slightly negative slope, with a negative Eu anomaly (Fig. 4.12 D).

4.6.4 REE minerals

The average compositions of synchysite and bastnasite, and xenotime and monazite are summarized in Tables 4.7 and 4.8, respectively. The mineral formula of synchysite was calculated by normalizing Y + REE to Ca content (1 a.p.f.u.), and the bastnasite mineral

formula was calculated by normalizing the total cations to 1 a.p.f.u. Xenotime and monazite mineral formulas were calculated based on 4 oxygens.

Calcium and yttrium are the main constituents of synchysite with average concentrations of 18.9 ± 1.90 wt. % and 28.29 ± 5.24 wt.%, respectively. The synchysite contains 14.52 ± 1.34 wt.% REE comprising mostly Dy, Er, Gd, and Ce. The rest of the REE are present in concentrations ranging from near detection limit to < 1 %. The REE pattern of synchysite in a chondrite-normalized diagram (Fig. 4.13 A) displays an overall positive slope with a concave HREE pattern due to the low Yb and Lu contents.

Bastnasite is Ce-rich with an average of 31.1 ± 3.4 wt% and has variable concentrations of La and Nd (14.6 ± 6.7 and 14.2 ± 5.2 wt%, respectively). In a chondrite-normalized REE diagram, bastnasite displays a negative slope with a slight positive Gd anomaly and HREE that are near or below the detection limits (Fig. 4.13 B).

Xenotime contains an average concentration of 43.43 ± 2.5 wt. % Y_2O_3 , 27.33 ± 0.3 wt. % P_2O_5 , 2.6 ± 2.0 wt. % ThO_2 , 17.28 ± 0.5 wt. % $\Sigma HREE$, and 3.0 ± 2.6 wt. % SiO_2 . In a chondrite-normalized REE diagram (Fig. 4.13 C), xenotime displays a positive slope with most of the LREE at or below the detection limit.

Monazite belongs to the Ce variety and contains an average of 35.95 ± 0.7 wt. % Ce_2O_3 , 22.01 ± 3.2 wt. % La_2O_3 , 8.26 ± 1.3 wt. % Nd_2O_3 , 2.74 ± 0.3 wt. % Pr_2O_3 , and 28.04 ± 0.7 wt. % P_2O_5 . On a chondrite-normalized REE diagram (Fig. 4.13 D), monazite has a negative REE pattern and is depleted in HREE and Y, with concentrations of these elements being below the detection limit.

4.7 Discussion

4.7.1 Magmatic evolution

Jabal Sayid shows a typical A-type alkaline granite composition with alkalinity index (A.I. = molar ratio of Na+K/Al) ranging from 1.0 to 1.11 values with sodic amphibole and aegirine as the only mafic minerals. Moreover, Jabal Sayid displays a characteristic within-plate A-type granite composition (Fig. 4. 8 B and C).

The aegirine granite in Jabal Sayid was interpreted to be genetically related to the Sayid complex, and it is considered the most magmatically evolved granitic unit of the complex (Harris et al., 1986; Moghazi et al., 2015). The progressively more negative Eu anomaly suggests that the granite evolution involved fractionation of feldspar (Fig. 4.8 A).

However, Harris et al. (1986) argued that the negative Eu anomaly in the alkaline granite could not be produced by only feldspar fractionation given the low Ca content in the syenogranite (monzogranite in Harris et al., (1986)). Moghazi et al. (2015) suggested that the fractionation of alkali feldspar contributed to the negative Eu anomaly but suggested fluid interaction must have played a role, in order to explain the variations in the REE and HFSE contents. Harris et al. (1986) argued that fractionation of alkali feldspar would move the composition toward CaO apex in $\text{Al}_2\text{O}_3\text{-CaO-(K}_2\text{O+Na}_2\text{O)}$, and instead they proposed that volatiles may have contributed to the negative Eu anomaly in the alkaline granite.

The absence of primary accessory minerals, such as zircon and pyrochlore, in the aegirine granite near the mineralization is atypical. Magmatic zircon has been reported previously from this unit and was used to estimate the age of the alkaline rock in Jabal Sayid (sample SAY-5; Moghazi et al., 2015); however, it was sampled from an alkaline granite near the center of the complex, south of the mineralized units. In the current work, the samples were collected from the northern part of the complex and near the mineralized units, where aegirine is the main mafic mineral (arfvedsonite and riebeckite are relics; Fig 4.4 D). Alkali feldspar granite (aegirine granite in this work) are interpreted to be more evolved because they are from the apical zone of the complex (Hackett, 1986). Therefore, the absence of zircon and other rare-metal minerals could be attributed to the increase in the solubility in the granitic melt due to the increase in volatiles, such as F. According to experimental work, the solubilities of HFSE minerals are positively affected by melt alkalinity and the melt content of F. As alkaline silicate melt evolved by fractional crystallization, the ratio of network-formers, such as SiO_4 and AlO_4 , and network modifiers, such as Na, K, Ca, Mn, Fe^{2+} , and Li, changes in favor to the latter (Linnen, 1998; Linnen and Keppler, 1997). This would lead to an increase in solubilities of zircon that are needed to stabilize alkali-zirconosilicate species in the melt. Moreover, the presence of flux components, F in particular, will have the same effect as network

modifiers by depolymerizing the silicate melt and increases NBO (Aseri et al., 2014; Bartels et al., 2010; Fiege et al., 2011; Keppler, 1996; Linnen, 1998; Linnen and Keppler, 2002, 1997), and melt viscosity (Giordano et al., 2004)

The chemical composition of aegirine shows an elevated concentration of Zr. For example, prismatic aegirine contains up to 0.26 wt.% ZrO₂, whereas acicular aegirine contains up to 1.1 wt.% ZrO₂. This agrees with previous observations of up to a weight percent concentration of Zr in aegirine from other deposits (Dyulgerov and Platevoet, 2006; Kogarko, 2016; Njonfang and Nono, 2003). This also may suggest that the melt was enriched in Zr in addition to other HFSE, such as Hf, because Hf in alkaline melts has a higher aegirine/melt partitioning coefficient relative to Zr (Kogarko, 2015). Furthermore, this also suggests that the low ratio Zr/Hf in the aegirine granite (34) is due to a magmatic process rather than interaction with an aqueous fluid.

4.7.2 Mineralization and Hydrothermal alteration

The main mineralization in Jabal Sayid is hosted by the pegmatite sheets and the oxidized granite. Furthermore, the mineralization is marked by intense hematization and the crystallization of abundant zircon, bastnasite, synchysite, and pyrochlore, in addition to variable amounts of monazite, xenotime, and thorite. Based on the paragenetic sequence of ore minerals, the mineralization can be classified into two stages: late-magmatic to early hydrothermal and hydrothermal.

4.7.2.1 Late magmatic to early hydrothermal stage (transitional stage)

Mineralization in Jabal Sayid is limited to the pegmatite sheets and the oxidized granite. The intensive hematization that is associated with the mineralization has obscured the primary mineralogy. This is a common phenomenon that was observed in similar rare-metal alkaline granites around the world (Gysi and Williams-Jones, 2013; Kovalenko, 1995; Miller, 1996; Salvi and Williams-Jones, 1990). This led many authors to speculate about the original mineralogy from the shape and mineral assemblage in the pseudomorphs. For example, in Strange Lake, Canada, primary HFSE minerals (elpidite) are completely altered and was identified by the shape of the pseudomorph (Gysi and Williams-Jones, 2013; Salvi and Williams-Jones, 1990). Similarly, quartz-gittinsite

pseudomorphs are interpreted to have replaced elpidite in Khaldzan-Buregtey, Western Mongolia (Kovalenko, 1995). In Jabal Sayid, the earliest crystallization of rare-metal minerals is exceptionally well preserved in the border zone of the pegmatite and the partially altered aegirine granite near the mineralized units. This demonstrates that the crystallization of Zircon-1 is through the alteration of prismatic aegirine to zircon, quartz, and hematite (Fig. 4.4 E and F Fig. 4.4 M and N). The crystallization of Zircon-1 is also associated with acicular aegirine that shows no sign of alteration (Fig. 4.4 E, M, and N). This suggests that both acicular aegirine and Zircon-1 are formed by hydrothermal processes. However, in the border zone of the pegmatite sheets, acicular aegirine occurs in an intergranular texture, with albite and microcline, as well as inclusions in snowball quartz (Fig. 4.4 M to P). The origin of the snowball texture has been attributed to either magmatic (Costi et al., 2009; Kovalenko, 1995; Poutiainen and Scherbakova, 1998), or metasomatic processes (Kempe, 1999). Muller and Seltmann (1999) concluded that this texture is an indication of a fluid-saturated melt enriched in F and Li. Miller (1996) and Siegel et al., (2017) reported snowball quartz in the Strange Lake peralkaline granitic pegmatite, Canada, which was interpreted as a late-stage growth from an interstitial residual melt. Given that the pegmatite represents a late-magmatic stage and the border zone displays a typical magmatic texture (Fig. 4.4 P), whereas in the aegirine granite it is associated with the secondary minerals, such as zircon and hematite, it is more likely that acicular aegirine was formed from a transitional stage in a fluid-saturated melt environment.

Another way to assess the origin of the acicular aegirine and Zircon-1 is by using the morphology and chemistry of zircon (Corfu et al., 2003; Erdmann et al., 2013; Fu et al., 2009; Hoskin and Schaltegger, 2003; Pupin, 1980; Schaltegger, 2007). Magmatic zircon commonly display a prismatic shape and display narrow-spaced oscillatory zoning (Erdmann et al., 2013; Hoskin and Schaltegger, 2003; Pupin, 1980). Zircon-1 occurs as subhedral to anhedral equant bipyramid crystals (Fig. 4.5 A to C). Most crystals lack oscillatory zoning, but where present, it is widely spaced (Fig. 4.5 A and B). These characteristics are commonly attributed to hydrothermal zircon or zircon formed by a fluid-rich melt (Corfu et al., 2003; Erdmann et al., 2013; Hoskin and Schaltegger, 2003; Schaltegger, 2007). Chemistry can also be used to interpret the magmatic or

hydrothermal origin of zircon. For example, magmatic zircon is characterized by a low abundance of LREE and non-formula elements, whereas hydrothermal zircon has high concentrations of non-formula elements, such as Li, Fe, Ca, Nb, and Ta (Fu et al., 2009; Hoskin, 2005; Pettke et al., 2005; Wu et al., 2018). Zircon-1 associated with acicular aegirine is characterized by high concentrations of Li, Nb, and Ta. Furthermore, in the zircon discrimination diagram proposed by Hoskin (2005), Zircon-1 plotted near the hydrothermal field (Fig. 4.11 B and C). This suggests that Zircon-1 is formed by a hydrothermal process.

The acicular aegirine and Zircon-1 show characteristics of late-magmatic (acicular aegirine) and hydrothermal crystallization (Zircon-1). Therefore, the crystallization of acicular aegirine and Zircon-1 potentially records the transitional stage between magmatic and hydrothermal environments.

4.7.2.2 Hydrothermal stage

The hematization of acicular aegirine and the crystallization of HFSE and REE minerals took place during the hydrothermal stage. During this stage, zircon continued to crystallize as a replacement after acicular aegirine or as aggregates of zircon associated with hematite and bastnasite (Fig. 4.5 D E). In the oxidized granite, Zircon-2 is secondary and has a chemical composition that is characterized by high concentrations of REE and Y. In the zircon discrimination diagram proposed by Hoskin (2005), Zircon-2 plots near the hydrothermal field (Fig. 4.11 B and C). Moreover, Zircon-2 occurs as a replacement mineral associated with hematite in the oxidized granite (Fig. 4.5 D and E).

In the border zone of the pegmatite sheets and the oxidized granite, hematite, zircon-1 and bastnasite are precipitated along the grain boundaries (Fig. 4.4 N and P). Monazite and bastnasite are the earliest REE phases to have crystallized, which were then replaced by synchysite and xenotime (Fig. 4.6 C to H). Pyrochlore may have crystallized with monazite and bastnasite; however, it was altered to Y-rich pyrochlore \pm aeschynite (4.7 C). The last mineralization stage is marked by crystallization of Y-rich minerals, such as xenotime, synchysite, and Y-pyrochlore \pm aeschynite. This is demonstrated by the alteration of monazite, bastnasite and pyrochlore.

In the pegmatite sheets, Zircon-3 commonly occurs in the pseudomorphs that formed as aggregates of zircon in veinlets with synchysite (Fig. 4.5 F and Fig. 4.6 A and B). Its chemical composition is different from Zircon-1 and 2 and characterized by high concentrations of HREE + Y and low LREE (Fig. 4.11 A). In Hoskin (2005) zircon discrimination diagrams (Fig. 13 B and C), Zircon-3 plots near the magmatic field and away from Zircon-1 and 2 when La concentration is compared to the chondrite-normalized Sm/La ratio (chondrite values from McDonough and Sun, 1995) (Fig. 13 B). In Figure 4.13 (C), all zircon types plot outside the discrimination field due to the low Ce anomaly values of these zircon. Although Zircon-3 in Figure 4.11 (B) plots near the magmatic discrimination field, which may suggest magmatic origin, the morphology and texture of Zircon-3 indicates hydrothermal origin. The low LREE content in Zircon-3 could be inherited from the melt or be due to co-crystallization with a LREE-rich phase. Co-existing phases with Zircon-3 that could possibly fractionate REE are pyrochlore, synchysite, and monazite. Pyrochlore contains up to 9 wt.% LREE (Table 4.6), and synchysite contains up to 3.11 wt.% LREE (Table 4.7). Monazite contains an average of 70.15 wt.% LREE (Table 4.8), but it occurs in low abundances. However, the same minerals co-exist with Zircon-1 and Zircon-2 in the oxidized granite and the border of the pegmatite, yet Zircon-1 and 2 do not show low LREE contents (Fig. 4.13 A). Therefore, it is more likely that the low LREE content in Zircon-3 is due to crystallization from an environment that had low LREE concentration. The possible mechanism that fractionated REE is by an early deposition of LREE minerals at the border zone of the pegmatite, which would deplete the residual melt (the core of the pegmatite) in LREE. This is supported by the mineralogy of the border zone, where it shows abundant bastnasite and monazite relative to the core. Similar REE behavior was reported from Nechalacho Layered Suite, Canada, where the fractionation REE was attributed to the early crystallization of LREE-rich pyrochlore, fluorbritholite-(Ce), and REE-fluorocarbonate (Möller and Williams-Jones, 2016).

4.8 Conclusion

Jabal Sayid is characterized by mineralogy and chemistry that is typical of A-type alkaline granite that formed in a within-plate tectonic environment. The whole-rock

chondrite-normalized REE pattern shows a progressive increase in Eu anomaly, which is interpreted to reflect extreme feldspar fractionation. The absence of HFSE and REE in the aegirine granite near the mineralization was probably due to increased solubility of HFSE and REE minerals due to the increase in volatiles and fluxes at the late magmatic stage. Based on textural observation and the morphology of ore minerals, the mineralization took place in two stages. The first stage is demonstrated by the alteration of prismatic aegirine and the crystallization of Zircon-1, hematite, and quartz with fresh acicular aegirine. This stage shows magmatic (acicular aegirine forming snowball texture in intergranular albite and microcline matrix) and hydrothermal (Zircon-1 chemistry and morphology) characteristics. The hydrothermal stage is demonstrated by the hematization of acicular aegirine and the crystallization of Zircon-2 (in the oxidized granite), Zircon-3 (in the pegmatite core), REE-fluorocarbonate (bastnasite and synchysite), monazite, and xenotime. The early crystallization of bastnasite and monazite led to the concentration of HREE in the residual melt, which led to the late alteration of monazite and bastnasite by synchysite and xenotime.

4.9 References

- Agar, R.A., 1992. The tectono-metallogenic evolution of the Arabian Shield. *Precambrian Res.* 58, 169–194. [https://doi.org/10.1016/0301-9268\(92\)90118-8](https://doi.org/10.1016/0301-9268(92)90118-8)
- Aseri, A.A., Linnen, R.L., Che, X.D., Thibault, Y., Holtz, F., 2014. Effects of fluorine on the solubilities of Nb, Ta, Zr and Hf minerals in highly fluxed water-saturated haplogranitic melts. *Ore Geol. Rev.*
- Bartels, a., Holtz, F., Linnen, R.L., 2010. Solubility of manganotantalite and manganocolumbite in pegmatitic melts. *Am. Mineral.* 95, 537–544. <https://doi.org/10.2138/am.2010.3157>
- Boily, M., Williams-Jones, A.E., 1994. The role of magmatic and hydrothermal processes in the chemical evolution of the Strange Lake plutonic complex, Quebec-Labrador. *Contrib. to Mineral. Petrol.* <https://doi.org/10.1007/BF00310609>
- Boynton, W. V., 1984. *Cosmochemistry of the Rare Earth Elements: Meteorite Studies.*

- Dev. Geochemistry 2, 63–114. <https://doi.org/10.1016/B978-0-444-42148-7.50008-3>
- Caruba, R., Baumer, A., Ganteaume, M., Iacconi, P., 1985. An experimental study of hydroxyl groups and water in synthetic and natural zircons: a model of the metamict state. *Am. Mineral.* 70, 1224–1231.
- Corfu, F., Hanchar, J.M., Hoskin, P.W.O., Kinny, P., 2003. Atlas of zircon textures. *Rev. Mineral. Geochemistry* 53, 469–500. <https://doi.org/10.2113/0530469>
- Costi, H.T., Dall’Agnol, R., Pichavant, M., Rämö, O.T., 2009. The peralkaline tin-mineralized madeira cryolite albite-rich granite of pitinga, amazonian craton, brazil: Petrography, mineralogy and crystallization processes. *Can. Mineral.* 47, 1301–1327. <https://doi.org/10.3749/canmin.47.6.1301>
- Drysdall, a. R., Jackson, N.J., Ramsay, C.R., Douch, C.J., Hackett, D., 1984. Rare element mineralization related in Precambrian alkali granites in the Arabian shield. *Econ. Geol.* 79, 1366–1377. <https://doi.org/10.2113/gsecongeo.79.6.1366>
- Dyulgerov, M.M., Platevoet, B., 2006. Unusual Ti and Zr aegirine-augite and potassic magnesio-arfvedsonite in the peralkaline potassic oversaturated Buhovo-Seslavtzi complex , Bulgaria 127–138. <https://doi.org/10.1127/0935-1221/2006/0018-0127>
- Erdmann, S., Wodicka, N., Jackson, S.E., Corrigan, D., 2013. Zircon textures and composition: refractory recorders of magmatic volatile evolution? *Contrib. to Mineral. Petrol.* 165, 45–71. <https://doi.org/10.1007/s00410-012-0791-z>
- Feng, Y., Samson, I.M., 2015. Replacement processes involving high field strength elements in the T Zone, Thor Lake rare-metal deposit. *Can. Mineral.* 53, 31–60. <https://doi.org/10.3749/canmin.1400028>
- Fiege, A., Kirchner, C., Holtz, F., Linnen, R.L., Dziony, W., 2011. Lithos Influence of fluorine on the solubility of manganotantalite (MnTa_2O_6) and manganocolumbite (MnNb_2O_6) in granitic melts — An experimental study. *Lithos* 122, 165–174. <https://doi.org/10.1016/j.lithos.2010.12.012>

- Fron del, C., 1953. Hydroxyl substitution in thorite and zircon. *Am. Mineral.* 38, 1007–1018.
- Fu, B., Mernagh, T.P., Kita, N.T., Kemp, A.I.S., Valley, J.W., 2009. Distinguishing magmatic zircon from hydrothermal zircon: A case study from the Gidginbung high-sulphidation Au-Ag-(Cu) deposit, SE Australia. *Chem. Geol.* 259, 131–142. <https://doi.org/10.1016/j.chemgeo.2008.10.035>
- Geisler, T., Rashwan, A.A., Rahn, M.K.W., Poller, U., Zwingmann, H., Pidgeon, R.T., Schleicher, H., Tomaschek, F., 2003. Low-temperature hydrothermal alteration of natural metamict zircons from the Eastern Desert, Egypt. *Mineral. Mag.* <https://doi.org/10.1180/0026461036730112>
- Giordano, D., Romano, C., Dingwell, D.B.B., Poe, B., Behrens, H., 2004. The combined effects of water and fluorine on the viscosity of silicic magmas. *Geochim. Cosmochim. Acta* 68, 5159–5168. <https://doi.org/10.1016/j.gca.2004.08.012>
- Gysi, A.P., Williams-Jones, A.E., 2013. Hydrothermal mobilization of pegmatite-hosted REE and Zr at Strange Lake, Canada: A reaction path model. *Geochim. Cosmochim. Acta* 122, 324–352. <https://doi.org/10.1016/j.gca.2013.08.031>
- Hackett, D., 1986. Mineralized aplite-pegmatite at Jabal Sa'id, Hijaz region, Kingdom of Saudi Arabia. *J. African Earth Sci.* 4, 257–267. [https://doi.org/10.1016/S0899-5362\(86\)80087-2](https://doi.org/10.1016/S0899-5362(86)80087-2)
- Harris, N.B.W., Marzouki, F.M.H., Ali, S., 1986. The Jabel Sayid complex, Arabian Shield: geochemical constraints on the origin of peralkaline and related granites. *J. Geol. Soc. London.* 143, 287–295. <https://doi.org/10.1144/gsjgs.143.2.0287>
- Hoskin, P.W.O., 2005. Trace-element composition of hydrothermal zircon and the alteration of Hadean zircon from the Jack Hills, Australia. *Geochim. Cosmochim. Acta* 69, 637–648. <https://doi.org/10.1016/j.gca.2004.07.006>
- Hoskin, P.W.O., Schaltegger, U., 2003. The composition of zircon and igneous and metamorphic petrogenesis. *Rev. Mineral. Geochemistry* 53, 27–62.

<https://doi.org/10.2113/0530027>

- Irber, W., 1999. The lanthanide tetrad effect and its correlation with K/Rb, Eu/Eu*, Sr/Eu, Y/Ho, and Zr/Hf of evolving peraluminous granite suites. *Geochim. Cosmochim. Acta* 63, 489–508. [https://doi.org/10.1016/S0016-7037\(99\)00027-7](https://doi.org/10.1016/S0016-7037(99)00027-7)
- Johnson, P.R., 2006. Explanatory notes to the map of Proterozoic geology of western Saudi Arabia, Saudi Geological Survey Technical Report SGS-TR-2006-4.
- Johnson, P.R.R., Andresen, A., Collins, A.S.S., Fowler, A.R.R., Fritz, H., Ghebreab, W., Kusky, T., Stern, R.J.J., 2011. Late Cryogenian-Ediacaran history of the Arabian-Nubian Shield: A review of depositional, plutonic, structural, and tectonic events in the closing stages of the northern east African Orogen. *J. African Earth Sci.* 61, 167–232. <https://doi.org/10.1016/j.jafrearsci.2011.07.003>
- Kempe, U., 1999. Magmatic and Metasomatic Processes During Formation of the Nb-Zr-REE Deposits Khaldzan Buregte and Tsakhir (Mongolian Altai): Indications from a Combined CL-SEM Study. *Mineral. Mag.* 63, 165–177. <https://doi.org/10.1180/002646199548402>
- Kepler, H., 1996. Constraints from partitioning experiments on the composition of subduction-zone fluids. *Nature*. <https://doi.org/10.1038/380237a0>
- Kogarko, L.N., 2016. Geochemistry of fractionation of coherent elements (Zr and Hf) during the profound differentiation of peralkaline magmatic systems: A case study of the Lovozero Complex. *Geochemistry Int.* 54, 1–6. <https://doi.org/10.1134/S0016702916010079>
- Kogarko, L.N., 2015. Fractionation of zirconium in pyroxenes of alkaline magmas. *Geochemistry Int.* 53, 1–8. <https://doi.org/10.1134/S0016702915010048>
- Kovalenko, V.I., 1995. The peralkaline granite-related Khaldzan-Buregtey rare metal (Zr, Nb, REE) deposit, western Mongolia. *Econ. Geol.* 90, 530–547. <https://doi.org/10.2113/gsecongeo.90.3.530>

- Küster, D., 2009. Granitoid-hosted Ta mineralization in the Arabian-Nubian Shield: Ore deposit types, tectono-metallogenic setting and petrogenetic framework. *Ore Geol. Rev.* 35, 68–86. <https://doi.org/10.1016/j.oregeorev.2008.09.008>
- Linnen, R.L., 1998. The solubility of Nb-Ta-Zr-Hf-W in granitic melts with Li and Li + F: Constraints for mineralization in rare metal granites and pegmatites. *Econ. Geol.* 93, 1013–1025. <https://doi.org/10.2113/gsecongeo.93.7.1013>
- Linnen, R.L., Keppler, H., 2002. Melt composition control of Zr/Hf fractionation in magmatic processes. *Geochim. Cosmochim. Acta* 66, 3293–3301. [https://doi.org/10.1016/S0016-7037\(02\)00924-9](https://doi.org/10.1016/S0016-7037(02)00924-9)
- Linnen, R.L., Keppler, H., 1997. Columbite solubility in granitic melts: consequences for the enrichment and fractionation of Nb and Ta in the Earth's crust. *Contrib. to Mineral. Petrol.* 128, 213–227. <https://doi.org/10.1007/s004100050304>
- Linnen, R.L., Samson, I.M., Williams-Jones, A.E., Chakhmouradian, A.R., 2014. Geochemistry of the rare-earth element, Nb, Ta, Hf, and Zr deposits, in: *Treatise on Geochemistry*. Elsevier, pp. 543–568. <https://doi.org/10.1016/B978-0-08-095975-7.01124-4>
- Lumpkin, G.R., Ewing, R.C., 1996. Geochemical alteration of pyrochlore group minerals: Betafite subgroup. *Am. Mineral.* 81, 1237–1248.
- Mathieu, R., Zetterström, L., Cuney, M., Gauthier-Lafaye, F., Hidaka, H., 2001. Alteration of monazite and zircon and lead migration as geochemical tracers of fluid paleocirculations around the Oklo-Okélobondo and Bangombé natural nuclear reaction zones (Franceville basin, Gabon). *Chem. Geol.* 171, 147–171. [https://doi.org/10.1016/S0009-2541\(00\)00245-X](https://doi.org/10.1016/S0009-2541(00)00245-X)
- McDonough, W.F., Sun, S. -s., 1995. The composition of the Earth. *Chem. Geol.* 120, 223–253. [https://doi.org/https://doi.org/10.1016/0009-2541\(94\)00140-4](https://doi.org/https://doi.org/10.1016/0009-2541(94)00140-4)
- Miller, R.R., 1996. Structural and textural evolution of the strange Lake Peralkaline rare-element (NYF) granitic pegmatite, Quebec-Labrador. *Can. Mineral.* 34, 349–371.

- Moghazi, A.-K.M., Iaccheri, L.M., Bakhsh, R.A., Kotov, A.B., Ali, K.A., 2015. Sources of rare-metal-bearing A-type granites from Jabel Sayed complex, Northern Arabian Shield, Saudi Arabia. *J. Asian Earth Sci.* 107, 244–258.
<https://doi.org/10.1016/j.jseaes.2015.04.042>
- Moghazi, A.M., Ali, K.A., Wilde, S.A., Zhou, Q., Andersen, T., Andresen, A., El-enen, M.M.A., Stern, R.J., 2012. Lithos Geochemistry , geochronology , and Sr – Nd isotopes of the Late Neoproterozoic Wadi Kid volcano-sedimentary rocks , Southern Sinai , Egypt : Implications for tectonic setting and crustal evolution. *LITHOS* 154, 147–165. <https://doi.org/10.1016/j.lithos.2012.07.003>
- Möller, V., Williams-Jones, A.E., 2017. Magmatic and hydrothermal controls on the mineralogy of the Basal Zone, Nechalacho REE-Nb-Zr Deposit, Canada☀. *Econ. Geol.* 112, 1823–1856. <https://doi.org/10.5382/econgeo.2017.4531>
- Möller, V., Williams-Jones, A.E., 2016. PPetrogenesis of the Nechalacho Layered Suite, Canada: Magmatic evolution of a REE–Nb-rich nepheline syenite intrusion. *J. Petrol.* 57, 229–276. <https://doi.org/10.1093/petrology/egw003>
- Morimoto, N., 1988. Nomenclature of Pyroxenes. *Mineral. Petrol.* 39, 55–76.
<https://doi.org/10.1007/BF01226262>
- Mysen, B.O., Ryerson, F.J., Virgo, D., 1981. The structural role of phosphorus in silicate melts. *Am. Mineral.* 66, 106–117. [https://doi.org/0003-w4x/8|/0102-0106\\$02.00](https://doi.org/0003-w4x/8|/0102-0106$02.00)
- Nasdala, L., Kronz, A., Wirth, R., Váczi, T., Pérez-Soba, C., Willner, A., Kennedy, A.K., Váczi, T., Pérez-Soba, C., Willner, A., Kennedy, A.K., Váczi, T., Pérez-Soba, C., Willner, A., Kennedy, A.K., 2009. The phenomenon of deficient electron microprobe totals in radiation-damaged and altered zircon. *Geochim. Cosmochim. Acta* 73, 1637–1650. <https://doi.org/10.1016/j.gca.2008.12.010>
- Nehlig, P., Genna, A., Asfirane, F., 2002. A review of the Pan-African evolution of the Arabian shield. *GeoArabia* 7, 103–124.
- Njonfang, E., Nono, A., 2003. Clinopyroxene from some felsic alkaline rocks of the

- Cameroon Line , central Africa : petrological implications 15, 527–542.
<https://doi.org/10.1127/0935-1221/2003/0015-0527>
- Paton, C., Hellstrom, J., Paul, B., Woodhead, J., Hergt, J., 2011. Iolite: Freeware for the visualisation and processing of mass spectrometric data. *J. Anal. At. Spectrom.* 26, 2508–2518.
- Pearce, J.A., Harris, N.B.W., Tindle, A.G., 1984. Trace element distribution diagrams for the tectonic interpretation of granitic rocks. *J. Petrol.* 25, 956–983.
<https://doi.org/10.1093/petrology/25.4.956>
- Pettke, T., Audéat, A., Schaltegger, U., Heinrich, C. a., 2005. Magmatic-to-hydrothermal crystallization in the W-Sn mineralized Mole Granite (NSW, Australia). Part II: Evolving zircon and thorite trace element chemistry. *Chem. Geol.* 220, 191–213.
<https://doi.org/10.1016/j.chemgeo.2005.02.017>
- Piilonen, P.C., McDonald, A.M., Poirier, G., Rowe, R., Larsen, A.O., 2012. The mineralogy and crystal chemistry of alkaline pegmatites in the Larvik Plutonic Complex, Oslo rift valley, Norway. Part 1. Magmatic and secondary zircon: implications for petrogenesis from trace-element geochemistry. *Mineral. Mag.* 76, 649–672. <https://doi.org/10.1180/minmag.2012.076.3.15>
- Poutiainen, M., Scherbakova, T.F., 1998. Fluid and melt inclusion evidence for the origin of idiomorphic quartz crystals in topaz-bearing granite from the Salmi batholith, Karelia, Russia. *Lithos* 44, 141–151. [https://doi.org/10.1016/S0024-4937\(98\)00052-8](https://doi.org/10.1016/S0024-4937(98)00052-8)
- Pupin, J.P., 1980. Zircon and granite petrology. *Contrib. to Mineral. Petrol.* 73, 207–220.
<https://doi.org/10.1007/BF00381441>
- Radain, A., 1979. Petrogenesis of Some Pearalkaline and Non-peralkaline Post-tectonic Granite in The Arabian Shield. The University of Western Ontario.
- Radain, A.A.M., Fyfe, W.S., Kerrich, R., 1981. Origin of Peralkaline Granites of Saudi Arabia. *Contrib. Miner. Pet.* 358–366. <https://doi.org/10.1007/BF00398932>

- Robinson, F.A., Foden, J.D., Collins, A.S., Payne, J.L., 2014. Arabian Shield magmatic cycles and their relationship with Gondwana assembly: Insights from zircon U–Pb and Hf isotopes. *Earth Planet. Sci. Lett.* 408, 207–225.
<https://doi.org/10.1016/j.epsl.2014.10.010>
- Rule, A.C., Radke, F., 1988. Baileychlorite, the Zn end member of the trioctahedral chlorite series. *Am. Mineral.* 73, 135–139.
- Salvi, S., Fontan, F., Monchoux, P., Williams-Jones, A. E., Moine, B., 2000. Hydrothermal mobilization of high field strength elements in Alkaline Igneous Systems: Evidence from the Tamazeght complex (Morocco). *Econ. Geol.* 95, 559–575. <https://doi.org/10.2113/gsecongeo.95.3.559>
- Salvi, S., Williams-Jones, A.E., 1996. The role of hydrothermal processes in concentrating high-field strength elements in the Strange Lake peralkaline complex, northeastern Canada. *Geochim. Cosmochim. Acta* 60, 1917–1932.
[https://doi.org/10.1016/0016-7037\(96\)00071-3](https://doi.org/10.1016/0016-7037(96)00071-3)
- Salvi, S., Williams-Jones, A.E., 1990. The role of hydrothermal processes in the granite-hosted Zr, Y, REE deposit at Strange Lake, Quebec/Labrador: Evidence from fluid inclusions. *Geochim. Cosmochim. Acta* 54, 2403–2418.
[https://doi.org/10.1016/0016-7037\(90\)90228-D](https://doi.org/10.1016/0016-7037(90)90228-D)
- Schaltegger, U., 2007. Hydrothermal zircon. *Elements* 3, 51–79.
<https://doi.org/10.2113/gselements.3.1.51>
- Siegel, K., Vasyukova, O. V., Williams-Jones, A.E., 2018. Magmatic evolution and controls on rare metal-enrichment of the Strange Lake A-type peralkaline granitic pluton, Québec-Labrador. *Lithos* 308–309, 34–52.
<https://doi.org/10.1016/j.lithos.2018.03.003>
- Siegel, K., Williams-Jones, A.E., van Hinsberg, V.J., 2017. The amphiboles of the REE-rich A-type peralkaline Strange Lake pluton – fingerprints of magma evolution. *Lithos* 288–289, 156–174. <https://doi.org/10.1016/j.lithos.2017.07.012>

- Smith, D.G.W., Jorre, L. de St., Reed, S.J.B., Long, J.V.P., 1991. Zonally metamictized and other zircons from Thor Lake, Northwest Territories. *Can Miner.*
- Sorensen, H., 1992. Agpaitic nepheline syenites : a potential source of rare elements 7, 417–427.
- Speer, A., 1982. Zircon, in: Ribbe, P.H. (Ed.), *Orthosilicate*. Mineralogical Society of America, Blacksburg, pp. 67–112.
- Staatz, M.A., Brownfield, I.K., 1985. *Mineralogy of drill cores from Jabal Sa'id*. Denver.
- Stern, R.J., 1994. Arc assembly and continental collision in the Neoproterozoic East African Orogen: Implication for the Consolidation of Gondwanaland. *Ann. Rev. Earth Planet Sci.* 22, 319–351.
- Stern, R.J., Ali, K.A., Lie, J.P., Johnson, P.R., Kozdroj, W., Kattan, F.H., 2010. Distribution and significance of pre-Neoproterozoic zircons in juvenile Neoproterozoic Igneous rocks of the Arabian-Nubian Shield. *Am. J. Sci.* 310, 791–811. <https://doi.org/10.2475/09.2010.02>
- Stoeser, D.B., 1986. Distribution and tectonic setting of plutonic rocks of the Arabian Shield. *J. African Earth Sci.* 4, 21–46. [https://doi.org/10.1016/S0899-5362\(86\)80066-5](https://doi.org/10.1016/S0899-5362(86)80066-5)
- Turkistany, A.R., Ramsay, C.R., 1982. Mineralized apogranite associated with alkali granite at Jabal Sa'id, Kingdom of Saudi Arabia. *Deputy Ministry Miner. Resour.* 78–88.
- Vasyukova, O., Williams-Jones, A.E., 2014. Fluoride-silicate melt immiscibility and its role in REE ore formation: Evidence from the Strange Lake rare metal deposit, Quebec-Labrador, Canada. *Geochim. Cosmochim. Acta* 139, 110–130. <https://doi.org/10.1016/j.gca.2014.04.031>
- Vasyukova, O. V., Williams-Jones, A.E., Blamey, N.J.F.F., 2016. Fluid evolution in the Strange Lake granitic pluton, Canada: Implications for HFSE mobilisation. *Chem.*

Geol. 444, 83–100. <https://doi.org/10.1016/j.chemgeo.2016.10.009>

Wang, R.C., Chen, X.M., Hu, H., Liu, C.S., Xu, S.J., Fontan, F., de Parseval, P., 2003.

Accessory minerals in the Xihuashan Y-enriched granitic complex, southern China: A record of magmatic and hydrothermal stages of evolution. *Can. Mineral.* 41, 727–748.

Whalen, J.B., Currie, K.L., Chappell, B.W., 1987. A-type granites: geochemical

characteristics, discrimination and petrogenesis. *Contrib. to Mineral. Petrol.* 95, 407–419. <https://doi.org/10.1007/BF00402202>

Wu, M., Tian, B., Zhang, D., Xu, G., Xu, W., Qiu, K., 2018. Zircon of the No. 782

deposit from the Great Xing'an Range in NE China: Implications for Nb-REE-Zr mineralization during magmatic-hydrothermal evolution. *Ore Geol. Rev.* 102, 284–299.

<https://doi.org/10.1016/j.oregeorev.2018.09.006>

Table 4-1 Summary of the main rock units at Jabal Sayid mineralization

Rock units	Description
Aegirine granite	Medium-grained to porphyritic grey to light pink granite. Quartz, plagioclase, microcline-perthite, and aegirine are the main rock-forming minerals. Aegirine is the main mafic mineral followed by arfvedsonite, which occurs as remnants. Secondary minerals include zircon, pyrochlore, hematite, and fluorite. The secondary minerals are associated with altered mafic minerals arfvedsonite and aegirine.
Oxidized granite	Dark red medium-grained consists of quartz, pseudomorphs, microcline, and minor albite. Rare-metal minerals include zircon, bastnasite, pyrochlore group mineral, monazite, and xenotime. Other minerals include fluorite, hematite, sericite, and chlorite (chamosite?). Partially altered acicular aegirine trapped in quartz is common.
Pegmatite sheets	A reddish coarse-grained pegmatite sheets with or without a well-developed quartz and K-feldspar cores. Quartz, microcline, and pseudomorphs are the main rock-forming minerals. Rare-metal minerals include synchysite, bastnasite, pyrochlore, xenotime, zircon, and thorite. Other minerals include hematite and fluorite.

Table 4-2 List of common minerals in Jabal Sayid with abbreviation and formula

Mineral	Symbol	Formula
Quartz	Qtz	SiO ₂
Albite	Ab	NaAlSi ₃ O ₈
Microcline	Mc	KAlSi ₃ O ₈
Aegirine	Aeg	NaFeSi ₂ O ₆
Alkali feldspar	Kfs	(K,Na)AlSi ₃ O ₈
Arfvedsonite	Arf	Na ₃ Fe ₅ Si ₈ O ₂₂ (OH,F) ₂
Zircon	Zrn	ZrSiO ₄
Pyrochlore	Pcl	(Ca,Na,Pb,Ln,Y,U) ₂ Nb ₂ (O,OH) ₆ (O,OH,F,□)
Synchysite	Schy	CaY(CO ₃) ₂ F
Bastnasite	Bst	(Ce,La,Nd)(CO ₃)F
Xenotime	Xtm	(Y,Yb)PO ₄
Monazite	Mnz	(Ce,La,Nd)PO ₄
Fluorite	Fl	(Ca _{1-x} Y _x)F _{2+x}
Sericite	Ser	KAl ₂ (Si ₃ Al)O ₁₀ (OH,F) ₂
Thorite	Thr	ThSiO ₄
Hematite	Hem	Fe ₂ O ₃
Aeschynite	Achy	(Y,Ln,Ca,Th)(Ti,Nb) ₂ (O,OH) ₆

Table 4-3 Whole-rock chemical analyses of Jabal Sayid granite

	Oxidized granite			Aegirine granite			
	JSA1	JSA6B	JSA13	JSA6A	JSA7	JSA10A	JSA10B
F	0.18	0.1	0.21	0.01	0.09	0.1	0.03
SiO ₂	72.62	74.56	69.56	74.88	74.88	74.8	76.28
Al ₂ O ₃	3.75	7.58	4.87	10.9	11.06	10.82	10.25
Fe ₂ O ₃ (T)	11.54	5.25	15.45	3.86	2.95	3.94	3.84
MnO	0.027	0.453	0.025	0.047	0.087	0.043	0.022
MgO	0.67	0.25	0.09	0.2	0.21	0.2	0.24
CaO	1.3	0.36	0.56	0.31	0.77	0.4	0.35
Na ₂ O	0.11	2.04	0.22	4.36	4.09	4.86	3.74
K ₂ O	2.5	3.56	2.66	3.85	3.97	3.71	3.87
TiO ₂	0.563	0.451	0.444	0.079	0.058	0.072	0.076
P ₂ O ₅	0.13	0.01	0.02	0.01	0.01	0.01	0.01
LOI	2.7	1.33	1.97	0.64	1.08	0.5	0.68
Total	96.1	95.9	96.1	99.1	99.3	99.5	99.4
Be	41	13	35	4	11	4	6
Cr	30	30	30	30	30	30	30
Cu	20	10	20	10	10	10	10
Zn	550	3280	720	170	270	340	280
Ga	32	57	37	40	43	44	44
Ge	6	7	7	2	2	2	3
As	28	28	25	5	5	5	8
Rb	369	415	386	225	314	215	252
Sr	59	73	31	6	18	6	6
Y	7091	1256	7043	111	108	103	225
Zr	7211	11190	7759	663	651	901	859
Nb	1400	1910	830	38	87	46	156
Mo	2	2	2	2	2	2	2
In	0.9	0.3	0.6	0.2	0.2	0.2	0.2
Sn	275	68	187	9	11	8	26
Sb	2.1	0.9	2.2	0.5	0.8	< 0.5	1.1
Cs	3.5	2.6	3.3	0.9	2.6	0.5	0.7
Ba	37	210	30	21	18	10	17
Bi	0.4	3.1	0.5	0.4	0.4	0.4	0.4
La	1010	751	919	53.5	87.6	47.6	166
Ce	2180	2110	2160	133	219	121	528
Pr	261	275	281	17.2	28	15.4	71
Nd	1120	1140	1290	71.6	114	64.4	294
Sm	540	276	658	19.9	29.5	17.9	86
Eu	34.7	12.9	42.5	0.96	1.27	0.85	3.94
Gd	838	270	1010	19.7	26.1	18.4	73.7
Tb	188	41.1	217	3.6	4.1	3.2	10.7
Dy	1380	246	1480	22.4	22.7	20.2	49.3

Continue Table 4.3							
Ho	292	49.1	296	4.4	4.1	3.9	7.1
Er	823	150	831	11.4	11.4	11	15.9
Tm	116	24	117	1.43	1.69	1.5	1.95
Yb	669	167	683	8.3	10.8	8.8	11.2
Lu	81.8	26.6	82.2	1.13	1.65	1.19	1.55
Hf	117	240	132	14.4	14	18.4	19.2
Ta	192	169	96.1	5.4	8.5	5.5	10
W	7	4	7	2	2	2	2
Tl	1.8	1.8	1.7	1.4	1.6	1	1.4
Pb	424	751	504	37	50	50	176
Th	1080	63.9	5350	15.5	23.3	18.4	56.2
U	331	284	689	7.1	15.6	12.4	32.4
Na/K	0.04	0.57	0.08	1.13	1.03	1.31	0.97
LREE	5111.00	4552.00	5308.00	295.20	478.10	266.30	1145.00
HREE	4422.50	986.70	4758.70	73.32	83.81	69.04	175.34
Σ REE	9533.50	5538.70	10066.70	368.52	561.91	335.34	1320.34
Eu/Eu*	0.159	0.145	0.160	0.149	0.141	0.144	0.152
Zr/Hf	61.6	46.6	58.8	46.0	46.5	49.0	44.7
Nb/Ta	7.3	11.3	8.6	7.0	10.2	8.4	15.6
(La/Yb) _N	1.01	3.00	0.90	4.30	5.41	3.61	9.88
(Gd/Yb) _N	1.00	1.29	1.18	1.90	1.93	1.67	5.26
(La/Sm) _N	1.17	1.70	0.87	1.68	1.86	1.66	1.21
A.I.	0.77	0.95	0.66	1.04	1.00	1.11	1.00
Chondrite normalized values are from McDonough and Sun (1995). A.I agpaitic index = the molar ratio of Na+K/Al. Total iron reported as Fe ₂ O ₃ (T).							

Table 4-4 EMP analyses of Aegirine

		Prismatic Aegirine		Acicular Aegirine	
	LOD (% oxide)	Average (N=12)	±	Average (N=4)	±
Na ₂ O	0.03	12.2	0.5	12.2	0.6
MgO	0.02	b.d.	-	b.d.	-
F	0.23	b.d.	-	b.d.	-
Al ₂ O ₃	0.03	0.4	0.1	0.3	0.1
SiO ₂	0.06	50.4	0.9	50.2	1.3
ZrO ₂	0.03	0.1	0.1	1.0	0.3
Fe ₂ O ₃	0.03	29.48	3.8	23.78	4.5
FeO		3.05	2.9	5.5	3.8
MnO	0.01	0.1	0.1	0.2	0.0
ThO ₂	0.03	b.d.	-	b.d.	-
Nb ₂ O ₅	0.02	b.d.	-	b.d.	-
ZnO	0.02	0.1	0.1	0.1	0.0
CaO	0.02	0.7	0.5	0.2	0.0
TiO ₂	0.02	0.6	0.3	2.5	0.3
Total		97.3	1.7	96.1	1.7
atom per formula unit					
M2 site	Na	0.94		0.95	
	Ca	0.03		0.01	
	Fe ²⁺	0.02		0.04	
Total M2		0.97		0.95	
M1 site	Fe ³⁺	0.88		0.72	
	Mg	0.00		0.00	
	Mn	0.00		0.01	
	Al	0.02		0.02	
	Ti	0.01		0.08	
	Zr	0.00		0.01	
	Fe ²⁺	0.08		0.14	
Total M1	Si	1.00		0.99	
T site	Si	2.00		2.00	
	Al	0.00		0.00	
	Ti	0.00		0.00	
	Zr	0.00		0.01	
Total T		2.00		2.00	

LOD, limit of detection; b.d, below detection limit; error is one sigma standard deviation.

Table 4-5 Average EMP and LA-ICP-MS analyses of zircon

		Zircon-1			Zircon-2			Zircon-3		
	LOD (%)	Ave.(N=7)	(+/-)	a.p.f.u ¹	Ave.(N=28)	(+/-)	a.p.f.u	Ave.(N=15)	(+/-)	a.p.f.u
SiO ₂	0.04	29.74	0.11	0.93	26.43	1.60	0.84	22.86	1.05	0.73
Al ₂ O ₃	0.02	0.34	0.17	0.01	0.25	0.27	0.01	0.22	0.09	0.01
TiO ₂	0.02	0.13	0.03	0.00	b.d.			b.d.		0.00
P ₂ O ₅	0.03	b.d.		0.00	1.00	0.87	0.03	b.d.		0.00
B site				0.94			0.88			0.74
ZrO ₂	0.09	60.53	1.59	0.92	49.18	2.59	0.76	47.44	1.19	0.74
HfO ₂	0.06	1.15	0.46	0.01	0.68	0.26	0.01	0.64	0.22	0.01
CaO	0.02	0.19	0.07	0.01	0.58	0.24	0.02	0.41	0.11	0.01
ThO ₂	0.04	0.07	0.07	0.00	1.06	1.11	0.01	0.06	0.04	0.00
Y ₂ O ₃	0.04	1.08	1.29	0.02	7.32	1.57	0.12	10.60	0.55	0.18
UO ₂	0.03	0.12	0.02	0.00	0.71	0.22	0.00	0.61	0.60	0.00
FeO	0.02	1.13	0.44	0.03	1.61	0.54	0.04	0.29	0.31	0.01
REE	0.04	1.09	0.34	0.04	3.36	0.2	0.03	4.87	0.42	0.05
PbO	0.03	0.18	0.09	0.00	0.12	0.05	0.00	0.16	0.07	0.00
A site				1.00			1.00			1.00
Total		95.76	0.75	1.94	92.81	2.37	1.87	90.60	0.99	1.74
Zr/Hf		60.96	0.4		86.02	0.5		82.21	0.3	
REE (%)		1.34	0.77		3.99	0.82		5.10	0.64	
LREE (%)		0.49	0.22		0.65	0.20		0.58	0.11	
HREE (%)		0.83	0.56		3.32	0.90		4.49	0.67	

elements ppm	Trace (LA-ICP-MS)					
	Zircon-1		Zircon-2		Zircon-3	
	Average (N=4)	(+/-)	Average (N=4)	(+/-)	Average (N=3)	(+/-)
Li	3	2	6	1	27	7
Al	998	107	631	154	2365	538
Si	109000	18735	113500	5745	160000	16391
P	197	16	908	111	91	31
Sc	436	17	494	12	578	23
Ti	132	11	191	21	423	78
Fe	1470	692	6598	1715	3773	1936
Y	75400	2252	48925	3226	17203	12505
Nb	219	8	944	135	1823	352
Sn	1143	81	460	159	933	242
La	1	0	65	15	49	12

Ce	4	1	231	28	193	92
Pr	1	0	32	6	56	22
Nd	10	3	170	22	488	203
Sm	140	2	316	29	648	322
Eu	23	2	48	3	53	31
Gd	1317	18	1823	161	1294	833
Tb	795	9	827	91	327	231
Dy	9940	171	7960	916	2406	1998
Ho	2597	112	1783	192	527	448
Er	8253	515	5715	525	1780	1410
Tm	1317	65	1010	94	374	269
Yb	8667	448	7970	582	3935	2531
Lu	837	81	913	84	525	276
Hf	3073	266	4945	1025	8563	2382
Ta	25	2	41	5	277	46
Pb	342	18	353	33	1362	529
Th	603	414	20275	3340	309	127
U	2560	121	3098	629	681	178

LOD: limit of detection of EMPA in oxide %; Ave.: average; N: number of analyses points; +/-: 1 σ stander deviation; a.p.f.u: atom per formula unit calculated by normalizing to M site assuming full occupancy. Trace elements concentrations in zircon are the average obtained by the LA-ICP-MS. b.d.: below detection limit of EMPA.

Table 4-6 Average EMP analyses of pyrochlore

Pyrochlore					Altered pyrochlore		
	LOD (ppm element)	Ave. (N=7)	(+/-)	Ave. a.p.f.u	Ave. (N=2)	(+/-)	Ave. a.p.f.u
Nb ₂ O ₅	425	42.1	4.4	1.48	37.9	0.2	1.39
Ta ₂ O ₅	671	3.5	0.6	0.07	1.1	1.0	0.02
TiO ₂	247	2.5	0.1	0.15	2.8	2.0	0.17
SiO ₂	455	3.9	2.2	0.30	5.1	1.0	0.41
B site				2.00			2.00
Na ₂ O	224	0.5	0.4	0.07	0.1	0.1	0.01
La ₂ O ₃	1413	1.8	0.9	0.05	0.2	0.2	0.01
Ce ₂ O ₃	1168	5.6	1.6	0.16	1.2	1.2	0.04
Gd ₂ O ₃	702	b.d.			3.9	4.5	0.11
CaO	152	3.8	1.2	0.32	2.3	0.4	0.20
ThO ₂	400	0.2	0.3	0.00	1.1	0.1	0.02
Y ₂ O ₃	487	0.4	0.2	0.02	16.5	2.8	0.71
Nd ₂ O ₃	442	1.6	0.5	0.02	1.4	1.7	0.04
Pr ₂ O ₃	836	0.5	0.2	0.05	0.3	0.3	0.01
Dy ₂ O ₃	451	0.4	0.3	0.00	4.2	0.7	0.11
Ho ₂ O ₃	926	b.d.			0.8	0.6	0.02
Lu ₂ O ₃	515	b.d.			0.2	0.2	0.00
UO ₂	323	2.3	1.5	0.00	0.7	0.3	0.01
MnO	273	0.6	0.7	0.04	0.1	0.1	0.01
Sm ₂ O ₃	726	0.4	0.2	0.01	1.9	2.2	0.05
Tb ₂ O ₃	421	b.d.			0.7	0.4	0.02
FeO	180	1.8	0.8	0.12	2.8	1.1	0.19
Er ₂ O ₃	420	b.d.			2.9	3.3	0.08
Tm ₂ O ₃	421	b.d.			0.5	0.6	0.01
Yb ₂ O ₃	411	0.2	0.1	0.00	2.3	2.9	0.06
PbO	441	25.8	6.6	0.55	1.8	0.6	0.04
A site				1.4			1.7
F	1747	0.1	0.1		0.1	0.0	
F=2O		-0.05			-0.03		
Total		98.34		3.4	93.22		3.7
Nb/Ta		12.10			34.14		

LOD: limit of detection of EMPA. Ave.: average; N: number of analyses points; +/-: 1 σ standard deviation.; a.p.f.u: atom per formula unit calculated by normalizing to B site assuming full occupancy. b.d., at or below detection limit.

Table 4-7 Average EMP analyses of synchysite and bastnasite

	Synchysite			Bastnasite		
	Average (N=7)	±	Average a.p.f.u	Average (N=9)	±	Average a.p.f.u
CaO	18.89	1.9	1.0	0.3	0.1	0.01
La ₂ O ₃	0.41	0.2	0.0	14.2	6.7	0.19
Ce ₂ O ₃	1.04	0.4	0.0	31.1	3.4	0.41
Gd ₂ O ₃	1.98	0.3	0.0	1.6	1.7	0.02
ThO ₂	0.92	1.0	0.0	0.8	0.6	0.01
Y ₂ O ₃	28.29	5.2	0.7	1.0	0.7	0.02
Nd ₂ O ₃	0.77	0.2	0.0	14.2	5.2	0.23
Pr ₂ O ₃	0.14	0.1	0.0	3.6	1.0	0.05
Eu ₂ O ₃	0.04	0.0	0.0	0.1	0.1	0.00
Dy ₂ O ₃	4.41	0.3	0.1	0.6	0.6	0.01
Ho ₂ O ₃	0.93	0.1	0.0	0.1	0.1	0.00
Lu ₂ O ₃	0.04	0.0	0.0	0.0	0.0	0.00
Sm ₂ O ₃	0.75	0.1	0.0	3.3	2.0	0.04
Tb ₂ O ₃	0.53	0.1	0.0	0.2	0.2	0.00
Er ₂ O ₃	2.33	0.3	0.0	0.1	0.1	0.00
Tm ₂ O ₃	0.25	0.0	0.0	0.0	0.0	0.00
Yb ₂ O ₃	0.92	0.2	0.0	0.1	0.1	0.00
PbO	0.33	0.0	0.0	0.0	0.0	0.00
F	4.74	0.3		7.1	0.8	
-O=F2	-2.0			-3.16		
Total	65.7		2.0	75.2		0.99
*CO ₂	32.3			21.6		

*CO₂ calculated by the difference of the total oxides to 100. LOD, the limit of detection;
b.d, below detection limit; error is one sigma standard deviation.

Table 4-8 Average EMP analyses of xenotime and monazite

	Xenotime			Monazite		
	Average (N=3)	±	Average a.p.f.u	Average (N=5)	±	Average a.p.f.u
F	3.02	0.3		0.74	0.0	
SiO ₂	3.28	0.3	0.12	0.73	0.5	0.03
Al ₂ O ₃	0.13	0.1	0.01	0.01	0.0	<0.001
La ₂ O ₃	0.48	0.6	0.01	22.03	3.2	0.32
Ce ₂ O ₃	0.69	0.9	0.01	35.96	0.7	0.52
Gd ₂ O ₃	0.20	0.0	0.00	0.22	0.2	<0.001
CaO	0.45	0.6	0.02	0.03	0.0	<0.001
ThO ₂	2.26	2.0	0.02	0.40	0.2	<0.001
P ₂ O ₅	27.33	0.3	0.84	28.41	0.7	0.96
Y ₂ O ₃	43.43	2.5	0.84	0.04	0.0	<0.001
Nd ₂ O ₃	0.16	0.2	0.00	8.26	1.3	0.12
Pr ₂ O ₃	0.07	0.0	0.00	2.75	0.3	0.04
Eu ₂ O ₃	0.04	0.0	0.00	0.04	0.0	<0.001
Dy ₂ O ₃	2.26	0.3	0.03	0.05	0.0	<0.001
Ho ₂ O ₃	1.02	0.1	0.01	0.05	0.0	<0.001
Lu ₂ O ₃	0.76	0.1	0.01	0.05	0.0	<0.001
UO ₂	0.07	0.0	0.00	0.03	0.0	<0.001
Sm ₂ O ₃	0.18	0.0	0.00	0.93	0.5	0.01
Tb ₂ O ₃	0.10	0.0	0.00	0.03	0.0	<0.001
FeO	1.07	0.4	0.03	0.02	0.0	<0.001
Er ₂ O ₃	5.18	0.2	0.06	0.03	0.0	<0.001
Tm ₂ O ₃	1.03	0.0	0.01	0.03	0.0	<0.001
Yb ₂ O ₃	6.75	0.1	0.07	0.04	0.0	<0.001
PbO	0.44	0.1	0.04	0.0		<0.001
Total	100.40		2.12	100.85		2.00

Error is one sigma standard deviation.

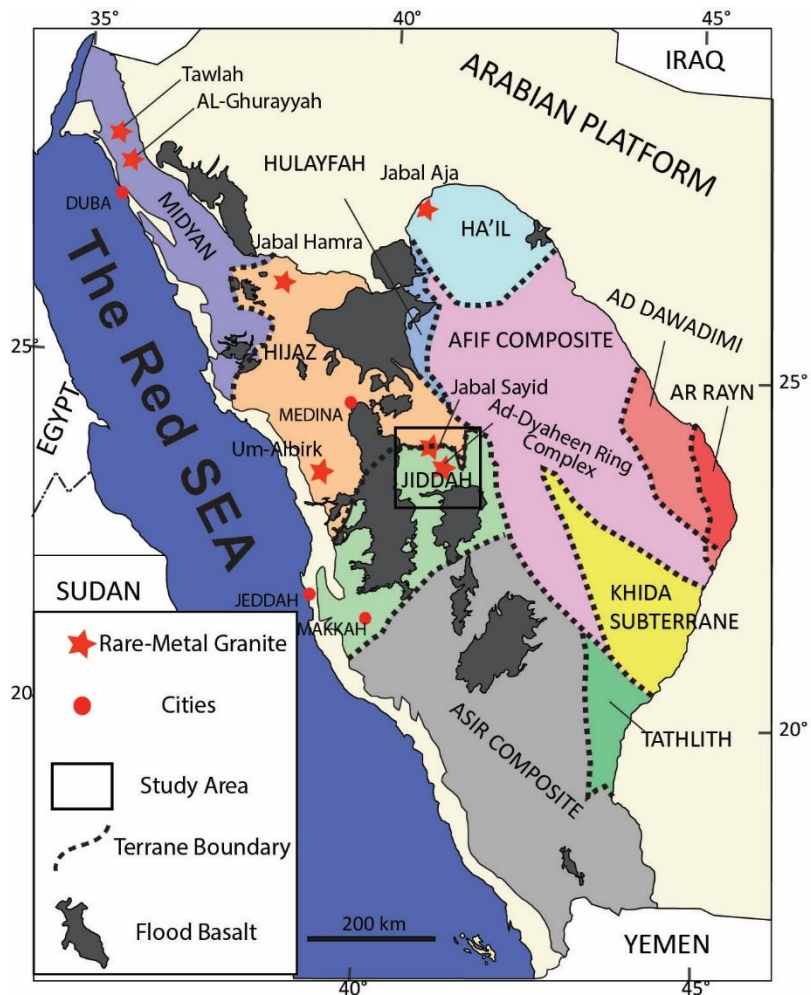


Figure 4-1 A geological map of the Arabian Shield showing the different terranes that constitute the Shield. The red stars are the locations of some important occurrences of rare-metal granite including Jabal Sayid deposit. The study is shown in the black box (modified after Johnson and Kattan 2012).

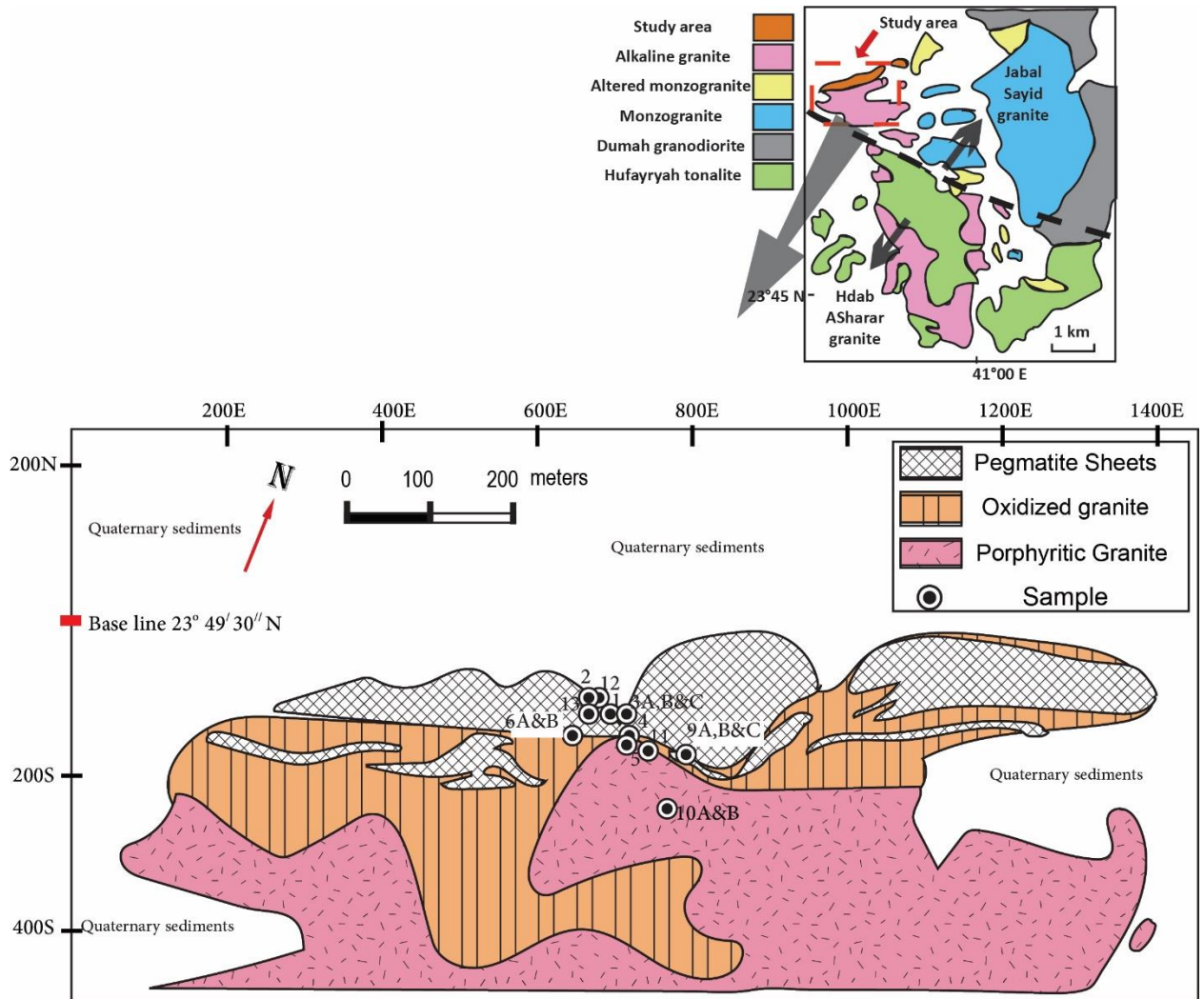


Figure 4-2 Geological map of Jabal Sayid deposit (modified after Hackett, 1986) and the location of samples. At the top right corner is a general geological map of Jabal Sayid complex (Modified after Turkistany et al., 1982). The study area is denoted by a dashed orange line.

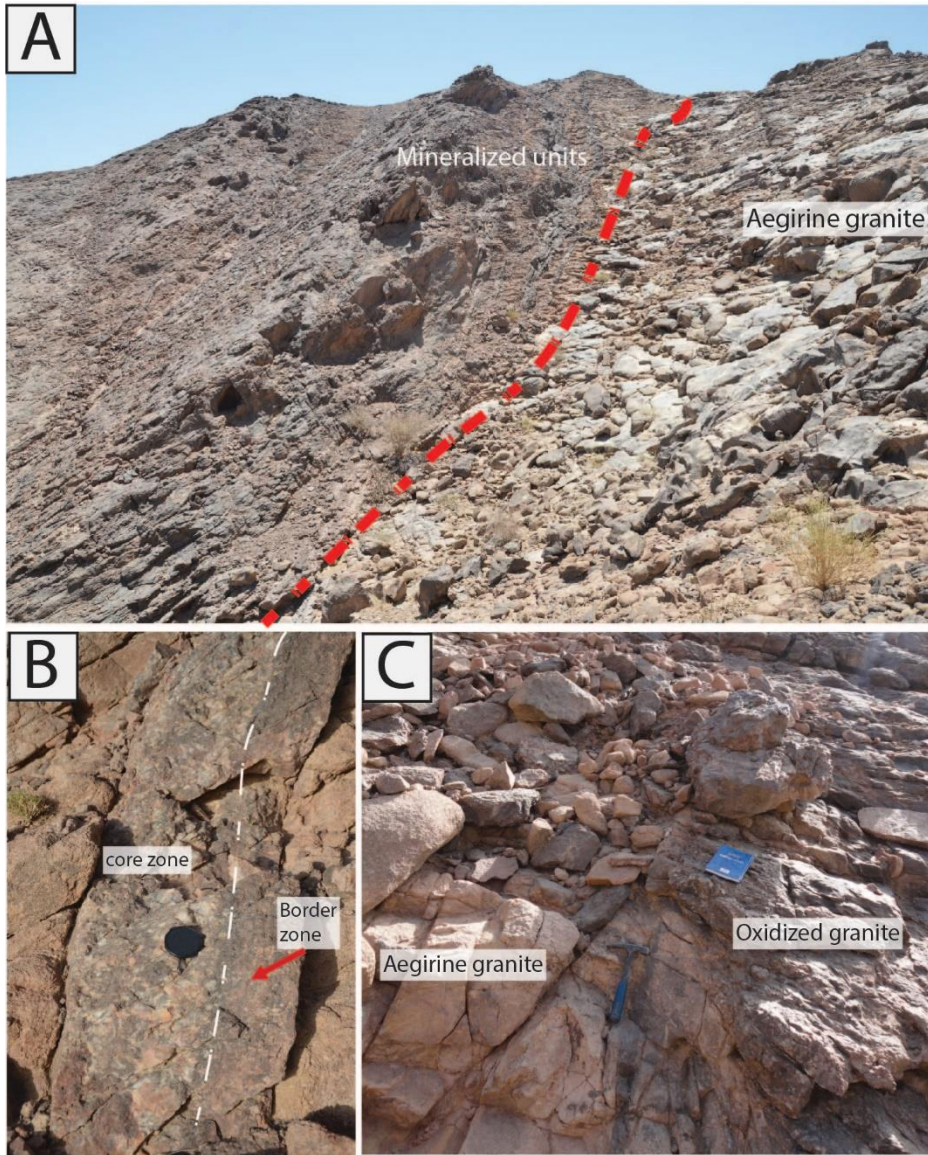


Figure 4-3 The main rock units in the Jabal Sayid mineralization area. **A)** Looking southeast, an outcrop of the mineralized units and the aegirine granite. **B)** A photo of the pegmatite sheets showing the contact with the aegirine granite. **C)** A photo of the contact between the oxidized granite and the aegirine granite.

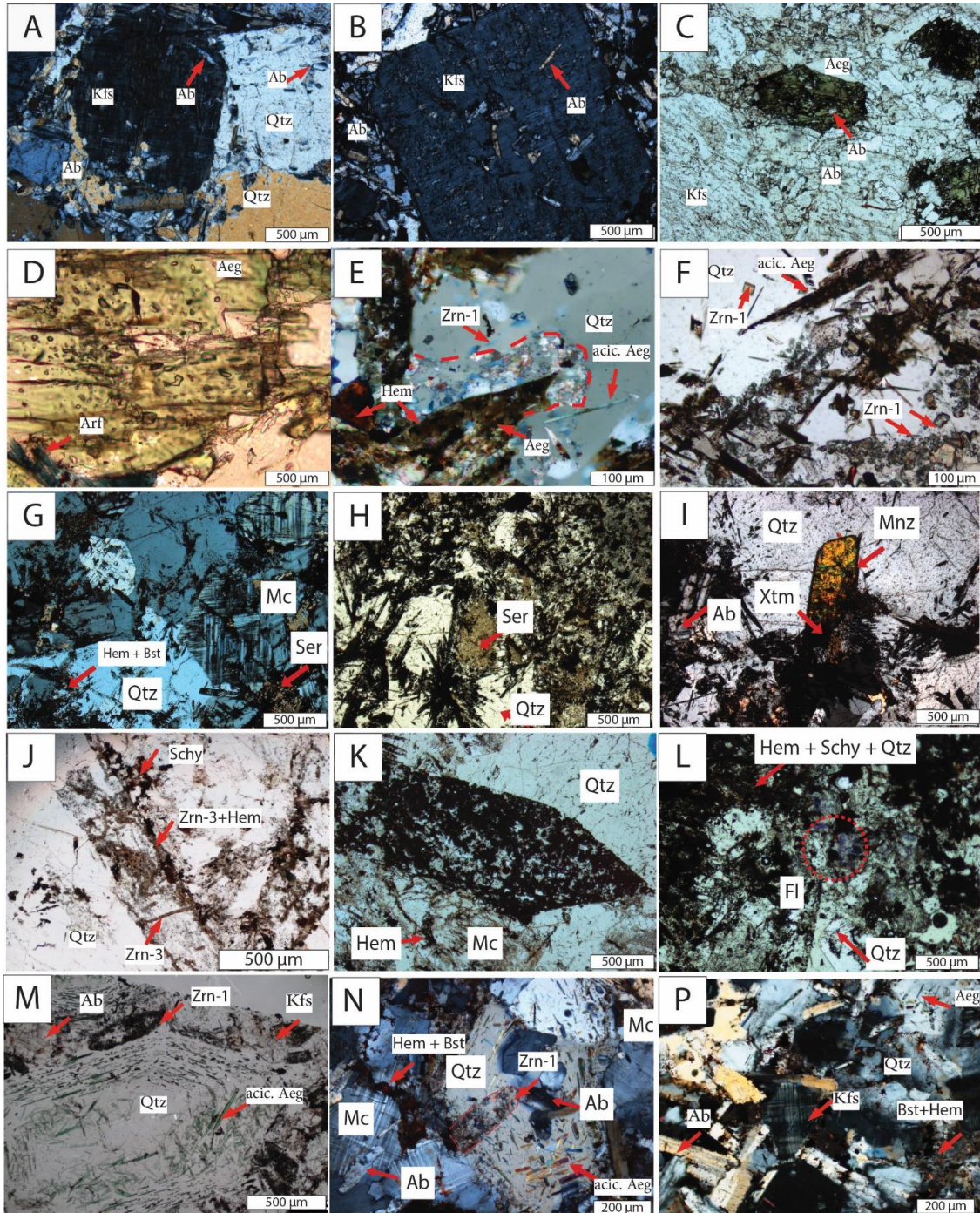


Figure 4-4 Petrography of the aegirine granite. A) Crossed polarized light image (CPL) of subhedral alkali feldspar and quartz phenocrysts with albite inclusions from the aegirine granite. B) CPL image of euhedral alkali feldspar crystals with albite inclusions. C) A plane-polarized light (PPL) image of prismatic aegirine crystals in albite, and quartz in a perthite matrix. Albite occurs as inclusion in the

aegirine D) PPL close up image of prismatic aegirine crystal showing abundant fluid inclusions and a relic of arfvedsonite. E) PPL image of a prismatic aegirine partially replaced by Zircon-1, hematite and quartz, and associated with fresh acicular aegirine. The red dashed lines show the original shape of the prismatic aegirine. F) PPL image of altered acicular aegirine associated with zircon (Zircon-1) in a quartz matrix. G) CPL image showing large microcline crystals and quartz that contain acicular pseudomorph after aegirine from the oxidized granite. H) PPL image of altered acicular aegirine and sericite in quartz matrix from the oxidized granite. I) CPL image of partially altered monazite to xenotime and bastnasite from the oxidized granite. J) PPL image of a large Zircon-3 -hematite-rich pseudomorph in a quartz matrix from the core of the pegmatite sheet. K) PPL of a large pseudomorph in a quartz matrix from the core of the pegmatite. The pseudomorph consists of hematite, Zircon3, quartz and Synchysite (shown in Fig. 4.6 A and B). L) PPL image showing fluorite with hematite and synchysite from the core of the pegmatite. M) PPL of large snowball quartz contains inclusion of fresh acicular aegirine from the border zone. Zircon-1-rich pseudomorph on the top of the image, which is part of the mineralization associated with the transition stage. N) CPL of large snowball quartz from the border zone, contains fresh acicular aegirine and trapped Zircon-1 pseudomorphs, which is part of the mineralization associated with the transition stage. Bastnasite and hematite occur between grain boundaries. Bastnasite and hematite are part of the mineralization that occurs in the hydrothermal stage. P) CPL image of albite, quartz, and microcline from the border zone form a typical magmatic intergranular texture. Abbreviations: Qtz: quartz, Ab: albite, Kfs: alkali feldspar, Zrn: zircon, Aeg: aegirine, Arfv: arfvedsonite, acic. Aeg: acicular aegirine, Bst: bastnasite, Schy: synchysite

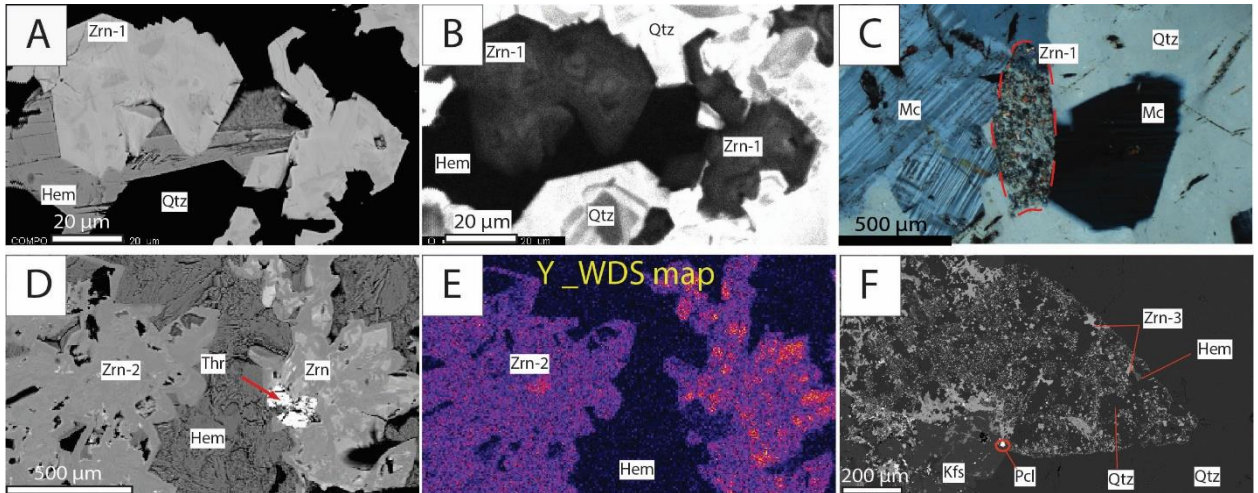


Figure 4-5 A) BSE image of Zircon-1 associated with hematite from the aegirine granite B) CL image of Zircon-1 in A. C) CPL image of Zircon-2 rich pseudomorph trapped in a quartz crystal with microcline from the pegmatite boundary. D) BSE image of Zircon-2 in a hematite matrix showing a core of Y-rich zircon and resorbed precipitation texture of Y low zircon from the oxidized granite. E) WDS X-ray map of Zircon-2 internal Y content in D. F) BSE image of a large pseudomorph from the pegmatite core showing Zircon-3 forming veinlets with synchysite and hematite.

Abbreviations Qtz: quartz, Mc: microcline, PCL: pyrochlore, Mnz: monazite, Zrn: zircon, Xtm: xenotime, Hem: hematite.

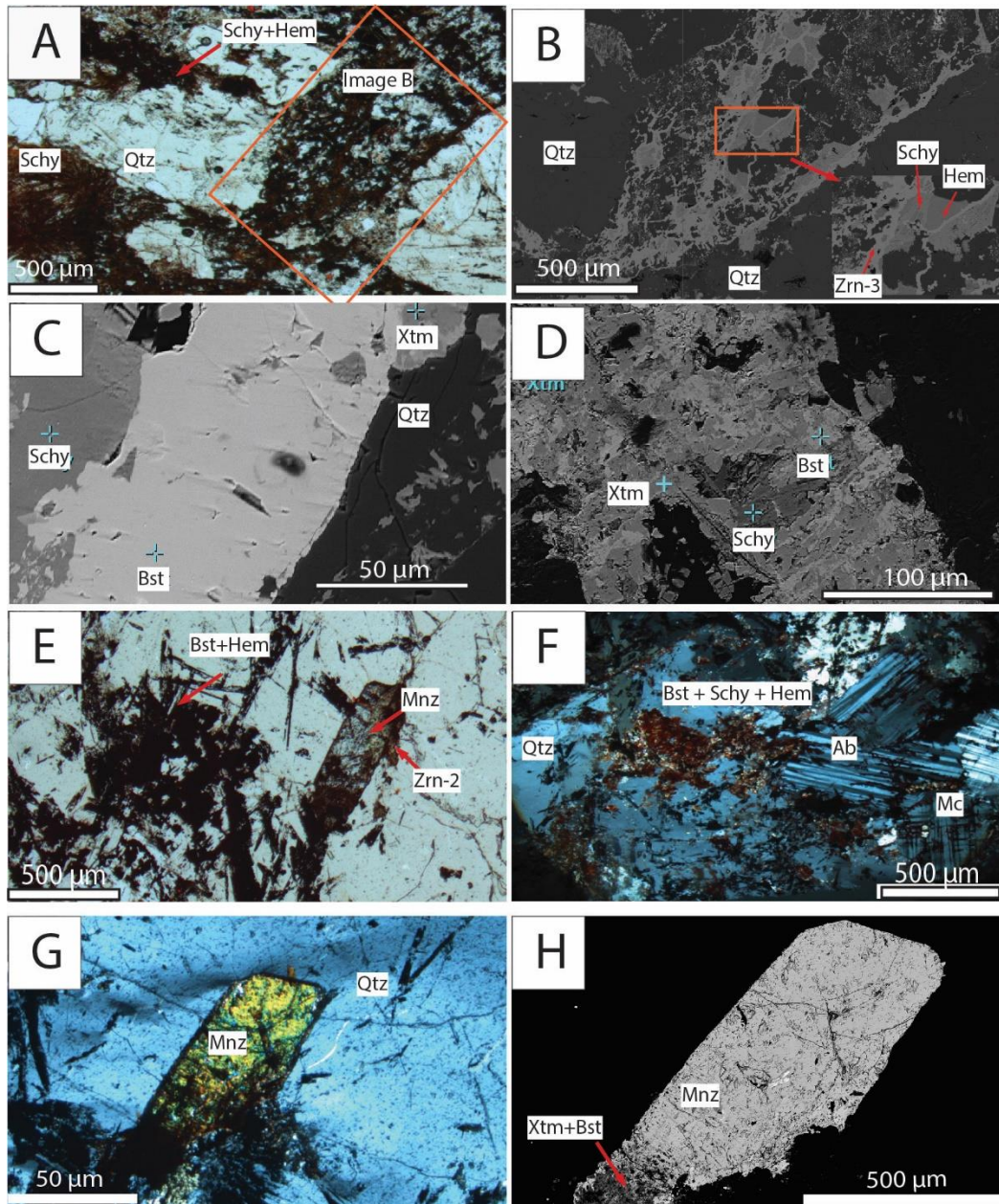


Figure 4-6 A) PPL image of large pseudomorphs and acicular synchysite with hematite in a quartz matrix from the core of the pegmatite sheet show B) BSE image of the large pseudomorph in A showing Zircon-3 forming veinlets with synchysite and hematite. C) BSE image of bastnasite that is partially replaced by synchysite and xenotime from the oxidized granite. D) Another BSE image of intensely altered bastnasite that is replaced by synchysite and xenotime. E) PPL image of altered aegirine that is replaced by bastnasite and hematite, and a partially altered

monazite associated with Zircon-2 from the oxidized granite. F) CPL image of aggregates of bastnasite, synchysite, and hematite enclosed by quartz that contains altered acicular aegirine. G) and H) are CPL and BSE images of monazite with partial alteration of xenotime and bastnasite from the oxidized granite.

Abbreviations. Qtz: quartz, Mc: microcline, Ab: albite, Bst: bastnasite, Sych: synchysite, Mnz: monazite, Zrn: zircon, Xtm: xenotime, Hem: hematite.

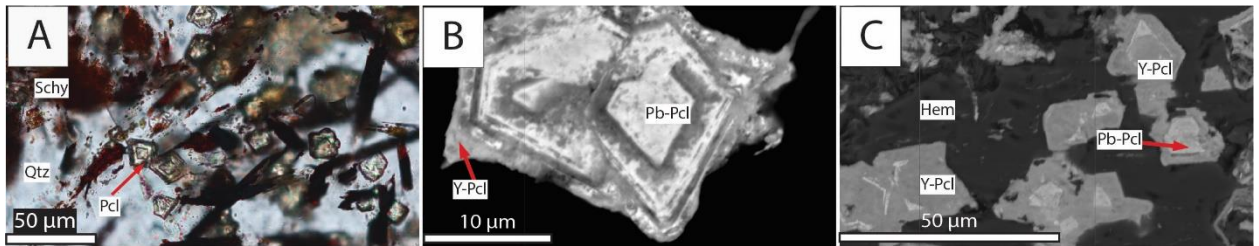


Figure 4-7 A) PPL image of pyrochlore crystals from a pegmatite core. B) BSE image of partially altered pyrochlore that is replaced by Y-rich pyrochlore from a pegmatite core. C) BSE image of pyrochlore in hematite matrix that shows intense alteration to Y-rich pyrochlore.

Abbreviations: Qtz: quartz, PCL: pyrochlore, Schy: synchysite, Hem: hematite.

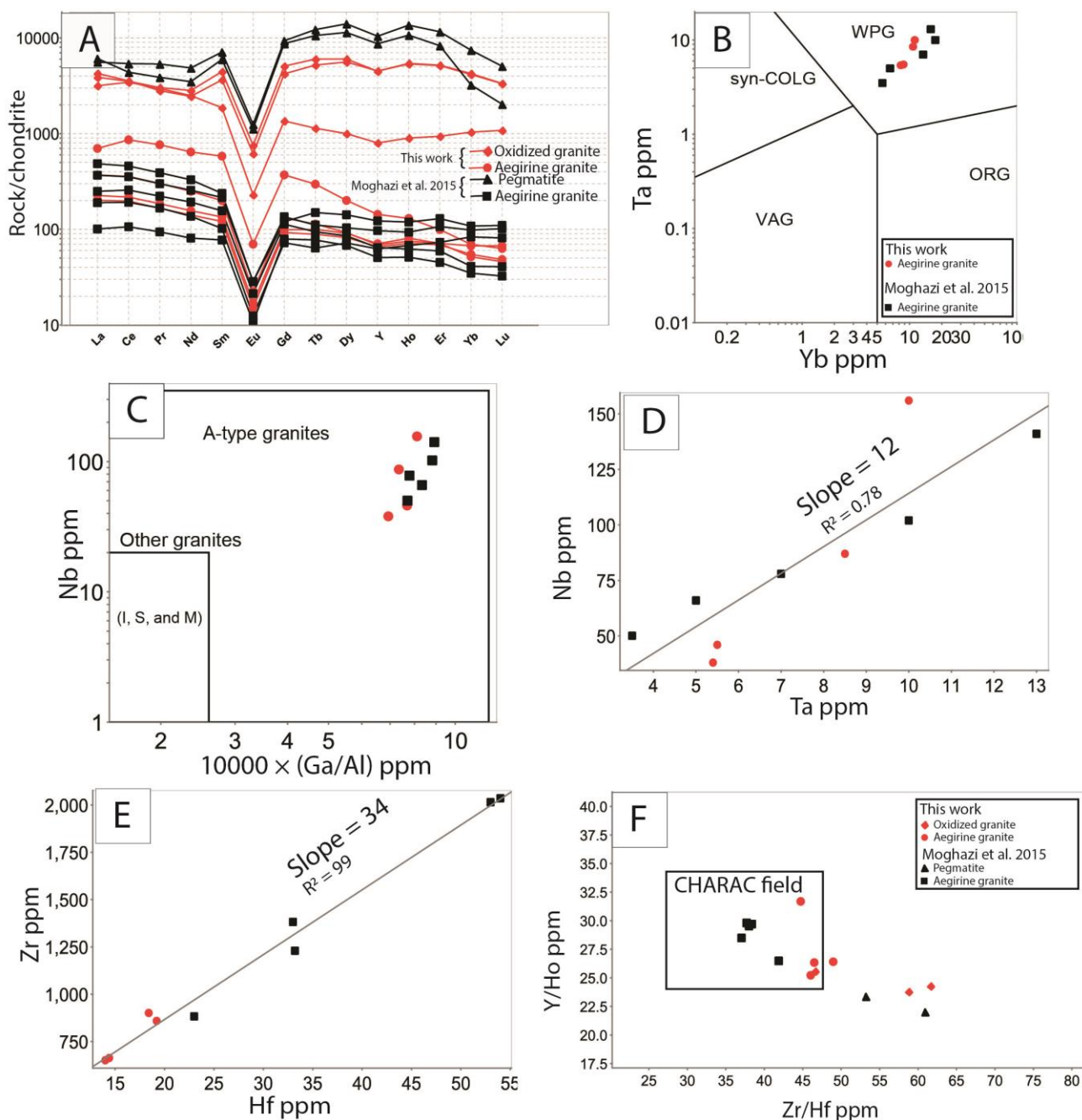
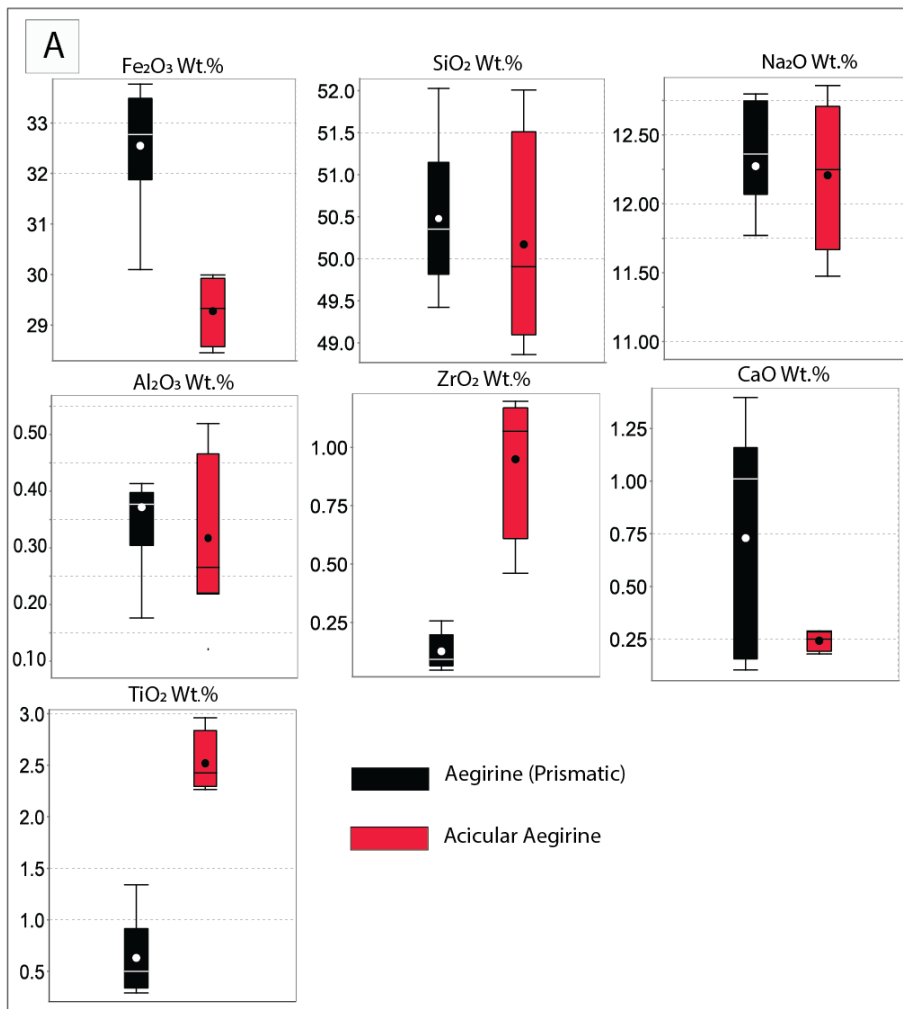


Figure 4-8 Whole-rock lithogeochemistry data of this work compared to previous works data. **A)** Chondrite-normalized REE pattern of the aegirine granite (chondrite values are from McDonough and Sun, 1995). **B)** Yb vs. Ta tectonic discrimination diagram (Pearce et al. 1984) showing the within-plate tectonic settings of Jabal Sayid aegirine granite. **C)** Ratio of Ga/Al vs. Nb concentration in ppm (Whalen et al. 1987) showing the alkalinity nature of Jabal Sayid aegirine

granite. D) Ta vs. Nb concentrations. The solid line is a least-square fit has a slope value of 12. E) Hf vs. Zr concentration in ppm forming a trend with a slope of 34. F) The ratio of Zr/Hf vs. Y/Ho of the aegirine granite, oxidized granite, the pegmatite sheets. The box represents the range of charge-and-radius -controlled field proposed by Bau (1996).



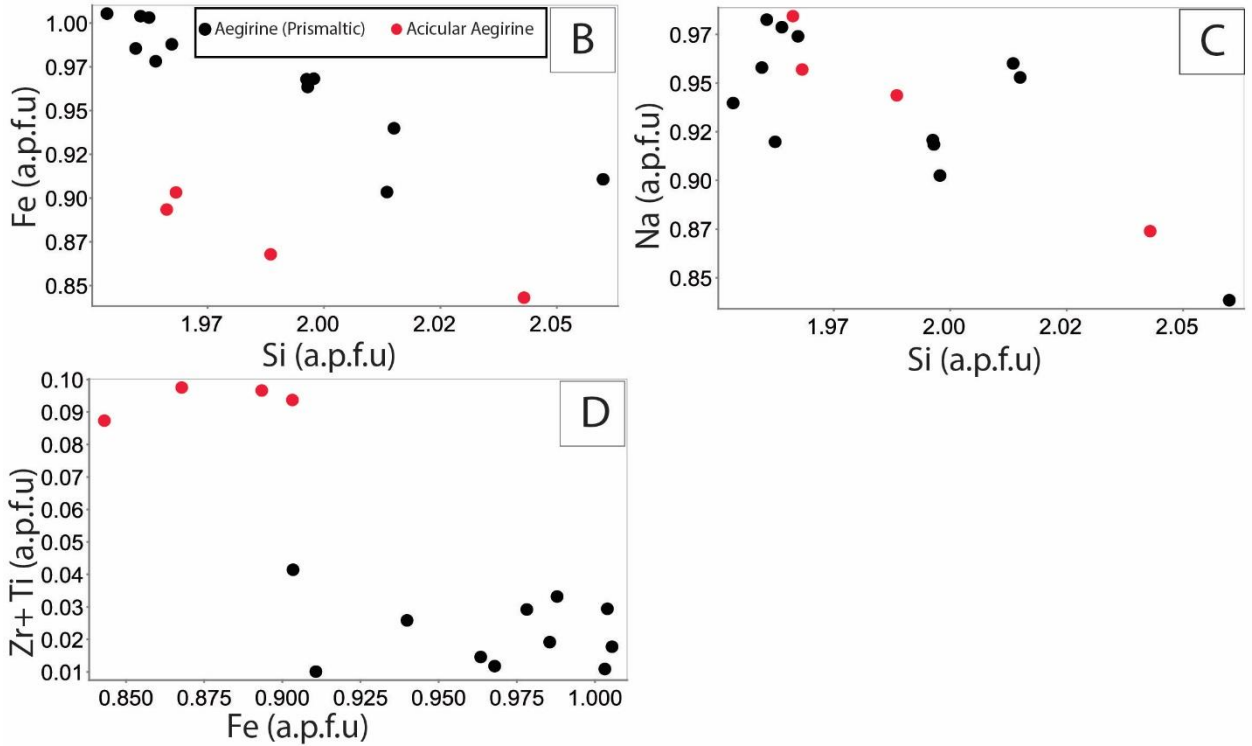


Figure 4-9 Chemical composition of Aegirine. A) Box and whisker plot showing the variation in the chemical composition of prismatic aegirine and acicular aegirine. B) and C) Si correlates negatively with Fe and Na in atom per formula unit. Prismatic aegirine and acicular aegirine form two different trends in Figure B. Figures D) show the elevated concentration of Zr + Ti in acicular aegirine that is associated with low Fe.

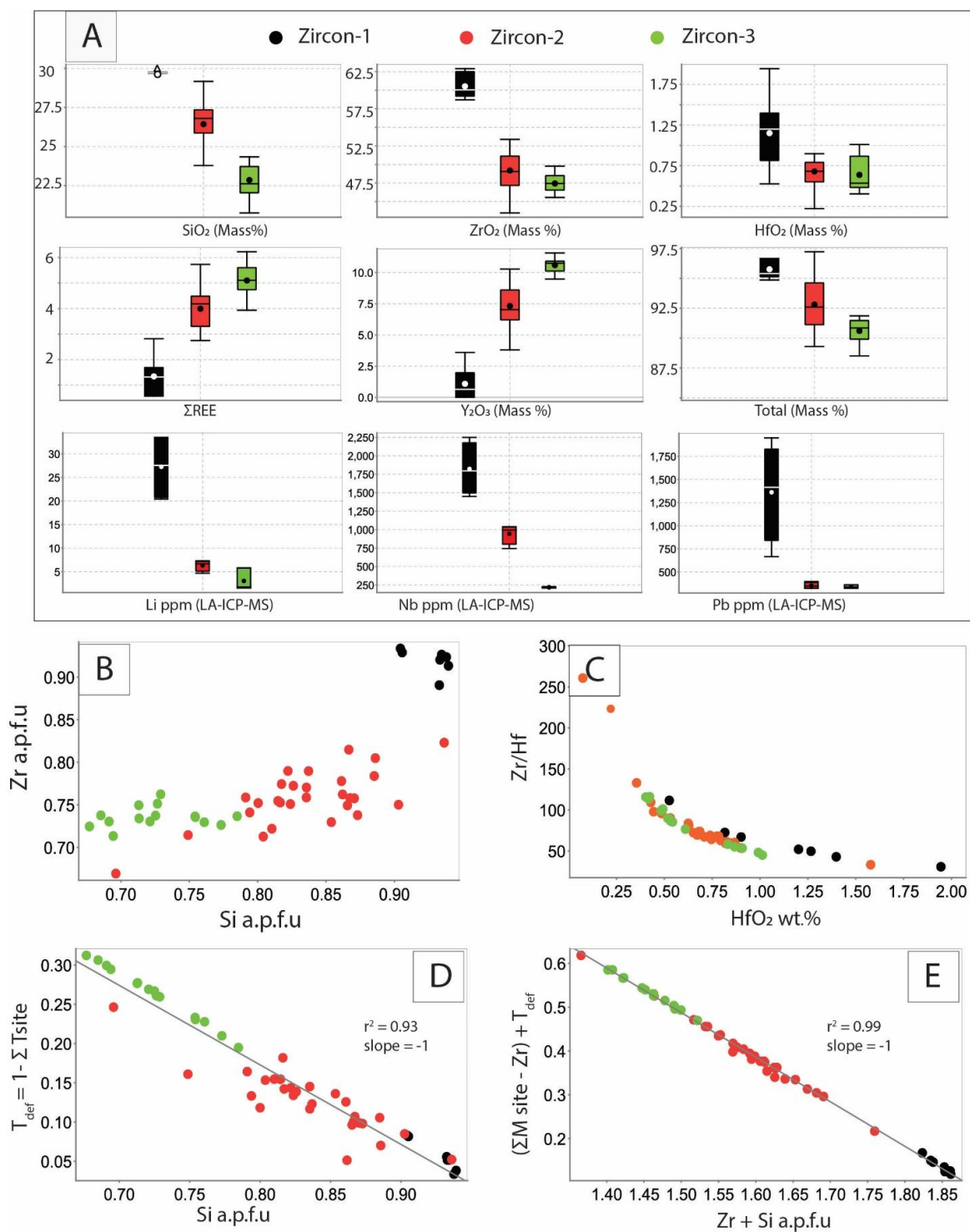


Figure 4-10 A) Box and whisker plot showing variations in the chemical composition of zircon types. B) Zr vs. Si in atom per formula unit (a.p.f.u). C) The ratio of Zr/Hf forms a smooth curve with HfO₂ concentration. The Zr/Hf ratio is generally higher than the ratio in the whole-rock suggesting other minerals control these elements. D)

The deficiency in the filling of T site ($T_{\text{def}} = 1 - \text{cations total of T site}$) forms a strong correlation with Si a.p.f.u. the line represents least square fit with a slope of -0.9. F)

A plot the shows the main substitution mechanism as $M^{n+} + (OH)_n^- + (4-n) H^+ = Si^{4+} + Zr^{4+}$; where M = REE, Y, Fe, Al, and Ca (Caruba et al., 1985).

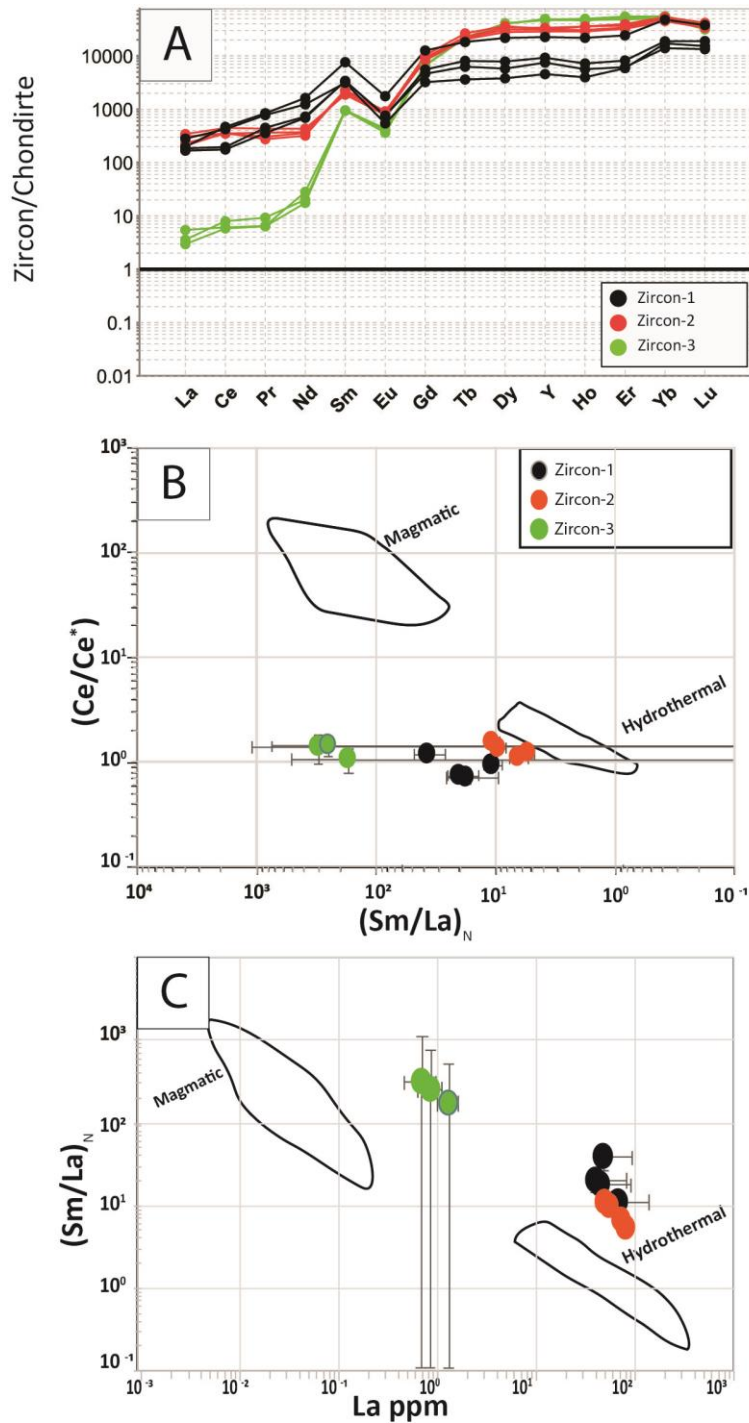


Figure 4-11 A) Chondrite-normalized REE diagram of the three main zircon types in Jabal Sayid (chondrite values are from McDonough and Sun, 1995). B) Zircon discrimination of chondrite-normalized ratio of Sm/La with La ppm. C) a discrimination diagram where the chondrite normalized ratios of Ce/Ce* and

Sm/La are plot against each other. The grey fields in Figures A and C represent magmatic and hydrothermal zircon (modified after Hoskin, 2005).

$$Ce/Ce^* = \frac{\left(\frac{Ce_{in\ rock}}{Ce_{in\ chondrite}}\right)}{\sqrt{\frac{La_{in\ rock}}{La_{in\ chondrite}} \times \frac{Pr_{in\ rock}}{Pr_{in\ chondrite}}}}, Sm/La_N = \frac{\left(\frac{Sm_{in\ rock}}{Sm_{in\ chondrite}}\right)}{\left(\frac{La_{in\ rock}}{La_{in\ chondrite}}\right)}. \text{ Chondrite values are}$$

from McDonough and Sun (1995).

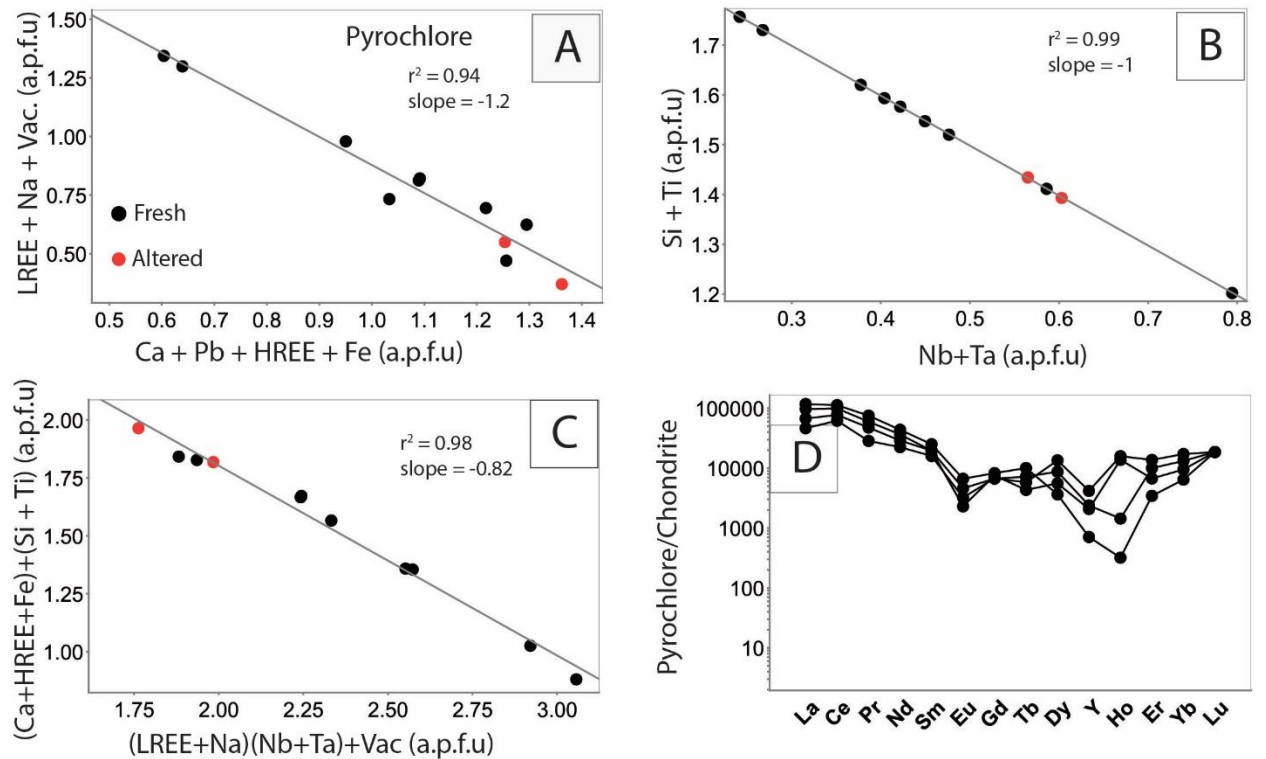


Figure 4-12 A) A diagram shows the main substitution mechanism in A site. B) A diagram shows the main substitution mechanism in B site. C) is the main substitution mechanism in pyrochlores. Vac is the vacancy in A site calculated as 1 – total A site cations. D) Is a chondrite-normalized REE diagram of fresh pyrochlores from Jabal Sayid. Most values are above the EMPA detection limit, except for Eu where one half of the detection limit was plotted.

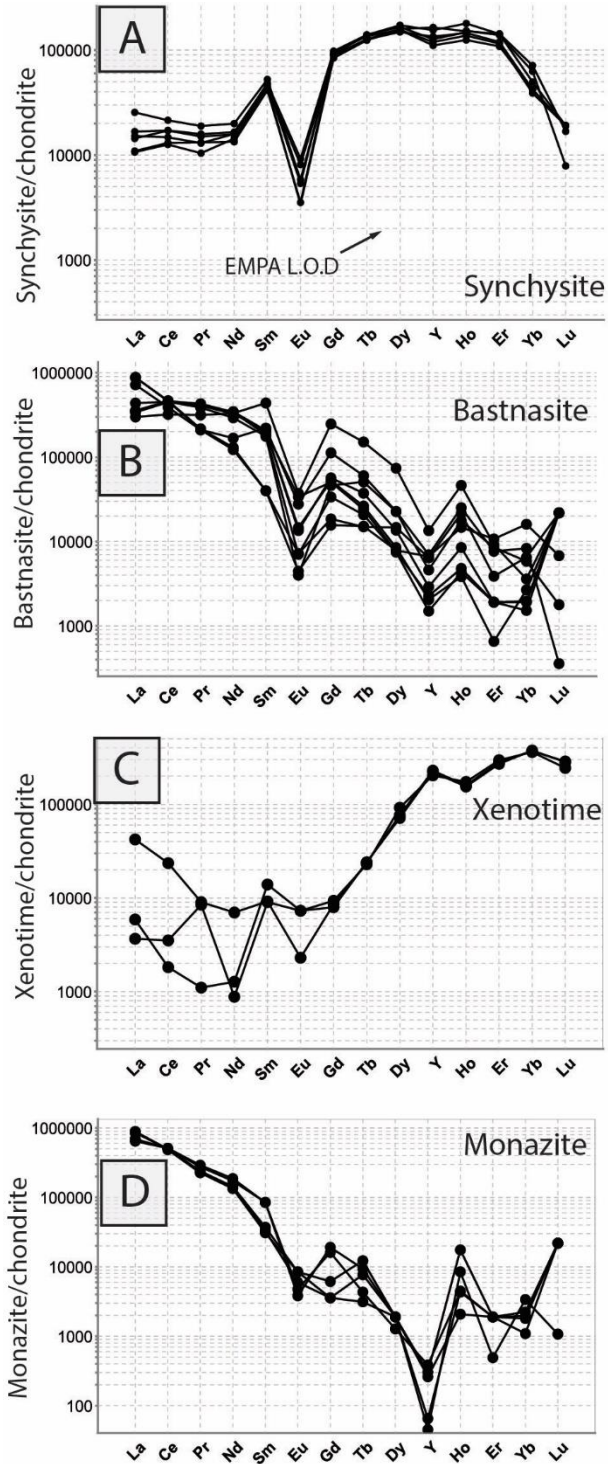


Figure 4-13 Chondrite normalized REE pattern of synchysite in A, bastnasite in B, xenotime in C, and monazite in D. One half of the EMP detection limit were plotted for REE value below the detection limit.

Chapter 5

5 Rare-metal mineralization at Dyaheen ring complex, the Arabian Shield, Saudi Arabia: petrography, lithogeochemistry, and mineral chemistry

5.1 Introduction

The common use of high field strength elements (HFSE) and rare earth elements (REE) in advanced industries has led to the surge in demand for these elements. The most common use of Nb is for the steel and superalloy industry; Ta is mainly used to manufacture capacitors for electronics; Zr is used for ceramics, foundry sand, and refractories; Hf is used for superalloy manufacturing; and REE is used for catalysts, ceramics and glass, and metallurgical and alloy applications (U.S. Geological Survey, Mineral Commodity Summaries, 2019).

Primary deposits of HFSE and REE are usually associated with carbonatites (e.g. Bayan Obo, China; Nolan Bore, Australia; Mountain Pass, USA/Canada), alkaline/peralkaline granite (e.g. Ilímaussaq, Greenland; Lovozero and Khibiny, Russia; Nechalacho, Canada), and metaluminous and peraluminous granites and pegmatites (e.g. Pitinga, Brazil; Yichyan, China; Tanco, Canada) (Linnen et al., 2014; Möller et al., 1989). Rare-metal alkaline/peralkaline granites contain high concentrations of Nb, Ta, Zr, Y, and REE, especially the heavy rare earth elements (HREE; Tb, Dy, Ho, Er, Tm, Yb, and Lu). Generally, alkaline granites are characterized by an alkalinity index (A.I.) of > 1 , where $A.I. = \frac{Na + K}{Al}$ (Marks and Markl, 2017). Moreover, alkaline granites can be classified according to their silica saturation into silica over-saturated (quartz-bearing rocks) and silica saturated (feldspar-bearing rocks)/undersaturated (feldspathoids-bearing rocks) (Linnen et al., 2014). The silica saturated/undersaturated peralkaline granites are commonly given the name agpaitic when the A.I. is equal or larger than 1.2, whereas those with an A.I. of < 1.2 are known as miaskitic. The mineralogy of agpaitic and miaskitic granites are distinct; agpaitic granites are characterized by complex zirconosilicate minerals, such as eudialyte ($Na_4[Ca,REE]_2[Fe,Mn]ZrSi_8O_{22}[Oh,Cl]_2$) and rinkite

($[\text{Ca,REE}]_4\text{Na}[\text{Na,Ca}]_2\text{Ti}[\text{Si}_2\text{O}_7]_2\text{F}_2[\text{O,F}]_2$), whereas miaskitic granites have simpler ore mineral composition, such as zircon, ilmenite, and pyrochlore (Möller and Williams-Jones, 2017; Piilonen et al., 2012; Sorensen, 1992). Nevertheless, the term miaskitic has been used to describe silica-bearing alkaline granites with mineralogy similar to the traditional silica-undersaturated miaskitic rocks (Siegel et al., 2018).

Several studies have investigated the processes where metals in this type of rock reach economical concentrations (Boily and Williams-Jones, 1994; Feng and Samson, 2015; Gysi and Williams-Jones, 2013; Kovalenko, 1995; Möller and Williams-Jones, 2016; Salvi et al., 2000; Salvi and Williams-Jones, 1990; Vasyukova and Williams-Jones, 2014; Vasyukova et al., 2016; Wang et al., 2003). The main hypotheses regarding the formation of this kind of deposits include: 1) a magmatic model due to extreme fractionation (Kovalenko, 1995); 2) a magmatic and hydrothermal model where magmatic process enriched the residual melt in HFSE and REE, and the metals were increased to economical concentrations during a later hydrothermal stage (Boily and Williams-Jones, 1994a; Gysi and Williams-Jones, 2013; S Salvi et al., 2000; Salvi and Williams-Jones, 1996); 3) a fluoride-silicate melt immiscibility modal where the fluoride melt fractionated LREE and enriched the silicate melt in HFSE ((Siegel et al., 2017; Vasyukova and Williams-Jones, 2014; Vasyukova et al., 2016).

The Arabian Shield hosts one of the largest alkaline granite fields in the world and these granites form about 2 % of the shield's area. The granites were emplaced between 680 to 510 Ma (Kröner and Stern, 2005; Moghazi et al., 2011; Stoeser, 1986), several rare-metal alkaline granite deposits formed during this period, such as Al-Ghurayyah, Jabal Sayid, Um-Alberak, Jabal Tawlah, and Dyaheen ring complex (Fig. 5.1) economic potentials, such as Al-Ghurayyah, Jabal Sayid,.

Hadb AdDyaheen ring complex (referred to as Dyaheen below) is a subcircular body located approximately 300 km northeast of Jeddah, Saudi Arabia. The granitic body is a silica-saturated alkaline granite, which is related to late Neoproterozoic magmatism (613 ± 4 Ma to 625 ± 11 Ma from U-Pb zircon age dating; Ali et al., 2014). The ore reserve has not been estimated. The lithology and chemistry of Dyaheen were investigated as part

of a regional study of alkaline magmatism in the Arabian Shield (Jackson, 1986; Radain, 1979). Dyaheen received studies that focused on its genesis and age (Ali et al., 2014; Moghazi et al., 2011). It is located near rare-metal mineralization at Jabal Sayid, and it was suggested that they have the same source (Radain, 1979). Moreover, they share similar host rock composition and age (593 ± 2 Ma, Moghazi et al., 2015). However, the two deposits show different mineralization styles, in which the mineralization in Dyaheen is in quartz veins and aegirine-rich dykes, whereas at Jabal Sayid, the mineralization is hosted by pegmatite sheets and an oxidized granite. Another important feature that distinguishes the two deposits is the absence of intense hematization at Dyaheen, where the mineralization is associated with relatively fresh rock (most aegirine is fresh). This allows a comparison between two deposits that share the same source and are hosted by rocks with similar compositions but have different mineralization styles. Moreover, most rare-metal alkaline granites are associated with intense post-magmatic alteration that destroys and obscures magmatic and early hydrothermal mineral assemblages (Kovalenko et al., 2007; Miller, 1996; Salvi and Williams-Jones, 1996, 1991). Thus, the nature of this stage is not well documented. At Dyaheen, the late-magmatic to early-hydrothermal stage mineral assemblages are preserved, which gives the opportunity for understanding the nature of this stage that is commonly obscure in similar deposits.

The objectives of this study are to assess the magmatic evolution of Dyaheen ring complex and hydrothermal stages, and their roles in the formation of rare-metal alkaline deposits are evaluated. This will be accomplished by field mapping, petrographic and lithogeochemical analyses of Dyaheen rock units and characterizing the evolution of HFSE and REE through the morphology and chemistry of their host minerals.

Dyaheen is located 30 km south of Jabal Sayid rare-metal granite (Fig. 5.1). The granite complex is about 8.5 km by 11.5 km is oval-shaped, with an elevated rim (Fig. 5.2). The complex intruded granodiorite, quartz-diorite, and diorite (Radain, 1979). The complex consists of three main rock units, namely monzogranite, amphibole-biotite granite, and aegirine granite (Fig. 5.2 and Table 5.1). The core of the complex consists of a light-grey, moderately to highly weathered, coarse-grained monzogranite. The monzogranite is mantled by amphibole-biotite granite. The amphibole-biotite granite forms the bulk of the

complex area, which occurs as ring dykes surrounding the monzogranite except at northern margin. The amphibole-biotite granite has a variable color ranging from gray to reddish-brown and shows a variable grain size ranging from medium-grained to porphyritic. The amphibole-biotite contains isolated bodies of microgranite that have complex contacts with the amphibole-biotite granite. These contact relationships were not investigated in the current study. Pegmatite dykes and miarolitic cavities are common in the amphibole-biotite granite. They consist of amphibole, alkali feldspar, and quartz where they form large crystals that are up to 5 cm long (Fig. 5.3 A). The aegirine granite is medium-grained to slightly porphyritic and pinkish-grey in color. The contact of amphibole-biotite granite and aegirine granite (outer rim), where exposed, is sharp to irregular. The aegirine granite is cut by several aplite dykes and quartz veins and pods. Highly mineralized aegirine dykes were observed to crosscut the host aegirine granite. The aegirine dykes are 10 to 20 cm wide and display comparable major mineral compositions to the aegirine granite (Fig. 5.3 B). High radiation was detected at the aegirine granite dykes and near quartz veins and pods reaching values of more than 10000 counts per second (cps) total alpha, beta, and gamma radiation measured using a handheld Technical Association radiation detector. Locally, quartz veins that crosscut the aegirine granite display ductile deformation (Fig. 5.3 C).

5.2 Methodology

Samples from the monzogranite, amphibole-biotite granite, aegirine granite, pegmatite, aegirine dykes, and quartz veins were collected. In addition to the mineralized units, the sampling focused on the amphibole-biotite granite and aegirine granite located at the western outer rim of the complex, as well as monzogranite from the core. Polished thin sections were prepared at the Department of Earth Sciences at the University of Western Ontario, Canada, and the Faculty of Earth Sciences, at the King Abdul Aziz University, Jeddah, Saudi Arabia. Polished thin section slides were studied using a petrographic microscope and a scanning electron microscope equipped with energy dispersive spectroscopy (SEM-EDS) to obtain mineralogical, texture, and semi-quantitative mineral compositions. The analyses were performed at the Department of Earth Sciences at the University of Western Ontario, Canada. Major and trace element mineral compositions

and backscattered electron images (BSEI) were obtained using a JEOL-JCM 6000 benchtop SEM equipped with EDS (B-SEM). Data were collected at 15 kV acceleration voltage at high vacuum mode. Quantitative mineral compositions, cathodoluminescence (CL), and EDS analyses were determined on a JEOL JXA-8530F field-emission electron microprobe (EMPA) at Earth and Planetary Materials Analysis Laboratory at the University of Western Ontario, Canada. The analytical conditions of the EPMA were 20 kV probe current, 40-60 nA accelerating voltage, and beam diameter ranging from 1 to 15 micrometer. The standards were synthetic zircon for Zr and Si, rutile for Ti, albite for Na and Al, fayalite for Fe for iron in aegirine, fluorite for F, orthoclase for K, anorthite for Ca. Pure metal standards (serial 2AG-METM25-44, Astimex Standards Limited) were used for Fe in oxide accessory minerals, Mn, Nb, Ta, Hf, Pb, Th, and U.

Smithsonian REE phosphate (NMNH 168484-116499) standard was used for REE analysis. In order to resolve the REE peak and background overlaps, corrections were made by performing a slow scan on WDS crystals (LIF, LIFH, and LIFL) to identify the elements with peak and background overlaps. The amount of overlap that contributes to the main peak was measured and then subtract from the main peak (elements overlap, and the amount of overlaps are given in Appendix B).

Ages were determined from U-Pb analyses of zircon. The zircon crystals were selected from the mineralized quartz veins from sample V16. Ages were determined at the University of Toronto using a laser-ablation ICP/MS technique. A NWR excimer laser was used with 20 microns beam diameter, 7 to 10 Hz repetition rate, at an energy of 3.6-4.3 J/cm² energy. The ICP system is an Agilent 7900 ICP-MS. Ar gas flow was 0.85 L/min, with 20 milliseconds were used as wash delay. The analyzed isotopes were ⁸⁸Sr, ²⁰⁶Pb, ²⁰⁷Pb, ²⁰⁸Pb, ²³²Th, ²³⁸U. Strontium was used as an indicator of alteration where high Sr indicates excessive alteration of zircon before starting the analyses, and the analyzed spots were pre-ablated to clean them from any dust or unwanted material on the surface. To avoid losing U with drilling, a rastering technique was followed to obtain a large material amount with less drilling. In samples where the desired areas for analysis are zoned, a line technique was followed. Data reduction was performed using a program written by Davis (1982). Two zircon standards were used: sample DD91-1 from Lac

Fourniere pluton, the Pontiac and Abitibi subprovinces, Quebec (Davis, 2002), and sample DD85-17 from mafic tonalite, Marmion batholith, south-central Wabigoon subprovince, Canada (Tomlinson et al., 2003).

To obtain the trace element content of zircon, grains were analyzed by laser ablation inductively coupled plasma mass spectrometry (LA-ICP-MS) at the Great Lakes Institute for Environmental Research (GLIER) at the University of Windsor, Ontario, Canada. Zircon-1, Zircon-2, and Zircon-3 (classification discussed below) were analyzed on a Photon-Machines 193 nm ArF excimer laser with 20 micrometer beam diameter, 20 Hz repetition rate, and 1.63 J/cm² energy. The ICP system is an Agilent 7900 ICP-MS. Ar gas flow was 0.82 L/Min, and 30 millisecond were used as wash delay. NIST 610 was used as an external standard, and the concentration of Zr obtained using EMPA was used as an internal standard. In zoned grains, the average concentration of Zr of the ablated area was used as the internal standard. The data processing and data reduction were done using IGORPro and Iolite software (Paton et al., 2011). The isotopes list and the average detection limits are summarized in Appendix C.

Lithochemical analyses the monzogranite, the amphibole-biotite, the aegirine granite, aegirine dykes, and quartz veins were carried out by Activation Laboratories Ltd (Actlabs), Ancaster, Ontario, Canada. Samples were crushed and pulverized (using mild steel). Rock powders were fused with lithium metaborate/tetraborate and then digested in a weak nitric acid solution. Major and trace elements were analyzed using an inductively coupled plasma-mass spectrometry (ICP/ICP-MS) technique. Analytical precision was calculated from duplicate analyses and ranges from 0.1 to 5 relative % for major elements, 0.5 to 8 relative % for REE and HFSE, and up to 20 % for other trace elements. Fluorine analysis was performed following ion-selective electrode technique. In this technique, samples were fused with lithium metaborate/tetraborate in an induction furnace to release the fluoride ions to the matrix and then dissolved in dilute nitric acid. Next, the solution was complexed with ionic strength adjusted with ammonium citrate buffer before the analysis.

5.3 Petrography

5.3.1 Monzogranite

The monzogranite is medium-grained and shows a moderate to a high degree of weathering, which is characterized by the formation of clay minerals after plagioclase. It consists of 35 to 40 % quartz, 35 % zoned plagioclase, 25 to 30 alkali feldspar, 5-10 % biotite all estimated visually in volume %. Accessory minerals include titanite, magnetite, zircon, and apatite. Plagioclase (An_{16-24} determined based on the extinction angle) is the most abundant mineral and displays oscillatory zoning but has undergone selective alteration of the core (to clay minerals) over the rim (Fig. 5.4.A). Alkali feldspar occurs as large anhedral crystals (≈ 1 mm) with a micro-perthite texture. Biotite is strongly pleochroic ranging from brown to green color and is partially replaced by chlorite along edges. It occurs as 200 μm to 1 mm flakes and locally contains inclusions of apatite and magnetite. Titanite is the most abundant accessory mineral, which occurs as light brown euhedral to subhedral crystals that are 500 μm in length (Fig. 5.4 B). Magnetite is the second most abundant accessory mineral and occurs as medium-grained euhedral to subhedral grains that locally have partially been replaced by hematite. Small apatite crystals (10 to 50 μm) are associated with biotite and magnetite. Secondary minerals include chlorite and fluorite that replaced biotite, and clay minerals after plagioclase.

5.3.2 Amphibole-biotite granite

This unit is moderately to highly weathered. It consists of 30 to 35 % quartz, 20 to 25 % plagioclase, 30 % alkali feldspar, 5-10 % sodic amphibole, and biotite. Accessory minerals include titanite, zircon, and magnetite \pm ilmenite. Secondary minerals are clay minerals, sericite, fluorite, chlorite, and minor calcite. This unit displays variable textures and occurs as microgranite, medium-grained, and porphyritic granite. The alkali feldspar is perthite that is partially replaced by sericite. Locally perthite occurs as euhedral phenocrysts. Quartz occurs as fine-grained rounded crystals (20 μm) and locally forms a myrmekitic texture with perthite. Plagioclase, has a composition of An_{15-30} , estimated by the plagioclase extinction angle, occurs as tabular crystals showing simple albite twinning. It is highly weathered and altered to clay minerals. Sodic amphibole is present as

dark blueish-green anhedral crystals that are replaced by biotite and contain inclusions of magnetite and titanite (Fig. 5.4 C). Biotite is reddish-yellow to brown color with weak pleochroism. Biotite occurs as a replacement of the sodic amphibole (Fig. 5.4 C) or as individual mineral. Magnetite and titanite are the most common accessory phases and show a close association with amphibole (commonly as inclusion in amphibole). Other less common accessory minerals are apatite and zircon. In highly altered samples, amphibole is completely replaced by hematite, fluorite, and zircon. Zircon is more abundant in altered samples relative to unaltered samples.

5.3.3 Aegirine granite

The aegirine granite consists of 35-40 % quartz, 30 % albite, 20 % microcline, and 7 to 10 % aegirine and amphibole. Quartz is present as large anhedral rounded grains (1 cm) containing inclusions of albite and aegirine \pm pyrochlore (Fig. 5.4 D). Additionally, quartz occurs as a fine-grained matrix mineral with albite. Albite occurs as subhedral lath-shaped crystals forming the bulk of groundmass minerals (Fig. 5.4 D and E). Microcline is present as anhedral crystals rimmed by lath-shaped albite (Fig. 5.4 F). Locally, microcline-perthite were observed as 1 mm subhedral crystals. Aegirine occurs as deep green to pale olive-green subhedral crystals that range in length from 100 μ m to 500 μ m. Sodic amphibole occurs as strongly perchloric deep blue to blue subhedral crystals, is in planar contact with aegirine, and contains inclusions of albite and quartz (Fig. 5.4 E). In rocks near the mineralization, aegirine is the stable mafic phase, whereas all of the sodic amphibole is altered to hematite \pm fluorite, and zircon (Fig. 5.4 G). In fresh aegirine granite, pyrochlore is the only accessory mineral that was observed, which occurs as trace euhedral yellow inclusions in phenocrysts of quartz and aegirine.

5.3.4 Alteration

The main alteration event observed in the amphibole-biotite granite and the aegirine granite is calcite, fluorite and hematite alterations (Fig. 5.4 G to L). The amphibole-biotite granite near the aegirine granite shows a variable alteration of amphibole and biotite granite to hematite \pm fluorite and zircon (Fig. 5.4 G to L). Calcite veins are common in highly altered samples, associated with biotite, hematite, zircon, and fluorite

(Fig. 5.4 H to J). Locally, this alteration events altered titanite to calcite and rutile (Fig. 5.4 L)

Altered aegirine granite is distinguished by its darker color due to the higher abundance of hematite and zircon (Fig. 5.4 M and N). In the altered aegirine granite, zircon is the most common accessory mineral and typically associated with hematite and fluorite around altered aegirine. The altered aegirine granite is generally present near quartz veins and pods.

5.3.5 Mineralization

Zr, Nb, and REE mineralization in Dyaheen occurs in an aegirine dykes, pegmatites, and quartz veins and pods that crosscut the aegirine granite at the western outer rim of the complex. The aegirine dykes consists of 40 % quartz, 30 % albite, 10 K-feldspar, and 7 % aegirine. Zircon is the most common accessory mineral and occurs as aggregates or isolated crystals (Fig. 5.5 A). The zircon occurs as reddish-brown subhedral prismatic crystals ($\approx 200 \mu\text{m}$) with abundant hematite inclusions (Fig. 5.5 B). Pyrochlore is the second most common accessory mineral and occurs as rounded yellow to brown grains that are $50 \mu\text{m}$ across. Other accessory minerals include bastnasite and fergusonite that usually occur in complex clusters of crystals with pyrochlore and zircon.

The quartz vein and pods in Dyaheen are characterized by the presence of perthite, aegirine, and abundant disseminated pyrochlore and zircon (Fig. 5.5 D to F) in addition to gadolinite, and britholite \pm bastnasite. The quartz veins show a variable degree of ductile deformation (Fig. 5.3 C). Locally, aegirine occurs as fine-grained needle-shaped crystals that are 50 to $100 \mu\text{m}$ long (Fig. 5.5 D and E). Accessory ore minerals in the quartz veins and pods include zircon, pyrochlore, fergusonite, and REE-silicate (britholite). Some quartz veins and pods contain show hematite, willemite (ZnSiO_4), and zircon that are arranged in a prismatic shape that are interpreted as pseudomorphs. The pseudomorphs have crystal habit similar to that of aegirine, which suggests that aegirine was the precursor mineral. Additionally, the quartz veins locally contain sphalerite.

5.4 Morphology of ore minerals

Various rare-metal minerals occur in the Dyaheen ring complex; however, the common rare-metal minerals are zircon, pyrochlore, fergusonite, gadolinite, and bastnasite \pm britholite and monazite. These minerals occur in the altered aegirine granite, the aegirine dykes, and the quartz veins. Fergusonite is most commonly found in pegmatite from the amphibole granite, as well as in some quartz pods hosted by the aegirine granite. Major rock-forming and ore minerals observed in Dyaheen are summarized in Table 5.2.

5.4.1 Zircon

Zircon is present in variable concentrations in all rock units at Dyaheen except for the fresh aegirine granite at the rim of the complex. Zircon is very rare in the monzogranite and the amphibole-biotite granite. It occurs as light-grey subhedral prismatic crystals that are 10 μm long (Fig. 5.6 A). The core contains abundant U and Y-rich mineral inclusions (Fig. 5.6 B). In the pegmatite dykes from the amphibole-biotite granite, zircon is reddish and subhedral crystals that are 500 μm long. It is mineral inclusion-rich and highly porous with hematite, fergusonite, pyrochlore, and fluorite inclusions (Fig. 5.6 C and D). Moreover, it is associated with fergusonite, which is altered to pyrochlore and fluorite. In the aegirine granite, the zircon abundance is higher in samples that show hematite alteration of aegirine. It occurs as light-grey subhedral to equant anhedral crystals that range in size from 100 to 300 μm long (Fig. 5.6 E and F). No zoning or mineral inclusions were observed in this zircon. In the mineralized aegirine dykes, zircon is present as aggregates of reddish-brown equant-shaped subhedral crystals that are 500 μm long (Fig 5.6 G). It shows spotted to patchy zonation of Hf. Zircon in this unit commonly is associated with pyrochlore (Fig. 5.6 H). In the quartz veins, the morphology of zircon is similar to that from the aegirine dykes. It occurs as aggregates of reddish-brown subhedral to anhedral crystals that are 100 to 300 μm across (Fig. 5.6 I). Zircon commonly has a spongy texture and contains inclusions of aegirine, thorite, hematite, and pyrochlore (Fig. 5.6 J and K). It is associated with pyrochlore, gadolinite, bastnasite, britholite, and complex REE-Ti-silicate.

5.4.2 Fergusonite and pyrochlore

Fergusonite is the main Nb mineral in the pegmatite from the amphibole-biotite granite and some of the quartz vein samples. However, it is rare in the aegirine dykes and quartz veins that contain aegirine. Fergusonite occurs as light-yellow prismatic crystals that are 200 μm to 1 mm long (Fig. 5.7 A to C). It is well zoned (Fig. 5.7 B) due to the variation in Y, Th, U, Ti, and Yb (discussed below) and is altered to pyrochlore (Pb-rich) at the rim. Fluorite is locally associated with pyrochlore replacement (Fig. 5.7 B).

Pyrochlore is more common in the aegirine granite, aegirine dykes, and aegirine-rich quartz veins. Pyrochlore in the pegmatite occurs as a replacement after fergusonite (Fig. 5.7 A to C). Pyrochlore in the fresh aegirine granite is Pb-rich, is rare, and only found as inclusions in aegirine crystals. It forms yellow to reddish-yellow subhedral crystals that are less than 50 μm across. In the aegirine dykes, pyrochlore occurs as yellow to reddish-yellow subhedral to anhedral equant shaped crystals that are 10 to 100 μm across (Fig. 5.5 C). In BSE images, pyrochlore commonly varies from well-zoned to patchy zoning. Most of the well-zoned crystals are affected by alteration (Fig. 5.7 D). The zonation is due to the internal variation in Nb, Pb, Ti, Ta, Y, and LREE (La, Ce, Pr, Gd, and Sm) concentrations in the pyrochlore. In the quartz veins, abundant pyrochlore crystals are associated with aegirine (Fig. 5.5 D and E). Pyrochlore occurs as yellow to reddish-yellow bipyramid crystals that are 10 to 25 μm across. The pyrochlore is replaced by Pb-poor and Y and REE-rich pyrochlore. Moreover, the pyrochlore crystals are surrounded by veinlets of complex Nb-rich minerals that are Y and REE (Fig. 5.5 F).

5.4.3 Y and REE minerals

All minerals where Y and REE are essential elements excluding Nb oxide minerals will be referred to as REE minerals. The main REE minerals in Dyaheen are gadolinite, bastnasite, and a complex REE-Pb-Ti-silicate \pm britholite. Monazite is rare, and it was only observed in one sample from a highly sheared aegirine quartz vein.

Gadolinite is the dominant REE phase and commonly occurs in the quartz veins. It was identified from its stoichiometry using electron microprobe analyses (see below). Two types of gadolinite were observed in Dyaheen quartz veins: early and late gadolinite. The

early type is associated with fergusonite and displays oscillatory zoning that is clear in BSE images and WDS maps (Fig. 5.8 A). The late type occurs as overgrowths on the early type (Fig. 5.8 B and C). The zones in both types are defined by Y, Ce, Nd concentrations (Fig. 5.8 A). The late gadolinite contains numerous inclusions and veinlets of bastnasite, which occurs as veinlets at the rim or crosscutting gadolinite, and pyrochlore (Fig. 5.8 B and C).

Bastnasite is the second most common REE mineral. It occurs mainly in the quartz veins associated with gadolinite, pyrochlore and zircon. Bastnasite occurs as euhedral to subhedral prismatic crystals that are 100- 500 μm long and as veinlets in the gadolinite (Fig. 5.8 D).

5.5 Litho geochemistry

Representative whole-rock analyses for fresh host rock, mineralized granite, mineralized dykes, and veins from Dyaheen are given in Table 5.3. It should be noted that the monzogranite sample displays an intermediate to high level of weathering. The amphibole-biotite granite and the aegirine granite and show intermediate to low weathering, which mostly affected the feldspar and replaced to clay minerals.

The major oxide compositions of Dyaheen rocks from this study, as well as those from Moghazi et al. (2011) are shown in Figure 5.9. The major compositions of all oxides except Na_2O show a continuous trend from monzogranite to aegirine granite. The monzogranite composition from this work and Moghazi et al. (2011) shows a relatively high SiO_2 content, which could be related to the high degree of weathering observed in this rock. The contents of TiO_2 , Al_2O_3 , MgO , CaO , P_2O_5 , and to a lesser extent K_2O decrease with increasing SiO_2 , whereas Fe_2O_3 increases slightly (Fig. 5.9 A to H). Na_2O does not show a distinct trend. The trace element contents of the Dyaheen rock units generally increase from the monzogranite to the aegirine granite (Table 5.3). The average concentrations (here and below, \pm represents 1 σ standard deviations) of Zr, Nb, Y, and total REE (lanthanides) are 168 ± 82 ppm, 13 ± 6 ppm, 13 ± 6 ppm, and 138 ± 48 ppm; respectively, in the monzogranite (average monzogranite composition from this work and Moghazi et al., 2011), 745 ± 849 ppm, 37 ± 19 ppm, 63 ± 25 ppm, and 318 ± 198 ppm;

respectively, in the amphibole-biotite granite, and 2846 ± 1802 ppm, 68 ± 49 ppm, 190 ± 31 ppm, and 462 ± 74 ppm; respectively, in the aegirine granite. The plots of geochemically coherent elements Zr-Hf, Nb-Ta, and Y-Ho show positive correlation (Fig. 5.10 A to C). In a chondrite normalized REE diagram (Fig. 5.10 D), the monzogranite displays a negative slope with negative Eu anomaly (0.57; Boynton, 1984) and La/ Yb chondrite normalized ratio of 12.1. The amphibole-biotite granite and the aegirine granite show relatively similar slopes (Fig. 5.10 E) that are flat to slightly negative with La/ Yb chondrite normalized ratios ranging from 9.7 to 3.7 in the amphibole-biotite granite and from 4.1 to 0.74 in the aegirine granite. The amphibole-biotite granite and the aegirine granite REE patterns have pronounced negative Eu anomalies that range 0.41 to 0.14 in the amphibole-biotite granite and 0.16 to 0.13 in the aegirine granite. The Eu anomaly was plotted against La/Yb (chondrite normalized), CaO and Nb (Fig. 5.10 F to H), and the plots show positive correlations between La/Yb and CaO and Eu anomaly from the monzogranite to the amphibole-biotite granite and the aegirine granite, whereas Nb displays a negative correlation, which would be predicted from fractional crystallization process because it is an incompatible element. These correlations with Eu anomaly are less clear at low Eu values (< 0.2). The concentration of Ba shows a positive correlation with Sr with most of the monzogranite samples plotted at high Ba and Sr, whereas the aegirine granite and the amphibole-biotite plot at low values and are consistent with trends that would be predicted for fractionation crystallization of feldspar minerals.

In the aegirine dykes, trace elements concentrations increase significantly and are highly variable with average Zr, Nb, Y, and REE concentrations of 6419 ± 2970 , 1830 ± 1201 , 1266 ± 199 , and 10343 ± 3867 , respectively. In a chondrite normalized REE diagram (Fig. 5.10 E), the aegirine dykes displays a similar slope to the amphibole-biotite granite and the aegirine granite; however, it contains one order of magnitude more REE. The aegirine granite displays a negative Eu anomaly of 0.15 ± 0.01 and La/Yb chondrite normalized ratio of 7 ± 4 .

5.6 U-Pb zircon age dating

The age of the mineralization in Dyaheen was estimated from zircon clusters from quartz vein sample HDA11. Two types of zircon clusters were recognized, inclusion-free clear zircon clusters (V16) and dark-brown and inclusion-rich clusters (V10). The clear zircon locally contains cracks extended from the core to the rim (Fig. 5.11 A). The second cluster (V10) is inclusion-rich and highly porous and is inclusion-rich, which made the analyses challenging (Fig. 5.11 B). The age date was determined from the inclusion-free clear zircon. The $^{206}\text{Pb}/^{238}\text{U}$ versus $^{207}\text{Pb}/^{235}\text{U}$ isochron plot for the analyzed zircon is shown in Figure 5.11 (C). The estimated age of the clear zircon clusters 645 ± 70 Ma.

5.7 Mineral chemistry

5.7.1 Amphibole and aegirine

The compositions of amphibole and aegirine from the amphibole-biotite granite, pegmatite granite, aegirine granite, aegirine dykes, and aegirine from the quartz vein were obtained using EMPA and are summarized in Table 5.4. The amphibole mineral formula was calculated based on the general formula $\text{AB}_2\text{C}_5\text{T}_8\text{O}_{22}\text{W}_2$ where A= vacancy (\square), Na^+ , K^+ , Ca^{2+} , Pb^{2+} , Li^+ ; B= Na^+ , Ca^{2+} , Mn^{2+} , Mn^{3+} , Fe^{3+} , Al^{3+} , Ti^{4+} , Li^+ ; C= Zn , V^{3+} , Ni^{2+} , Sc^{3+} , Cr^{3+} , Zr^{4+} ; T= Si^{4+} , Al^{3+} , Ti^{4+} ; W= (OH), F, Cl, O^{2-} (Hawthorne et al., 2012), and using Locock (2014) Excel spreadsheet. The overall site occupancies are in agreement with the general formula except for the T site where it shows values > 8 , which could be related to an overestimation of SiO_2 . Moreover, A site shows an excess of Na, which is a problem that has been observed before in Jabal Sayid granite (Turkistany and Ramsay, 1982) and was attributed to Na and Ca into the C site.

The aegirine mineral formula was calculated based on the general formula $\text{M}_2\text{M}_1\text{T}_2\text{O}_6$ where M2= Na , Ca^{2+} , Li^+ , Mn^{2+} , Fe^{2+} , Mg^{2+} ; M1= Al^{3+} , Ti^{4+} , Fe^{3+} , Ti^{3+} , Zn^{2+} , Mg^{2+} , Fe^{2+} , Mn^{2+} ; T= Si^{4+} , Al^{3+} , Fe^{3+} (Morimoto, 1988) and the cations were calculated first by normalizing to 4 atoms then $\text{Fe}^{3+}/\text{Fe}^{2+}$ ratio was adjusted to achieve 6 oxygen total. The EMPA analyses display variable totals and < 100 that indicate the presence of other elements. However, a slow scan performed on the WDS crystals (TAP, LIF, LDE1, PETL) did not show the presence of any elements detectable by the EMP. Most of the

sites fulfilled the general formula cations siting except for M2 where it has > 1 cations total. This could be due to element that were not analyzed, such as Li.

The amphibole in the amphibole-biotite granite is arfvedsonite where $Mg/(Mg+Fe^{2+}) < 0.5$, $Al < Fe^{3+}$ and Si is > 7.5 all in atom per formula unit (a.p.f.u) (Hawthorne and Oberti, 2007). All trace elements are below the detection limit of the EMP. The main differences between amphibole from different rock units are their contents of Ca, Mg, Ti, and Al. Amphibole from the porphyritic amphibole-biotite granite is characterized by high Ca content relative to amphibole from other units and displays a negative correlation with Na, which increases to a maximum in the aegirine granite (Fig. 5.12 A).

The aegirine from the aegirine granite, aegirine dykes, and the quartz veins have comparable major element compositions. The only difference that may distinguish aegirine in different rock units from each other are Fe, Mn, Mg, and Zn (Fig 5.12 B). Aegirine from the quartz veins shows the highest Mn, Zn, and Mg and the lowest Fe. Locally, the rim of aegirine from the altered aegirine granite shows a comparable Fe to aegirine from the quartz vein (Fig 5.12 C). Moreover, Fe and Ti show a negative correlation where Ti increases with decreasing Fe.

5.7.2 Zircon

The composition of zircon from the altered aegirine granite, aegirine dykes, and quartz veins were obtained from EMP analyses of the major and trace elements, and LA-ICP-MS for trace elements (Table 5.5). The zircon mineral formula was calculated based on 4 oxygens according to the empirical zircon formula $Zr_1Si_1O_4$ (Speer, 1982). Hafnium can enter zircon structure by a simple substitution where 1 atom of Hf substitutes for 1 atom of Zr^{4+} (Hoskin, 2003), which stoichiometrically can be represented by $(Zr_{1-x}Hf_x)SiO_4$. A coupled substitution is common in zircon, where REE^{3+} and P^{5+} substitute for Zr^{4+} and Si^{4+} , which stoichiometrically can be represented by $(Zr_{1-x}REE_x)(Si_{1-y}P_y)O_4$ (Hoskin, 2003; Speer, 1982).

The composition of zircon from the altered aegirine granite is characterized by high SiO_2 , ZrO_2 , and HfO_2 , and very low trace element concentrations (Fig. 5.13 A). In contrast,

zircon from the aegirine dykes and quartz veins are characterized by high concentrations of trace elements where the aegirine dykes zircon show significantly higher concentrations relative to zircon from the quartz vein zircon (Fig. 5.13 A). In Figure 5.13 B, the plot of Hf with the Zr/Hf ratio shows the zircon from the aegirine granite has the highest Hf and the lowest Zr/Hf ratio, whereas zircon from the aegirine dykes and quartz veins have the lowest Hf contents and the highest Zr/Hf ratio. This diagram also compares the Zr-Hf composition of the zircon (symbols with black ring) with the host rock whole-rock analyses from which the zircon came (unfiled circles). Zircon from the aegirine dykes show Zr/Hf ratio that is much higher than the whole-rock, whereas zircon from the aegirine granite and quartz veins show similar Zr/Hf ratios. The total REE (Σ REE), Y, and P, in atom per formula unit (a.p.f.u), show a positive correlation with the Zr and Si (in a.p.f.u) contents of the zircon from the altered aegirine granite and quartz veins, whereas the aegirine dykes zircon show more complex substitution that involves Nb (up to 0.03 Nb a.p.f.u, Fig. 5.13 D and E). In a chondrite normalized REE diagram (Fig. 5.13 F), the majority of data points of zircon from the altered aegirine granite and quartz veins have positive slopes with positive Ce and Sm anomalies and negative Eu anomaly. The majority of the aegirine dykes zircon displays flat slopes with a negative Eu anomaly (Fig. 5.13 D). In order to distinguish magmatic and hydrothermal zircon, the discrimination diagrams of Hoskin, (2005) were used (Fig. 5.14). In Figure 5.14 (A), chondrite normalized ratios of Sm/LaN ($\text{Sm/LaN} = \text{Sm}_{\text{rock}}/\text{Sm}_{\text{chondrite}}/(\text{La}_{\text{rock}}/\text{La}_{\text{chondrite}})$) were plotted against $\text{Ce/Ce}^* (= [\text{Ce}_{\text{rock}}/\text{Ce}_{\text{chondrite}}] / \sqrt{((\text{La}_{\text{rock}}/\text{La}_{\text{chondrite}}) \times (\text{Pr}_{\text{rock}}/\text{Pr}_{\text{chondrite}}))})$ (chondrite values are from McDonough and Sun, 1995), and the data compared to magmatic zircon Types-1, 2, and hydrothermal zircon Type- 4 from Al-Ghurayyah (Chapter 3), and the hydrothermal zircon (Zircon-1,2, and 3) from Jabal Sayid (from Chapter 4). The zircon from the altered aegirine granite plot in the hydrothermal region and outside the hydrothermal region, forming a trend toward low Sm/LaN and Ce/Ce*. This trend also overlaps with the composition of Type-4 zircon from Al-Ghurayyah, and Zircon-1, 2, and 3 from Jabal Sayid. The aegirine dykes zircon and quartz veins zircon plot in, or near the hydrothermal region. In Figure 5.14 (B), most of the data plots in the area between the magmatic and hydrothermal regions and near magmatic zircon (Types-1

and 2 zircon) from the altered aegirine granite. The zircon from the aegirine dykes and quartz veins plot in or near the hydrothermal region.

5.7.3 Fergusonite and pyrochlore

The chemical compositions of fergusonite and pyrochlore obtained by EMPA are summarized in Table 5.6. The mineral stoichiometries were calculated by normalizing the B site according to the general fergusonite formula ABO_4 where A = REE, Y Ca, U, and Th, and B = Nb, Ta, and Ti (Tomašić et al., 2006). The total of A site ranged between 0.99 in the fresh parts of the crystals and 1.05 in the altered parts. Fergusonite displays oscillatory chemical zoning (Fig. 5.7 C), defined by the general increase in LREE (LREE = La, Ce, Pr, Nd, Eu, and Gd), U, and Th, and decreases in Y from cores to rims. The substitution is controlled by Y+HREE (HREE = Tb, Dy, Ho, Er, Tm, Yb, and Lu) for LREE (Fig. 5.15 A). At the altered rim, HREE content increases, whereas Y decreases, which could be due to alteration. In a chondrite normalized REE diagram (Fig. 5.15 B), fergusonite is characterized by a positive REE slope and concave HREE pattern due to low Yb and Lu concentrations in the fresh part. The part near the altered rim shows increases in Yb and Lu and has a steeper positive REE pattern. The concentrations of LREE increase from core to rim, whereas the altered zones generally show less enriched patterns and higher Yb and Lu concentrations.

Pyrochlore chemistry from the aegirine granite, aegirine dykes, pegmatite, and quartz vein are given in Table 5.6. The stoichiometry was calculated on the basis of two B-site cations according to the general formula of pyrochlore group minerals $A_{2-m}B_2X_{6-w}Y_{1-n} \cdot pH_2O$, where A = Na, Ca, Fe^{2+} , REE, Pb, Y, U, and Th; B = Nb, Ta, Ti, Al, Fe^{3+} , and Sn; X = O and OH; and Y = O, OH, and F, with $m = 0 - 1.7$, $w = 0 - 0.7$, and $n = 0 - 1$ are vacancies in A, X, and Y, respectively, and $p = 0 - 2$ H_2O molecules in defect pyrochlore (Lumpkin and Ewing, 1996). The dominant pyrochlore type is plumbopyrochlore, where Pb is the most abundant element in the A site other than Na and Ca (Hogarth, D, 1977) (Fig. 5.16). Other pyrochlore types include yttropyrochlore ($Y + \Sigma HREE > Ce + \Sigma LREE$) and ceriopyrochlore ($Ce + \Sigma LREE > Y + \Sigma HREE$). Moreover, in addition to high Pb concentrations in the late pyrochlore, it also contains higher Si concentration. The amounts of Nb and Y+REE in atom per formula unit decrease with

increasing Pb and Si (Fig. 5.17 A and B). Furthermore, the amount of vacancy in the A site decreases with increasing Pb and decreases with increasing Y and REE (HREE in particular) due to the valence difference between Pb^{2+} and $\text{REE}+\text{Y}^{3+}$ (Fig. 5.17 C to E). The main substitution mechanism in pyrochlore is demonstrated in Figure 5.17 (F) where $\text{Si}^{4+} + (\text{Pb}^{2+}, \text{Fe}^{3+}, \text{U}^{4+}) = (\text{Nb}^{5+}, \text{Ti}^{4+}, \text{Ta}^{5+}) + (\text{Ca}^{2+}, \Sigma\text{YREE}^{2+}, \text{vacancy})$.

5.7.4 REE minerals

Electron microprobe analyses of gadolinite and bastnasite from quartz veins are summarized in Table 5.7. The structural formula of gadolinite was calculated based on the general formula of gadolinite group minerals $\text{A}_2\text{M Q}_2\text{T}_2\text{O}_8(\text{O}, \text{OH}, \text{F})_2$ where A= REE, Y, Ca, U, Th, Pb, Mn and Na; and M= Fe, Mg, Cu, Al, Zn, and vacancy; Q= B, Be, and Li; T= Si, P, As, B, Be, and S (Bačík et al., 2017). The mineral was first identified by EDS and then analyzed by electron microprobe. The analytical totals were always low, which suggests the presence of other elements that were not analyzed. Thus, a slow scan was performed on the WDS crystals (TAP, LIF, LDE1, PETL) and did not show any elements that can be detectable by the EMP. The concentrations of other element concentrations match their concentrations in gadolinite. Moreover, Be is a major constituent of gadolinite, and it is not detectable by the EMP. Thus, Be concentration was estimated based on 1:1 ratio of Si to Be. The formula was calculated by normalizing Si to 2 atoms and normalized A and M sites according to Si atoms. The M site has a total <1, which represents vacancy in this site (Demartin et al., 1993; Lyalina et al., 2014).

Bastnasite mineral formula was calculated by normalizing the total cations to 1 assuming full occupancy $\text{REE}(\text{CO}_3)\text{F}$ (Voncken, 2016). The concentration of CO_2 was estimated by difference.

The early gadolinite is characterized by alternating zones defined by Y + HREE and LREE (Fig 5.8 A to C). This type has higher Ca relative to the late type. The late gadolinite is less-well zoned and commonly occurs at the rim of the early type and shows wide zoning defined by Ca and LREE. Late gadolinite in the deformed quartz veins is the dominant type where the early type is replaced by the late type (Fig. 5.8 B). Generally, the early gadolinite has high LREE and low HREE relative to the late type; however, Ce

concentrations in both types are comparable (Fig. 5.17 A). In a chondrite normalized REE diagram (Fig. 5.18 B), early gadolinite shows a flat to slightly positive REE pattern with a normalized La/Yb ratio ranging between 0.1 to 1.7 and an Eu anomaly of between 0.08 and 0.17. The late type has higher Yb and Lu values, thus indicating a less fractionated pattern with a normalized La/Yb ranging from 0.12 to 0.2 and an Eu anomaly ranging from 0.09 to 0.14 (Fig. 5.17 B).

Bastnasite is Ce-rich in addition to other LREE where their concentration follow the order Ce > Nd > La > Sm > Pr > Gd > Eu. The total HREE concentrations in bastnasite is 2.0 wt. %, and the average Y₂O₃ is 3.1 wt. %. The compositions of bastnasite veinlets in gadolinite and bastnasite crystals are nearly identical. The REE chondrite normalized pattern of bastnasite shows a negative slope with an average La/Yb ratio of 74.2 ± 39 and Eu anomaly of 0.14 ± 0.03 (Fig. 5.18 C).

5.8 Discussion

The alkaline nature of Dyaheen granites is demonstrated by the low aluminum saturation index (ASI) ranging from 0.83 to 1 in the aegirine granite and from 1.02 to 1.11 in the amphibole-biotite granite, where ASI = the molar ratio of Al/(Na+K) (Shand, 1943). Moreover, the presence of alkali-minerals, such as arfvedsonite, and aegirine, in addition to the high concentrations of Nb, Zr, Y, and REE (specially, Nb and Y), are characteristic features of A-type alkaline granite (Dostal, 2016; Küster, 2009; Salvi and Williams-Jones, 2005; Sorensen, 1992; Yang et al., 2014). The age of the granite was previously estimated from the U-Pb isotope analyses of zircon to be 625 ± 11 Ma for the amphibole-biotite granite, and 613 ± 4 Ma for a monzogranite (Ali et al., 2014). In the present study, the age of the mineralization was estimated from zircon from quartz veins, which yielded an age of 645 ± 70 Ma. This shows that the mineralization and the granite emplacement are, within error, coeval. Moreover, the estimated age of the nearby Jabal Sayid deposits, located 30 km southeast Dyaheen, is 593.4 ± 2.4 Ma, which is within the error range of Dyaheen ring complex, consistent with the interpretation that both deposits are part of Jabal Sayid complex (Radain, 1979). The mineralization in Dyaheen shares some characteristics of the mineralization in Jabal Sayid in terms of the common occurrence of late aegirine and mineralization within aegirine-rich dykes and quartz veins. However,

Dyaheen mineralization lacks the hematization observed in Jabal Sayid. The common presence of hydrothermal perthite and the ductile deformation observed in the quartz veins that crosscut the aegirine granite indicate that the mineralization was formed at high temperature and probably at the late-magmatic to early-hydrothermal stage. Therefore, Dyaheen Jabal Sayid might represent different transitional to hydrothermal stages in which Dyaheen represents an early hydrothermal stage, and Jabal Sayid represents a more advanced hydrothermal stage.

5.8.1 Magmatic evolution

The Dyaheen major oxide compositions display a progressive evolution toward the rim of the complex (Fig. 5.9 and Table 5.8). The decreases in the Al, Ca, Mg, and Ti oxides with increasing silica content from the monzogranite to the amphibole-biotite granite and aegirine granite suggest that the evolution of the Dyaheen was mostly controlled by the fractionation of feldspar, titanite, and Mg-rich phases, such as biotite and amphibole (Rollinson, 2014). Moreover, in the Quartz-Albite-Orthoclase (Qtz-Ab-Or) normative composition (Fig. 5.19 A), most of the monzogranite samples lie at the fluorine-free minimum and trend toward a higher F concentration. This supports magmatic crystallization because the concentration of volatiles increases with magma evolution (Baker and Alletti, 2012; London et al., 1988; Manning, 1981). Furthermore, in Figure 2.10 (D and E), the progressive increase in Eu anomaly from the monzogranite to the aegirine granite indicates feldspar fractionation (Harris et al., 1986; Hassanen, 1997; Qiu et al., 2019).

The effect of feldspar fractionation on the magma trace element content can be seen in Figure 5.10 (I and J). Strontium shows a positive correlation with the Eu anomaly. Moreover, Sr and Ba show a positive correlation, which suggests that plagioclase and K-feldspar crystallization played a major role in the magma evolution. In order to quantitatively evaluate the degree of feldspar fractionation, Sr and Ba are modeled assuming perfect Rayleigh fractionation. The average composition of the monzogranite from this work and Moghazi et al. (2011) was used as the initial composition. The values of partitioning coefficients (D) are from Nash and Crecraft (1985) for plagioclase (An_{30}) and K-feldspar (Table 5.8). In Figure 5.19 (B), Dyaheen samples form a straight line

between monzogranite and aegirine granite. The diagram shows that the formation of the aegirine granite from the monzogranite requires 40 to 50 % feldspar fractionation, whereas for the amphibole-biotite granite it ranges from less than 10% up to 40 % feldspar fractionation (the average composition is plotted at 30 %). Furthermore, the calculated Eu anomaly assuming 20 % feldspar fractionation is comparable to the value of the amphibole-biotite, whereas at 40 % feldspar fractionation, the value is similar to the aegirine granite (Fig. 5.19 C, and Table 5.8). However, the degree of REE enrichment, especially HREE, which led to the flat REE pattern in the amphibole-biotite granite and aegirine granite cannot be reproduced by feldspar fractionation. The flat REE pattern could be explained by: 1) early fractionation of a LREE-rich phase that depleted the residual melt in LREE, or 2) metasomatic alteration and/or the formation of late-stage REE phases. Apatite is a common early magmatic phase in the monzogranite and amphibole-granite, which could control LREE content. Similar observations have been reported from other granitic rocks (Condie, 1978; Hassanen, 1997; Miller and Mittlefehldt, 1982; Taylor et al., 1981) and these authors suggested that this pattern is due to the crystallization of monazite and allanite, which depleted the residual melt in LREE. However, this does not explain the enrichment of HREE relative to LREE and the narrow range of enrichment of LREE compared to the wide range of enrichment of HREE. Enrichment of HREE elsewhere was attributed to interaction with volatiles, especially F in the melt. (Hassanen, 1997; Monecke et al., 2002). Although the decrease in La/Yb_N and CaO, and the increase in Nb with decreasing Eu anomaly support a magmatic process, at low Eu anomaly values (<0.2) the magmatic trends are not clear, and the data points are scattered, which suggests a non-magmatic behavior (Fig. 5.10 F to H). In the amphibole-biotite, some amphibole underwent fluorite-hematite alteration and crystallization of zircon (Fig. 5.4 J to N). Zircon is known to have HREE mineral/melt partitioning coefficients > 22 (Thomas et al., 2002). Zircon in the aegirine granite is also associated with hematization. The composition of zircon and the morphology indicate that it was formed in late-magmatic to hydrothermal conditions (discussed below). The presence of aegirine in the quartz veins and the aegirine dykes suggests that aegirine is a late phase. Additionally, aegirine occurs as inclusions in zircon from the quartz veins. The comparable aegirine composition from the altered and fresh aegirine granites (with

fresh amphibole replaced by aegirine) and the aegirine from quartz veins and aegirine dykes (Fig. 5.12 B and C) support the formation of aegirine from a late-magmatic to hydrothermal environment. Thus, the aegirine granite is interpreted to represent a metasomatized granite.

5.8.2 Mineralization

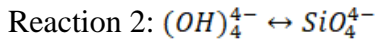
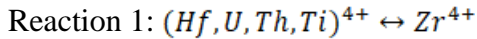
5.8.2.1 Zircon crystallization environment

Zircon is a common mineral associated with other HFSE-bearing minerals in Dyaheen. Moreover, zircon can host significant concentrations of trace elements. Therefore, the crystallization of zircon impacts the behavior of trace elements (Belousova et al., 2002) thus, zircon chemistry can reflect the environment of crystallization.

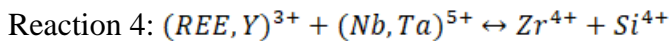
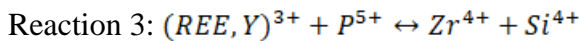
Zircon morphology and chemistry have been used to study changes in crystallization environment (Corfu et al., 2003; Erdmann et al., 2013; Fu et al., 2009; Hoskin and Schaltegger, 2003; Pupin, 1980; Schaltegger, 2007). Zircon in Dyaheen is abundant in the altered aegirine and amphibole-biotite granites in addition to the aegirine dykes and quartz veins. In unaltered rock, zircon is present as small ($\approx 10 \mu\text{m}$) prismatic crystals that show oscillatory zoning (Fig 5.6 A and B). The prismatic shape, oscillatory zoning, and the intergranular texture indicate that it was formed in a magmatic environment (Corfu et al., 2003; Pidgeon, 1992; Silver and Deutsch, 1963). By contrast, zircon from the aegirine dykes, quartz veins, and altered aegirine granite are anhedral to subhedral equant crystals, lack or show patchy zoning and have a spongy texture with abundant fluid and mineral inclusions (Fig. 5.6 C to J). These are characteristic features of hydrothermal zircon or magmatic zircon that has undergone interaction with a fluid phase (Schaltegger, 2007).

The trace element contents in zircon have been used to discriminate hydrothermal and magmatic zircon signatures (Chen and Zhou, 2017; Corfu et al., 2003; Fu et al., 2009; Hoskin, 2005; Hoskin and Schaltegger, 2003; Pettke et al., 2005; Schaltegger, 2007; Wu et al., 2018; Yang et al., 2014). The incorporation of trace elements in zircon can occur through:

simple substitution



or coupled substitution



(Hoskin and Schaltegger, 2003; and references therein). Several studies on distinguishing magmatic and hydrothermal zircon have shown that hydrothermal zircon has higher abundances of non-essential elements, higher LREE concentrations, and lack a Ce anomaly (Belousova et al., 2006; Feng, 2014; Fu et al., 2009; Hoskin and Schaltegger, 2003; Wu et al., 2018). Zircon in the altered aegirine granite, aegirine dykes, and quartz veins show distinct mineral compositions (Fig. 5.13). Zircon from the altered aegirine granite show the lowest concentrations of non-essential elements and the highest Si, Zr, and Hf contents (Fig. 5.13 A). In Figure 5.13 (B), Zr/Hf ratio and Hf have a negative correlation showing zircon from the aegirine granite with low Zr/Hf ratio and zircon from the aegirine dykes and quartz veins with high Zr/Hf ratio. The high Zr/Hf ratio of aegirine dykes relative to the whole-rock suggests that this ratio is controlled by a phase (or phases) other than zircon. Zirconium concentration in aegirine can reach up to weight percent levels (Dyulgerov and Platevoet, 2006; Kogarko, 2016; Njonfang and Nono, 2003) and the partitioning coefficient of Hf between aegirine and alkaline granitic melt is greater than that of Zr (Kogarko, 2016). The high Zr/Hf ratio in zircon from the aegirine dykes suggests that aegirine formed earlier than zircon, which led to the increase in Zr/Hf ratio of the residual melt/fluid at the late-magmatic to early-hydrothermal stage. If, zircon crystallized after aegirine, the Zr/Hf ratio would be high. This timing is supported by aegirine inclusions in zircon from the quartz veins (Fig. 5.6 K).

Figure 9.13 (C) illustrates that trace element substitutions in zircon from the altered aegirine granite and quartz veins occurred via coupled substitution $(\text{REE}, \text{Y})^{3+} + \text{P}^{5+} \leftrightarrow \text{Zr}^{4+} + \text{Si}^{4+}$. Zircon from the aegirine dykes show a more complex substitution mechanism involving other trace elements $(\text{REE}, \text{Y})^{3+} + \text{Nb}^{5+} + \text{Ta}^{5+} \leftrightarrow \text{Zr}^{4+} + \text{Si}^{4+}$ (Fig. 5.13 D). The chondrite-normalized REE pattern for zircon shows distinct patterns (Fig. 5.13 E). Zircon from the altered aegirine granite and most of the zircon from the quartz vein have positive REE trends with variable positive Ce anomalies. Zircon from the aegirine dykes have a flat to a slightly positive REE pattern similar to patterns commonly reported for hydrothermal zircon (Hoskin, 2005; Kebede et al., 2007; Pettke et al., 2005; Wu et al., 2018). Although zircon from the altered aegirine granite and quartz veins show low LREE content and positive Ce anomaly, their morphology and their host rock mineral composition (hosted by quartz veins and altered aegirine granite) suggest that they are of a hydrothermal origin or were affected by hydrothermal fluids. Pettke et al. (2005) reported an indistinguishable positive Ce anomaly and REE pattern from hydrothermal zircon and late magmatic zircon. The zircon diagrams of Hoskin (2005) were used for additional discrimination between the zircon types (Fig. 5.14). The compositions of zircon from Al-Ghurayyah and Jabal Sayid were also plotted for comparison. All zircon types plotted inside or near the hydrothermal field and away from the magmatic field. This further supports the morphological and textural observations that indicate that these zircon formed in late-magmatic to metasomatic environments. Zircon from quartz veins and aegirine dykes show the most distinct hydrothermal characteristics in both chemical compositions and textural relationships and, given the mode of occurrence of the vein hosted zircon, have an indisputable hydrothermal origin. The high trace element concentrations, such as LREE, Nb, and Ta in the zircon from the aegirine dykes, suggest their high abundances in the metasomatic environment from which this zircon has crystallized.

5.8.2.2 Evolution of mineralization

The main mineralization in Dyaheen is concentrated in the aegirine granite, aegirine dykes, and quartz veins. Disseminated mineralization is observed in the amphibole granite, where zircon and bastnasite have replaced amphibole. The common presence of

perthite in aegirine dykes and in quartz veins suggests the formation at high temperature (Bowen and Tuttle, 1950). In this stage, REE and HFSE are controlled by early formed phases zircon, fergusonite, gadolinite, and pyrochlore \pm monazite, which were later replaced by bastnasite and britholite. This stage is generally not preserved in similar rare-metal alkaline granites, such as Strange Lake and Khaldzan-Buregtey (Kovalenko et al., 2007; Miller, 1996; Salvi and Williams-Jones, 1996, 1991).

According to the textural and mineral relationships of HFSE and REE minerals, there are at least three main mineralization stages. These stages can be seen clearly in the early crystallized phases, such as fergusonite (first stage), which is usually replaced by Pb-pyrochlore (second stage) during subsequent hydrothermal events. Fergusonite also occurs in pegmatites where it shows the same morphology and replacement by Pb-pyrochlore (Fig. 5.7 B), which also supports the early crystallization of fergusonite. The first stage shows an increase in LREE concentrations indicated by zoning in fergusonite (Fig. 5.7 C). The gadolinite associated with fergusonite is also zoned and shows the same trend of increasing LREE toward the rim (Fig. 5.8 A and C). This trend is expected as the early crystallizing phases are HREE-rich phases, such as zircon, fergusonite, and gadolinite (Tables 5, 6, and 7). The second stage is marked by the alteration of fergusonite and the crystallization of Pb-pyrochlore (Fig. 5.7 C). The fergusonite rim near the Pb-rich pyrochlore shows increases in HREE contents whereas Y decreased. This stage also led to the crystallization of the late gadolinite that is HREE enriched (Fig. 5.8 A to C and Fig. 5.18 A and B). The third stage is demonstrated by the formation of bastnasite as veinlets in gadolinite and as individual crystals in quartz veins (Fig. 5.8 B to D).

5.9 Conclusion

Dyaheen ring complex shows a typical A-type alkaline rock chemical signature that is characterized by low Ca, Mg, and P and high Fe, Nb, Zr, Y, and REE. The estimated age of the mineralization indicates that mineralization is cogenetic with the host granites. The progressively more developed Eu anomaly in addition to the strong correlation between Sr and Ba suggest a major role of feldspar fraction in the evolution of the Dyaheen ring complex. Feldspar fractionation modeling suggests that the development of amphibole-

biotite melt from the monzogranite requires 10 to 20 % feldspar fractionation, whereas aegirine granite requires up to 40 % feldspar fraction. The fractionation model reproduced the Eu anomalies in the amphibole-biotite granite and the aegirine granite. However, the amount of REE enrichment, HREE in particular, cannot be reproduced only by feldspar fractional crystallization. The possible cause of the enrichment in REE concentration is interaction with fluid phases during a late-magmatic to post-magmatic stage. This is manifested by the alteration of amphibole and the formation of secondary zircon that are associated with hematite and fluorite. Moreover, the composition of aegirine from the aegirine granite is comparable to the aegirine from the quartz veins, which indicate that aegirine is a metasomatic phase. The mineralization event took place at high temperatures that might be at a late-magmatic to early hydrothermal stage. Based on the morphology of ore minerals, the mineralization took place in three stages. The first stage occurred during late-magmatic to early hydrothermal conditions by the crystallization of fergusonite, zircon, and early gadolinite. The second stage is manifested by the alteration of fergusonite to Pb-pyrochlore and the alteration of early gadolinite to HREE-rich late gadolinite. The third stage is marked by the crystallization of bastnasite as veinlets in the late gadolinite or as individual crystals.

5.10 References

- Ali, K.A., Jeon, H., Andresen, A., Li, S.-Q., Harbi, H.M., Hegner, E., 2014. U–Pb zircon geochronology and Nd–Hf–O isotopic systematics of the Neoproterozoic Hadb adh Dayheen ring complex, Central Arabian Shield, Saudi Arabia. *Lithos*.
<https://doi.org/10.1016/j.lithos.2014.07.030>
- Bačík, P., Miyawaki, R., Atencio, D., Cámara, F., Fridrichová, J., 2017. Nomenclature of the gadolinite supergroup. *Eur. J. Mineral.* 29, 1067–1082.
<https://doi.org/10.1127/ejm/2017/0029-2659>
- Baker, D.R., Alletti, M., 2012. Fluid saturation and volatile partitioning between melts and hydrous fluids in crustal magmatic systems: The contribution of experimental measurements and solubility models. *Earth-Science Rev.* 114, 298–324.
<https://doi.org/10.1016/j.earscirev.2012.06.005>

- Belousova, E. a., Griffin, W.L., O'Reilly, S.Y., 2006. Zircon crystal morphology, trace element signatures and Hf isotope composition as a tool for oetrogenetic modelling: Examples from Eastern Australian granitoids. *J. Petrol.* 47, 329–353.
<https://doi.org/10.1093/petrology/egi077>
- Belousova, E.A., Griffin, W.L., O'Reilly, S.Y., Fisher, N.I., 2002. Igneous zircon: Trace element composition as an indicator of source rock type. *Contrib. to Mineral. Petrol.* 143, 602–622. <https://doi.org/10.1007/s00410-002-0364-7>
- Boily, M., Williams-Jones, A. E., 1994a. The role of magmatic and hydrothermal processes in the chemical evolution of the Strange Lake plutonic complex, Quebec-Labrador. *Contrib. to Mineral. Petrol.* 118, 33–47.
<https://doi.org/10.1007/BF00310609>
- Boily, M., Williams-Jones, A.E., 1994b. The role of magmatic and hydrothermal processes in the chemical evolution of the Strange Lake plutonic complex, Quebec-Labrador. *Contrib. to Mineral. Petrol.* <https://doi.org/10.1007/BF00310609>
- Bowen, N.L., Tuttle, Of., 1950. The System NaAlSi₃O₈-KAlSi₃O₈-H₂O. *J. Geol.* 58, 489–511.
- Boynton, W. V., 1984. Cosmochemistry of the Rare Earth Elements: Meteorite Studies. *Dev. Geochemistry* 2, 63–114. <https://doi.org/10.1016/B978-0-444-42148-7.50008-3>
- Brun, J.P., Pons, J., 1981. Strain patterns of pluton emplacement in a crust undergoing non-coaxial deformation, Sierra Morena, Southern Spain. *J. Struct. Geol.* 3, 219–229. [https://doi.org/10.1016/0191-8141\(81\)90018-3](https://doi.org/10.1016/0191-8141(81)90018-3)
- Chen, W.E.I.T.E.I.T., Zhou, M.-F., 2017. Hydrothermal alteration of magmatic zircon related to NaCl-rich brines: Diffusion-reaction and dissolution-reprecipitation processes. *Am. J. Sci.* 317, 177–215. <https://doi.org/10.2475/02.2017.02>
- Condie, K.C., 1978. Geochemistry of Proterozoic granitic plutons from New Mexico, U.S.A. *Chem. Geol.* 21, 131–149. [https://doi.org/10.1016/0009-2541\(78\)90010-4](https://doi.org/10.1016/0009-2541(78)90010-4)
- Corfu, F., Hanchar, J.M., Hoskin, P.W.O., Kinny, P., 2003. Atlas of zircon textures. *Rev.*

- Mineral. Geochemistry 53, 469–500. <https://doi.org/10.2113/0530469>
- Demartin, F., Pilati, T., Diella, V., 1993. A CRYSTAL.CHEMICAL INVESTIGATION OF ALPINE GADOLINIT. *Can. Mineral.* 30, 127–136.
- Dostal, J., 2016. Rare metal deposits associated with alkaline/peralkaline igneous rocks. *Rev. Econ. Geol* 18, 33–54.
- Dyulgerov, M.M., Platevoet, B., 2006. Unusual Ti and Zr aegirine-augite and potassic magnesio-arfvedsonite in the peralkaline potassic oversaturated Buhovo-Seslavytzi complex , Bulgaria 127–138. <https://doi.org/10.1127/0935-1221/2006/0018-0127>
- Erdmann, S., Wodicka, N., Jackson, S.E., Corrigan, D., 2013. Zircon textures and composition: refractory recorders of magmatic volatile evolution? *Contrib. to Mineral. Petrol.* 165, 45–71. <https://doi.org/10.1007/s00410-012-0791-z>
- Feng, Y., 2014. Hydrothermal geochemistry and mineralizing processes in the T Zone , Thor Lake Rare-element deposit , Northwest Territories 341.
- Feng, Y., Samson, I.M., 2015. Replacement processes involving high field strength elements in the T Zone, Thor Lake rare-metal deposit. *Can. Mineral.* 53, 31–60. <https://doi.org/10.3749/canmin.1400028>
- Fu, B., Mernagh, T.P., Kita, N.T., Kemp, A.I.S., Valley, J.W., 2009. Distinguishing magmatic zircon from hydrothermal zircon: A case study from the Gidginbung high-sulphidation Au-Ag-(Cu) deposit, SE Australia. *Chem. Geol.* 259, 131–142. <https://doi.org/10.1016/j.chemgeo.2008.10.035>
- Gysi, A.P., Williams-Jones, A.E., 2013. Hydrothermal mobilization of pegmatite-hosted REE and Zr at Strange Lake, Canada: A reaction path model. *Geochim. Cosmochim. Acta* 122, 324–352. <https://doi.org/10.1016/j.gca.2013.08.031>
- Harris, N.B.W., Marzouki, F.M.H., Ali, S., 1986. The Jabel Sayid complex, Arabian Shield: geochemical constraints on the origin of peralkaline and related granites. *J. Geol. Soc. London.* 143, 287–295. <https://doi.org/10.1144/gsjgs.143.2.0287>
- Hassanen, M.A., 1997. Post-collision, A-type granites of Homrit Waggat Complex,

- Egypt: Petrological and geochemical constraints on its origin. *Precambrian Res.* 82, 211–236.
- Hawthorne, F.C., Oberti, R., 2007. Classification of the amphiboles. *Rev. Mineral. Geochemistry* 67, 55–88. <https://doi.org/10.2138/rmg.2007.67.2>
- Hawthorne, F.C., Oberti, R., Harlow, G.E., Maresch, W. V., Martin, R.F., Schumacher, J.C., Welch, M.D., 2012. Ima report: Nomenclature of the amphibole supergroup. *Am. Mineral.* 97, 2031–2048. <https://doi.org/10.2138/am.2012.4276>
- Hogarth, D. D., 1977. Classification and nomenclature of the pyrochlore group. *Am. Mineral.* 62, 403–410.
- Hoskin, P.W.O., 2005. Trace-element composition of hydrothermal zircon and the alteration of Hadean zircon from the Jack Hills, Australia. *Geochim. Cosmochim. Acta* 69, 637–648. <https://doi.org/10.1016/j.gca.2004.07.006>
- Hoskin, P.W.O., Schaltegger, U., 2003. The composition of zircon and igneous and metamorphic petrogenesis. *Rev. Mineral. Geochemistry* 53, 27–62. <https://doi.org/10.2113/0530027>
- Jackson, N.J., 1986. Mineralization associated with felsic plutonic rocks in the Arabian Shield. *J. African Earth Sci.* 4, 213–227. [https://doi.org/10.1016/S0899-5362\(86\)80083-5](https://doi.org/10.1016/S0899-5362(86)80083-5)
- Kebede, T., Horie, K., Hidaka, H., Terada, K., 2007. Zircon “microvein” in peralkaline granitic gneiss, western Ethiopia: Origin, SHRIMP U-Pb geochronology and trace element investigations. *Chem. Geol.* 242, 76–102. <https://doi.org/10.1016/j.chemgeo.2007.03.014>
- Kogarko, L.N., 2016. Geochemistry of fractionation of coherent elements (Zr and Hf) during the profound differentiation of peralkaline magmatic systems: A case study of the Lovozero Complex. *Geochemistry Int.* 54, 1–6. <https://doi.org/10.1134/S0016702916010079>
- Kovalenko, V.I., 1995. The peralkaline granite-related Khaldzan-Buregtey rare metal (Zr, Nb, REE) deposit, western Mongolia. *Econ. Geol.* 90, 530–547.

<https://doi.org/10.2113/gsecongeo.90.3.530>

Kovalenko, V.I., Yarmolyuk, V. V., Kozlovsky, a. M., Kovach, V.P., Sal'nikova, E.B., Kotov, a. B., Vladykin, N. V., 2007. Two types of magma sources of rare-metal alkali granites. *Geol. Ore Depos.* 49, 442–466.

<https://doi.org/10.1134/S1075701507060025>

Kröner, A., Stern, R.J., 2005. AFRICA | Pan-African Orogeny. *Encycl. Geol.* 1, 1–12.

<https://doi.org/10.1016/B0-12-369396-9/00431-7>

Küster, D., 2009. Granitoid-hosted Ta mineralization in the Arabian-Nubian Shield: Ore deposit types, tectono-metallogenetic setting and petrogenetic framework. *Ore Geol. Rev.* 35, 68–86. <https://doi.org/10.1016/j.oregeorev.2008.09.008>

Linnen, R.L., Samson, I.M., Williams-Jones, A.E., Chakhmouradian, A.R., 2014.

Geochemistry of the rare-earth element, Nb, Ta, Hf, and Zr deposits, in: *Treatise on Geochemistry*. Elsevier, pp. 543–568. <https://doi.org/10.1016/B978-0-08-095975-7.01124-4>

Locock, A.J., 2014. An Excel spreadsheet to classify chemical analyses of amphiboles following the IMA 2012 recommendations. *Comput. Geosci.* 62, 1–11.

<https://doi.org/10.1016/j.cageo.2013.09.011>

London, D., Hervig, R.L., Morgan, G.B., 1988. Melt-vapor solubilities and elemental partitioning in peraluminous granite-pegmatite systems: experimental results with Macusani glass at 200 MPa. *Contrib. to Mineral. Petrol.* 99, 360–373.

<https://doi.org/10.1007/BF00375368>

Lumpkin, G.R., Ewing, R.C., 1996. Geochemical alteration of pyrochlore group minerals: Betafite subgroup. *Am. Mineral.* 81, 1237–1248.

Lyalina, L.M., Selivanova, E.A., Savchenko, Y.E., Zozulya, D.R., Kadyrova, G.I., 2014. Minerals of the gadolinite-(Y)-hingganite-(Y) series in the alkali granite pegmatites of the Kola Peninsula. *Geol. Ore Depos.* 56, 675–684.

<https://doi.org/10.1134/S1075701514080042>

Manning, D. a. C., 1981. The effect of fluorine on liquidus phase relationships in the

- system Q-Ab-Or with excess water at 1 kb. *Contrib. Miner. Pet.* 76, 205–215.
- Marks, M.A.W., Markl, G., 2017. A global review on agpaitic rocks. *Earth-Science Rev.* 173, 229–258. <https://doi.org/10.1016/j.earscirev.2017.06.002>
- Miller, C.F., Mittlefehldt, D.W., 1982. Depletion of light rare-earth elements in felsic magmas. *Geology* 10, 129–133.
- Miller, R.R., 1996. Structural and textural evolution of the strange Lake Peralkaline rare-element (NYF) granitic pegmatite, Quebec-Labrador. *Can. Mineral.* 34, 349–371.
- Moghazi, A.-K.M., Iaccheri, L.M., Bakhsh, R.A., Kotov, A.B., Ali, K.A., 2015. Sources of rare-metal-bearing A-type granites from Jabel Sayed complex, Northern Arabian Shield, Saudi Arabia. *J. Asian Earth Sci.* 107, 244–258. <https://doi.org/10.1016/j.jseaes.2015.04.042>
- Moghazi, A.M., Harbi, H.M., Ali, K.A., 2011. Geochemistry of the Late Neoproterozoic Hadb adh Dayheen ring complex, Central Arabian Shield: Implications for the origin of rare-metal-bearing post-orogenic A-type granites. *J. Asian Earth Sci.* 42, 1324–1340. <https://doi.org/10.1016/j.jseaes.2011.07.018>
- Möller, P., Černý, P., Saupe, F., 1989. Rare earth mineral deposits and their industrial importance, in: *Lanthanides, Tantalum and Niobium*. Springer Berlin Heidelberg, Berlin, Heidelberg, pp. 171–188. https://doi.org/10.1007/978-3-642-87262-4_6
- Möller, V., Williams-Jones, A.E., 2017. Magmatic and hydrothermal controls on the mineralogy of the Basal Zone, Nechalacho REE-Nb-Zr Deposit, Canada. *Econ. Geol.* 112, 1823–1856. <https://doi.org/10.5382/econgeo.2017.4531>
- Möller, V., Williams-Jones, A.E., 2016. Petrogenesis of the Nechalacho Layered Suite, Canada: Magmatic evolution of a REE–Nb-rich nepheline syenite intrusion. *J. Petrol.* 57, 229–276. <https://doi.org/10.1093/petrology/egw003>
- Monecke, T., Kempe, U., Monecke, J., Sala, M., Wolf, D., 2002. Tetrad effect in rare earth element distribution patterns: A method of quantification with application to rock and mineral samples from granite-related rare metal deposits. *Geochim. Cosmochim. Acta* 66, 1185–1196. [https://doi.org/10.1016/S0016-7037\(01\)00849-3](https://doi.org/10.1016/S0016-7037(01)00849-3)

- Morimoto, N., 1988. Nomenclature of Pyroxenes. *Mineral. Petrol.* 39, 55–76.
<https://doi.org/10.1007/BF01226262>
- Nash, W.P., Crecraft, H.R., 1985. Partition coefficients for trace elements in silicic magmas. *Geochim. Cosmochim. Acta* 49, 2309–2322. [https://doi.org/10.1016/0016-7037\(85\)90231-5](https://doi.org/10.1016/0016-7037(85)90231-5)
- Njonfang, E., Nono, A., 2003. Clinopyroxene from some felsic alkaline rocks of the Cameroon Line , central Africa : petrological implications 15, 527–542.
<https://doi.org/10.1127/0935-1221/2003/0015-0527>
- Paton, C., Hellstrom, J., Paul, B., Woodhead, J., Hergt, J., 2011. Iolite: Freeware for the visualisation and processing of mass spectrometric data. *J. Anal. At. Spectrom.* 26, 2508–2518.
- Pettke, T., Audétat, A., Schaltegger, U., Heinrich, C. a., 2005. Magmatic-to-hydrothermal crystallization in the W-Sn mineralized Mole Granite (NSW, Australia). Part II: Evolving zircon and thorite trace element chemistry. *Chem. Geol.* 220, 191–213.
<https://doi.org/10.1016/j.chemgeo.2005.02.017>
- Pidgeon, R.T., 1992. Recrystallisation of oscillatory zoned zircon: some geochronological and petrological implications. *Contrib. to Mineral. Petrol.* 110, 463–472. <https://doi.org/10.1007/BF00344081>
- Piilonen, P.C., McDonald, A.M., Poirier, G., Rowe, R., Larsen, A.O., 2012. The mineralogy and crystal chemistry of alkaline pegmatites in the Larvik Plutonic Complex, Oslo rift valley, Norway. Part 1. Magmatic and secondary zircon: implications for petrogenesis from trace-element geochemistry. *Mineral. Mag.* 76, 649–672. <https://doi.org/10.1180/minmag.2012.076.3.15>
- Pupin, J.P., 1980. Zircon and granite petrology. *Contrib. to Mineral. Petrol.* 73, 207–220.
<https://doi.org/10.1007/BF00381441>
- Qiu, K., Yu, H., Wu, M., Geng, J., Ge, X., Gou, Z., Taylor, R.D., 2019. Discrete Zr and REE mineralization of the Baerzhe rare-metal deposit, China. *Am. Mineral.* 104, 1487–1502. <https://doi.org/10.2138/am-2019-6890>

- Radain, A., 1979. Petrogenesis of Some Pearalkaline and Non-peralkaline Post-tectonic Granite in The Arabian Shield. The University of Western Ontario.
- Rollinson, H.R., 2014. Using geochemical data: evaluation, presentation, interpretation. Routledge.
- Salvi, Stefano, Fontan, F., Monchoux, P., Williams-Jones, a. E., Moine, B., 2000. Hydrothermal mobilization of high field strength elements in Alkaline Igneous Systems: Evidence from the Tamazeght complex (Morocco). *Econ. Geol.* 95, 559–575. <https://doi.org/10.2113/gsecongeo.95.3.559>
- Salvi, S, Fontan, F., Monchoux, P., Williams-Jones, A., Moine, B., 2000. Hydrothermal Mobilisation of High Field Strength Elements in Alkaline Igenous Systems: Evidence from the Tamazeght Complex (Morocco). *Econ. Geol.* 95 SRC-, 559–576.
- Salvi, S., Williams-jones, A.E., 2005. Alkaline granite-syenite deposits, in: Linnen, R.L., Samson, I.M. (Eds.), *Rare-Elements Geochemistry and Mineral Depoists*. Geological Asociation of Canada, St. Catharine, p. 315.
- Salvi, S., Williams-Jones, A.E., 1996. The role of hydrothermal processes in concentrating high-field strength elements in the Strange Lake peralkaline complex, northeastern Canada. *Geochim. Cosmochim. Acta* 60, 1917–1932. [https://doi.org/10.1016/0016-7037\(96\)00071-3](https://doi.org/10.1016/0016-7037(96)00071-3)
- Salvi, S., Williams-Jones, A.E., 1991. Reply to Comment by T. C. Birkett and R. R. Miller on “The role of hydrothermal processes in the granite-hosted Zr, Y, REE deposit at Strange Lake, Quebec/Labrador: Evidence from fluid inclusions.” *Geochim. Cosmochim. Acta* 55, 3447–3449. [https://doi.org/10.1016/0016-7037\(91\)90504-X](https://doi.org/10.1016/0016-7037(91)90504-X)
- Salvi, S., Williams-Jones, A.E., 1990. The role of hydrothermal processes in the granite-hosted Zr, Y, REE deposit at Strange Lake, Quebec/Labrador: Evidence from fluid inclusions. *Geochim. Cosmochim. Acta* 54, 2403–2418. [https://doi.org/10.1016/0016-7037\(90\)90228-D](https://doi.org/10.1016/0016-7037(90)90228-D)
- Schaltegger, U., 2007. Hydrothermal zircon. *Elements* 3, 51–79.

<https://doi.org/10.2113/gselements.3.1.51>

Schaltegger, U., Pettke, T., Audétat, A., Reusser, E., Heinrich, C. a., 2005. Magmatic-to-hydrothermal crystallization in the W-Sn mineralized Mole Granite (NSW, Australia). Part I: Crystallization of zircon and REE-phosphates over three million years - A geochemical and U-Pb geochronological study. *Chem. Geol.* 220, 215–235. <https://doi.org/10.1016/j.chemgeo.2005.02.018>

Shand, S.J., 1943. Eruptive rocks. *Geol. Mag.* 81, 137–138. <https://doi.org/DOI:10.1017/S0016756800075026>

Siegel, K., Vasyukova, O. V., Williams-Jones, A.E., 2018. Magmatic evolution and controls on rare metal-enrichment of the Strange Lake A-type peralkaline granitic pluton, Québec-Labrador. *Lithos* 308–309, 34–52. <https://doi.org/10.1016/j.lithos.2018.03.003>

Siegel, K., Williams-Jones, A.E., van Hinsberg, V.J., 2017. The amphiboles of the REE-rich A-type peralkaline Strange Lake pluton – fingerprints of magma evolution. *Lithos* 288–289, 156–174. <https://doi.org/10.1016/j.lithos.2017.07.012>

Silver, L.T., Deutsch, S., 1963. Uranium-Lead Isotopic Variations in Zircons: A Case Study. *J. Geol.* 71, 721–758. <https://doi.org/10.1086/626951>

Sorensen, H., 1992. Agpaitic nepheline syenites : a potential source of rare elements 7, 417–427.

Speer, A., 1982. Zircon, in: Ribbe, P.H. (Ed.), *Orthosilicate*. Mineralogical Society of America, Blacksburg, pp. 67–112.

Stoeser, D.B., 1986. Distribution and tectonic setting of plutonic rocks of the Arabian Shield. *J. African Earth Sci.* 4, 21–46. [https://doi.org/10.1016/S0899-5362\(86\)80066-5](https://doi.org/10.1016/S0899-5362(86)80066-5)

Taylor, R.P., Strong, D.F., Fryer, B.J., 1981. Volatile control of contrasting trace element distributions in peralkaline granitic and volcanic rocks. *Contrib. to Mineral. Petrol.* 77, 267–271. <https://doi.org/10.1007/BF00373542>

- Thomas, J.B., Bodnar, R.J., Shimizu, N., Sinha, A.K., 2002. Determination of zircon/melt trace element partition coefficients from SIMS analysis of melt inclusions in zircon. *Geochim. Cosmochim. Acta* 66, 2887–2901. [https://doi.org/10.1016/S0016-7037\(02\)00881-5](https://doi.org/10.1016/S0016-7037(02)00881-5)
- Tomašić, N., Gajović, A., Bermanec, V., Su, D.S., Rajić Linarić, M., Ntaflos, T., Schlögl, R., 2006. Recrystallization mechanisms of fergusonite from metamict mineral precursors. *Phys. Chem. Miner.* 33, 145–159. <https://doi.org/10.1007/s00269-006-0061-6>
- Turkistany, A.R., Ramsay, C.R., 1982. Mineralized apogranite associated with alkali granite at Jabal Sa'id, Kingdom of Saudi Arabia. *Deputy Ministry Miner. Resour.* 78–88.
- Vasyukova, O., Williams-Jones, A.E., 2014. Fluoride-silicate melt immiscibility and its role in REE ore formation: Evidence from the Strange Lake rare metal deposit, Quebec-Labrador, Canada. *Geochim. Cosmochim. Acta* 139, 110–130. <https://doi.org/10.1016/j.gca.2014.04.031>
- Vasyukova, O. V., Williams-Jones, A.E., Blamey, N.J.F.F., 2016. Fluid evolution in the Strange Lake granitic pluton, Canada: Implications for HFSE mobilisation. *Chem. Geol.* 444, 83–100. <https://doi.org/10.1016/j.chemgeo.2016.10.009>
- Voncken, J.H.L., 2016. *The Rare Earth Elements : an Introduction.* <https://doi.org/10.1007/978-3-319-26809-5>
- Wang, R.C., Chen, X.M., Hu, H., Liu, C.S., Xu, S.J., Fontan, F., de Parseval, P., 2003. Accessory minerals in the Xihuashan Y-enriched granitic complex, southern China: A record of magmatic and hydrothermal stages of evolution. *Can. Mineral.* 41, 727–748.
- Wu, M., Tian, B., Zhang, D., Xu, G., Xu, W., Qiu, K., 2018. Zircon of the No. 782 deposit from the Great Xing'an Range in NE China: Implications for Nb-REE-Zr mineralization during magmatic-hydrothermal evolution. *Ore Geol. Rev.* 102, 284–299. <https://doi.org/10.1016/j.oregeorev.2018.09.006>

Yang, W.-B., Niu, H.-C., Shan, Q., Sun, W.-D., Zhang, H., Li, N.-B., Jiang, Y.-H., Yu, X.-Y., 2014. Geochemistry of magmatic and hydrothermal zircon from the highly evolved Baerzhe alkaline granite: implications for Zr–REE–Nb mineralization. *Miner. Depos.* 49, 451–470. <https://doi.org/10.1007/s00126-013-0504-1>

Table 5-1 Summary of the main rock units at Dyaheen

Rock Unit	Description	Weathering/alteration/ Mineralization
Monzogranite	Light-grey medium-grained granite. Plagioclase is zoned with a selective alteration. Alkali feldspar occurs as perthite. Biotite is the main mafic mineral	Moderately to highly weathered. Apatite, titanite, and magnetite are the main accessory minerals. Zircon present, but very rare
Amphibole-biotite granite	Dark-grey to reddish-brown medium-grained to porphyritic granite. Host most of the pegmatite and miarolitic cavities in Dyaheen. Quartz, plagioclase, perthite (to microcline perthite), sodic amphibole and biotite are the main rock-forming minerals.	Variable alteration to hematite, calcite, and fluorite after sodic amphibole. Titanite, magnetite are the main accessories. Zircon occurs as secondary minerals with the alteration
Aegirine granite	Light-grey medium-grained to porphyritic granite. Aegirine occurs with amphibole as a replacement. Quartz, albite, microcline, and aegirine/amphibole are the main rock-forming minerals.	Altered rocks show reddish color due to hematization. Pyrochlore and zircon are the main rare-metal phases.
Aegirine dykes	Similar to the aegirine granite, but darker. Aegirine, quartz, albite, and perthite are the main rock-forming minerals.	Locally hematitized. Zircon, pyrochlore, bastnasite, and fergusonite are the main rare-metal minerals
Quartz veins	Crosscut the aegirine granite and show deformation. Mostly aegirine and perthite rich.	Gadolinite, bastnasite, britholite, zircon, and pyrochlore are the main rare-metal minerals

Table 5-2 List of common minerals at Dyaheen with abbreviations and formulas

Mineral	Symbols	Formula
Quartz	Qtz	SiO ₂
Albite	Ab	NaAlSi ₃ O ₈
Microcline	Mc	KAlSi ₃ O ₈
Aegirine	Aeg	NaFeSi ₂ O ₆
Alkali feldspar	Kfs	(K,Na)AlSi ₃ O ₈
Arfvedsonite	Arf	Na ₃ Fe ₅ Si ₈ O ₂₂ (OH,F) ₂
Zircon	Zrn	ZrSiO ₄
Pyrochlore	Pcl	(Ca,Na,Pb,Ln,Y,U) ₂ Nb ₂ (O,OH) ₆ (O,OH,F,□)
Gadolinite	Gdt	(YREE) ₂ FeBe ₂ Si ₂ O ₁₀
Bastnasite	Bst	(Ce,La,Nd)(CO ₃)F
Britholite	Brth	(Y,REE,Ca) ₅ (SiO ₄) ₃ (OH)
Fergusonite	Frg	YREENbO ₄
Monazite	Mnz	(Ce,La,Nd)PO ₄
Fluorite	Fl	(Ca _{1-x} Y _x)F _{2+x}
Sericite	Ser	KAl ₂ (Si ₃ Al)O ₁₀ (OH,F) ₂
Thorite	Thr	ThSiO ₄
Hematite	Hem	Fe ₂ O ₃
Titanite	Tnt	CaTiSiO ₂
Calcite	Cal	CaCO ₃
Rutile	Rt	TiO ₂
Magnetite	Mag	Fe ₃ O ₄
Apatite	Ap	Ca ₅ (PO ₄) ₃ (F,Cl,OH)

Table 5-3 Whole-rock Analyses of main rock units at Dyaheen

	Aegirine Dikes		Aegirine Granite				Amphibole-biotite Granite						Monzogranite
	HDA8	HDA19	HDA1-A	HAD1-B	HDA9	HDA17	HDA26	HDA27	HDA28	HDA29	HDA36	HDA38	HDA39
F	0.01	0.12	0.02	0.22	0.01	0.17	0.4	0.12	0.09	0.01	0.18	0.02	0.08
SiO ₂	83.44	81.85	74.6	74.7	75.12	73.29	71.4	70.73	69.22	74.86	73.72	76.28	71.69
Al ₂ O ₃	5.02	3.97	11.18	11.56	10.65	11.23	12.99	13.41	14.11	12.17	12.8	12.4	14.71
Fe ₂ O ₃ (T)	4.28	3	4.32	2.88	4.14	3.86	3.08	2.51	2.34	3.03	2.59	1.24	2.28
MnO	0.21	0.119	0.03	0.046	0.055	0.072	0.043	0.049	0.041	0.025	0.035	0.014	0.033
MgO	0.14	0.2	0.03	0.09	0.06	0.05	0.38	0.53	0.63	0.19	0.17	0.05	0.62
CaO	0.21	1.48	0.08	0.27	0.26	0.45	1.56	1.75	1.65	0.13	0.64	0.22	1.85
Na ₂ O	3.43	1.28	5.68	5.25	4.97	4.55	4.71	4.94	5.32	4.05	4.5	4.7	4.22
K ₂ O	1.12	2.96	3.7	3.33	3.47	3.86	4.62	4.02	4.19	3.98	4.44	4.03	3.86
TiO ₂	0.287	0.373	0.116	0.072	0.091	0.072	0.282	0.319	0.343	0.063	0.1	0.02	0.293
P ₂ O ₅	0.03	0.45	0.01	0.03	0.01	0.01	0.03	0.05	0.08	0.01	0.01	0.01	0.09
LOI	0.57	1.53	0.16	0.26	0.39	0.43	1	1.3	1.22	0.56	0.47	0.21	0.64
Total	98.7	97.3	99.9	98.7	99.2	98.0	100.5	99.7	99.2	99.1	99.7	99.2	100.4
Be	114	27	12	8	17	16	8	8	15	8	11	3	4
Cr	50	30	30	40	30	40	30	40	30	30	40	40	40
Cu	10	10	10	10	10	10	10	20	10	10	30	90	50
Zn	3820	1810	270	340	450	260	130	160	120	240	190	60	70
Ga	47	51	59	47	48	56	27	27	25	48	44	41	24
Ge	7	9	3	3	3	3	2	1	2	2	2	2	1
As	13	23	5	5	5	10	5	5	5	5	5	5	5
Rb	141	383	525	455	361	508	302	200	298	439	279	195	166
Sr	17	41	4	50	7	16	106	317	251	17	67	42	401
Y	1407	1125	181	220	149	208	37	70	37	84	87	19	14
Zr	4319	8519	2644	2090	1244	5407	339	777	287	120	2201	185	168
Nb	981	2680	32	34	71	137	36	62	22	15	50	13	10
Mo	2	2	2	2	2	2	2	2	2	2	2	2	3
In	0.5	2	0.2	2	0.2	2	2	2	2	2	2	2	0.2
Sn	157	44	59	18	27	15	5	7	8	5	7	2	3
Sb	1.3	1.6	1.7	1.1	0.7	2	0.7	0.7	0.7	0.8	0.6	1.2	1.1
Cs	1.6	2.6	2.2	3.9	1.8	2.8	2.7	4.9	11.4	3.6	4.2	2.7	5.2
Ba	56	74	9	115	22	66	266	660	709	82	189	75	767
Bi	0.8	8	1.2	0.5	0.4	3.6	0.6	0.4	0.4	1.5	0.4	0.4	0.4
La	836	2530	56.9	49.2	68.9	59.8	48.6	38.3	37.7	45	106	7.5	25.2
Ce	3480	5990	125	122	200	166	107	84.7	73.5	84.3	351	33.1	52.5
Pr	340	688	15.4	15.8	23.8	24.4	12.5	10.2	8.76	12.1	27.6	2.47	5.64
Nd	1360	2460	57.9	66.7	98.6	107	47.4	39.5	33.6	55.6	103	10.2	20.2
Sm	406	446	13.2	20.1	28	31.8	9.5	10.4	6.5	15.4	19.4	2.7	3.9
Eu	19.6	17.1	0.51	1.14	1.36	1.61	0.77	1.05	0.88	0.76	0.85	0.19	0.64
Gd	371	279	10.2	23.9	28	32.6	7.9	11.1	6.5	16.6	15	2.7	3
Tb	60.7	37.4	2.3	4.2	4.7	5.4	1.3	2	1	2.3	2.4	0.5	0.4

Continue Table 5.3													
Dy	337	212	21.1	29.2	26.7	35.7	7.4	13.2	5.8	12.3	14.7	3.4	2.5
Ho	59.2	45.2	6.2	6.4	5.1	7.5	1.3	2.5	1.1	2.2	3	0.6	0.5
Er	161	154	27.7	20.7	14.3	24.2	3.7	7.4	3.1	5.4	9.9	2	1.4
Tm	22.6	25.4	6.09	3.58	2.15	3.88	0.57	1.07	0.43	0.68	1.58	0.32	0.21
Yb	138	170	51.7	26.6	14.2	27.9	3.9	6.9	2.6	4	11.1	2.4	1.4
Lu	17.2	22.8	8.45	4.14	2.17	4.5	0.61	1.03	0.41	0.6	1.89	0.36	0.21
Hf	81.4	156	164	70.5	30.7	127	8.9	20.7	7.3	3.6	44	6.2	4
Ta	73.3	224	3.9	4.8	6.3	14.7	2.6	5.2	1.7	1.3	4.4	2.8	1.4
W	5	5	3	4	2	3	3	3	2	3	2	7	3
Tl	1.7	2.6	3.7	2.9	2.2	6.1	2	1.4	2.2	2.1	1.4	0.9	0.8
Pb	984	3420	32	27	62	59	22	38	47	19	30	15	19
Th	289	800	76.6	29.2	16.9	31.7	10.9	23	12.2	4.3	28.3	10.2	11.3
U	193	386	5	17.4	11.3	18.2	4.1	11.1	5.1	2.2	12	4.9	3
Na/K	3.06	0.43	1.54	1.58	1.43	1.18	1.02	1.23	1.27	1.02	1.01	1.17	1.09
ASI	0.73	0.75	0.84	0.94	0.89	0.96	1.02	1.07	1.06	1.11	1.05	1.03	1.32
LREE	6422	12114	268	274	419	389	225	183	160	212	607	56	107
HREE	1186	963	134	120	99	143	27	46	22	45	60	12	10
TREE	7608	13076	403	394	518	532	252	229	182	257	667	68	118
Eu/Eu*	0.15	0.15	0.13	0.16	0.15	0.15	0.27	0.30	0.42	0.15	0.15	0.22	0.58
La/Yb	4.04	9.92	0.73	1.23	3.23	1.43	8.31	3.70	9.67	7.50	6.37	2.08	12.00
Gd/Yb	2.15	1.31	0.16	0.72	1.58	0.93	1.62	1.29	2.00	3.32	1.08	0.90	1.71
La/Sm	1.29	3.55	2.69	1.53	1.54	1.18	3.20	2.30	3.63	1.83	3.41	1.74	4.04
Abbreviations: Fe ₂ O ₃ (T), total iron; ASI, aluminium saturation index; LREE, light rare earth elements; HREE, heavy rare earth elements.													

Table 5-4 Table Average EMPA of amphibole and aegirine from Dyaheen

	L.O.D	Average amphibole N=12	±		Average Aegirine N=34	±
SiO ₂	0.09	51.1	0.9	SiO ₂	50.59	0.9
Al ₂ O ₃	0.08	0.7	0.4	Al ₂ O ₃	0.39	0.1
F	0.00	1.8	0.5	F	N.A	N.A
Na ₂ O	0.05	7.6	0.6	Na ₂ O	12.46	0.41
MgO	0.07	3.2	2.8	MgO	0.1	0.1
CaO	0.06	0.7	0.8	CaO	0.59	0.6
TiO ₂	0.07	0.6	0.2	TiO ₂	0.95	0.1
K ₂ O	0.05	1.8	0.5	K ₂ O	0.0	0.0
FeO	0.05	23.8	3.3	FeO	2.36	1.32
Fe ₂ O ₃		4.2	3.5	Fe ₂ O ₃	29.07	1.27
MnO	0.05	1.0	0.3	MnO	0.31	0.30
ZnO	0.04			ZnO	0.11	0.1
Total		96.3		Total	98.03	
Atom per formula unit						
Si	8.2			Si	1.95	
ΣT	8.2			Ti	0.03	
Ti	0.1			Al	0.02	
Al	0.1			ΣT	2.0	
Fe ³⁺	0.6			Fe ³⁺	0.94	
Fe ²⁺	3.2			Fe ²⁺	0.04	
Mn	0.1			Mn	0.01	
Mg	0.7			Mg	0.01	
ΣC	4.8			ΣM1	1.0	
Ca	0.1			Fe ²⁺	0.04	
Na	1.9			Ca	0.02	
ΣB	2.0			K	0.0	
K	0.4			Na	0.93	
Na	0.6			Zn	0.0	
ΣA	1.0			ΣM2	1.0	
F	0.9					

L.O.D. limit of detection. N.A. analyses not available. Fe²⁺ was estimated from aegirine stoichiometry where Fe³⁺ to Fe²⁺ ratio was adjusted to achieve 6 oxygen totals.

Table 5-5 Average EMPA of zircons from Dyaheen

	L.O.D	Altered aegirine granite N= 5	±	a.p.f.u	Aegirine dyke N = 7	±	a.p.f.u	Quartz veins N = 29	±	a.p.f.u
SiO ₂	0.08	32.71	0.10	1.004	29.33	1.22	0.95	31.67	1.34	1.00
P ₂ O ₅	0.07	b.d	b.d	b.d	0.31	0.07	0.01	0.36	0.24	0.01
ΣB site				1.00			0.96			1.01
ZrO ₂	0.12	63.47	0.72	0.950	56.94	2.01	0.90	59.74	3.77	0.92
HfO ₂	0.08	1.33	0.16	0.012	0.62	0.13	0.01	1.10	0.53	0.01
CaO	0.02	b.d	b.d	b.d	1.08	0.50	0.04	0.08	0.11	0.00
ThO ₂	0.05	b.d	b.d	b.d	0.69	0.73	0.01	0.20	0.19	0.00
Y ₂ O ₃	0.06	1.26	0.41	0.021	1.75	1.00	0.03	2.59	2.23	0.04
Dy ₂ O ₃	0.05	0.16	0.08	0.002	0.31	0.12	0.00	0.30	0.29	0.00
UO ₂	0.03	0.08	0.06	0.006	0.75	0.27	0.05	0.11	0.07	0.01
Tb ₂ O ₃	0.04	b.d	b.d	b.d	b.d	b.d	b.d	b.d	b.d	b.d
FeO	0.02	0.05	0.05	0.001	1.55	1.23	0.04	0.13	0.13	0.00
Er ₂ O ₃	0.04	0.16	0.03	0.002	0.23	0.12	0.00	0.33	0.24	0.00
Yb ₂ O ₃	0.04	0.25	0.02	0.002	0.48	0.16	0.00	0.48	0.17	0.00
PbO	0.04	b.d	b.d	b.d	0.23	0.16	0.00	0.08	0.08	0.00
ΣA site				1.00			1.07			0.98
Total		99.97		2.00	94.44		2.03	97.75		1.99
REE		1.06			1.37			1.53		
Zr/Hf		47.6	0.12		91.7	0.21		54.5	0.49	

L.O.D. limit of detection. b.d at or below the detection limit. N is the number of analyses. ± is 1 σ standard deviation.

Table 5-6 Average EMP analyses of pyrochlore from Dyaheen

	L.O.D	Average Pb- Pyrochlore N=15	±	Average Yttrropyrochlore N=3	±	Average Fergusonite N=6	±	
F	0.18	0.18	0.2	0.21	0.1	F	0.13	0.2
SiO ₂	0.10	5.54	2.6	6.55	1.2	SiO ₂		
Na ₂ O	0.03	0.19	0.3			Na ₂ O		
MgO	0.01	0.02	0.0			MgO		
La ₂ O ₃	0.16	0.70	0.8	0.62	0.1	La ₂ O ₃	0.22	0.1
Ce ₂ O ₃	0.14	3.26	2.1	2.87	0.8	Ce ₂ O ₃	0.79	0.5
Gd ₂ O ₃	0.08	0.53	0.3	1.64	0.3	Gd ₂ O ₃	2.32	0.8
TiO ₂	0.04	3.86	1.8	3.87	3.5	TiO ₂	0.96	0.1
CaO	0.02	2.55	0.8	2.63	0.5	CaO	0.22	0.3
ThO ₂	0.05	0.29	0.7	1.75	2.1	ThO ₂	0.50	0.2
Nb ₂ O ₅	0.06	35.06	11.3	39.86	3.7	Nb ₂ O ₅	46.47	1.8
Y ₂ O ₃	0.06	2.99	2.3	9.29	1.8	Y ₂ O ₃	28.80	1.1
Nd ₂ O ₃	0.05	1.44	0.7	2.54	0.2	Nd ₂ O ₃	0.88	0.5
Pr ₂ O ₃	0.10	0.37	0.2	0.53	0.1	Pr ₂ O ₃	0.15	0.1
Dy ₂ O ₃	0.05	0.75	0.5	2.44	0.3	Dy ₂ O ₃	5.32	1.1
Ho ₂ O ₃	0.11	b.d.		0.45	0.1	Ho ₂ O ₃	1.20	0.1
Lu ₂ O ₃	0.06	b.d.		0.04	0.0	Lu ₂ O ₃	0.11	0.2
UO ₂	0.04	2.65	1.0	1.40	0.4	UO ₂	1.06	0.5
Ta ₂ O ₅	0.08	2.46	1.4	1.46	0.5	Ta ₂ O ₅	0.69	0.2
MnO	0.03	0.15	0.2	0.67	0.9	MnO	b.d.	
Sm ₂ O ₃	0.08	0.56	0.2	1.46	0.2	Sm ₂ O ₃	0.95	0.3
Tb ₂ O ₃	0.05	0.11	0.1	0.34	0.0	Tb ₂ O ₃	0.64	0.2
FeO	0.03	1.84	0.9	2.14	0.9	FeO	b.d.	
Er ₂ O ₃	0.05	0.39	0.3	1.26	0.3	Er ₂ O ₃	3.39	0.2
Tm ₂ O ₃	0.05	0.10	0.0	0.20	0.0	Tm ₂ O ₃	0.44	0.1
Yb ₂ O ₃	0.05	0.33	0.3	0.75	0.2	Yb ₂ O ₃	2.09	1.0
PbO	0.04	29.23	11.5	9.44	7.0	PbO	0.58	0.1

Table 5.6 *continue*

Total	95.9		Total	97.87
Atom per formula unit				
	Pb-Pyrochlore	Average Ytropyrochlore	Fergusonite	
Si	0.4	0.4	Si	0.0
Nb	1.2	1.2	Nb	0.9
Ta	0.1	0.03	Ta	0.01
Ti	0.2	0.2	Ti	0.03
Fe	0.1	0.1	Fe	0.0
ΣB	2.0	2.0	ΣB	1.0
Na	0.0	0.0	Na	0.0
La	0.0	0.02	La	0.0
Ce	0.1	0.1	Ce	0.01
Gd	0.0	0.04	Gd	0.03
Ca	0.2	0.2	Ca	0.01
Th	0.0	0.03	Th	0.01
Y	0.1	0.3	Y	0.7
Nd	0.0	0.1	Nd	0.01
Pr	0.0	0.01	Pr	0.0
Dy	0.0	0.05	Dy	0.1
Ho		0.01	Ho	0.02
Lu		0.0	Lu	0.0
U	0.5	0.2	U	0.01
Mn	0.0	0.04	Mn	
Sm	0.0	0.03	Sm	0.01
Tb	0.0	0.01	Tb	0.01
Er	0.0	0.03	Er	0.05
Tm	0.0	0.0	Tm	0.01
Yb	0.0	0.02	Yb	0.03
Pb	0.6	0.2	Pb	0.01
ΣA	1.5	1.2	ΣA	1.0

L.O.D. limit of detection. b.d. at or below detection limit. N is the number of analyses. \pm is 1 σ standard deviation.

Table 5-7 Average EMP analyses of gadolinite and bastnasite from

Gadolinite	Early			Late			Bastnasite		
	LOD	Average N=1	±	Average N=4	±	Average N=8	±		
F	0.20	b.d		b.d		F	4.8	1.2	
SiO ₂	0.08	25.15	0.8	24.75	0.2	SiO ₂	0.5	0.4	
Al ₂ O ₃	0.03	0.16	0.5		0.0	Al ₂ O ₃	b.d	-	
La ₂ O ₃	0.14	0.83	0.7	1.23	0.4	La ₂ O ₃	9.4	1.9	
Ce ₂ O ₃	0.11	3.21	1.4	3.85	0.5	Ce ₂ O ₃	28.1	2.6	
Gd ₂ O ₃	0.08	3.19	1.1	1.20	0.4	Gd ₂ O ₃	2.9	0.6	
CaO	0.02	2.52	1.3	0.87	0.1	CaO	2.6	2.5	
ThO ₂	0.05	0.53	0.8	0.03	0.0	ThO ₂	0.2	0.1	
P ₂ O ₅						P ₂ O ₅	0.6	1.0	
Y ₂ O ₃	0.06	27.55	1.5	29.70	0.5	Y ₂ O ₃	3.1	1.6	
Nd ₂ O ₃	0.05	3.01	1.7	1.60	0.7	Nd ₂ O ₃	14.6	1.2	
Pr ₂ O ₃	0.10	0.63	0.3	0.40	0.1	Pr ₂ O ₃	3.6	0.2	
Eu ₂ O ₃	0.04	0.09	0.0	0.04	0.0	Eu ₂ O ₃	0.1	0.0	
Dy ₂ O ₃	0.05	4.43	0.9	2.88	0.3	Dy ₂ O ₃	1.2	0.3	
Ho ₂ O ₃	0.09	0.86	0.1	0.91	0.0	Ho ₂ O ₃	0.1	0.0	
Lu ₂ O ₃	0.05	0.05	0.0	0.52	0.1	Lu ₂ O ₃	0.0	0.0	
UO ₂	0.03	0.03	0.0	0.02	0.0	UO ₂	0.0	0.0	
Sm ₂ O ₃	0.07	1.56	0.5	0.75	0.3	Sm ₂ O ₃	3.7	0.7	
Tb ₂ O ₃	0.04	0.64	0.2	0.30	0.1	Tb ₂ O ₃	0.3	0.1	
FeO	0.02	7.58	1.2	9.11	0.5	FeO	1.0	1.5	
Er ₂ O ₃	0.04	2.16	0.1	3.77	0.3	Er ₂ O ₃	0.2	0.1	
Tm ₂ O ₃	0.04	0.25	0.0	0.68	0.1	Tm ₂ O ₃	0.1	0.0	
Yb ₂ O ₃	0.04	1.03	0.3	4.60	0.7	Yb ₂ O ₃	0.1	0.0	
PbO	0.04	0.32	0.2	0.30	0.0	PbO	0.3	0.2	
CO ₂ *	-					CO ₂ *	22.3		
Be*	-	10.47	0.3	10.30	0.1	Be*	-		
Total		96.29		97.79		Total	100.0		

Continue Table 5.7

Atom per formula unit				
Gadolinite	Early	Late	Bastnasite	
Al	0.0	0.0	Si	0.0
La	0.0	0.0	Al	-
Ce	0.1	0.1		
Gd	0.1	0.0	La	0.1
Ca	0.2	0.1	Ce	0.3
Th	0.0	0.0	Gd	0.0
Y	1.2	1.3	Ca	0.1
Nd	0.1	0.0	Th	0.0
Pr	0.0	0.0	P	0.0
Eu	0.0	0.0	Y	0.1
Dy	0.1	0.1	Nd	0.2
Ho	0.0	0.0	Pr	0.0
Lu	0.0	0.0	Eu	0.0
U	0.0	0.0	Dy	0.0
Sm	0.0	0.0	HO	0.0
Tb	0.0	0.0	Lu	0.0
Er	0.1	0.1	U	0.0
Tm	0.0	0.0	Sm	0.0
Yb	0.0	0.1	Tb	0.0
Pb	0.0	0.0	Fe	0.0
A	2.0	2.0	Er	0.0
Fe	0.5	0.6	Tm	0.0
Mn	0.0	0.0	Yb	0.0
M	0.5	0.6	Pb	0.0
Be	2.0	2.0	Total	1.0
Si	2.0	2.0		
Total	6.5	6.6		

LOD, limit of detection of EMP. * CO₂ in bastnasite was calculated by difference. * Be concentration was calculated from stoichiometry, assuming full site occupation. ± is 1 σ standard deviation.

Table 5-8 Feldspar fractionation model for Dyaheen

	D ¹ Plg	D ¹ Kfs	C° (Ave. Monzogranite composition)	10% feldspar fractionation	20% feldspar fractionation	30% feldspar fractionation	40% feldspar fractionation	Ave. Amphibole- Biotite granite	Ave. Aegirine granite
La	0.3	0.05	33.4	36.5	40.2	44.9	51.1	64.2	63.8
Ce	0.21	0.41	66.8	72.9	80.4	89.8	102.1	125.3	148.3
Nd	0.17	0.02	29.0	31.8	35.4	40.0	45.9	73.3	88.0
Sm	0.14	0.014	4.4	4.9	5.4	6.1	7.1	17.1	22.2
Eu	4.2	3.5	0.7	0.6	0.5	0.4	0.3	1.2	1.1
Gd	0.09	0.011	3.2	3.6	4.0	4.5	5.2	15.8	20.7
Tb	0.9	0.09	0.4	0.4	0.5	0.5	0.5	2.4	3.0
Dy	0.064	0.006	2.5	2.7	3.0	3.5	4.0	15.4	18.3
Er	0.055	0.006	1.4	1.6	1.7	2.0	2.3	8.9	12.1
Yb	0.0701	0.006	1.4	1.5	1.7	1.9	2.2	8.2	14.8
Sr	7.3	1.6	311.0	222.0	152.3	99.3	60.7	147.67	15.83
Ba	1.6	9.7	614.8	546.9	479.9	413.8	348.7	312.37	31.42
Eu anomaly			0.56	0.42	0.31	0.21	0.14	0.24	0.15
Qtz _N			0.33						
Ab _N			0.55						
Or _N			0.13						

1 Plagioclase and K-feldspar partitioning coefficient are from Nash and Crecraft, (1985). C° initial melt compositing.

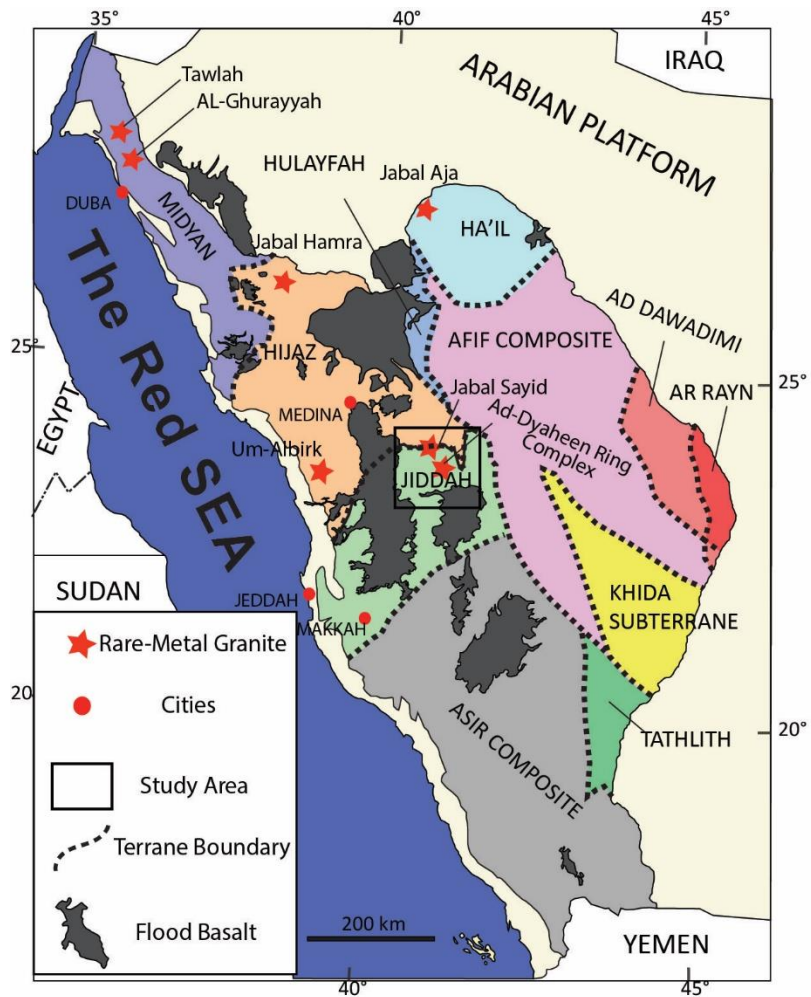


Figure 5-1 A geological map showing the different terrane in the Arabian Shield. The red stars are the location of some important rare-metal alkaline granite in the Arabian Shield. The box is showing the location of the study area. (modified after Johnson and Kattan 2012).

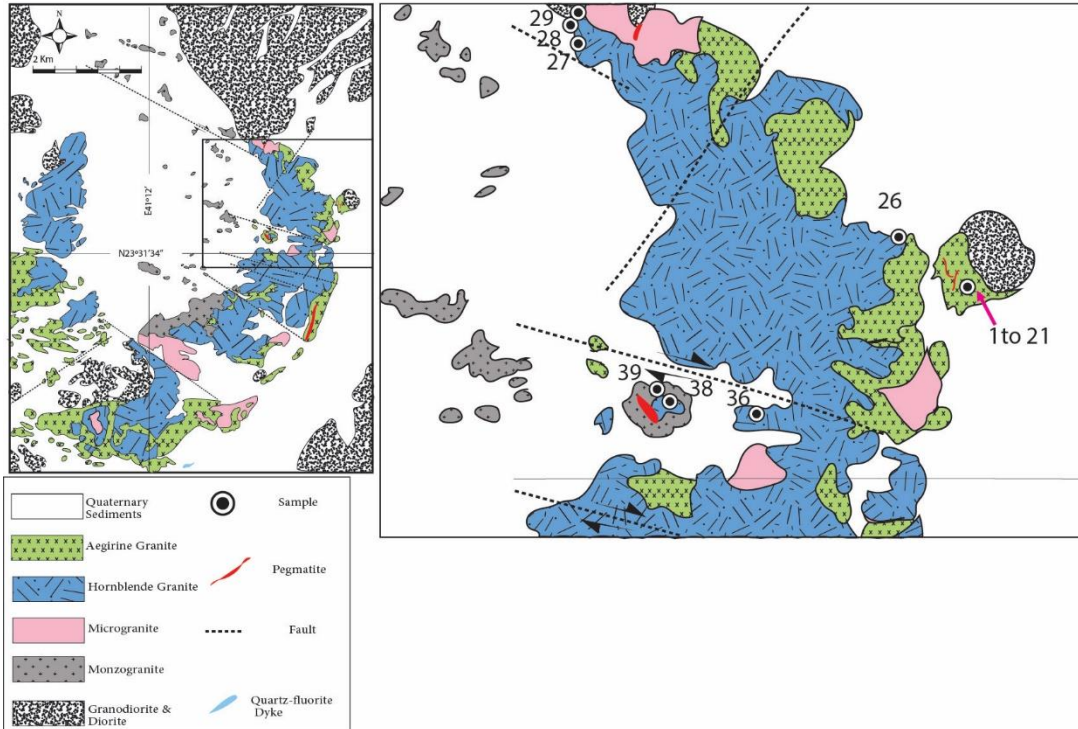


Figure 5-2 Geological map of Dyaheen ring complex showing the major rock units and the sample locations (Modified after Radain, 1979).

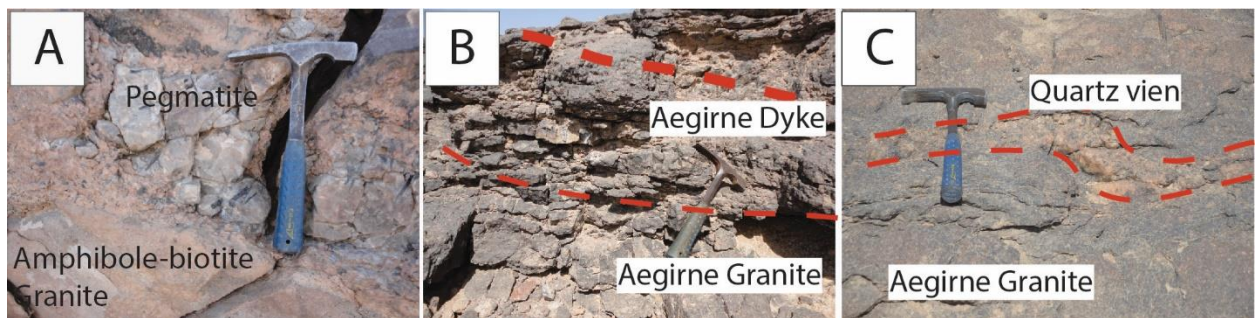


Figure 5-3 Photos of mineralized rocks in Dyaheen ring complex. A) Pegmatite dyke in the amphibole-biotite granite. B) Aegirine dyke crosscut aegirine granite. C) Ductile quartz vein crosscut altered aegirine granite.

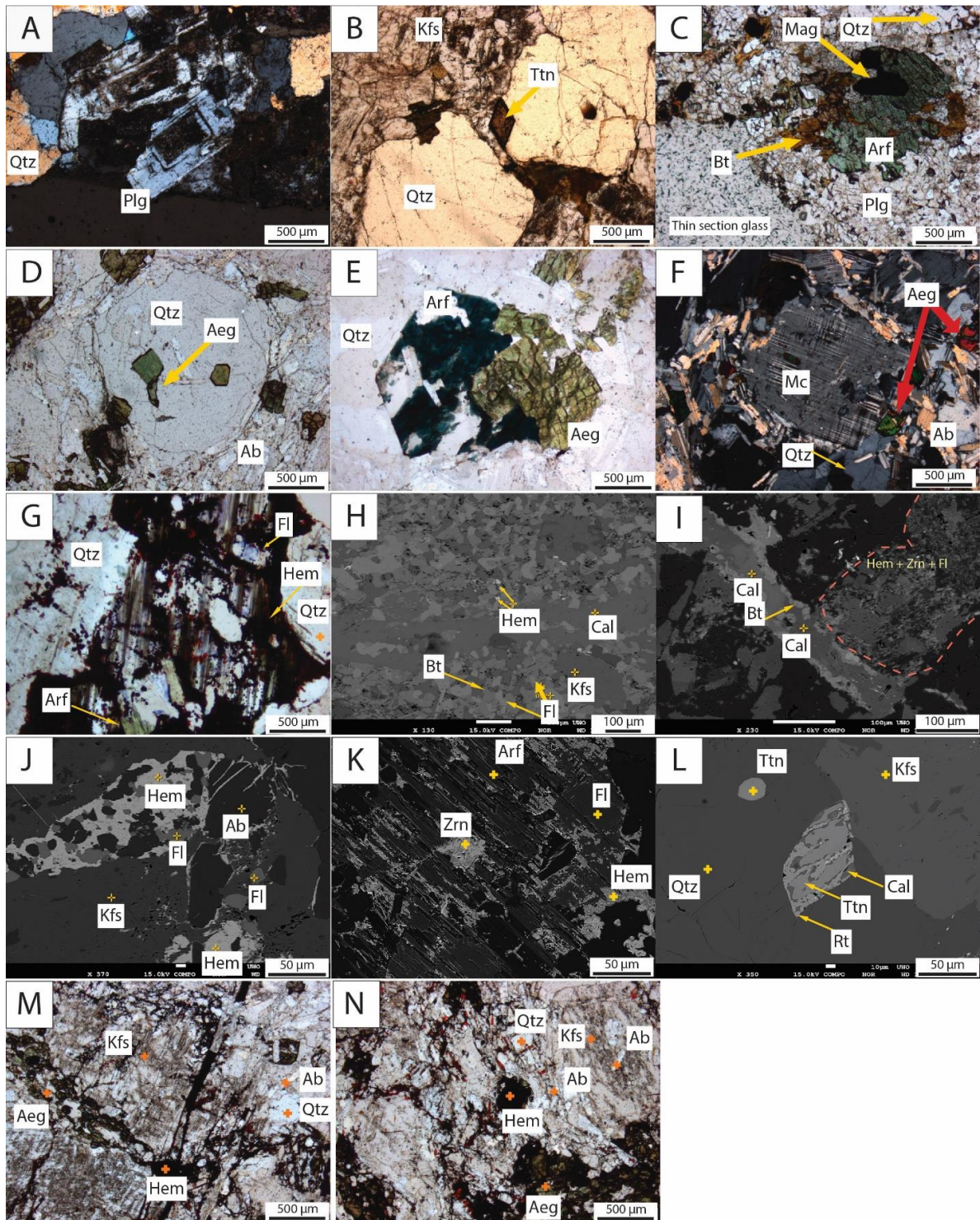


Figure 5-4 Major rock-forming minerals and alteration minerals in Dyaheen. A) Cross polarized light (CPL) image showing highly selective alteration of highly zoned plagioclase associated with quartz from the monzogranite. B) Plane polarized light (PPL) image of titanite associated with alkali feldspar and quartz from the

monzogranite. C) PPL image sodic amphibole with magnetite inclusion. Amphibole is replaced to biotite in a quartz plagioclase matrix from the amphibole-biotite granite. D) PPL image of rounded quartz crystals surrounded by albite crystals and contains inclusions of aegirine from the aegirine granite. E) PPL image of sodic amphibole replaced by aegirine from the aegirine granite. F) CPL image of irregular microcline crystal with albite inclusions in quartz, albite, and aegirine matrix from the aegirine granite. G) PPL image of altered sodic amphibole that is replaced by hematite and fluorite from the amphibole-biotite granite. H) Backscattered electron image (BSEI) of a calcite veinlet associated with albite, biotite, hematite, and fluorite from the amphibole-biotite granite. I) BSEI of calcite veinlets with biotite crosscutting sodic amphibole crystals from the amphibole-biotite granite. the dashed line shows the border of a pseudomorph that contains zircon, hematite, and fluorite. J) BSEI of hematite and fluorite alteration from the amphibole-biotite granite. H) BSEI of fine-grained zircon, fluorite, and hematite replacing sodic amphibole from the amphibole-biotite granite. L) fresh and altered titanite from the altered amphibole-biotite granite. Altered titanite is replaced by calcite and rutile. N) and M) PPL variable degree of hematization associated with fresh aegirine, microcline-perthite, and quartz from the altered aegirine granite.

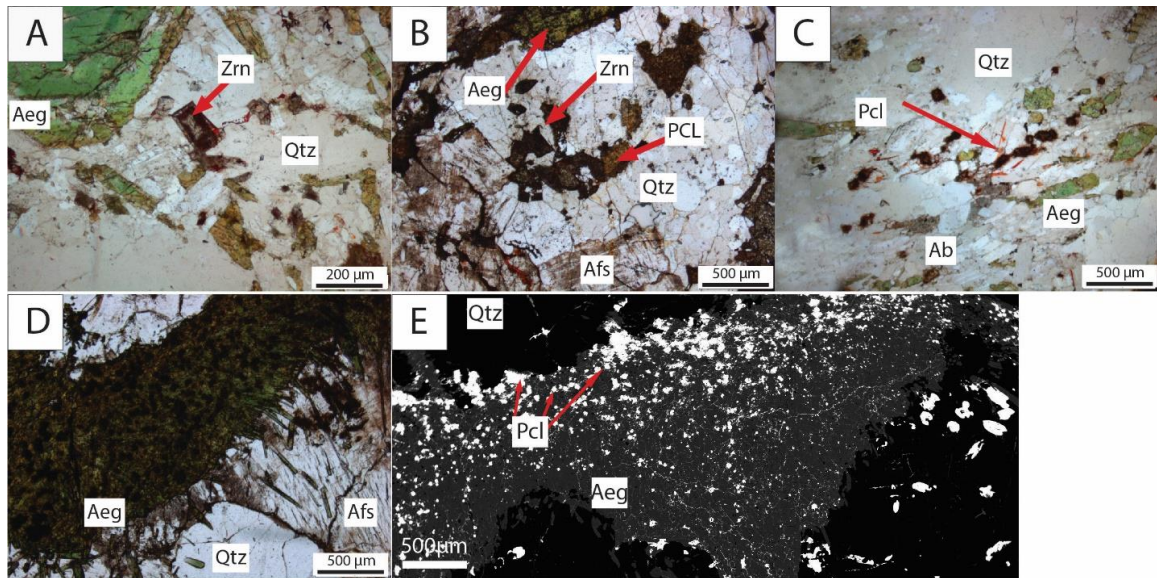


Figure 5-5 Rock-forming mineral and rare-metal minerals from the aegirine dykes and the quartz veins. A) PPL image of zircons in albite quartz matrix and variable crystal sizes of aegirine from the aegirine dyke. B) PPL image of zircon and pyrochlore in quartz and albite matrix, and large aegirine and perthite crystals from the aegirine dyke. C) PPL image of highly altered rounded pyrochlore crystals from the aegirine dyke. D) PPL of a cluster of acicular aegirine with dark pyrochlore crystals from the deformed quartz vein (Fig. 5.3 C). E) BSEI of image D showing bright pyrochlore inclusion in aegirine.

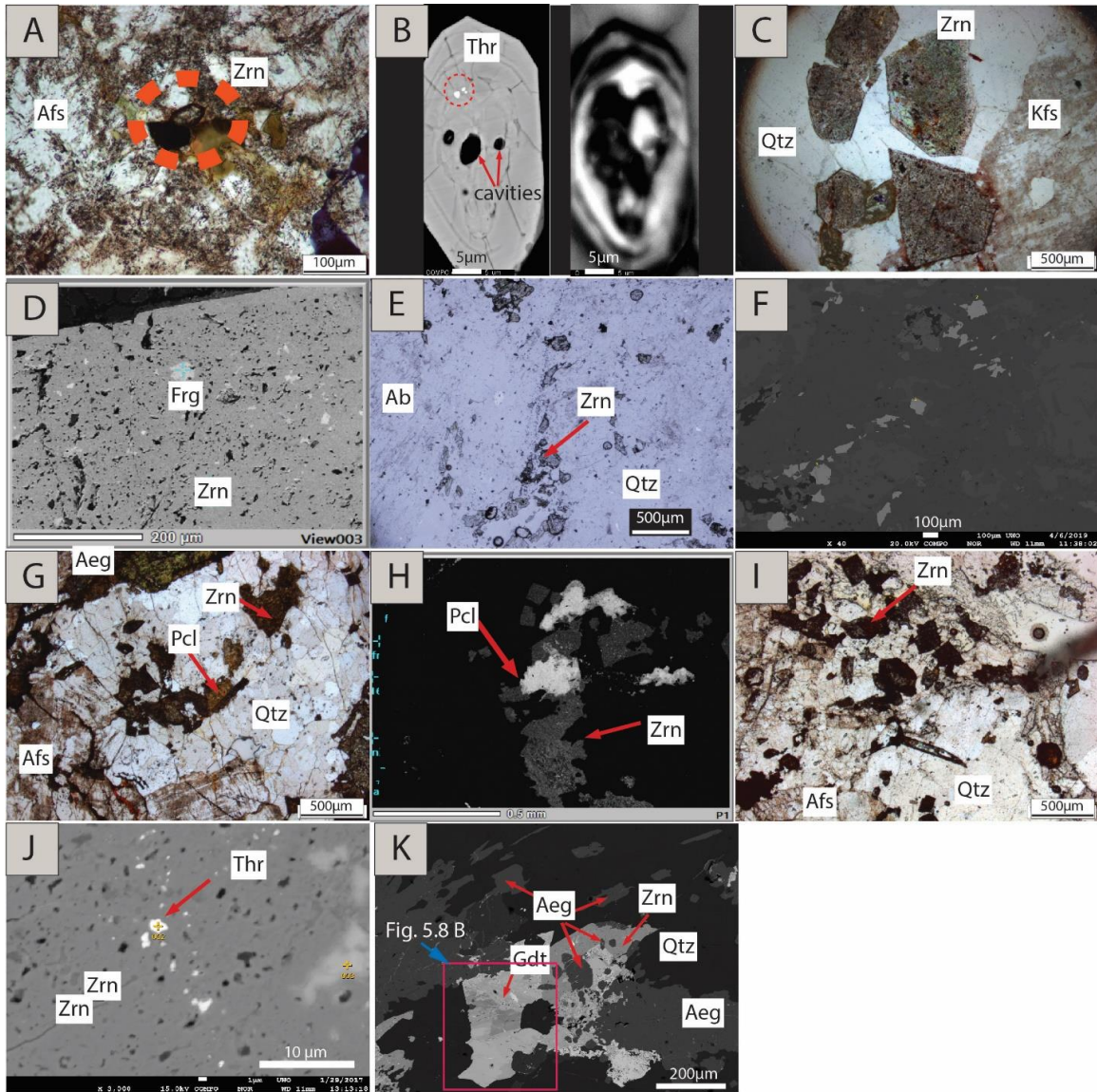


Figure 5-6 Zircon crystals morphology in Dyaheen. A) PPL image of a prismatic zircon associated with alkali weathered alkali feldspar from the monzogranite. B) BSEI and cathodoluminescence (CL) image of zircon in image A. C) PPL image of inclusion-rich zircon from pegmatites. D) BSEI of the spongy texture of zircon in D. E) PPL image of light irregular zircon crystals from the aegirine granite. F) BSEI of zircon in E. G) and H) are PPL and BSEI of zircons from the aegirine dyke . I) PPL image of a cluster of zircons from the quartz veins. J) BSI image of a spongy texture in zircon from the quartz veins. K) BSEI zircon and gadolinite with inclusions of aegirine from the quartz veins. A close-up image of the gadolinite is in Fig. 5.8 B.

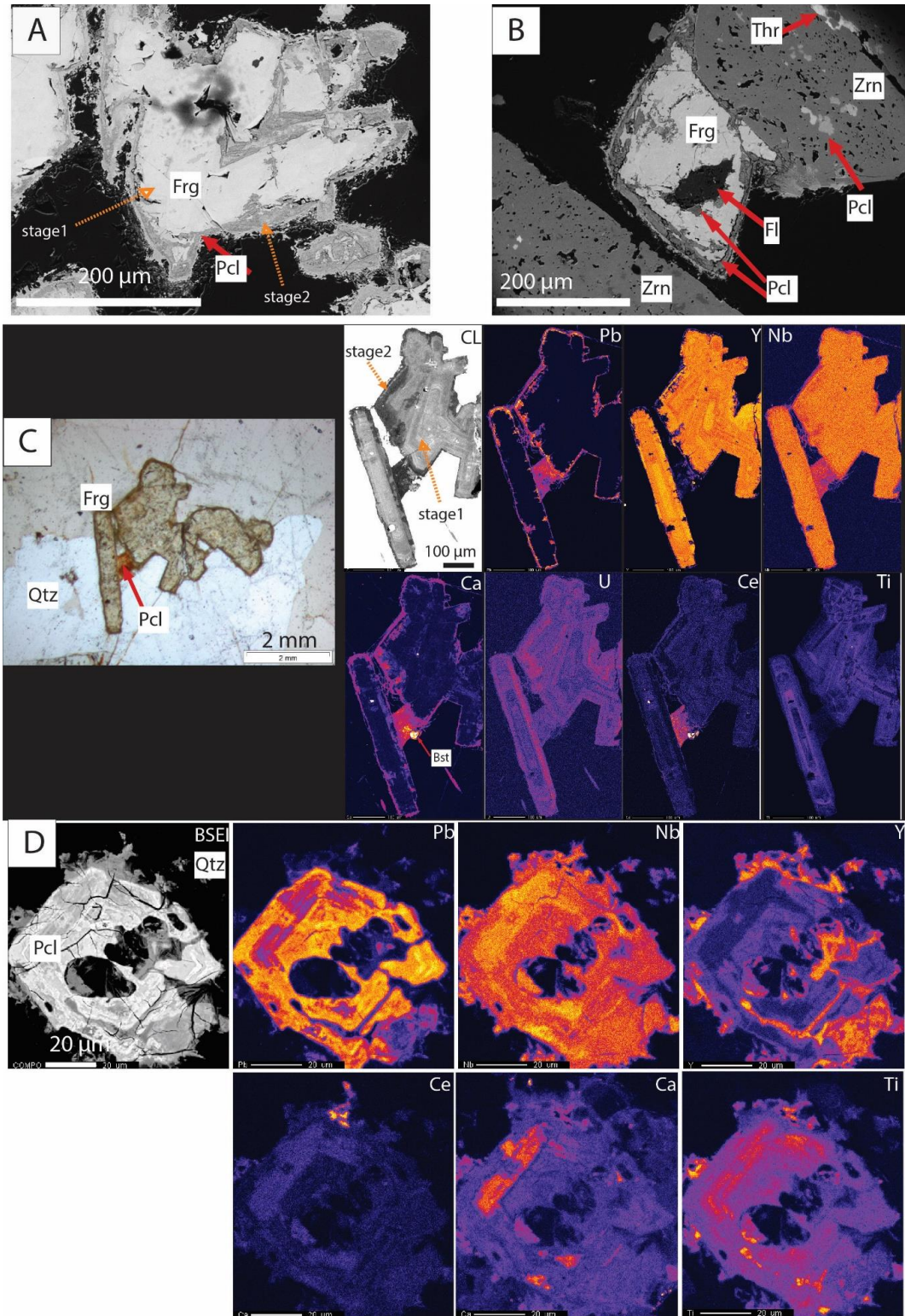


Figure 5-7 Morphology and internal chemistry of fergusonite and pyrochlore from Dyaheen. A) and B) are BSEI's of fergusonite crystals from pegmatite that are

replaced by pyrochlore. Stage 1 represents the earliest mineralization in Dyaheen, which is replaced by stage 2 represented by Pb-rich pyrochlore. C) PPL, CL, and wavelength dispersive x-ray spectroscopy (WDS)) maps showing the variable internal chemistry of fergusonite from a ductile quartz vein. D) BSEI and WDS maps show the variable internal chemistry of pyrochlore from the aegirine dyke.

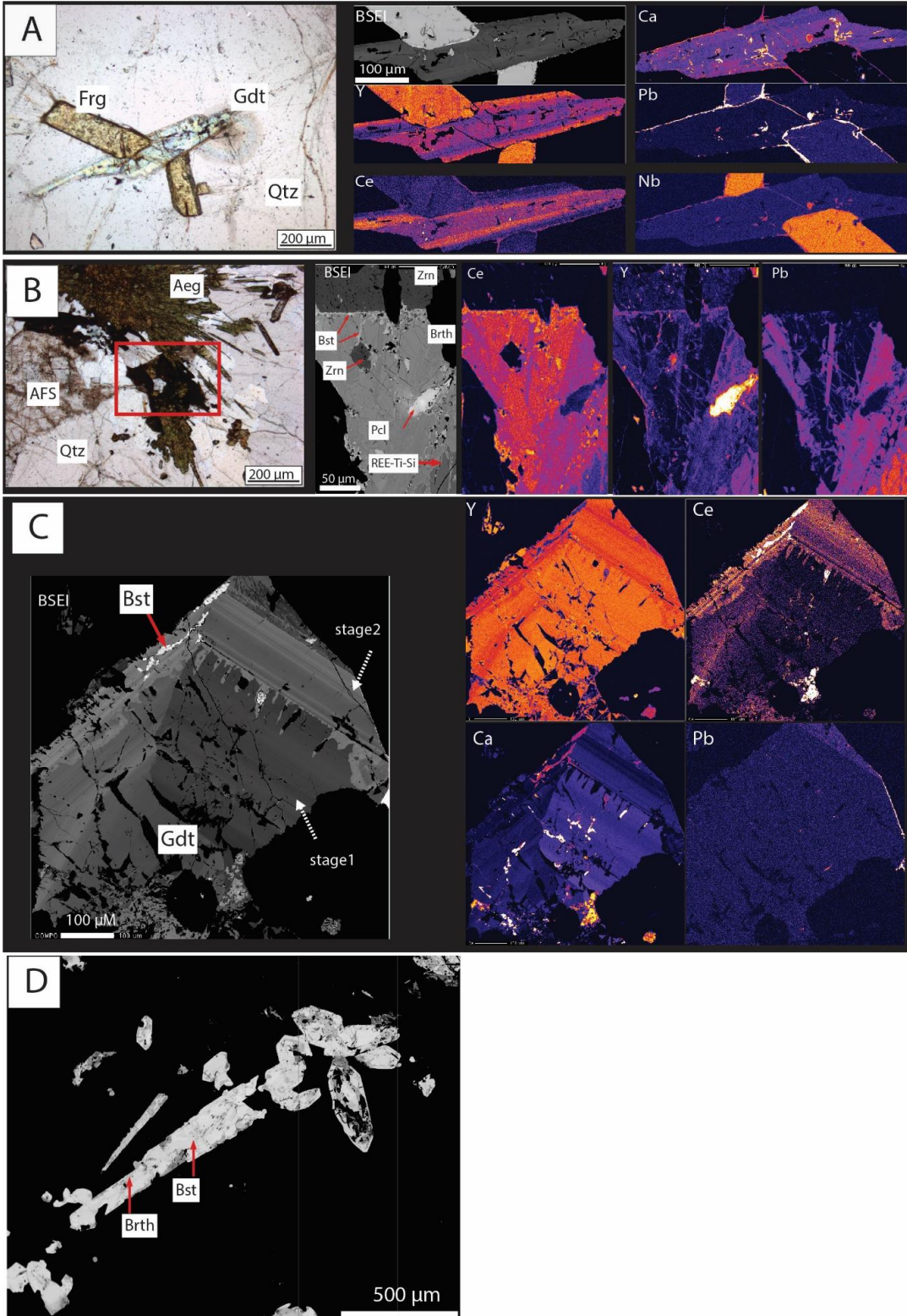


Figure 5-8 Morphology and chemistry of gadolinite and bastnasite. A) PP image, BSEI and WDS maps of early gadolinite associated with fergusonite in quartz

matrix from a ductile, quartz vein. B) PP image, BSEI and WDS maps of late gadolinite from a ductile quartz vein. C) PP image, BSEI, and WDS maps of early gadolinite from a ductile quartz vein. D) BSEI of bastnasite and britholite from a ductile quartz vein.

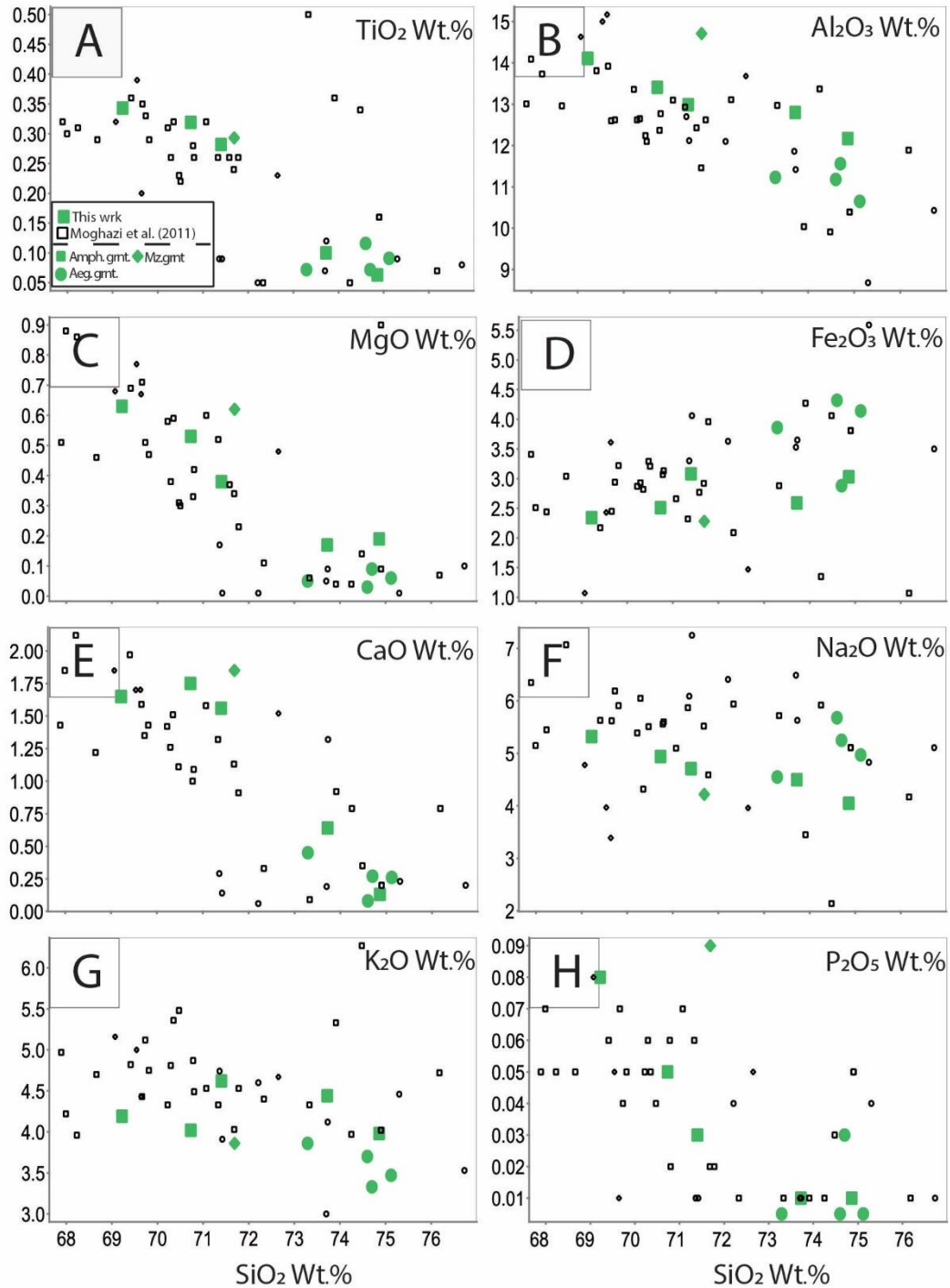


Figure 5-9 A plot of SiO₂ and major oxides concentrations of the main rock units in Dyaheen. Black symbols are from Moghazi et al. (2011). Abbreviations: Amph. grnt, amphibole-biotite granite; Aeg. grnt., aegirine granite; Mz.grnt, Monzogranite.

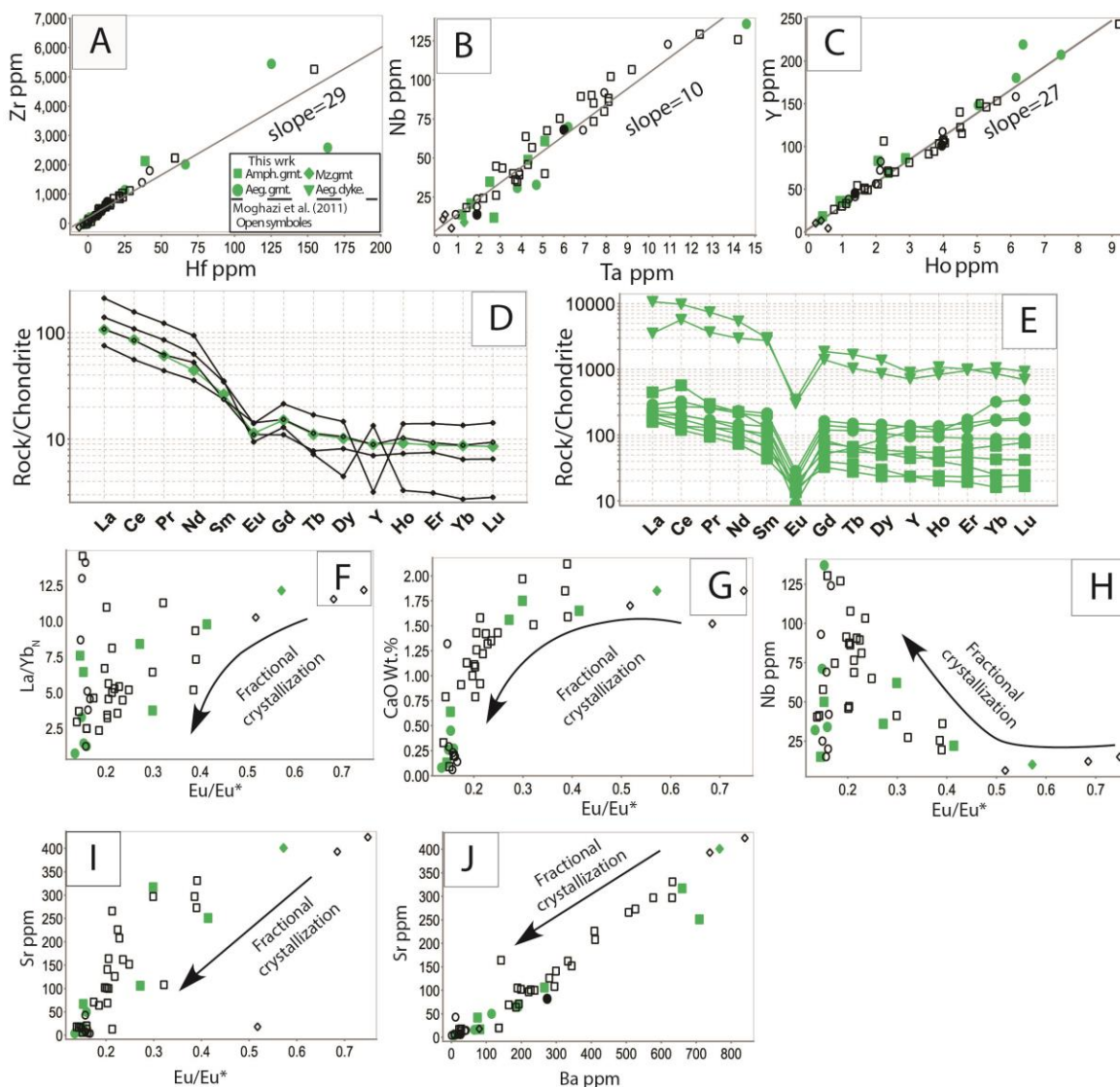


Figure 5-10 Trace element composition of Dyaheen. A) to C) plots to show the correlation between chemically coherent pairs. D) monzogranite REE chondrite normalized diagram. E) Chondrite normalized REE diagram for the amphibole-biotite granite, aegirine granite, and the aegirine dykes. Chondrite values are from McDonough and Sun, (1995). F) to I) plot of Eu anomaly ($=Eu_N/[\sqrt{Sm_N \cdot Gd_N}]$) and chondrite normalized ratio of La/Yb, CaO wt. %, Nb ppm, and Sr ppm. J) a plot of Ba ppm and Sr ppm showing a positive correlation. Arrows resemble the evolution trend of the magma.

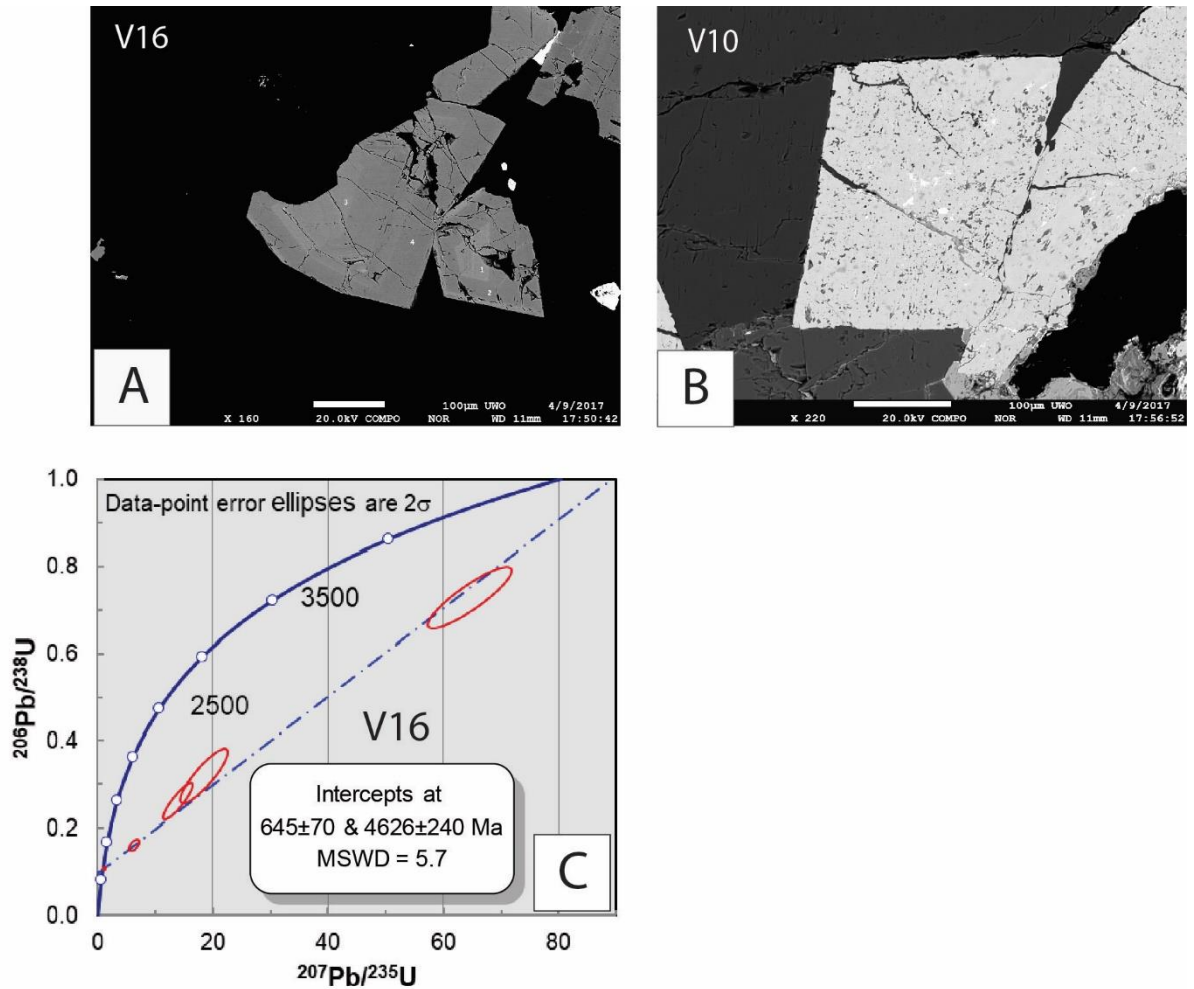


Figure 5-11 U-Pb zircon age dating of two zircons from aegirine-rich quartz vein from Dyaheen. Red circles represent analysis points. A) Clear and Inclusion-free zircon from the quartz vein that crosscut the aegirine dyke. B) Dark color, inclusion-rich zircons from the same associated with the clear-zircon. C) Estimated zircon U-Pb age of the clear zircon type.

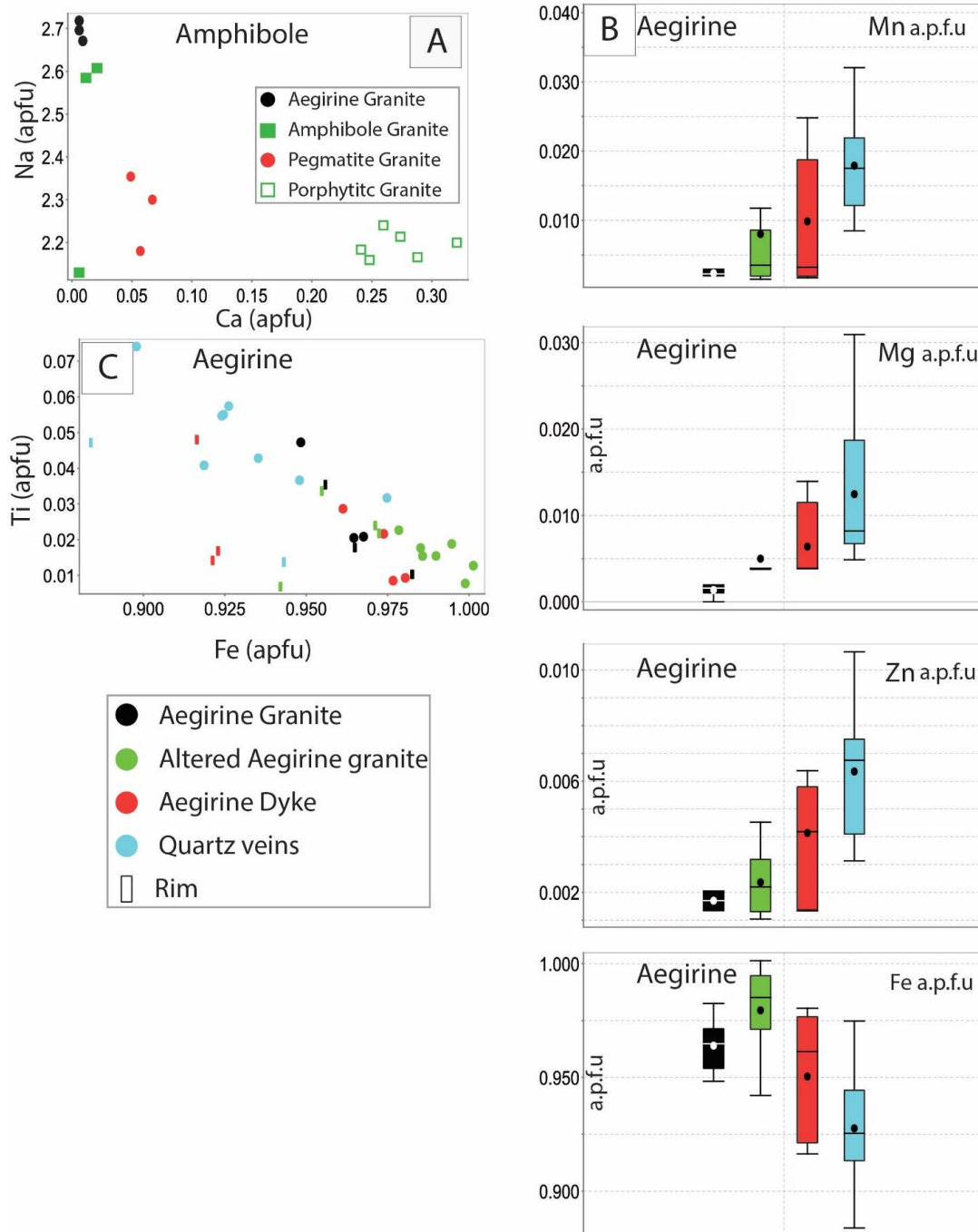


Figure 5-12 Amphibole and aegirine composition from different rock units in Dyaheen. A) Ca and Na content of amphibole in atom per formula unit. B) Variation in trace elements concentration in aegirine from different rock units. C) Fe and Ti in a.p.f.u, showing a negative correlation.

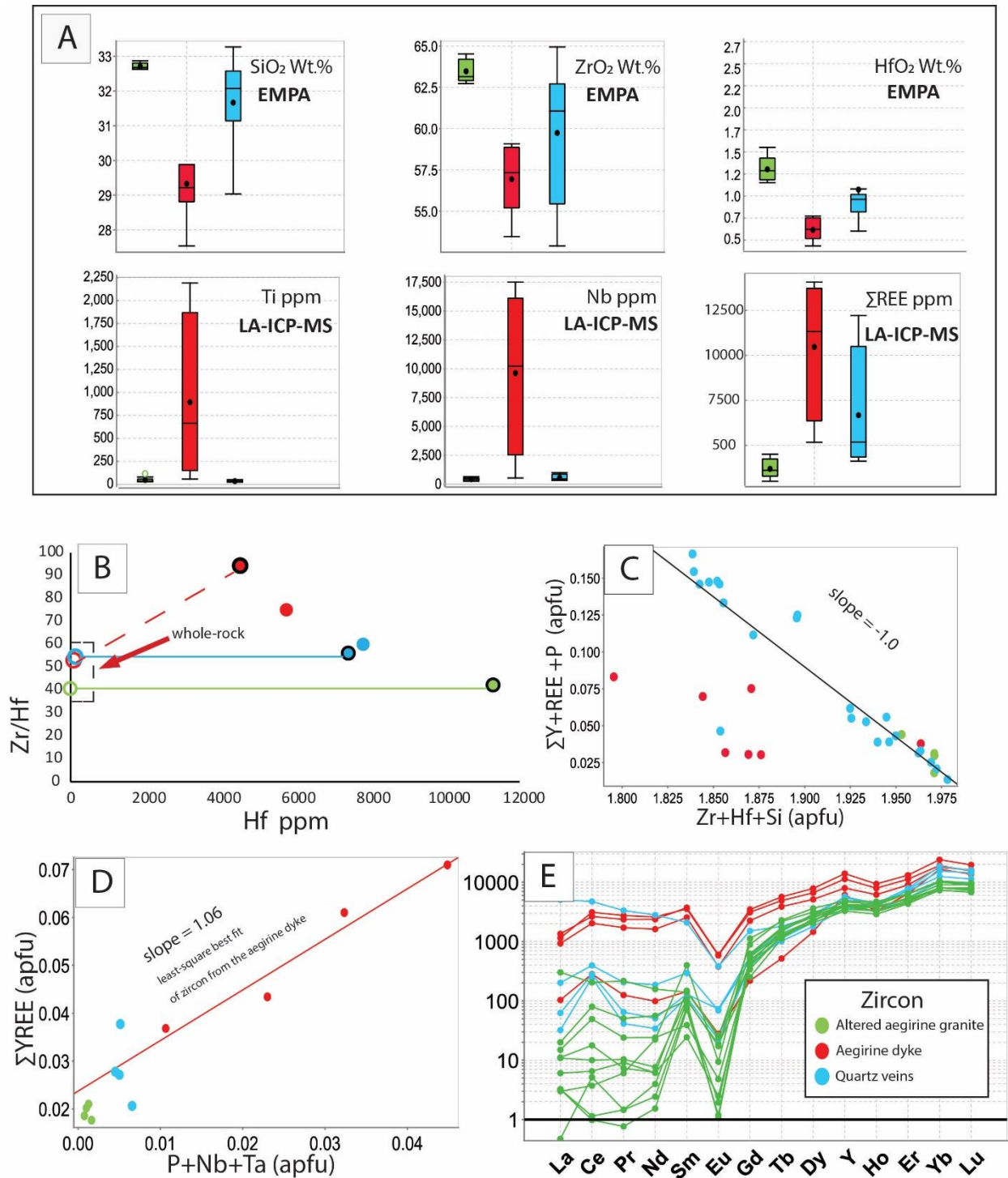


Figure 5-13 Zircon composition from different rock units in Dyaheen. A) Box and whisker plot showing the variable composition of zircons from Dyaheen. B) Hf vs. the ratio of Zr/Hf. Symbols with black rings represent zircons that have samples

with whole-rock analyses, which are demonstrated by unfilled circles in the small dashed box. Solid lines represent the tie-line between Hf and Zr/Hf in the host rock and zircons. The dashed line represents the assumed tie line of zircons from the aegirine granite. C) the substitution of $Zr+Si$ by $REE+P$ is followed by most of the zircons from the aegirine granite and the quartz veins. D) Zircons from the aegirine granite show more complex substitutions that involve Nb and Ta. The slope reflects a least-square fit of aegirine dykes (red circles) zircon data points E) Zircon/chondrite normalized REE patterns of the different zircon types. Chondrite values are from McDonough and Sun (1995).

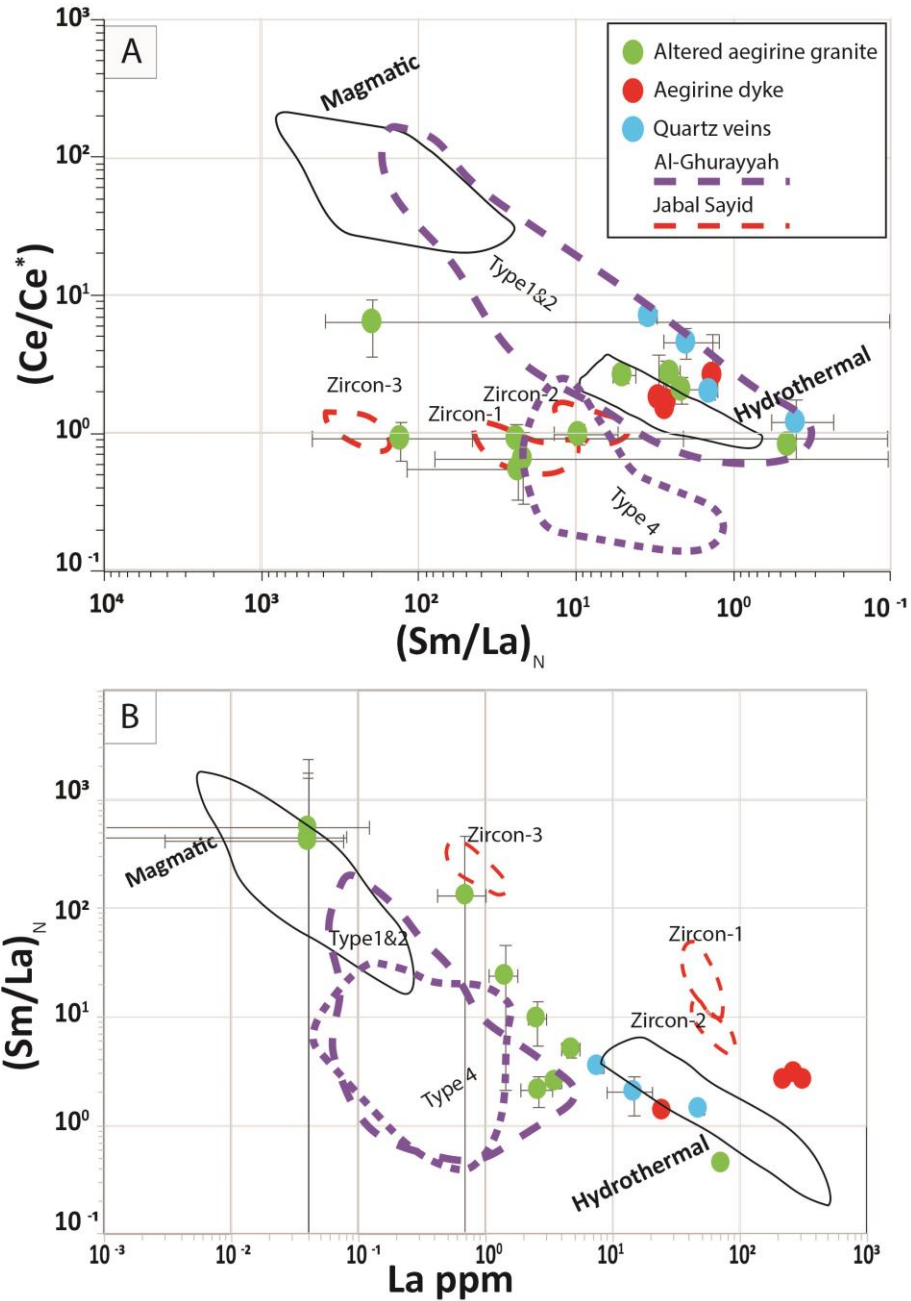


Figure 5-14 Zircon discrimination of Ce/Ce^* versus Sm/La_N in A) and Sm/La_N versus

La ppm in B) (modified after Hoskin, 2005). $Ce/Ce^* = (Ce/Ce_{chondrite}) /$

$$\sqrt{\left(\frac{La}{La_{chondrite}}\right) \times \left(\frac{Pr}{Pr_{chondrite}}\right)}, \quad (Sm/La)_N = (Sm/Sm_{chondrite}) / (La/La_{chondrite}).$$

Chondrite values are from McDonough and Sun (1995). Purple regions are for zircons from Al-Ghurayyah, and red regions are for zircons from Jabal Sayid

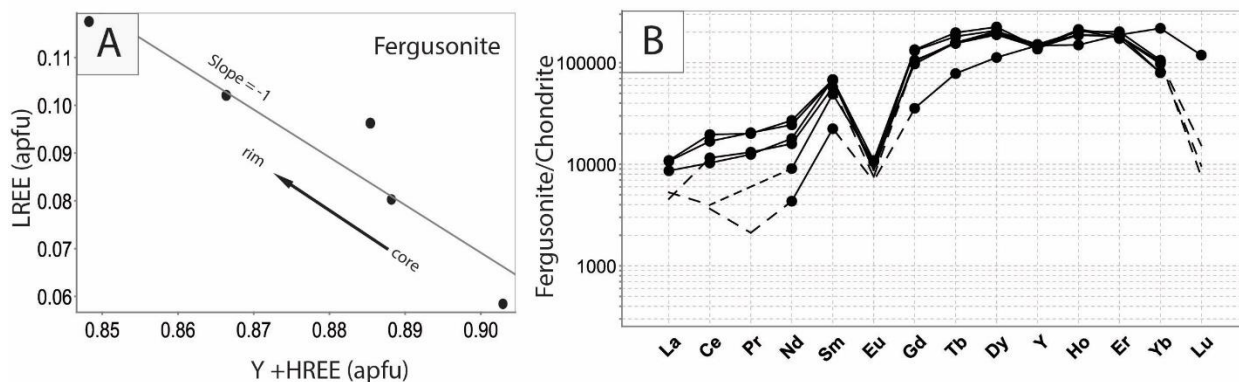


Figure 5-15 Fergusonite chemistry. A) substitution of Y+HREE by LREE that increases from core to rim. The slope of -1 reflects the ideal substitution of LREE for HREE. B) Chondrite normalized REE pattern of Fergusonite. Elements with values below the detection limit are omitted, and the dashed lines show the potential trend. Chondrite's values are from McDonough and Sun (1995).

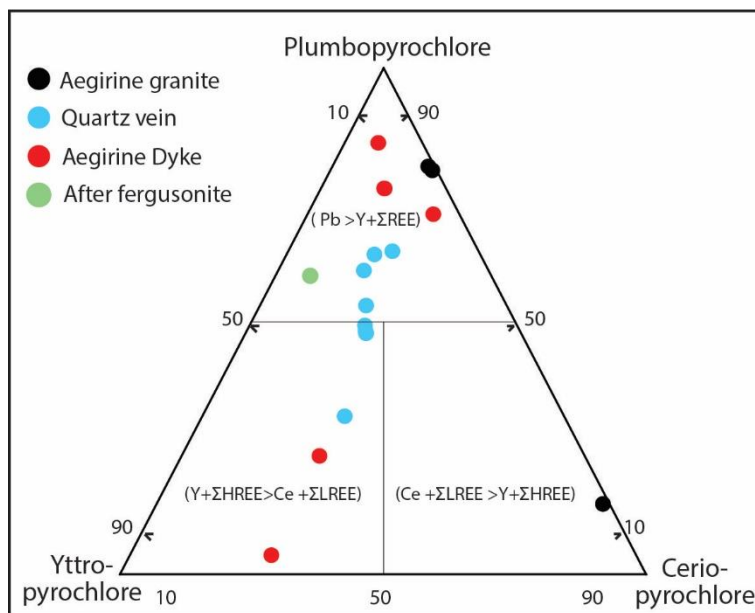


Figure 5-16 Nomenclature of pyrochlore group minerals in Dyaheen. The diagram shows the main elements (in atom per formula units) that are present in the A site of pyrochlore.

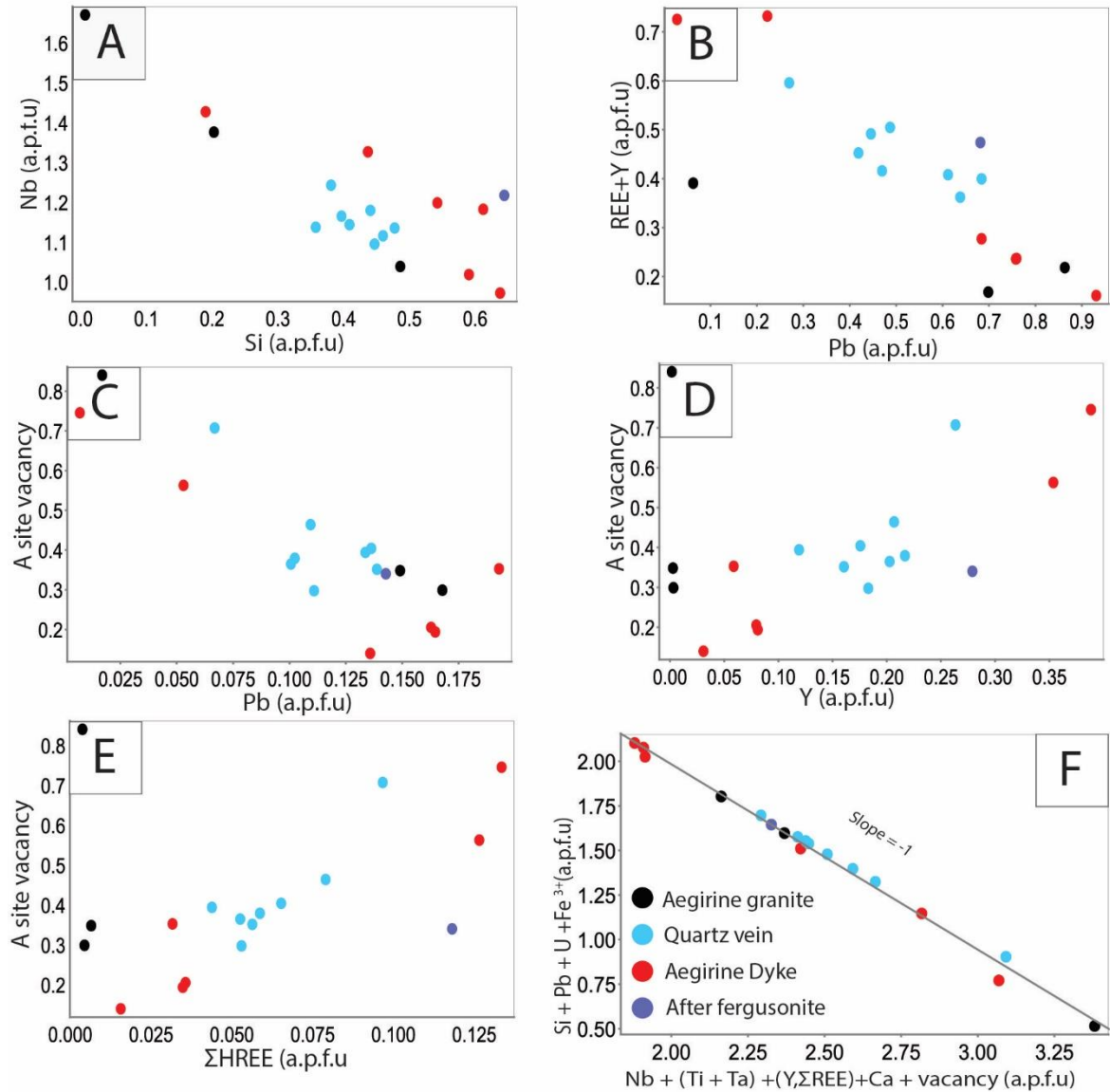


Figure 5-17 Pyrochlore chemistry. A) Nb substitution by Si in a.p.f.u. B) substitution of REE+Y by Pb. C) The decrease in A site vacancy as Pb content increases in pyrochlore. D) The Increase of vacancy in A site as Y content increases in pyrochlore. E) The increase in A site vacancy as the total HREE increase in pyrochlore. F) The slope of -1 reflects the ideal substitutions mechanism in pyrochlore.

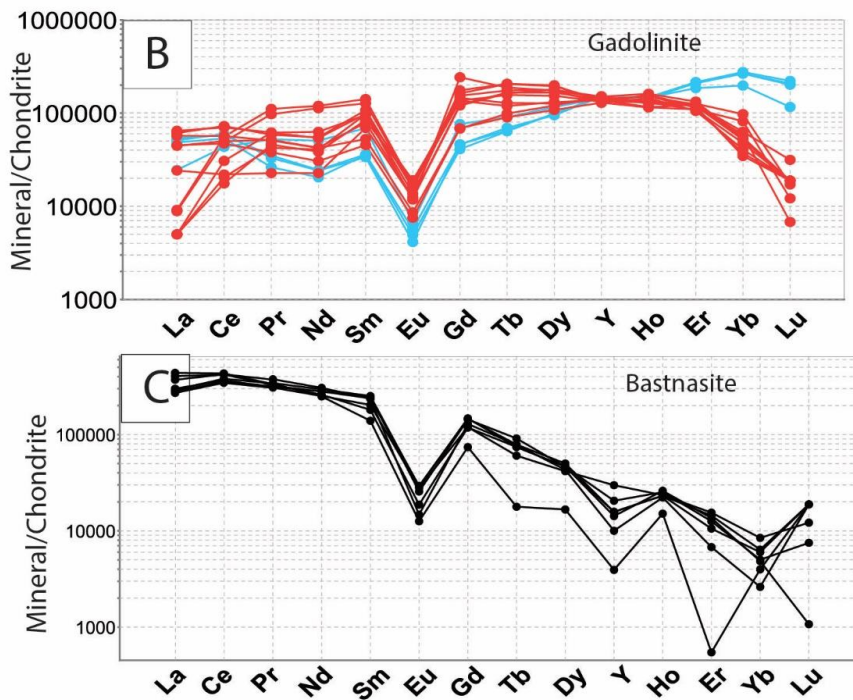
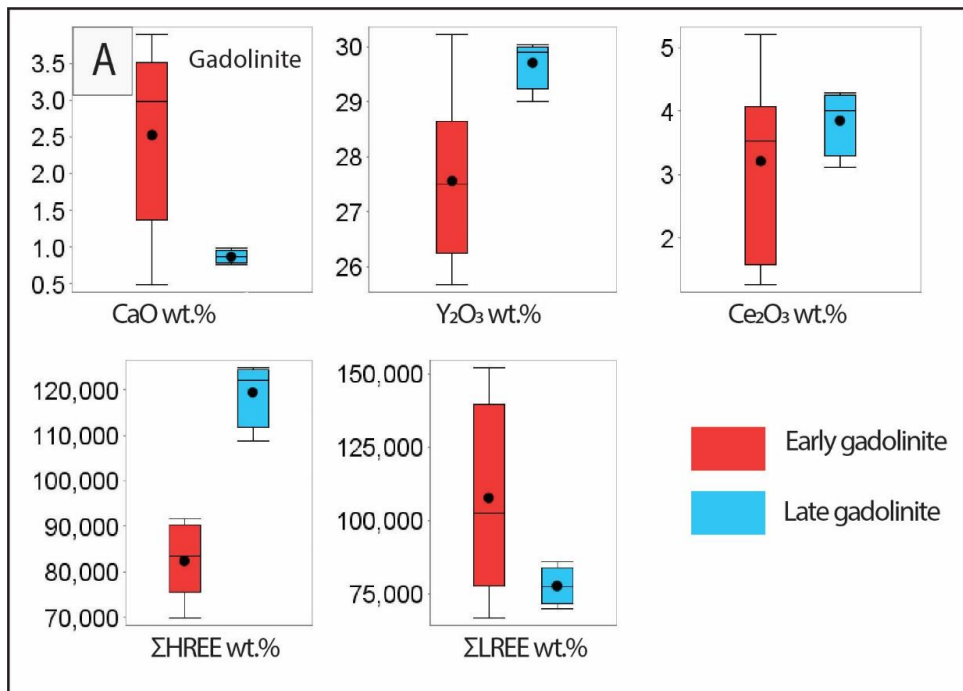


Figure 5-18 Gadolinite and bastnasite chemistry. A) Box and whisker plot show the variable composition of the gadolinite types. B) Chondrite normalized REE diagram of early and late gadolinite. C) Chondrite normalized REE diagram of bastnasite. Chondrite's values are from McDonough and Sun (1995).

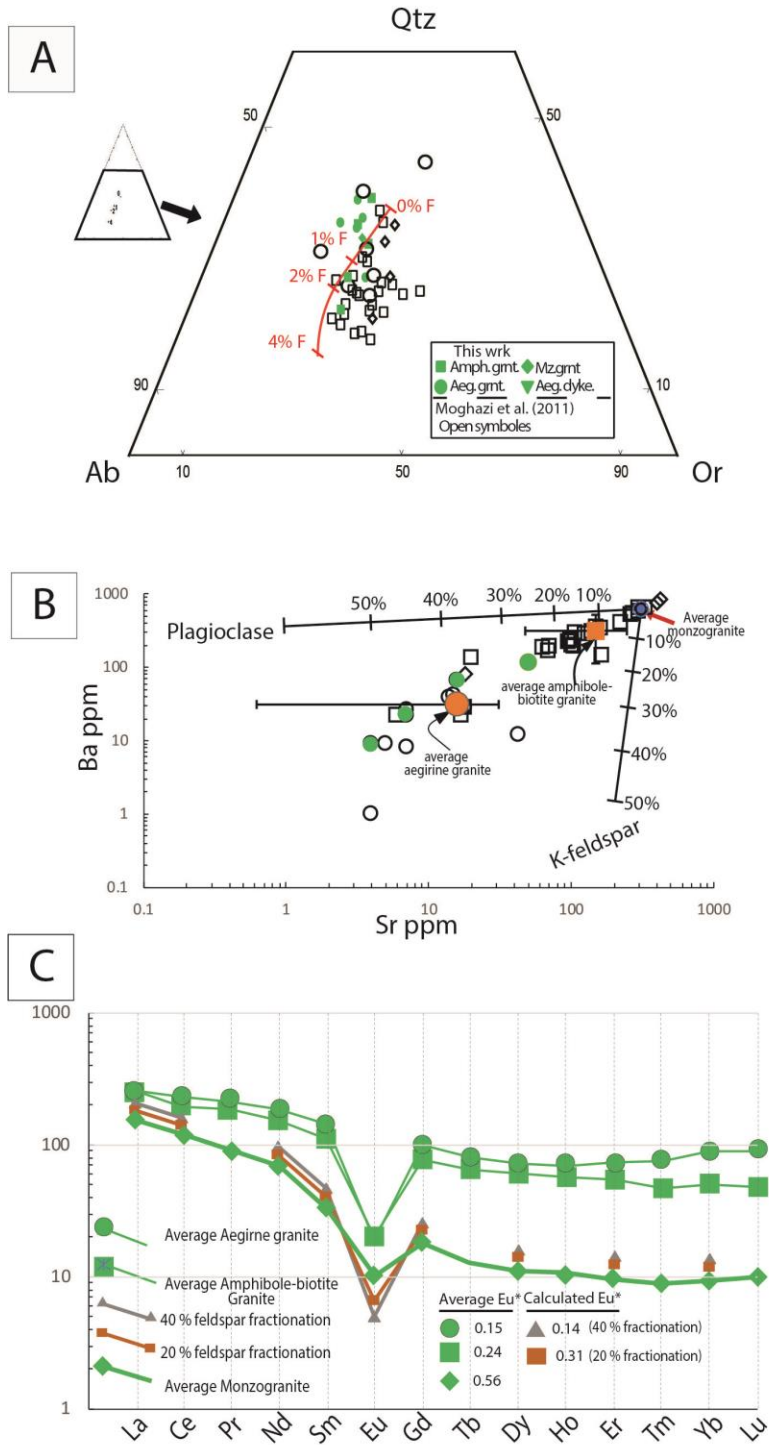


Figure 5-19 A) normalized quartz-albite-orthoclase diagram of rocks from Dyaheen. The red line represents the change in granite minima as the F concentration increases in the granitic system at 2 kbars (Manning, 1981). B) Sr Vs. Ba that are

commonly controlled by plagioclase and K-feldspar. Plagioclase and K-feldspar vectors were plotted, assuming perfect Rayleigh fractionation. The annotated percentages represent the degree of feldspars fractionation. C) Chondrite normalized REE diagram after 20% and 40 feldspars fractionations from the monzogranite. Chondrite's values are from McDonough and Sun (1995).

Chapter 6

6 Conclusion

6.1 Introduction

Rare-metal alkaline granites contain high concentrations of high field strength elements (HFSE) and rare earth elements (REE). In the Arabian Shield these types of granites formed in a post-orogenic tectonic setting. Several studies have investigated the mineralized rare-metal granites in the Arabian Shield (Ali et al., 2014; Drysdall et al., 1984; du Bray, 1986; Elliott, 1983; Elliott et al., 2002; Hackett, 1986; Moghazi et al., 2015, 2011; Qadhi and Moufti, 2008; Radain et al., 1981; Staatz and Brownfield, 1986; Turkistany and Ramsay, 1982), and the most important rare-metal deposits include Al-Ghurayyah, Jabal Tawlah, Umm Al-Birak, Jabal Sayid, Jabal Hamara, and Jabal Aja (Fig. 6.1). Drysdall et al. (1984) classified rare-metal granites of the Arabian Shield into Jabal Sayid type and Al-Ghurayyah type, based on geochemical, geological characteristics, host rock, and the associated minerals. The Jabal Sayid type is characterized by the associated granitic rocks having low Al and Na and high Fe, K/Na and high REE. Moreover, the granites of this type have normative mineralogy of a hematitic silexite. The main minerals of this type include quartz, K-feldspar and hematite with little or no albite. Jabal Sayid and Jabal Hamra are two examples of this type. In the Al-Ghurayyah type the associated granitic rocks have a major oxides composition similar to the average alkaline granite (Creaser et al., 1991), which is characterized by high Na, K, Fe and low Ca, and Al (see below). The mineralization is disseminated in porphyritic to microgranite granite. Major rock-forming minerals include microcline, albite, quartz, sodic amphibole, and zircon. The main feature of this type is the strong enrichment of HREE. Examples of this type include Al-Ghurayyah, Jabal Tawlah, and Umm Al-Birak.

This chapter draws comparisons between Al-Ghurayyah, Jabal Sayid, and Dyaheen in terms of their geology, granite ages, lithology, ore minerals, and minerals chemistry. The

different types of mineralization are evaluated within the context of the tectonic evolution of the Arabian Shield.

6.2 Geology and petrography

The rare-metal deposits at Al-Ghurayyah, Jabal Sayid, and Dyaheen share similarities in terms of elemental enrichment, and the relationships of this enrichment with the host rocks. However, there are distinct differences in terms of the style of mineralization, size, lithology of the host rock, and the nature of the mineralization. These characteristics are summarized in Table 6.1.

The granites and associated deposits form sharp contacts with the country rocks (Fig. 6.2). For example, Al-Ghurayyah has a sharp contact with the meta-volcanic rock of Silasia formation without brecciation or deformed contacts (Fig. 6.2 A). Jabal Sayid complex and Dyaheen are also in sharp contact with the diorite rocks that they intruded (Fig. 6.2 B & C) (Moghazi et al., 2015, 2011; Radain, 1979; Turkistany and Ramsay, 1982).

The granites associated with the deposits studied have variable compositions and sizes. Al-Ghurayyah occurs as 900 m subcircular body that consists of microgranitic to porphyritic granites (more abundant) with quartz, albite, and microcline as the main minerals. The granites are subsolvus with two feldspars, mafic minerals are rare, and where present are mostly sodic amphibole. Zircon and pyrochlore are the main accessory minerals, and they form an intergranular texture with the rock-forming minerals. Trilithionite mica occurs in the porphyritic granite and forms an intergranular texture with the rock-forming minerals, and inclusions in microcline and quartz phenocrysts. Columbite and secondary zircon \pm rutile occurs as secondary minerals with chlorite and muscovite that are associated with silicification.

Jabal Sayid is an alkaline granite with a composition that has evolved from monzogranitic intrusion to an alkaline granite (Harris et al., 1986; Moghazi et al., 2015). The intrusion covers an area of 30 km², with the mineralized part occurs within an oval-shaped region 2 km long and 150 m wide along the northern part of the intrusion (Fig. 6.2

B). The alkaline granite has microgranite to porphyritic texture and consists of quartz, plagioclase, perthite/microcline-perthite, sodic amphibole and aegirine. The aegirine occurs in two types: an early large prismatic crystal and a late acicular crystal. At the northern part of the granite and near the mineralized units, zircon, pyrochlore, and bastnasite occur as secondary minerals associated with hematized acicular aegirine. The main mineralization is limited to the oxidized granite and the pegmatite sheets.

Dyaheen ring complex displays a compositional evolution trend from monzogranite to amphibole-biotite granite. The ring complex is an 8.5 km by 11.5 km oval shape. The amphibole-biotite consists of quartz, plagioclase, perthite, and amphibole as the main rock-forming minerals. Titanite, magnetite, zircon, and apatite are the main accessory minerals. Fluorite, hematite, and calcite occur as secondary minerals. Most mineralization is associated with altered granite and aegirine dyke and quartz veins.

6.2.1 Mineralization styles and alteration

Al-Ghurayyah, Jabal Sayid, and Dyaheen each have distinct mineralization styles and alteration stages. The main mineralization in Al-Ghurayyah is disseminated in the porphyritic granite and the marginal unit, or as an aggregate mineralization style in a composite-body and mineralized quartz veins. The main rare-metal minerals are zircon and pyrochlore in the disseminated mineralization style and zircon, columbite, rutile, xenotime, cassiterite in the aggregate mineralization style. The early mineralization is magmatic and pyrochlore that is disseminated in the porphyritic granite and the marginal unit. Columbite occurs in the porphyritic granite; however, it is associated with secondary zircon and rutile in the porphyritic granite that shows silicification.

The main alteration event is demonstrated by the intense silicification of the porphyritic granite and the leaching of Na. Columbite, rutile in addition to secondary zircon are associated with this stage. The compositions of columbite and the secondary zircon associated with the aggregate mineralization style are comparable to the compositions of zircon and columbite associated with the silicification event. The lack of sodic amphibole in the porphyritic granite suggests it has undergone alteration. However, the absence of pseudomorphs in the porphyritic granite suggests the amphibole was replaced in an early

stage probably due to interaction with more evolved melt. The presence of columbite is a distinguishing feature of Al-Ghurayyah because columbite is absent in Jabal Sayid and Dyaheen.

The main characteristic feature of Jabal Sayid is the strong hematization that is associated with the mineralization. Most of the mineralization is coeval with the hematization of acicular aegirine. Based on textural and morphological observations of ore minerals, the mineralization occurred in two main stages. The first stage consists of alteration of early prismatic aegirine and the crystallization of zircon, hematite, and quartz with fresh acicular aegirine. Both magmatic textures (acicular aegirine forming snowball texture in intergranular albite and microcline matrix) and hydrothermal textures (typical chemistry and morphology of hydrothermal zircon) are characteristic of this stage. This is interpreted to reflect crystallization at the transition between magmatic and hydrothermal environments. The second stage is hydrothermal, and it is marked by the hematization of acicular aegirine and the crystallization of Zircon-2 (in the oxidized granite), Zircon-3 (in the pegmatite core), REE-fluorocarbonate (bastnasite and synchysite), monazite, and xenotime. The core of the pegmatite sheets is enriched in synchysite with little to no bastnasite. The bastnasite is enriched in the border zone of the pegmatite and the oxidized granite. At the end of the second stage, monazite, pyrochlore, and bastnasite were not stable and were replaced by xenotime and synchysite, whereas pyrochlore was replaced by Y-rich pyrochlore.

Dyaheen shows an evolution from monzogranite to alkaline amphibole granite, similar to Jabal Sayid. The mineralization style in Dyaheen is also similar to Jabal Sayid where the mineralization concentrated in the most evolved unit, which are aegirine dyke and quartz veins. Furthermore, the late-magmatic to early-hydrothermal stage is marked by the formation of aegirine that occurs in the aegirine dykes and quartz veins, and associated with zircon, pyrochlore, gadolinite, and bastnasite. The differences between the two deposits are manifested by the absence of the extreme hematization and the occurrence of gadolinite as the main Y+REE mineral in addition to zircon and pyrochlore at Dyaheen. Textural and mineral relationships of HFSE and REE minerals show at least three main mineralization stages. These stages can be seen clearly in the early crystallized phases,

such as fergusonite and gadolinite (first stage), which is usually replaced by Pb-pyrochlore and HREE-rich gadolinite (second stage) during subsequent hydrothermal events. The occurrence of fergusonite in pegmatites from the amphibole-granite indicate the early crystallization of fergusonite (Chapter 5). The third stage is demonstrated by the formation of bastnasite as veinlets in the gadolinite and as individual crystals in the quartz veins (Chapter 5, Fig. 5.8 B to D).

6.3 Chemistry

The average compositions of fresh and altered/mineralized granites Al-Ghurayyah, Jabal Sayid, and Dyaheen are given in Table 6.2. The Nb vs Y tectonic discrimination diagram of Pearce et al, (1984) was used to evaluate the tectonic setting of the three areas (Fig. 6.3 A). The granites from the three deposits all plot in the within-plate tectonic field. Dyaheen and Jabal Sayid display similar Nb and Y values, and they cluster near each other. Al-Ghurayyah samples have higher Nb and Y values and plot at the upper-right portion of the within-plate field. Furthermore, Al-Ghurayyah shows the highest aluminum saturation index ($ASI = \frac{\text{molar Al}}{[\text{Na} + \text{K}]}$ (Shand, 1943)) with an average of 1.12 ± 0.05 (error = 1σ standard deviation), whereas Jabal Sayid and Dyaheen have average ASI values of 0.96 ± 0.1 and 0.96 ± 0.05 , respectively (Fig. 6.3 B). Moreover, primary trillithionite is present at Al-Ghurayyah, which is a mineral that is not common in alkaline granites, but is reported at other locations (Li alteration occurs as an alteration event, e.g. Nechalacho, Canada, Feng and Samson, 2015). Nevertheless, Al-Ghurayyah shows characteristics that are consistent with alkaline granites, such as the trace element enrichments and the presence of sodic amphibole (although it is altered in most studied samples).

The variation in the major oxide and trace element compositions are shown in Figure 6.4 A. The samples from all deposits are least altered and show slight to moderate weathering. Jabal Sayid alkaline granite differs from the other deposits by its high SiO_2 and low Na_2O contents. Al-Ghurayyah is distinct by the high Al_2O_3 and F contents and the low MgO and K_2O . Dyaheen is generally similar to Jabal Sayid in terms of Mg, Fe, and K oxides, but it has a higher Ti content. Trace element compositions also show variations between the three deposits, and Al-Ghurayyah shows the highest

concentrations of HFSE and REE. This is expected because the mineralization in Al-Ghurayyah dominantly occurs in the porphyritic granite, whereas in Jabal Sayid and Dyaheen the mineralization is concentrated in the apical part (Jabal Sayid) or as quartz veins and aegirine dykes that crosscut the most evolved unit in Dyaheen. Comparing Dyaheen to Jabal Sayid, Dyaheen shows HREE, Zr, and Hf contents relative to Jabal Sayid. All studied rare-metal deposits show high enrichment of Nb, Zr, Y, and REE with different enrichment proportions of each element. The rare-metal enrichments follow the order $Zr > Nb > Y > REE$ at Al-Ghurayyah and $Zr > REE > Y > Nb$ at Jabal Sayid and Dyaheen. The variations in trace element concentrations of the three deposits are also shown by the chondrite normalized spider diagram in Figure 6.4 (B). All deposits show negative P, Ti, and K anomalies and a positive Rb anomaly. Jabal Sayid and Dyaheen show negative F, Pb anomalies, and flat Sn anomaly, whereas Al-Ghurayyah shows a flat F anomaly, and positive Pb and Sn anomalies. The best separation of Jabal Sayid and Dyaheen from Al-Ghurayyah is best illustrated by a chondrite normalized REE diagram (Fig. 6.4 C). All deposits show a well developed negative Eu anomaly. The REE pattern for Al-Ghurayyah shows a positive slope and strong HREE enrichment, whereas Jabal Sayid shows a negative slope. Dyaheen shows a high variation in REE concentration with a flat slope. Geochemically coherent element pairs Zr-Hf, and Nb-Ta were plotted against each other (Fig. 6.5). In Al-Ghurayyah, Zr and Hf have a ratio lower than the chondrite value (38), whereas Jabal Sayid and Dyaheen granites fall along or near the chondrite value. All samples have an Nb/Ta ratio near 10, which is close to the crustal ratio of 11-12 (Green, 1995).

Al-Ghurayyah zircon were classified in terms of the morphology and the host rock into 4 types. Type-1 and 2 occur in the porphyritic granite and the marginal unit, whereas Type-3 and Type-4 occur in the composite-body and the mineralized quartz veins. Secondary zircon is also present in the porphyritic granite as a replacement on Type-1 and 2.

In Jabal Sayid, all zircon is interpreted to have occurred during the alteration of prismatic and acicular aegirine. The zircon are classified based on the host rock into Zircon-1 in the aegirine granite, Zircon-2 in the oxidized granite, and Zircon-3 in the pegmatite. They commonly occur as a replacement mineral in the pseudomorphs and the matrix with

hematite. In the pseudomorphs, they occur as aggregates of small crystals that are arranged to form veinlets. Most of the zircon is unzoned; however, they show bimodal zoning and a resorbed reprecipitation texture where they are zoned. At Dyaheen, magmatic zircon is rare and only occur as fine elongated prismatic crystals (about 10 μm long). Moreover, the magmatic zircon is well zoned and show oscillatory zoning that was overprinted by secondary zircon. The secondary zircon is common in altered amphibole and the aegirine granite. It is associated with hematite and fluorite alteration of amphibole and aegirine. Moreover, the secondary zircon also occurs in the aegirine dykes and the quartz veins. The secondary zircon occurs as subhedral to anhedral equant crystals 100 to 300 μm across that are larger than the magmatic zircon. The secondary zircon lacks oscillatory zoning; however, it locally shows bimodal zoning. In the aegirine dyke and quartz veins, zircon is fluid and mineral inclusion-rich and show spongy texture.

The chemistry of zircon from the three deposits shows variable chemical compositions among zircon types from the same deposits and among other deposits. The four types of zircon from Al-Ghurayyah are distinguished by Hf and the LREE (La, Ce, Pr, Nd, Sm) relative to Jabal Sayid and Dyaheen zircon. Type-1 and 2 zircon have lower Hf and higher Y+REE contents relative to Type-3 and 4. Type-3 and 4 have the highest Hf content and the lowest REE concentration of zircon from the three deposits. In Jabal Sayid, zircon have distinctly higher abundances of Y and REE compared to Al-Ghurayyah (Fig. 6.6 A). The composition of Zircon-2 from the oxidized granite and Zircon-3 from the pegmatite sheets are comparable, and they are characterized by high Y content, which can reach up to 15 wt. %. Zircon-1 have a lower Y content and higher Hf concentration. All zircon types in Jabal Sayid are secondary based on the textural observations (Chapter 3). Dyaheen has variable zircon compositions. Zircon from the aegirine dyke have the highest trace element concentrations, and they are comparable to Zircon-2 and 3 from Jabal Sayid. The aegirine granite zircon have the lowest trace elements concentrations and the highest Hf content. Figure 6.6 (A) shows a comparison of the average chondrite normalized REE concentration of the different zircon types from the three deposits. Zircon from Al-Ghurayyah have the steepest positive REE pattern with La_N/Yb_N (chondrite value are from Boynton, 1984) ranging between 4.0×10^{-5} to 1.4×10^{-4} and display a negative Eu anomaly in all types and a positive Ce anomaly for

Type-1 and 2. Zircon-3 from the pegmatite sheets from Jabal Sayid and zircon from the aegirine granite from Dyaheen also have steep positive REE patterns (La_N/Yb_N 7.3×10^{-5} and 3.8×10^{-3} , respectively), but they lack a positive Ce anomaly. The other zircon types from Jabal Sayid have higher LREE content and are more enriched in HREE relative to the Zircon-3. Dyaheen zircon from the aegirine dyke and the quartz veins have the highest LREE and show near-flat REE patterns. They have a similar HREE enrichment to Al-Ghurayyah zircon.

From Table 6.2, the mineralized sample from Jabal Sayid and Dyaheen experienced increases in heavy REE (HREE = Gd, Tb, Dy, Ho, Er, Tm, Yb, and Lu) +Y concentrations, whereas in Al-Ghurayyah all samples show high HREE concentrations and show tetrad effect (Chapter 2). In order to evaluate the tetrad effect, the total tetrad effect was calculated according to Monecke et al. (2002) method from tetrad 1 ($T_1 = La, Ce, Pr, \text{ and } Nd$), 3 ($T_3 = Gd, Tb, Dy, \text{ and } Ho$) and 4 ($T_4 = Er, Tm, Yb, \text{ and } Lu$), where the total tetrad effect (T) is :

$$T = \sqrt{\frac{1}{2N} \times \sum_{i=1}^N \left(\left[\frac{X_{Bi}}{X_{Ai}^{2/3} \times X_{Di}^{1/3}} - 1 \right]^2 + \left[\frac{X_{Ci}}{X_{Ai}^{1/3} \times X_{Di}^{2/3}} - 1 \right]^2 \right)}$$

Where X_{Ai} is the chondrite normalized concentration of the first element in the tetrad, X_{Bi} and X_{Ci} are the chondrite normalized concentrations of the middle elements, and X_{Di} is the normalized concentration of the last element in the tetrad. The result of the total tetrad effect was plotted with K/Rb, Zr/Hf, and Y/Ho (Fig. 6.7). The calculated total tetrad effect of the three deposits shows that Al-Ghurayyah has the highest total tetrad effect with values larger than the limit of visible tetrad (Monecke et al., 2002). By contrast, only a few of the altered amphibole granite and mineralized samples from Dyaheen and an altered aegirine granite from Jabal Sayid show a total tetrad effect. The tetrad effect was attributed to the interaction of silicate magma with aqueous fluid (Bau, 1996; Irber, 1999; McLennan, 1994; Peretyazhko and Savina, 2010). Peretyazhko and Savina, (2010) proposed that the M shape tetrad effect commonly seen in rare-metal granitoid rock

occurs due to fluoride-silicate liquid immiscibility in F-rich magma chambers where the fluoride melt is characterized by the presence of a W-shaped tetrad. In Figure 6.7 (A), the ratio of K/Rb in Dyaheen and Jabal Sayid granites is at the minimum K/Rb in crustal rocks (150 to 350, Taylor, 1965) and do not show total tetrad effect. Al-Ghurayyah samples show values below the minimum crustal values and show tetrad effect. The K/Rb ratio in Al-Ghurayyah granite decreases with increasing the total tetrad values. In Figure 6.7 (B), the ratio of Zr/Hf was plotted with the total tetrad effect values. Most of Dyaheen samples were plotted in the charge-and-radius-controlled field (CHARAC) defined by Bau (1996), whereas Jabal Sayid and Al-Ghurayyah samples were plotted outside the CHARAC field. In Figure 6.7 C, most of the samples fall in CHARAC field of Y/Ho and do not show any correlation with the amount of the tetrad (Fig. 6.7 C).

According to Bau (1996), the deviation of ratio indicates a non-magmatic environment. Irber (1999) pointed out that a highly fractionated ratio is not a characteristic of silicate melts. However, as shown in Figure 6.7, samples that are mineralized or show post-magmatic alteration (square symbols) from the three deposits commonly have the same total tetrad effect as the fresh samples. This indicates that the variation in the ratios of chemically coherent elements is not exclusively due to interactions with aqueous fluid. For example, some authors argued that the deviation of Zr/Hf from the chondrite ratio is due magmatic processes (Kogarko, 2016; Linnen and Keppler, 2002). The deviation of Zr/Hf is due to the higher Hf content in Al-Ghurayyah, which is a characteristic of secondary zircon (Chapter 3). Furthermore, zircon from the aegirine dyke in Dyaheen have an average Zr/Hf ratio of ≈ 95 , whereas the ratio of the whole-rock is ≈ 50 . This indicates that Hf is being controlled by a mineral (or minerals) other than zircon. Another mineral that is present with zircon and might partition Zr and Hf is aegirine, which is known to have high concentrations of Zr (Dyulgerov and Platevoet, 2006; Kogarko, 2016; Njonfang and Nono, 2003). Hafnium has a higher partition coefficient than Zr in aegirine structure (Kogarko, 2016). Thus, if aegirine crystallizes before zircon this could cause an increase in the ratio of Zr/Hf in the zircon. Therefore, the ratio of chemically coherent pairs and the amount of tetrad effect cannot distinguish non-magmatic, and other factors such as textures and minerals chemistry should also be taken into consideration.

The morphology and the internal chemistry of zircon were considered as a very useful tool to track the change in the magma evolution and to distinguish magmatic and hydrothermal crystallization environments (Chen and Zhou, 2017; Corfu et al., 2003; Fu et al., 2009; Hoskin, 2005; Hoskin and Schaltegger, 2003; Pettke et al., 2005; Schaltegger, 2007; Wu et al., 2018; Yang et al., 2014). In Al-Ghurayyah, the oscillatory zoning of Type-1 and the typical magmatic intergranular texture that Type-1 and 2 forms in the matrix indicate magmatic formation. By contrast, Type-3 and 4 occur in quartz veins and the composite-body, that were interpreted to resample hydrothermal fluid, lack oscillatory zoning and display spongy texture (Type-3). Moreover, they have chemical composition comparable to the secondary zircon associated with the alteration events in the porphyritic granites. In Jabal Sayid, all zircon types are associated with alteration. Zircon-1 shows textural relationships with albite, microcline, and snowball quartz that resemble magmatic texture. This type might have crystallized from a transitional environment. In Dyaheen, the morphology and textural relationships show that it is not a magmatic. The zircon occurs with alteration in the aegirine granite and amphibole-biotite granite, or in quartz veins and aegirine dykes.

In order to discriminate between zircon types using their trace element compositions, Ce anomaly was plotted with chondrite normalized Sm/La in Figure 6.6 (B), and chondrite normalized Sm/La was plotted with La concentration in ppm in Figure 6.6 (C) (Hoskin, 2005). In Figure 6.6 (B), most of the zircon data fall outside the designated fields for magmatic and hydrothermal zircon. Al-Ghurayyah Type-1 and 2 zircon formed a trend between the magmatic and hydrothermal zircon. Type-4 zircon from Al-Ghurayyah plotted near the hydrothermal field. All zircon types from Dyaheen are partially to completely within the hydrothermal field. Jabal Sayid zircon plotted outside the designated fields, and formed a trend toward lower $(\text{Sm/La})_N$ values. In Figure 6.6 (C), Type-1 and 2 zircon from Al-Ghurayyah also fall partially in the magmatic field and spread in the area between the magmatic and hydrothermal fields. Zircon from the aegirine granite from Dyaheen plotted in the area between the magmatic field, and the hydrothermal field, with some data falling in the hydrothermal field. Zircon from the aegirine dykes and quartz veins from Dyaheen plotted near and in the hydrothermal field, respectively. All zircon from Jabal Sayid plotted outside the designated magmatic and

hydrothermal fields with zircon from the oxidized granite and aegirine granite plotting near the hydrothermal field, whereas zircon from the pegmatite sheets plotted closer to hydrothermal field. It has been suggested that magmatic zircon generally has a lower LREE content and shows a positive Ce anomaly (Belousova et al., 2006; Hoskin and Schaltegger, 2003; Wu et al., 2018). However, late-magmatic zircon could be difficult to distinguish from hydrothermal zircon (Pettke et al., 2005). Moreover, Ce anomaly can be obscured or absent due to the crystallization of Ce-rich minerals prior or coeval to zircon crystallization (Lv et al., 2018). Furthermore, it seems that Hoskins (2005) diagrams could not discriminate magmatic zircon and hydrothermal zircon from Jabal Sayid as well as Type-4 zircon from Al-Ghurayyah.

This suggests that zircon chemistry cannot be used solely to discriminate between magmatic and hydrothermal zircon. Thus, morphology and textural relationships of zircon with associated minerals should be taken into consideration.

6.4 Age and source

The rare-metal alkaline granite deposits in the Arabian Shield were emplaced during the post-tectonic plutonic activity that intruded the shield between 680 to 550 Ma (Nehlig et al., 2002). The ages of the studied deposits were estimated from U-Pb isotopes from zircon. Al-Ghurayyah yields an estimated age of 554 ± 89 Ma from zircon from the porphyritic granite and from 631 ± 7 to 647 ± 34 Ma from zircon from the mineralized quartz veins (Chapter 2). The estimated age of zircon from the feldspar granite in Jabal Sayid yields an age of 593 ± 2.4 Ma (Moghazi et al., 2015). The age of Dyaheen was estimated by U-Pb in zircon from the monzogranite and amphibole-biotite granite by Ali et al., (2014), which are of 625 ± 11 Ma and 613 ± 4 Ma, respectively. In Chapter 5, the age of the mineralization at Dyaheen was estimated from zircon from the mineralized quartz veins and yielded an age of 645 ± 70 Ma. The ages of the studied rare-metal granites are consistent with the post-tectonic plutonic activity age and in agreement with their trace elements compositions that indicate a within-plate tectonic environment.

The source of anorogenic A-type alkaline granites is a subject of an ongoing debate. Many genetic models have been proposed to describe the geneses of this type of rock.

The proposed models include: 1) residual-modal where A-type granite is a result of high-temperature partial melting of granulitic rock that had previously generated an I-type magma (Barker et al., 1975; Collins et al., 1982; Landenberger and Collins, 1996); 2) fractionation of alkaline mantle-derived basalt with or without crustal assimilation (Bonin, 2007; Eby, 1992, 1990; Frost and Frost, 2011; Kemp et al., 2006; Turner et al., 1992; Zhang et al., 2012); 3) melting of lower crust under fluxing of mantle-derived volatiles, melting of lower crust by internal radiogenic heat production, or by underplating mantle derived magma (Brown, 1994; Frost et al., 2002); 4) high temperature melting of I-type tonalitic granites (Creaser et al., 1991).

The genesis and development of the Arabian-Nubian Shield has been investigated by a number of studies (Ali et al., 2014, 2009; Moghazi et al., 2015, 2012; Stern, 2002, 1994; Stern and Johnson, 2010). Stern and Johnson (2010) concluded that Sm-Nd isotope compositions revealed that the lower crust is formed by juvenile materials from the mantle, and the Nd model age of the lower crust is close to the age of the Arabian-Nubian Shield. Moreover, Stern et al. (2010) excluded the involvement of pre-Neoproterozoic crust in the formation of the Arabian-Nubian Shield. The $\epsilon\text{Nd}(t)$ of the Arabian Shield ranges from $\sim +4$ to $\sim +10$ (Moghazi et al., 2012). Thus, partial melting of the lower part of the juvenile Arabian Shield crust with/without direct contribution from the upper mantle material led to the formation of the post-orogenic alkaline granites (Ali et al., 2014; Eyal et al., 2010; Moghazi et al., 2015)

The Sm-Nd isotope compositions of Al-Ghurayyah, Jabal Sayid, and Dyaheen granites have been estimated by several studies (Ali et al., 2014; Moghazi et al., 2015; Qadhi and Moufti, 2008). Qadhi and Moufti (2008) reported an initial ϵNd that ranges from +5.8 to +5.6 from the porphyritic granite. Moghazi et al. (2015) reported an initial ϵNd of +4.9 to 5.3 for the feldspar alkaline granite in Jabal Sayid. In Dyaheen, Ali et al. (2014) reported an initial ϵNd of +4.1 to 5.3 for the monzogranite, the amphibole-biotite granite, and the aegirine granite. These values are within the Arabian Shield range, which was interpreted to resemble juvenile crust (Stern et al., 2010). Ali et al. (2014) concluded that the magma source of Dyaheen is derived from the mixing of arc-related crustal protolith and a subduction-overprinted mantle source. However, Moghazi et al. (2015) discounted both a

direct source from the depleted mantle, or a hybridized source due to the high volume of granites over mafic rocks and the rare presence of intermediate rocks. Instead they argued that a hybridization process would lead to scattering isotope signatures of Sm-Nd, whereas Jabal Sayid shows restricted ϵNd values. Moreover, Moghazi et al. (2015) interpreted the source of Jabal Sayid granite to be from partial melting of the lower crust of the juvenile Arabian Shield.

Although Qadhi and Mufti (2008) did not fully discuss the magma source of Al-Ghurayyah, they did suggest that the source was from the partial melting of either mantle or juvenile crust.

In summary, the ϵNd of the three deposits all fall in the range +4.1 to +5.8 and are within the range of the Arabian-Nubian Shield, which indicates that they have the same magma source. Given the positive ϵNd of the studied rare-metal granites, the most plausible model of magma source is the partial melting of the lower crust of the Arabian shield. The variation in mineralization style and mineral enrichment are most likely due to late magmatic to post-magmatic processes.

6.5 Emplacement and evolution of rare-metal deposits in the Arabian Shied

As discussed above, the age and isotopic signatures of the three deposits signify that they all formed from a melt that was derived from the partial melting of juvenile crust. Figure (6.8) summaries the process that Al-Ghurayyah and Jabal Sayid granite took from the source to the final crystallization. Dyaheen evolution path is equivalent to Jabal Sayid but lacks the final hematization event.

The heat source for the crustal melting was likely supplied by the upwelling of the asthenosphere after crustal-mantle thickening and the delamination of the mantle lithosphere (Avigad and Gvirtzman, 2009; Eyal et al., 2010; Moghazi et al., 2011)(Fig. 6.8 A). It has been suggested that alkaline granite magma in the Arabian-Nubian Shield may have been generated by about 20 % partial melting of calc-alkaline basaltic rock (Eyal et al. 2010). The three studied granites show that they have undergone extreme

fractionation by mainly feldspar in addition to other mafic minerals. This led to the accumulation of the incompatible elements in the residual melt. The variations between the three deposits most likely took place during late-magmatic to hydrothermal stages. These variations are manifested in the style of mineralization, late-stage gangue minerals, and the type of rare-metal minerals. Therefore, it is more convenient to compare the three deposits by the characteristics of their late-magmatic stage and hydrothermal stage. Nevertheless, distinguishing the late-magmatic stage from hydrothermal stage is challenging as there is no unequivocal evidence that can distinguish the two stages. Thus, the classification of stages is based on the dominance of one stage on the other, which was assessed by the texture, mineralogy, and mineral morphology and chemistry.

6.5.1 Late-magmatic stage

A common feature observed in Jabal Sayid and Dyaheen is the crystallization of a late-magmatic to early-metasomatic aegirine. By contrast, Al-Ghurayyah lacks aegirine, which is probably due to the higher Al content in Al-Ghurayyah granite, which led to the crystallization of albite during this stage (Fig. 6.8 B-1). This stage is widespread at Al-Ghurayyah, and is associated with the crystallization of magmatic zircon (Type-1 and 2) and pyrochlore (PCL-1 and 2) based on the intergranular textures of both minerals. Another unique observation about Al-Ghurayyah is the occurrence of trillithionite within the magmatic assemblage, which is not observed at Jabal Sayid and Dyaheen. This indicates that the granitic melt of Al-Ghurayyah was enriched in Li in addition to F, which helped to concentrate incompatible elements.

At Jabal Sayid and Dyaheen, the formation of late-aegirine is limited to rock units that are close to the mineralization at Jabal Sayid and the most evolved unit at Dyaheen ring complex. The aegirine formed by replacing the sodic amphibole or forming individual crystals (Fig. 6.8 C-1). Only weak mineralization is observed, and most of the mineralization occurs later, during the hydrothermal stage.

6.5.2 Hydrothermal stage

The beginning of the hydrothermal stage in Al-Ghurayyah can be inferred by the alteration of the magmatic zircon (Type-1 and 2) to form secondary zircon, and the

alteration of the pyrochlore to form columbite in the porphyritic granite and the marginal unit. Moreover, this stage is characterized by silicification, the formation of fan-shaped muscovite, and the alteration of albite. The mineral chemistry of zircon indicates that it was formed in a hydrothermal environment. Moreover, the chemistry of zircon and columbite from the silicified granite overlap with the chemistry of these minerals from the quartz veins and the composite-body.

In Jabal Sayid, the early mineralization is at the transition stage between magmatic and hydrothermal environments, demonstrated by the alteration of the prismatic aegirine and the crystallization of Zircon-1 with acicular aegirine, whereas most of the rare-metal minerals occur later during the hydrothermal stage. This was followed by the alteration of the acicular aegirine and the crystallization of zircon, bastnasite, thorite, pyrochlore, and monazite. At the late hydrothermal stage, pyrochlore and monazite are altered, and replaced by Y-rich pyrochlore, whereas monazite and bastnasite are replaced by synchysite and monazite.

At Dyaheen, the hydrothermal alteration is not as intense relative to Jabal Sayid. The hydrothermal stage is manifested by the alteration of the aegirine granite and the amphibole granite. At this stage, quartz veins and pods and aegirine dykes crosscut the aegirine granite, and aegirine and amphibole were replaced by hematite, zircon, and fluorite. The aegirine dyke is highly mineralized and shows major mineral composition comparable to the aegirine granite. The quartz veins show ductile deformation and contain perthite, which implies that they were formed at high temperatures. Thus, it is more likely that the aegirine dykes and ductile quartz veins represent a transitional environment between the magmatic and hydrothermal stages. Based on the textural and morphological relationships of the ore minerals from the quartz veins and the aegirine dykes, there are at least three main mineralization stages. The first stage occurs during late-magmatic to early hydrothermal by the crystallization of fergusonite, zircon, and early gadolinite. The second stage is manifested by the alteration of fergusonite to Pb-pyrochlore and the alteration of early gadolinite to HREE-rich late gadolinite. The third stage is marked by the crystallization of bastnasite as veinlets the late gadolinite or as individual crystals.

6.6 Conclusion

The current work provides petrographical and lithogeochemical data of the mineralization associated with silica-rich alkaline granites at Al-Ghurayyah, Jabal Sayid, and Dyaheen. Moreover, this work also presents the first detailed work on the chemistry and morphology of the ore minerals at these deposits and has characterized the magmatic and hydrothermal stages and their contributions to the mineralization. Al-Ghurayyah, Jabal Sayid, and Dyaheen display variable styles of mineralization ranging from disseminated in Al-Ghurayyah, localized mineralization in hematized granite and pegmatite sheets at Jabal Sayid, and localized mineralization without hematization in quartz veins and aegirine granite and dykes at Dyaheen. All fresh rocks from three deposits show a typical alkaline A-type alkaline granite lithogeochemistry and mineralogically are characterized by the occurrence of sodic amphibole and aegirine and the high concentrations of Na, K, Fe, Nb, Ta, Zr Y, and REE, and the low concentrations of Ca and Al. The estimated ages of the granites from the current study and previous studies are consistent with the interpretation that they are post-tectonic granites. Furthermore, the three deposits have the trace element signature of a within-plate tectonic setting. The ϵNd of the three deposits range from +4.1 to +5.8, which indicates that they have the same magma source.

All three deposits show extreme feldspar fractionation indicated by the negative Eu anomalies, which led to the increase the concentrations of incompatible elements in the residual melt. Additionally, the high magma content of volatiles and fluxes, such as F, and Li, and the alkalinity of the melt would increase the solubility of HFSE and REE minerals and decrease the solidus temperature of the granite. The variations between the three deposits mainly occur in the late-magmatic to the hydrothermal stages, which is manifested in the variations in the ore minerals and the associated gangue minerals. The current work showed that earliest HFSE and REE mineralization occur during a late-magmatic stage in Al-Ghurayyah and a transitional stage in Jabal Sayid and Dyaheen. The mineralization continued to the hydrothermal stage hydrothermal fluid exsolved from the melt.

The nature of the late stage melt and the fluid phase associated with silica-rich rare-metal alkaline granites in the Arabian Shield remains poorly understood. In fact, there have

been no fluid inclusion or melt inclusion studies on any of the rare-metal deposits in the Arabian Shield. Understanding the composition of the late melt and the crystallization temperature as well as the temperature and composition of the hydrothermal fluid are the next crucial step to constructing a model that explains the behavior of HFSE and REE at these deposits.

6.7 References

- Ali, K.A., Jeon, H., Andresen, A., Li, S.-Q., Harbi, H.M., Hegner, E., 2014. U–Pb zircon geochronology and Nd–Hf–O isotopic systematics of the Neoproterozoic Hadb adh Dayheen ring complex, Central Arabian Shield, Saudi Arabia. *Lithos*.
<https://doi.org/10.1016/j.lithos.2014.07.030>
- Ali, K.A., Stern, R.J., Manton, W.I., Kimura, J., Khamees, H.A., 2009. Geochemistry , Nd isotopes and U – Pb SHRIMP zircon dating of Neoproterozoic volcanic rocks from the Central Eastern Desert of Egypt : New insights into the ~ 750 Ma crust-forming event. *Precambrian Res.* 171, 1–22.
<https://doi.org/10.1016/j.precamres.2009.03.002>
- Avigad, D., Gvirtzman, Z., 2009. Tectonophysics Late Neoproterozoic rise and fall of the northern Arabian – Nubian shield : The role of lithospheric mantle delamination and subsequent thermal subsidence. *Tectonophysics* 477, 217–228.
<https://doi.org/10.1016/j.tecto.2009.04.018>
- Barker, F., Wones, D.R., Sharp, W.N., Desborough, G.A., 1975. The Pikes Peak Batholith, Colorado Front Range, and a model for the origin of the gabbro-anorthosite- syenite-potassic granite suite. *Precambrian Res.* 2, 97–160.
- Bau, M., 1996. Controls on the fractionation of isovalent trace elements in magmatic and aqueous systems: evidence from Y/Ho, Zr/Hf, and lanthanide tetrad effect. *Contrib Miner. Pet.* 123, 323–333. <https://doi.org/10.1007/s004100050317>
- Belousova, E. a., Griffin, W.L., O’Reilly, S.Y., 2006. Zircon crystal morphology, trace element signatures and Hf isotope composition as a tool for oetrogenetic modelling:

- Examples from Eastern Australian granitoids. *J. Petrol.* 47, 329–353.
<https://doi.org/10.1093/petrology/egi077>
- Bonin, B., 2007. A-type granites and related rocks: Evolution of a concept, problems and prospects. *Lithos* 97, 1–29. <https://doi.org/10.1016/j.lithos.2006.12.007>
- Boynton, W. V., 1984. Cosmochemistry of the Rare Earth Elements: Meteorite Studies. *Dev. Geochemistry* 2, 63–114. <https://doi.org/10.1016/B978-0-444-42148-7.50008-3>
- Brown, M., 1994. The generation , segregation , ascent and emplacement of granite magma : the migmatite-to-crustally-derived granite connection in thickened orogens 36, 83–130.
- Chen, W.E.I.T.E.I.T., Zhou, M.-F., 2017. Hydrothermal alteration of magmatic zircon related to NaCl-rich brines: Diffusion-reaction and dissolution-reprecipitation processes. *Am. J. Sci.* 317, 177–215. <https://doi.org/10.2475/02.2017.02>
- Collins, W.J., Beams, S.D., White, A.J.R., Chappell, B.W., 1982. Nature and origin of A-type granites with particular reference to southeastern Australia. *Contrib. to Mineral. Petrol.* 80, 189–200. <https://doi.org/10.1007/BF00374895>
- Corfu, F., Hanchar, J.M., Hoskin, P.W.O., Kinny, P., 2003. Atlas of zircon textures. *Rev. Mineral. Geochemistry* 53, 469–500. <https://doi.org/10.2113/0530469>
- Creaser, R.A., Price, R.C., Wormald, R.J., 1991. A-type granites revisited: Assessment of a residual-source model. *Geology* 19, 163–166.
- Drysdall, a. R., Jackson, N.J., Ramsay, C.R., Douch, C.J., Hackett, D., 1984. Rare element mineralization related in Precambrian alkali granites in the Arabian shield. *Econ. Geol.* 79, 1366–1377. <https://doi.org/10.2113/gsecongeo.79.6.1366>
- du Bray, E.A., 1986. Specialized granitoids in the southeastern Arabian Shield-case history of a regional assessment. *J. African Earth Sci.* 4, 169–176.
[https://doi.org/10.1016/S0899-5362\(86\)80077-X](https://doi.org/10.1016/S0899-5362(86)80077-X)

- Dyulgerov, M.M., Platevoet, B., 2006. Unusual Ti and Zr aegirine-augite and potassic magnesio-arfvedsonite in the peralkaline potassic oversaturated Buhovo-Seslavitzi complex , Bulgaria 127–138. <https://doi.org/10.1127/0935-1221/2006/0018-0127>
- Eby, G.N., 1992. Chemical subdivision of the A-type granitoids : Petrogenetic and tectonic implications. *Geology* 20, 641–644.
- Eby, G.N., 1990. The A-type granitoids : A review of their occurrence and chemical characteristics and speculations on their petrogenesis. *Lithos* 26, 115–134.
- Elliott, J.E., 1983. Peralkaline and peraluminous Granites and Related Mineral Deposits of the Arabian Shield, Kingdom of Saudi Arabia.
- Elliott, J.E., Al-Yazidi, S., Al-Eissa, A., Al-Shammeri, A., Hashem, A.I., Tarabulsi, Y., 2002. Exploration of the Ghurayyah radioactive granite, Kingdom of Saudi Arabia. *Saudi Geol. Surv.* open-file, x.
- Eyal, M., Litvinovsky, B., Jahn, B.M., Zanzilevich, A., Katzir, Y., 2010. Origin and evolution of post-collisional magmatism : Coeval Neoproterozoic calc-alkaline and alkaline suites of the Sinai Peninsula. *Chem. Geol.* 269, 153–179.
<https://doi.org/10.1016/j.chemgeo.2009.09.010>
- Feng, Y., Samson, I.M., 2015. Replacement processes involving high field strength elements in the T Zone, Thor Lake rare-metal deposit. *Can. Mineral.* 53, 31–60.
<https://doi.org/10.3749/canmin.1400028>
- Frost, C.D., Frost, B.R., 2011. On Ferroan (A-type) Granitoids : their Compositional Variability and Modes of Origin Fe-index. *Juornal Petrol.* 52, 39–53.
<https://doi.org/10.1093/petrology/egq070>
- Frost, C.D., Frost, B.R., Bell, J.M., Chamberlain, K.R., 2002. The relationship between A-type granites and residual magmas from anorthosite: evidence from the northern Sherman batholith, Laramie Mountains, Wyoming, USA. *Pre* 119, 45–71.
- Fu, B., Mernagh, T.P., Kita, N.T., Kemp, A.I.S., Valley, J.W., 2009. Distinguishing

magmatic zircon from hydrothermal zircon: A case study from the Gidginbung high-sulphidation Au-Ag-(Cu) deposit, SE Australia. *Chem. Geol.* 259, 131–142.

<https://doi.org/10.1016/j.chemgeo.2008.10.035>

Green, T.H., 1995. Significance of Nb/Ta as an indicator of geochemical processes in the crust_mantle system. *Geochemical Geol.* 120, 347.

Hackett, D., 1986. Mineralized aplite-pegmatite at Jabal Sa'id, Hijaz region, Kingdom of Saudi Arabia. *J. African Earth Sci.* 4, 257–267. [https://doi.org/10.1016/S0899-5362\(86\)80087-2](https://doi.org/10.1016/S0899-5362(86)80087-2)

Harris, N.B.W., Marzouki, F.M.H., Ali, S., 1986. The Jabel Sayid complex, Arabian Shield: geochemical constraints on the origin of peralkaline and related granites. *J. Geol. Soc. London.* 143, 287–295. <https://doi.org/10.1144/gsjgs.143.2.0287>

Hoskin, P.W.O., 2005. Trace-element composition of hydrothermal zircon and the alteration of Hadean zircon from the Jack Hills, Australia. *Geochim. Cosmochim. Acta* 69, 637–648. <https://doi.org/10.1016/j.gca.2004.07.006>

Hoskin, P.W.O., Schaltegger, U., 2003. The composition of zircon and igneous and metamorphic petrogenesis. *Rev. Mineral. Geochemistry* 53, 27–62. <https://doi.org/10.2113/0530027>

Irber, W., 1999. The lanthanide tetrad effect and its correlation with K/Rb, Eu/Eu*, Sr/Eu, Y/Ho, and Zr/Hf of evolving peraluminous granite suites. *Geochim. Cosmochim. Acta* 63, 489–508. [https://doi.org/10.1016/S0016-7037\(99\)00027-7](https://doi.org/10.1016/S0016-7037(99)00027-7)

Kemp, A.I.S., Hawkesworth, C.J., Paterson, B.A., Kinny, P.D., 2006. Episodic growth of the Gondwana supercontinent from hafnium and oxygen isotopes in zircon. *Nature* 439, 580–583. <https://doi.org/10.1038/nature04505>

Kogarko, L.N., 2016. Geochemistry of fractionation of coherent elements (Zr and Hf) during the profound differentiation of peralkaline magmatic systems: A case study of the Lovozero Complex. *Geochemistry Int.* 54, 1–6. <https://doi.org/10.1134/S0016702916010079>

- Landenberger, B., Collins, W.J., 1996. Derivation of A-type granites from a dehydrated charnockitic lower crust: Evidence from the Chaelundi Complex. *J. Petrol.*
<https://doi.org/10.1093/petrology/37.1.145>
- Linnen, R.L., Keppler, H., 2002. Melt composition control of Zr/Hf fractionation in magmatic processes. *Geochim. Cosmochim. Acta* 66, 3293–3301.
[https://doi.org/10.1016/S0016-7037\(02\)00924-9](https://doi.org/10.1016/S0016-7037(02)00924-9)
- Lv, Z.H., Zhang, H., Tang, Y., 2018. Lanthanide tetrads with implications for liquid immiscibility in an evolving magmatic-hydrothermal system: Evidence from rare earth elements in zircon from the No. 112 pegmatite, Kelumute, Chinese Altai. *J. Asian Earth Sci.* 164, 9–22. <https://doi.org/10.1016/j.jseaes.2018.05.031>
- McLennan, S.M., 1994. Rare earth element geochemistry and the tetrad effect. *Geochim. Cosmochim. Acta* 58, 2025–2033.
- Moghazi, A.-K.M., Iaccheri, L.M., Bakhsh, R.A., Kotov, A.B., Ali, K.A., 2015. Sources of rare-metal-bearing A-type granites from Jabel Sayed complex, Northern Arabian Shield, Saudi Arabia. *J. Asian Earth Sci.* 107, 244–258.
<https://doi.org/10.1016/j.jseaes.2015.04.042>
- Moghazi, A.M., Ali, K.A., Wilde, S.A., Zhou, Q., Andersen, T., Andresen, A., El-enen, M.M.A., Stern, R.J., 2012. Lithos Geochemistry , geochronology , and Sr – Nd isotopes of the Late Neoproterozoic Wadi Kid volcano-sedimentary rocks , Southern Sinai , Egypt : Implications for tectonic setting and crustal evolution. *LITHOS* 154, 147–165. <https://doi.org/10.1016/j.lithos.2012.07.003>
- Moghazi, A.M., Harbi, H.M., Ali, K.A., 2011. Geochemistry of the Late Neoproterozoic Hadb adh Dayheen ring complex, Central Arabian Shield: Implications for the origin of rare-metal-bearing post-orogenic A-type granites. *J. Asian Earth Sci.* 42, 1324–1340. <https://doi.org/10.1016/j.jseaes.2011.07.018>
- Monecke, T., Kempe, U., Monecke, J., Sala, M., Wolf, D., 2002. Tetrad effect in rare earth element distribution patterns: A method of quantification with application to

- rock and mineral samples from granite-related rare metal deposits. *Geochim. Cosmochim. Acta* 66, 1185–1196. [https://doi.org/10.1016/S0016-7037\(01\)00849-3](https://doi.org/10.1016/S0016-7037(01)00849-3)
- Nehlig, P., Genna, A., Asfirane, F., 2002. A review of the Pan-African evolution of the Arabian shield. *GeoArabia* 7, 103–124.
- Njonfang, E., Nono, A., 2003. Clinopyroxene from some felsic alkaline rocks of the Cameroon Line , central Africa : petrological implications 15, 527–542. <https://doi.org/10.1127/0935-1221/2003/0015-0527>
- Peretyazhko, I.S., Savina, E.A., 2010. Tetrad effects in the rare earth element patterns of granitoid rocks as an indicator of fluoride-silicate liquid immiscibility in magmatic systems. *Petrology* 18, 514–543. <https://doi.org/10.1134/S086959111005005X>
- Pettke, T., Audétat, A., Schaltegger, U., Heinrich, C. a., 2005. Magmatic-to-hydrothermal crystallization in the W-Sn mineralized Mole Granite (NSW, Australia). Part II: Evolving zircon and thorite trace element chemistry. *Chem. Geol.* 220, 191–213. <https://doi.org/10.1016/j.chemgeo.2005.02.017>
- Qadhi, T., Moufti, A., 2008. Geochemical characteristic of the rare-metal rich granite in the Ghurayyah-Dubbagh Area, north western Arabian Shield, Saudi Arabia. *Ann. Geol. Surv. Egypt* XXX, 149.
- Radain, A., 1979. Petrogenesis of Some Pearalkaline and Non-peralkaline Post-tectonic Granite in The Arabian Shield. The University of Western Ontario.
- Radain, A.A.M., Fyfe, W.S., Kerrich, R., 1981. Origin of Peralkaline Granites of Saudi Arabia. *Contrib. Miner. Pet.* 358–366. <https://doi.org/10.1007/BF00398932>
- Schaltegger, U., 2007. Hydrothermal zircon. *Elements* 3, 51–79. <https://doi.org/10.2113/gselements.3.1.51>
- Shand, S.J., 1943. Eruptive rocks. *Geol. Mag.* 81, 137–138. <https://doi.org/DOI:10.1017/S0016756800075026>

- Staatz, M.H., Brownfield, I.K., 1986. Trace-and minor-element mineralogy of the microgranite at Ghurayyah, Kingdom of Saudi Arabia.
- Stern, R.J., 2002. Crustal evolution in the East African Orogen : a neodymium isotopic perspective 34, 109–117.
- Stern, R.J., 1994. ARC Assembly and continental collision in the Neoproterozoic East African Orogen: implications for the consolidation of Gondwanaland. *Annu. Rev. Earth Planet. Sci.* 22, 319–351.
<https://doi.org/10.1146/annurev.ea.22.050194.001535>
- Stern, R.J., Ali, K.A., Lie, J.P., Johnson, P.R., Kozdroj, W., Kattan, F.H., 2010. Distribution and significance of pre-Neoproterozoic zircons in juvenile Neoproterozoic Igneous rocks of the Arabian-Nubian Shield. *Am. J. Sci.* 310, 791–811. <https://doi.org/10.2475/09.2010.02>
- Stern, R.J., Johnson, P., 2010. Continental lithosphere of the Arabian Plate : A geologic , petrologic , and geophysical synthesis. *Earth Sci. Rev.* 101, 29–67.
<https://doi.org/10.1016/j.earscirev.2010.01.002>
- Taylor, S.R., 1965. The application of trace element data to problems in petrology. *Phys. Chem. Earth* 6, 133–213. [https://doi.org/https://doi.org/10.1016/0079-1946\(65\)90014-5](https://doi.org/10.1016/0079-1946(65)90014-5)
- Turkistany, A.R., Ramsay, C.R., 1982. Mineralized apogranite associated with alkali granite at Jabal Sa'id, Kingdom of Saudi Arabia. *Deputy Minstry Miner. Resour.* 78–88.
- Turner, S.P., Foden, J.D., Morrison, R.S., 1992. Derivation of some A-type magmas by fractionation of basaltic magma : An example from the Padthaway Ridge , South Australia. *Lithos* 28, 151–179.
- Wu, M., Tian, B., Zhang, D., Xu, G., Xu, W., Qiu, K., 2018. Zircon of the No. 782 deposit from the Great Xing'an Range in NE China: Implications for Nb-REE-Zr mineralization during magmatic-hydrothermal evolution. *Ore Geol. Rev.* 102, 284–

299. <https://doi.org/10.1016/j.oregeorev.2018.09.006>

Yang, W.-B., Niu, H.-C., Shan, Q., Sun, W.-D., Zhang, H., Li, N.-B., Jiang, Y.-H., Yu, X.-Y., 2014. Geochemistry of magmatic and hydrothermal zircon from the highly evolved Baerzhe alkaline granite: implications for Zr–REE–Nb mineralization. *Miner. Depos.* 49, 451–470. <https://doi.org/10.1007/s00126-013-0504-1>

Zhang, X., Yuan, L., Xue, F., Zhang, Y., 2012. Contrasting Triassic ferroan granitoids from northwestern Liaoning , North China : Magmatic monitor of Mesozoic decratonization and a craton – orogen boundary. *Lithos* 144–145, 12–23. <https://doi.org/10.1016/j.lithos.2012.03.022>

Table 6-1 Main characteristics of the rare-metal deposits in the current study

Deposit	Petrography of the host rock	Mineralization	Aeg, reserve, and grade
Al-Ghurayyah	Light-pink to light grey medium-grained to porphyritic granite. Consists mainly of 35-45% quartz, 25-35% albite, 20-25% microcline, and 0- <5% sodic amphibole. Accessory minerals include trillithionite, zircon, and pyrochlore. Quartz and microcline occur as large phenocrysts displaying snowball quartz that contain albite inclusions along growth planes. Fresh sodic amphibole is rare and mostly altered to chlorite and hematite. Altered granites show high quartz and muscovite contents with hematite staining.	Two mineralization styles: 1- disseminated in the porphyritic granite and the marginal unit. the common rare-metal minerals include zircon and pyrochlore in non-silicified rocks, and columbite, and rutile \pm REE-fluorocarbonate in silicified granite. 2- aggregate style in quartz veins and the composite-body. The common rare-metal minerals include zircon, columbite, rutile, and xenotime \pm REE-fluorocarbonate.	The age was estimated from U-Pb zircon and yielded an age ranges from 554 ± 89 to 647 ± 32 Ma from. The estimated reserve is 385×10^6 tons that have a grade of 245 g/t Ta ₂ O ₅ , 2840 g/t Nb ₂ O ₅ , 8915 g/t ZrO ₂ , and 1270 g/t Y ₂ O ₃
Jabal Sayid	The fresh host rock adjacent to the mineralized units is a medium-grained to porphyritic aegirine/amphibole granite. It consists of 45% quartz, 30 K-feldspar, 15-20 albite, and 5-10% aegirine and amphibole. Quartz and K-feldspar locally occur as phenocryst that contains inclusions of albite and fine quartz. No rare-metal phases were observed in the fresh granites.	The mineralization is limited to the oxidized granite and the pegmatite sheets. The oxidized granite consists of 40-45% quartz and 10-15% microcline, and 25-30% acicular pseudomorphs. The main rare-metal minerals are zircon, pyrochlore, monazite, bastnasite, xenotime, and thorite \pm synchysite. Fluorite is widespread, and it is associated with irregular hematite.	The age was estimated from U-Pb zircon system, and the alkali granite yielded an age of 593 ± 2.4 Ma (Moghazi et al., 2015). The estimated reserve is 58×10^6 tons containing 450 ppm La, 1040 ppm Ce, 3325 ppm Y, 1077 Nb, and over 19000 ppm Zr.

Dyaheen	<p>The Dyaheen ring complex consists of three main rock units. 1- monzogranite (core), which consists of plagioclase, alkali feldspar, and quartz. Accessory minerals include magnetite, titanite, apatite, and zircon. 2- amphibole-biotite (core to rim), which consists of plagioclase, quartz, perthite, sodic amphibole, and biotite. Accessory minerals include titanite, magnetite, and zircon. 3- aegirine granite (rim), which consists of albite, perthite, aegirine, and amphibole. In fresh granites, only pyrochlore observed as inclusions in quartz and aegirine. Altered aegirine granite contains hematite veinlets, disseminated zircons, and pseudomorphs after sodic amphibole.</p>	<p>Locally, amphibole-biotite granite displays calcite alteration, which occurs as veinlets. Amphibole was replaced by hematite and fluorite with variable amounts of zircon \pm fluorocarbonate. Mineralization occurs in altered aegirine granite, aegirine dykes, and quartz veins and pods. Locally, pegmatite hosted by amphibole-biotite granite contains fergusonite, pyrochlore, and zircons. The mineralization occurs in 2 stages. Stage 1 is early and resulted in the crystallization of fergusonite and Y-gadolinite. Stage 2 is late and led to the alteration of Pb-pyrochlore and the alteration of the Y-gadolinite to LREE-rich gadolinite and bastnasite.</p>	<p>The ages of the monzogranite and the amphibole-biotite and granite were estimated by U-Pb isotopes from zircon and yielded an age of 613 ± 4 Ma and 625 ± 11 Ma, respectively (Ali et al., 2014). The mineralization age was estimated by U-Pb isotopes from zircons from quartz veins and yielded an age of 651 ± 70 Ma. The reserve and the grade have not been estimated.</p>
---------	---	---	--

Table 6-2 Average whole-rock analyses of fresh and altered/mineralized granites at the studied rare-metals

	Al-Ghurayyah				Jabal Sayid				Dyaheen			
	Granite		Silicified		Granite		Oxidized granite		Aegirine Granite		Mineralized dykes	
	average	±	average	±	average	±	average	±	average	±	average	±
SiO ₂	72.1	1.3	83.3	5.7	75.2	0.7	72.2	2.5	72.8	2.2	82.6	1.1
TiO ₂	0.1	0.0	0.1	0.0	0.1	0.0	0.5	0.1	0.2	0.1	0.3	0.1
Al ₂ O ₃	13.1	1.3	6.9	3.5	10.8	0.4	5.4	2.0	12.2	1.2	4.5	0.7
Fe ₂ O ₃	2.3	0.9	2.1	0.4	3.6	0.5	10.7	5.1	3.2	0.8	3.6	0.9
MnO	0.1	0.0	0.0	0.0	0.0	0.0	0.2	0.2	0.0	0.0	0.2	0.1
MgO	0.1	0.0	0.1	0.0	0.2	0.0	0.3	0.3	0.2	0.2	0.2	0.0
CaO	0.7	0.8	0.2	0.1	0.5	0.2	0.7	0.5	0.8	0.7	0.8	0.9
Na ₂ O	5.2	1.0	0.9	1.5	4.3	0.5	0.8	1.1	5.0	0.4	2.4	1.5
K ₂ O	2.9	0.7	4.4	1.0	3.9	0.1	2.9	0.6	4.0	0.5	2.0	1.3
P ₂ O ₅	0.0	0.0	0.1	0.1	0.0	0.0	0.1	0.1	0.0	0.0	0.2	0.3
LOI*	1.1	0.4	0.6	0.2	0.7	0.2	2.0	0.7	0.7	0.4	1.1	0.7
Total	97.7	0.7	98.6	0.3	99.2	0.1	95.9	0.0	99.2	0.7	98.0	1.1
F (wt. %)	0.4	0.5	0.0	0.1	0.1	0.0	0.2	0.1	0.2	0.1	0.1	0.1
Sr ppm	30	40	10	4	9	6	54	21	102	119	29	17
Ba ppm	27	12	37	12	17	5	92	102	255	279	65	13
Ni ppm	16	13	10	0	10	0	10	0	15	5	10	0
Cr ppm	22	8	40	14	30	0	30	0	35	5	40	14
Zr ppm	5359	2068	3872	1596	769	130	8720	2157	1874	1678	6419	2970
Sc ppm	1	0	1	1	1	0	1	1	2	1	1	0
Be ppm	9	2	9	8	6	3	30	15	12	4	71	62
V ppm	4	2	5	3	3	0	7	3	13	11	8	7
Co ppm	1	0	1	0	1	0	1	0	2	1	3	1

Table 6.2 Continue

Cu ppm	5	0	44	43	5	0	17	6	11	9	5	0
Zn ppm	1218	903	1080	650	265	70	1517	1529	240	114	2815	1421
Ga ppm	66	8	32	18	43	2	42	13	42	14	49	3
Ge ppm	5	1	4	1	2	1	7	1	2	1	8	1
As ppm	3	0	7	5	4	3	27	2	3	3	18	7
Rb ppm	881	308	1603	733	252	45	390	23	366	118	262	171
Y ppm	880	316	1104	428	137	59	5130	3355	124	75	1266	199
Nb ppm	1208	285	1303	243	82	54	1380	540	56	37	1831	1201
Mo ppm	3	4	12	9	1	1	1	1	1	0	2	1
In ppm	0	0	1	1	0	0	1	0	0	0	0	0
Sn ppm	70	17	344	265	14	8	177	104	18	18	101	80
Sb ppm	1	0	2	1	1	0	2	1	1	1	1	0
Cs ppm	2	1	4	2	1	1	3	0	4	3	2	1
Bi ppm	8	3	8	3	0	0	1	2	1	1	4	5
La ppm	55	18	42	4	89	54	893	131	58	22	1683	1198
Ce ppm	148	62	122	11	250	190	2150	36	154	90	4735	1775
Pr ppm	17	5	13	1	33	26	272	10	17	7	514	246
Nd ppm	48	15	35	4	136	108	1183	93	69	30	1910	778
Sm ppm	23	7	17	3	38	32	491	196	17	9	426	28
Eu ppm	0.5	0.1	0.5	0.3	2	1	30	15	1	0	18	2
Gd ppm	32	9	27	7	34	26	706	387	17	10	325	65
Tb ppm	14	4	14	4	5	4	149	94	3	2	49	16
Dy ppm	140	43	147	48	29	14	1035	685	19	11	275	88
Ho ppm	37	12	41	14	5	1	212	141	4	2	52	10
Er ppm	148	52	171	52	12	2	601	391	14	9	158	5
Tm ppm	29	11	35	9	2	0	86	53	2	2	24	2
Yb ppm	218	83	259	61	10	1	506	294	18	17	154	23

Table 6.2 Continue

Lu ppm	32	13	39	10	1	0	64	32	3	3	20	4
Hf ppm	268	118	216	138	17	3	163	67	59	58	119	53
Ta ppm	166	42	134	15	7	2	152	50	5	4	149	107
W ppm	10	4	8	2	2	0	6	2	3	1	5	0
Tl ppm	3	1	6	3	1	0	2	0	3	2	2	1
Pb ppm	421	330	593	152	78	65	560	170	40	15	2202	1723
Th ppm	528	397	520	232	28	19	2165	2805	29	21	545	361
U ppm	122	47	107	16	17	11	435	222	11	5	290	136
Nb/Ta	7		10		12		9		11		12	
Zr/Hf	20		18		45		53		32		54	
Eu/Eu*	0.05		0.07		0.14		0.15		0.18		0.15	
La/Yb	0.1		0.2		6.0		1.7		3.0		7.4	
T _{1,3,4}	0.35		0.37		0.09		0.1		0.1		0.14	

LOL loss on ignition. Error represents 1 σ standard deviation. Total iron is reported as Fe₂O₃. Eu/Eu* = Eu_{normalized} / sqrt(Sm_{normalized} / Gd_{normalized}). T_{1,2,3}; is the total tetrad effect of tetrad 1, 2, and 4 calculated following Monecke et al., (2002) method.

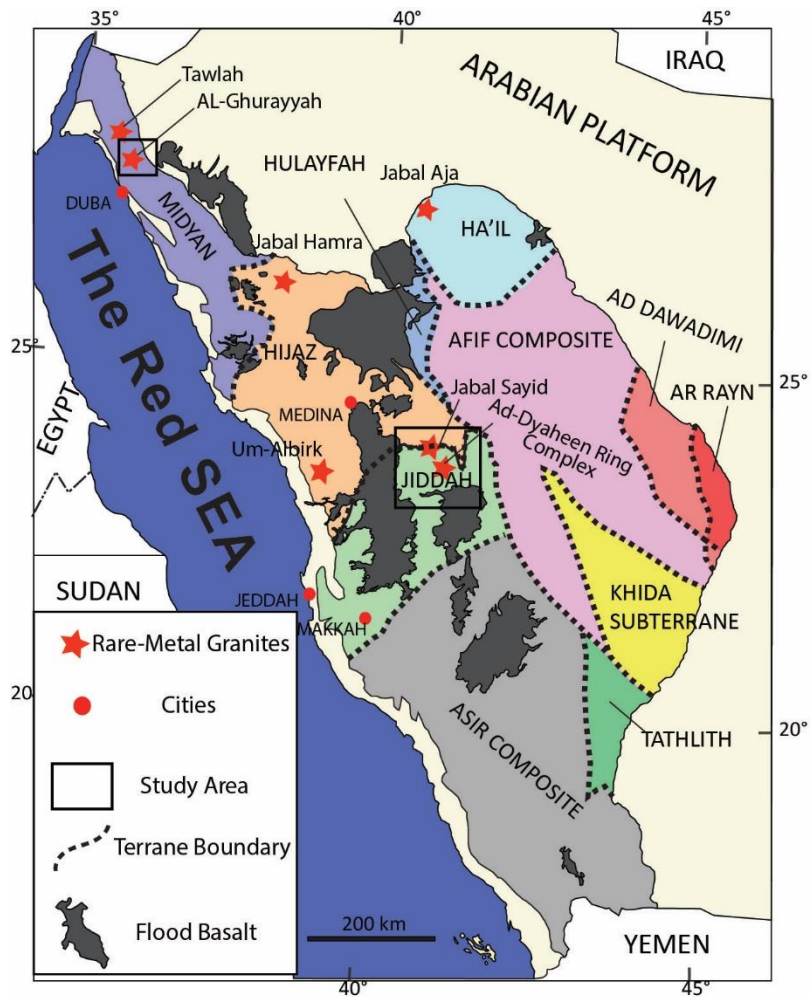


Figure 6-1 A geological map showing the different terrane in the Arabian Shield. The red stars are the location of some important rare-metal alkaline granite in the Arabian Shield. The study areas (modified after Johnson and Kattan 2012).

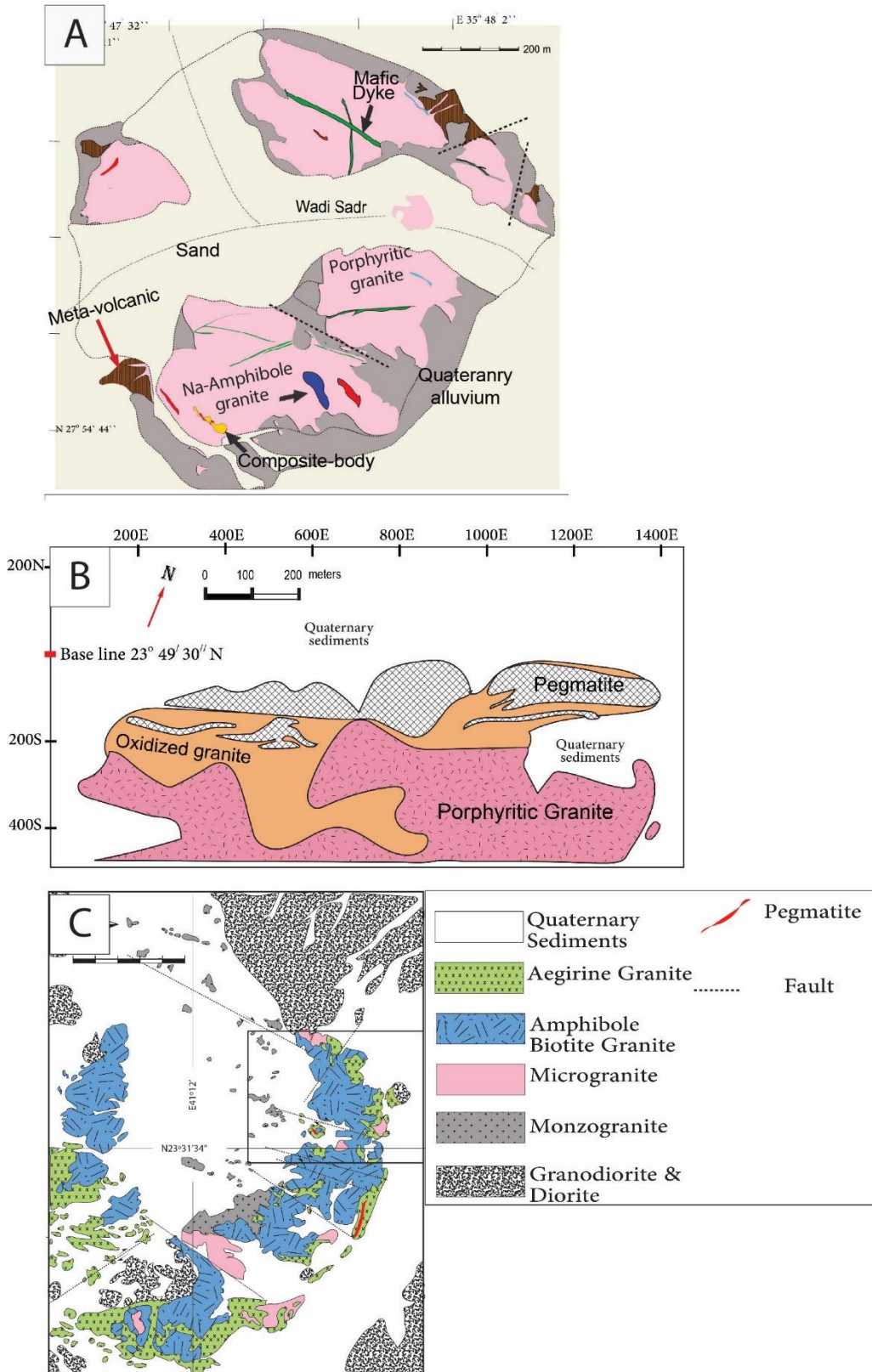


Figure 6-2 Simplified geological maps from Al-Ghurayyah (A), Jabal Sayid (B), and Dyaheen

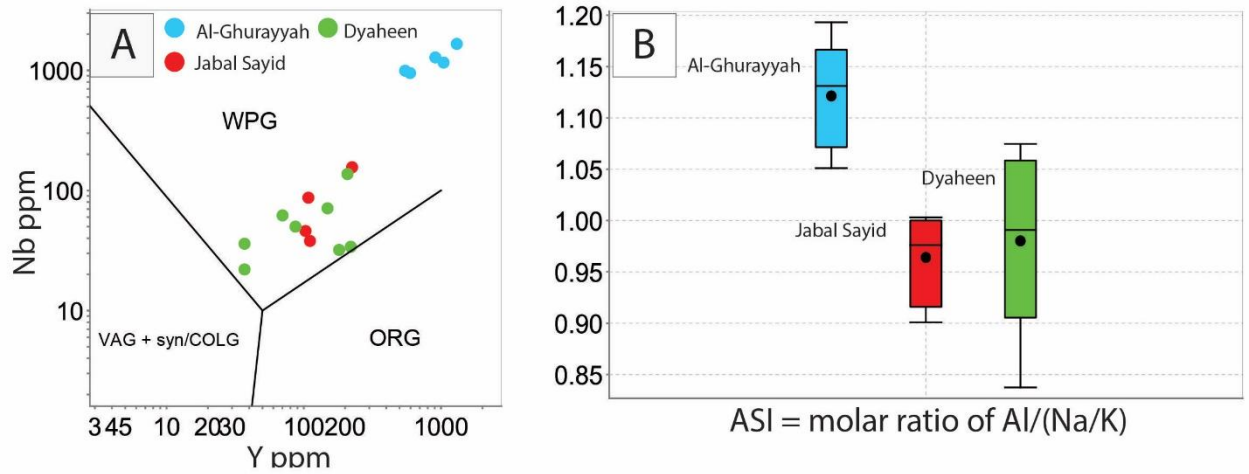


Figure 6-3 A) Y vs. Nb ppm tectonic settings discrimination diagram (Pearce et al. 1984). B) Variation in aluminum saturation index (ASI) of the three deposits (Shand 1943).

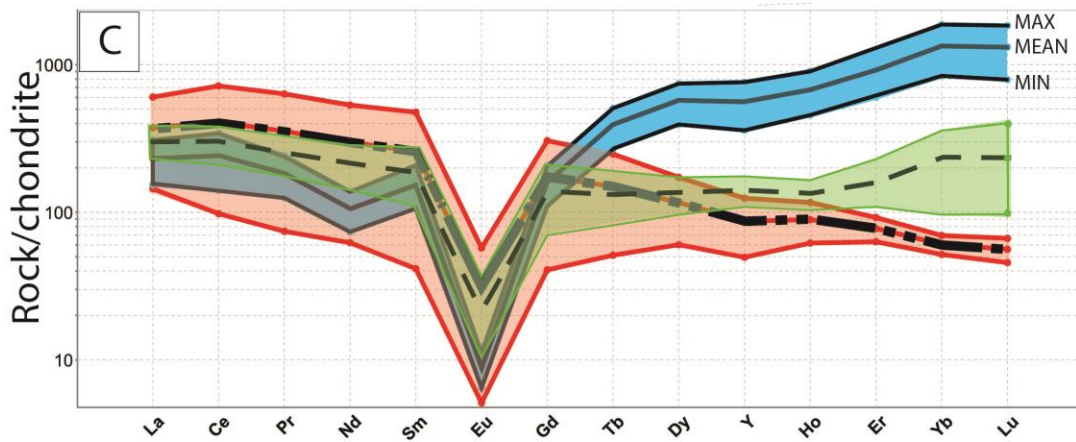
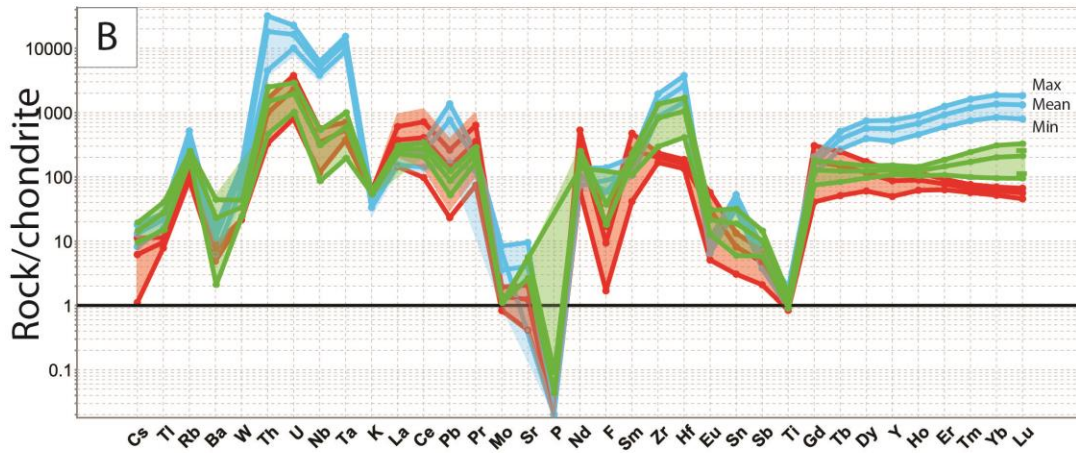
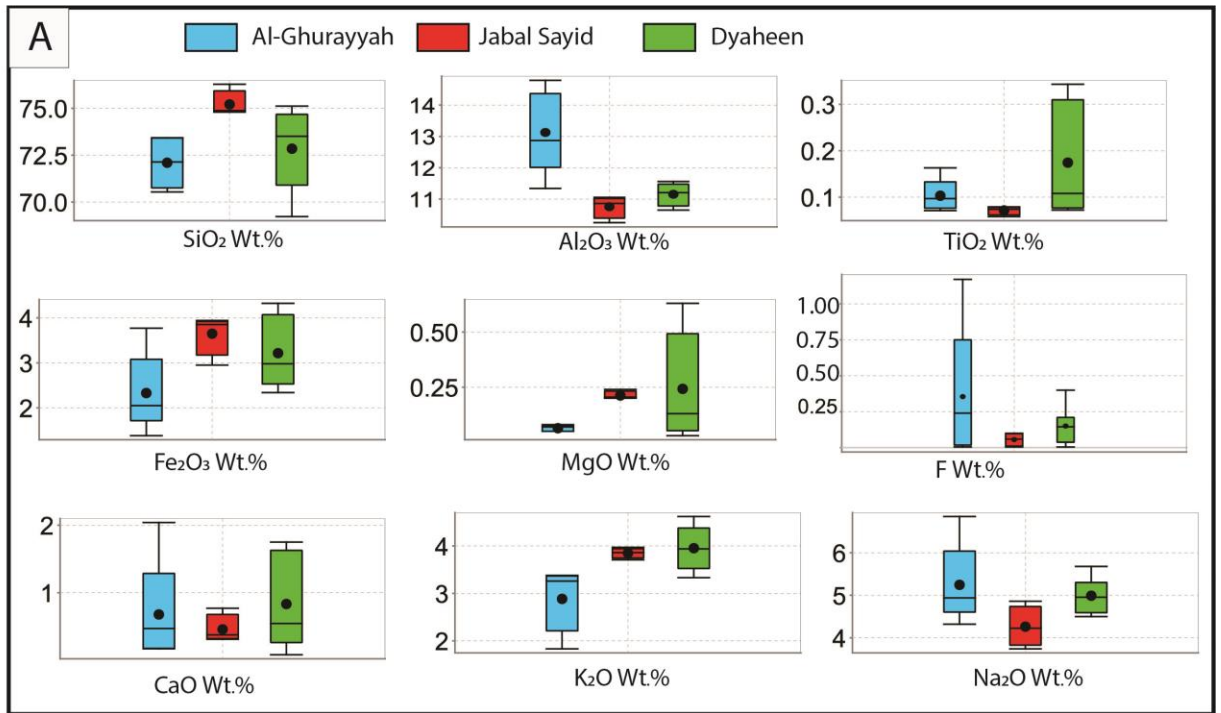


Figure 6-4 A) Box and whiskers plot show the variability in Major oxide composition of the studied areas. B) A chondrite normalized spider diagram showing the mean, max, and min normalized concentrations of REE elements in the fresh studied granites. C) chondrite normalized REE diagram showing the mean, max, and min normalized concentrations of REE elements in the studied granites. Normalized values are from McDonough and Sun (1995).

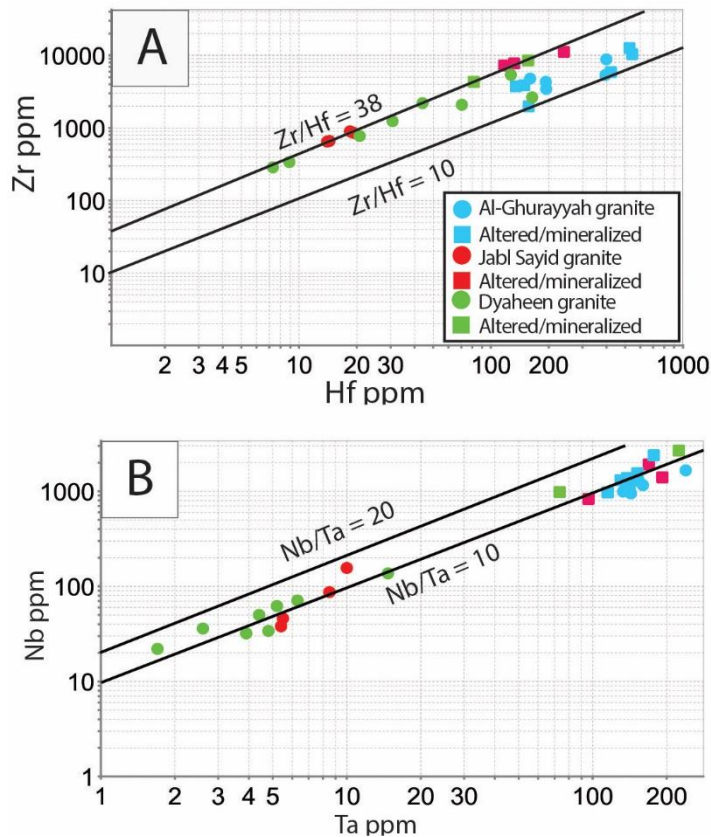


Figure 6-5 A) plot of the granite concentrations of Hf ppm and Zr ppm in (A) and Ta ppm vs Nb ppm in (B). The line represents the slope values of Zr/Hf and Nb/Ta.

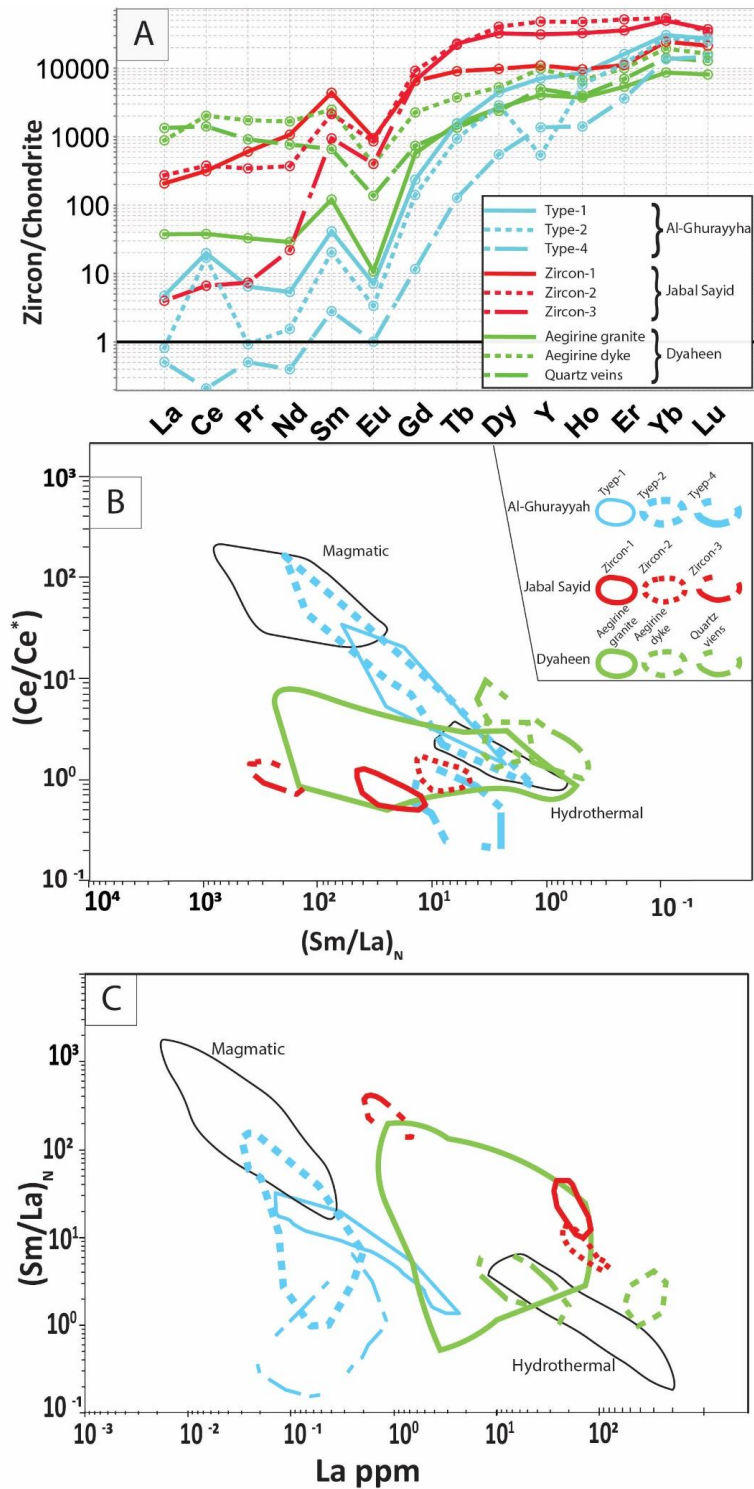


Figure 6-6 A) Chondrite normalized average REE concentration of zircons from the studied areas Zircon discrimination of Ce/Ce* versus Sm/La_N in B) and Sm/La_N versus La ppm in C) (modified after Hoskin, 2005). Ce/Ce* = (Ce/Ce_{chondrite})/

$\sqrt{((La/La_{chondrite}) \times (Pr/Pr_{chondrite}))}$,

$(Sm/La)_N = (Sm/Sm_{chondrite}) / (La/La_{chondrite})$. Chondrite's values are from

McDonough and Sun (1995). Purple regions are for zircons from Al-Ghurayyah and red regions are for zircons from Jabal Sayid.

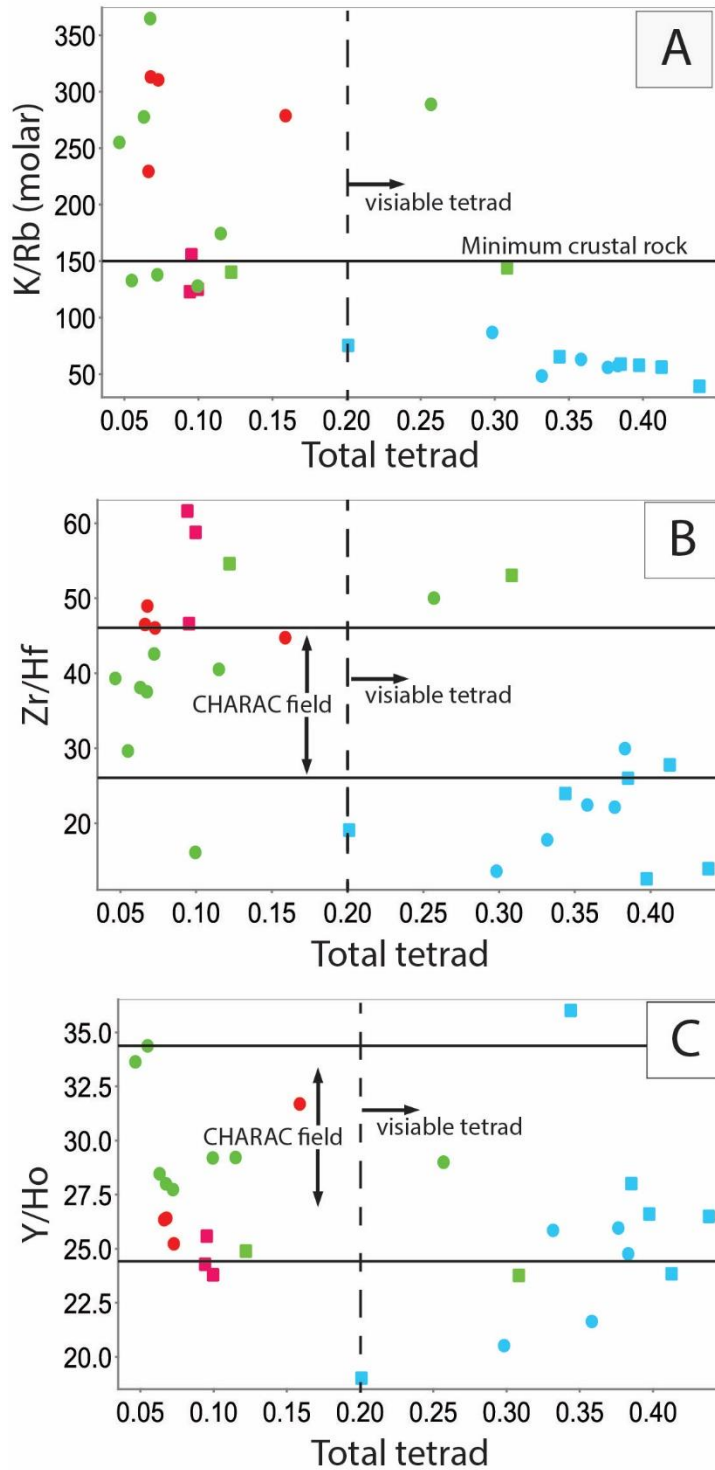


Figure 6-7 Total tetrad effect plot against the ratio of K/Rb in (A), Zr/Hf in (B), and Y/Ho in (C). These elements are sensitive to the change in melt composition (Irber, 1999). Solid lines show the range of CHARAC whereas the dashed line show the

minimum value of visible total tetrad effect. The symbols are the same as in Figure 6.5.

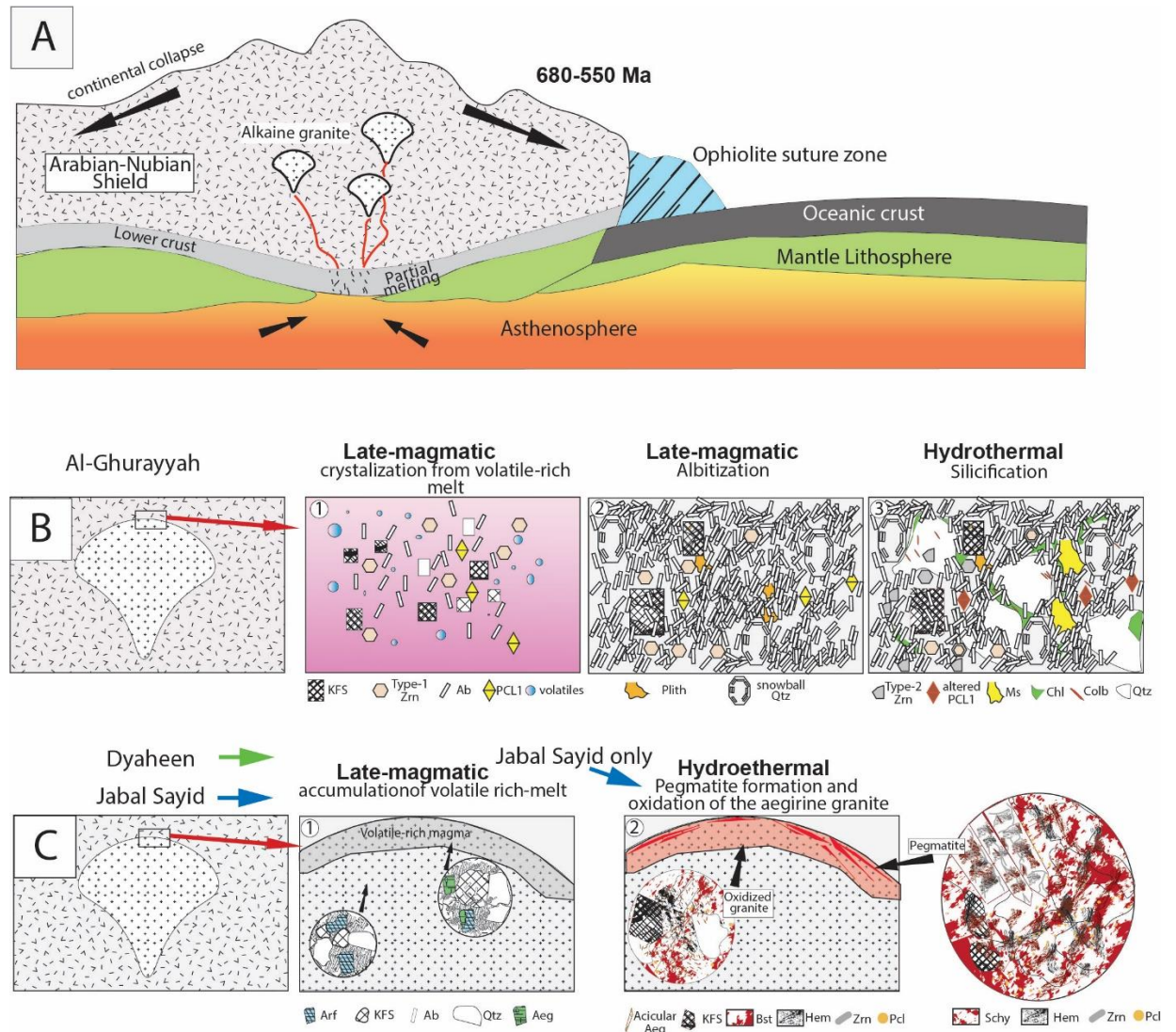


Figure 6-8 Cartoon to illustrate the emplacement of the alkaline granite during the post-tectonic time period. The main processes that took place during the late magmatic stage and the hydrothermal stage in Al-Ghurayyah (B) and Jabal Sayid and Dyaheen (C). Abbreviation: Arf, arfvedsonite; Kfs, K-feldspar; Ab, albite; Aeg, aegirine; Bst, bastnasite; Hem, hematite; Zrn, zircon; Pcl, pyrochlore; Plith, polyolithionite; Ms, muscovite; Chl, chlorite; Colb, columbite; Qtz, quartz.

Appendices

Appendix A: List of Al-Ghurayyah samples, whole-rock analyses, zircon age data

List of all samples from Al-Ghurayyah		EMP analyses						
	Description	Whole-rock	Zircon	Pyrochlore	Columbite	Mica	Albite	Kfeldspar
GHA1A	Fine-grained dark color marginal unit	√	√	√	√	√	√	√
GHA1B	Fine-grained light-pink marginal unit		√	√	√		√	√
GHA1C	Contact with the marginal unit. Coarse-grained and porphyritic (qtz+k-feld) 1000cps	√	√	√	√	√	√	√
GHA2A	quartz vein with Qtz+k-feld.		√		√			
GHA2B	contact microgranite along GHA2A. Shows mineralization of zircon							
GHA3A	Quartz zone (Composite-body)							
GHA3B	Zircon-columbite zone (Composite-body)		√		√			
GHA3C	K-feldspar zone (Composite-body)							
GHA3D	Zircon Mica Zone. high cps (10000) (Composite-body)		√		√	√		
GHA3E	Zircon Mica Zone. high cps (10000) (Composite-body)		√		√	√		
GHA4A	Highly silicified granite. medium-grained (Hematized)		√		√	√		
GHA4B	coarse-grained pink granite (hematized)		√		√	√		
GHA5	Amphibole-bearing granite (microgranite). Medium-grained	√	√	√	√	√	√	√
GHA6	pink fluorite granite							
GHA7	Altered dark-grey granite microgranite.	√	√	√				
GHA8	mineralized quartz vein		√	√		√		
GHA9A	mineralized quartz vein							
GHA9B	mineralized quartz vein							
GHA10	light pink microgranite		√	√				
GHA12	Coarse-grained granite							

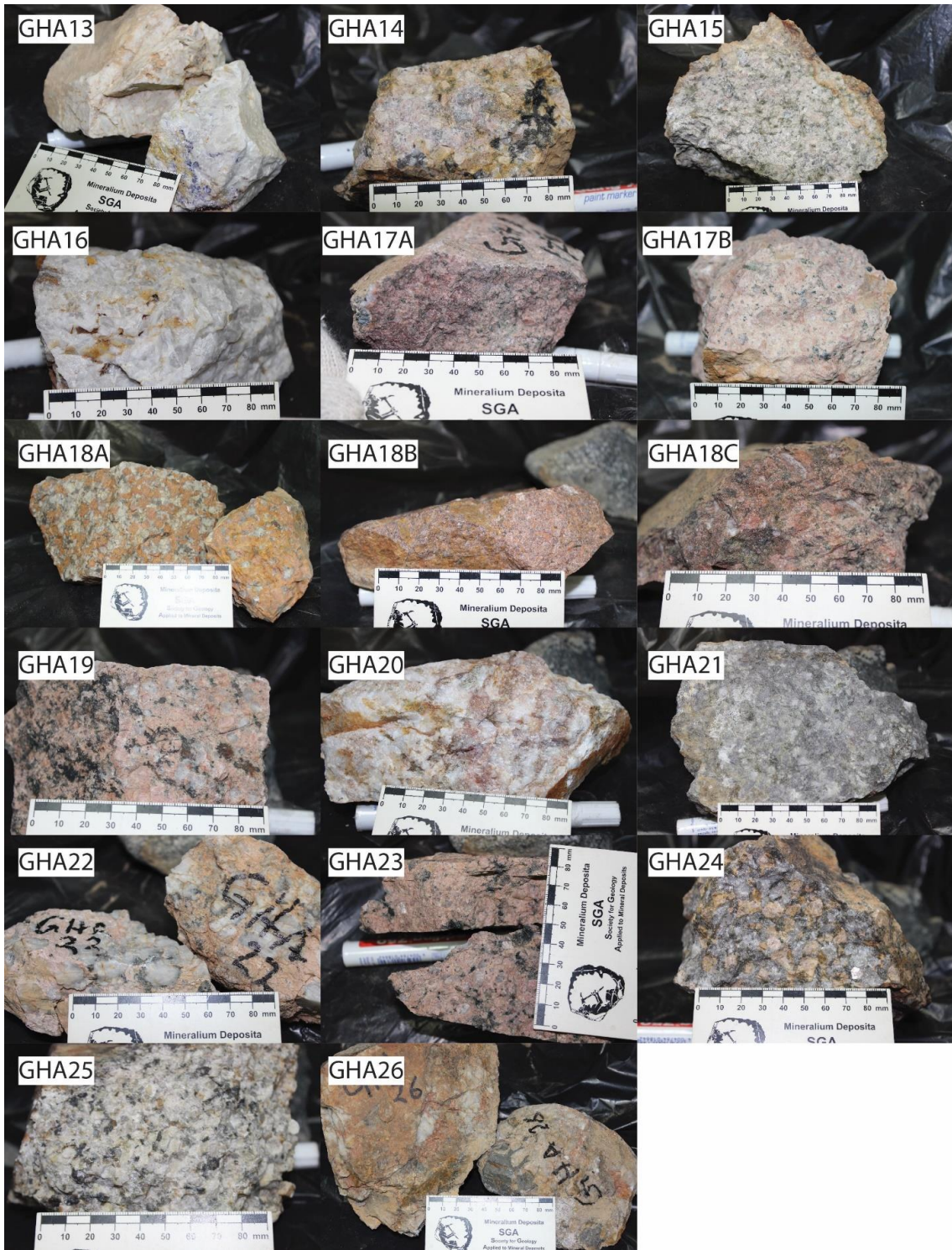
GHA13A	pegmatite dyke				
GHA13B	qtz vein or pegmatite with purple fluorite				
GHA14	Highly weathered coarse-grained pink granite				
GHA15	Microgranite with chlorite.				
GHA16	white qtz vein with some fluorite				
GHA17A	coarse-grained pink granite with amphibole	v			
GHA17B	medium to fine-grained granite	v			
GHA18A	coarse-grained granite	v			
GHA18B	microgranite	v			
GHA18C	red -altered granite	v			
GHA19	Coarse-grained pink granite				
GHA20	qtz vein parallel to mafic dyke and (younger than mineralization)				
GHA21	Green Porphyritic granite near fault zone				
GHA22	miarolitic cavities of qtz + k-feld and amphibole and weathered				
GHA23	pink coarse-grained amphibole granite				
GHA24	chloritized amphibole granite along fault zone	v			v
GHA25	coarse-grained amphibole granite	v	v		v
GHA26	qtz vein with mafic xenolith	v	v	v	v

List of Al-Ghurayyah samples with GPS coordinates			
Sample	GPS coordinates	Sample	GPS coordinates
GHA1A	N20 02.946 E41 56.650	GHA12	N20 02.050 E41 57.125
GHA1B	“	GHA13A	N20 02.071 E41 57.262
GHA1C	“	GHA13B	“
GHA2A	N20 02.417 E41 56.326	GHA14	N20 02.010 E41 57.300
GHA2B	“	GHA15	N20 01.969 E41 57.111
GHA3A	N20 02.436 E41 56.270	GHA16	“
GHA3B	“	GHA17A	N20 01.729 E41 56.976
GHA3C	“	GHA17B	“
GHA3D	“	GHA18A	N20 03.149 E41 56.506
GHA3E	“	GHA18B	“
GHA4A	N20 02.439 E41 56.141	GHA18C	“
GHA4B	“	GHA19	N20 02.877 E41 57.523
GHA5	N20 02.411 E41 56.036	GHA20	N20 02.867 E41 57.471
GHA6	N20 02.381 E41 56.069	GHA21	N20 02.854 E41 57.377
GHA7	N20 02.376 E41 56.104	GHA22	N20 02.841 E41 57.352
GHA8	N20 02.376 E41 56.104	GHA23	N20 02.925 E41 57.224
GHA9A	N20 02.001 E41 56.980	GHA24	N20 02.950 E41 57.218
GHA9B	“	GHA25	N20 02.965 E41 57.050
GHA10	N20 02.024 E41 57.000	GHA26	N20 02.967 E41 57.044

Photos of hand specimens from Al-Ghurayyah 1-2



Photos of hand specimens from Al-Ghurayyah 2-2



Appendix B : EMP chemical analyses for ore and rock-forming minerals from Al-Ghurayyah

EMP REE elements overlap and the amount of correction

Element	Interference	Correction amount
Eu (L α)	Pr (L β)	0.3633
Eu (L α)	Nd (L α)	0.0228
Gd (L α)	Ce (L α)	0.15101
Dy (L α)	Eu (L α)	0.01613
Er (L α)	Tb(L α)	0.0769
Tm (L α)	Sm (L β)	0.21271
Lu (L α)	Ho (L β)	0.1638
Lu (L α)	Dy (L α)	0.1031

Example:

Element	Net(cps)
Ce	0.7
Gd	14.7

$$14.7 \text{ (Gd Net)} - 0.15101 \times 0.7 \text{ (Ce Net)} = 14.59 \text{ (Gd cps)}$$

EMP analyses of zircons from Al-Ghurayyah. \pm is 1 σ standard deviation

LA-ICP-MS analyses of zircons from Al-Ghurayyah

	Type-1	Type-1	Type-1	Type-2	Type-2	Type-2	Type-2	Type-2	Type-2
label	GHA1C_Zrn2_03 (core)	GHA5_C3_02 (Primary_type1)	GHA5_C4_02 (Primary_type1)	GHA1C_Zrn1_01	GHA1C_Zrn1_02	GHA1C_Zrn1_03	GHA5_C3_01 (secondary_type-2)	GHA5_C4_01 (secondary_type-2)	GHA10_Zrn2_01
Li ppm	109.0	2.2	4.7	36.0	30.0	8.9	30.6	26.0	
Al ppm	1520.0	26.8	44.0	259.0	570.0	300.0	338.0	540.0	65.0
Si ppm	167000.0	164000.0	159000.0	168000.0	171000.0	158000.0	170000.0	172500.0	152000.0
P ppm	1710.0	880.0	1101.0	880.0	537.0	974.0	1182.0	722.0	1890.0
Sc ppm	553.0	554.0	544.0	565.0	548.0	539.0	595.0	563.0	610.0
Ti ppm	78.0	26.7	24.4	46.3	64.0	51.1	48.8	25.7	31.4
Fe ppm	512.0	66.6	66.6	39.0	64.0	254.0	420.0	244.0	66.6
Y ppm	N.A	N.A	N.A	N.A	N.A	N.A	N.A	N.A	N.A
Nb ppm	760.0	344.0	382.0	170.0	235.0	283.0	333.0	174.0	672.0
Sn ppm	195.0	7.0	6.8	75.0	57.0	68.0	34.6	7.9	6.8
La ppm	3.1	0.2	0.1	0.1	0.1	0.2	0.5	0.5	0.1
Ce ppm	8.8	7.1	4.9	1.6	0.4	0.3	6.8	6.4	24.6
Pr ppm	0.8	0.0	0.0	0.0	0.0	0.0	0.1	0.1	0.0
Nd ppm	2.8	0.4	0.5	0.1	1.1	0.2	0.6	0.7	1.6
Sm ppm	4.1	2.4	1.9	1.2	0.4	0.1	4.4	2.1	6.0
Eu ppm	0.2	0.2	0.3	0.1	0.1	0.0	0.4	0.1	0.5
Gd ppm	33.6	34.4	39.4	7.0	1.8	1.4	31.8	11.3	62.0
Tb ppm	40.9	41.1	50.2	11.9	3.3	4.7	36.8	15.5	73.2
Dy ppm	846.0	820.0	1038.0	278.0	119.0	207.0	771.0	340.0	1423.0
Ho ppm	382.0	351.0	461.0	140.0	80.8	149.0	332.0	153.0	607.0

Er ppm	2370.0	1970.0	2490.0	1048.0	793.0	1500.0	1810.0	919.0	3330.0
Tm ppm	555.0	464.0	551.0	319.0	272.0	509.0	423.0	258.0	760.0
Yb ppm	5100.0	4100.0	4380.0	3530.0	3120.0	6140.0	3880.0	2660.0	6380.0
Lu ppm	742.0	530.0	595.0	529.0	474.0	842.0	535.0	418.0	809.0
Hf ppm	13800.0	10860.0	10700.0	13600.0	31400.0	24600.0	8970.0	10940.0	8130.0
Ta ppm	77.9	45.5	40.4	29.8	32.9	52.2	49.4	36.2	65.2
Pb ppm	280.0	54.0	74.3	52.0	28.9	45.0	62.6	39.0	184.0
Th ppm	995.0	819.0	1006.0	377.0	372.0	640.0	774.0	579.0	1430.0
U ppm	208.0	121.3	93.5	315.0	2.9	17.7	305.0	115.3	991.0
Total trace	5932.9	2326.5	2777.1	2240.1	1929.7	2439.9	3158.0	2265.1	5335.4
REE	10089.3	8320.8	9612.3	5866.0	4866.0	9353.9	7832.3	4784.6	13477.0
	GHA10_Zrn1_01	GHA10_Zrn1_02	GHA3B_Ty pe2_01	GHA3B_Ty pe2_02	GHA3B_Ty pe2_03	GHA26_ty pe3_01	GHA26_typ e3_02	GHA26_typ e3_03	GHA26 _type3 _04
lable	126.0	1.6	0.4	0.5	1.1	7.3	2.6	8.7	10.9
Li ppm	870.0	42.0	0.4	1.2	39.8	890.0	836.0	628.0	526.0
Al ppm	180000.0	172000.0	149600.0	177000.0	185000.0	165000.0	142000.0	152600.0	165000.0
Si ppm	1820.0	1640.0	245.0	197.0	56.0	76.0	117.0	218.0	320.0
P ppm	554.0	600.0	570.0	531.0	595.0	569.0	602.0	555.0	604.0
Sc ppm	43.0	25.6	22.9	25.6	81.0	2420.0	1658.0	1990.0	2237.0
Ti ppm	610.0	93.0	66.6	66.6	89.0	3980.0	3240.0	3330.0	2880.0
Fe ppm	N.A	N.A	370.1	370.1	370.1	1236.3	4079.0	3811.2	3042.2
Y ppm	605.0	517.0	97.6	108.9	1830.0	565.0	877.0	435.0	454.0
Nb ppm	31.0	6.1	3.9	17.0	171.0	6200.0	4150.0	6110.0	7480.0
Sn ppm	0.2	0.1	0.1	0.1	1.0	0.1	0.1	0.3	0.2
La ppm	24.0	19.3	0.2	0.1	6.0	0.0	0.2	0.1	0.1
Ce ppm	0.1	0.2	0.0	0.0	1.0	0.0	0.1	0.1	0.0

Pr ppm	0.7	0.6	0.2	0.2	4.6	0.2	0.2	0.2	0.2
Nd ppm	6.0	4.0	0.2	0.3	0.2	0.2	1.1	0.4	0.2
Sm ppm	0.3	0.1	0.1	0.1	0.2	0.1	0.1	0.1	0.1
Eu ppm	61.6	46.3	0.8	0.8	20.2	0.8	7.6	1.2	2.6
Gd ppm	70.6	54.2	1.8	1.2	15.1	1.7	18.7	2.2	2.1
Tb ppm	1367.0	1153.0	61.1	31.7	176.0	44.5	564.0	65.0	44.8
Dy ppm	569.0	476.0	37.6	17.8	54.9	24.8	328.0	27.7	24.5
Ho ppm	3080.0	2530.0	358.0	155.0	357.0	184.0	2380.0	211.0	177.0
Er ppm	666.0	561.0	138.7	63.5	140.0	68.0	736.0	77.5	65.8
Tm ppm	5290.0	4630.0	1870.0	965.0	2340.0	892.0	7490.0	1020.0	837.0
Yb ppm	706.0	610.0	363.0	203.0	509.0	149.0	1118.0	190.0	158.0
Lu ppm	7880.0	7820.0	30100.0	33600.0	37600.0	23900.0	23500.0	24700.0	27500.0
Hf ppm	60.5	60.5	26.9	26.6	116.0	98.5	64.2	75.3	83.7
Ta ppm	118.0	78.3	16.5	8.2	37.1	42.1	38.4	63.0	53.7
Pb ppm	1360.0	977.0	253.0	58.5	426.0	30.4	84.1	32.6	31.5
Th ppm	705.0	536.0	27.5	5.2	5.4	0.5	49.0	23.1	17.4
U ppm	5738.5	3884.1	694.1	448.7	2763.5	10329.8	7876.3	9583.7	11214.2
Total trace	11841.5	10084.8	2831.7	1438.7	3625.2	1365.4	12644.0	1595.8	1312.6

EMPA of Zircons from Al-Ghurayyah

		GHA1C2_2z_01		GHA4B_C1_01		GHA4B_C1_02		GHA4B_C1_03	
	LOD	type-1	±	type-1	±	type-1	±	type-1	±
HfO2	0.06	1.44	0.01	1.89	0.01	1.82	0.01	2.20	0.02
SiO2	0.04	32.64	0.02	31.55	0.02	31.18	0.02	31.55	0.02
TiO2	0.02	b.d.		0.12	0.01	0.11	0.00	0.16	0.01
ThO2	0.04	0.24	0.01	0.18	0.01	0.29	0.01	0.29	0.01
ZrO2	0.09	61.82	0.22	61.79	0.22	60.68	0.22	61.10	0.22
P2O5	0.03	0.60	0.01	0.37	0.00	0.53	0.01	0.39	0.00
Y2O3	0.04	1.48	0.03	1.17	0.02	1.64	0.03	1.25	0.03
Dy2O3	0.04	0.19	0.03	0.13	0.02	0.16	0.03	b.d.	
UO2	0.03	b.d.		b.d.		b.d.		b.d.	
Er2O3	0.04	0.46	0.04	0.36	0.03	0.46	0.04	0.35	0.03
Yb2O3	0.04	0.73	0.01	0.67	0.01	0.81	0.01	0.71	0.01
Total		99.59		98.23		97.67		97.99	
	LOD	GHA4B_cluster1_01		GHA4B_cluster1_02		GHA4B_cluster1_03		GHA4B_cluster1_04	
		type-1	±	type-1	±	type-1	±	type-1	±
HfO2	0.06	1.66	0.01	1.82	0.01	1.91	0.01	2.09	0.01
SiO2	0.04	31.80	0.02	31.70	0.02	31.59	0.02	31.19	0.02
ThO2	0.04	0.10	0.00	0.10	0.00	0.12	0.01	0.13	0.01
ZrO2	0.09	b.d.		b.d.		0.15	0.01	0.29	0.01
P2O5	0.03	64.15	0.23	63.29	0.23	62.35	0.22	61.29	0.22
Y2O3	0.04	0.40	0.00	0.29	0.00	0.36	0.00	0.46	0.00
Dy2O3	0.04	0.58	0.01	0.87	0.02	1.12	0.02	1.47	0.03
UO2	0.03	b.d.		b.d.		0.14	0.02	0.16	0.03
Er2O3	0.04	b.d.		b.d.		b.d.		b.d.	
Yb2O3	0.04	0.13	0.01	0.29	0.03	0.39	0.03	0.49	0.04
Total		0.29	0.00	0.55	0.00	0.67	0.01	0.93	0.01
		99.10		98.92		98.79		98.48	
		GHA4B_cluster2_01		GHA4B_cluster1_05		GHA4B_cluster2_02		GHA4B_cluster2_03	
	LOD	type-1	±	type-1	±	type-1	±	type-1	±
HfO2	0.06	1.40	0.01	2.02	0.01	1.69	0.01	1.56	0.01
SiO2	0.04	31.88	0.02	32.14	0.02	31.46	0.02	31.12	0.02
TiO2	0.02	0.08	0.00	0.13	0.01	0.11	0.00	0.11	0.00
ThO2	0.04	b.d.		b.d.		0.22	0.01	0.25	0.01
ZrO2	0.09	64.39	0.23	64.67	0.23	61.47	0.22	61.48	0.22
P2O5	0.03	0.41	0.00	0.17	0.00	0.37	0.00	0.56	0.01
Y2O3	0.04	0.36	0.01	0.24	0.00	1.52	0.03	1.70	0.03
Dy2O3	0.04	b.d.		b.d.		0.20	0.03	0.22	0.03
UO2	0.03	0.12	0.27	b.d.		b.d.		b.d.	
Er2O3	0.04	0.19	0.02	0.12	0.01	0.48	0.04	0.51	0.04
Yb2O3	0.04	0.55	0.00	0.28	0.00	0.83	0.01	0.86	0.01
Total		99.38		99.77		98.33		98.34	

Continue EMPA of Zircons from Al-Ghurayyah											
		GHA4B_cluster2_04			GHA4B_cluster2_05			GHA4B_cluster2_06		GHA4B_cluster2_07	
	LOD	type-1	±	type-1	±	type-1	±	type-1	±		
HfO2	0.06	1.75	0.01	2.18	0.02	b.d.			2.22	0.02	
SiO2	0.04	31.45	0.02	31.35	0.02	30.78	0.02	31.88	0.02	0.02	
TiO2	0.02	0.13	0.01	0.14	0.01	0.13	0.01	0.14	0.01	0.01	
ThO2	0.04	0.18	0.01	0.32	0.01	0.28	0.01	b.d.			
ZrO2	0.09	61.74	0.22	61.03	0.22	60.98	0.22	63.84	0.23		
P2O5	0.03	0.44	0.00	0.42	0.00	0.62	0.01	0.34	0.00		
Y2O3	0.04	1.31	0.03	1.47	0.03	0.62	0.01	0.13	0.00		
Dy2O3	0.04	b.d.		0.14	0.02	b.d.		b.d.			
UO2	0.03	b.d.		b.d.		b.d.		b.d.			
Er2O3	0.04	0.36	0.03	0.47	0.04	0.35	0.03	0.15	0.01		
Yb2O3	0.04	0.64	0.01	0.89	0.01	0.92	0.01	0.54	0.00		
Total		98.01		98.41		94.66		99.25			
		GHA5_C3_01			GHA5_C3_02			GHA5_C3_03		GHA5_C3_04	
	LOD	type-1	±	type-1	±	type-1	±	type-1	±		
HfO2	0.06	1.54	0.01	1.59	0.01	1.71	0.01	1.74	0.01	0.01	
SiO2	0.04	31.28	0.02	31.21	0.02	31.24	0.02	31.21	0.02	0.02	
TiO2	0.02	0.09	0.00	0.08	0.00	0.12	0.00	0.12	0.00	0.00	
ThO2	0.04	0.25	0.01	0.17	0.01	0.16	0.01	0.17	0.01	0.01	
ZrO2	0.09	62.38	0.22	61.93	0.22	62.04	0.22	62.18	0.22	0.22	
P2O5	0.03	0.44	0.00	0.42	0.00	0.38	0.00	0.41	0.00	0.00	
Y2O3	0.04	1.29	0.03	1.35	0.03	1.27	0.03	1.33	0.03	0.03	
Dy2O3	0.04	0.15	0.02	0.18	0.03	0.15	0.02	0.16	0.03	0.03	
UO2	0.03	b.d.		b.d.		b.d.		b.d.			
Er2O3	0.04	0.39	0.03	0.45	0.04	0.40	0.04	0.39	0.03	0.03	
Yb2O3	0.04	0.65	0.01	0.72	0.01	0.68	0.01	0.65	0.01	0.01	
Total		98.47		98.10		98.14		98.36			
		GHA5_C3_05			GHA5_C4_01			GHA5_C4_02		GHA5_C4_03	
	LOD	type-1	±	Type-1	±	Type-1	±	Type-1	±		
HfO2	0.06	2.07	0.01	1.80	0.01	1.73	0.01	1.61	0.01	0.01	
SiO2	0.04	31.90	0.02	31.42	0.02	31.86	0.02	31.27	0.02	0.02	
TiO2	0.02	0.12	0.00	0.10	0.00	0.12	0.01	0.09	0.00	0.00	
ThO2	0.04	0.12	0.00	0.10	0.00	0.12	0.01	0.09	0.00	0.00	
ZrO2	0.09	b.d.		0.27	0.01	b.d.		0.17	0.01	0.01	
P2O5	0.03	64.36	0.23	62.13	0.22	64.32	0.23	60.92	0.22	0.22	
Y2O3	0.04	0.18	0.00	0.40	0.00	0.23	0.01	0.41	0.00	0.00	
Dy2O3	0.04	b.d.	0.00	1.28	0.03	0.15	0.01	1.44	0.03	0.03	
UO2	0.03	b.d.		0.13	0.02	b.d.		b.d.			
Er2O3	0.04	b.d.		b.d.		b.d.		b.d.			
Yb2O3	0.04	b.d.		0.33	0.03	b.d.		0.44	0.04	0.04	
Total		0.35	0.00	0.58	0.00	0.53	0.01	0.72	0.01	0.01	
		98.98		98.43		98.93		97.07			

Continue EMPA of Zircons from Al-Ghurayyah											
	LOD	GHA8_C4_01		GHA8_C4_02		GHA8_C4_03		GHA8_C4_04		GHA8_C4_05	
		type-1	±	type-1	±	type-1	±	type-1	±	type-1	±
HfO2	0.06										
SiO2	0.04	1.57	0.01	1.76	0.01	1.82	0.01	1.99	0.01	2.06	0.01
TiO2	0.02	31.06	0.02	31.46	0.02	31.06	0.02	31.52	0.02	31.04	0.02
ThO2	0.04	0.09	0.00	0.10	0.00	0.12	0.00	0.15	0.01	0.14	0.01
ZrO2	0.09	0.30	0.01	b.d.		0.64	0.02	0.21	0.01	0.29	0.01
P2O5	0.03	60.33	0.22	64.02	0.23	59.77	0.21	62.21	0.22	62.36	0.22
Y2O3	0.04	0.57	0.01	0.37	0.00	0.44	0.00	0.28	0.00	0.17	0.01
Dy2O3	0.04	1.47	0.03	0.28	0.01	1.32	0.03	0.61	0.01	0.62	0.01
UO2	0.03	b.d.		b.d.		b.d.		b.d.		b.d.	
Er2O3	0.04	b.d.		b.d.		b.d.		b.d.		b.d.	
Yb2O3	0.04	0.47	0.04	0.14	0.01	0.45	0.04	0.22	0.02	0.16	0.01
Total		0.90	0.01	0.55	0.00	1.31	0.01	0.70	0.01	0.51	0.01
		96.75		98.68		96.91		97.89		97.36	

Continue EMPA of Zircons from Al-Ghurayyah											
Type-2	GHA1A_zrn_a1_01				GHA1A_zrn_a1_07		GHA1A_zrn_a1_08		GHA1b_a8_01		
	Type-2			Type-2			Type-2			Type-2	
	LOD		±		±		±		±		
HfO2	0.06	2.17	0.02	2.97	0.02	2.26	0.02	2.00	0.02	0.02	
SiO2	0.04	32.40	0.01	33.47	0.50	30.29	0.01	32.42	0.02	0.02	
Al2O3	0.02	b.d.		0.55	0.00	b.d.		b.d.			
TiO2	0.02	b.d.		b.d.		b.d.		b.d.			
ThO2	0.04	b.d.		0.12	0.21	0.15	0.21	0.13	0.23		
ZrO2	0.09	63.66	0.00	59.53	0.00	58.70	0.00	64.31	0.00	0.00	
P2O5	0.03	0.22	0.01	0.19	0.01	0.13	0.00	0.23	0.00	0.00	
Y2O3	0.04	0.33	0.03	0.38	0.00	b.d.		0.22	0.00	0.00	
Ho2O3	0.09	b.d.		b.d.		b.d.		b.d.			
Lu2O3	0.05	b.d.		b.d.		b.d.		b.d.			
UO2	0.03	b.d.		0.11	0.01	0.14	0.00	b.d.			
Sm2O3	0.07	b.d.		b.d.		b.d.		b.d.			
Tb2O3	0.04	b.d.		b.d.		b.d.		b.d.			
FeO	0.02	0.06	0.02	0.26	0.02	0.11	0.01	b.d.			
Er2O3	0.04	0.21	0.00	0.21	0.00	b.d.		0.17	0.00	0.00	
Tm2O3	0.04	b.d.		b.d.		b.d.		b.d.			
Yb2O3	0.04	0.70	0.00	0.56	0.01	0.32	0.09	0.48	0.00	0.00	
PbO	0.03	b.d.		b.d.		b.d.		b.d.			
Total		99.75		98.36		92.09		99.96			
	GHA1b_a8_02				GHA1b_a8_03		GHA1c2_a13_03		GHA1C2_1z_01		
	Type-2			Type-2			Type-2			Type-2	
	LOD		±		±	brighter	±	bright	±		
HfO2	0.06	2.22	0.02	2.58	0.02	4.35	0.02	3.55	0.02	0.02	
SiO2	0.04	32.69	0.01	33.22	0.91	32.60	0.00	33.12	0.01	0.01	
Al2O3	0.02	b.d.		1.00	0.00	b.d.		b.d.			
TiO2	0.02	b.d.		b.d.		b.d.		b.d.			
ThO2	0.04	0.14	0.23	b.d.		0.28	0.22	b.d.			
ZrO2	0.09	63.32	0.00	59.24	0.00	60.86	0.00	62.99	0.00	0.00	
P2O5	0.03	0.22	0.00	0.15	0.01	0.29	0.01	0.16	0.00	0.00	
Y2O3	0.04	0.21	0.03	0.28	0.00	0.44	0.03	b.d.			
Ho2O3	0.09	b.d.		b.d.		b.d.		b.d.			
Lu2O3	0.05	b.d.		b.d.		0.16	0.00	b.d.			
UO2	0.03	b.d.		b.d.		b.d.		b.d.			
Sm2O3	0.07	b.d.		b.d.		b.d.		b.d.			
Tb2O3	0.04	b.d.		b.d.		b.d.		b.d.			
FeO	0.02	b.d.		1.95	0.01	b.d.		b.d.			
Er2O3	0.04	0.19	0.00	0.17	0.00	0.32	0.00	b.d.			
Tm2O3	0.04	b.d.		b.d.		b.d.		b.d.			
Yb2O3	0.04	0.47	0.00	0.43	0.03	0.95	0.01	0.34	0.03	0.03	
PbO	0.03	b.d.		b.d.		b.d.		b.d.			
Total		99.46		99.01		100.25		100.15			

Continue EMPA of Zircons from Al-Ghurayyah										
	GHA1C2_1z_02				GHA1C2_2z_02		GHA7_F13		GHA7_F13_02	
	Type-2			Type-2		Type-2		Type-2		
	LOD	bright	±	bright	±		±		±	
HfO2	0.06	3.83	0.02	2.05	0.02	1.14	0.02	3.37	0.02	
SiO2	0.04	32.54	0.06	32.46	0.03	31.39	0.00	31.57	0.04	
Al2O3	0.02	0.06	0.00	b.d.		b.d.		b.d.		
TiO2	0.02	b.d.		b.d.		b.d.		b.d.		
ThO2	0.04	b.d.		0.39	0.23	b.d.		b.d.		
ZrO2	0.09	62.18	0.00	62.93	0.01	62.14	0.00	59.33	0.00	
P2O5	0.03	0.30	0.00	0.55	0.01	b.d.		b.d.		
Y2O3	0.04	0.15	0.00	0.36	0.00	0.75	0.00	b.d.		
Ho2O3	0.09	b.d.		b.d.		b.d.		b.d.		
Lu2O3	0.05	b.d.		b.d.		b.d.		b.d.		
UO2	0.03	b.d.		b.d.		b.d.		b.d.		
Sm2O3	0.07	b.d.		b.d.		b.d.		b.d.		
Tb2O3	0.04	b.d.		b.d.		b.d.		b.d.		
FeO	0.02	0.06	0.02	0.39	0.02	b.d.		0.08	0.00	
Er2O3	0.04	0.22	0.00	0.24	0.00	b.d.		b.d.		
Tm2O3	0.04	b.d.		b.d.		b.d.		b.d.		
Yb2O3	0.04	0.68	0.00	0.83	0.00	0.46	0.00	0.34	0.00	
PbO	0.03	b.d.		b.d.		b.d.		b.d.		
Total		100.01		100.20		95.87		94.69		
	GHA4B_C6_01				GHA4B_C6_02		GHA4B_C6_03		GHA4B_C6_04	
	Type-2			Type-2		Type-2		Type-2		
	LOD		±	bright	±		±		±	
HfO2	0.06	2.19	0.02	1.95	0.02	2.37	0.02	2.49	0.02	
SiO2	0.04	32.36	0.00	31.53	0.00	31.95	0.00	31.86	0.00	
Al2O3	0.02	b.d.		b.d.		b.d.		b.d.		
TiO2	0.02	0.14	0.00	0.13	0.01	0.15	0.00	0.18	0.00	
ThO2	0.04	b.d.		0.16	0.22	b.d.		b.d.		
ZrO2	0.09	64.74	0.00	62.02	0.00	63.52	0.00	62.55	0.00	
P2O5	0.03	b.d.		0.35	0.02	0.22	0.01	0.24	0.01	
Y2O3	0.04	b.d.		1.17	0.02	0.47	0.00	0.56	0.00	
Ho2O3	0.09	b.d.		b.d.		b.d.		b.d.		
Lu2O3	0.05	b.d.		b.d.		b.d.		b.d.		
UO2	0.03	b.d.		b.d.		b.d.		b.d.		
Sm2O3	0.07	b.d.		b.d.		b.d.		b.d.		
Tb2O3	0.04	b.d.		b.d.		b.d.		b.d.		
FeO	0.02	b.d.		b.d.		b.d.		b.d.		
Er2O3	0.04	b.d.		0.37	0.00	0.22	0.00	0.21	0.00	
Tm2O3	0.04	b.d.		b.d.		b.d.		b.d.		
Yb2O3	0.04	b.d.		0.69	0.00	0.41	0.00	0.50	0.00	
PbO	0.03	b.d.		b.d.		b.d.		b.d.		
Total		99.43		98.35		99.31		98.59		

Continue EMPA of Zircons from Al-Ghurayyah							
		GHA5_C5_01		GHA5_C5_02		GHA5_C5_03	
		Type-2		Type-2		Type-2	
	LOD		±		±		±
HfO2	0.06	1.87	0.02	1.74	0.02	6.59	0.02
SiO2	0.04	31.77	0.00	31.26	0.00	31.88	0.00
Al2O3	0.02	b.d.		b.d.		b.d.	
TiO2	0.02	0.11	0.01	0.10	0.01	0.43	0.00
ThO2	0.04	0.18	0.23	0.15	0.22	b.d.	
ZrO2	0.09	62.99	0.00	61.91	0.00	60.18	0.00
P2O5	0.03	0.31	0.02	0.29	0.02	0.12	0.01
Y2O3	0.04	0.90	0.00	1.16	0.00	b.d.	
Ho2O3	0.09	b.d.		b.d.		b.d.	
Lu2O3	0.05	b.d.		b.d.		b.d.	
UO2	0.03	b.d.		b.d.		b.d.	
Sm2O3	0.07	b.d.		b.d.		b.d.	
Tb2O3	0.04	b.d.		b.d.		b.d.	
FeO	0.02	b.d.		b.d.		b.d.	
Er2O3	0.04	0.25	0.00	0.41	0.00	0.13	0.00
Tm2O3	0.04	b.d.		b.d.		b.d.	
Yb2O3	0.04	0.45	0.00	0.69	0.00	0.46	0.00
PbO	0.03	b.d.		b.d.		b.d.	
Total		98.84		97.70		99.79	

Continue EMPA of Zircons from Al-Ghurayyah									
Type-3									
name		GHA2b_a20_03		GHA2b_a20_03.2		GHA2b_a20_03.3		GHA2b_a20_04	
Types	LOD	Type-3	±	Type-3	±	Type-3	±	Type-3	±
HfO2	0.06	4.07	0.03	3.17	0.02	3.75	0.03	4.25	0.03
SiO2	0.04	32.73	0.02	33.13	0.02	34.19	0.02	32.71	0.02
Al2O3	0.02	b.d.		b.d.		b.d.		b.d.	
TiO2	0.02	b.d.		b.d.		b.d.		b.d.	
ThO2	0.04	b.d.		b.d.		b.d.		b.d.	
ZrO2	0.09	62.89	0.22	62.85	0.22	63.87	0.23	63.09	0.23
P2O5	0.03	b.d.		b.d.		b.d.		b.d.	
Y2O3	0.04	b.d.		b.d.		b.d.		b.d.	
Ho2O3	0.09	b.d.		b.d.		b.d.		b.d.	
Lu2O3	0.05	b.d.		b.d.		b.d.		b.d.	
UO2	0.03	b.d.		b.d.		b.d.		b.d.	
Sm2O3	0.07	b.d.		b.d.		b.d.		b.d.	
Tb2O3	0.04	b.d.		b.d.		b.d.		b.d.	
FeO	0.02	0.06	0.00	0.09	0.00	0.21	0.00	0.05	0.00
Er2O3	0.04	b.d.		b.d.		b.d.		b.d.	
Tm2O3	0.04	b.d.		b.d.		b.d.		b.d.	
Yb2O3	0.04	0.20	0.00	0.14	0.00	b.d.		0.21	0.00
PbO	0.03	b.d.		b.d.		b.d.		b.d.	
Total		99.95		99.38		102.02		100.32	
Type-3									
name		GHA2b_a20_06		GHA3E1_Y13_02		GHA3b_Cluster2_1		GHA3b_Cluster2_2	
Types	LOD	Type-3	±	Type-3	±	Type-3	±	Type-3	±
HfO2	0.06	4.15	0.03	3.82	0.03	3.56	0.02	4.07	0.03
SiO2	0.04	32.91	0.02	32.22	0.02	31.96	0.02	31.51	0.02
Al2O3	0.02	b.d.		b.d.		b.d.		b.d.	
TiO2	0.02	b.d.		b.d.		0.21	0.01	0.27	0.01
ThO2	0.04	b.d.		b.d.		b.d.		b.d.	
ZrO2	0.09	63.61	0.23	61.71	0.22	63.71	0.23	62.98	0.23
P2O5	0.03	b.d.		b.d.		0.17	0.00	0.18	0.00
Y2O3	0.04	b.d.		b.d.		b.d.		b.d.	
Ho2O3	0.09	b.d.		b.d.		b.d.		b.d.	
Lu2O3	0.05	b.d.		b.d.		b.d.		b.d.	
UO2	0.03	b.d.		b.d.		b.d.		b.d.	
Sm2O3	0.07	b.d.		b.d.		b.d.		b.d.	
Tb2O3	0.04	b.d.		b.d.		b.d.		b.d.	
FeO	0.02	b.d.		b.d.		b.d.		0.45	0.01
Er2O3	0.04	0.16	0.01	b.d.		b.d.		b.d.	
Tm2O3	0.04	b.d.		b.d.		b.d.		b.d.	
Yb2O3	0.04	0.27	0.00	0.25	0.00	0.37	0.00	0.38	0.00
PbO	0.03	b.d.		b.d.		b.d.		b.d.	
Total		101.10		97.99		99.98		99.84	

Continue EMPA of Zircons from Al-Ghurayyah							
Type-3							
Types	LOD	Type-3	±	Type-3	±	Type-3	±
HfO2	0.06	5.48	0.04	3.10	0.02	1.83	0.01
SiO2	0.04	32.13	0.02	31.46	0.02	30.02	0.02
Al2O3	0.02	b.d.		b.d.		b.d.	
TiO2	0.02	0.35	0.01	0.21	0.01	0.16	0.01
ThO2	0.04	b.d.		3.35	0.12	0.81	0.03
ZrO2	0.09	61.68	0.22	61.03	0.22	59.22	0.21
P2O5	0.03	0.16	0.00	0.24	0.00	0.47	0.00
Y2O3	0.04	b.d.		0.14	0.00	0.60	0.01
Ho2O3	0.09	b.d.		b.d.		b.d.	
Lu2O3	0.05	b.d.		b.d.		b.d.	
UO2	0.03	b.d.		b.d.		b.d.	
Sm2O3	0.07	b.d.		b.d.		b.d.	
Tb2O3	0.04	b.d.		b.d.		b.d.	
FeO	0.02	0.44	0.01	b.d.		4.65	0.09
Er2O3	0.04	b.d.		b.d.		0.14	0.01
Tm2O3	0.04	b.d.		b.d.		b.d.	
Yb2O3	0.04	0.36	0.00	0.27	0.00	0.55	0.00
PbO	0.03	b.d.		b.d.		b.d.	
Total		100.59		99.79		98.46	

Continue EMPA of Zircons from Al-Ghurayyah											
Type-4	GHA26_a17_01		GHA26_a17_02		GHA26_a17_03		GHA26_a17_04		GHA3b_Cluster3_1_4		
Types	Type-4		Type-4		Type-4		Type-4		Type-4		
LOD	±		±		±		±		±		
HfO2	0.06	3.22	0.02	3.08	0.02	3.59	0.02	2.93	0.02	3.24	0.02
SiO2	0.04	31.88	0.02	31.68	0.02	31.81	0.02	31.82	0.02	32.26	0.02
Al2O3	0.02	0.20	0.18	0.19	0.17	0.11	0.10	b.d.		b.d.	
TiO2	0.02	0.55	0.02	0.58	0.02	0.70	0.03	0.64	0.03	0.21	0.01
ThO2	0.04	b.d.		b.d.		b.d.		0.17	0.01	b.d.	
ZrO2	0.09	60.25	0.22	60.55	0.22	60.60	0.22	58.93	0.21	64.21	0.23
P2O5	0.03	0.11	0.00	b.d.		b.d.		b.d.		0.10	0.00
Y2O3	0.04	0.52	0.01	0.48	0.01	0.16	0.00	1.71	0.03	b.d.	
Ho2O3	0.09	b.d.		b.d.		b.d.		b.d.		b.d.	
Lu2O3	0.05	b.d.		b.d.		b.d.		0.23	0.27	b.d.	
UO2	0.03	b.d.		b.d.		b.d.		b.d.		b.d.	
Sm2O3	0.07	b.d.		b.d.		b.d.		b.d.		b.d.	
Tb2O3	0.04	b.d.		b.d.		b.d.		b.d.		b.d.	
FeO	0.02	0.73	0.01	0.85	0.02	0.64	0.01	0.38	0.01	b.d.	
Er2O3	0.04	0.20	0.02	0.18	0.02	b.d.		0.23	0.02	b.d.	
Tm2O3	0.04	b.d.		b.d.		b.d.		b.d.		b.d.	
Yb2O3	0.04	0.63	0.01	0.52	0.00	0.17	0.00	1.38	0.01	0.30	0.00
PbO	0.03	b.d.		b.d.		b.d.		b.d.		b.d.	
Total		98.27		98.10		97.78		98.41		100.31	
LOD	GHA26_a17_05		GHA3b_Cluster1_1		GHA3b_Cluster1_2		GHA3b_Cluster1_3				
Type-4	Type-4		Type-4		Type-4		Type-4				
LOD	±		±		±		±				
HfO2	0.06										
SiO2	0.04										
Al2O3	0.02	4.29	0.03	3.94	0.03	3.38	0.02	3.47	0.02		
TiO2	0.02	32.93	0.02	32.50	0.02	32.19	0.02	32.32	0.02		
ThO2	0.04	0.09	0.08	b.d.		b.d.		b.d.			
ZrO2	0.09	0.32	0.01	0.23	0.01	0.22	0.01	0.22	0.01		
P2O5	0.03	b.d.		b.d.		b.d.		b.d.			
Y2O3	0.04	58.64	0.21	62.95	0.23	63.52	0.23	63.29	0.23		
Ho2O3	0.09	b.d.		b.d.		0.17	0.00	0.12	0.00		
Lu2O3	0.05	0.42	0.01	b.d.		b.d.		b.d.			
UO2	0.03	b.d.		b.d.		b.d.		b.d.			
Sm2O3	0.07	b.d.		b.d.		b.d.		b.d.			
Tb2O3	0.04	b.d.		b.d.		b.d.		b.d.			
FeO	0.02	b.d.		b.d.		b.d.		b.d.			
Er2O3	0.04	b.d.		b.d.		b.d.		b.d.			
Tm2O3	0.04	0.74	0.01	b.d.		b.d.		b.d.			
Yb2O3	0.04	0.18	0.02	b.d.		b.d.		b.d.			
PbO	0.03	b.d.		b.d.		b.d.		b.d.			
Total		0.62	0.00	0.13	0.00	0.34	0.00	0.25	0.00		
		b.d.		b.d.		b.d.		b.d.			
		98.21		99.74		99.81		99.67			

LOD, limit of detection. b.d. at or below detection limit

EMP analyses of pyrochlore (PCL-1) from Al-Ghurayyah

	LOD	GHA10_pcl_4_06			GHA10_pcl_4_05			GHA5_pcl_01		GHA5_pcl_02	
		Type 1	±	Type 1	±	Type 1	±	Type 1	±		
F	0.18	4.28	0.47	5.35	0.59	1.15	0.13	1.01	0.11		
Na2O	0.03	6.22	0.21	6.65	0.23	0.87	0.03	0.39	0.01		
La2O3	0.16	2.69	0.48	2.62	0.46	2.75	0.49	2.28	0.40		
Ce2O3	0.14	8.49	0.61	7.95	0.57	7.91	0.57	6.31	0.45		
Gd2O3	0.08	0.41	0.06	0.39	0.06	0.42	0.07	0.46	0.07		
TiO2	0.04	4.04	0.07	4.14	0.07	4.34	0.07	4.51	0.08		
CaO	0.02	0.87	0.01	0.97	0.01	0.91	0.01	1.06	0.01		
ThO2	0.05	0.20	0.02	0.18	0.01	0.27	0.02	0.80	0.07		
Nb2O5	0.06	53.95	0.67	55.08	0.69	56.29	0.70	57.38	0.72		
Y2O3	0.06	0.83	0.08	0.95	0.09	1.08	0.10	1.82	0.18		
Nd2O3	0.05	1.77	0.14	1.69	0.13	1.73	0.13	1.67	0.13		
Pr2O3	0.10	0.84	0.24	0.76	0.22	0.74	0.22	0.61	0.18		
Eu2O3	0.05	b.d.		b.d.		b.d.		b.d.			
Dy2O3	0.05	0.27	0.05	0.31	0.06	0.33	0.06	0.67	0.12		
Ho2O3	0.11	b.d.		b.d.		b.d.		b.d.			
Lu2O3	0.06	b.d.		b.d.		b.d.		b.d.			
UO2	0.04	5.86	0.18	5.85	0.18	6.28	0.19	5.24	0.16		
Ta2O5	0.08	4.56	0.14	4.64	0.14	4.71	0.14	4.69	0.14		
MnO	0.03	0.12	1.05	0.13	1.11	b.d.		b.d.			
Sm2O3	0.08	0.55	0.12	0.55	0.12	0.49	0.11	0.71	0.15		
Tb2O3	0.05	b.d.		b.d.		b.d.		b.d.			
FeO	0.03	b.d.		b.d.		0.10	0.01	b.d.			
Er2O3	0.05	b.d.		b.d.		0.15	0.04	0.22	0.06		
Tm2O3	0.05	b.d.		b.d.		b.d.		b.d.			
Yb2O3	0.05	b.d.		b.d.		0.15	0.04	0.14	0.04		
PbO	0.04	1.68	0.07	1.77	0.08	2.80	0.12	2.73	0.12		
SnO2	0.03	0.25	0.05	0.29	0.05	0.18	0.03	0.14	0.03		
Total		98.29	0.00	100.62	0.00	93.80	0.00	93.13	0.00		

Continue PCL-1

	GHA5_pcl_03			GHA5_pcl2_01			GHA5_pcl2_02			GHA5_pcl2_03		
	LOD	Type 1	±	Type 1	±	Type 1	±	Type 1	±	Type 1	±	
F	0.18	1.60	0.17	1.36	0.15	1.68	0.18	1.08	0.12			
Na2O	0.03	0.43	0.01	0.10	0.00	2.74	0.09	b.d.				
La2O3	0.16	1.29	0.23	1.68	0.30	2.66	0.47	2.44	0.43			
Ce2O3	0.14	3.37	0.24	6.61	0.47	7.36	0.53	7.48	0.54			
Gd2O3	0.08	0.51	0.08	0.28	0.04	0.57	0.09	0.41	0.07			
TiO2	0.04	5.45	0.09	5.93	0.10	5.42	0.09	5.07	0.09			
CaO	0.02	1.22	0.02	2.09	0.03	1.16	0.02	1.14	0.02			
ThO2	0.05	5.39	0.45	0.42	0.03	0.77	0.06	0.31	0.03			
Nb2O5	0.06	55.36	0.69	52.00	0.65	57.18	0.71	55.98	0.70			
Y2O3	0.06	4.45	0.43	1.09	0.11	2.11	0.20	1.97	0.19			
Nd2O3	0.05	1.14	0.09	1.63	0.13	1.70	0.13	1.76	0.14			
Pr2O3	0.10	0.33	0.09	0.67	0.19	0.72	0.21	0.65	0.19			
Eu2O3	0.05	b.d.		b.d.		b.d.		b.d.				
Dy2O3	0.05	1.27	0.23	0.42	0.08	0.70	0.13	0.61	0.11			
Ho2O3	0.11	b.d.		b.d.		b.d.		b.d.				
Lu2O3	0.06	b.d.		b.d.		b.d.		b.d.				
UO2	0.04	0.91	0.03	9.31	0.28	2.56	0.08	4.41	0.13			
Ta2O5	0.08	3.56	0.11	3.20	0.10	3.65	0.11	4.32	0.13			
MnO	0.03	b.d.		b.d.		b.d.		b.d.				
Sm2O3	0.08	0.61	0.13	0.47	0.10	0.53	0.12	0.60	0.13			
Tb2O3	0.05	b.d.		b.d.		b.d.		b.d.				
FeO	0.03	0.12	0.01	0.29	0.02	b.d.		b.d.				
Er2O3	0.05	0.73	0.21	b.d.		0.27	0.08	0.27	0.08			
Tm2O3	0.05	0.18	0.08	b.d.		b.d.		b.d.				
Yb2O3	0.05	0.77	0.20	b.d.		b.d.		0.31	0.08			
PbO	0.04	2.10	0.09	3.76	0.16	2.19	0.10	3.48	0.15			
SnO2	0.03	0.21	0.04	0.36	0.07	0.19	0.03	0.29	0.05			
Total		91.37	0.00	91.98	0.00	94.55	0.00	92.96	0.00			

EMP analyses of pyrochlore (PCL-2) from Al-Ghurayyah.

	LOD	GHA1a_pcl_A1_01		GHA1a_pcl_A1_02		GHA1a_pcl_A5_01		GHA1a_pcl_A5_02	
		Type 2	±	Type 2	±	Type 2	±	Type 2	±
F	0.18	b.d.		b.d.		b.d.		b.d.	
SiO ₂	0.10	b.d.		b.d.		b.d.		0.53	0.88
Na ₂ O	0.03	7.49	1.50	7.46	1.49	6.46	1.29	2.83	0.57
La ₂ O ₃	0.16	1.60	1.23	1.23	0.95	1.32	1.02	0.87	0.67
Ce ₂ O ₃	0.14	4.25	0.78	3.14	0.57	3.75	0.68	2.74	0.50
Gd ₂ O ₃	0.08	b.d.		b.d.		b.d.		b.d.	
TiO ₂	0.04	4.54	0.08	3.81	0.06	4.23	0.07	3.98	0.07
CaO	0.02	5.37	0.06	4.81	0.06	7.86	0.09	8.06	0.09
ThO ₂	0.05	4.14	0.38	0.77	0.07	3.12	0.29	0.77	0.07
Nb ₂ O ₅	0.06	57.06	0.55	52.14	0.51	55.96	0.54	50.59	0.49
Y ₂ O ₃	0.06	1.63	0.11	1.33	0.09	1.97	0.13	4.86	0.32
Nd ₂ O ₃	0.05	0.75	0.10	0.56	0.07	0.61	0.08	0.49	0.06
Pr ₂ O ₃	0.10	0.33	1.09	b.d.		0.32	1.07	b.d.	
Eu ₂ O ₃	0.05	b.d.		b.d.		b.d.		b.d.	
Dy ₂ O ₃	0.05	0.48	0.05	0.35	0.03	0.58	0.05	0.96	0.09
Ho ₂ O ₃	0.11	b.d.		b.d.		b.d.		b.d.	
Lu ₂ O ₃	0.06	b.d.		b.d.		b.d.		b.d.	
UO ₂	0.04	0.40	0.01	4.87	0.16	2.34	0.08	6.53	0.21
Ta ₂ O ₅	0.08	4.74	0.16	3.51	0.12	4.21	0.14	4.23	0.14
MnO	0.03	b.d.		b.d.		b.d.		0.11	0.29
Sm ₂ O ₃	0.08	0.30	0.05	0.27	0.05	0.29	0.05	0.26	0.05
Tb ₂ O ₃	0.05	b.d.		b.d.		b.d.		b.d.	
FeO	0.03	0.12	0.01	0.16	0.01	0.41	0.02	2.92	0.17
Er ₂ O ₃	0.05	0.21	0.03	0.16	0.02	0.36	0.05	1.10	0.16
Tm ₂ O ₃	0.05	b.d.		b.d.		0.15	0.04	0.30	0.08
Yb ₂ O ₃	0.05	0.18	0.02	b.d.		0.30	0.03	1.19	0.13
PbO	0.04	2.66	0.15	4.33	0.25	2.87	0.17	2.55	0.15
SnO ₂	0.03	0.19	0.04	0.13	0.03	0.15	0.03	0.11	0.02
Total		96.43		89.01		97.25		96.00	

Continue PCL-2

	LOD	GHA1a_pcl_A5_03		GHA1a_pcl_A6_01		GHA1a_pcl_A6_02		GHA1A_COLB-pcl_01	
		Type 2	±	Type 2	±	Type 2	±	Type 2	±
F	0.18	b.d.		b.d.		b.d.		1.54	13.59
SiO2	0.10	b.d.		b.d.		b.d.		0.87	1.42
Na2O	0.03	3.93	0.79	7.17	1.44	5.13	1.03	2.08	0.42
La2O3	0.16	1.36	1.05	1.39	1.07	1.18	0.90	1.02	0.78
Ce2O3	0.14	3.81	0.70	3.90	0.71	3.50	0.64	2.72	0.50
Gd2O3	0.08	b.d.		b.d.		b.d.		b.d.	
TiO2	0.04	4.11	0.07	4.41	0.07	4.56	0.08	4.72	0.08
CaO	0.02	8.17	0.10	6.27	0.07	7.80	0.09	9.00	0.11
ThO2	0.05	1.04	0.09	4.57	0.42	1.75	0.16	0.75	0.07
Nb2O5	0.06	53.29	0.52	57.76	0.56	54.72	0.53	47.87	0.46
Y2O3	0.06	3.61	0.23	1.69	0.11	1.55	0.10	2.49	0.16
Nd2O3	0.05	0.77	0.10	0.67	0.09	0.63	0.08	0.50	0.07
Pr2O3	0.10	b.d.		b.d.		b.d.		b.d.	
Eu2O3	0.05	b.d.		b.d.		b.d.		b.d.	
Dy2O3	0.05	0.95	0.09	0.52	0.05	0.47	0.04	0.73	0.07
Ho2O3	0.11	b.d.		b.d.		b.d.		b.d.	
Lu2O3	0.06	b.d.		b.d.		b.d.		b.d.	
UO2	0.04	4.32	0.14	0.65	0.02	5.66	0.18	8.11	0.26
Ta2O5	0.08	4.10	0.14	4.08	0.14	4.37	0.15	4.33	0.15
MnO	0.03	0.13	0.34	b.d.		b.d.		0.32	0.82
Sm2O3	0.08	0.40	0.07	0.34	0.06	0.31	0.06	0.34	0.06
Tb2O3	0.05	b.d.		b.d.		b.d.		b.d.	
FeO	0.03	2.13	0.13	0.49	0.03	0.61	0.04	3.72	0.22
Er2O3	0.05	0.88	0.12	0.30	0.04	0.28	0.04	0.63	0.09
Tm2O3	0.05	0.25	0.06	b.d.		b.d.		0.18	0.05
Yb2O3	0.05	0.92	0.10	0.24	0.03	0.26	0.03	0.64	0.07
PbO	0.04	2.36	0.14	2.50	0.14	4.39	0.25	2.94	0.17
SnO2	0.03	0.13	0.03	0.18	0.04	0.18	0.04	b.d.	
Total		96.64		97.11		97.33		95.49	

Continue PCL-2

	LOD	GHA1b_pcl_01		GHA1b_pcl_02		GHA1b_pcl_A7_01		GHA1b_pcl_A7_02	
		Type 2	±	Type 2	±	Type 2	±	Type 2	±
F	0.18	b.d.		b.d.		b.d.		b.d.	
SiO2	0.10	b.d.		b.d.		b.d.		0.34	0.55
Na2O	0.03	5.14	1.03	3.77	0.75	5.15	1.03	3.62	0.72
La2O3	0.16	1.68	1.29	1.66	1.27	1.93	1.48	1.70	1.30
Ce2O3	0.14	4.54	0.83	4.14	0.76	4.67	0.85	3.99	0.73
Gd2O3	0.08	b.d.		b.d.		b.d.		b.d.	
TiO2	0.04	3.53	0.06	5.20	0.09	3.76	0.06	4.75	0.08
CaO	0.02	8.23	0.10	8.53	0.10	6.37	0.07	8.49	0.10
ThO2	0.05	0.33	0.03	0.41	0.04	0.38	0.03	0.41	0.04
Nb2O5	0.06	56.64	0.55	53.23	0.52	58.11	0.56	53.76	0.52
Y2O3	0.06	1.37	0.09	1.97	0.13	1.04	0.07	1.84	0.12
Nd2O3	0.05	0.95	0.13	1.01	0.13	1.08	0.14	0.99	0.13
Pr2O3	0.10	0.38	1.27	0.35	1.18	0.42	1.42	0.34	1.15
Eu2O3	0.05	b.d.		b.d.		b.d.		b.d.	
Dy2O3	0.05	0.39	0.04	0.50	0.05	0.29	0.03	0.60	0.06
Ho2O3	0.11	b.d.		b.d.		b.d.		b.d.	
Lu2O3	0.06	b.d.		b.d.		b.d.		b.d.	
UO2	0.04	4.31	0.14	4.78	0.16	4.26	0.14	4.90	0.16
Ta2O5	0.08	4.19	0.14	3.78	0.13	4.21	0.14	4.17	0.14
MnO	0.03	b.d.		b.d.		b.d.		b.d.	
Sm2O3	0.08	0.44	0.08	0.35	0.06	0.31	0.06	0.30	0.05
Tb2O3	0.05	b.d.		b.d.		b.d.		b.d.	
FeO	0.03	0.35	0.02	0.78	0.05	0.17	0.01	0.71	0.04
Er2O3	0.05	0.25	0.04	0.39	0.06	0.16	0.02	0.40	0.06
Tm2O3	0.05	b.d.		0.16	0.04	b.d.		b.d.	
Yb2O3	0.05	0.25	0.03	0.49	0.05	0.17	0.02	0.39	0.04
PbO	0.04	3.39	0.20	2.35	0.14	2.53	0.15	2.46	0.14
SnO2	0.03	0.12	0.02	0.19	0.04	0.16	0.03	0.16	0.03
Total		96.48		94.02		95.18		94.28	

Continue PCL-2

	LOD	GHA1b_pcl_A7_03		GHA1b_pcl_A8_01		GHA1b_pcl_A8_02		GHA1b_pcl_A8_03	
		Type 2	±	Type 2	±	Type 2	±	Type 2	±
F	0.18	b.d.		b.d.		b.d.		b.d.	
SiO2	0.10	b.d.		b.d.		b.d.		b.d.	
Na2O	0.03	4.62	0.92	5.19	1.04	4.95	0.99	4.92	0.99
La2O3	0.16	1.87	1.43	1.99	1.53	1.97	1.51	1.72	1.32
Ce2O3	0.14	4.52	0.82	4.61	0.84	4.66	0.85	4.36	0.80
Gd2O3	0.08	b.d.		b.d.		b.d.		b.d.	
TiO2	0.04	4.87	0.08	3.00	0.05	3.54	0.06	5.07	0.09
CaO	0.02	6.82	0.08	6.20	0.07	6.84	0.08	8.15	0.10
ThO2	0.05	0.89	0.08	0.66	0.06	0.80	0.07	0.65	0.06
Nb2O5	0.06	54.54	0.53	58.45	0.57	58.25	0.57	53.86	0.52
Y2O3	0.06	1.19	0.08	0.90	0.06	1.00	0.07	1.01	0.07
Nd2O3	0.05	1.02	0.13	1.08	0.14	1.16	0.15	1.08	0.14
Pr2O3	0.10	0.40	1.35	0.40	1.35	0.36	1.20	0.42	1.39
Eu2O3	0.05	b.d.		b.d.		b.d.		b.d.	
Dy2O3	0.05	0.39	0.04	0.28	0.03	0.28	0.03	0.33	0.03
Ho2O3	0.11	b.d.		b.d.		b.d.		b.d.	
Lu2O3	0.06	b.d.		b.d.		b.d.		b.d.	
UO2	0.04	3.93	0.13	3.34	0.11	3.12	0.10	4.63	0.15
Ta2O5	0.08	4.11	0.14	4.69	0.16	4.73	0.16	3.64	0.12
MnO	0.03	b.d.		b.d.		b.d.		b.d.	
Sm2O3	0.08	0.43	0.08	0.34	0.06	b.d.		0.32	0.06
Tb2O3	0.05	b.d.		b.d.		b.d.		b.d.	
FeO	0.03	0.22	0.01	0.20	0.01	0.25	0.01	0.39	0.02
Er2O3	0.05	0.19	0.03	0.15	0.02	0.21	0.03	0.16	0.02
Tm2O3	0.05	b.d.		b.d.		b.d.		b.d.	
Yb2O3	0.05	0.20	0.02	0.21	0.02	0.19	0.02	0.21	0.02
PbO	0.04	2.46	0.14	2.75	0.16	2.60	0.15	3.61	0.21
SnO2	0.03	0.16	0.03	0.14	0.03	0.17	0.03	0.17	0.03
Total		92.82		94.57		95.07		94.69	

Continue PCL-2

	LOD	GHA1b_pcl_A8_04		GHA1b_pcl_A9_01		GHA1b_pcl_A9_02		GHA1b_pcl_A9_03	
		Type 2	±	Type 2	±	Type 2	±	Type 2	±
F	0.18	b.d.		b.d.		b.d.		b.d.	
SiO2	0.10	b.d.		b.d.		b.d.		b.d.	
Na2O	0.03	4.98	1.00	6.26	1.25	4.50	0.90	5.45	1.09
La2O3	0.16	1.67	1.28	1.76	1.36	1.73	1.33	2.10	1.62
Ce2O3	0.14	4.90	0.89	4.31	0.79	4.73	0.86	4.91	0.90
Gd2O3	0.08	b.d.		b.d.		b.d.		b.d.	
TiO2	0.04	4.71	0.08	2.74	0.05	4.72	0.08	4.64	0.08
CaO	0.02	6.50	0.08	5.95	0.07	5.36	0.06	5.94	0.07
ThO2	0.05	1.31	0.12	0.64	0.06	0.83	0.08	1.33	0.12
Nb2O5	0.06	55.15	0.53	58.63	0.57	54.56	0.53	55.19	0.54
Y2O3	0.06	1.14	0.07	1.13	0.07	1.17	0.08	1.19	0.08
Nd2O3	0.05	1.05	0.14	0.99	0.13	1.03	0.14	1.04	0.14
Pr2O3	0.10	0.37	1.24	0.36	1.19	0.39	1.32	0.38	1.26
Eu2O3	0.05	b.d.		b.d.		b.d.		b.d.	
Dy2O3	0.05	0.41	0.04	0.38	0.04	0.42	0.04	0.39	0.04
Ho2O3	0.11	b.d.		b.d.		b.d.		b.d.	
Lu2O3	0.06	b.d.		b.d.		b.d.		b.d.	
UO2	0.04	2.87	0.09	3.49	0.11	3.52	0.11	2.58	0.08
Ta2O5	0.08	3.85	0.13	4.90	0.17	3.84	0.13	3.80	0.13
MnO	0.03	b.d.		b.d.		0.17	0.43	b.d.	
Sm2O3	0.08	0.39	0.07	0.32	0.06	0.35	0.06	0.44	0.08
Tb2O3	0.05	b.d.		b.d.		b.d.		b.d.	
FeO	0.03	0.52	0.03	b.d.		0.59	0.03	0.42	0.02
Er2O3	0.05	0.18	0.03	0.19	0.03	0.17	0.02	0.19	0.03
Tm2O3	0.05	b.d.		b.d.		b.d.		b.d.	
Yb2O3	0.05	0.17	0.02	0.16	0.02	0.16	0.02	0.16	0.02
PbO	0.04	4.90	0.28	3.75	0.22	8.37	0.48	5.95	0.34
SnO2	0.03	0.14	0.03	0.14	0.03	0.15	0.03	0.15	0.03
Total		95.17		96.08		96.75		96.22	

Continue PCL-2

	LOD	GHA1b_pcl1_01		GHA1b_pcl1_02		GHA1b_pcl_A15_04	
		Type 2	±	Type 2	±	Type 2	±
F	0.18	4.70	0.51	4.96	0.54	b.d.	
SiO2	0.10	b.d.		b.d.		1.63	4.90
Na2O	0.03	4.85	0.17	4.36	0.15	1.89	0.07
La2O3	0.16	1.67	0.29	1.82	0.32	b.d.	
Ce2O3	0.14	4.72	0.34	4.45	0.32	0.82	0.06
Gd2O3	0.08	0.28	0.04	b.d.		b.d.	
TiO2	0.04	4.81	0.08	2.86	0.05	3.57	0.06
CaO	0.02	5.38	0.07	5.13	0.07	8.66	0.12
ThO2	0.05	1.38	0.11	0.45	0.04	0.90	0.07
Nb2O5	0.06	55.89	0.70	59.42	0.74	52.01	0.65
Y2O3	0.06	1.18	0.11	1.05	0.10	8.82	0.85
Nd2O3	0.05	0.99	0.08	0.97	0.08	0.29	0.02
Pr2O3	0.10	0.39	0.11	0.33	0.10	b.d.	
Eu2O3	0.05	b.d.		b.d.		b.d.	
Dy2O3	0.05	0.36	0.07	0.37	0.07	1.21	0.22
Ho2O3	0.11	b.d.		b.d.		b.d.	
Lu2O3	0.06	b.d.		b.d.		b.d.	
UO2	0.04	3.04	0.09	4.37	0.13	5.39	0.16
Ta2O5	0.08	4.00	0.12	4.12	0.12	4.03	0.12
MnO	0.03	b.d.		b.d.		0.32	2.73
Sm2O3	0.08	0.33	0.07	0.37	0.08	0.31	0.07
Tb2O3	0.05	b.d.		b.d.		b.d.	
FeO	0.03	0.45	0.03	0.23	0.02	1.51	0.10
Er2O3	0.05	0.18	0.05	0.19	0.05	0.99	0.29
Tm2O3	0.05	b.d.		b.d.		0.23	0.11
Yb2O3	0.05	0.15	0.04	0.17	0.04	0.91	0.24
PbO	0.04	2.94	0.13	2.72	0.12	4.02	0.17
SnO2	0.03	0.18	0.03	0.29	0.05	0.19	0.04
Total		97.85		98.62		97.69	

EMP analyses of pyrochlore (PCL-3) from Al-Ghurayyah

LOD	GHA1C2_a11_01		GHA26_colb_03		GHA10_pcl_4_01	
	Type 3	±	Type 3	±	Type 3	±
0.18	1.25	0.14	0.78	0.08	b.d.	
0.03	0.10	0.00	0.10	0.00	0.10	0.00
0.16	b.d.		b.d.		b.d.	
0.14	b.d.		b.d.		b.d.	
0.08	0.61	0.10	0.50	0.08	0.37	0.06
0.04	1.88	0.03	1.22	0.02	5.77	0.10
0.02	1.25	0.02	1.69	0.02	1.55	0.02
0.05	0.58	0.05	2.36	0.19	0.66	0.05
0.06	44.34	0.55	40.15	0.50	44.11	0.55
0.06	29.41	2.84	25.98	2.51	11.63	1.12
0.05	b.d.		b.d.		b.d.	
0.10	b.d.		b.d.		b.d.	
0.05	b.d.		b.d.		b.d.	
0.05	3.16	0.57	2.97	0.54	1.92	0.35
0.11	0.92	1.45	0.80	1.27	0.40	0.64
0.06	0.23	0.84	0.35	1.31	b.d.	
0.04	2.06	0.06	4.97	0.15	3.19	0.10
0.08	0.97	0.03	1.16	0.03	4.36	0.13
0.03	0.50	4.24	0.70	6.02	1.39	11.89
0.08	0.33	0.07	0.30	0.06	0.29	0.06
0.05	0.28	0.26	0.27	0.25	0.19	0.17
0.03	1.17	0.08	0.77	0.05	5.78	0.38
0.05	3.22	0.94	2.96	0.86	1.53	0.45
0.05	0.55	0.25	0.51	0.23	0.33	0.15
0.05	3.28	0.85	3.35	0.86	1.57	0.41
0.04	0.56	0.02	0.38	0.02	7.98	0.35
0.03	0.12	0.02	b.d.		0.24	0.04
	96.99	0.00	92.54	0.00	94.13	0.00

LOD, limit of detection. b.d. at or below detection limit

EMPA of columbite from Al-Ghurayyah

Comment	LOD	GHA25_Nb_oxides_2		GHA25_Nb_oxides_2		GHA25_Nb_oxides_1		GHA25_Nb_oxides_1	
		COLB1	±	COLB1	±	COLB1	±	COLB1	±
SiO2	0.10	b.d.		b.d.		1.64	1.99	b.d.	
Na2O	0.03	b.d.		b.d.		b.d.		b.d.	
MgO	0.10	b.d.		b.d.		b.d.		b.d.	
La2O3	0.03	b.d.		b.d.		b.d.		b.d.	
Ce2O3	0.01	b.d.		0.05	0.26	b.d.		0.06	0.34
Gd2O3	0.16	b.d.		b.d.		b.d.		b.d.	
TiO2	0.14	5.43	0.14	4.84	0.13	3.75	0.10	3.77	0.10
CaO	0.08	b.d.		b.d.		0.67	0.20	b.d.	
ThO2	0.04	b.d.		b.d.		0.48	5.58	b.d.	
Nb2O5	0.02	63.92	0.99	66.02	1.02	57.06	0.89	65.74	1.02
Y2O3	0.06	0.58	0.08	0.21	0.03	4.26	0.62	0.19	0.03
Nd2O3	0.05	b.d.		b.d.		b.d.		b.d.	
Pr2O3	0.10	b.d.		b.d.		b.d.		b.d.	
Eu2O3	0.05	b.d.		b.d.		b.d.		b.d.	
Dy2O3	0.05	0.48	0.02	0.36	0.01	0.84	0.03	0.25	0.01
Ho2O3	0.11	b.d.		b.d.		b.d.		b.d.	
Lu2O3	0.06	b.d.		b.d.		b.d.		b.d.	
UO2	0.04	2.95	4.17	1.42	2.00	2.28	3.23	0.95	1.34
Ta2O5	0.08	5.13	0.31	5.39	0.32	6.15	0.37	6.73	0.40
MnO	0.03	6.27	0.29	6.84	0.31	3.82	0.18	4.50	0.21
Sm2O3	0.08	b.d.		b.d.		b.d.		b.d.	
Tb2O3	0.05	b.d.		b.d.		b.d.		b.d.	
FeO	0.03	12.29	0.33	12.65	0.34	11.31	0.30	15.13	0.40
Er2O3	0.05	0.20	0.04	b.d.		0.71	0.14	b.d.	
Tm2O3	0.05	b.d.		b.d.		0.21	0.06	b.d.	
Yb2O3	0.05	0.25	0.02	b.d.		0.66	0.05	b.d.	
PbO	0.04	0.75	0.11	0.45	0.06	1.97	0.28	0.54	0.08
SnO2	0.03	0.76	0.15	0.81	0.16	0.44	0.09	0.54	0.11
Total		99.633		99.60		97.02		99.08	

Continue columbite

GHA25_pcl2_03		GHA25_pcl2_04		GHA25_pcl1_05		GHA25_pcl1_06		GHA10_pcl_4_03	
COLB1	±	COLB1	±	COLB1	±	COLB4	±	COLB1	±
b.d.		b.d.		b.d.		b.d.		b.d.	
b.d.		b.d.		b.d.		b.d.		b.d.	
b.d.		b.d.		b.d.		b.d.		b.d.	
b.d.		b.d.		b.d.		b.d.		b.d.	
b.d.		0.10	0.55	b.d.		0.04	0.24	0.09	0.50
b.d.		b.d.		b.d.		b.d.		b.d.	
5.43	0.14	5.13	0.13	5.45	0.14	5.54	0.14	6.24	0.16
b.d.		b.d.		b.d.		b.d.		0.29	0.09
b.d.		b.d.		b.d.		b.d.		0.25	2.86
62.00	0.96	63.91	0.99	63.61	0.99	63.09	0.98	64.80	1.01
0.57	0.08	0.47	0.07	0.55	0.08	0.49	0.07	0.56	0.08
b.d.		b.d.		b.d.		b.d.		b.d.	
b.d.		b.d.		b.d.		b.d.		b.d.	
b.d.		b.d.		b.d.		b.d.		b.d.	
0.39	0.01	0.39	0.01	0.33	0.01	0.41	0.01	0.39	0.01
b.d.		b.d.		b.d.		b.d.		b.d.	
b.d.		b.d.		b.d.		b.d.		b.d.	
2.81	3.97	2.21	3.12	4.48	6.33	4.18	5.90	0.37	0.52
6.98	0.42	6.23	0.37	5.51	0.33	5.60	0.33	4.31	0.26
6.58	0.30	6.30	0.29	5.31	0.24	6.56	0.30	2.26	0.10
0.27	0.09	b.d.		b.d.		b.d.		b.d.	
b.d.		b.d.		b.d.		b.d.		b.d.	
12.01	0.32	12.66	0.34	12.79	0.34	11.83	0.32	15.58	0.42
0.19	0.04	b.d.		0.17	0.03	b.d.		0.29	0.06
0.15	0.04	0.15	0.04	b.d.		b.d.		b.d.	
0.23	0.02	0.19	0.02	0.26	0.02	0.25	0.02	0.41	0.03
0.56	0.08	0.69	0.10	0.70	0.10	0.82	0.12	0.61	0.09
0.78	0.16	0.77	0.15	0.49	0.10	0.71	0.14	0.36	0.07
99.36		100.24		100.35		100.42		97.72	

Continue columbite

GHA10_pcl_4_04		GHA7_pcl1_01		GHA7_pcl1_03		GHA1a_a3_02		GHA10_complex1&2_	
COLB1	±	COLB1	±	COLB1	±	COLB1	±	COLB2	±
b.d.		b.d.		0.32	0.38	3.21	3.90	b.d.	
b.d.		b.d.		b.d.		0.72	2.16	b.d.	
b.d.		b.d.		b.d.		b.d.		b.d.	
b.d.		b.d.		b.d.		b.d.		b.d.	
b.d.		b.d.		0.09	0.52	b.d.		b.d.	
b.d.		b.d.		b.d.		b.d.		b.d.	
7.02	0.18	2.67	0.07	3.77	0.10	4.88	0.13	5.02	0.13
0.36	0.11	0.27	0.08	0.45	0.13	b.d.		b.d.	
0.22	2.53	b.d.		0.18	2.03	b.d.		b.d.	
64.50	1.00	68.06	1.06	65.04	1.01	65.07	1.01	69.34	1.08
0.79	0.11	1.95	0.28	3.32	0.48	b.d.		1.09	0.16
b.d.		b.d.		b.d.		b.d.		b.d.	
b.d.		b.d.		b.d.		b.d.		b.d.	
b.d.		b.d.		b.d.		b.d.		b.d.	
0.47	0.02	0.58	0.02	0.68	0.02	0.16	0.01	0.49	0.02
b.d.		b.d.		b.d.		b.d.		b.d.	
b.d.		b.d.		b.d.		b.d.		b.d.	
0.23	0.32	0.89	1.25	1.04	1.47	b.d.		b.d.	
3.77	0.23	5.07	0.30	4.42	0.26	1.93	0.12	0.57	0.03
2.62	0.12	5.08	0.23	2.13	0.10	3.11	0.14	8.66	0.40
b.d.		b.d.		b.d.		b.d.		b.d.	
b.d.		b.d.		b.d.		b.d.		b.d.	
15.10	0.40	13.09	0.35	14.65	0.39	16.48	0.44	10.41	0.28
0.37	0.07	0.35	0.07	0.57	0.11	0.37	0.07	0.42	0.08
0.17	0.05	b.d.		b.d.		b.d.		b.d.	
0.64	0.05	0.43	0.04	0.55	0.05	0.52	0.04	1.15	0.09
0.60	0.08	0.35	0.05	0.96	0.14	0.23	0.03	0.27	0.04
0.52	0.10	0.23	0.05	0.34	0.07	0.74	0.15	0.31	0.06
98.37		99.95		99.51		98.32		98.40	

Continue columbite

GHA1C2_a11_02		GHA1C2_A11_02		GHA1C2_a11_03		GHA1C2_a11_04		GHA1C2_a14_01	
COLB2	±	COLB2	±	COLB2	±	COLB2	±	COLB2	±
b.d.		b.d.		b.d.		b.d.		0.54	0.65
b.d.		b.d.		b.d.		b.d.		b.d.	
b.d.		b.d.		b.d.		b.d.		b.d.	
b.d.		b.d.		b.d.		b.d.		0.10	0.54
0.07	0.41	b.d.		0.06	0.34	b.d.		0.08	0.42
b.d.		b.d.		b.d.		b.d.		b.d.	
2.12	0.05	2.98	0.08	2.64	0.07	3.94	0.10	8.62	0.22
b.d.		b.d.		b.d.		b.d.		0.85	0.25
b.d.		b.d.		b.d.		b.d.		1.11	12.84
72.15	1.12	69.81	1.08	70.77	1.10	66.99	1.04	58.13	0.90
b.d.		b.d.		0.18	0.03	0.75	0.11	4.29	0.62
b.d.		b.d.		b.d.		b.d.		b.d.	
b.d.		b.d.		b.d.		b.d.		b.d.	
b.d.		b.d.		b.d.		b.d.		b.d.	
0.34	0.01	b.d.		0.38	0.01	0.42	0.01	1.05	0.03
b.d.		b.d.		b.d.		b.d.		b.d.	
b.d.		b.d.		b.d.		b.d.		b.d.	
0.13	0.18	0.22	0.31	0.14	0.20	0.21	0.30	1.03	1.46
4.56	0.27	4.68	0.28	4.80	0.29	4.48	0.27	3.90	0.23
8.16	0.37	8.33	0.38	8.30	0.38	7.66	0.35	3.18	0.15
b.d.		b.d.		b.d.		b.d.		b.d.	
b.d.		b.d.		b.d.		b.d.		b.d.	
12.15	0.33	12.20	0.33	12.15	0.33	12.83	0.34	12.05	0.32
b.d.		b.d.		b.d.		0.18	0.04	0.79	0.15
b.d.		b.d.		b.d.		b.d.		0.20	0.06
0.18	0.01	0.26	0.02	0.21	0.02	0.27	0.02	0.77	0.06
0.29	0.04	0.29	0.04	0.26	0.04	0.36	0.05	0.38	0.05
1.30	0.26	0.74	0.15	1.07	0.21	0.80	0.16	0.92	0.18
102.12		100.33		101.57		99.65		99.05	

Continue columbite

GHA26_colb_01		GHA26_colb_02		GHA4B_C8-02		GHA4B_C8-03		GHA4B_C8-04	
COLB2	±	COLB2	±	COLB2	±	COLB2	±	COLB2	±
b.d.		b.d.		b.d.		b.d.		b.d.	
b.d.		b.d.		b.d.		b.d.		b.d.	
b.d.		b.d.		b.d.		b.d.		b.d.	
b.d.		b.d.		b.d.		b.d.		b.d.	
b.d.		0.05	0.30	b.d.		b.d.		b.d.	
b.d.		b.d.		b.d.		b.d.		b.d.	
2.26	0.06	3.40	0.09	0.82	0.02	1.14	0.03	0.95	0.02
b.d.		b.d.		b.d.		b.d.		b.d.	
b.d.		b.d.		b.d.		b.d.		b.d.	
72.05	1.12	69.14	1.07	75.53	1.17	75.19	1.17	74.35	1.15
0.36	0.05	1.08	0.16	b.d.		b.d.		b.d.	
b.d.		b.d.		b.d.		b.d.		b.d.	
b.d.		b.d.		b.d.		b.d.		b.d.	
b.d.		b.d.		b.d.		b.d.		b.d.	
0.50	0.02	0.56	0.02	b.d.		b.d.		b.d.	
b.d.		b.d.		b.d.		b.d.		b.d.	
b.d.		b.d.		b.d.		b.d.		b.d.	
0.15	0.21	0.28	0.39	b.d.		b.d.		b.d.	
3.59	0.21	3.07	0.18	2.13	0.13	2.51	0.15	2.91	0.17
11.52	0.53	9.34	0.43	10.15	0.47	9.20	0.42	9.51	0.44
b.d.		b.d.		b.d.		b.d.		b.d.	
b.d.		b.d.		b.d.		b.d.		b.d.	
8.68	0.23	9.47	0.25	10.81	0.29	11.81	0.32	11.18	0.30
0.18	0.04	0.32	0.06	b.d.		b.d.		b.d.	
b.d.		b.d.		b.d.		b.d.		b.d.	
0.42	0.03	0.64	0.05	b.d.		b.d.		b.d.	
0.30	0.04	0.84	0.12	b.d.		b.d.		b.d.	
0.26	0.05	0.36	0.07	0.12	0.02	0.13	0.03	0.12	0.02
100.88		99.27		99.77		100.30		99.31	

Continue columbite

GHA3E_COLB-pcl_13		GHA3E_COLB-pcl_14		GHA3E_COLB-pcl_15		GHA1C2_01		GHA3B_C12-01	
COLB3	±	COLB3	±	COLB3	±	COLB3	±	COLB3	±
b.d.		b.d.		b.d.		b.d.		b.d.	
b.d.		b.d.		b.d.		b.d.		b.d.	
b.d.		b.d.		b.d.		b.d.		b.d.	
b.d.		b.d.		0.10	0.54	b.d.		b.d.	
0.07	0.36	b.d.		b.d.		0.05	0.28	b.d.	
b.d.		b.d.		b.d.		b.d.		b.d.	
2.99	0.08	3.61	0.09	3.10	0.08	4.14	0.11	b.d.	
b.d.		b.d.		b.d.		b.d.		b.d.	
b.d.		b.d.		0.13	1.54	b.d.		b.d.	
71.66	1.11	65.82	1.02	65.52	1.02	68.88	1.07	76.49	1.19
0.22	0.03	0.26	0.04	0.66	0.10	b.d.		b.d.	
b.d.		b.d.		b.d.		b.d.		b.d.	
b.d.		b.d.		b.d.		b.d.		b.d.	
b.d.		b.d.		b.d.		b.d.		b.d.	
b.d.		b.d.		0.23	0.01	b.d.		b.d.	
b.d.		b.d.		b.d.		b.d.		b.d.	
b.d.		b.d.		b.d.		b.d.		b.d.	
b.d.		0.70	0.98	0.59	0.83	0.28	0.39	b.d.	
3.16	0.19	6.86	0.41	6.19	0.37	4.35	0.26	3.04	0.18
10.10	0.46	5.21	0.24	8.24	0.38	6.21	0.29	11.33	0.52
b.d.		b.d.		b.d.		b.d.		b.d.	
b.d.		b.d.		b.d.		b.d.		b.d.	
10.79	0.29	15.10	0.40	11.86	0.32	13.73	0.37	9.40	0.25
b.d.		b.d.		0.20	0.04	0.22	0.04	b.d.	
b.d.		b.d.		b.d.		b.d.		b.d.	
0.30	0.02	b.d.		0.29	0.02	0.36	0.03	b.d.	
0.23	0.03	0.28	0.04	0.32	0.05	0.28	0.04	b.d.	
b.d.		b.d.		b.d.		0.94	0.19	b.d.	
100.14		98.62		97.96		100.26		100.85	

Continue columbite

GHA3B_C12-02		GHA3B_C12-03		GHA3B_C07-02		GHA3B_C07-04		GHA3B_C13-01	
COLB3	±	COLB3	±	COLB3	±	COLB3	±	COLB3	±
b.d.		b.d.		b.d.		b.d.		b.d.	
b.d.		b.d.		b.d.		b.d.		b.d.	
b.d.		b.d.		b.d.		b.d.		b.d.	
b.d.		b.d.		b.d.		b.d.		b.d.	
b.d.		b.d.		b.d.		b.d.		b.d.	
b.d.		b.d.		b.d.		b.d.		b.d.	
0.45	0.01	0.48	0.01	1.60	0.04	1.19	0.03	4.18	0.11
b.d.		b.d.		b.d.		b.d.		b.d.	
b.d.		b.d.		b.d.		b.d.		b.d.	
76.31	1.18	76.00	1.18	75.45	1.17	75.81	1.18	65.85	1.02
b.d.		b.d.		0.19	0.03	0.33	0.05	0.43	0.06
b.d.		b.d.		b.d.		b.d.		b.d.	
b.d.		b.d.		b.d.		b.d.		b.d.	
b.d.		b.d.		b.d.		b.d.		b.d.	
b.d.		b.d.		b.d.		b.d.		b.d.	
b.d.		b.d.		b.d.		b.d.		b.d.	
b.d.		b.d.		b.d.		b.d.		b.d.	
b.d.		b.d.		b.d.		b.d.		1.11	1.56
2.98	0.18	2.88	0.17	1.88	0.11	1.60	0.10	6.13	0.37
11.39	0.52	11.31	0.52	8.87	0.41	8.97	0.41	10.87	0.50
b.d.		b.d.		b.d.		b.d.		b.d.	
b.d.		b.d.		b.d.		b.d.		b.d.	
9.55	0.26	9.55	0.26	12.02	0.32	11.72	0.31	8.24	0.22
b.d.		b.d.		b.d.		b.d.		b.d.	
b.d.		b.d.		b.d.		b.d.		b.d.	
b.d.		b.d.		b.d.		b.d.		b.d.	
b.d.		b.d.		b.d.		b.d.		b.d.	
b.d.		b.d.		0.15	0.03	0.09	0.02	0.57	0.11
100.93		100.42		100.39		99.92		98.18	

Continue columbite

GHA3B_C13-02		GHA3B_C13-03		GHA6_colb1_01		GHA6_colb1_02		GHA6_colb1_03	
COLB3	±	COLB3	±	COLB3	±	COLB3	±	COLB3	±
b.d.		b.d.		b.d.		b.d.		b.d.	
b.d.		b.d.		b.d.		b.d.		b.d.	
b.d.		b.d.		b.d.		b.d.		b.d.	
b.d.		b.d.		b.d.		b.d.		b.d.	
b.d.		b.d.		b.d.		0.06	0.35	0.07	0.37
b.d.		b.d.		b.d.		b.d.		b.d.	
1.54	0.04	1.91	0.05	0.53	0.01	2.49	0.06	2.40	0.06
b.d.		b.d.		b.d.		b.d.		b.d.	
b.d.		b.d.		b.d.		b.d.		b.d.	
74.70	1.16	74.96	1.16	74.87	1.16	73.61	1.14	67.19	1.04
0.50	0.07	0.18	0.03	0.19	0.03	b.d.		b.d.	
b.d.		b.d.		b.d.		b.d.		b.d.	
b.d.		b.d.		b.d.		b.d.		b.d.	
b.d.		b.d.		b.d.		b.d.		b.d.	
b.d.		b.d.		0.40	0.01	0.37	0.01	0.36	0.01
b.d.		b.d.		b.d.		b.d.		b.d.	
b.d.		b.d.		b.d.		b.d.		b.d.	
b.d.		b.d.		b.d.		b.d.		b.d.	
1.85	0.11	1.96	0.12	3.00	0.18	1.56	0.09	7.18	0.43
9.25	0.43	8.91	0.41	10.42	0.48	11.24	0.52	10.34	0.48
b.d.		b.d.		b.d.		b.d.		b.d.	
b.d.		b.d.		b.d.		b.d.		b.d.	
11.08	0.30	11.95	0.32	10.37	0.28	9.72	0.26	9.89	0.26
b.d.		b.d.		b.d.		b.d.		b.d.	
b.d.		b.d.		b.d.		b.d.		b.d.	
b.d.		b.d.		0.28	0.02	0.46	0.04	0.23	0.02
b.d.		b.d.		0.32	0.04	0.32	0.05	0.29	0.04
0.21	0.04	0.15	0.03	b.d.		0.28	0.06	0.45	0.09
99.39		100.21		100.99		100.72		99.20	

Continue columbite

GHA6_colb2_01		GHA6_colb2_02		GHA6_colb3_01		GHA6_colb3_02	
COLB3	±	COLB3	±	COLB3	±	COLB3	±
b.d.		b.d.		b.d.		b.d.	0.00
b.d.		b.d.		b.d.		b.d.	0.00
b.d.		b.d.		b.d.		b.d.	0.00
b.d.		b.d.		b.d.		b.d.	0.00
b.d.		b.d.		b.d.		b.d.	0.00
b.d.		b.d.		b.d.		b.d.	0.04
1.12	0.03	1.83	0.05	1.16	0.03	0.96	0.02
b.d.		b.d.		b.d.		b.d.	0.00
b.d.		b.d.		b.d.		b.d.	0.00
76.08	1.18	74.62	1.16	75.45	1.17	72.54	1.13
0.19	0.03	0.68	0.10	0.36	0.05	b.d.	0.02
b.d.		b.d.		b.d.		b.d.	0.16
b.d.		b.d.		b.d.		b.d.	0.00
b.d.		b.d.		b.d.		b.d.	0.14
0.35	0.01	0.40	0.01	0.34	0.01	0.33	0.01
b.d.		b.d.		b.d.		b.d.	0.00
b.d.		b.d.		b.d.		b.d.	0.00
b.d.		b.d.		b.d.		b.d.	0.02
1.54	0.09	1.45	0.09	1.42	0.08	5.42	0.32
9.83	0.45	10.06	0.46	7.53	0.35	7.07	0.33
b.d.		b.d.		b.d.		b.d.	0.05
b.d.		b.d.		b.d.		b.d.	0.04
11.10	0.30	10.35	0.28	13.01	0.35	13.36	0.36
b.d.		0.22	0.04	0.19	0.04	b.d.	0.01
b.d.		b.d.		b.d.		b.d.	0.02
0.17	0.01	0.53	0.04	0.35	0.03	b.d.	0.01
0.28	0.04	0.28	0.04	0.34	0.05	0.29	0.04
0.09	0.02	0.26	0.05	0.10	0.02	0.08	0.02
101.31		101.12		100.58		100.95	

LOD, limit of detection. b.d., at or below detection limit

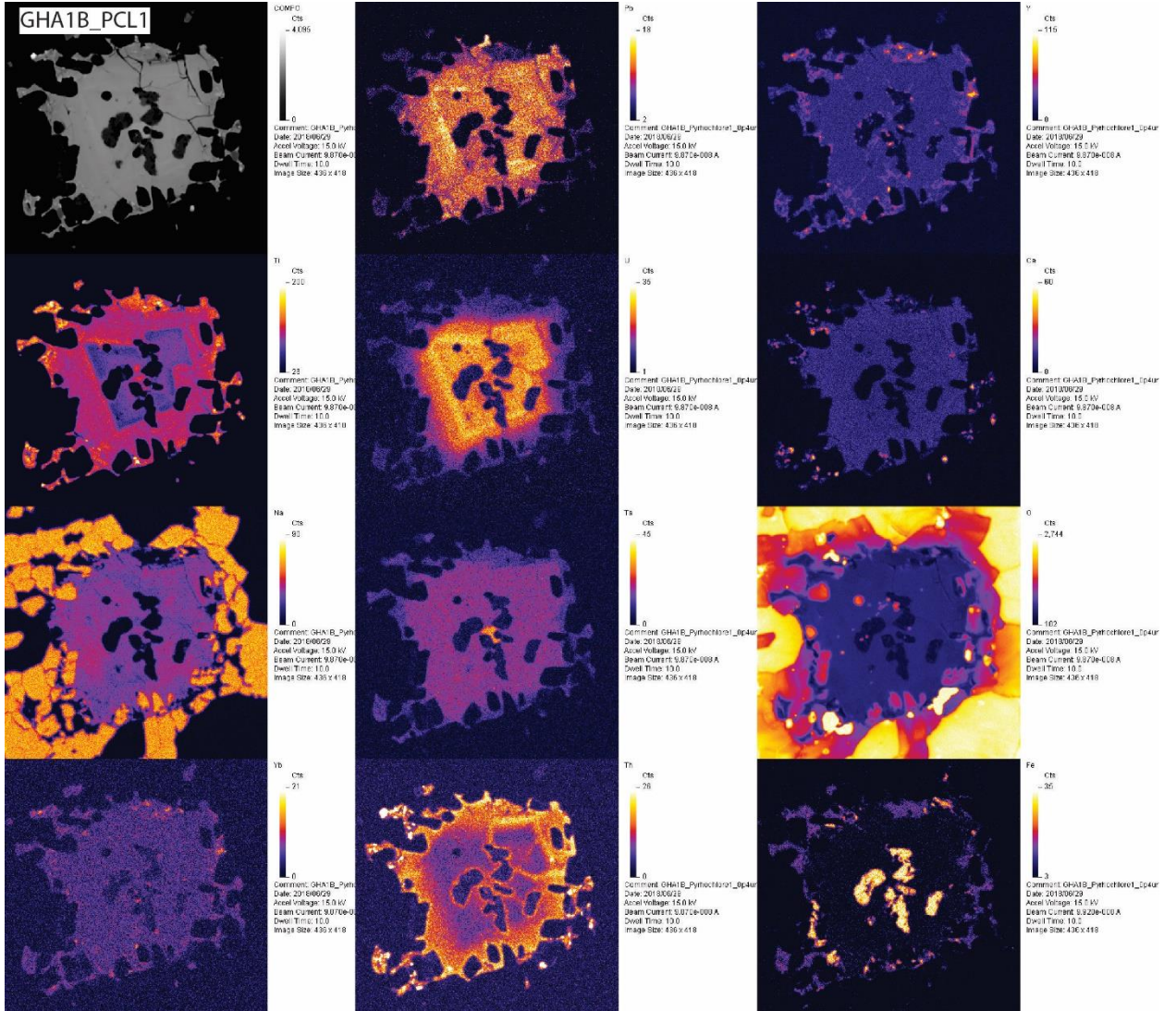
EMP analyses of mica minerals

Comment	Type	Na2O	SiO2	MgO	F	Al2O3	TiO2	CaO	Cl	K2O	ZnO	FeO	MnO	SrO	Total	Li*
GHA1c2_F7_02	Li.mica	0.02	59.82	0.01	8.53	12.29	0.67	0.02	0.00	11.01	0.26	1.93	0.04	0.00	94.59	7.35
GHA1c2_F7_03	Li.mica	0.02	60.26	0.00	8.64	13.74	0.11	0.00	0.00	11.41	0.33	1.76	0.11	0.00	96.42	7.36
GHA1c2_F7_04	Li.mica	0.07	53.22	0.01	6.56	19.02	0.01	0.03	0.00	10.61	1.10	6.96	0.50	0.00	98.08	7.35
GHA1c2_F7_05	Li.mica		57.64	0.00	8.06	12.15	0.50	0.02	0.00	10.71	0.83	3.72	0.02	0.00	93.64	7.35
GHA1c2_P17_01	Li.mica	0.04	61.54	0.03	7.77	12.84	0.41	0.01	0.01	10.78	0.28	2.15	0.01	0.00	95.88	7.34
GHA1c2_P17_02	Li.mica		58.93	0.01	8.00	13.24	0.61	0.01	0.01	10.97	0.38	3.01	0.04	0.00	95.20	7.35
GHA1c2_P17_03	Li.mica		54.68	0.05	6.59	19.69	0.02	0.01	0.00	10.59	0.64	4.95	0.07	0.00	97.28	7.33
GHA1c2_P17_04	Li.mica	0.03	49.61	0.08	6.97	20.25	-0.01	0.05	0.01	10.34	1.29	10.05	0.02	0.00	98.72	7.31
GHA1A_MS_01	Li.mica		58.37	3.36	9.06	11.46	0.12	0.01	0.00	10.81	0.98	2.77	0.02	0.00	96.95	5.77
GHA1A_MS_02	Li.mica		58.82	0.69	8.96	13.29	0.64	0.01	0.00	11.04	0.50	2.73	0.02	0.00	96.71	6.97
GHA1A_MS_03	Li.mica	0.01	56.77	0.62	8.03	12.22	2.55	0.06	0.00	10.78	0.43	4.74	0.11	0.00	96.31	7.00
GHA1A_MS_04	Li.mica		59.96	0.66	9.04	13.94	0.04	0.05	0.00	11.50	0.36	1.22	0.01	0.00	96.76	6.98
GHA1C2MS_01	Li.mica		60.00	0.00	8.11	13.42	0.20	0.00	0.00	10.93	0.32	2.34	0.03	0.00	95.34	7.36
GHA1C2MS_02	Li.mica		56.57	0.08	7.86	15.88	0.03	0.02	0.00	10.52	0.76	4.88	0.03	0.00	96.64	7.31
GHA1C2MS_03	Li.mica		50.08	0.09	6.76	19.12	0.12	0.02	0.00	10.66	1.26	9.07	0.07	0.00	97.25	7.30
GHA4b_mica_2	Muscovite	0.08	47.4	0.05	0.9	34.36	0.04	0.1	0	10.5	0.1	3.06	0.02		96	
GHA4b_mica_3	Muscovite	0.12	47.9	0.05	1	32.51	0.07	0.1	0	10.8	0.1	4.61	0.05		95.7	
GHA4b_mica_4	Muscovite	0.11	47.5	0.06	0.8	32.7	0.08	0	0	10.6	0.1	4.41	0.04		95.2	
GHA4b_mica_5	Muscovite	0.09	48.8	0.02	1.4	32.09	0.09	0.1	0	10.5	0.1	4.74	0.07		96.6	
GHA3E_mica_1	Fe-mica	0.02	43.8	1.16	2	9.595	3.74	0.1	0.01	9.13	0.1	26.1	0.16		93.9	
GHA3E_mica_2	Fe-mica	0.06	47.9	0.84	2.1	23.71	0.73	0.1	0.01	9.69	0.1	12	0.09		95.7	
GHA3E_mica_3	Fe-mica	0.07	43.8	1.35	2.6	8.407	3.82	0.1	0	9.27	0.1	27.5	0.18		96.3	
GHA3E_mica_4	Fe-mica	0.04	43	0.88	2.1	9.928	2.67	0	0	9.2	0.1	28.4	0.2		95.4	

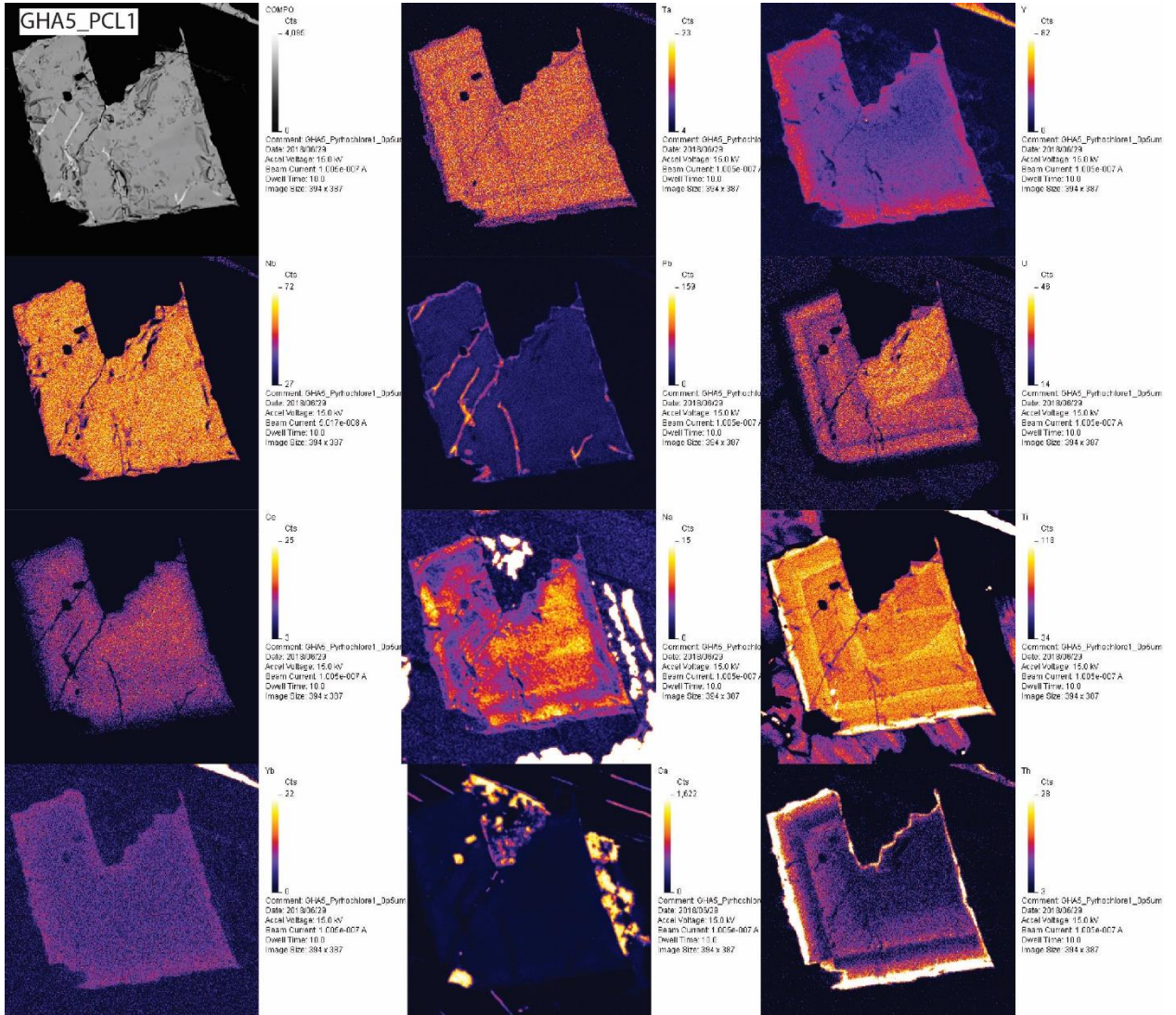
*calculated. Li-mica is trillithionite. Fe-mica is siderophyllite.

WDS-Xray maps of pyrochlore

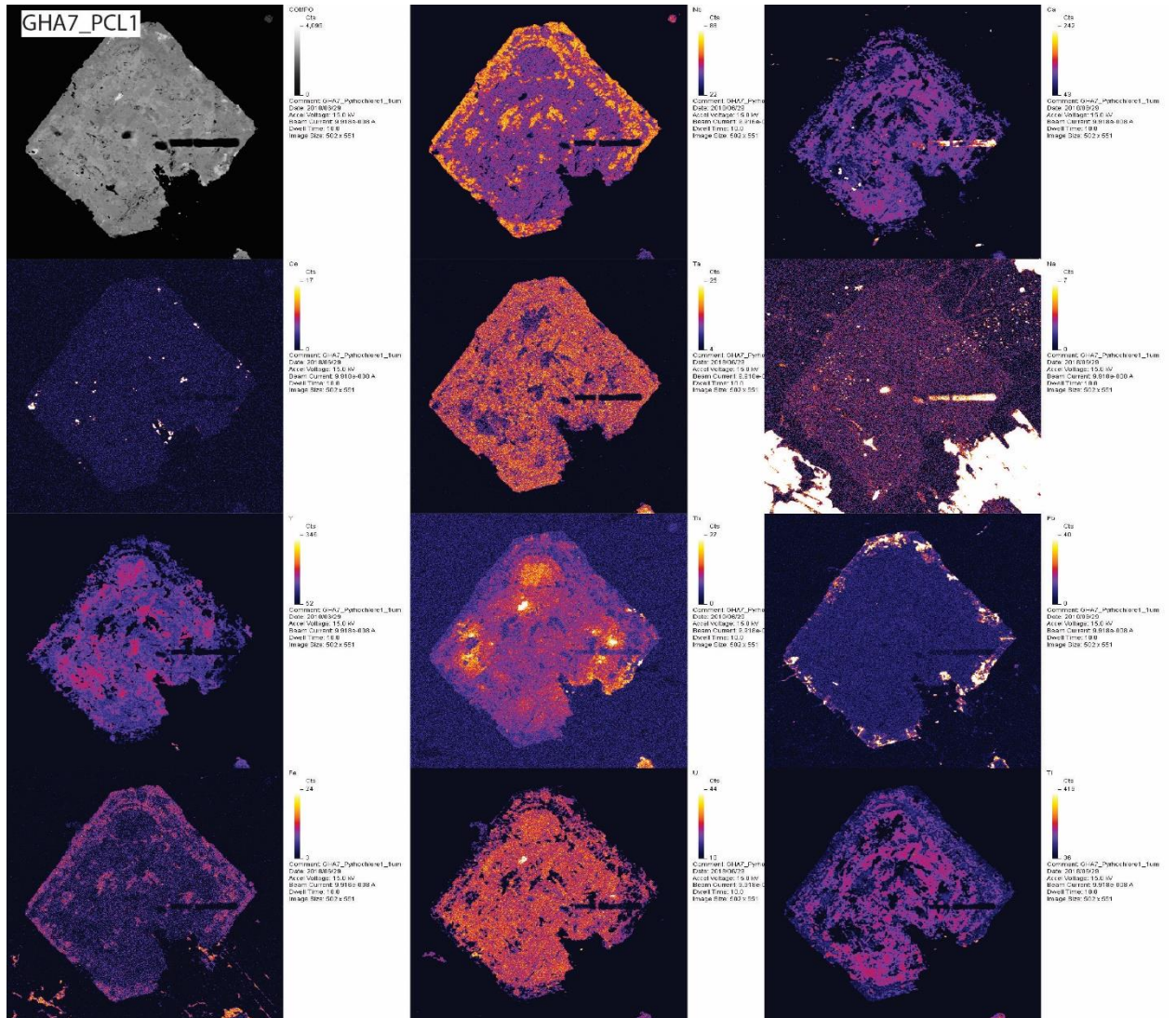
PCL-2



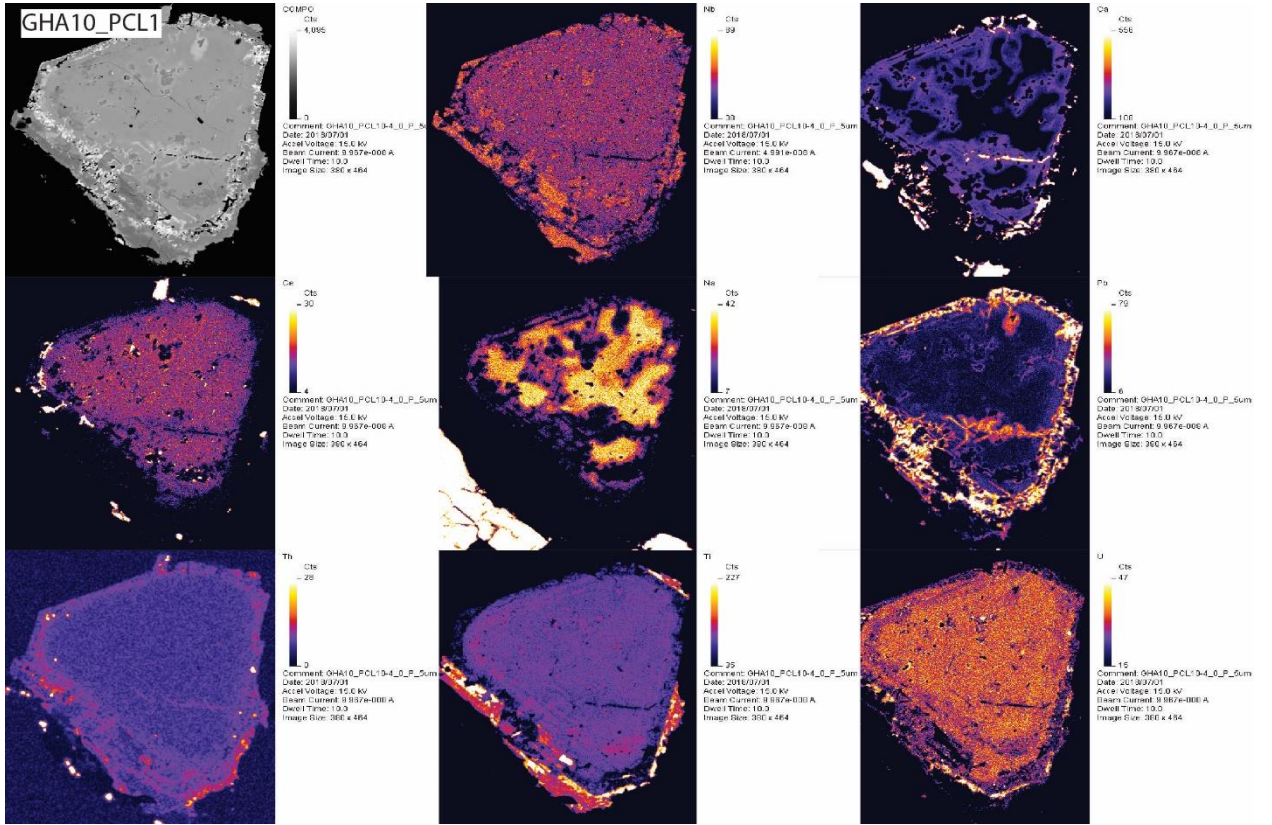
PCL-1



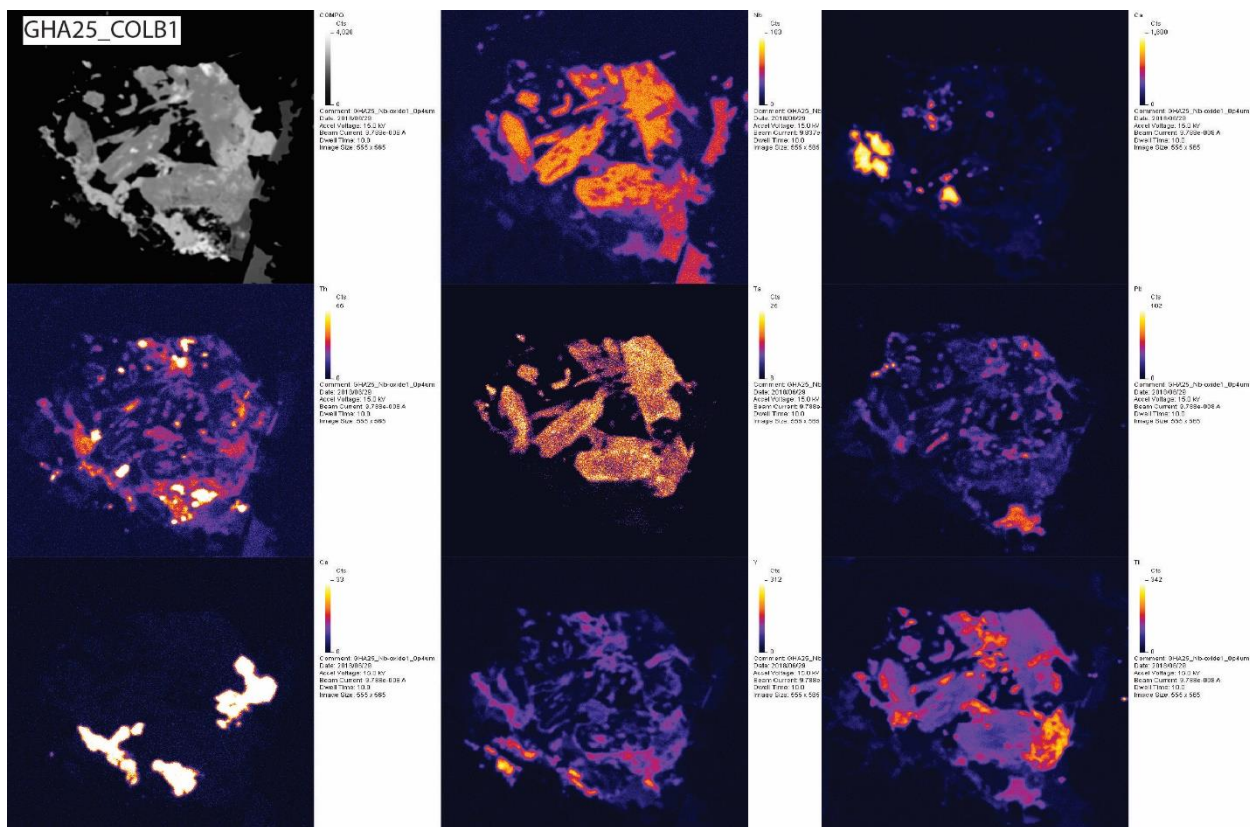
PCL-1



PCL-1



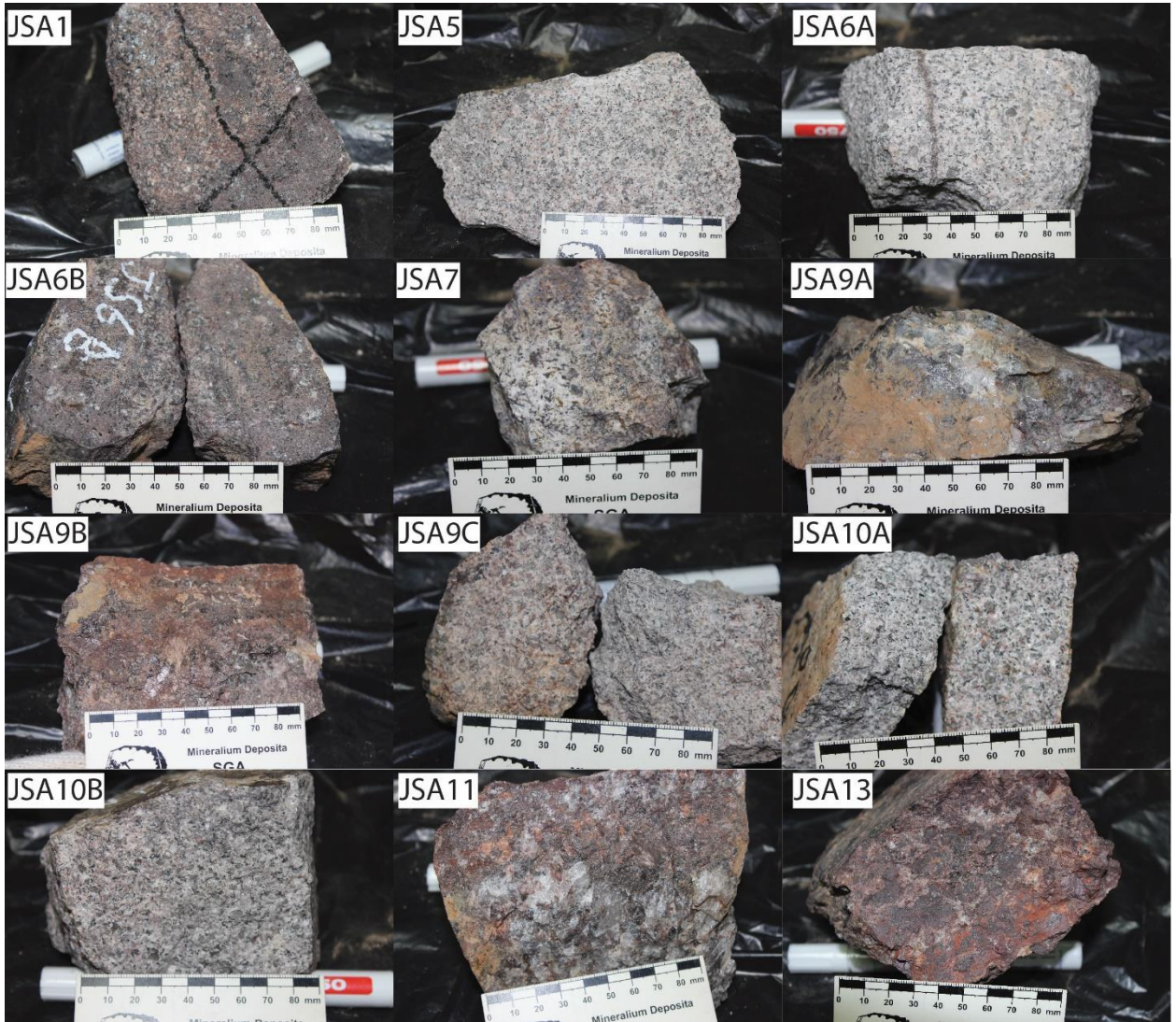
WDS-Xray maps of Columbite (COLB-1).



List of Jabal Said Samples

Appendix C: List of Jabal Sayid samples, whole-rock analyses, and mineral chemistry

	Description	EEMPA							
		Whole-rock	Zircon	Pyrochlore	Bastnasite	Monazite	Synchysite	Xenotime	Aegirine
JSA1	highly red-brown hematized granite. Original mineralogy cannot be distinguished	√	√	√	√	√		√	
JSA5	Highly silicified granite.		√						
JSA6A	Aegirine granite at contact with a pegmatite dyke	√			√				
JSA6B	Pegmatite dyke (10 cm) with well-developed core.	√	√						√
JSA7	Highly weathered granite aegirine granite	√	√						
JSA9A	Quartz and alkali feldspar rich core from the pegmatite sheets		√						
JSA9B	Fine-grained boarder zone of a pegmatite sheets		√						
JSA9C	Coarse-grained aegirine granite in contact with pegmatite		√						
JSA10A	Porphyritic aegirine granite that shows slight alteration	√							√
JSA10B	Porphyritic aegirine granite that shows high alteration	√			√				
JSA11	Pegmatite with well-developed		√	√	√	√	√	√	
JSA13	Highly hematized granite		√						



Oxide and elements detection limit using fusion ICP and ICP-MS in ppm, except where noted

Oxide/Element	LOD*	Oxide/Element	LOD	Oxide/Element	LOD	Oxide/Element	LOD
Al ₂ O ₃	0.01%	Ba	3	Pb	2	Zr	4
CaO	0.01%	Be	1	Rb	2	La	0.1
Fe ₂ O ₃	0.01%	Bi	0.4	Sb	0.5	Ce	0.1
K ₂ O	0.01%	Co	1	Sc	1	Pr	0.05
MgO	0.01%	Cr	20	Sn	1	Nd	0.1
MnO	0.00%	Cs	0.5	Sr	2	Sm	0.1
Na ₂ O	0.01%	Cu	10	Ta	0.1	Eu	0.05
P ₂ O ₅	0.01%	Ga	1	Th	0.1	Gd	0.1
SiO ₂	0.01%	Ge	1	Tl	0.1	Tb	0.1
TiO ₂	0.00%	Hf	0.2	U	0.1	Dy	0.1
LOI	0.01%	In	0.2	V	5	Ho	0.1
F ¹		Mo	2	W	1	Er	0.1
Ag	0.5	Nb	1	Y	2	Tm	0.05
As	5	Ni	20	Zn	30	Yb	0.1
*Limit of detection. 1 analyzed using fusion ISE							

EMP analyses of aegirine from Jabal Sayid. \pm is 3 σ standard deviations. LOD is limit of detection in oxide percent

Comment	Type	Na ₂ O		MgO		F		Al ₂ O ₃		SiO ₂		ZrO ₂		FeO		MnO		ZnO	
LOD		0.03	\pm	0.02	\pm	0.23	\pm	0.03	\pm	0.06	\pm	0.03	\pm	0.03	\pm	0.01	\pm	0.02	\pm
JSA9_1	Prs.aeg	12.14	0.02	0.01	0.00	0.26	0.00	0.40	0.00	51.14	0.03	0.10	0.01	32.71	0.04	0.05	0.00	0.06	0.02
JSA9_2	Prs.aeg	11.76	0.02	0.00	0.00	0.12	0.00	0.42	0.00	50.47	0.03	0.10	0.01	32.42	0.04	0.02	0.00	0.04	0.01
JSA9_3	Prs.aeg	12.11	0.02	0.01	0.00	0.24	0.00	0.38	0.00	50.92	0.03	0.10	0.01	32.73	0.04	0.04	0.00	0.01	0.00
JSA9_4	Prs.aeg	10.93	0.02	0.01	0.00	0.12	0.00	0.39	0.00	52.05	0.03	0.08	0.00	30.50	0.04	0.05	0.00	0.05	0.02
JSA9_5	Prs.aeg	12.46	0.02	0.01	0.01	0.24	0.00	0.30	0.00	50.66	0.03	0.07	0.00	30.13	0.04	0.51	0.05	0.28	0.09
JSA9_6	Prs.aeg	12.50	0.02	0.00	0.00	0.24	0.00	0.34	0.00	51.24	0.03	0.26	0.02	31.68	0.04	0.06	0.01	0.05	0.02
JSA10A-1	Prs.aeg	12.76	0.02	0.00	0.00	0.12	0.00	0.29	0.00	49.97	0.02	0.18	0.01	33.26	0.04	0.07	0.01	0.06	0.02
JSA10A-2	Prs.aeg	12.75	0.02	0.01	0.01	0.12	0.00	0.66	0.00	49.60	0.02	0.21	0.01	32.75	0.04	0.08	0.01	0.04	0.01
JSA10A-3	Prs.aeg	12.75	0.02	0.01	0.01	0.09	0.00	0.19	0.00	49.32	0.02	0.07	0.00	33.48	0.05	0.12	0.01	0.06	0.02
JSA10A-2_1	Prs.aeg	12.03	0.02	0.01	0.00	0.12	0.00	0.38	0.00	49.75	0.02	0.05	0.00	33.71	0.05	0.06	0.01	0.02	0.01
JSA10A-2_2	Prs.aeg	12.21	0.02	0.01	0.00	0.12	0.00	0.38	0.00	49.21	0.02	0.12	0.01	33.57	0.05	0.05	0.00	0.03	0.01
JSA10A-2_3	Prs.aeg	12.60	0.02	0.00	0.00	0.12	0.00	0.40	0.00	49.98	0.02	0.26	0.01	33.32	0.04	0.07	0.01	0.03	0.01
JSA6B-1	acic.aeg	12.86	0.02	0.01	0.00	0.03	0.00	0.31	0.00	49.80	0.02	1.21	0.07	29.99	0.04	0.22	0.02	0.11	0.03
JSA6A-2	acic.aeg	12.25	0.02	0.01	0.01	0.11	0.00	0.22	0.00	48.86	0.02	1.10	0.06	29.72	0.04	0.30	0.03	0.13	0.04
JSA6A-3	acic.aeg	12.24	0.02	0.01	0.01	0.12	0.00	0.52	0.00	50.02	0.03	0.47	0.03	28.94	0.04	0.21	0.02	0.10	0.03
JSA6A-4	acic.aeg	11.48	0.02	0.00	0.00	0.12	0.00	0.23	0.00	52.01	0.03	1.06	0.06	28.45	0.04	0.23	0.02	0.10	0.03
Comment	Type	CaO		TiO ₂															
LOD		0.02	\pm	0.02															
JSA9_1	Prs.aeg	1.00	0.00	0.43															
JSA9_2	Prs.aeg	1.07	0.00	0.35															
JSA9_3	Prs.aeg	1.03	0.00	0.33															
JSA9_4	Prs.aeg	1.03	0.00	0.29															
JSA9_5	Prs.aeg	0.19	0.00	1.34															
JSA9_6	Prs.aeg	0.12	0.00	0.70															
JSA10A-1	Prs.aeg	0.14	0.00	1.01															
JSA10A-2	Prs.aeg	0.16	0.00	0.84															
JSA10A-3	Prs.aeg	0.09	0.00	0.94															
JSA10A-2_1	Prs.aeg	1.40	0.01	0.33															
JSA10A-2_2	Prs.aeg	1.19	0.01	0.51															
JSA10A-2_3	Prs.aeg	1.31	0.01	0.48															
JSA6B-1	acic.aeg	0.23	0.00	2.47															
JSA6A-2	acic.aeg	0.29	0.00	2.38															
JSA6A-3	acic.aeg	0.18	0.00	2.96															
JSA6A-4	acic.aeg	0.27	0.00	2.27															

Prs.aeg, Prismatic aegirine; acic.aeg, Acicular aegirine

EMP analyses of zircon from Jabal Sayid. \pm is 3σ standard deviations. LOD is limit of detection in oxide percent. b.d., at or below detection limit.

Type		Zircon-1	Zircon-1	Zircon-1	Zircon-1	Zircon-1	Zircon-1	Zircon-1
Comment	LOD	JSA6a_a21_01	JSA6a_a21_02	JSA6a_a21_03	JSA6a_a21_04	JSA6a_a21_05	JSA6a_a21_06	JSA6a_a21_07
HfO2	0.06	1.398	1.945	0.526	0.816	0.901	1.266	1.201
SiO2	0.04	29.743	29.62	29.984	29.699	29.737	29.719	29.711
Al2O3	0.02	0.639	0.309	0.237	0.512	0.251	0.213	0.234
La2O3	0.11	b.d.	b.d.	b.d.	b.d.	b.d.	b.d.	b.d.
Ce2O3	0.09	b.d.	b.d.	b.d.	b.d.	b.d.	b.d.	b.d.
Gd2O3	0.07	b.d.	b.d.	0.305	b.d.	b.d.	b.d.	b.d.
TiO2	0.02	0.156	0.11	0.076	0.097	0.148	0.15	0.153
CaO	0.02	0.234	0.2	b.d.	0.209	0.144	0.241	0.227
ThO2	0.04	b.d.	b.d.	0.238	b.d.	b.d.	b.d.	b.d.
ZrO2	0.09	60.059	59.906	58.703	59.21	60.453	62.911	62.501
P2O5	0.03	b.d.	b.d.	b.d.	b.d.	b.d.	b.d.	b.d.
Y2O3	0.04	0.638	0.472	3.604	1.964	0.881	b.d.	b.d.
Nd2O3	0.04	b.d.	b.d.	b.d.	b.d.	b.d.	b.d.	b.d.
Pr2O3	0.08	b.d.	b.d.	b.d.	b.d.	b.d.	b.d.	b.d.
Eu2O3	0.04	b.d.	b.d.	b.d.	b.d.	b.d.	b.d.	b.d.
Dy2O3	0.04	b.d.	0.151	0.575	0.298	0.152	b.d.	b.d.
Ho2O3	0.09	b.d.	b.d.	b.d.	b.d.	b.d.	b.d.	b.d.
Lu2O3	0.05	b.d.	b.d.	b.d.	b.d.	b.d.	b.d.	b.d.
UO2	0.03	0.102	b.d.	0.099	0.12	0.116	0.146	0.141
Sm2O3	0.07	b.d.	b.d.	0.225	b.d.	b.d.	b.d.	b.d.
Tb2O3	0.04	b.d.	b.d.	b.d.	b.d.	b.d.	b.d.	b.d.
FeO	0.02	1.185	1.206	0.455	0.795	1.003	1.543	1.757
Er2O3	0.04	b.d.	0.136	0.385	0.174	0.186	b.d.	b.d.
Tm2O3	0.04	b.d.	b.d.	b.d.	b.d.	b.d.	b.d.	b.d.
Yb2O3	0.04	0.176	0.455	0.627	0.283	0.516	b.d.	b.d.
PbO	0.03	0.341	0.138	0.133	0.271	0.149	0.106	0.113
Total		95.137	95.402	96.67	94.867	95.314	96.62	96.306
Type		Zircon-2	Zircon-2	Zircon-2	Zircon-2	Zircon-2	Zircon-2	Zircon-2
Comment	LOD	JSA1_c1_a26_01	JSA1_c1_a26_02	JSA1_c1_a26_03	JSA1_a28_01	JSA1_a28_02	JSA1_a28_03	JSA1_a28_04
HfO2	0.06	0.625	0.784	0.739	0.709	0.531	0.672	0.674
SiO2	0.04	27.108	28.653	26.837	27.983	26.856	26.924	27.932
Al2O3	0.02	0.319	0.312	0.552	0.114	0.453	0.536	b.d.
La2O3	0.11	b.d.	b.d.	b.d.	b.d.	b.d.	b.d.	b.d.
Ce2O3	0.09	b.d.	b.d.	b.d.	b.d.	b.d.	b.d.	b.d.
Gd2O3	0.07	b.d.	b.d.	0.3	0.276	0.274	0.28	0.31
TiO2	0.02	b.d.	b.d.	b.d.	b.d.	b.d.	b.d.	0.104
CaO	0.02	0.58	0.457	0.515	0.4	0.611	0.548	0.508
ThO2	0.04	0.971	0.629	0.673	0.359	0.403	0.435	0.347
ZrO2	0.09	52.266	53.376	50.965	47.673	47.927	46.664	48.953
P2O5	0.03	0.78	1.225	0.395	0.233	0.468	0.258	0.281
Y2O3	0.04	3.807	5.456	8.483	8.212	7.34	8.603	8.589
Nd2O3	0.04	b.d.	b.d.	b.d.	b.d.	b.d.	b.d.	b.d.
Pr2O3	0.08	b.d.	b.d.	b.d.	b.d.	b.d.	b.d.	b.d.
Eu2O3	0.04	b.d.	b.d.	b.d.	b.d.	b.d.	b.d.	b.d.
Dy2O3	0.04	0.715	0.726	1.162	1.181	1.12	1.13	1.168
Ho2O3	0.09	b.d.	0.272	0.33	0.282	b.d.	b.d.	b.d.
Lu2O3	0.05	b.d.	0.158	b.d.	b.d.	b.d.	b.d.	b.d.
UO2	0.03	0.681	0.559	0.766	0.684	0.932	0.733	0.663
Sm2O3	0.07	b.d.	b.d.	b.d.	b.d.	b.d.	b.d.	b.d.
Tb2O3	0.04	b.d.	b.d.	0.133	b.d.	b.d.	b.d.	b.d.
FeO	0.02	1.764	1.349	1.281	1.462	1.678	1.427	2.474
Er2O3	0.04	0.947	1.104	0.987	0.954	0.822	0.92	0.958
Tm2O3	0.04	0.168	0.178	0.129	b.d.	b.d.	0.137	0.147
Yb2O3	0.04	1.203	1.458	0.988	0.858	0.733	0.949	0.893
PbO	0.03	0.153	0.149	0.179	0.189	0.139	0.183	0.199
Type		92.583	97.225	95.98	92.146	90.907	90.911	94.68

Continue zircon analyses

Point		Zircon-2	Zircon-2	Zircon-2	Zircon-2	Zircon-2	Zircon-2	Zircon-2
Comment	LOD	JSA1_a28_05	JSA1_C1_1_1	JSA1_C1_1_2	JSA1_C1_1_3	JSA1_C1_1_4	JSA1_C1_2_1	JSA1_C1_2_2
HfO2	0.06	0.82	0.776	0.486	0.793	0.867	0.685	0.827
SiO2	0.04	26.837	26.881	23.787	26.432	26.532	26.377	26.056
Al2O3	0.02	b.d.	b.d.	0.549	b.d.	b.d.	b.d.	b.d.
La2O3	0.11	b.d.	b.d.	b.d.	b.d.	b.d.	b.d.	b.d.
Ce2O3	0.09	b.d.	b.d.	b.d.	b.d.	b.d.	b.d.	b.d.
Gd2O3	0.07	0.399	0.302	0.354	0.396	0.315	0.274	0.367
TiO2	0.02	b.d.	0.224	0.108	0.193	0.132	0.093	0.09
CaO	0.02	0.31	0.807	0.833	0.662	0.684	0.529	0.932
ThO2	0.04	0.467	0.482	0.408	0.684	0.261	0.581	0.484
ZrO2	0.09	48.659	52.856	46.526	49.968	52.267	50.576	50.619
P2O5	0.03	3.146	1.562	2.513	1.579	1.165	1.219	1.415
Y2O3	0.04	6.589	6.077	10.028	6.54	5.421	7.163	6.185
Nd2O3	0.04	b.d.	b.d.	b.d.	b.d.	b.d.	b.d.	b.d.
Pr2O3	0.08	b.d.	b.d.	b.d.	b.d.	b.d.	b.d.	b.d.
Eu2O3	0.04	b.d.	b.d.	b.d.	b.d.	b.d.	b.d.	b.d.
Dy2O3	0.04	1.448	0.874	0.849	0.719	0.905	0.981	0.768
Ho2O3	0.09	b.d.	b.d.	b.d.	b.d.	b.d.	b.d.	b.d.
Lu2O3	0.05	b.d.	b.d.	b.d.	b.d.	b.d.	b.d.	b.d.
UO2	0.03	0.485	0.932	0.655	0.892	0.919	0.796	0.917
Sm2O3	0.07	b.d.	b.d.	b.d.	0.252	b.d.	b.d.	0.239
Tb2O3	0.04	0.125	b.d.	b.d.	b.d.	b.d.	b.d.	b.d.
FeO	0.02	1.619	3.296	1.742	2.088	2.119	1.513	1.88
Er2O3	0.04	1.297	0.597	0.66	0.407	0.701	0.832	0.442
Tm2O3	0.04	0.224	b.d.	b.d.	b.d.	b.d.	0.138	b.d.
Yb2O3	0.04	1.525	0.639	0.831	0.356	0.632	0.843	0.419
PbO	0.03	0.224	b.d.	0.106	b.d.	0.117	0.117	b.d.
Total		94.704	91.473	90.995	92.385	90.84	92.56	91.013
Type		Zircon-2	Zircon-2	Zircon-2	Zircon-2	Zircon-2	Zircon-2	Zircon-2
Comment	LOD	JSA1_C1_2_3	JSA1_C1_2_4	JSA1_C1_2_5	JSA1_C13_1	JSA1_C13_2	JSA1_C13_3	JSA1_C13_5
HfO2	0.06	0.769	0.652	0.429	0.746	0.899	0.444	0.612
SiO2	0.04	26.762	24.476	24.491	26.352	25.806	22.054	25.715
Al2O3	0.02	b.d.	b.d.	b.d.	0.634	0.404	0.9	0.565
La2O3	0.11	b.d.	b.d.	b.d.	b.d.	b.d.	b.d.	b.d.
Ce2O3	0.09	b.d.	b.d.	b.d.	b.d.	b.d.	b.d.	b.d.
Gd2O3	0.07	0.377	0.459	0.261	b.d.	0.309	0.271	0.225
TiO2	0.02	0.083	0.073	b.d.	b.d.	0.091	b.d.	b.d.
CaO	0.02	0.58	0.751	0.565	0.578	0.464	1.227	0.591
ThO2	0.04	0.412	0.316	0.412	0.447	0.727	1.446	0.624
ZrO2	0.09	51.763	47.166	46.864	47.898	48.226	43.47	46.978
P2O5	0.03	1.403	2.851	2.583	0.701	0.911	0.845	0.478
Y2O3	0.04	6.665	8.926	9.001	8.85	8.124	10.277	9.535
Nd2O3	0.04	b.d.	0.152	b.d.	b.d.	b.d.	b.d.	b.d.
Pr2O3	0.08	b.d.	b.d.	b.d.	b.d.	b.d.	b.d.	b.d.
Eu2O3	0.04	b.d.	b.d.	b.d.	b.d.	b.d.	b.d.	b.d.
Dy2O3	0.04	0.732	0.704	1.009	1.214	1.242	1.398	1.311
Ho2O3	0.09	b.d.	b.d.	b.d.	0.303	0.274	0.322	b.d.
Lu2O3	0.05	b.d.	b.d.	b.d.	b.d.	b.d.	b.d.	b.d.
UO2	0.03	0.937	0.486	0.957	0.838	0.595	1.164	0.964
Sm2O3	0.07	0.231	0.272	b.d.	b.d.	b.d.	b.d.	b.d.
Tb2O3	0.04	b.d.	b.d.	b.d.	b.d.	0.127	b.d.	b.d.
FeO	0.02	1.459	0.95	1.15	2.646	1.1	1.586	1.53
Er2O3	0.04	0.444	0.352	0.82	1.184	1.121	1.313	1.028
Tm2O3	0.04	b.d.	b.d.	0.136	0.188	0.18	0.213	0.158
Yb2O3	0.04	0.477	0.342	0.87	1.233	1.263	1.434	0.959
PbO	0.03	b.d.	b.d.	0.143	b.d.	0.121	b.d.	b.d.
Total		93.267	92.419	92.618	94.053	93.281	89.302	94.539

Continue zircon analyses

Type		Zircon-2	Zircon-2	Zircon-2	Zircon-2	Zircon-2	Zircon-2	Zircon-2
Comment	LOD	JSA13_P18_01	JSA13_P18_02	JSA13_P182_01	JSA13_P182_02	JSA13_P183_01	JSA13_P183_02	JSA13_X6_01
HfO2	0.06	0.855	0.628	1.578	0.681	0.355	0.22	b.d.
SiO2	0.04	28.158	27.596	29.168	26.942	26.596	27.429	23.316
Al2O3	0.02	b.d.	0.07	0.074	0.216	0.739	0.414	b.d.
La2O3	0.11	b.d.	b.d.	b.d.	b.d.	b.d.	b.d.	b.d.
Ce2O3	0.09	b.d.	b.d.	b.d.	b.d.	b.d.	b.d.	b.d.
Gd2O3	0.07	0.351	0.326	0.399	0.226	0.289	0.286	b.d.
TiO2	0.02	0.088	b.d.	0.084	b.d.	b.d.	b.d.	b.d.
CaO	0.02	0.197	0.585	0.253	0.88	0.672	0.587	b.d.
ThO2	0.04	0.997	2.382	0.86	2.405	3.46	4.124	3.817
ZrO2	0.09	51.132	51.112	52.572	50.162	47.213	49.131	44.076
P2O5	0.03	0.214	0.344	0.242	0.393	0.323	0.333	b.d.
Y2O3	0.04	6.882	6.116	5.346	6.292	6.581	6.345	7.466
Nd2O3	0.04	b.d.	b.d.	b.d.	b.d.	b.d.	b.d.	b.d.
Pr2O3	0.08	b.d.	b.d.	b.d.	b.d.	b.d.	b.d.	b.d.
Eu2O3	0.04	b.d.	b.d.	b.d.	b.d.	b.d.	b.d.	b.d.
Dy2O3	0.04	1.108	1.062	0.891	0.978	1.03	1.055	1.141
Ho2O3	0.09	b.d.	0.289	b.d.	b.d.	b.d.	b.d.	b.d.
Lu2O3	0.05	0.288	0.26	0.212	0.261	0.184	0.189	0.234
UO2	0.03	0.308	0.523	0.317	0.494	0.549	0.632	0.451
Sm2O3	0.07	b.d.	b.d.	b.d.	b.d.	b.d.	b.d.	b.d.
Tb2O3	0.04	b.d.	b.d.	b.d.	b.d.	b.d.	b.d.	b.d.
FeO	0.02	1.125	1.227	0.595	1.676	1.416	1.464	1.531
Er2O3	0.04	0.923	0.862	0.643	0.885	0.832	0.878	b.d.
Tm2O3	0.04	0.166	0.129	b.d.	0.165	0.151	0.147	b.d.
Yb2O3	0.04	1.293	1.078	0.831	1.128	1.067	1.117	0.881
PbO	0.03	b.d.	b.d.	b.d.	b.d.	0.141	0.182	b.d.
Total		94.538	94.99	94.645	94.504	92.033	94.941	85.148
Type		Zircon-3	Zircon-3	Zircon-3	Zircon-3	Zircon-3	Zircon-3	Zircon-3
Comment	LOD	JSA11_a29_01	JSA11_a29_02	JSA11_a29_03	SA11_a29_06	SA11_a31_01	SA11_a31_02	A11_a31_03
HfO2	0.06	0.418	0.492	0.525	0.423	0.483	0.403	0.518
SiO2	0.04	23.728	23.474	24.341	23.568	23.895	24.202	23.673
Al2O3	0.02	0.325	0.293	0.439	0.191	0.24	0.328	0.222
La2O3	0.11	b.d.	b.d.	b.d.	b.d.	b.d.	b.d.	b.d.
Ce2O3	0.09	b.d.	b.d.	b.d.	b.d.	b.d.	b.d.	b.d.
Gd2O3	0.07	0.269	b.d.	0.28	0.266	b.d.	b.d.	0.238
TiO2	0.02	b.d.	b.d.	b.d.	b.d.	b.d.	b.d.	b.d.
CaO	0.02	0.539	0.486	0.656	0.463	0.37	0.448	0.431
ThO2	0.04	b.d.	b.d.	b.d.	b.d.	b.d.	b.d.	b.d.
ZrO2	0.09	47.443	49.768	46.84	49.131	47.841	46.62	46.543
P2O5	0.03	b.d.	b.d.	0.113	b.d.	0.121	0.128	b.d.
Y2O3	0.04	10.797	10.696	9.897	10.912	10.802	10.746	10.836
Nd2O3	0.04	b.d.	b.d.	b.d.	b.d.	b.d.	b.d.	b.d.
Pr2O3	0.08	b.d.	b.d.	b.d.	b.d.	b.d.	b.d.	b.d.
Eu2O3	0.04	b.d.	b.d.	b.d.	b.d.	b.d.	b.d.	b.d.
Dy2O3	0.04	1.217	1.212	1.029	1.262	1.274	1.152	1.261
Ho2O3	0.09	b.d.	b.d.	b.d.	0.382	0.359	0.338	0.327
Lu2O3	0.05	b.d.	b.d.	b.d.	b.d.	0.164	0.257	b.d.
UO2	0.03	1.112	0.7	2.648	0.388	0.421	0.562	0.444
Sm2O3	0.07	b.d.	b.d.	0.224	b.d.	b.d.	b.d.	b.d.
Tb2O3	0.04	b.d.	b.d.	b.d.	b.d.	b.d.	b.d.	b.d.
FeO	0.02	0.148	0.123	0.114	0.466	0.157	0.099	0.106
Er2O3	0.04	1.064	1.01	0.881	1.175	1.407	1.56	1.36
Tm2O3	0.04	0.186	0.162	0.135	0.178	0.217	0.28	0.206
Yb2O3	0.04	1.051	0.901	0.783	1.17	1.66	2.067	1.562
PbO	0.03	0.199	0.204	0.339	0.189	0.217	0.205	0.173
Total		89.15	90.29	89.626	90.688	90.097	89.912	88.521

Continue zircon analyses

Comment	LOD	JSA11_Map1_1	JSA11_Map1_2	JSA11_Map1_3	JSA11_Map1_4	JSA11_Map2_1	JSA11_Map2_2	JSA11_Map2_3
HfO2	0.06	0.534	1.012	0.543	0.991	0.907	0.61	0.867
SiO2	0.04	21.868	20.756	22.343	22.043	22.618	22.157	22.181
Al2O3	0.02	0.207	0.182	0.159	0.144	0.125	0.137	0.163
La2O3	0.11	b.d.	b.d.	b.d.	b.d.	b.d.	b.d.	b.d.
Ce2O3	0.09	b.d.	b.d.	b.d.	b.d.	b.d.	b.d.	b.d.
Gd2O3	0.07	0.221	0.281	0.298	0.296	0.255	0.278	0.258
TiO2	0.02	b.d.	0.105	0.077	0.078	0.085	b.d.	0.089
CaO	0.02	0.471	0.312	0.296	0.392	0.23	0.307	0.439
ThO2	0.04	b.d.	b.d.	0.121	b.d.	0.178	b.d.	b.d.
ZrO2	0.09	46.07	45.554	46.402	47.756	48.502	46.756	47.813
P2O5	0.03	b.d.	b.d.	b.d.	b.d.	0.167	0.094	b.d.
Y2O3	0.04	11.57	10.122	11.273	10.597	9.486	10.997	9.975
Nd2O3	0.04	b.d.	b.d.	b.d.	b.d.	b.d.	b.d.	b.d.
Pr2O3	0.08	b.d.	b.d.	b.d.	b.d.	b.d.	b.d.	b.d.
Eu2O3	0.04	b.d.	b.d.	b.d.	b.d.	b.d.	b.d.	b.d.
Dy2O3	0.04	1.434	1.448	1.43	1.408	1.302	1.324	1.262
Ho2O3	0.09	0.343	0.34	0.345	0.358	0.296	0.312	0.289
Lu2O3	0.05	0.157	b.d.	b.d.	b.d.	b.d.	b.d.	b.d.
UO2	0.03	0.452	0.191	0.449	0.32	0.338	0.572	0.338
Sm2O3	0.07	b.d.	b.d.	b.d.	b.d.	b.d.	b.d.	b.d.
Tb2O3	0.04	b.d.	b.d.	b.d.	0.13	b.d.	b.d.	b.d.
FeO	0.02	0.096	0.898	0.108	0.619	0.197	0.116	0.11
Er2O3	0.04	1.553	1.277	1.246	1.217	1.112	1.152	1.171
Tm2O3	0.04	0.26	0.195	0.207	0.181	0.158	0.189	0.194
Yb2O3	0.04	1.698	1.146	1.131	1.122	1.091	1.232	1.341
PbO	0.03	0.123	0.124	0.104	b.d.	0.106	0.129	b.d.
Total		90.851	91.077	91.862	91.226	91.704	91.711	90.855
Type		Zircon-3						
Comment	LOD	JSA11_Map2_4						
HfO2	0.06	0.832						
SiO2	0.04	21.983						
Al2O3	0.02	0.134						
La2O3	0.11	b.d.						
Ce2O3	0.09	b.d.						
Gd2O3	0.07	0.306						
TiO2	0.02	0.079						
CaO	0.02	0.259						
ThO2	0.04	b.d.						
ZrO2	0.09	48.517						
P2O5	0.03	b.d.						
Y2O3	0.04	10.319						
Nd2O3	0.04	b.d.						
Pr2O3	0.08	b.d.						
Eu2O3	0.04	b.d.						
Dy2O3	0.04	1.183						
Ho2O3	0.09	b.d.						
Lu2O3	0.05	b.d.						
UO2	0.03	0.271						
Sm2O3	0.07	b.d.						
Tb2O3	0.04	b.d.						
FeO	0.02	1.016						
Er2O3	0.04	1.108						
Tm2O3	0.04	0.166						
Yb2O3	0.04	1.183						
PbO	0.03	b.d.						
Total		91.472						

LA-ICP-MS analyses of zircon from Jabal Sayid

Comments	Li_ppm_m7	Al_ppm_m27	Si_ppm_m29	P_ppm_m31	Sc_ppm_m45	Ti_ppm_m48	Fe_ppm_m57	Y_ppm_m89	Nb_ppm_m93
LOD	0.3	0.6	1294	34	0.6	0.9	54	0.05	0.05
JSA11_Y_01	1.56	923	115000	186	423	130	1180	73200	226
JSA11_Y_02	5.8	1121	124000	189	455	144	2260	75300	220.6
JSA11_Y_03	1.81	950	88000	215	429	121.2	970	77700	210
JSA13_P18_01	7	560	114000	780	484	203	5060	44900	746
JSA13_P18_02	6.4	820	106000	910	491	159	9000	52800	974
JSA13_P18_03	7.3	465	114000	1050	512	198	6560	49000	1040
JSA13_P18_04	4.7	680	120000	890	490	203	5770	49000	1016
JSA6A_Zrn_01	21.9	2250	146000	130	546	347	5210	7150	1640
JSA6A_Zrn_02	33.5	2800	181000	97	602	531	4820	11760	1950
JSA6A_Zrn_03	33.2	2760	165000	80	584	417	4110	14500	1450
JSA6A_Zrn_04	20.4	1650	148000	55	578	396	950	35400	2250
Comments	Sn_ppm_m120	La_ppm_m139	Ce_ppm_m140	Pr_ppm_m141	Nd_ppm_m146	Sm_ppm_m147	Eu_ppm_m153	Gd_ppm_m157	Tb_ppm_m159
LOD	1	0.03	0.04	0.03	0.13	0.16	0.05	0.19	0.02
JSA11_Y_01	1190	0.7	3.56	0.59	8	138.7	23	1332	786
JSA11_Y_02	1050	1.29	3.74	0.6	12.9	141.7	24.4	1297	797
JSA11_Y_03	1190	0.85	4.87	0.86	9.2	138.8	20.4	1321	803
JSA13_P18_01	620	49.2	220	25.4	146	338	48	1640	741
JSA13_P18_02	240	81.2	273	40.1	198	278	44.2	1830	824
JSA13_P18_03	500	72.8	215	33.7	170	307	48.4	2030	953
JSA13_P18_04	480	54.9	214	28.3	164	340	51.5	1790	788
JSA6A_Zrn_01	612	66.5	259	72	563	463	30.6	641	130.3

JSA6A_Zrn_02	1110	43.8	120	41.6	333	495	42.8	920	227
JSA6A_Zrn_03	880	39.7	107.9	33.1	315	504	41.5	1106	291
JSA6A_Zrn_04	1129	46.7	286	77.9	742	1130	99	2510	659
Comments	Ho_ppm_m165	Er_ppm_m167	Tm_ppm_m169	Yb_ppm_m171	Lu_ppm_m175	Hf_ppm_m177	Ta_ppm_m181	Pb_ppm_m208	Th_ppm_m232
LOD	0.03	0.16	0.03	0.20	0.03	0.17	0.03	0.13	0.05
JSA11_Y_01	2570	7730	1250	8150	772	2930	27.3	340	279
JSA11_Y_02	2720	8760	1320	8900	810	3380	22.6	361	461
JSA11_Y_03	2500	8270	1380	8950	928	2910	23.7	325	1070
JSA13_P18_01	1570	5130	926	7240	825	5470	40.3	334	17400
JSA13_P18_02	1940	6330	1144	8660	1025	3940	37.4	361	24200
JSA13_P18_03	1950	5930	988	7940	915	4250	48.9	396	21900
JSA13_P18_04	1670	5470	982	8040	888	6120	38.1	322	17600
JSA6A_Zrn_01	217	942	229	2760	376	7900	244	1370	129.2
JSA6A_Zrn_02	307	987	214	2250	329	8880	274	1950	321
JSA6A_Zrn_03	393	1310	276	3030	466	11600	247	1460	423
JSA6A_Zrn_04	1190	3880	775	7700	930	5870	342	667	364

EMP analyses of pyrochlore from Jabal Sayid. \pm is 3σ standard deviations. LOD is limit of detection in oxide percent

Comment	LOD	JSA11_a29_01	JSA11_a29_02	JSA11_a29_03	JSA11_a32_01	JSA11_a32_02	JSA11_a32_03	JSA11_a32_04	JSA11_a32_06	JSA10b_A23_04
	error									
notes		primary	primary	primary	primary	primary	primary	primary	alt	alt
F	0.177	0.07	0.04	0.18	0.17	0.18	0.03	0.13	0.06	0.06
	\pm	0.23	0.12	0.57	0.53	0.57	0.09	0.42	0.20	0.19
SiO ₂	0.099	3.90	2.84	1.47	3.45	4.23	4.38	1.48	4.43	5.78
	\pm	0.11	0.08	0.04	0.10	0.12	0.13	0.04	0.13	0.17
Na ₂ O	0.032	0.24	0.19	0.54	0.49	0.35	1.19	1.02	0.04	0.14
	\pm	0.27	0.22	0.62	0.57	0.40	1.37	1.17	0.05	0.16
MgO	0.013	0.00	0.01	0.01	0.01	0.00	0.01	0.01	0.01	0.01
	\pm	0.00	0.04	0.04	0.04	0.00	0.04	0.04	0.04	0.04
La ₂ O ₃	0.160	0.68	1.08	1.94	1.87	1.29	2.70	3.27	0.10	0.40
	\pm	0.49	0.78	1.39	1.35	0.93	1.94	2.36	0.07	0.28
Ce ₂ O ₃	0.135	4.61	4.21	5.75	5.55	4.45	7.11	8.09	0.34	2.02
	\pm	0.74	0.68	0.93	0.89	0.72	1.14	1.30	0.05	0.33
Gd ₂ O ₃	0.079	0.13	0.05	0.18	0.15	0.16	0.17	0.19	0.64	7.07
	\pm	0.02	0.01	0.02	0.02	0.02	0.02	0.02	0.08	0.93
TiO ₂	0.041	2.19	2.27	2.32	2.45	2.60	2.50	2.44	4.23	1.39
	\pm	0.04	0.04	0.04	0.04	0.04	0.04	0.04	0.07	0.02
CaO	0.021	3.29	3.68	2.45	3.54	3.80	3.49	2.99	2.02	2.52
	\pm	0.05	0.06	0.04	0.06	0.06	0.06	0.05	0.03	0.04
ThO ₂	0.049	1.01	0.04	0.04	0.01	0.06	0.00	0.04	1.07	1.20
	\pm	6.45	0.26	0.26	0.04	0.35	0.01	0.26	6.83	7.69
Nb ₂ O ₅	0.057	39.89	40.60	44.43	43.55	41.39	49.45	51.18	37.82	38.07
	\pm	0.45	0.45	0.50	0.49	0.46	0.55	0.57	0.42	0.43
Y ₂ O ₃	0.060	0.69	0.32	0.20	0.48	0.83	0.41	0.14	18.50	14.52
	\pm	0.11	0.05	0.03	0.08	0.14	0.07	0.02	3.01	2.36
Nd ₂ O ₃	0.050	0.98	1.41	1.70	1.54	1.19	1.95	2.33	0.19	2.65
	\pm	0.10	0.15	0.18	0.17	0.13	0.21	0.25	0.02	0.28
Pr ₂ O ₃	0.095	0.17	0.37	0.56	0.52	0.31	0.65	0.82	0.08	0.46
	\pm	0.19	0.40	0.61	0.57	0.34	0.71	0.90	0.09	0.50
Eu ₂ O ₃	0.050	0.02	0.01	0.04	0.00	0.02	0.02	0.04	0.04	0.27

	±	0.02	0.00	0.04	0.00	0.02	0.01	0.04	0.04	0.25
Dy ₂ O ₃	0.052	0.35	0.16	0.17	0.25	0.38	0.16	0.10	4.72	3.76
	±	0.06	0.03	0.03	0.05	0.07	0.03	0.02	0.88	0.70
Ho ₂ O ₃	0.106	0.03	0.03	0.09	0.01	0.10	0.09	0.00	1.22	0.43
	±	0.17	0.21	0.61	0.06	0.64	0.56	0.01	7.92	2.82
Lu ₂ O ₃	0.059	0.05	0.01	0.05	0.05	0.05	0.05	0.05	0.27	0.05
	±	0.12	0.02	0.12	0.12	0.12	0.12	0.12	0.60	0.12
UO ₂	0.038	1.63	1.95	1.60	1.45	3.09	1.07	1.06	0.91	0.47
	±	0.09	0.11	0.09	0.08	0.17	0.06	0.06	0.05	0.03
Ta ₂ O ₅	0.085	3.89	4.31	2.54	4.25	3.73	3.86	3.46	1.82	0.40
	±	0.13	0.14	0.08	0.14	0.12	0.13	0.11	0.06	0.01
MnO	0.032	0.22	0.26	0.32	0.21	0.23	0.07	0.09	0.23	0.02
	±	0.03	0.04	0.04	0.03	0.03	0.01	0.01	0.03	0.00
Sm ₂ O ₃	0.082	0.35	0.32	0.28	0.34	0.27	0.34	0.43	0.32	3.46
	±	0.06	0.06	0.05	0.06	0.05	0.06	0.08	0.06	0.61
Tb ₂ O ₃	0.048	0.05	0.01	0.04	0.03	0.02	0.02	0.04	0.34	0.97
	±	0.09	0.01	0.07	0.05	0.04	0.03	0.07	0.55	1.57
FeO	0.025	2.12	3.14	2.61	1.57	1.94	0.92	0.69	2.06	3.62
	±	0.04	0.07	0.05	0.03	0.04	0.02	0.01	0.04	0.08
Er ₂ O ₃	0.048	0.19	0.08	0.05	0.18	0.25	0.12	0.06	5.23	0.58
	±	0.05	0.02	0.02	0.05	0.07	0.04	0.02	1.55	0.17
Tm ₂ O ₃	0.048	0.09	0.08	0.07	0.08	0.12	0.10	0.04	0.90	0.11
	±	0.03	0.03	0.02	0.03	0.04	0.03	0.01	0.28	0.04
Yb ₂ O ₃	0.047	0.21	0.17	0.09	0.24	0.32	0.17	0.12	4.40	0.27
	±	0.03	0.02	0.01	0.03	0.04	0.02	0.02	0.61	0.04
PbO	0.041	34.08	32.54	30.14	25.71	28.89	15.36	17.96	2.25	1.44
	±	1.06	1.01	0.94	0.80	0.90	0.48	0.56	0.07	0.04
SnO ₂	0.026	0.10	0.07	0.06	0.08	0.11	0.06	0.05	0.13	0.02
	±	0.03	0.02	0.02	0.02	0.03	0.02	0.01	0.04	0.01
Total		101.20	100.25	99.90	98.21	100.35	96.44	98.31	94.38	92.17

EMPA analyses of Synchysite from Jabal Sayid. \pm is 3 σ standard deviations. LOD is limit of detection in oxide percent

Comment	LOD	JSA11_0_01	JSA11_0_02	JSA11_0_03	JSA11_31_01	JSA11_31_02	JSA11_31_03	JSA11_31_04
	Error							
F	0.17	4.90	4.30	4.61	5.20	4.54	4.77	4.89
	\pm	1.95	1.71	1.83	2.07	1.81	1.90	1.94
SiO ₂	0.02	0.08	0.11	0.13	0.05	0.02	0.02	0.02
	\pm	0.00	0.00	0.00	0.00	0.00	0.00	0.00
La ₂ O ₃	0.14	0.42	0.30	0.46	0.71	0.30	0.25	0.40
	\pm	0.67	0.47	0.74	1.12	0.48	0.40	0.63
Ce ₂ O ₃	0.12	1.06	0.90	1.23	1.54	0.94	0.40	1.23
	\pm	0.60	0.51	0.69	0.87	0.53	0.22	0.69
Gd ₂ O ₃	0.07	2.24	1.92	2.17	2.07	2.11	1.34	2.03
	\pm	0.54	0.47	0.52	0.50	0.51	0.32	0.49
CaO	0.02	18.12	16.03	17.38	18.49	20.40	21.11	20.71
	\pm	0.56	0.50	0.54	0.57	0.63	0.65	0.64
ThO ₂	0.04	2.12	1.70	2.15	0.04	0.03	0.27	0.16
	\pm	0.57	0.45	0.58	0.01	0.01	0.07	0.04
Y ₂ O ₃	0.06	25.30	22.08	23.75	26.77	30.84	36.54	32.76
	\pm	1.02	0.89	0.96	1.08	1.24	1.47	1.32
Nd ₂ O ₃	0.04	0.85	0.76	0.88	1.06	0.71	0.31	0.84
	\pm	0.17	0.16	0.18	0.22	0.14	0.06	0.17
Pr ₂ O ₃	0.08	0.14	0.11	0.17	0.21	0.14	0.02	0.16
	\pm	0.19	0.15	0.23	0.27	0.19	0.02	0.22
Eu ₂ O ₃	0.04	0.06	0.02	0.04	0.04	0.02	0.02	0.05
	\pm	0.49	0.18	0.29	0.31	0.19	0.18	0.43
Dy ₂ O ₃	0.05	4.68	4.39	4.41	4.20	4.86	3.83	4.49
	\pm	0.17	0.16	0.16	0.15	0.17	0.14	0.16
Ho ₂ O ₃	0.09	0.92	0.78	0.86	0.91	1.12	0.96	0.94
	\pm	0.14	0.12	0.13	0.14	0.17	0.14	0.14
Lu ₂ O ₃	0.05	0.01	0.05	0.05	0.05	0.05	0.02	0.05
	\pm	0.00	0.01	0.01	0.01	0.01	0.00	0.01

Sm ₂ O ₃	0.07	0.83	0.77	0.82	0.90	0.71	0.46	0.79
	±	0.23	0.21	0.23	0.25	0.20	0.13	0.22
Tb ₂ O ₃	0.04	0.58	0.52	0.56	0.53	0.58	0.39	0.53
	±	0.21	0.18	0.20	0.19	0.21	0.14	0.19
Er ₂ O ₃	0.03	2.27	1.99	2.11	2.18	2.60	2.54	2.61
	±	0.06	0.05	0.05	0.06	0.07	0.06	0.07
Tm ₂ O ₃	0.04	0.25	0.19	0.24	0.22	0.24	0.30	0.32
	±	0.02	0.02	0.02	0.02	0.02	0.03	0.03
Yb ₂ O ₃	0.04	0.82	0.77	0.71	0.77	0.91	1.15	1.31
	±	0.02	0.02	0.02	0.02	0.02	0.03	0.03
PbO	0.04	0.32	0.35	0.32	0.26	0.38	0.34	0.32
	±	0.04	0.05	0.04	0.04	0.05	0.05	0.04
Total		66.0	58.0	63.0	66.2	71.5	75.0	74.6

EMP analyses of bastnasite from Jabal Sayid. ± is 3 σ standard deviations. LOD is limit of detection in oxide percent

	LOD	JSA11_07	JSA6Aa22_01	JSA10b-a24_01	JSA10b-a24_02	JSA10b-a24_03	JSA10b-a24_04	JSA1_a26_04	JSA1_a26_05	JSA1_a26_06
	Error									
F	0.20	5.81	6.48	7.20	7.23	6.80	6.95	8.03	7.40	8.28
	±	0.59	0.66	0.73	0.73	0.69	0.70	0.81	0.75	0.84
SiO ₂	0.02	0.14	0.04	0.10	0.09	0.08	0.10	0.02	0.02	0.02
	±	0.03	0.01	0.02	0.02	0.02	0.02	0.01	0.00	0.00
La ₂ O ₃	0.18	8.31	12.11	9.88	9.70	9.42	9.81	19.93	24.53	24.21
	±	2.07	3.02	2.46	2.42	2.35	2.44	4.96	6.11	6.03
Ce ₂ O ₃	0.15	22.97	32.49	33.10	32.44	32.09	32.19	27.96	32.86	33.40
	±	2.03	2.88	2.93	2.87	2.84	2.85	2.48	2.91	2.96
Gd ₂ O ₃	0.08	5.66	1.06	0.77	1.20	1.16	1.30	2.58	0.42	0.36
	±	0.49	0.09	0.07	0.10	0.10	0.11	0.22	0.04	0.03
CaO	0.02	0.33	0.24	0.34	0.15	0.16	0.19	0.44	0.34	0.44
	±	0.15	0.11	0.15	0.07	0.07	0.08	0.20	0.15	0.19
ThO ₂	0.05	0.13	0.70	0.38	0.46	0.36	0.58	2.18	1.47	0.59
	±	0.03	0.15	0.08	0.10	0.08	0.12	0.46	0.31	0.13
Y ₂ O ₃	0.06	2.68	0.92	0.30	0.41	0.45	0.58	1.39	1.28	1.32

	±	6.36	2.18	0.71	0.97	1.07	1.37	3.30	3.03	3.13
Nd ₂ O ₃	0.06	17.58	15.58	18.16	18.40	18.26	17.35	8.94	6.52	6.93
	±	2.43	2.16	2.52	2.55	2.53	2.40	1.24	0.90	0.96
Pr ₂ O ₃	0.11	3.43	4.19	4.65	4.41	4.43	4.42	2.28	2.28	2.35
	±	1.29	1.57	1.74	1.65	1.66	1.66	0.86	0.86	0.88
Eu ₂ O ₃	0.05	0.24	0.03	0.05	0.10	0.22	0.09	0.18	0.05	0.03
	±	0.10	0.01	0.02	0.04	0.09	0.04	0.07	0.02	0.01
Dy ₂ O ₃	0.05	2.08	0.64	0.21	0.24	0.22	0.38	0.64	0.41	0.22
	±	2.37	0.72	0.24	0.27	0.24	0.44	0.73	0.47	0.25
Ho ₂ O ₃	0.11	0.29	0.11	0.03	0.02	0.03	0.05	0.16	0.14	0.09
	±	0.84	0.32	0.08	0.07	0.09	0.15	0.46	0.39	0.27
Lu ₂ O ₃	0.06	0.06	0.01	0.06	0.06	0.06	0.06	0.00	0.06	0.02
	±	0.47	0.04	0.47	0.47	0.47	0.47	0.01	0.47	0.15
UO ₂	0.04	0.02	0.04	0.01	0.02	0.04	0.00	0.02	0.05	0.00
	±	0.10	0.25	0.05	0.11	0.25	0.01	0.12	0.27	0.02
Sm ₂ O ₃	0.09	7.50	3.02	3.17	3.54	3.43	3.53	3.78	0.68	0.69
	±	0.88	0.35	0.37	0.42	0.40	0.41	0.44	0.08	0.08
Tb ₂ O ₃	0.05	0.63	0.21	0.09	0.11	0.10	0.16	0.25	0.06	0.06
	±	0.68	0.23	0.09	0.12	0.11	0.17	0.27	0.07	0.07
FeO	0.02	0.02	2.00	0.01	0.02	0.05	0.08	0.28	0.33	0.11
	±	0.03	2.61	0.02	0.02	0.06	0.11	0.36	0.43	0.14
Er ₂ O ₃	0.03	0.17	0.16	0.03	0.01	0.03	0.03	0.14	0.07	0.20
	±	0.64	0.59	0.13	0.05	0.13	0.13	0.53	0.27	0.75
Tm ₂ O ₃	0.05	0.03	0.01	0.05	0.05	0.02	0.03	0.06	0.05	0.02
	±	0.02	0.01	0.03	0.03	0.02	0.02	0.04	0.03	0.02
Yb ₂ O ₃	0.05	0.07	0.11	0.04	0.05	0.03	0.04	0.15	0.12	0.29
	±	0.06	0.10	0.03	0.04	0.03	0.03	0.14	0.11	0.26
PbO	0.04	0.04	0.07	0.04	0.02	0.02	0.04	0.07	0.07	0.03
	±	0.09	0.19	0.11	0.05	0.04	0.11	0.19	0.18	0.07
Total		78.15	80.21	78.65	78.72	77.46	77.97	79.48	79.21	79.65

EMP analyses of monazite from Jabal Sayid. \pm is 3 σ standard deviations. LOD is limit of detection in oxide percent

Comment	LOD	JSA11-31_05	JSA11-31_06	JSA1a25_01	JSA1a25_02	JSA1a25_03
	Error					
F	0.18882	0.78	0.71	0.73	0.73	0.77
	\pm	0.08	0.07	0.07	0.07	0.08
SiO ₂	0.01656	0.22	0.24	1.07	0.93	1.17
	\pm	0.05	0.06	0.25	0.22	0.27
Al ₂ O ₃	0.0126	0.01	0.01	0.01	0.01	0.01
	\pm	0.03	0.03	0.03	0.03	0.03
La ₂ O ₃	0.18036	17.93	19.29	24.81	24.38	23.73
	\pm	4.46	4.80	6.18	6.07	5.91
Ce ₂ O ₃	0.15246	36.76	36.44	35.68	34.97	35.93
	\pm	3.26	3.23	3.16	3.10	3.18
Gd ₂ O ₃	0.08198	0.37	0.44	0.08	0.08	0.14
	\pm	0.03	0.04	0.01	0.01	0.01
CaO	0.01888	0.04	0.04	0.02	0.02	0.01
	\pm	0.02	0.02	0.01	0.01	0.01
ThO ₂	0.05164	0.60	0.60	0.20	0.20	0.38
	\pm	0.13	0.13	0.04	0.04	0.08
P ₂ O ₅	0.04554	28.35	29.66	28.08	28.27	27.67
	\pm	0.00	0.00	0.00	0.00	0.00
Y ₂ O ₃	0.0606	0.08	0.05	0.01	0.01	0.06
	\pm	0.00	0.00	0.00	0.00	0.00
Nd ₂ O ₃	0.06086	9.97	9.22	7.32	7.14	7.63
	\pm	0.00	0.00	0.00	0.00	0.00
Pr ₂ O ₃	0.11102	3.17	3.00	2.51	2.46	2.60
	\pm	0.00	0.00	0.00	0.00	0.00
Eu ₂ O ₃	0.0551	0.03	0.03	0.04	0.06	0.06
	\pm	0.00	0.00	0.00	0.00	0.00
Dy ₂ O ₃	0.05364	0.04	0.05	0.05	0.05	0.05
	\pm	0.00	0.00	0.00	0.00	0.00

Ho2O3	0.10964	0.03	0.01	0.03	0.05	0.11
	±	0.00	0.00	0.00	0.00	0.00
Lu2O3	0.06136	0.06	0.06	0.06	0.00	0.06
	±	0.00	0.00	0.00	0.00	0.00
UO2	0.04152	0.03	0.03	0.01	0.04	0.02
	±	0.00	0.00	0.00	0.00	0.00
Sm2O3	0.08532	1.45	1.46	0.57	0.53	0.64
	±	0.00	0.00	0.00	0.00	0.00
Tb2O3	0.0496	0.02	0.04	0.01	0.03	0.05
	±	0.00	0.00	0.00	0.00	0.00
FeO	0.02084	0.03	0.02	0.02	0.01	0.01
	±	0.00	0.00	0.00	0.00	0.00
Er2O3	0.03466	0.03	0.03	0.03	0.01	0.03
	±	0.00	0.00	0.00	0.00	0.00
Tm2O3	0.04912	0.02	0.02	0.00	0.05	0.05
	±	0.00	0.00	0.00	0.00	0.00
Yb2O3	0.04826	0.04	0.03	0.04	0.06	0.02
	±	0.00	0.00	0.00	0.00	0.00
PbO	0.04308	0.04	0.04	0.03	0.04	0.04
	±	0.00	0.00	0.00	0.00	0.00
Total		100.07	101.53	101.43	100.14	101.26

EMP analyses of xenotime from Jabal Sayid. ± is 3 σ standard deviations. LOD is limit of detection in oxide percent

Comment	LOD	JSA1_01	JSA1_02	JSA1_03
F	0.37	2.74	3.07	3.26
	±	0.6	0.7	0.7
SiO ₂	0.13	3.48	2.93	3.43
	±	0.1	0.1	0.1
Al ₂ O ₃	0.02	0.15	0.20	0.05
	±	0.4	0.6	0.2
La ₂ O ₃	0.07	0.10	1.17	0.16

	±	0.0	0.0	0.0
Ce ₂ O ₃	0.15	0.25	1.69	0.13
	±	0.0	0.0	0.0
Gd ₂ O ₃	0.11	0.18	0.20	0.21
	±	0.0	0.0	0.0
CaO	0.06	0.09	0.16	1.10
	±	0.1	0.2	1.2
ThO ₂	0.03	2.27	0.30	4.21
	±	0.7	0.1	1.4
P ₂ O ₅	0.05	27.32	27.06	27.63
	±	0.5	0.5	0.5
Y ₂ O ₃	0.06	44.11	45.57	40.61
	±	0.7	0.7	0.6
Nd ₂ O ₃	0.06	0.05	0.37	0.07
	±	0.0	0.0	0.0
Pr ₂ O ₃	0.06	0.09	0.10	0.01
	±	0.4	0.4	0.0
Eu ₂ O ₃	0.08	0.05	0.02	0.05
	±	1.0	0.3	1.0
Dy ₂ O ₃	0.05	2.02	2.16	2.60
	±	0.1	0.1	0.1
Ho ₂ O ₃	0.07	0.97	1.00	1.08
	±	0.1	0.1	0.1
Lu ₂ O ₃	0.09	0.79	0.80	0.68
	±	0.1	0.1	0.0
UO ₂	0.05	0.07	0.03	0.11
	±	0.2	0.1	0.2
Sm ₂ O ₃	0.05	0.16	0.16	0.24
	±	0.1	0.1	0.1
Tb ₂ O ₃	0.07	0.10	0.10	0.10

	±	0.05	0.05	0.05
FeO	0.04	1.43	0.56	1.21
	±	0.07	0.03	0.06
Er ₂ O ₃	0.02	4.95	5.18	5.41
	±	0.1	0.1	0.1
Tm ₂ O ₃	0.04	1.00	1.04	1.06
	±	0.07	0.07	0.07
Yb ₂ O ₃	0.05	6.87	6.78	6.62
	±	0.1	0.1	0.1
PbO	0.04	0.51	0.43	0.38
	±	0.1	0.1	0.1
Total		99.7	101.1	100.4

HDA.11	Qtz vein with high cps around 3000	√						
HDA.19	Sub-horizontal qtz vien shows alteration halos. The vein dips 20 deg nw and strikes 240ne	√	√				√	
HDA.20	A- qtz vein + amphibole with about 3000 cps radiation.			√				
HDA.21	Gray amphibole granite.							
HDA.22	Qtz amphibole vein							
HDA.24	A small deformed Qtz vein with high radioactivity	√	√	√	√	√		
HDA.25	Marialitic cavities consist of qtz+ k-feld- mafic minerals (amphibole)	√	√					
HDA.26	Porphyritic amphibole granite. Large k-feldspar crystal in a medium grained granite matrix. This could be a different phase of the regular amphibole granite	√						√
HDA.27	Red amphibole granite.	√						
hda28	Amphibole granite	√						
HDA.29	Amphibole-biotite granite at the center	√						

	of the intrusion				
HDA.30	Marialitic cavities isolated by red amphibole granite.	√	√	√	√
HAD 32	Pink microgranite granite				
HAD 33	microgranite granite (gray to pinkish) with gray xenolith				
HDA34	Qtz amphibole marialitic cavities.			√	√
HDA35	Gray monzogranite with amphibole				
HDA36	Gray to white pink granite. No amphibole minerals	√			
HDA37	Pink porphyritic granite				
HAD 38	Light pink to gray granite on the contact with the monzogranite	√			
HDA39	Monzogranite on contact with pink to gray granite	√			

Sample	GPS coordinates
HDA.1	N 23 33 31.7 E 41 14 32.8
HDA.5	N 23 33 33.1 E 41 14 38.9
HDA.6	N 23 33 32 E 41 14 39.2
HDA.7	N23 33 32.8 E 41 14 39.1

HDA.8		
HDA.9	N 23 33 32.9	E 41 14 39.3
HDA.10	N23 33 32.5	E 41 14
HDA.11	N23 33 32.3	E 41 14 38.7
HDA.19	N23 33 37.3	E41 14 37.0
HDA.20	N23 33 37.2	E 41 14 38.4
HDA.21	N23 33 37.5	E41 14 37.4
HDA.22	N23 33 37.4	E41 14 37.1
HDA.24	N23 33 36.8	E41 14 37.7
HDA.25	N23 33 38.0	E41 14 36.5
HDA.26	N23 33 45.4	E 41 14 11.2
HDA.27		
hda28		
HDA.29	N23 34 26.1	E41 13 27.9
HDA.30	N23 39 19.2	E41 13 30.8
HAD 32	N23 34 07.8	E41 13 29.7
HAD 33	N23 33 15.4	E41 13 36.6
HDA34		
HDA35		
HDA36	N23 33 18.2	E41 13 28.1
HDA37		
HAD 38	N23 33 18.9	E41 13 15.7
HDA39		

photos of samples from Dyaheen



U-Pb zircon age date of zircon from the quartz veins

Analysis					Concordia:					Ages Ma								
	207Pb/206Pb	SigM	206Pb/238U	SigM	207Pb/235U	SigM	206Pb/238U	SigM	RhoXY	SigM	207Pb/206Pb	SigM	207Pb/235U	SigM	206Pb/238U	SigM	%Disc	SigM
DD91-1-2.1	0.1836	0.0009	0.4601	0.0027														
DD85-17-1.1	0.2263	0.0011	0.5410	0.0029														
HDA11-V16.1	0.0796	0.0042	0.0981	0.0013	1.1596	0.063	0.107082665	0.001	0.260	0.007	1161	101	782	29	656	9	46	5
HDA11-V16.2	0.3919	0.0134	0.2417	0.0156	13.9866	1.029	0.262255996	0.017	0.884	0.405	3859	51	2749	68	1501	86	68	2
HDA11-V16.3	0.2870	0.0135	0.1499	0.0051	6.2977	0.370	0.161454767	0.006	0.589	0.100	3379	72	2018	51	965	31	77	1
HDA11-V16.4	0.4273	0.0190	0.2996	0.0239	18.5140	1.705	0.319645137	0.026	0.873	0.253	3983	66	3017	86	1788	124	63	3
HDA11-V16.5	0.6577	0.0135	0.6899	0.0271	64.6248	2.976	0.72792691	0.029	0.882	0.333	4610	31	4248	45	3526	107	30	3
DD91-1-2.2	0.1845	0.0011	0.4462	0.0029														
DD85-17-2.1	0.2237	0.0011	0.5572	0.0033														

EMP analyses of zircons from Dyaheen. LOD is ppm element. \pm is 2 sigma standard deviation

Point	LOD (element ppm)	HDA9_zrn_01	HDA9_zrn_02	HDA9_zrn_03	HDA9_zrn_04	HDA9_zrn_05	HDA7 (N2) a33_01	HDA7 (N2) a33_02
Type		Aeg.grt	Aeg.grt	Aeg.grt	Aeg.grt	Aeg.grt	aeg.dyke	aeg.dyke
HfO2	629	1.3	1.3	1.2	1.2	1.6	0.5	0.8
\pm		0.06	0.06	0.06	0.06	0.06	0.05	0.05
SiO2	370	32.6	32.6	32.7	32.7	32.9	29.0	29.9
\pm		0.12	0.12	0.12	0.12	0.12	0.11	0.11
Al2O3	174	0.03	0.0	0.0	0.0	0.0	0.1	0.0
\pm		0.05	0.05	0.01	0.03	0.05	0.01	0.01
La2O3	1347	0.0	0.0	0.1	0.0	0.0	0.0	0.0
\pm		0.06	0.05	0.21	0.07	0.05	0.07	0.07
Ce2O3	1022	0.1	0.2	0.0	0.1	0.1	0.0	0.0
\pm		0.05	0.06	0.06	0.06	0.06	0.05	0.05
Gd2O3	712	0.1	0.2	0.1	0.2	0.2	0.2	0.1
\pm		0.03	0.03	0.03	0.03	0.03	0.31	0.03
TiO2	254	0.0	0.0	0.0	0.0	0.0	0.0	0.0
\pm		0.01	0.01	0.02	0.01	0.02	0.01	0.01
CaO	158	0.0	0.0	0.0	0.0	0.0	1.4	1.2
\pm		0.01	0.01	0.01	0.01	0.01	0.02	0.02
ThO2	412	0.0	0.0	0.1	0.1	0.1	0.2	0.1
\pm		0.03	0.01	0.04	0.04	0.08	0.04	0.04
ZrO2	906	63.9	63.1	64.5	62.7	63.1	57.3	59.1
\pm		0.50	0.50	0.50	0.49	0.50	0.47	0.48
P2O5	322	0.1	0.0	0.1	0.1	0.1	0.3	0.2

±		0.02	0.02	0.02	0.02	0.02	0.02	0.02
Y2O3	461	1.2	1.1	0.7	1.8	1.4	0.9	0.9
±		0.06	0.06	0.05	0.07	0.06	0.05	0.05
Nd2O3	450	0.1	0.0	0.0	0.1	0.1	0.0	0.0
±		0.08	0.03	0.02	0.03	0.03	0.02	0.02
Pr2O3	850	0.0	0.0	0.0	0.0	0.0	0.1	0.0
±		0.05	0.04	0.05	0.05	0.02	0.15	0.04
Eu2O3	446	0.0	0.0	0.0	0.0	0.0	0.0	0.0
±		0.02	0.02	0.09	0.02	0.02	0.03	0.01
Dy2O3	459	0.1	0.2	0.1	0.2	0.2	0.2	0.2
±		0.03	0.03	0.03	0.03	0.03	0.03	0.03
Ho2O3	950	0.1	0.0	0.0	0.0	0.0	0.0	0.0
±		0.14	0.05	0.05	0.05	0.05	0.02	0.05
Lu2O3	529	0.0	0.0	0.1	0.0	0.0	0.0	0.0
±		0.02	0.03	0.03	0.00	0.01	0.01	0.02
UO2	344	0.0	0.0	0.2	0.1	0.1	0.7	0.8
±		0.03	0.03	0.03	0.03	0.03	0.03	0.03
Sm2O3	734	0.1	0.2	0.1	0.2	0.2	0.1	0.1
±		0.03	0.03	0.03	0.03	0.03	0.03	0.03
Tb2O3	427	0.0	0.0	0.0	0.0	0.0	0.0	0.0
±		0.02	0.03	0.00	0.02	0.02	0.03	0.06
FeO	177	0.0	0.1	0.0	0.0	0.0	2.7	1.0
±		0.01	0.01	0.01	0.04	0.01	0.03	0.02
Er2O3	427	0.2	0.1	0.1	0.2	0.2	0.1	0.1
±		0.02	0.03	0.02	0.03	0.03	0.02	0.02
Tm2O3	429	0.0	0.0	0.0	0.1	0.0	0.0	0.0
±		0.01	0.01	0.04	0.02	0.01	0.02	0.01
Yb2O3	422	0.3	0.2	0.2	0.2	0.3	0.3	0.4
±		0.02	0.02	0.02	0.02	0.02	0.02	0.02
PbO	355	0.0	0.0	0.0	0.0	0.0	0.2	0.2
±		0.03	0.04	0.03	0.03	0.02	0.04	0.04
Total		100.4	99.7	100.4	100.3	100.8	94.4	95.4

Point	HDA7_(N2)_a33_03	HDA7_(N2)_a33_04	HDA8_a35_01	HDA8_a35_02	HDA8_a35_03	HDA10_a36_01	HDA10_a36_02	HDA10_a36_03
Type	aeg.dyke	aeg.dyke	aeg.dyke	aeg.dyke	aeg.dyke	qtz.vein	qtz.vein	qtz.vein
HfO2	0.8	0.7	0.4	0.6	0.6	1.0	1.0	1.0
±	0.05	0.05	0.05	0.05	0.05	0.05	0.05	0.05
SiO2	29.3	27.5	29.2	31.6	28.8	32.4	32.6	32.2
±	0.11	0.11	0.11	0.12	0.11	0.12	0.12	0.12
Al2O3	0.1	0.1	0.0	0.0	0.1	0.1	0.0	0.0
±	0.01	0.01	0.01	0.00	0.01	3.91	0.05	0.05
La2O3	0.0	0.1	0.1	0.1	0.1	0.1	0.1	0.1
±	0.05	0.07	0.14	0.07	0.09	0.21	0.21	0.21
Ce2O3	0.0	0.4	0.0	0.1	0.0	0.0	0.0	0.1
±	0.05	0.06	0.05	0.06	0.05	0.05	0.05	0.06
Gd2O3	0.0	0.1	0.1	0.0	0.1	0.1	0.1	0.1
±	0.03	0.03	0.03	0.03	0.03	0.03	0.03	0.03
TiO2	0.0	0.2	0.0	0.0	0.0	0.0	0.0	0.0
±	0.01	0.02	0.02	0.01	0.03	0.01	0.02	0.02
CaO	0.9	1.0	1.5	0.0	1.4	0.0	0.0	0.0
±	0.02	0.02	0.02	0.01	0.02	0.01	0.01	0.01
ThO2	0.1	0.1	1.4	1.6	1.4	0.5	0.4	0.6
±	0.04	0.04	0.05	0.06	0.06	0.04	0.04	0.04
ZrO2	57.8	53.5	55.2	58.9	56.8	59.5	60.1	59.0
±	0.47	0.45	0.46	0.48	0.47	0.48	0.48	0.48
P2O5	0.3	0.3	0.4	0.3	0.4	0.2	0.2	0.2
±	0.02	0.02	0.02	0.02	0.02	0.02	0.02	0.02
Y2O3	1.0	1.9	3.1	3.2	1.4	1.4	1.5	1.7
±	0.05	0.07	0.08	0.09	0.06	0.06	0.06	0.07

Nd ₂ O ₃	0.0	0.2	0.2	0.0	0.0	0.1	0.0	0.0
±	0.02	0.03	18.29	0.02	0.04	0.08	0.02	0.03
Pr ₂ O ₃	0.0	0.0	0.0	0.0	0.0	0.0	0.0	0.1
±	0.06	0.05	0.04	0.04	0.05	0.05	0.07	0.15
Eu ₂ O ₃	0.0	0.0	0.0	0.0	0.0	0.0	0.0	0.0
±	0.02	0.01	0.02	0.02	0.02	0.06	0.02	0.03
Dy ₂ O ₃	0.2	0.5	0.4	0.2	0.3	0.2	0.2	0.2
±	0.03	0.03	0.03	0.03	0.03	0.03	0.03	0.03
Ho ₂ O ₃	0.0	0.0	0.1	0.0	0.0	0.0	0.1	0.1
±	0.05	0.05	0.05	0.05	0.05	0.03	0.05	0.05
Lu ₂ O ₃	0.0	0.0	0.0	0.1	0.1	0.0	0.0	0.1
±	0.02	0.01	0.02	0.02	0.02	0.02	0.43	0.50
UO ₂	0.5	0.4	1.3	0.8	0.7	0.2	0.2	0.2
±	0.03	0.03	0.04	0.03	0.03	0.03	0.03	0.03
Sm ₂ O ₃	0.1	0.2	0.1	0.1	0.1	0.1	0.1	0.1
±	0.03	0.03	0.03	0.03	0.03	0.03	0.03	0.03
Tb ₂ O ₃	0.0	0.1	0.1	0.0	0.0	0.0	0.0	0.0
±	0.06	0.02	0.08	0.02	0.03	0.04	0.02	0.02
FeO	3.1	2.5	0.3	0.1	1.0	0.3	0.0	0.0
±	0.03	0.03	0.01	0.01	0.02	0.01	0.01	0.01
Er ₂ O ₃	0.1	0.3	0.4	0.4	0.2	0.3	0.2	0.3
±	0.02	0.03	0.03	0.03	0.02	0.03	0.03	0.03
Tm ₂ O ₃	0.0	0.1	0.1	0.1	0.1	0.0	0.0	0.0
±	0.02	0.02	0.02	0.02	0.02	0.02	0.02	0.02
Yb ₂ O ₃	0.3	0.5	0.7	0.6	0.5	0.4	0.3	0.3
±	0.02	0.02	0.02	0.02	0.02	0.02	0.02	0.02
PbO	0.1	0.6	0.3	0.1	0.2	0.2	0.1	0.0

±	0.04	0.05	0.04	0.04	0.04	0.28	0.03	0.03
Total	95.1	91.4	95.5	99.0	94.3	97.3	97.5	96.6
Point	HDA10_a 37_04	HDA5_a41_0 1	HDA5_a41_02	HDA5_a41_03	HDA5_a41_04	HDA5_a41_05	HDA5_a41_06	HDA5_Q7_01
Type	qtz.vein	qtz.vein	qtz.vein	qtz.vein	qtz.vein	qtz.vein	qtz.vein	qtz.vein
HfO2	1.0	1.0	0.9	0.8	1.1	1.0	1.0	0.9
±	0.05	0.05	0.05	0.05	0.05	0.05	0.05	0.05
SiO2	32.2	33.1	33.3	32.9	33.1	32.6	33.2	32.5
±	0.12	0.12	0.12	0.12	0.12	0.12	0.12	0.12
Al2O3	0.0	0.0	0.0	0.0	0.0	0.0	0.0	0.0
±	0.05	0.05	0.05	0.05	0.05	0.05	0.05	0.05
La2O3	0.1	0.0	0.1	0.1	0.1	0.1	0.1	0.1
±	0.07	0.06	0.07	0.07	0.10	0.07	0.08	0.21
Ce2O3	0.2	0.0	0.0	0.0	0.1	0.0	0.0	0.1
±	0.06	0.05	0.06	0.02	0.17	0.05	0.05	0.07
Gd2O3	0.1	0.0	0.1	0.1	0.1	0.1	0.1	0.2
±	0.14	0.03	0.03	0.03	0.03	0.03	0.03	0.04
TiO2	0.1	0.1	0.0	0.0	0.0	0.0	0.0	0.0
±	0.02	0.12	0.01	0.01	0.01	0.23	0.06	0.01
CaO	0.0	0.0	0.0	0.0	0.0	0.0	0.0	0.0
±	0.01	0.01	0.01	0.01	0.01	0.00	0.01	0.01
ThO2	0.4	0.4	0.1	0.0	0.0	0.1	0.0	0.1
±	0.04	0.63	0.03	0.04	0.03	0.04	0.04	0.03
ZrO2	62.3	63.8	62.5	63.0	64.9	63.7	62.8	57.7
±	0.49	0.49	0.49	0.49	0.50	0.49	0.49	0.47
P2O5	0.3	0.2	0.3	0.4	0.1	0.3	0.3	0.4
±	0.02	0.02	0.02	0.02	0.02	0.02	0.02	0.02
Y2O3	1.9	0.6	1.1	1.5	0.4	1.1	0.8	5.3

PbO	0.0	0.0	0.0	0.0	0.0	0.0	0.0	0.0
±	0.04	0.04	0.05	0.03	0.03	0.03	0.03	0.03
Total	100.4	100.3	99.6	100.5	100.9	100.0	99.4	100.1
Point	HDA5_Q7_02	HDA5_Q7_03	HDA5_Q7_04	HDA5_Q7_05	HDA19_a44_01	HDA19_a44_02	HDA19_a44_03	HDA19_a44_04
Type	qtz.vein	qtz.vein	qtz.vein	qtz.vein	qtz.vein	qtz.vein	qtz.vein	qtz.vein
HfO2	0.9	0.7	1.0	0.6	0.9	0.7	0.7	1.1
±	0.05	0.05	0.05	0.05	0.05	0.05	0.05	0.06
SiO2	32.4	32.3	32.8	31.8	29.0	29.0	29.7	28.7
±	0.12	0.12	0.12	0.12	0.11	0.11	0.11	0.11
Al2O3	0.0	0.0	0.0	0.2	0.2	0.2	0.1	0.2
±	0.05	0.01	0.01	0.01	0.01	0.01	0.01	0.01
La2O3	0.1	0.0	0.0	0.1	0.1	0.1	0.1	0.0
±	0.11	0.11	0.06	0.11	0.07	0.06	0.07	0.06
Ce2O3	0.1	0.1	0.1	0.1	0.1	0.1	0.1	0.0
±	0.07	0.07	0.07	0.06	0.15	0.06	0.20	0.05
Gd2O3	0.2	0.0	0.0	0.0	0.2	0.2	0.1	0.3
±	0.03	0.03	0.03	0.03	0.04	0.04	0.03	0.04
TiO2	0.0	0.0	0.0	0.0	0.1	0.1	0.1	0.1
±	0.00	0.06	0.01	0.01	0.02	0.02	0.02	0.02
CaO	0.0	0.1	0.0	0.0	0.2	0.3	0.1	0.3
±	0.01	0.01	0.01	0.01	0.01	0.01	0.01	0.01
ThO2	0.0	0.1	0.0	0.1	0.3	0.3	0.4	0.3
±	0.03	0.03	0.05	0.04	0.04	0.04	0.04	0.04
ZrO2	58.3	62.6	61.7	62.4	53.8	53.3	55.9	54.3
±	0.47	0.49	0.49	0.49	0.46	0.45	0.47	0.46
P2O5	0.5	0.7	0.4	0.5	0.8	0.6	0.9	0.6
±	0.03	0.03	0.02	0.03	0.03	0.03	0.03	0.03

Y ₂ O ₃	5.2	2.1	2.1	1.8	6.4	6.0	5.4	5.7
±	0.11	0.07	0.07	0.07	0.12	0.11	0.11	0.11
Nd ₂ O ₃	0.0	0.0	0.0	0.0	0.1	0.1	0.0	0.0
±	0.03	0.02	0.02	0.02	0.03	0.03	0.03	0.03
Pr ₂ O ₃	0.0	0.0	0.1	0.1	0.1	0.1	0.1	0.1
±	0.05	0.03	0.05	0.08	0.15	0.15	0.15	0.15
Eu ₂ O ₃	0.0	0.0	0.0	0.0	0.0	0.0	0.0	0.0
±	0.03	0.01	0.07	0.07	0.07	0.07	0.07	0.07
Dy ₂ O ₃	0.6	0.2	0.2	0.1	0.8	0.8	0.7	0.7
±	0.03	0.03	0.03	0.03	0.03	0.03	0.03	0.03
Ho ₂ O ₃	0.0	0.0	0.0	0.1	0.1	0.1	0.2	0.2
±	0.05	0.05	0.05	0.05	0.05	0.05	0.05	0.05
Lu ₂ O ₃	0.1	0.1	0.1	0.1	0.1	0.1	0.1	0.0
±	0.03	0.03	0.03	0.03	0.01	0.02	0.01	0.01
UO ₂	0.1	0.1	0.0	0.2	0.1	0.2	0.2	0.1
±	0.03	0.03	0.03	0.03	0.03	0.03	0.03	0.03
Sm ₂ O ₃	0.1	0.1	0.1	0.1	0.2	0.2	0.2	0.2
±	0.03	0.03	0.03	0.03	0.03	0.03	0.03	0.03
Tb ₂ O ₃	0.0	0.0	0.0	0.0	0.1	0.1	0.1	0.1
±	0.02	0.02	0.03	0.06	0.02	0.02	0.02	0.02
FeO	0.0	0.3	0.1	0.4	0.1	0.2	0.1	0.2
±	0.01	0.01	0.01	0.01	0.01	0.01	0.01	0.01
Er ₂ O ₃	0.6	0.3	0.3	0.3	0.7	0.7	0.7	0.6
±	0.03	0.03	0.03	0.03	0.03	0.03	0.03	0.03
Tm ₂ O ₃	0.1	0.1	0.1	0.1	0.1	0.1	0.1	0.1
±	0.03	0.03	0.03	0.03	0.02	0.02	0.02	0.02
Yb ₂ O ₃	0.7	0.5	0.5	0.5	0.7	0.7	0.7	0.6

±	0.02	0.02	0.02	0.02	0.02	0.02	0.02	0.02
PbO	0.0	0.1	0.0	0.1	0.1	0.4	0.2	0.2
±	0.03	0.03	0.03	0.03	0.04	0.04	0.04	0.04
Total	100.2	100.6	99.9	99.7	95.5	94.9	97.1	95.0
Point	HDA19_a 44_05	HDA19_01	HDA19_02	HDA19_03				
Type	qtz.vein	qtz.vein	qtz.vein	qtz.vein				
HfO2	0.7	1.0	1.0	0.9				
±	0.05	0.06	0.06	0.05				
SiO2	29.3	31.1	31.2	30.7				
±	0.11	0.12	0.12	0.12				
Al2O3	0.1	0.6	0.7	0.5				
±	0.01	0.01	0.02	0.01				
La2O3	0.0	0.0	0.2	0.2				
±	0.07	0.03	0.11	0.29				
Ce2O3	0.0	0.1	0.1	0.0				
±	0.08	0.07	0.07	0.07				
Gd2O3	0.2	0.3	0.2	0.2				
±	0.03	0.04	0.03	0.04				
TiO2	0.1	0.2	0.2	0.2				
±	0.02	0.02	0.02	0.02				
CaO	0.2	0.2	0.4	0.3				
±	0.01	0.01	0.01	0.01				
ThO2	0.4	0.3	0.2	0.6				
±	0.04	0.04	0.03	0.04				
ZrO2	54.9	54.7	55.0	52.9				
±	0.46	0.46	0.46	0.45				
P2O5	0.8	0.4	0.2	0.6				

±	0.03	0.03	0.02	0.03				
Y ₂ O ₃	5.6	5.3	4.4	5.6				
±	0.11	0.11	0.10	0.11				
Nd ₂ O ₃	0.0	0.2	0.3	0.2				
±	0.02	0.03	0.03	0.03				
Pr ₂ O ₃	0.1	0.0	0.1	0.1				
±	0.15	0.05	0.05	0.08				
Eu ₂ O ₃	0.0	0.0	0.0	0.0				
±	0.02	0.02	0.02	0.02				
Dy ₂ O ₃	0.8	0.6	0.4	0.6				
±	0.03	0.03	0.03	0.03				
Ho ₂ O ₃	0.1	0.2	0.1	0.2				
±	0.05	0.05	0.05	0.05				
Lu ₂ O ₃	0.1	0.1	0.1	0.1				
±	0.02	0.03	0.03	0.03				
UO ₂	0.1	0.1	0.0	0.1				
±	0.03	0.03	0.03	0.03				
Sm ₂ O ₃	0.2	0.3	0.2	0.2				
±	0.03	0.03	0.03	0.03				
Tb ₂ O ₃	0.1	0.1	0.0	0.0				
±	0.02	0.02	0.02	0.02				
FeO	0.0	0.2	0.3	0.2				
±	0.01	0.01	0.01	0.01				
Er ₂ O ₃	0.7	0.6	0.5	0.6				
±	0.03	0.03	0.03	0.03				
Tm ₂ O ₃	0.1	0.2	0.1	0.1				
±	0.02	0.03	0.03					

Yb2O3	0.7	0.6	0.6	0.7				
±	0.02	0.02	0.02	0.02				
PbO	0.1	0.1	0.2	0.1				
±	0.04	0.03	0.03	0.03				
Total	95.6	97.7	97.2	96.1				

LA-ICP-MS analyses of zircons from Dyaheen

	LOD ppm	HDA7_N11_01	HDA7_N11_02	HDA7_N11_03	HDA7_N11_04_1	HDA10_a37_01	HDA10_a37_02	HDA10_a37_03	HDA10_a37_04	HDA9_P9_01	HDA9_P9_02
Li_ppm_m7	1	58	17	63	31	6	6	8	10	1	1
Al_ppm_m27	12	223	1160	690	640	898	56	360	109	2	1
Si_ppm_m29	1064	135000	135000	137000	160000	163000	162000	188000	153000	178000	137000
P_ppm_m31	29	1420	860	1150	1430	790	677	670	580	29	29
Sc_ppm_m45	1	564	554	582	584	599	560	592	578	592	595
Ti_ppm_m48	1	57	428	2190	900	50	25	38	26	35	32
Fe_ppm_m57	48	7200	62300	14400	9700	69300	7300	7400	400	48	48
Y_ppm_m89	1	9600	12490	17800	21900	5740	8010	8940	8580	5150	5480
Nb_ppm_m93	1	545	8560	11900	17500	999	319	485	427	503	317
Sn_ppm_m120	1	7	121	79	63	82	10	23	14	257	114
La_ppm_m139	1	25	220	272	320	48	8	1200	15	0	1
Ce_ppm_m140	1	174	1246	1910	1620	243	150	2900	172	3	1
Pr_ppm_m141	1	12	159	255	219	19	4	310	6	0	0
Nd_ppm_m146	1	45	739	1190	1083	85	16	1280	23	2	1
Sm_ppm_m147	1	21	376	524	551	44	17	310	19	14	12
Eu_ppm_m153	1	2	21	33	34	4	1	22	4	0	0

Gd_ppm_m157	1	44	447	619	690	96	77	300	112	97	109
Tb_ppm_m159	1	19	140	177	204	37	41	65	53	46	49
Dy_ppm_m163	1	358	1263	1630	1930	442	517	660	724	508	569
Ho_ppm_m165	1	178	337	433	511	178	212	239	241	158	182
Er_ppm_m167	1	1019	1440	1800	2100	880	1191	1260	1140	693	775
Tm_ppm_m169	1	281	315	377	459	182	275	309	238	144	149
Yb_ppm_m171	1	2660	2860	3070	3860	1630	2480	2960	2010	1180	1283
Lu_ppm_m175	1	336	398	380	482	237	354	392	279	167	198
Hf_ppm_m177	1	3230	3770	3410	3370	6260	5670	5880	5930	12200	11600
Ta_ppm_m181	1	284	413	478	999	90	76	56	84	128	102
Pb_ppm_m208	1	840	1470	1290	1570	1040	370	410	113	1	1
Th_ppm_m232	1	4100	2670	4830	26200	660	835	790	1460	22	25
U_ppm_m238	1	7000	5280	6440	10500	1295	1105	718	1470	421	338

Continue zircon LA-ICP-MS analyses

	HDA9_p9_03	HDA9_p9_04	HDA9_Zrm1_01	HDA9_Zrm1_02	HDA9_Zrm2_01	HDA9_Zrm2_02	HDA9_Zrm3_01	HDA9_Zrm3_02
Li_ppm_m7	0	2	0	1	1	1	1	0
Al_ppm_m27	2	6	2	10	1	22	5	12
Si_ppm_m29	139000	171000	165000	164000	147000	150000	181000	162000
P_ppm_m31	29	29	61	58	30	29	29	40
Sc_ppm_m45	592	587	600	636	574	581	608	624
Ti_ppm_m48	29	116	30	29	30	48	47	79
Fe_ppm_m57	48	63	48	68	48	48	48	84
Y_ppm_m89	6010	6460	6170	6510	6620	7260	7620	6480

Nb_ppm_m93	272	615	320	476	262	410	530	663
Sn_ppm_m120	76	168	7	7	12	25	121	188
La_ppm_m139	1	1	3	4	5	72	1	3
Ce_ppm_m140	1	2	11	30	49	125	4	6
Pr_ppm_m141	0	1	1	2	5	20	1	1
Nd_ppm_m146	1	10	3	11	26	72	3	3
Sm_ppm_m147	11	59	4	6	15	21	22	16
Eu_ppm_m153	0	1	0	0	1	2	1	1
Gd_ppm_m157	117	224	68	79	50	83	177	124
Tb_ppm_m159	58	79	46	44	40	56	82	62
Dy_ppm_m163	637	771	548	552	610	703	894	676
Ho_ppm_m165	203	215	174	178	224	237	257	202
Er_ppm_m167	872	821	727	787	1024	1008	1027	835
Tm_ppm_m169	170	145	149	145	207	191	199	154
Yb_ppm_m171	1459	1180	1294	1310	1690	1630	1620	1290
Lu_ppm_m175	223	168	184	178	240	217	223	191
Hf_ppm_m177	11060	11000	10800	10900	10100	10370	9900	10800
Ta_ppm_m181	107	121	116	89	97	56	77	113
Pb_ppm_m208	1	4	1	1	1	4	3	2
Th_ppm_m232	23	74	15	21	18	50	46	37
U_ppm_m238	338	778	283	417	533	502	473	369

EMPA analyses of pyrochlore from Dyaheen. Limit of detection is ppm element. \pm is 1σ standard deviation.

Comment	LOD (ppm element)	HDA1_a42_pcl_01	HDA1_a42_pcl_02	HDA1_a43_pcl_01	HDA8_PCL_2_01	HDA8_PCL_2_03	HDA8_PCL_1_01	HDA8_PCL_1_03
F	2493	0.3	0.1	0.1	0.3	0.0	0.0	0.4
\pm		0.1	0.1	0.1	0.3	0.0	0.0	0.4
SiO ₂	305	6.2	2.4	0.1	6.6	7.6	2.3	7.7
\pm		0.0	0.0	0.0	0.0	0.0	0.0	0.0
Na ₂ O	403	0.2	0.2	0.8				
\pm		0.0	0.0	0.0	0.0	0.0	0.0	0.0
MgO	122	0.0	0.0	0.0		0.0	0.0	0.0
\pm		0.0	0.0	0.0	0.0	0.0	0.0	0.0
La ₂ O ₃	1688	0.4	0.9	3.4	0.6	0.2	0.9	0.3
\pm		0.1	0.1	0.1	0.0	0.0	0.1	0.0
Ce ₂ O ₃	1447	4.3	4.0	9.6	2.0	0.8	3.6	1.8
\pm		0.1	0.1	0.1	0.3	0.3	0.4	0.4
Gd ₂ O ₃	804	0.1	0.1	0.2	1.8	0.3	0.4	0.5
\pm		0.0	0.0	0.0	0.1	0.0	0.0	0.0
TiO ₂	306	2.7	2.6	3.7	0.9	0.6	4.4	4.3
\pm		0.0	0.0	0.0	0.0	0.0	0.2	0.2
CaO	179	3.9	2.5	3.4	2.7	1.6	2.7	2.0
\pm		0.02	0.01	0.02	0.02	0.02	0.02	0.02
ThO ₂	489	0.0	0.0	0.0	4.1	2.8		0.0
\pm		0.02	0.00	0.02	0.06	0.05	0.00	0.03
Nb ₂ O ₅	441	29.5	35.6	59.8	44.2	32.6	37.7	29.4
\pm		0.12	0.13	0.17	0.22	0.17	0.19	0.17
Y ₂ O ₃	438	0.1	0.1	0.1	11.0	1.4	0.7	2.0
\pm		0.01	0.06	0.02	0.18	0.03	0.00	0.01
Nd ₂ O ₃	441	0.5	1.2	2.6	2.4	0.7	1.8	1.1
\pm		0.16	0.34	1.15	0.02	0.02	0.08	0.02
Pr ₂ O ₃	992	0.1	0.3	0.9	0.4	0.1	0.5	0.2
\pm		0.00	0.01	0.01	0.01	0.00	0.01	0.01
Eu ₂ O ₃	513	0.0	0.0	0.0	0.1	0.0		0.0
\pm		0.00	0.00	0.00	0.01	0.00	0.00	0.00
Dy ₂ O ₃	519	0.1	0.0	0.1	2.7	0.5	0.3	0.6
\pm		0.09	0.00	0.01	0.29	0.31	0.06	0.19
Ho ₂ O ₃	1045	0.0	0.0	0.0	0.5	0.1	0.1	0.0
\pm		0.00	0.03	0.00	0.01	0.00	0.00	0.00
Lu ₂ O ₃	588	0.0	0.0	0.0				0.0
\pm		0.00	0.00	0.00	0.00	0.00	0.00	0.05
UO ₂	396	2.5	1.9	2.8	1.0	2.0	3.1	3.7
\pm		2.48	8.24	2.75	0.08	31.28	53.83	0.99

Ta2O5	628	5.9	3.4	4.8	1.8	1.9	2.5	2.5
±		0.06	0.04	0.04	0.03	0.03	0.04	0.04
MnO	369	0.0	0.0	0.1	1.7	0.1	0.9	0.1
±		0.00	0.00	0.00	0.09	0.01	50.90	0.02
Sm2O3	800	0.2	0.3	0.4	1.6	0.4	0.5	0.5
±		0.01	0.03	0.41	0.04	0.01	0.01	0.00
Tb2O3	471	0.0	0.0	0.0	0.4	0.1	0.0	0.1
±		0.00	0.00	0.00	0.00	0.01	0.00	0.01
Fe2O3	205	3.2	2.7	1.5	3.1	2.1	0.8	1.6
±		0.34	0.18	0.08	0.07	0.14	0.04	0.08
Er2O3	458	0.0	0.0	0.0	1.5	0.2	0.0	0.3
±		0.00	0.01	0.00	0.08	0.05	0.52	0.09
Tm2O3	454	0.1	0.1	0.1	0.2	0.0	0.1	0.1
±		0.00	0.00	0.00	0.00	0.00	0.03	0.01
Yb2O3	445	0.0	0.0	0.0	0.9	0.3	0.1	0.4
±		0.04	0.07	0.02	0.05	0.07	0.01	0.06
PbO	410	33.3	37.5	3.8	1.6	43.1	30.3	36.8
±		3.41	7.06	0.55	0.03	2.31	4.00	1.53
SnO2	223	0.0	0.0	0.0	0.1	0.0	0.1	0.1
±		0.00	0.00	0.00	0.00	0.00	0.00	0.00
SrO	500	0.1	0.0	0.1	0.0	0.0	0.0	0.0
Total		93.71	95.93	98.45	94.03	99.42	93.63	96.35
Comment	HDA8_PCL 1_04	HDA8_PCL 1_05	HDA10_a3 8_pcl_01	HDA10_a3 8_pcl_02	HDA10_a3 8_pcl_03	HDA10_a3 8_pcl_04	HDA10_a3 8_pcl_05	HDA10_a3 8_pcl_06
F	0.7	0.2	0.0	0.0	0.1	0.0	0.2	0.1
±	0.7	0.2	0.0	0.0	0.1	0.0	0.1	0.1
SiO2	8.2	7.8	6.4	5.5	6.5	0.0	5.3	0.6
±	0.0	0.0	0.0	0.0	0.0	0.0	0.0	0.0
Na2O			0.0	0.0	0.0	0.4	0.0	0.4
±	0.0	0.0	0.0	0.0	0.0	0.0	0.0	0.0
MgO	0.0		0.0	0.0	0.0	0.0	0.0	0.0
±	0.0	0.0	0.0	0.0	0.0	0.0	0.0	0.0
La2O3	0.4	0.6	0.3	0.7	0.5	2.3	0.7	2.0
±	0.0	0.0	0.1	0.1	0.1	0.1	0.1	0.1
Ce2O3	2.1	2.9	2.7	3.5	3.0	9.4	3.7	7.9
±	0.5	0.4	0.1	0.1	0.1	0.1	0.1	0.1
Gd2O3	0.4	1.8	0.8	0.8	0.7	0.5	1.3	0.5
±	0.0	0.1	0.0	0.0	0.0	0.0	0.0	0.0
TiO2	3.4	2.9	4.8	5.3	4.8	6.3	7.8	5.6
±	0.2	0.1	0.0	0.0	0.0	0.0	0.0	0.0
CaO	2.5	2.1	2.4	3.0	2.4	9.2	3.1	8.6
±	0.02	0.02	0.01	0.02	0.01	0.03	0.02	0.02

ThO2	0.1	1.1	0.0	0.0	0.0	0.1	0.1	0.0
±	0.03	0.04	0.00	0.02	0.02	0.02	0.02	0.02
Nb2O5	27.7	38.0	33.6	35.6	35.0	53.1	37.5	51.6
±	0.16	0.20	0.13	0.13	0.13	0.16	0.14	0.16
Y2O3	1.9	9.5	4.4	5.6	4.9	0.6	7.4	0.7
±	0.01	0.07	0.15	0.20	0.27	0.07	0.30	0.07
Nd2O3	0.9	2.8	1.5	2.0	1.8	4.3	2.4	3.5
±	0.02	0.03	0.02	0.03	0.03	0.20	0.03	0.15
Pr2O3	0.3	0.5	0.3	0.5	0.4	1.2	0.6	0.9
±	0.01	0.01	0.01	0.01	0.01	0.01	0.01	0.01
Eu2O3		0.1	0.0	0.0	0.0	0.1	0.1	0.1
±	0.00	0.01	0.00	0.00	0.00	0.00	0.00	0.00
Dy2O3	0.5	2.5	1.3	1.1	1.1	0.9	2.1	0.9
±	0.53	0.22	0.20	0.11	0.13	0.05	0.16	0.06
Ho2O3	0.1	0.5	0.2	0.2	0.2	0.0	0.4	0.0
±	0.00	0.01	0.00	0.00	0.00	0.00	0.00	0.00
Lu2O3	0.0	0.1	0.0	0.0	0.0	0.0	0.0	0.0
±	0.00	0.00	0.00	0.00	0.00	0.00	0.00	0.00
UO2	3.3	1.9	2.3	2.7	4.0	2.3	1.3	3.1
±	1.18	0.14	0.28	0.41	0.61	0.86	0.11	1.63
Ta2O5	2.7	0.8	1.6	1.7	1.6	1.2	1.8	2.3
±	0.04	0.03	0.02	0.02	0.01	0.01	0.03	0.02
MnO	0.1	0.3	0.1	0.1	0.1	2.3	0.0	2.0
±	0.03	0.02	0.00	0.00	0.00	0.06	0.00	0.03
Sm2O3	0.4	1.6	0.7	0.8	0.8	1.0	1.2	0.9
±	0.00	0.02	0.07	0.07	0.08	0.18	0.07	0.13
Tb2O3	0.1	0.4	0.2	0.2	0.1	0.1	0.3	0.0
±	0.01	0.01	0.01	0.02	0.01	0.00	0.47	0.00
Fe2O3	2.3	1.7	1.5	2.1	2.6	1.3	1.6	1.1
±	0.14	0.04	0.05	0.06	0.08	0.03	0.03	0.03
Er2O3	0.3	1.2	0.6	0.6	0.5	0.1	1.0	0.1
±	0.07	0.07	0.06	0.05	0.07	0.02	0.05	0.03
Tm2O3	0.1	0.2	0.1	0.1	0.1	0.1	0.2	0.0
±	0.01	0.00	0.00	0.00	0.00	0.00	0.00	0.00
Yb2O3	0.3	0.8	0.4	0.4	0.3	0.1	0.6	0.1
±	0.06	0.04	0.01	0.01	0.01	0.01	0.01	0.02
PbO	36.3	11.8	30.4	22.8	24.7	2.2	14.9	6.2
±	1.51	0.26	2.71	2.15	2.43	0.26	0.97	0.82
SnO2	0.1	0.1	0.1	0.1	0.2	0.1	0.1	0.1
±	0.00	0.00	0.00	0.00	0.01	0.01	0.00	0.01
SrO	0.0	0.0	0.0	0.0	0.0	0.3	0.0	0.3
Total	95.21	93.98	96.54	95.40	96.26	99.35	95.39	99.37

Comment	HDA10_PC L1_LIGHT_ 01	HDA10_PC L1_LIGHT_ 02	HDA10_PC L1_DARK_ 01	HDA10_PC L1_DARK_ 02	HDA19_a4 9_pcl_01	HDA24_4_ 07		
F	0.1	0.1	0.2	0.1	0.1	0.2		
±	0.1	0.1	0.2	0.1	0.1	0.2		
SiO2	5.4	4.8	5.5	6.5	1.2	8.1		
±	2.5	8.7	5.5	6.5	0.0	0.0		
Na2O					0.0			
±	0.0	0.0	0.0	0.0	0.0	0.0		
MgO	0.0	0.0			0.0	0.0		
±	0.0	0.0	0.0	0.0	0.0	0.0		
La2O3	0.4	0.7	0.7	0.5	1.5	0.2		
±	0.0	0.0	0.0	0.0	0.1	0.0		
Ce2O3	2.8	3.1	3.4	3.4	6.6	0.8		
±	0.1	0.1	0.1	0.1	0.1	0.2		
Gd2O3	0.7	0.6	0.9	0.8	0.6	0.7		
±	0.0	0.0	0.0	0.0	0.0	0.1		
TiO2	4.7	4.8	5.7	5.5	4.7	0.8		
±	2.0	1.4	4.1	2.7	0.0	0.0		
CaO	2.2	2.2	2.5	2.4	5.2	2.7		
±	0.01	0.01	0.01	0.01	0.02	0.02		
ThO2	0.1	0.1	0.0	0.1	0.1	0.8		
±	0.00	0.00	0.00	0.00	0.02	0.04		
Nb2O5	31.8	34.6	34.1	35.0	44.5	33.9		
±	0.52	0.66	0.46	0.46	0.15	0.18		
Y2O3	3.7	2.8	5.2	5.5	0.4	6.6		
±	0.07	0.05	0.08	0.09	0.05	0.13		
Nd2O3	1.4	1.6	1.9	2.0	3.4	0.6		
±	0.17	0.16	0.17	0.15	0.24	0.01		
Pr2O3	0.3	0.4	0.5	0.5	0.8	0.1		
±	0.05	0.06	0.06	0.08	0.01	0.00		
Eu2O3	0.0	0.0	0.1	0.0	0.1			
±	0.00	0.00	0.00	0.00	0.00	0.00		
Dy2O3	1.0	0.8	1.4	1.0	0.5	1.4		
±	0.37	0.37	0.19	0.16	0.03	1.00		
Ho2O3	0.1	0.1	0.3	0.3	0.0	0.4		
±	0.02	0.03	0.04	0.06	0.00	0.01		
Lu2O3	0.0		0.0		0.0	0.1		
±	0.00	0.00	0.00	0.00	0.00	0.01		
UO2	2.0	2.3	2.1	3.7	2.8	1.4		
±	0.29	0.74	0.21	0.54	13.12	0.13		
Ta2O5	1.7	1.8	2.0	1.8	2.3	0.9		
±	0.02	0.02	0.03	0.02	0.02	0.03		

MnO	0.1	0.1	0.1	0.1	0.7	0.2		
±	0.01	0.01	0.01	0.01	0.01	0.01		
Sm2O3	0.7	0.7	0.9	0.7	0.9	0.4		
±	0.03	0.03	0.03	0.03	0.13	0.01		
Tb2O3	0.2	0.1	0.2	0.1	0.0	0.1		
±	0.02	0.02	0.02	0.02	0.00	0.01		
Fe2O3	0.9	0.9	1.6	2.6	0.2	1.2		
±	0.04	0.05	0.05	0.10	0.01	0.08		
Er2O3	0.5	0.4	0.7	0.5	0.0	1.1		
±	0.06	0.07	0.07	0.06	0.01	0.15		
Tm2O3	0.1	0.0	0.1	0.1	0.0	0.2		
±	0.00	0.00	0.00	0.00	0.00	0.00		
Yb2O3	0.3	0.3	0.5	0.3	0.1	1.3		
±	0.00	0.00	0.00	0.00	0.09	0.12		
PbO	31.0	29.8	24.4	22.5	17.8	31.9		
±	0.12	0.12	0.11	0.10	2.72	0.47		
SnO2	0.1	0.1	0.1	0.1	0.0			
±	0.01	0.01	0.01	0.01	0.00	0.00		
SrO	0.0	0.0	0.0	0.0	0.0	0.0		
Total	91.91	93.14	95.09	96.14	94.50	96.08		

EMP analyses of fergusonite from Dyaheen. Limit of detection is ppm element. ± is 1 σ standard deviation

Comment	LOD	HDA24_4_02	HDA24_4_03	HDA24_4_04	HDA24_4_05	HDA24_4_06	HDA24_1_01
Note		core	next_dark	next_light	alt	alt	
F	2626	0.0	0.1		0.0	0.4	0.0
±		0.1	0.3	0.0	0.1	0.9	0.0
SiO2	353					0.6	
±		0.0	0.0	0.0	0.0	0.5	0.0
Na2O	594						
±		0.0	0.0	0.0	0.0	0.0	0.0
MgO	143						
±		0.0	0.0	0.0	0.0	0.0	0.0
La2O3	1697	0.1	0.3	0.2	0.3		0.1

	±	0.1	0.1	0.1	0.1	0.0	0.1
Ce2O3	1353	0.3	1.4	0.7	1.2	0.3	0.8
	±	0.0	0.2	0.1	0.1	0.0	0.1
Gd2O3	842	2.2	3.0	3.1	2.4	0.8	2.4
	±	0.1	0.1	0.1	0.1	0.0	0.1
TiO2	287	0.9	0.9	1.1	0.9	1.0	1.0
	±	0.0	0.0	0.0	0.0	0.0	0.0
CaO	181	0.1	0.2	0.1	0.1	0.9	0.0
	±	0.0	0.0	0.0	0.0	0.1	0.0
ThO2	475	0.4	0.5	0.3	0.6	0.8	0.4
	±	0.0	0.0	0.0	0.0	0.1	0.0
Nb2O5	465	48.2	46.7	46.8	46.9	43.1	47.2
	±	0.2	0.2	0.2	0.2	0.2	0.2
Y2O3	497	30.2	27.1	28.4	28.1	29.4	29.5
	±	0.2	0.2	0.2	0.2	0.2	0.2
Nd2O3	516	0.5	1.4	1.0	1.3	0.2	0.8
	±	0.0	0.1	0.0	0.0	0.0	0.0
Pr2O3	968		0.2	0.1	0.2	0.0	0.1
	±	0.0	0.1	0.1	0.1	0.0	0.1
Eu2O3	518	0.1	0.1	0.1	0.1		0.0
	±	0.0	0.0	0.0	0.0	0.0	0.0
Dy2O3	533	5.8	5.9	6.3	5.3	3.2	5.5
	±	0.0	0.0	0.0	0.0	0.0	0.0
Ho2O3	1290	1.3	1.3	1.3	1.2	0.9	1.2
	±	0.0	0.0	0.1	0.0	0.0	0.0
Lu2O3	660	0.0			0.0	0.3	0.0
	±	0.0	0.0	0.0	0.0	0.0	0.0
UO2	387	0.8	0.9	0.6	0.9	2.0	1.0
	±	0.0	0.0	0.0	0.0	0.1	0.0

Ta2O5	710	1.1	0.5	0.4	0.5	0.8	0.8
	±	0.1	0.0	0.0	0.0	0.0	0.0
Continue fergusonite analyses							
MnO	258					0.2	
	±	0.0	0.0	0.0	0.0	0.2	0.0
Sm2O3	823	0.8	1.2	1.2	1.1	0.4	1.0
	±	0.0	0.0	0.0	0.0	0.0	0.0
Tb2O3	537	0.7	0.8	0.8	0.6	0.3	0.7
	±	0.0	0.0	0.0	0.0	0.0	0.0
FeO	205	0.0	0.0		0.0	0.1	
	±	0.0	0.0	0.0	0.0	0.2	0.0
Er2O3	487	3.7	3.2	3.4	3.3	3.4	3.3
	±	0.0	0.0	0.0	0.0	0.0	0.0
Tm2O3	489	0.5	0.4	0.4	0.4	0.6	0.4
	±	0.0	0.0	0.0	0.0	0.0	0.0
Yb2O3	483	1.9	1.5	1.5	1.9	4.0	1.8
	±	0.0	0.0	0.0	0.0	0.0	0.0
PbO	4333	0.6	0.5	0.5	0.5	0.7	0.6
	±	0.0	0.0	0.0	0.0	0.0	0.0
SnO2	0		0.0	0.0		0.0	
	±	0.0	0.0	0.0	0.0	0.0	0.0
Total		100.1	98.0	98.4	98.2	94.5	98.8

EMP analyses of gadolinite from Dyaheen. Limit of detection is ppm element. ± is 1 σ standard deviation

Comment	LOD	HDA10_a39_01	HDA10_a39_03	HDA10_a39_05	HDA24_3_01	HDA24_3_02	HDA24_3_03
F	2478	0.0	0.0	0.0	1.7	0.1	0.1
±		0.0	0.0	0.0	1.3	0.1	0.1
SiO2	306	24.8	24.9	24.9	25.8	26.1	24.5

±		0.7	0.7	0.7	0.7	0.7	0.6
Al ₂ O ₃	179	0.0	0.0	0.0	1.6	0.0	0.0
±		0.0	0.0	0.0	1.3	0.0	0.0
La ₂ O ₃	1605	1.4	1.3	1.5	1.3	1.6	1.8
±		0.9	0.8	0.9	0.8	1.0	1.1
Ce ₂ O ₃	1264	4.3	3.8	4.2	3.4	4.1	5.0
±		2.6	2.3	2.5	2.0	2.5	3.1
Gd ₂ O ₃	756	1.1	0.9	1.1	1.6	1.6	3.1
±		0.4	0.4	0.4	0.6	0.6	1.3
CaO	176	0.9	1.0	0.8	3.0	3.3	1.8
±		0.1	0.1	0.1	0.3	0.4	0.2
ThO ₂	465	0.0	0.0	0.0	0.1	0.2	0.0
±		0.0	0.0	0.0	0.1	0.1	0.0
Y ₂ O ₃	424	29.9	30.0	29.9	30.2	25.8	26.4
±		0.3	0.3	0.3	0.3	0.2	0.2
Nd ₂ O ₃	505	1.3	1.1	1.3	1.6	2.3	3.4
±		0.8	0.7	0.8	1.0	1.4	2.1
Pr ₂ O ₃	302	0.4	0.3	0.4	0.4	0.6	0.7
±		0.4	0.3	0.5	0.5	0.7	0.8
Eu ₂ O ₃	495	0.0	0.0	0.0	0.0	0.1	0.1
±		0.0	0.0	0.0	0.0	0.0	0.1
Dy ₂ O ₃	505	2.7	2.8	2.8	3.4	3.0	4.3
±		0.1	0.1	0.1	0.1	0.1	0.2
Ho ₂ O ₃	1011	0.9	0.9	0.9	0.8	0.7	0.8
±		2.3	2.2	2.4	2.0	1.8	2.1
Lu ₂ O ₃	570	0.6	0.6	0.6	0.0	0.0	0.1
±		0.4	0.4	0.4	0.0	0.0	0.0
UO ₂	381	0.0	0.0	0.0	0.1	0.0	0.0
±		0.0	0.0	0.0	0.1	0.0	0.0
Sm ₂ O ₃	785	0.6	0.6	0.6	0.8	0.9	1.6
±		0.2	0.2	0.2	0.2	0.2	0.4
Tb ₂ O ₃	456	0.3	0.3	0.3	0.4	0.4	0.7
±		0.3	0.3	0.3	0.4	0.4	0.7
FeO	201	9.1	8.8	8.7	7.8	6.1	7.7
±		0.1	0.1	0.1	0.1	0.1	0.1
Er ₂ O ₃	447	3.8	3.9	3.9	2.3	2.0	2.0
±		1.0	1.0	1.0	0.6	0.5	0.5
Tm ₂ O ₃	445	0.7	0.8	0.7	0.3	0.3	0.2
±		1.1	1.1	1.0	0.5	0.4	0.3
Yb ₂ O ₃	433	4.8	5.1	4.9	1.8	1.5	0.9
±		0.7	0.7	0.7	0.3	0.2	0.1
PbO	380	0.3	0.3	0.3	0.3	1.0	0.3
±		0.3	0.3	0.4	0.3	1.1	0.3

Nb2O5	91				0.2	0.1	0.1
±		0.0	0.0	0.0	0.0	0.0	0.0
TiO2	300				0.0	0.0	0.0
±		0.0	0.0	0.0	0.0	0.0	0.0
Ta2O5	760				0.0	0.0	0.2
±		0.0	0.0	0.0	0.0	0.0	0.5
WO3	23				0.2	0.1	0.3
±		0.0	0.0	0.0	0.1	0.1	0.2
MnO	262				0.0	1.1	0.8
±		0.0	0.0	0.0	0.0	0.2	0.2
Total		98.2	97.7	98.1	99.9	93.8	97.1
Comment	LOD	HDA24_3_04	HDA24_3_05	HDA24_3_06	HDA24_1_02	HDA24_1_03	HDA24_1_04
F	2478	0.1	0.1	0.0			
±		0.1	0.0	0.0	0.0	0.0	0.0
SiO2	306	25.6	24.6	26.4	25.2	25.0	25.2
±		0.7	0.7	0.7	0.7	0.7	0.7
Al2O3	179	0.0	0.0	0.0	0.0	0.0	0.0
±		0.0	0.0	0.0	0.0	0.0	0.0
La2O3	1605	1.2	1.7	0.7	0.1	0.1	0.1
±		0.8	1.0	0.4	0.1	0.1	0.1
Ce2O3	1264	3.6	5.2	1.6	1.3	2.2	1.5
±		2.2	3.2	1.0	0.8	1.3	0.9
Gd2O3	756	2.8	4.0	2.8	3.5	5.5	3.7
±		1.1	1.6	1.1	1.4	2.2	1.5
CaO	176	3.0	1.4	3.5	3.3	3.6	3.9
±		0.3	0.1	0.4	0.4	0.4	0.4
ThO2	465	0.1	0.0	0.0	1.9	1.7	1.8
±		0.0	0.0	0.0	1.3	1.2	1.2
Y2O3	424	27.5	26.2	29.9	28.6	25.7	27.7
±		0.2	0.2	0.3	0.3	0.2	0.3
Nd2O3	505	2.3	2.9	1.2	2.1	2.9	2.2
±		1.4	1.9	0.8	1.3	1.8	1.4
Pr2O3	302	0.6	0.6	0.2	0.5	0.7	0.5
±		0.7	0.8	0.3	0.6	0.8	0.6
Eu2O3	495	0.1	0.1	0.1	0.1	0.1	0.1
±		0.0	0.1	0.0	0.1	0.0	0.0
Dy2O3	505	4.7	5.6	5.0	5.0	4.9	5.5
±		0.2	0.2	0.2	0.2	0.2	0.2
Ho2O3	1011	0.9	1.0	1.0	0.9	0.9	0.9
±		2.2	2.5	2.6	2.4	2.3	2.4
Lu2O3	570	0.1	0.1	0.1	0.1	0.1	0.1
±		0.0	0.0	0.0	0.0	0.0	0.0

UO2	381	0.0	0.0	0.0	0.0	0.0	0.0
±		0.0	0.0	0.0	0.0	0.0	0.0
Sm2O3	785	1.4	1.8	1.2	1.4	1.7	1.7
±		0.4	0.5	0.3	0.4	0.5	0.4
Tb2O3	456	0.7	0.9	0.7	0.7	0.8	0.9
±		0.7	0.9	0.7	0.8	0.8	0.9
FeO	201	7.5	6.7	7.3	7.4	6.7	6.5
±		0.1	0.1	0.1	0.1	0.1	0.1
Er2O3	447	2.2	2.2	2.4	2.3	1.9	2.1
±		0.6	0.6	0.6	0.6	0.5	0.5
Tm2O3	445	0.2	0.2	0.3	0.2	0.2	0.2
±		0.3	0.3	0.5	0.3	0.3	0.4
Yb2O3	433	0.9	0.6	1.0	1.0	0.7	0.7
±		0.1	0.1	0.1	0.1	0.1	0.1
PbO	380	0.3	0.2	0.3	0.3	0.2	0.3
±		0.3	0.3	0.3	0.3	0.2	0.3
Nb2O5	91	0.1	0.0	0.1	0.1	0.1	0.1
±		0.0	0.0	0.0	0.0	0.0	0.0
TiO2	300	0.0	0.0	0.0	0.1	0.0	0.0
±		0.0	0.0	0.0	0.0	0.0	0.0
Ta2O5	760	0.1	0.3	0.3	0.0	0.1	0.0
±		0.2	0.6	0.5	0.0	0.1	0.1
WO3	23	0.3	0.4	0.2	0.3	0.3	0.4
±		0.1	0.2	0.1	0.2	0.2	0.2
MnO	262	0.9	1.6	1.4	0.0	0.0	0.0
±		0.2	0.4	0.3	0.0	0.0	0.0
Total		97.6	98.9	98.5	97.1	96.6	96.4

EMP analyses of bastnasite from Dyaheen. Limit of detection is ppm element. ± is 1 σ standard deviation

Comment		HDA10_a3 6_01	HDA10_a3 6_02	HDA10_a3 6_04	HDA10_a3 6_06	HDA10_a3 6_07	HDA10_RE E_Si_01	HDA10_RE E_Si_04
F	1279	3.0	5.7	5.5	5.0	5.4	3.2	5.9
±		0.1	0.1	0.1	0.1	0.1	0.1	0.1
SiO2	173	0.1	0.2	0.7	0.8	0.5	0.3	1.2
±		0.0	0.0	0.0	0.0	0.0	0.0	0.0
Al2O3	127	0.0	0.0	0.0	0.0	0.0		0.0
±		0.0	0.0	0.0	0.0	0.0	0.0	0.0
La2O3	1700	10.4	8.4	7.9	7.6	8.2	11.3	12.3
±		0.2	0.2	0.1	0.1	0.1	0.2	0.2
Ce2O3	815	30.5	26.5	25.6	25.0	27.5	30.5	31.2

±		0.3	0.2	0.2	0.2	0.2	0.3	0.3
Gd ₂ O ₃	815	3.0	3.4	3.3	2.7	3.4	2.7	1.7
±		0.0	0.0	0.0	0.0	0.0	0.0	0.0
CaO	187	0.1	4.5	2.2	6.5	4.0	0.5	0.4
±		0.0	0.1	0.0	0.1	0.1	0.0	0.0
ThO ₂	489	0.1	0.3	0.1	0.3	0.3	0.2	0.2
±		0.0	0.0	0.0	0.0	0.0	0.0	0.0
P ₂ O ₅	604	0.1	0.3	0.5	2.7	1.0	0.0	0.0
±		0.1	0.2	0.4	2.0	0.7	0.0	0.0
Y ₂ O ₃	601	2.0	3.1	3.1	5.9	2.8	4.1	0.8
±		0.1	0.1	0.1	0.2	0.1	0.1	0.0
Nd ₂ O ₃	605	16.3	15.0	15.0	13.4	15.7	13.8	13.3
±		0.1	0.1	0.1	0.1	0.1	0.1	0.1
Pr ₂ O ₃	1015	4.1	3.4	3.5	3.3	3.7	3.6	3.7
±		0.1	0.1	0.1	0.1	0.1	0.1	0.1
Eu ₂ O ₃	528	0.1	0.2	0.2	0.2	0.2	0.1	0.1
±		0.0	0.0	0.0	0.0	0.0	0.0	0.0
Dy ₂ O ₃	1065	1.2	1.4	1.3	1.2	1.3	1.3	0.5
±		0.0	0.0	0.0	0.0	0.0	0.0	0.0
Ho ₂ O ₃	1065	0.1	0.1	0.1	0.1	0.2	0.2	0.0
±		0.1	0.1	0.1	0.1	0.1	0.1	0.0
Lu ₂ O ₃	594	0.1	0.0	0.0	0.0	0.0	0.0	0.0
±		0.0	0.0	0.0	0.0	0.0	0.0	0.0
UO ₂	401	0.0	0.0	0.0	0.1	0.1	0.0	0.0
±		0.1	0.0	0.0	0.1	0.1	0.0	0.0
Sm ₂ O ₃	830	4.0	4.1	4.2	3.5	4.3	3.1	2.4
±		0.1	0.1	0.1	0.0	0.1	0.0	0.0
Tb ₂ O ₃	489	0.3	0.3	0.4	0.3	0.3	0.3	0.1
±		0.0	0.0	0.0	0.0	0.0	0.0	0.0
FeO	217	0.0	0.1	3.7	0.1	0.0	0.5	2.3
±		0.0	0.0	0.8	0.0	0.0	0.1	0.5
Er ₂ O ₃	342	0.1	0.3	0.2	0.3	0.2	0.2	0.0
±		0.0	0.1	0.0	0.1	0.1	0.1	0.0
Tm ₂ O ₃	482	0.0	0.1	0.1	0.1	0.0	0.0	0.0
±		0.0	0.0	0.0	0.0	0.0	0.0	0.0
Yb ₂ O ₃	472	0.0	0.1	0.1	0.2	0.1	0.1	0.1
±		0.0	0.0	0.0	0.0	0.0	0.0	0.0
PbO	405	0.0	0.3	0.2	0.8	0.2	0.2	0.2
±		0.0	0.1	0.0	0.1	0.0	0.0	0.0
Total		75.9	77.9	78.0	79.9	79.5	76.3	76.4

EMP analyses of arfvedsonite from Dyaheen. Limit of detection is ppm element. \pm is 1σ standard deviation

Comment	LOD	HDA-34A__02	HDA-34A__03	HDA-34A_rim_04	HDA-26_amph1_01	HDA-26_amph1_02
SiO2	465	50.1	50.1	49.5	51.6	50.7
\pm		0.1	0.1	0.1	0.1	0.1
Al2O3	403	1.0	1.1	1.4	0.2	0.9
\pm		0.0	0.0	0.0	0.0	0.0
F	3592	1.7	1.1	1.3	1.4	1.5
\pm		0.1	0.1	0.1	0.1	0.1
Na2O	400	7.5	7.0	7.3	7.3	7.0
\pm		0.1	0.1	0.1	0.1	0.1
MgO	322	0.8	0.6	0.7	6.5	6.1
\pm		0.0	0.0	0.0	0.1	0.1
CaO	266	0.3	0.3	0.4	1.6	1.7
\pm		0.0	0.0	0.0	0.1	0.1
TiO2	210	0.7	0.7	0.9	0.6	0.6
\pm		0.0	0.0	0.0	0.0	0.0
K2O	225	1.4	1.1	1.3	2.1	2.0
\pm		0.0	0.0	0.0	0.0	0.0
FeO	319	26.5	25.3	26.0	20.7	20.7
\pm		0.1	0.1	0.1	0.1	0.1
Fe2O3		5.9	7.9	6.6	4.4	3.5
\pm		0.0	0.0	0.0	0.0	0.0
MnO	218	1.0	0.9	0.9	0.8	0.8
\pm		0.1	0.1	0.1	0.1	0.1
Total		96.8	96.1	96.2	97.3	95.4
Comment	HDA-26_amph1_04	HDA-26_amph1_05	HDA-26_amph2_01	HDA-26_amph2_02	HDA-35_area2_K_in_amph_03	HDA-30A_area1_amph_01
SiO2	51.9	52.0	52.3	51.5	51.7	50.1
\pm	0.1	0.1	0.1	0.1	0.1	0.1
Al2O3	0.2	0.3	0.3	0.3	1.3	0.8
\pm	0.0	0.0	0.0	0.0	0.0	0.0
F	1.8	1.7	1.6	1.6	2.7	1.0
\pm	0.1	0.1	0.1	0.1	0.2	0.1
Na2O	7.2	7.3	7.5	7.2	8.2	6.8
\pm	0.1	0.1	0.1	0.1	0.1	0.1

MgO	6.9	6.7	6.4	6.3	2.1	0.7
±	0.1	0.1	0.1	0.1	0.0	0.0
CaO	1.5	1.5	1.6	1.9	0.1	0.0
±	0.1	0.0	0.1	0.1	0.0	0.0
TiO2	0.4	0.4	0.5	0.5	0.6	0.1
±	0.0	0.0	0.0	0.0	0.0	0.0
K2O	2.1	2.1	2.1	2.1	1.2	0.6
±	0.0	0.0	0.0	0.0	0.0	0.0
FeO	19.0	19.5	21.4	21.6	26.5	21.7
±	0.1	0.1	0.1	0.1	0.1	0.1
Fe2O3	6.2	6.2	3.8	3.5	0.0	12.4
±	0.0	0.0	0.0	0.0	0.0	0.0
MnO	0.8	0.8	0.7	0.7	1.3	0.6
±	0.1	0.1	0.1	0.1	0.1	0.0
Total	98.0	98.4	98.1	97.2	95.9	94.8
Comment	HDA1_k131 4-amph-4	HDA1_k131 4-amph-5	HDA1_k131 4-amph-6	porphyritic granite	aegirine granite	arfvedsonit e granite
SiO2	51.1	50.7	51.2	49.2	50.6	48.0
±	0.1	0.1	0.1	0.1	0.1	0.1
Al2O3	0.3	0.4	0.3	0.7	1.3	1.1
±	0.0	0.0	0.0	0.0	0.0	0.0
F	2.1	2.4	2.1			
±	0.2	0.2	0.2	0.0	0.0	0.0
Na2O	8.3	8.4	8.4	10.0	8.0	11.2
±	0.1	0.1	0.1	0.1	0.1	0.1
MgO	0.5	0.5	0.5	0.6	4.2	0.5
±	0.0	0.0	0.0	0.0	0.0	0.0
CaO	0.1	0.0	0.0	1.8	4.4	2.0
±	0.0	0.0	0.0	0.1	0.1	0.1
TiO2	0.4	0.5	0.6	0.6	0.3	0.6
±	0.0	0.0	0.0	0.0	0.0	0.0
K2O	2.3	2.3	2.3	2.3	2.6	1.6
±	0.0	0.0	0.0	0.0	0.0	0.0
FeO	28.1	27.1	27.7	10.5	7.7	9.7
±	0.1	0.1	0.1	0.0	0.0	0.0
Fe2O3	0.6	0.8	0.7	22.4	15.0	22.2
±	0.0	0.0	0.0	0.1	0.1	0.1
MnO	1.2	1.4	1.3			
±	0.1	0.1	0.1	0.0	0.0	0.0
Total	95.0	94.6	95.2	98.1	94.1	96.9

EMP analyses of aegirine from Dyaheen. Limit of detection is ppm element. \pm is 1σ standard deviation

Comment	LOD	HDA1_J9-1	HDA1_J9-2	HDA1_J9-3	HDA1_k131 4-aeg-1	HDA1_k131 4-aeg-2	HDA1_k131 4-aeg-3
SiO ₂	272	51.14	51.51	51.81	51.12	51.25	51.33
\pm		0.12	0.12	0.12	0.12	0.12	0.12
Al ₂ O ₃	149	0.27	0.39	0.32	0.27	0.48	0.46
\pm		0.01	0.01	0.01	0.01	0.02	0.02
MgO	137	0.01	0.03	0.03	-0.01	0.02	0.00
\pm		0.02	0.05	0.04	-0.02	0.03	0.00
Na ₂ O	215	12.39	12.65	12.76	12.76	12.71	12.57
\pm		0.10	0.10	0.10	0.10	0.10	0.10
K ₂ O	89	0.01	0.00	-0.01	0.00	-0.01	0.01
\pm		0.02	0.00	-0.02	-0.01	-0.01	0.01
TiO ₂	122	0.71	0.36	0.61	0.70	1.22	1.63
\pm		0.01	0.00	0.01	0.01	0.02	0.02
CaO	113	0.88	0.51	0.11	0.20	0.14	0.15
\pm		0.03	0.01	0.00	0.01	0.00	0.00
ZrO ₂	205	0.24	0.02	0.03	0.77	0.16	0.13
\pm		0.04	0.00	0.00	0.12	0.03	0.02
Fe ₂ O ₃	185	33.04	33.72	33.10	32.93	32.73	32.54
\pm		0.09	0.09	0.09	0.09	0.09	0.09
MnO	102	0.06	0.03	0.07	0.08	0.07	0.09
\pm		0.00	0.00	0.00	0.01	0.00	0.01
ZnO	168	0.02	0.02	0.07	0.05	0.03	0.03
\pm		0.00	0.00	0.02	0.01	0.01	0.01
Total		98.79	99.23	98.90	98.86	98.79	98.93
Comment	HDA10 aeg- 1	HDA10 aeg- 2	HDA10_ aeg-3	HDA8_F13- aeg-1	HDA8_F13- aeg-2	HDA8_F13- aeg-3	HDA8_L14- aeg-1
SiO ₂	50.06	51.73	50.90	50.88	51.47	51.52	51.31
\pm	0.12	0.12	0.12	0.12	0.12	0.12	0.12
Al ₂ O ₃	0.32	0.31	0.35	0.31	0.59	0.35	0.39
\pm	0.01	0.01	0.01	0.01	0.02	0.01	0.01
MgO	0.30	0.54	0.39	0.00	-0.01	0.07	0.00
\pm	0.41	0.75	0.54	-0.01	-0.02	0.09	0.00
Na ₂ O	12.36	12.32	12.19	12.50	12.62	12.86	11.64
\pm	0.10	0.10	0.10	0.10	0.10	0.10	0.09
K ₂ O	0.01	0.00	0.02	0.00	-0.01	0.00	0.00
\pm	0.01	-0.01	0.03	0.00	-0.02	0.00	0.01
TiO ₂	1.37	1.63	0.47	0.74	0.99	1.65	0.29
\pm	0.02	0.02	0.01	0.01	0.01	0.02	0.00

CaO	0.55	0.92	0.87	0.75	0.55	0.28	2.28
±	0.02	0.03	0.02	0.02	0.02	0.01	0.07
ZrO2	0.12	0.29	0.06	0.25	0.09	0.09	0.07
±	0.02	0.05	0.01	0.04	0.01	0.01	0.01
Fe2O3	30.71	30.45	31.97	33.18	33.11	31.44	33.59
±	0.08	0.08	0.09	0.09	0.09	0.09	0.09
MnO	0.36	0.68	0.36	0.06	0.05	0.50	0.10
±	0.02	0.04	0.02	0.00	0.00	0.03	0.01
ZnO	0.36	0.27	0.15	0.01	0.02	0.20	0.05
±	0.08	0.06	0.03	0.00	0.00	0.04	0.01
Total	96.51	99.13	97.72	98.66	99.45	98.95	99.71
Comment	HDA8_L14-aeg-3	HDA8_L14-aeg-4	HDA9-2	HDA9-3	HDA9-z9-1	HDA9-z9-2	HDA9-z9-3
SiO2	52.11	52.03	50.40	50.89	49.79	50.06	49.04
±	0.12	0.12	0.12	0.12	0.12	0.12	0.11
Al2O3	0.40	0.32	0.34	0.45	0.46	0.46	0.48
±	0.01	0.01	0.01	0.02	0.02	0.02	0.02
MgO	0.20	0.24	0.28	0.01	0.01	-0.01	0.00
±	0.28	0.34	0.39	0.01	0.02	-0.01	0.00
Na2O	13.21	12.25	11.22	12.51	12.50	12.63	12.29
±	0.10	0.10	0.09	0.10	0.10	0.10	0.10
K2O	0.00	-0.02	0.00	0.00	0.00	0.00	0.00
±	0.00	-0.03	0.00	0.00	0.00	0.00	0.01
TiO2	0.49	0.58	0.23	0.53	0.76	0.60	0.42
±	0.01	0.01	0.00	0.01	0.01	0.01	0.01
CaO	1.09	0.86	2.21	0.16	0.20	0.12	0.22
±	0.03	0.02	0.06	0.00	0.01	0.00	0.01
ZrO2	0.09	0.14	0.01	0.03	0.07	0.07	0.05
±	0.01	0.02	0.00	0.01	0.01	0.01	0.01
Fe2O3	31.95	31.78	31.70	33.46	32.72	33.06	33.04
±	0.09	0.09	0.09	0.09	0.09	0.09	0.09
MnO	0.58	0.76	1.20	0.06	0.35	0.19	0.17
±	0.04	0.05	0.07	0.00	0.02	0.01	0.01
ZnO	0.23	0.20	0.03	0.03	0.11	0.11	0.07
±	0.05	0.04	0.01	0.01	0.02	0.02	0.02
Total	100.34	99.15	97.62	98.14	96.98	97.29	95.78
Comment	HDA9-wv16_2	HDA9-wv16_3	HDA9-wv16_4	HDA9-wv16_5	HDA9-wv16_6	HDA19-R17_1	HDA19-R17_2
SiO2	50.82	50.00	49.23	50.16	50.88	49.87	49.62
±	0.12	0.12	0.11	0.12	0.12	0.12	0.12
Al2O3	0.50	0.43	0.44	0.48	0.37	0.37	0.37

±	0.02	0.02	0.02	0.02	0.01	0.01	0.01
MgO	0.00	0.00	0.00	0.01	-0.02	0.13	0.11
±	0.00	0.00	0.00	0.01	-0.02	0.18	0.15
Na2O	12.46	12.61	12.40	12.52	12.71	12.88	12.94
±	0.10	0.10	0.10	0.10	0.10	0.10	0.10
K2O	0.00	-0.01	0.00	0.00	0.00	0.00	0.01
±	0.00	-0.01	0.00	0.00	0.01	0.00	0.01
TiO2	0.82	1.13	0.63	0.26	0.74	1.84	1.85
±	0.01	0.02	0.01	0.00	0.01	0.03	0.03
CaO	0.39	0.21	0.15	0.25	0.18	0.14	0.14
±	0.01	0.01	0.00	0.01	0.01	0.00	0.00
ZrO2	0.14	0.18	0.11	0.06	0.04	0.33	0.33
±	0.02	0.03	0.02	0.01	0.01	0.05	0.05
Fe2O3	32.99	31.98	32.93	33.57	32.96	31.06	30.96
±	0.09	0.09	0.09	0.09	0.09	0.09	0.09
MnO	0.05	0.26	0.10	0.11	0.05	0.59	0.60
±	0.00	0.02	0.01	0.01	0.00	0.04	0.04
ZnO	0.01	0.16	0.06	0.05	0.03	0.24	0.23
±	0.00	0.03	0.01	0.01	0.01	0.05	0.05
Total	98.18	96.94	96.04	97.46	97.94	97.44	97.15
Comment	HDA19-Q1011_1	HDA19-Q1011_2	HDA19-Q1011_3	HDA19-Q1011_4	HDA19-Q1011_1	HDA19-Q1011_2	HDA19-Q1011_3
SiO2	49.37	50.34	49.53	49.79	49.37	50.34	49.53
±	0.12	0.12	0.12	0.12	0.12	0.12	0.12
Al2O3	0.38	0.38	0.36	0.53	0.38	0.38	0.36
±	0.01	0.01	0.01	0.02	0.01	0.01	0.01
MgO	0.12	0.15	0.20	0.08	0.12	0.15	0.20
±	0.16	0.21	0.27	0.12	0.16	0.21	0.27
Na2O	12.53	12.66	12.52	12.57	12.53	12.66	12.52
±	0.10	0.10	0.10	0.10	0.10	0.10	0.10
K2O	0.00	0.02	0.03	0.01	0.00	0.02	0.03
±	0.01	0.03	0.04	0.01	0.01	0.03	0.04
TiO2	1.06	1.45	1.23	2.50	1.06	1.45	1.23
±	0.01	0.02	0.02	0.03	0.01	0.02	0.02
CaO	0.25	0.18	0.73	0.23	0.25	0.18	0.73
±	0.01	0.01	0.02	0.01	0.01	0.01	0.02
ZrO2	0.08	0.25	0.11	0.55	0.08	0.25	0.11
±	0.01	0.04	0.02	0.09	0.01	0.04	0.02
Fe2O3	32.46	31.56	31.66	30.21	32.46	31.56	31.66
±	0.09	0.09	0.09	0.08	0.09	0.09	0.09
MnO	0.25	0.46	0.46	0.66	0.25	0.46	0.46
±	0.02	0.03	0.03	0.04	0.02	0.03	0.03

ZnO	0.13	0.24	0.11	0.26	0.13	0.24	0.11
±	0.03	0.05	0.02	0.06	0.03	0.05	0.02
Total	96.64	97.68	96.93	97.38	96.64	97.68	96.93

Figure BSEI of some zircons with EMPA analyses location

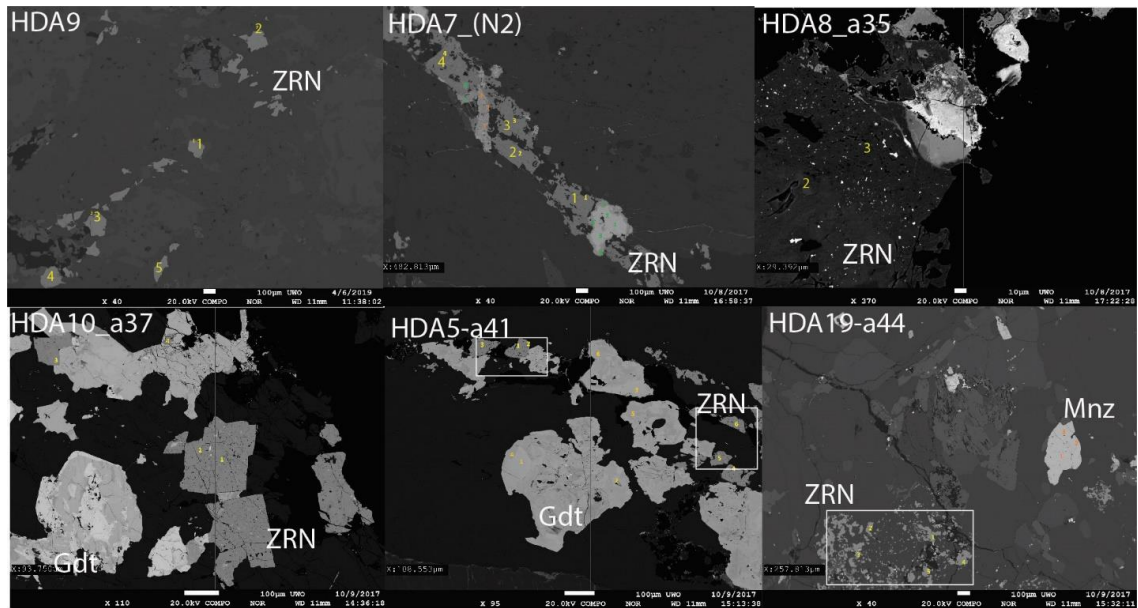
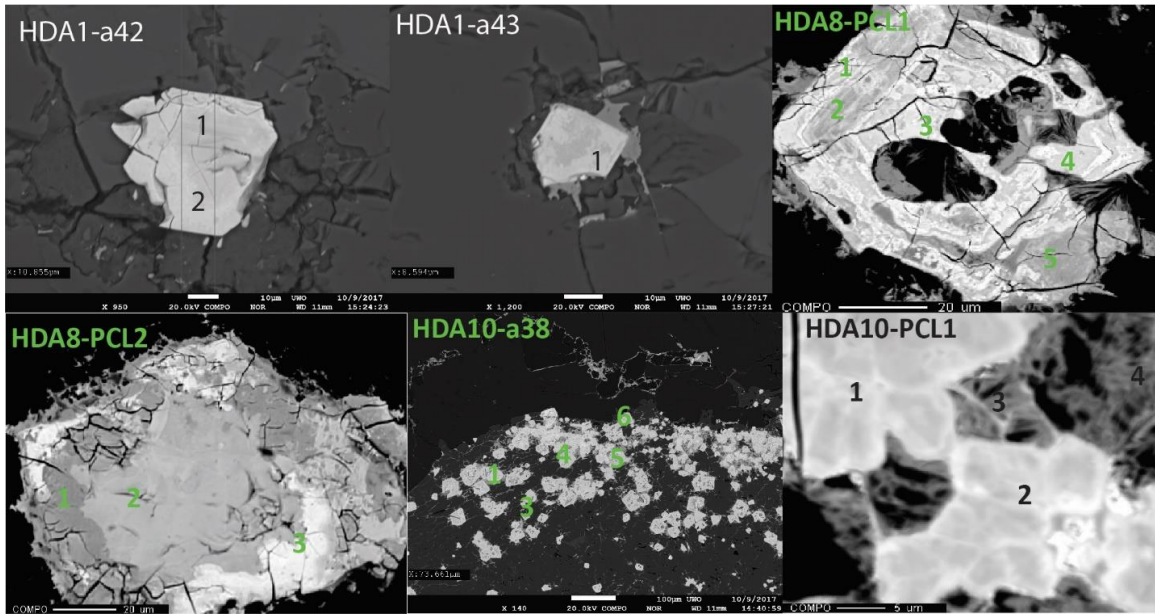
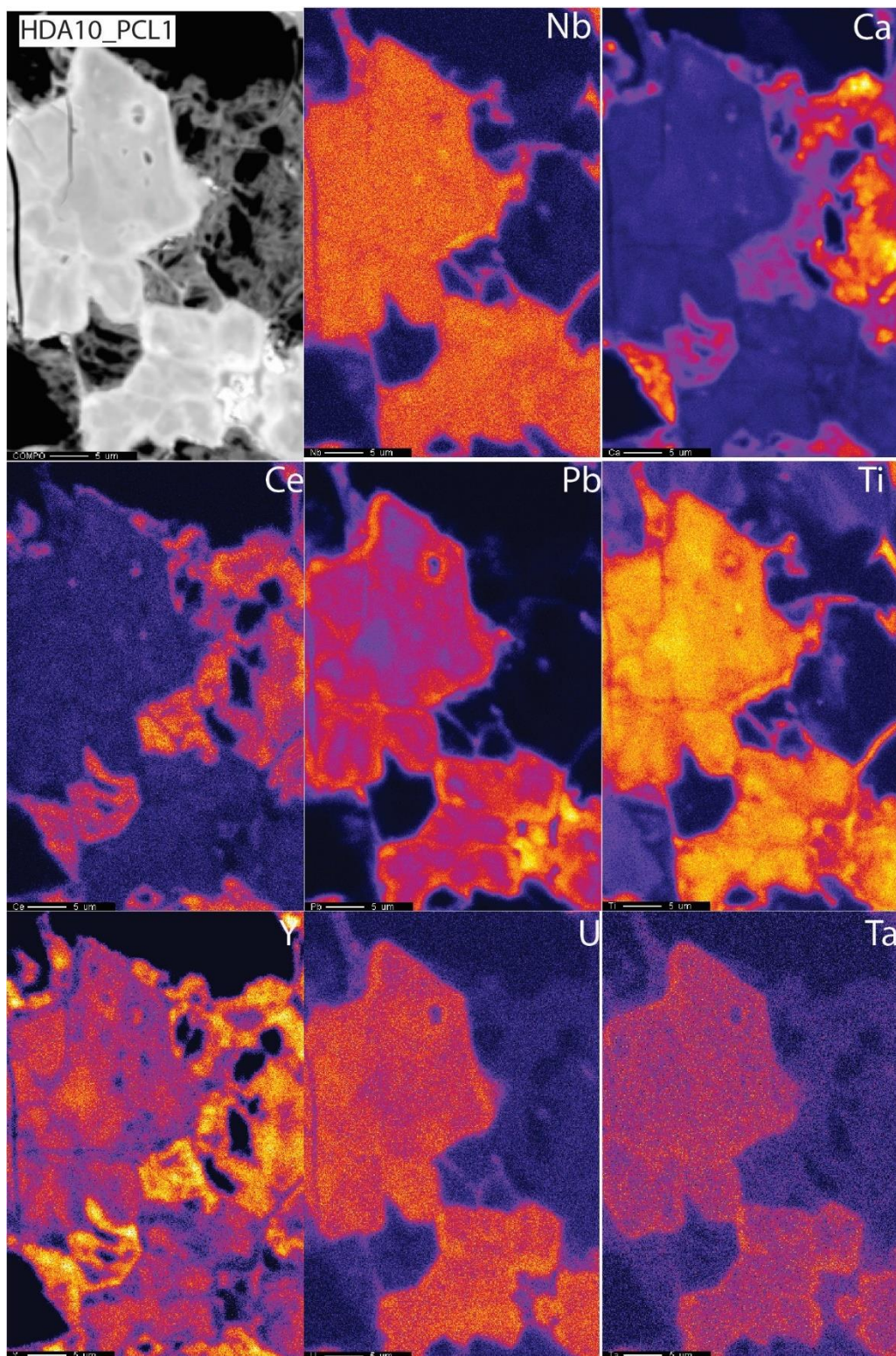
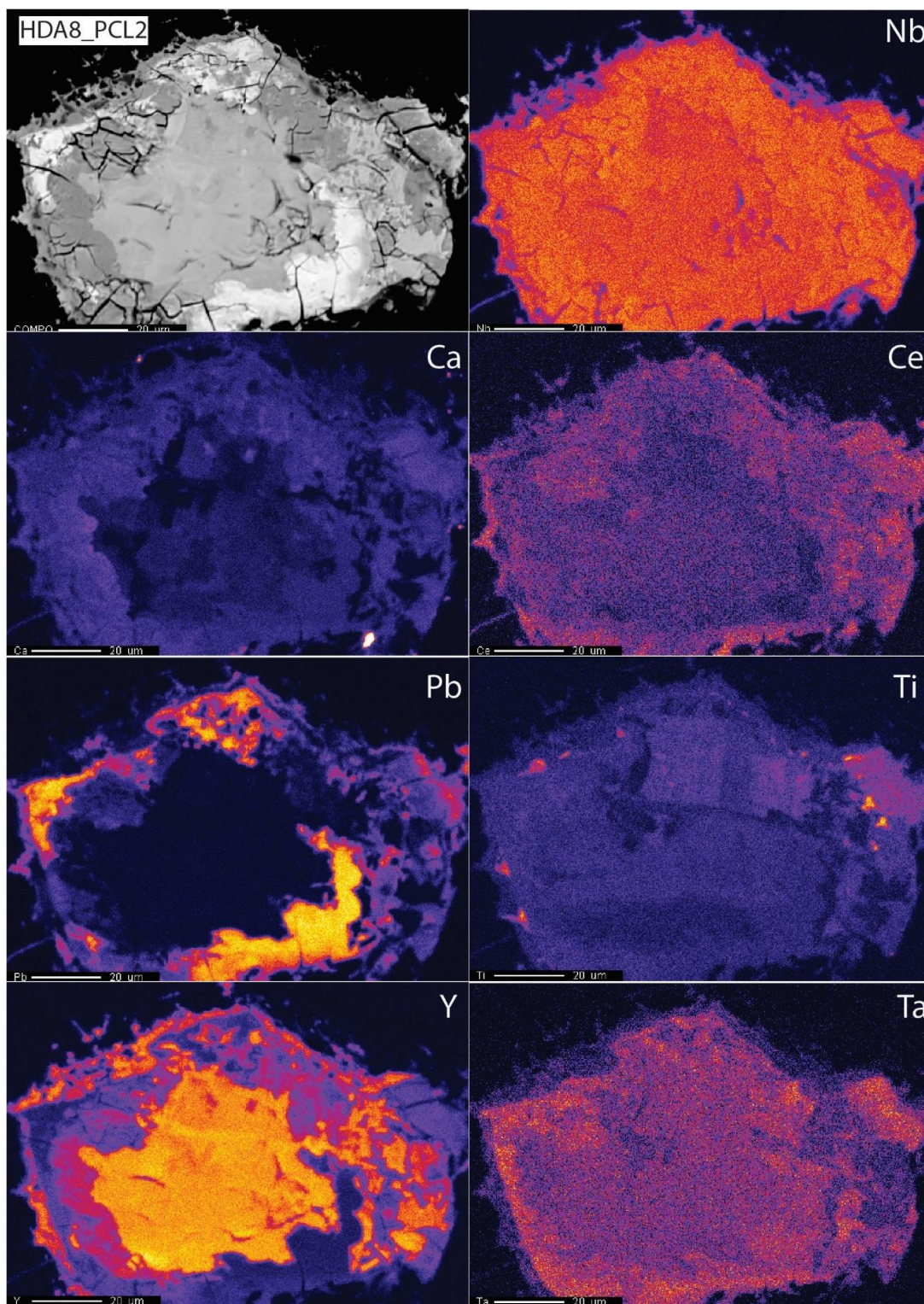


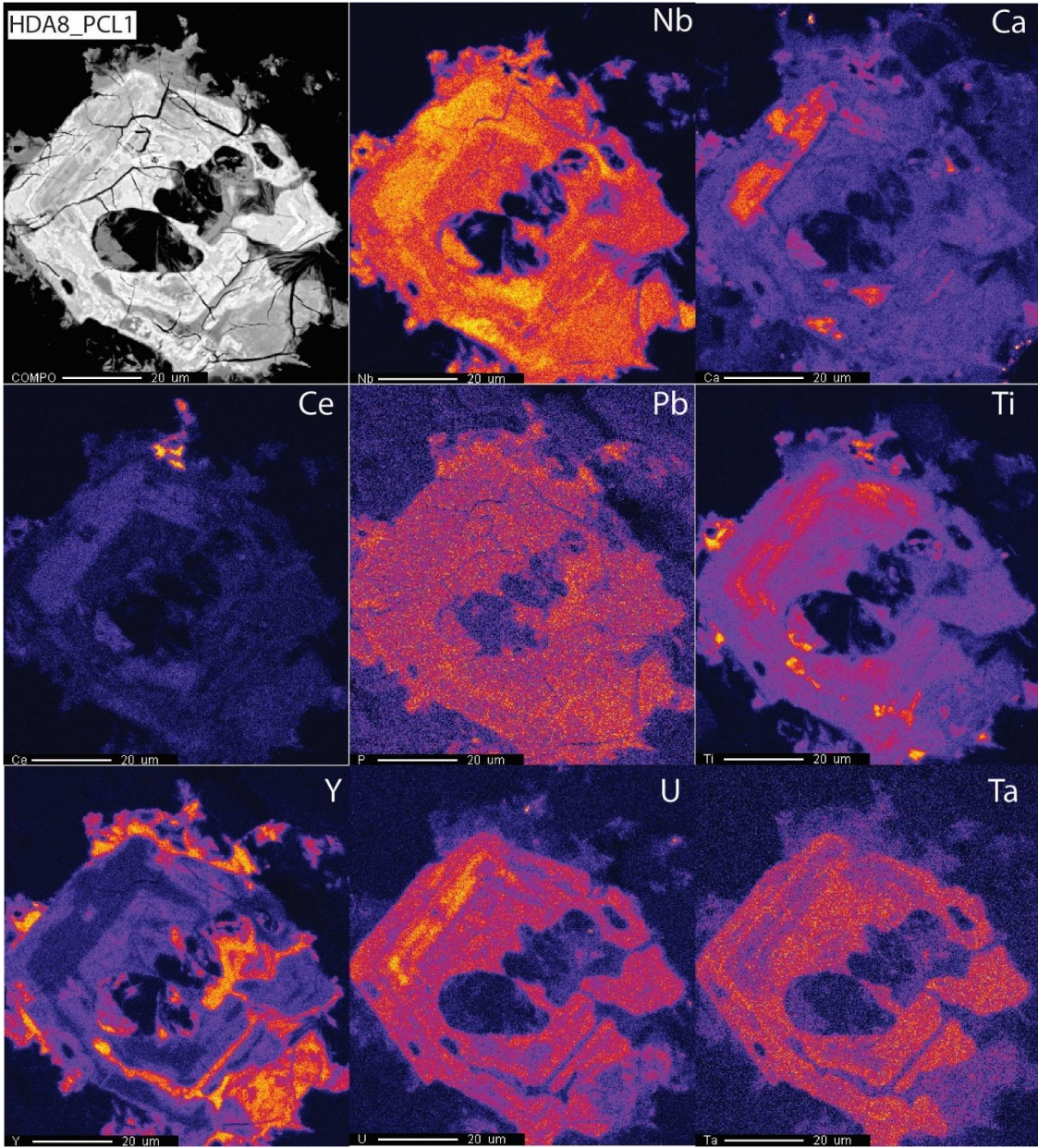
Figure BSEI of some pyrochlore with EMPA analyses location

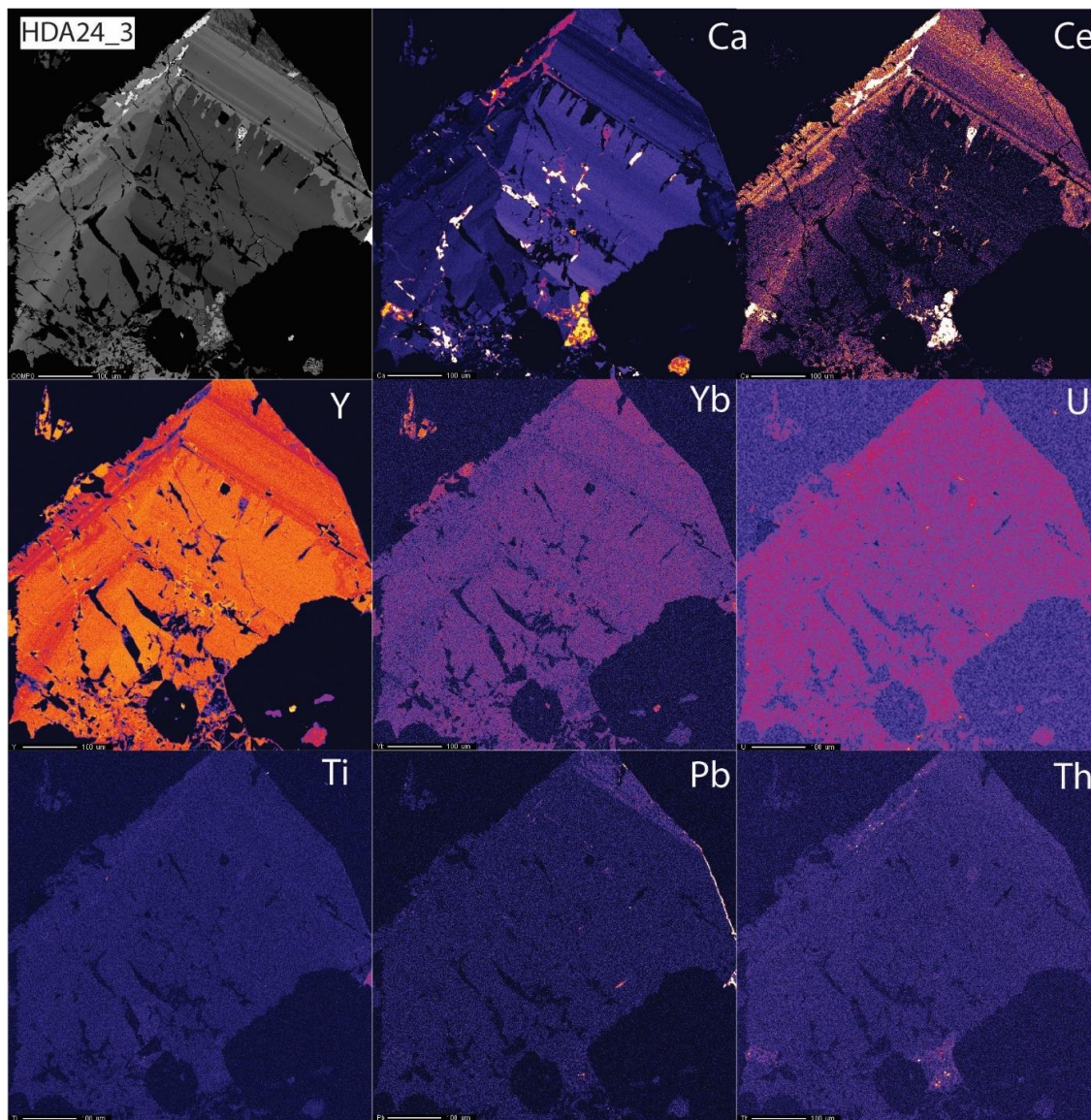


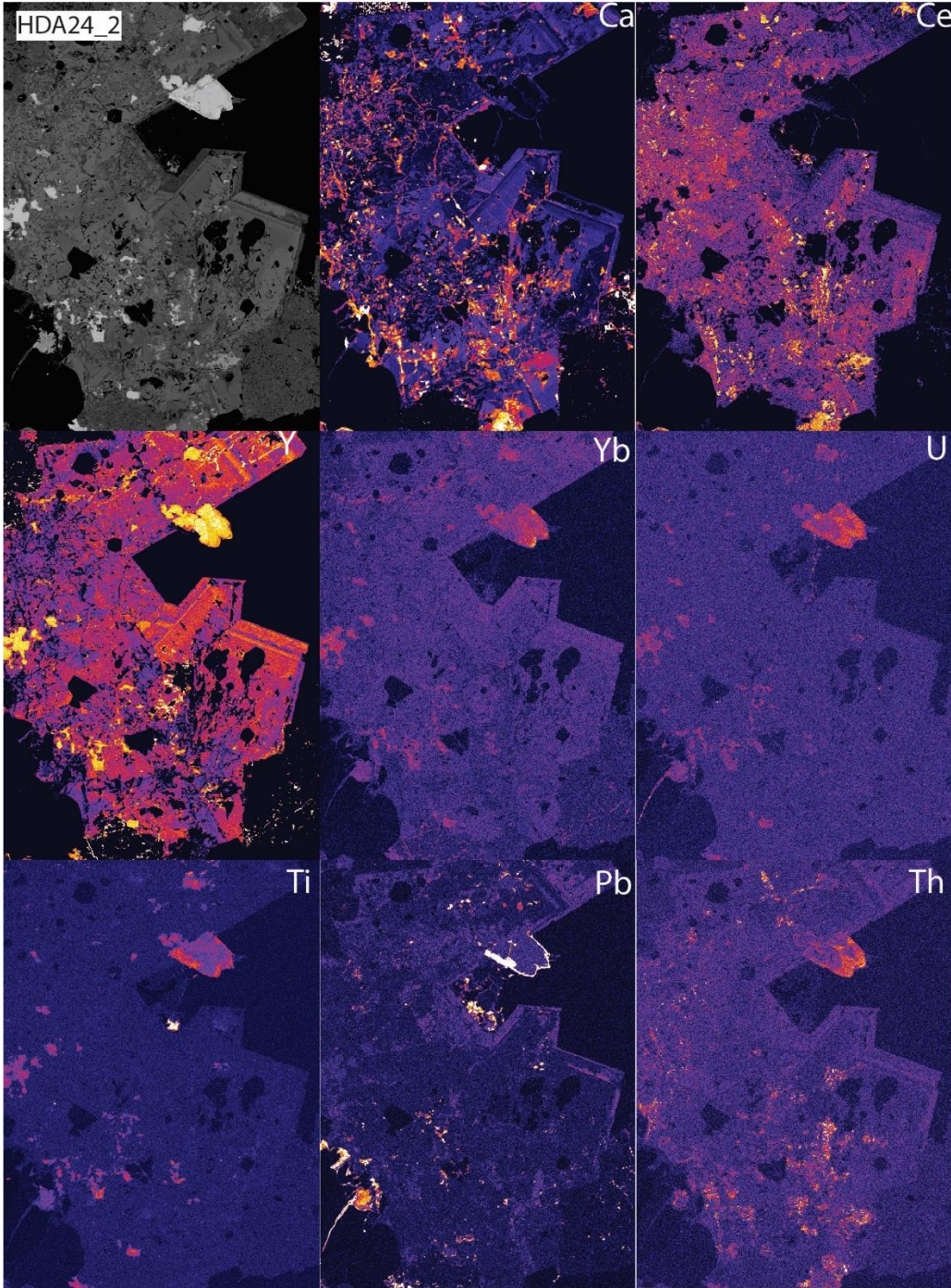
WDS maps for pyrochlore

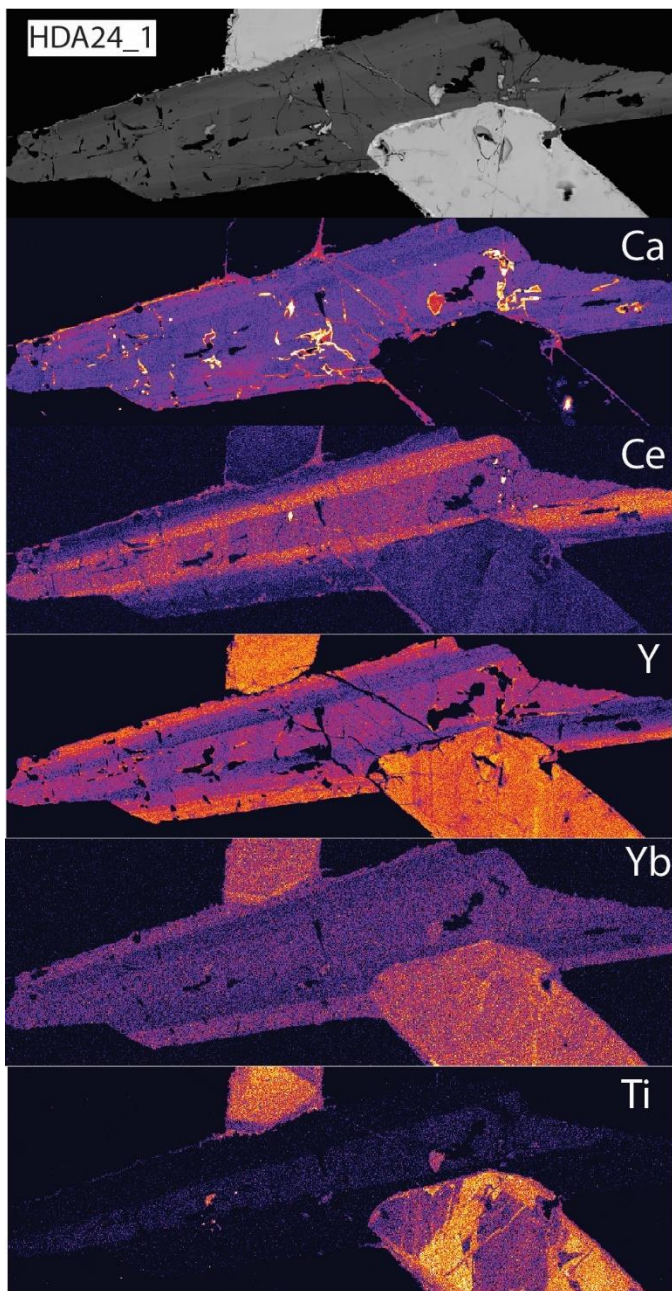


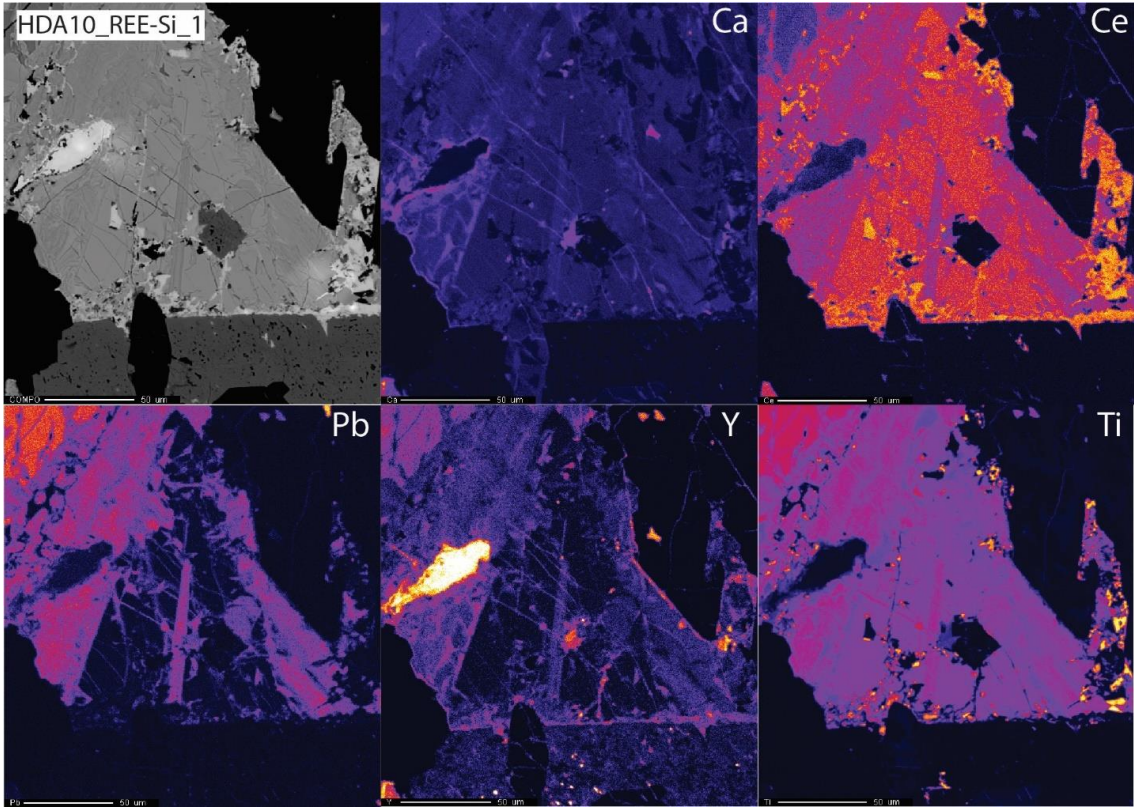




WDS maps for gadolinite







Curriculum Vitae

Name: Abdullah Ali Aseri

EDUCATION

Western University, Department of Earth Science - London, ON • Ph.D. in Geology – April 2020.

University of Waterloo, Department of Earth and Environmental Sciences - Waterloo, ON • Ph.D. in Geology – September 2012.

King Abdul Aziz University, Faculty of Earth Sciences - Jeddah, Saudi Arabia • B.Sc. in Geology – April 2007.

Work Experience

Electron Microprobe Operator, the University of Western Ontario, April – July 2017

Teaching Assistant, Optical mineralogy laboratory, King Abdul Aziz University, Saudi Arabia-2008 to 2009.

Teaching Assistant, rocks and minerals laboratory, King Abdul Aziz University, Saudi Arabia-2008 to 2009.

Gold mine geologist, Alamar gold mine, Saudi Arabia- 2007 to 2008

PUBLICATION

Aseri, A. A., Linnen, R. L., Che, X. D., Thibault, Y., & Holtz, F. (2015). Effects of fluorine on the solubilities of Nb, Ta, Zr and Hf minerals in highly fluxed water-saturated haplogranitic melts. *Ore Geology Reviews*, 64, 736-746.

Che, X. D., Linnen, R. L., Wang, R. C., Aseri, A., & Thibault, Y. (2013). Tungsten solubility in evolved granitic melts: An evaluation of magmatic wolframite. *Geochimica et Cosmochimica Acta*, 106, 84-98.